UNCLASSIFIED

THIS PAGE IS UNCLASSIFIED

AD855086

LIQUID PROPELLANT EXPLOSIVE HAZARDS

Final Report – December 1968

VOLUME 1 – TECHNICAL DOCUMENTARY REPORT

STATEMENT #2 UNCLASSIFIED

This document is subject ~~to special export~~ controls and each ~~transmittal to foreign government~~ nationals may be ~~made only with prior approval of~~

PREPARED UNDER CONTRACT AF 04 (611) 10739

FOR

AIR FORCE ROCKET PROPULSION LABORATORY

AIR FORCE SYSTEMS COMMAND

UNITED STATES AIR FORCE

EDWARDS, CALIFORNIA 93523

atter RPPRSTINFO

D D C

JUL 10 1969

C

URS SYSTEMS CORPORATION

LIQUID PROPELLANT EXPLOSIVE HAZARDS

Final Report – December 1968

VOLUME 1 - TECHNICAL DOCUMENTARY REPORT

by

A. B. Willoughby - C. Wilton

and J. Mansfield

URS Research Company
1811 Trousdale Drive
Burlingame, California 94010

This report has been reviewed and approved.

Robert L. Thomas

ROBERT L. THOMAS
Program Manager
Liquid Propellant Blast Hazards Program
Solid Rocket Division
Air Force Rocket Propulsion Laboratory

ABSTRACT

Project PYRO consisted of a comprehensive program to determine the blast and thermal characteristics of the three liquid propellant combinations in most common use in military missiles and space vehicles; liquid oxygen-RP-1 (LO_2/RP-1), liquid oxygen—liquid hydrogen (LO_2/LH_2), and nitrogen tetroxide/50% unsymmetrical dimethylhydrazine —50% hydrazine (N_2O_4/50% UDMH — 50% N_2H_4). During the course of the program some 270 tests were conducted with these propellant combinations on weight scales ranging from 200 lb to 100,000 lb. This basic explosive test program was supplemented by analytical and statistical studies, laboratory-scale experimental studies, simulation tests with inert propellant combinations and a series of high-explosive tests for calibration and evaluation purposes.

The basic test program was designed to investigate the explosive characteristics of the three propellant combinations for the most credible ways that the propellants might accidentally come into contact with each other and result in a significant explosion.

The results of the basic test program in conjunction with the analytical studies and prior information regarding liquid propellant explosive behavior were used as the basis for developing methods for predicting the blast and thermal environment that would be expected for any given missile or space vehicle system and any specified failure mode.

In the prediction method the thermal environment is given only as a function of propellant type, while the blast environment is given as a function of a number of controlling parameters. A failure mode analysis is required to select the appropriate values of the parameters needed to predict the blast environment for a specific system.

FOREWORD

This report was prepared by URS Systems Corporation, Burlingame, California, under Air Force Contract AF 04(611)-10739, which supported the NASA/USAF Liquid Propellant Blast Hazards Program (Project PYRO) conducted at the Air Force Rocket Propulsion Laboratory, Edwards Air Force Base, California. The URS support included establishing the overall design of the program; analyzing the test data; developing mathematical models relating the pertinent blast characteristics to the missile failure conditions; conducting exploratory studies; designing and constructing test articles; providing statistical, ordnance, and instrumentation consulting; and the writing of the technical reports.

The report is in three volumes: Volume 1, which is the Technical Documentary Report on the basic program; Volume 2, which contains the tabular blast, thermal and fragmentation data obtained during the program; and Volume 3, which presents prediction methods and recommendations for use of the PYRO data in predicting the explosive potential of full-scale missile failures.

ACKNOWLEDGEMENTS

The managers of Project PYRO for the URS Corporation gratefully acknowledge the contributions made to the program by representatives of the NASA, the Department of Defense, and SANDIA Corporation.

Our particular thanks are extended to the past and present members of the Steering Committee for their dedication in providing overall technical guidance to the program. These members were:

Mr. W. A. Riehl, Present Chairman, NASA, Marshall Space Flight Center, Alabama

Mr. H. C. Dyer, NASA, Marshall Space Flight Center, Alabama

Mr. John Atkins, NASA, Kennedy Space Center, Florida

Mr. L. Ullian, USAF, Patrick Air Force Base, Florida

Mr. F. D. Kite, SANDIA Corp., Albuquerque, New Mexico

Mr. R. H. Berry, SANDIA Corp., Albuquerque, New Mexico

Dr. J. B. Gayle, Past Chairman, NASA, Kennedy Space Center, Florida

Mr. P. King, Past Member, General Electric Co., Mississippi Test Facility

Our sincere thanks go to personnel at EAFB, Edwards, California, for their fine administrative and technical contributions to the project. Noted for their participation were:

Robert Thomas, Current Test Program Director	John Marshall, Past Test Program Director
Capt. Karl W. Joffs	Charles Cooke
Austin A. Dickinson	James Wanchek
Richard McQuown	

And our appreciation also to many other organizations and personnel who contributed to the project.

The authors also wish to gratefully acknowledge the technical contributions made to the program by the following URS staff members and consultants:

Mr. T. C. Goodale, Principal Chemist

Mr. J. V. Zaccor, Principal Physicist

Mr. J. Boyes, Test Engineer

Mr. Allen Saltzman, Technical Editor

Dr. S. Bessler, Statistical Consultant

CONTENTS

CONTENTS, cont.

CONTENTS, cont.

INDEX

Sections

Appendixes

ILLUSTRATIONS

ILLUSTRATIONS, cont.

ILLUSTRATIONS, cont.

ILLUSTRATIONS, cont.

ILLUSTRATIONS, cont.

ILLUSTRATIONS, cont.

ILLUSTRATIONS, cont.

TABLES

TABLES, cont.

TABLES, cont.

Section 1

INTRODUCTION AND BACKGROUND

Section 1
INTRODUCTION AND BACKGROUND

In the early 1950's there was relatively little need for accuracy in predicting the yield potential from liquid propellants used in missiles and aerospace vehicles. A conservative approach could be used to define the yield because the relatively small amounts of propellants involved did not require that total safety distances be very great. Launch vehicles contained no more than 100,000 to 300,000 lb of propellants, so that yield percentages up to 50% or greater resulted in clearance distances no greater than 2,000 to 3,000 ft. It was a common practice at that time to treat the explosive behavior of liquid propellants in the same fashion as that of standard solid high explosives. A given propellant combination was considered to have a fixed yield value and the same distribution of blast wave characteristics with distance as TNT. Thus the explosive potential could be represented by a single yield number relative to TNT.

It was recognized that this was only a crude approximation, since unlike normal high explosives, liquid propellants are not premixed and the explosive characteristics can vary widely depending on the degree of mixing, which in turn, depends on factors such as tank configuration, specific failure mode, and time of ignition. However, there was insufficient information available concerning the effect of these factor on explosive yield to provide the basis for deriving a better prediction method.

Until 1960 the quantities of propellants of interest remained relatively small, so that use of conservative and fixed yield values was not too much of a problem. Within the last few years, however, tremendous increases have occurred in vehicle propellant weights. Saturn-V contains almost 6 million lb of liquid propellants. These order-of-magnitude increases in propellant weights with their associated increases in required clearance distances no longer permit the luxury of ultraconservatism in determining propellant yields. Clearance distances for pre-launch, launch, and post-launch safety have become

critical because of their effects on other programs located nearby. Personnel
must be evacuated or given adequate protection. Launch vehicles and complexes
must be located at distances great enough to provide low hit probabilities in
case destruct action is required. All of these requirements add to costs in
time delays, required real estate, precount and countdown interference, and
facilities. These increased costs dictated the need for development of more
precise means of determining realistic and most probable yields in case of pre-
launch and launch abort.

In addition to siting and general operating criteria, the ability to pre-
dict propellant explosive characteristics is required to define hazard envel-
opes. These requirements generated the need for more detailed data concerning
the blast and thermal environments resulting from propellant explosions, e.g.,
peak overpressure, positive-phase impulse and duration, fireball temperature
and duration, and heat flux-time histories.

The strong requirement for an improved and more realistic method for pre-
dicting the environment from liquid propellant explosions and the lack of in-
formation on which to base such an improved method led the Air Force Eastern
Test Range and the NASA, who jointly had the prime concern for launching mis-
sile systems and space vehicles, to look to a new test program to better define
the problem. This resulted in Project PYRO, a combined experimental and ana-
lytical program to define the propellant blast environment for the three common
propellant combinations, liquid oxygen-RP-1, liquid oxygen — liquid hydrogen,
and nitrogen tetroxide/50% unsymmetrical dimethylhydrazine — 50% hydrazine.
The end result of the program is a method for predicting the blast and thermal
environment that would be expected for any given missile or space vehicle
for a wide range of failure modes.

This program was under the overall direction and sponsorship of the PYRO
Steering Committee, which consisted of representatives from NASA Marshall Space
Flight Center, NASA Kennedy Space Center, the Air Force Eastern Test range, and
the Sandia Corporation.

This is the final report of this program and consists of three volumes:
Volume 1, the comprehensive technical report on the basic program; Volume 2,
Test Data; and Volume 3, Prediction Methods. Volume 1 (herein) contains an in-
troduction, objectives, and general approach as the first three sections.
These are followed by the presentations of the hypergolic and cryogenic test
program, including test design, test conditions, results, and discussion of re-
sults in Sections 4 and 5, respectively. These sections also show the deriva-
tion of the methods for predicting blast yields. The results of the thermal
program, laboratory supporting programs, and a summary of the findings and con-
clusions are given in Sections 6, 7, and 8.

A glossary and appendices follow, including descriptions of the blast in-
strumentation system; the statistical procedures used in the analysis of the
blast data; and the thermal instrumentation system. The final appendix lists
a number of "ride along" R&D programs, which although not a part of Project
PYRO, used the blast and thermal environment provided by the liquid propellant
explosions, particularly on the large-scale tests, for a variety of experiments,
including structural response, ground shock measurement, cloud tracking, and
evaluation of instrumentation.

Section 2

OBJECTIVES

Section 2

OBJECTIVES

The overall objective of this program was to establish data and methods for predicting the credible damage potential which would be experienced from the accidental explosion of the liquid propellant combinations N_2O_4/50% UDMH – 50% N_2H_4, LO_2/RP-1, and LO_2/LH_2.

Based on experimentally derived data, analytical and statistical work, and laboratory studies, the end product would be a method for predicting the surface blast and thermal environment that would be expected for any given missile or space vehicle system for a wide range of failure modes.

Section 3

GENERAL APPROACH

Section 3

GENERAL APPROACH

This section of the report describes the general approach used in the selection of the test conditions for the PYRO program. It starts with a discussion of the fundamental differences expected in explosive behavior of hypergolic and cryogenic propellants and why these led to somewhat different approaches being used for the two classes of propellants. This is followed by a description of the general approach used for the hypergolic propellants. The last and major portion of this section covers in detail the rationale for the selection of the test conditions and parameter variations for the cryogenic propellant combinations.

The information available at the time the basic test design philosophy was being established indicated that hypergolic propellants tend to have significantly different explosive characteristics from cryogenic propellants. For cryogenic propellants, scaled model tests had indicated that significant explosive yields were possible for a large variety of missile and failure conditions (Refs. 3-1 to 3-6). Thus, it was clear that a comprehensive testing program would be necessary to evaluate the effect of the various important parameters of the process. It was less clear, however, that a comprehensive test program would be required for the hypergolic propellant combination since these propellants ignite on contact, and within a few milliseconds or tens of milliseconds (at ambient temperature), the reaction has proceeded far enough to produce visible flames. This spontaneous ignition behavior tends to limit the explosive potential of hypergolic propellants. In order for a propellant mixture to produce a large explosive yield, it is necessary for one of the propellants to be in a state of fine subdivision or solution and dispersed uniformly throughout the volume of the other propellant at the time of ignition. This permits the majority of the available reaction energy to be released fast enough to contribute to explosive effects. With hypergolic propellants, reaction starts on

initial contact and continues throughout the mixing process. Since the time involved in mixing the two propellant masses together to create the state of subdivision of one in the other required for explosive effects is usually long compared with the time interval required for their reaction to proceed to its completion spontaneously, it is difficult to get significant explosive effects from hypergolic propellants. Test results by other investigations (Refs. 3-7 to 3-9) tended to confirm this.

For this reason, the philosophy used for the testing of the N_2O_4/50% UDMH — 50% N_2H_4 propellant combination was to concentrate the initial testing on certain limiting conditions which tend to maximize the explosive yield. If under these conditions no significant yields were obtained, further testing with other failure conditions could be minimized.

From the foregoing it is evident that the most serious mixing conditions (with regard to explosive effects) for hypergolic propellants are those which:

1. Lead to extremely rapid mixing, or

2. Lead to confinement of the reacting products. (In this case, although the reaction itself need not be explosive, confinement of the reaction can build up pressures which can create significant blast effects if suddenly released.)

From a practical point of view, the specific failure modes which would lead to these conditions are high-velocity impact or an explosive-donor situation, which might occur if both cryogenic and hypergolic propellants are used in the same vehicle.

Accordingly, in the initial test program, the major effort was placed on these two failure modes. Two other conditions were selected for minor testing, command-destruct and confinement-by-the missile (the rapid removal of a diaphragm between the compartments containing the fuel and oxidizer). A 100-ft tower drop series was added to the program later.

This relatively simple upper limit approach was not practical for the cryogenic propellant combinations because of the anticipated large

number of conditions under which significant yields would be obtained and
the corresponding large number of potentially important variables.

The basic objective in the cryogenic test program was to test with
a limited number of generalized test configurations selected so that the
results from the tests would be generally applicable to any tankage configura-
tion and failure mode combination. The selection of the test configurations
was based on the generalized concept of the missile failure and explosive
process shown in Fig. 3-1 and described below.

Five basic variables of the initial configuration were considered of
prime concern with regard to the ultimate explosive yield. These were
the propellant type, the tank configuration, the failure mode, the launch-
pad geometry, and the ignition-source configuration. The tank configura-
tion, failure mode, and the launch-pad geometry, in turn, largely determine
the gross space – time history of the propellants, although the propellant
type may also play an important role. The gross space – time history of
the propellants, controlled by the boundary and initial conditions, determines
how the two propellants come into contact with each other and thereby
determines the explosive effects as a function of time. The time of ignition
depends on the ignition source configuration, the space time history of the
propellants and the propellant type.

The design approach used, which was termed the Generalized Propellant
Interaction Approach, was based on the assumption that although the detailed
course of propellant mixing may be too complicated to admit to detailed
analysis, propellants undergoing similar mixing conditions will lead to
mixtures having similar explosive properties. In other words, any time
two propellant masses interact or come into contact with each other in the
same fashion (and with the same constraints), it was assumed that the
explosive yield as a function of time after initial contact will be the
same. Further, it was assumed that all propellant spillage configurations
can be analyzed in terms of a few basic types of interactions, called basic
mixing modes.
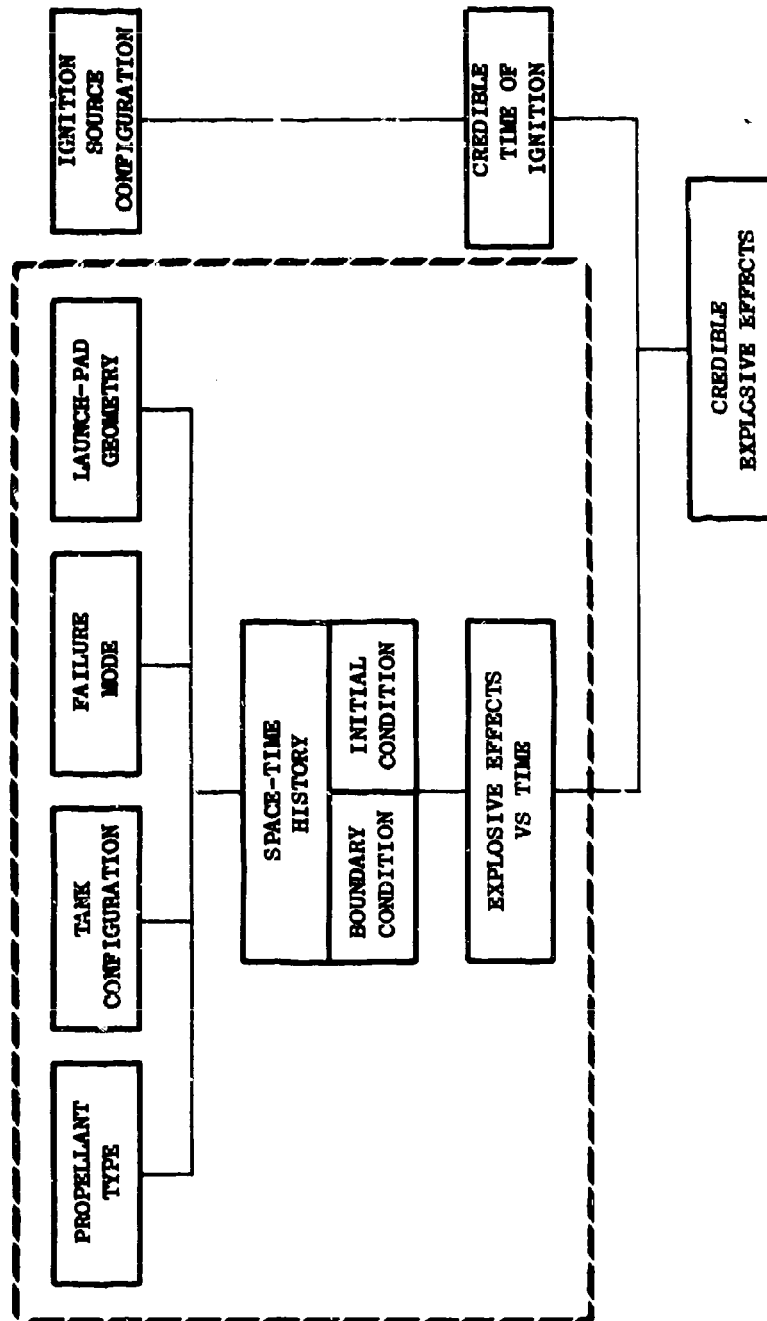
Fig. 3-1. Generalized Concept of the Missile Failure and Explosive Process

The objectives of the explosive testing were, first, to determine which parameters of potential interest in the interaction of two propellant masses have a significant influence on the explosive yield time relationship and, second, to determine the quantitative nature of the influence.

The main tasks in the overall design of the test program were to identify the parameters of potential interest, to establish the number of levels of each parameter for testing, and insofar as possible, to determine how best to scale the parameters for testing.

Since the basic mixing modes are really just convenient groupings of interaction types controlled by the same genera' parameters, it was appropriate to give general consideration to all the parameters of potential interest in the interaction of two propellant masses prior to selecting the basic mixing modes. For this, it was convenient to divide the parameters into the following general classes:

1. Specific properties of propellants

2. Initial conditions of propellants

3. Boundary conditions (nature of environment)

4. Ignition conditions

Although many of the specific properties of the propellants, such as density, viscosity, heat capacity, conductivity, boiling and freezing points, and heats of fusion and vaporization, were expected to be important in the mixing process, they were not subject to variation except in large discrete steps (that occur when propellant type changes), i.e., they were fixed once the propellant type and initial conditions were specified. Accordingly, the only parameter in Class 1 that entered directly into the test program design was the propellant type.

The initial conditions, i.e., the conditions at the time of first contact of one propellant with the other, consist of:

1. State of propellants

2. Spatial distribution of propellants

3. Velocity distribution of propellants

The <u>boundary conditions</u> consist of·

1. Spatial distribution of surfaces that control the flow of propellants during mixing

2. Characteristics of the air and surfaces through and along which the propellants fall or flow during mixing

The <u>ignition conditions</u> consist of:

1. Time of ignition (from first contact of propellants)

2. Nature of ignition source

Each class of conditions is discussed in the following, leading to the selection of the variables investigated.

INITIAL CONDITIONS

<u>State of Propellants</u>

In theory, the propellants could be in any of three states (gas, liquid, solid), or a mixture thereof. They also could be mixed with ambient gas (assumed to be air) in any proportion. In practice, however, for any given propellant, only certain states appeared reasonable. These are listed below:

1. RP-1: liquid state, negligible mixing with ambient air

2. LO_2: liquid state, negligible mixing with ambient air (Although LO_2 boils rapidly in ambient air or on contact with surfaces, primary concern is with large quantities and with massive spills, so that the fraction of LO_2 vaporized at the time of first contact is assumed negligible.)

3. LH_2: (a) liquid state, negligible mixing with ambient air, (b) gaseous state, mixed with ambient air, or (c) combination of (a) and (b)

Because of the low density of the gaseous H_2 (GH_2), it is not likely to react significantly with LO_2 but only with the gaseous oxygen of the air or that produced by vaporization of LO_2. Thus, the mixing process for GH_2, is entirely different from that for LO_2/RP-1 or LO_2/LH_2. Sufficient effort was not available during this program to conduct an investigation into GH_2/air mixture, however, some work has been done in this area by other investigators.

Spatial Distribution

With the foregoing assumptions, it would appear possible to describe the initial distribution of LO_2, LH_2, and RP-1 in terms of (1) the total weight (W), (2) the shape (with one or more variables), and (3) the position of the mass (with one or more variables). There were innumerable ways of characterizing shape; however, considering the generalized nature of the basic approach, it appeared adequate to use a single variable, L/D, which specifies the ratio of the average height (or length), L, of the propellant mass to a characteristic dimension, D, of a cross section normal to the height. In essence, this was equivalent to approximating all shapes by cylinders. Because gravitational potential varies with height, greater emphasis was given to it than to the other dimensions.

Since the initial conditions are defined as those which exist when the propellant massses first contact each other, and since the shape and weight are already specified, the only position variable necessary is orientation, i.e., which propellant is on top. This assumes that primary concern is with initial interfaces that are horizontal and, furthermore, that the cylinders are concentric. Considering initial vertical interfaces to be of secondary importance does not seem unreasonable, because it was unlikely that they could be very large and they would very likely be unstable (not persisting very long).[*] The justification for assuming concentricity is that this was a credible condition which tended to maximize mixing.

---

[*] This point is discussed in more detail later.

Velocity Distribution

Although it is possible to conceive of a wide variety of velocity
distributions at the time of initial contact, when consideration is given
to the mechanisms by which the propellant masses achieve their velocity
(primarily, gravitational or pressure forces), it did not seem unreason-
able to assume that the entire mass of one propellant will have the same
net translational velocity and that the rotational velocity will be small
compared to it.

BOUNDARY CONDITIONS

Space Distribution of Rigid Surfaces

The major types of rigid surfaces in the vicinity of launch sites that
can modify the flow of propellants during the mixing process are:

1. The vehicle itself

2. The basic launch-site geometry

3. Miscellaneous close-in launch facilities and structures, such as
   service towers, cribs, and flame deflectors.

In general, the sizes of surfaces in Item 3 tend to be much smaller
than those in 1 or 2, so that their effects were not included in the basic
program. Obviously, there are some exceptions. Perhaps most important
is the silo case, where the crib, platforms, and miscellaneous equipment
may significantly modify the flow. It is believed that these surfaces
were of too special a nature to be included as a generalized boundary
condition and that estimation of the blast effects from these special
cases would have to be made by considering various portions of the flow
separately (so that it would be possible to use a generalized boundary
condition for each), and combining results to get the overall effect.

The vehicle itself would affect the flow of fluid during the mixing
process in various ways, perhaps the most important of which occurs when,

due to internal failure, mixing starts inside the tank walls. Once the
propellants are outside the vehicle tankage, its role would tend to be
secondary, compared with the ground surface, in modifying the flow.[*]

For a flat-pad geometry, the ground surface is expected to be generally
flat or, at most, have small curvature since it is unlikely to have large
slopes over large areas.

Accordingly, we can conceive of two basic types of boundary conditions
w''ich depend on the extent of the rigid walls:

1. Confinement by the missile

2. Confinement by the ground surface

Actually, however, within the framework described above, there are two
other cases which were not included in the basic program. These are confine-
ment by the ground surface and vertical walls and no confinement, i.e.,
where mixing occurs in the absence of any confining surface.

The confinement-by-the-ground-surface-and-vertical-wall case, which
would most typically be the silo geometry was originally planned to be
included in the program but with less emphasis than the other cases. However,
as the program proceeded and the full extent of the testing needed for the
other cases became evident this case was essentially eliminated from the
program because it was of much less practical interest than the others.
The LO_2/RP-1 propellant combination in a silo geometry had been studied for
propellant weights up to 200-lb in previous URS programs (Refs. 3-3 and 3-5).
Information from these programs combined with the few tests with the LO_2/LH_2
propellant combination which were left in this program would provide at
least a minimum data base for this geometry.

---

[*]   How the vehicle fails is very important in determining the space — time
      history of the propellants; however, these effects were considered under
      initial rather than boundary conditions.

The no-confinement case was not included because of the very small
explosive yields anticipated for this condition. Unless there is a large
velocity difference between the two propellants (which is unlikely when
both are in free air), there are no significant forces holding the two
masses together. Thus, even a small pressure generated by vaporization
of a small amount of one of the propellants at the boundary between the
two masses would be sufficient to separate them and minimize mixing.
Confirmation of this concept has been obtained by experimental testing
of propellant quantities up to 250 lb (Ref. 3-4).

SUMMARY OF PARAMETERS

A summary of important parameters is presented in Table 3-1. Examina-
tion of this list suggests that the basic mixing modes are identified primarily
by the boundary conditions, although within each of the latter further
subdivision was necessary, particularly with regard to flow direction.
Using a breakdown by boundary conditions, it was possible to determine
which initial-condition parameters, and ranges in value, were appropriate
for each.

BASIC MIXING MODES

Confinement by the Missile

In this case an internal failure is assumed to occur, and one propellant
falls down into the other. This failure condition could occur in either
the static test stand, launch, or in-flight mode. Cause of failure could
be bulkhead rupture from overpressurization of a propellant compartment,
engine blowup sending fragments through the bulkheads, etc. The position
and velocity distributions of the lower propellant at the moment of first
contact are fairly well specified, since it is assumed to be in its original
configuration and to have zero velocity. Those of the upper propellant,
however, may have a large range of values, depending on how full the tanks
are and how large an opening is created between them. If a relatively
small opening is produced, the L/D ratio of the top propellant will be

Table 3-1

SUMMARY OF PARAMETERS

Propellant Properties

    P.T.   (propellant type)

Initial Conditions

    W   (weight)

    L/D   (length-to-diameter ratio)

    P.O. (propellant orientation)

    V_H (velocity, horizontal)

    V_V (velocity, vertical)

Boundary Conditions

    Confinement by the missile (CBM)

    Confinement by the ground surface (CBGS)

Ignition Conditions

    T   (time)

    I.T. (type)

---

effectively very much greater than that of the bottom one, and its total
weight (entering into the mixing at an early enough stage to be a matter
of concern) will be much smaller than that for the bottom one. In addition,
the top propellant will have an initial velocity given by the fluid head
in the top tank and the pressure differential between the two tanks. As
the opening between the tanks becomes larger, the L/D ratio and effective
weight of the upper propellant more nearly approaches the values they
originally had in the missile. In addition, at the time the opening between
the tanks is the full cross section of the original tank, the velocity
would reach the value given by the acceleration of gravity through the
distance of the ullage space in the lower tank, provided there was no
pressure difference between the two tanks.

In the case where the opening between the tanks is significantly less
that the full cross section of the vehicle, the different initial L/D
values for each propellant can be treated by assuming that the L/D ratio
refers to the over-all vehicle geometry and by defining a D_o/D_t ratio,
where D_o is the opening diameter and D_t the vehicle diameter. A sketch
of the CBM test configuration is presented in Fig. 3-2.

Duration of the confinement by the missile case is limited to the time
that the propellants remain confined by the walls of the vehicle. This time
is determined by the strength of the tankage, the rate of vaporization of
the cryogenic materials, the initial pressure in the tanks, and the initial
ullage space.

The parameters considered to be of primary interest for this case and
the initial ranges in values were as follows:

- **Propellant type**: two cases: $LO_2/RP-1$ and LO_2/LH_2

- **Propellant weight**: three values: 200-lb, 1,000-lb and 25,000-lb

- **L/D ratio**: two values: 5 and 1.8 (selected to span the range of
  credible missile geometries)

- **D_o/D_t ratio**: two values: 1 and 0.45

- **Time of ignition**: minimum of three values

- **Type of ignition**: two cases: detonator and squib
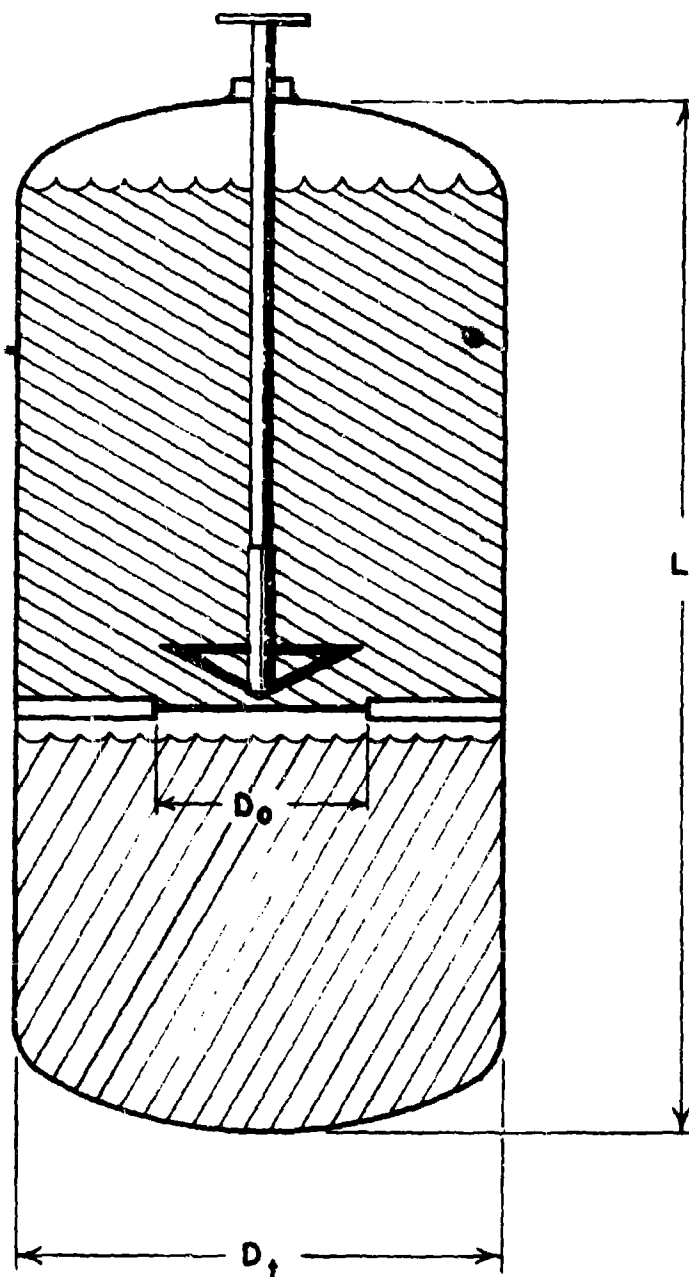
Fig. 3-2.   Confinement-by-the-Missile Test Configuration

Confinement by the Ground Surface

A relatively large range in initial conditions was appropriate for
this boundary condition because of the large variety of credible failure
modes. For example, this condition could occur in static test stand
operations from overpressurizing the tanks, where the tank could be split
open, and the propellants pour out on the test stand or ground surface.
It could also occur at the launch pad both by the overpressurization of
tanks described above or by the fallback or topple-over of the entire missile.
Probably the most severe failure mode under this category would be fallback
from a high altutude or powered flight impact at a high velocity. Certain
of the parameters selected for study were quite similar to those for the
previous case, although specific values were not identical. These include:
the propellant type, weight, and orientation and the time of ignition.

The major problem for this case was in establishing the appropriate
L/D and velocity conditions. This was complicated because, theoretically,
each of the two propellant masses may have a different L/D and magnitude
and direction of flow. Thus, there really were six parameters, and if each
were permitted to take on two values, 64 different combinations would be
obtained. Fortunately, certain of these combinations seemed so unlikely
they could be neglected. Considering first each parameter separately,
the following conclusions were reached:

- The reasonable L/D conditions were that both propellant masses
  may have high or low ratios or that the bottom propellant mass
  may have a low and the top one a high ratio. The converse of the
  latter condition was not assumed reasonable.

- The reasonable flow direction conditions were for both propellants
  to be moving either vertically or horizontally or for the top
  propellant to be moving vertically and the bottom propellant
  horizontally. The converse of the latter conditions was not assumed
  reasonable.

- The reasonable flow magnitude conditions were for both propellants
  to have either high or low velocity or for the top propellant to
  have a high and the bottom propellant to have low velocity. The
  converse of the latter condition was not assumed reasonable.

3-14

Considering next the interaction between parameters, divided into the three flow direction cases, the following conclusions were reached:

When both propellants were vertical:

Although all three flow-magnitude cases were credible, it is unlikely that the velocity of the top propellant would exceed that of the bottom by more than a factor of about two, so that it seemed reasonable to drop the case where the propellants had differing velocities.

Although all three L/D cases were possible, the credible ratios were all likely to be equal to or greater than typical missile values and the differences in ratios between the two propellants did not seem likely to be large. It appeared reasonable, therefore, to drop the case where the propellants had differing L/D ratios.

When both propellants were horizontal:

Only the relative velocity between propellants seemed important, so that two cases should suffice: the top propellant with a velocity high or low relative to the bottom propellant.

All three L/D cases are credible, except that it seemed possible to cover the cases of interest with only two values of L/D, since it is likely that all L/D ratios will be much less than typical missile values.

For both propellants flowing horizontally, the earlier assumptions that the initial interface between the two propellants was horizontal and that the propellant masses have concentric axes actually did not appear to correspond very closely to real situations. The most likely way to have both propellant masses flowing horizontally at the time of the first contact was for them to impact the ground separately and to flow into one another. This results in nonconcentric propellant masses, and at the moment of first contact, the interface was likely to be primarily vertical. However, this initial interface area would be quite small and because of density differences, it was anticipated that as the pools overlap, the interface would be primarily horizontal.

In spite of these differences, however, it was believed that the major features of this case were adequately simulated by the original assumptions of only horizontal interfaces and of concentric masses.

By using concentric masses, radial symmetry could be preserved, which simplified determination of the gross overlap area as a function of time and which, perhaps even more important, simplified interpretation of the resulting explosive phenomena.

In summary, the parameters considered of primary interest for the "confinement-by-the-ground-surface" case, and the initial ranges in values were as follows:

Basic Program: Vertical Flow Direction Case

Propellant type: two cases: LO_2/RP-1 and LO_2/LH_2

Propellant weight: 200, 1,000 and 25,000 lb

L/D ratio: two values 5 and 1.8 (selected to span the range of credible missile geometries)

Propellant orientation: two cases

Velocity: four values (~15, ~44, ~100, ~600 ft/sec)

Time of ignition: three values

Basic Program: Horizontal Direction Case

Propellant type: two cases: LO_2/RP-1 and LO_2/LH_2

Propellant weight: 200 lb

L/D ratio: two values (top propellant fixed at a typical in-tank value, bottom propellant variable)

Propellant orientation: one case: LO_2/RP-1, LH_2/LO_2

Velocity: two values (bottom propellant as near zero as practical, top propellant variable)

Time of ignition: three values

TEST PROGRAM MODIFICATIONS

Continually throughout the test program minor modifications were made to the outlined test series and a number of additional tests were added to investigate

in more detail those parameters showing a large effect on explosive yield. Type of ignition, for example, was dropped as a significant parameter early in the testing because it did not have a significant effect on yield, while much greater emphasis had to be given to time of ignition to properly evaluate its effect on yield. The full scope of the test program as actually conducted is described in Sections 4 and 5.

Section 3

REFERENCES

3-1   Condit, R. I., Explosive Potential of "ATLAS" Propellants (U),
        Final Report, BRC-57-6A1, Broadview Research Corporation, Burlingame,
        California, June 1957 (C)

3-2   Willoughby, A. B., J. V. Zaccor, J. Mills, J. Boyes, W. Nieth,
        An Investigation of the Integrity of Certain Test Assemblies Under
        Missile Failure Forces-Explosive Shock, Temperature, and Oxidation
        Test Program (U), Final Report, RD-58-2.1035-9, Broadview Research
        Corporation, Burlingame, California, July 1958 (C)

3-3   Broadview Research Corporation, 1/18 Scale Model Missile
        Tests, Phase IV, Frangible Silo Tests, Report No. RD-58-2.1039-10,
        Burlingame, California, Oct 1958

3-4   Broadview Research Corporation, 1/18 and 1/10 Scale Model Missile
        Tests, Phase V, Flat Pad Tests, Report No. RD-58-3.1039-11, Burlingame,
        California, Nov 1958

3-5   Willoughby, A. B., C. Wilton, and T. C. Goodale, A study of Atlas
        Missile Failure in Silos (U), Final Report, BRC 174-2, Broadview
        Research Corporation, Burlingame, California, Oct 1961 (C)

3-6   Arthur D. Little, Inc., Summary Report on a Study of the Blast Effect
        of the Saturn Vehicle, Report No. C-63850, Cambridge, Massachusetts,
        Feb 1962

3-7   Pesante, R. E., R. D. Erickson, D. G. Frutchery, and W. J. Helm,
        Blast and Fireball Comparison of Cryogenic and Hypergolic Propellants
        with Simulated Tankage, Report No. 0822-01(02)FP, Aerojet-General
        Corporation for NASA, June 1964

3-8   Martin Marietta Corporation, Titan II - Dyna-Soar Destruct Test
        and Analysis Report, ER 12269, March 1962

3-9   Rocketdyne, Research on Hazard Classification of New Liquid Rocket
        Propellants, Vols. I and II, for Rocket Test Annex, Space Systems
        Division, AF/SSD-TR-61-40, Oct 1961

Section 4

HYPERGOLIC PROPELLANT PROGRAM

Section 4
HYPERGOLIC PROPELLANT PROGRAM

This section of the report summarizes the existing information concerning the explosive potential of the hypergolic propellant combination nitrogen tetroxide/50% unsymmetrical dimethylhydrazine - 50% hydrazine (N_2O_4/50% UDMH - 50% N_2H_4). The summary is divided into three parts. Part 1 describes the tests conducted under the PYRO Program, Part 2 presents the information available from other sources, and Part 3 contains a summary of all the data and the conclusions.

Part 1 - PYRO TEST PROGRAM

The rationale behind the test design of the PYRO Hypergolic Test Program was presented in Section 3, the discussion of the general approach. One of the important points made in this discussion was that since it should be relatively difficult to obtain significant yields with hypergolic propellants because they ignite on contact, the major effort during the test program would be concentrated on the more severe mixing conditions.

From a practical point of view, the specific failure modes which could lead to these conditions are high-velocity impact, resulting from either powered impact or fallback from a high altitude, or an explosive-donor situation which might occur if both cryogenic and hypergolic propellants are used in the same vehicle.

Accordingly, in the initial test program, the major effort was placed on these two failure modes. Three other conditions were selected for minor testing: command-destruct in which the two propellant compartments were opened by explosive shaped charges; confinement-by-the-missile (the rapid removal of a diaphragm between the compartments containing the fuel and oxidizer); and tower drop, which simulated low-altitude fallback or seam rip.

HIGH-VELOCITY IMPACT TESTS

The high-velocity impact test series consisted of 15 tests in which 200- and 1000-lb quantities of the hypergolic propellant combination were propelled down a sled track at speeds ranging from 340 to 580 fps and allowed to impact on various target configurations.

The test parameters which were considered important for the high-velocity impact test condition were:

- Orientation of propellant tanks with respect to the impacted surface

- Velocity of impact

- Strength of propellant tanks

- Strength of impacted surface

- Geometry of impacted surface

Although there are innumerable tankage configurations that can be visualized for future hypergolic military and space vehicles, it was felt that the main features of the impact process could be studied using the conventional tankage configuration for existing vehicles, i.e., two cylin-drical tanks, one above the other, with the resultant length greater than the diameter. With this tankage configuration, two impacting geometries were of concern: impact on a surface normal to the cylindrical axis (nose-on impact) and impact on a surface parallel with the cylindrical axis (side-on impact).

Information furnished by AFRPL staff members indicated that a reasonable upper limit for nose-on impact of a missile (either from a high-altitude fallback or from turn-around and power impact) is about 500 to 600 fps. A value of 330 fps was selected as an upper limit for side-on impact.

The strength of the tank walls could influence the impact process under some circumstances. However, at the upper end of the impact velocity ranges of interest, pressures generated in the fluids by the impact significantly exceed the design pressure of the tanks. For this reason, tankage strengths were not considered as a significant parameter in the program.

The strength of the impacted surface could influence the impact process in two ways. For an ideal rigid surface, maximum pressures would be developed in the fluids at the moment of impact, which would lead to maximum initial velocities of the fluids after tank failure. For softer surfaces, the tank will be decelerated more slowly, and lower pressures will be generated in the impact process. However, some cratering of the surface would be expected, which could lead to confinement of the propellants after tank rupture. Since confinement and also high mixing velocity should tend to increase explosive effects, both of the above situations were of interest. For the soft-surface-cratering condition, it was necessary to decide on the type or types of surfaces to use or simulate. (In order to avoid simulation of the strength characteristics of real vehicles, it seemed easier to impact on a rigid surface with a preformed crater rather than attempting to actually create the crater during the impact process.) In a true fluid-fluid impact case with a roughly spherical impactor, a hemispherical crater is formed. Although few data are available regarding fluid-fluid impact for the case of impactors significantly longer than their diameters, it was anticipated that this would lead to deeper craters. Accordingly, for nose-on impact, two craters were used, a shallow crater, roughly hemispherical (depth equal to radius), and a deep crater with a depth three times the radius.

The initial geometry of the impacted surface is perhaps the most difficult of all the parameters to generalize. Simple depressions would act in a manner similar to craters, whose effects have already been discussed. Of perhaps more importance are sharp protuberances from the surface, which might increase the breakup of large fluid masses on impact, particularly those protuberances which might tend to force the propellants together. Accordingly, the geometry selected for the shallow crater, nose-

on impact test consisted of a hemispherical depression with a cylindrical
rod protruding from the center, the rod diameter being equal to one-third
the tank diameter and the crater diameter equal to twice the tank diameter.
For side-on impact, a flat surface with two parallel walls protruding from
the surface was selected. The parallel walls were normal to the tank axes
and approximately at the midpoints of the two tanks. This ensured that
at least half of each propellant mass was directed into the spa between
the walls.

Hardware and Test Design

The tanks required for this test condition were designed to be used
on the K-2 sled track located at the Naval Weapons Center, (formerly the
Naval Ordnance Test Station) China Lake, California. They were propelled
down this track by solid-motor propulsion units at speeds ranging from
340 to 580 fps and allowed to impact the various target configurations.

The criteria for the design of these tanks were determined by: (1)
the requirements to approximately simulate conventional vehicles with
regard to shape; (2) the desi ability of using minimum weight, strength,
and length-to-diameter ratios consistent with present and expected usage;
(3) compliance with the following operations restrictions imposed by the
Naval Weapons Center:

- Tanks should be capable of withstanding a 30-g load in
  any direction

- Tanks must be tested to 20 psi in either compartment
  with the other vented to the atmosphere.

Sketches of the aluminum tanks, designed to meet these require-
ments are presented in Figs. 4-1, 4-2, and 4-3. The tanks were designed,
in general, in accordance with the ASME code procedures outlined in Ref.
4-1, except that a working stress of 8,000 to 9,000 psi, instead of 6,000
psi, was utilized because of the nature of the vessel use. The tanks were
cylindrical with 2:1 ellipsoidal domed ends. The domed ends and the side
walls were 1/8 in. thick.
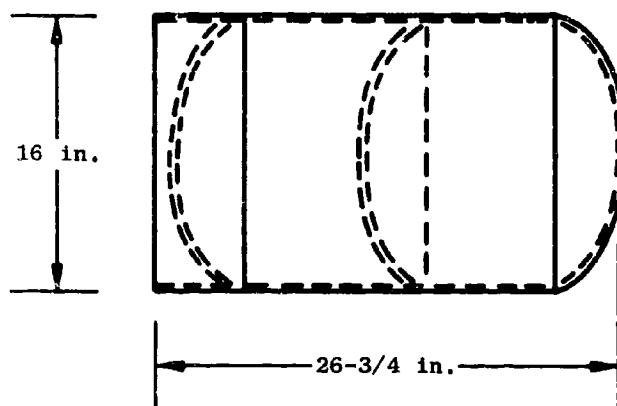
Fig. 4-1. Nose-on 200-lb, High-Velocity Impact Tank
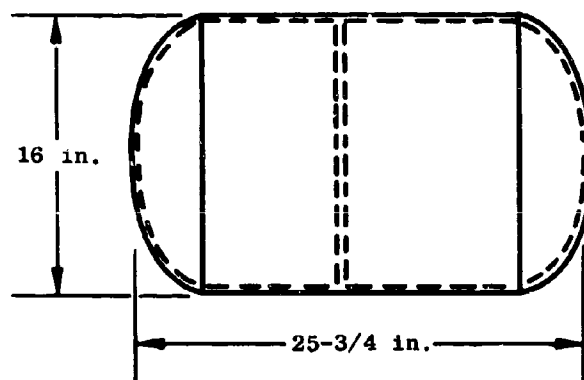
Fig. 4-2. Side-on, 200-lb, High-Velocity Impact Tank

4-5

26-1/4 in.

49 in.
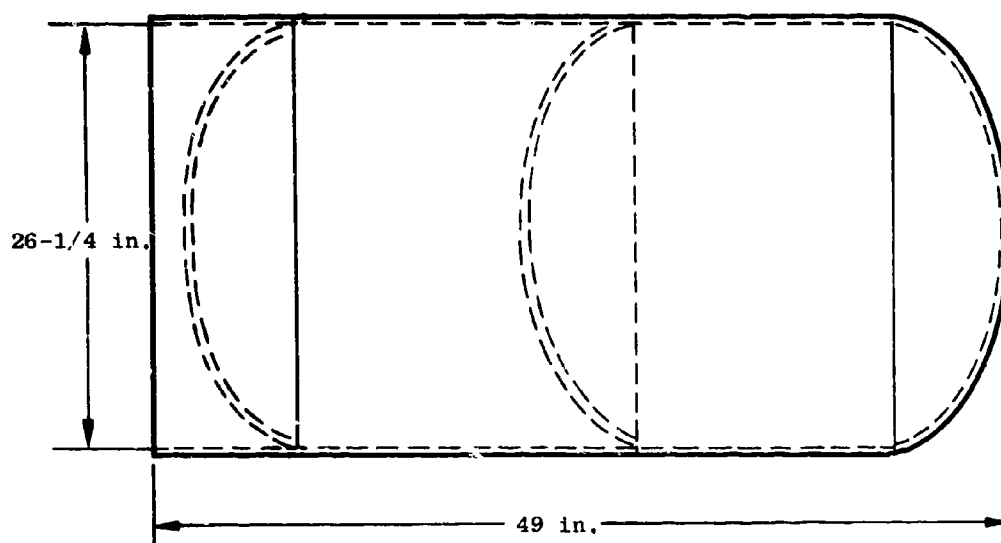
Fig. 4-3.   Nose-on, 1000-lb, High-Velocity Impact Tank

URS 652-35

The diaphragm design was of special interest. For the nose-on impact
tests, the critical design load condition for the diaphragm of the 16-in.
tank was 20 psi, imposed by both the static proof-test load and the 30-g
acceleration, and for the 26-in. tank, 37 psi, imposed by the 20-g accel-
eration. The required thickness of an elastic flat plate for these conditions
was approximately 3/16 in. and 9/16 in. for the 16- and 26-in.-diameter
tanks, respectively. This was considered unrealistic for the nose-on
impact configuration, since diaphragms of these thicknesses might be expected
to inhibit hypergolic impact mixing. Therefore, it was decided to utilize
an ellipsoidal diaphragm which permitted the use of the more realistic
material thicknesses of 1/16 in. for the 16- and 3/32 in. for the 26-in.
tanks. For the side-on impact test tank, it was decided to use the flat-
plate diaphragm. In this configuration, it would serve as a tank stiffener
and yet have negligible effect on fuel mixing at impact.

Four different target geometries were used: flat-wall, shallow-hole,
deep-hole, and parallel-wall. For the flat-wall target, a massive concrete
block was faced with a 1-in.-thick steel plate, 8 ft high, and 16 ft wide,
with a 12-in. splash shield around the edge. For the shallow-hole and
deep-hole test targets, the base was faced with concrete blocks 6 ft in cross
section and having cylindrical cavities. For the parallel-wall target, the
massive concrete base was faced with a steel plate from which two vertically
oriented walls protruded perpendicular to the plate. A diagonal brace
was placed between the vertical walls at the planned impact point of the
tank and a splash shield placed across the top of the vertical walls.
Sketches and photos of these target geometries are shown in Figs. 4-4 through
4-8.

In addition to the propellant tests, a series of high-explosive
calibration tests were conducted. The purpose of these tests was to obtain
suitable reference curves using the same basic geometry and height of burst
as in the propellant impact tests.

Fig. 4-4. Flat-Wall Target

32" DIA

6" DIA
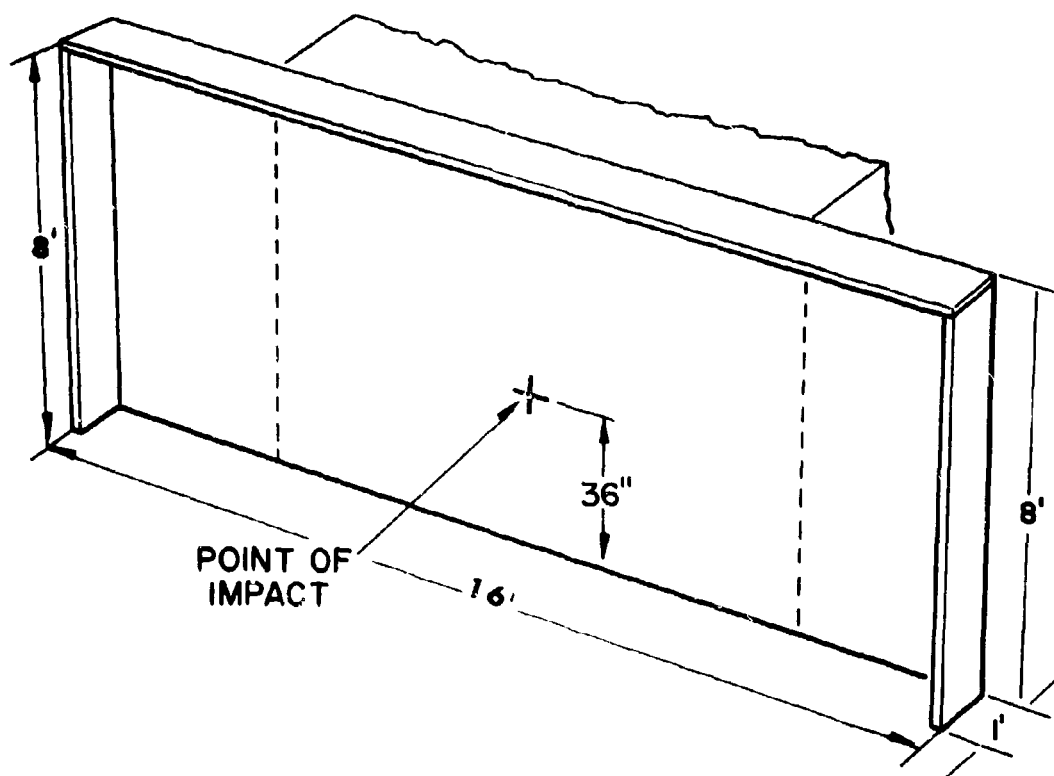
POINT OF
IMPACT
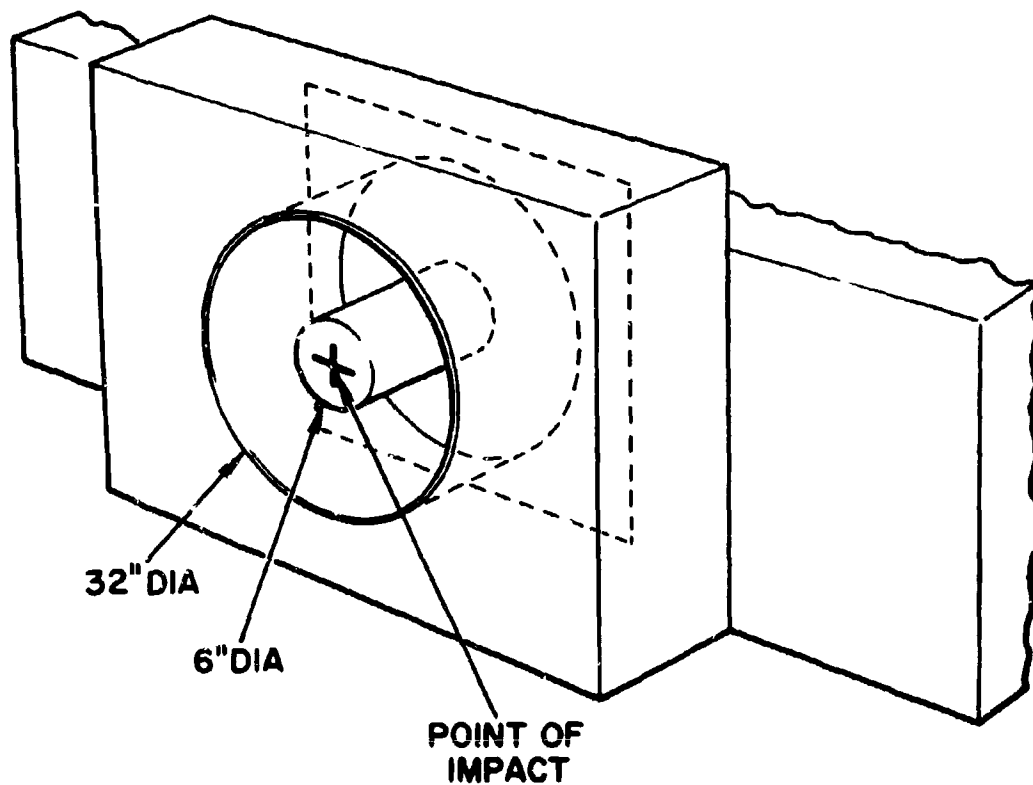
Fig. 4-5.   Shallow-Hole Target

It can be seen that, in general, the calibration results were as expected.
The transition is evident for peak pressure, being apparently well underway at
the 38-ft gauge station ($d/W^{1/3}$ of about 15). The impulse curve falls between
the two reference curves and, furthermore, has approximately the same shape,
suggesting either that the transition is complete at a distance closer than
the nearest station or that it commences at distances greater than the remote
stations. Since rarefactions from the target edges should commence decreasing
the impulse at smaller distances than peak pressure, and since the peak
pressure is apparently affected at close distances, presumably completing
its transition near the 38-ft gauge station, the impulse calibration curve
is probably that which would be obtained without the presence of the target.
The fact that its magnitude is approximately 25 percent greater than that
for the 18-lb TNT reference curve is not surprising, because of the differences
between TNT and pentolite and between a surface burst and a 3-ft HOB.

No significant differences in the gauge line magnitudes were apparent
for either pressure or impulse. The possibility of peak-pressure differences
occurring over the transition region might be anticipated but were not detectable.

Impact Test Results

The individual peak overpressure and positive-phase-impulse data are
presented in the data bank in Volume 2. The yield values which have been
computed from these data using the basic reference curves in Figs. 4-11 and
4-12 and multiplying by a factor of 1.18 to correct for the difference
between pentolite and TNT are presented in Table 4-2. From the data in
Table 4-2 it is evident that some of the computed yields tend to be distance-
dependent Yields computed from the overpressure for all gauge lines typi-
cally increase with increasing distance. Impulse yields for the 30-deg and
60-deg lines tend to decrease with increasing distance, while impulse yields
for the 90- and 180-deg lines tend to remain relatively constant with distance
or in some cases show a slight increase.

In addition, the data indicate that large shock wave asymmetries were
present, even at the outer gauge stations. This is particularly evident for
the deep-hole-target tests.

4-20

Table 4-2

EXPLOSIVE YIELDS FROM HYPERGOLIC IMPACT TESTS

TARGET GEOMETRY	TEST NO.	PROP. WEIGHT (lb)	IMPACT VELOCITY (ft/sec)	GAUGE LINE (deg)	YIELD (%) AT INDICATED NOMINAL DISTANCES (ft)									
					23		37		67		117		200	
					Y_P	Y_I	Y_P	Y_I	Y_P	Y_I	Y_P	Y_I	Y_P	Y_I
Flat Wall	001	200	570	30	8	24	13	17	-	-	-	-	-	-
				60	-	-	12	16	-	-	-	-	-	-
	007	200	340	30	2	6	-	-	-	-	-	-	-	-
				60	-	-	2	8	4	6	6	7	-	-
	068	200	566	30	7	35	12	25	12	15	18	14	-	-
				90	-	-	7	15	8	14	9	-	16*	18*
				180	-	-	-	-	-	-	-	-	-	-
	012	1000	570	30	-	-	6	21	-	-	-	-	-	-
				60	-	-	11	39	17	22	22	30	16	22
	072	1000	585	30	-	-	14	40	23	31	-	-	30	31
				90	-	-	5	18	10	17	8	13	12	19
				180	-	-	-	-	9	14	13	12	15	14
	073	1000	410	30	30	100	28	88	38	75	49	69	-	-
				90	-	-	16	15	13	17	17	23	-	-
				180	-	-	-	-	4	15	6	33	5*	20*
Shallow Hole	002	200	575	30	26	143	44	67	-	-	-	-	-	-
				60	-	-	-	-	-	-	-	-	-	-

* Non-classical

Y_P = yield by pressure

Y_I = yield by impulse

Table 4-2 (Cont.)

TARGET GEOMETRY	TEST NO.	PROP. WEIGHT (lb)	IMPACT VELOCITY (ft/sec)	GAUGE LINE (deg)	YIELD (%) AT INDICATED NOMINAL DISTANCES (ft)									
					23		37		67		117		200	
					Y_P	Y_I	Y_P	Y_I	Y_P	Y_I	Y_P	Y_I	Y_P	Y_I
Deep Hole	003	200	575	30	9	24	13	38	-	-	27	33	-	-
				60	8	17	13	27	-	-	-	-	-	-
	008	200	340	30	14	107	22	145	49	76	56	64	-	-
				60	6	9	-	-	-	-	-	-	-	-
	009	200	580	30	23	122	51	133	98	82	89	89	-	-
				60	11	14	-	-	-	-	-	-	-	-
	069	200	555	30	30	100	28	88	38	76	49	69	-	-
				90	-	-	16	15	13	17	17	23	-	-
				180	-	-	-	-	4	15	6	33	5*	20
	013	1000	570	30	-	-	16	-	41	-	51	-	28	-
				60	-	-	10	-	-	-	-	-	-	-
	074	1000	557	30	-	-	34	122	43	129	60	78	55	68
				90	-	-	5	23	16	31	20	39	24	42
				180	-	-	-	-	3	11	12	22	4	8
Parallel Wall	004	200	340	30	17	59	26	57	30	46	41	43	-	-
				60	10	46	15	41	-	-	-	-	-	-
	010	200	340	30	10	38	15	42	24	32	19	30	-	-
				60	7	26	-	-	-	-	-	-	-	-

Table 4-2 (Cont.)

TARGET GEOMETRY	TEST NO.	PROP. WEIGHT (lb)	IMPACT VELOCITY (ft/sec)	GAUGE LINE (deg)	YIELD (%) AT INDICATED NOMINAL DISTANCES (ft)									
					23		37		67		117		200	
					Y_P	Y_I	Y_P	Y_I	Y_P	Y_I	Y_P	Y_I	Y_P	Y_I
Deep Hole	003	200	575	30	9	24	13	38	-	-	27	33	-	-
				60	8	17	13	27	-	-	-	-	-	-
	008	200	340	30	14	107	22	145	49	76	56	64	-	-
				60	6	9	-	-	-	-	-	-	-	-
	009	200	580	30	23	122	51	133	98	82	89	89	-	-
				60	11	14	-	-	-	-	-	-	-	-
	069	200	555	30	30	100	28	88	38	76	49	69	-	-
				90	-	-	16	15	13	17	17	23	-	-
				180	-	-	-	-	4	15	6	33	5*	20
	013	1000	570	30	-	-	16	-	41	-	51	-	28	-
				60	-	-	10	-	-	-	-	-	-	-
	074	1000	557	30	-	-	34	122	43	129	60	78	55	68
				90	-	-	5	23	16	31	20	39	24	42
				180	-	-	-	-	3	11	12	22	4	8
Parallel Wall	004	200	340	30	17	59	26	57	30	46	41	43	-	-
				60	10	46	15	41	-	-	-	-	-	-
	010	200	340	30	10	38	15	42	24	32	19	30	-	-
				60	7	26	-	-	-	-	-	-	-	-

Fig. 4-7. Deep-Hole Target

4-11

The persistence of these blast asymmetries over the entire measuring
range tends to complicate the selection of appropriate terminal yield values
for these tests since the test geometry is not completely similar to the full-
scale case of concern. It will be recalled that these tests were intended to
simulate nose-on impact of a vehicle at high velocity onto the ground surface.
The flat-wall target was selected to simulate a rigid ground surface, in which
no impact cratering would occur, while the deep-hole target simulated a soft
ground surface, in which significant impact cratering would occur.

In the full-scale case of concern, it would be anticipated that blast
pressure would be radially symmetrical about the point of impact along the
ground surface and that blast asymmetry, if it existed, would occur in a
vertical plane, with the pressure directly above the impact point being the
highest. Such asymmetries are not of much concern since pressure along the
ground surface would be of most importance in the full-scale case.

In the test geometry, the tankage was accelerated along the ground sur-
face on a sled track and allowed to impact on a massive vertical target since
this was the only practical way to obtain the desired high velocities and the
required control on the impact point.

The important differences between the real and test geometries can be
understood by visualizing that the test geometry is created by rotating the
line of flight of the test tankage and a section of the ground surface the
size of the target through 90 deg, as shown in Fig. 4-13.

From Fig. 4-13, it appears that the pressures along the 90-deg gauge
line in the test geometry case would most nearly correspond to the pressures
along the ground surface in the real geometry. The pressures along the 30-
and 60-deg lines in the test geometry tend to correspond to those at 30 deg
and 60 deg from the vertical in the real geometry and thus would be higher
than the ground-surface value. The pressures along the 180-deg gauge lines
in the test geometry would tend to be lower than the ground-surface
pressure in the real geometry.

FULL-SCALE GEOMETRY
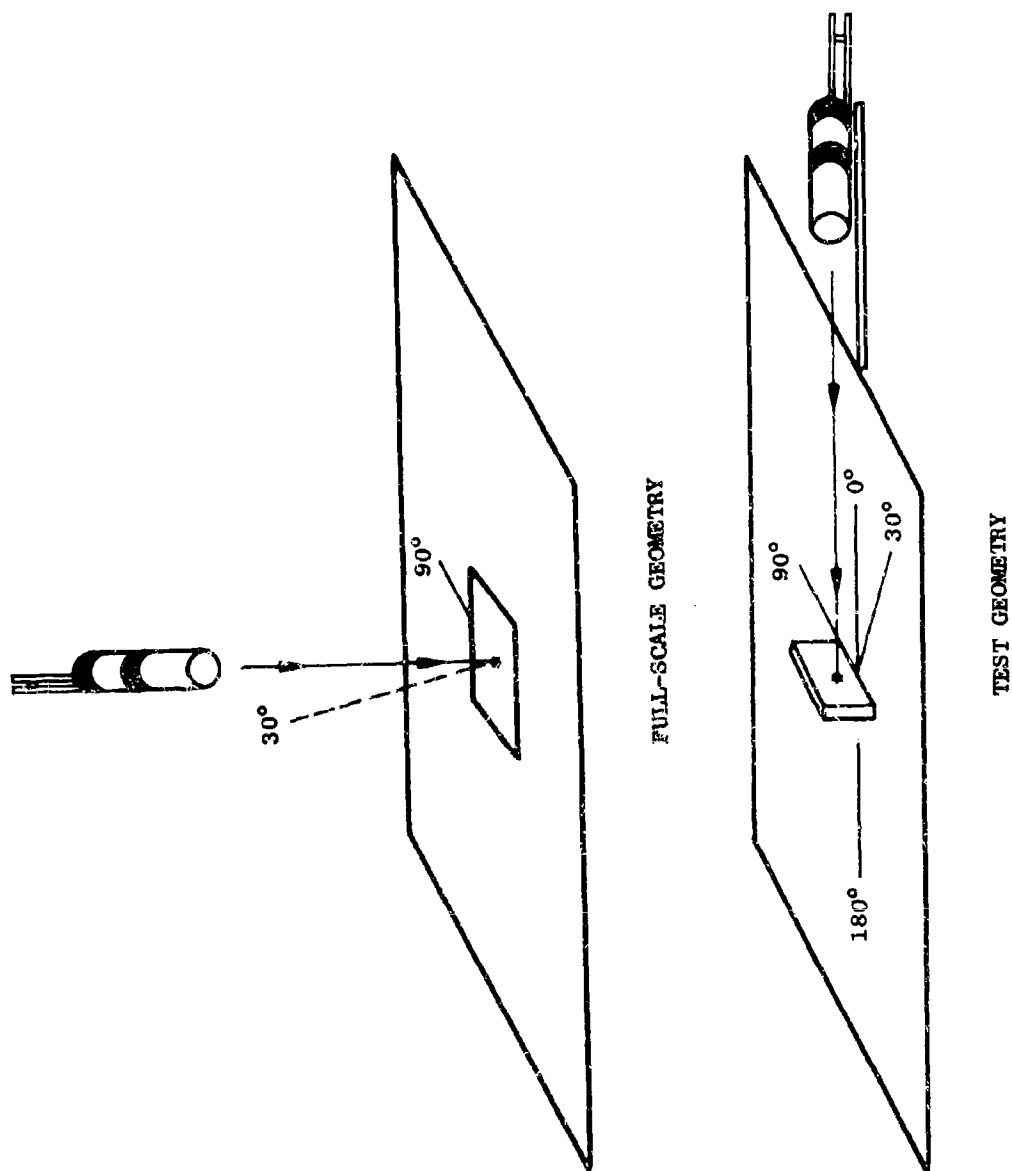
TEST GEOMETRY

Fig. 4-13. Sketch Indicating Differences Between Full-Scale and Test Geometry

POINT OF
IMPACT

16"

2'

6'
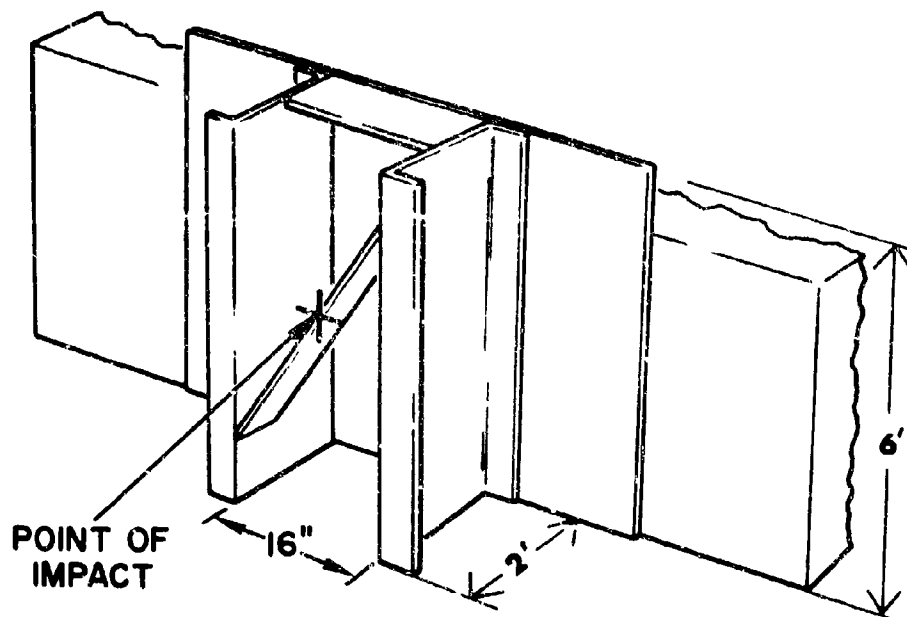
Fig. 4-8. Parallel-Wall Target

The test conditions for each of the propellant tests and the calibration tests are presented in Table 4-1.

These tests were conducted in two series. Test numbers 001 through 015 were conducted in May, June and July of 1964 and test numbers 065 through 081 were conducted in September and October of 1965. The tankage, test conditions and type of instrumentation were the same for both test series. The layout of the instrumentation system, however, was quite different.

The instrumentation layout used for the first series is shown in Fig. 4-9. The Kistler[*] gauges were installed in two gauge lines 30 and 60 deg from the track. For the second series of tests, the system was modified to obtain more information on the blast asymmetries. The 60-deg leg was moved to 90 deg and a third gauge line was added behind the target. This system is shown in Fig. 4-10. During this second series a gauge was installed on the target to obtain close-in blast information. The data from this gauge location are presented at the end of the high-velocity impact discussions.

During both test series, BRL[**] self-recording pressure-time gauges were also installed at all of the basic measuring stations and at several additional stations at longer distances. Since the pulse durations obtained from the tests were rather short for correct recording by the BRL gauges, particularly at the close-in stations, and since the Kistler system worked well, the major use of the BRL data was in checking blast asymmetry at long distances.

Calibration Tests

The calibration tests included eight with 18-lb pentolite spheres, one with a 105-lb sphere, and three with 216-lb spheres. The pentolite spheres in most cases were hung in fish nets at the horizontal center of a 5-ft-high, 13-ft-wide, 4-in.-thick backup plate; 3 ft above the ground surface and with the center of the charge approximately 1 ft in front of the plate.

---

[*] Quartz Piezoelectric Air Pressure gauges — Kistler Instrument Co. Models 601A.
[**] Ballistic Research Laboratory.

These considerations suggested two possible methods for estimating appropriate terminal yields:

1. Use value for 90-deg gauge line

2. Use average of maximum and minimum values where the minimum value corresponds to that for the 180-deg line and the maximum value to that along the line of flight (this value would have to be obtained by extrapolation)

A combination of the two methods was finally selected for computing the yields for the tests in the second test series. This method involved averaging the computed yields from the 0-, 90-, and 180-deg direction, with the 0-deg value obtained by extrapolation. (Plots demonstrating the method for obtaining the extrapolated value are given in Fig. 4-14.)

When data were available, the same method was used to obtain terminal yield estimates for the tests conducted during the first test series; however, for tests 002 and 007 sufficient data were not available to make this computation and thus the yields quoted are estimated values. The computed yield values for both test series are presented in Table 4-3.

Close-In Data

During the second high-velocity test series, effort was devoted to measuring the close-in blast environment overpressure. Gauges with a 0- to 30,000-psi pressure range were flush-mounted 2 ft from the point of impact in the flat-wall targets and on the lip of the deep-hole targets. Data were obtained from two tests: 069, a 200-lb deep-hole-target test; and 074, a 1000-lb deep-hole-target test.

The analog traces for these two tests have been redrawn and are presented in Fig. 4-15. Included are the approximate impact times of the tanks and the ignition times, which were obtained from the film records and the maximum peak overpressure values.
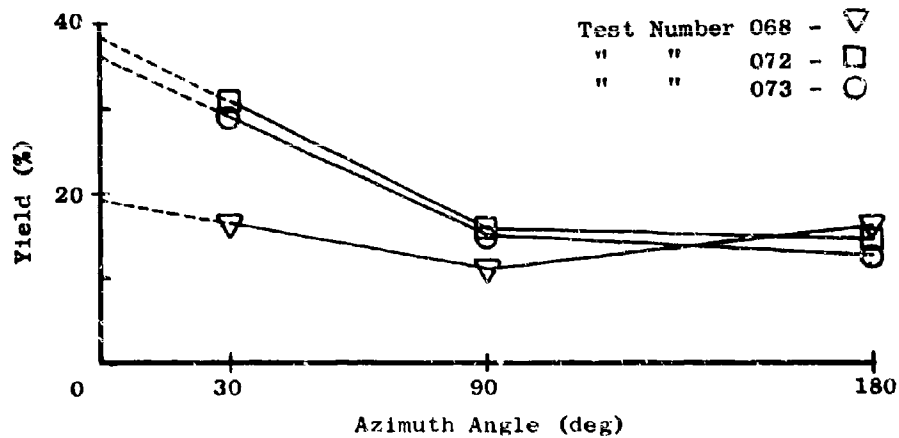
a. Flat-Wall Target Tests
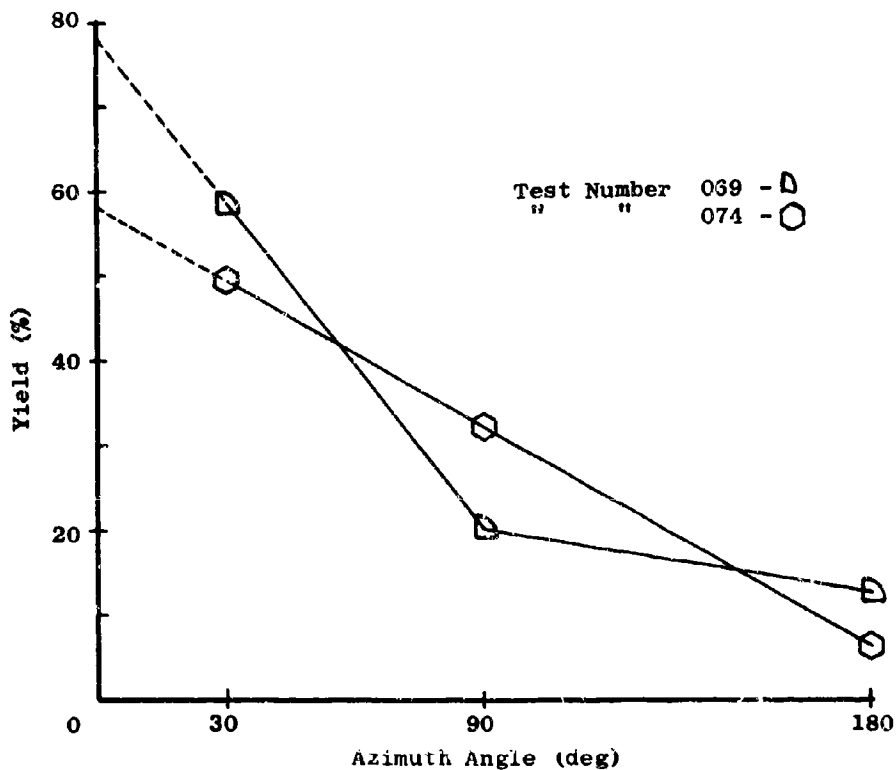
h. Deep-Hole Target Tests

Fig. 4-14. Plots of Yield as a Function of Azimuth Angle for Selected Hypergolic Impact Tests

Table 4-1

SUMMARY OF TEST CONDITIONS

TEST NO.	WEIGHT (lb)	TYPE	IMPACT VELOCITY (fps)	TARGET CONFIGURATION
01C	18	Pentolite	–	Flat Wall
02C	18	Pentolite	–	Flat Wall
03C	18	Pentolite	–	Flat Wall
001	200	N_2O_4/50-50	570	Flat Wall
002	200	N_2O_4/50-50	575	Shallow Hole
003	200	N_2O_4/50-50	575	Deep Hole
004	200	N_2O_4/50-50	340	Parallel Wall
006	18	Pentolite	–	Flat Wall
007	200	N_2O_4/50-50	340	Flat Wall
008	200	N_2O_4/50-50	340	Deep Hole
009	200	N_2O_4/50-50	580	Deep Hole
010	200	N_2O_4/50-50	340	Parallel Wall
011	18	Pentolite	–	Flat Wall
012	1000	N_2O_4/50-50	570	Flat Wall
013	1000	N_2O_4/50-50	570	Deep Hole
014	216	Pentolite	–	Flat Wall
015	216	Pentolite	–	Flat Wall
065	18	Pentolite	–	Flat Wall
067	18	Pentolite	–	Flat Wall
068	200	N_2O_4/50-50	566	Flat Wall
069	200	N_2O_4/50-50	535	Deep Hole
070	18	Pentolite	–	Flat Wall
071	105	Pentolite	·	Flat Wall
072	1000	N_2O_4/50-50	585	Flat Wall
073	1000	N_2O_4/50-50	410	Flat Wall
074	1000	N_2O_4/50-50	557	Deep Hole
081	216	Pentolite	–	Flat Wall

Table 4-3

TERMINAL YIELDS FROM HYPERGOLIC IMPACT TESTS

TARGET TYPE	PROPELLANT WEIGHT (lb)	VELOCITY	TEST NO.	TERMINAL YIELD (%)
Flat Wall	200	340	007	5
		570	001	13
		566	008	15
		410	073	21
	1000	570	012	15
		585	072	23
Shallow Hole	200	575	002	53
Deep Hole	200	340	008	38
		575	003	24
		560	009	56
		535	069	37
	1000	570	013	28
		557	074	34
Parallel Wall	200	340	004	33
		340	010	21
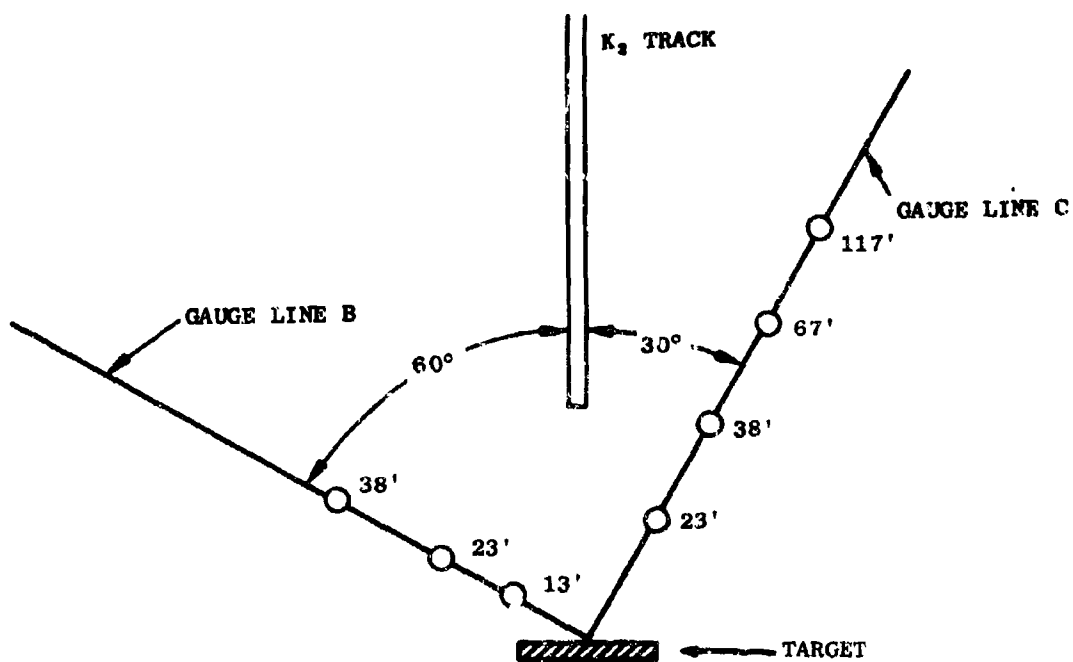
Fig. 4-9.   Pressure Sensor Locations for First Hypergolic
Impact Test Series

NOMINAL GZ-TO-STATION
DISTANCE (ft)

A	13
B	23
C	38
D	67
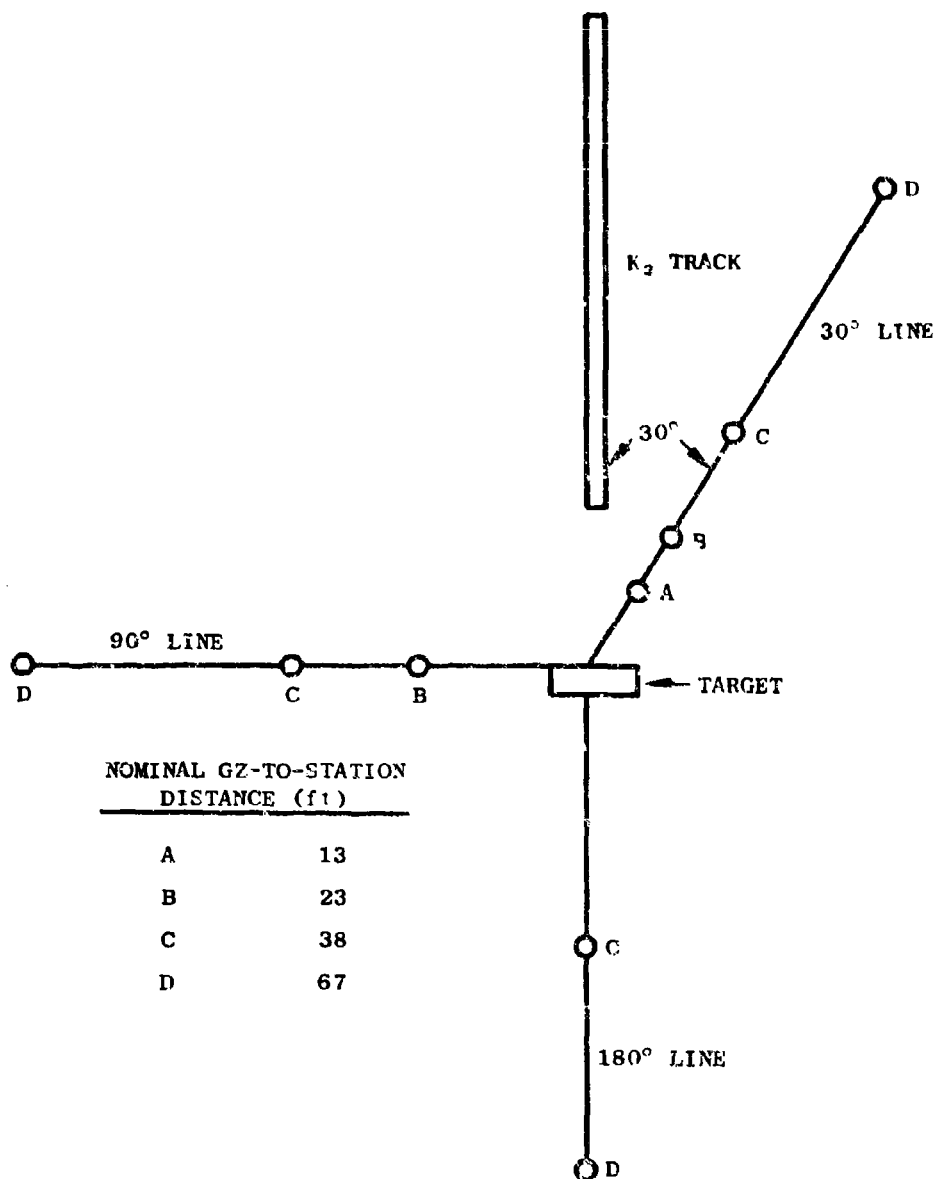
Fig. 4-10.   Pressure Sensor Locations for Second Hypergolic
Impact Test Series
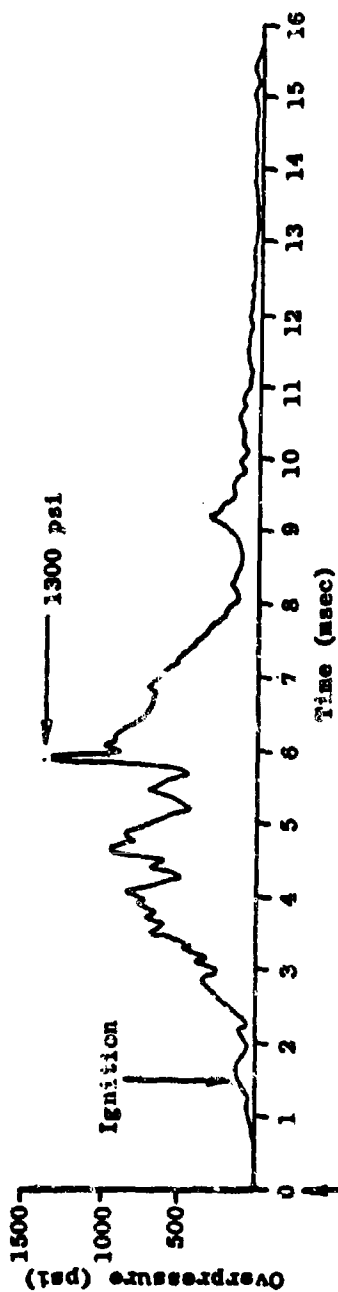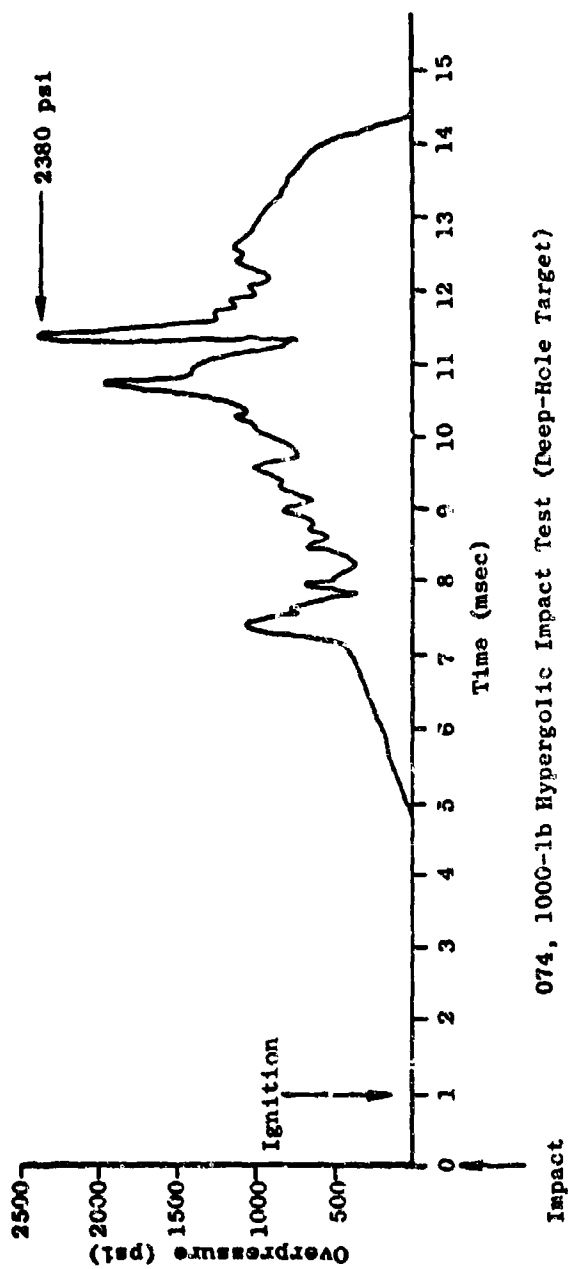
Fig. 4-15 Close-in Gauge Traces, Hypergolic Tests 069 and 074

The peak overpressure[*] and positive-phase-impulse data from these calibration tests are plotted as a function of scaled distance in Figs. 4-11 and 4-12, respectively.[**] It can be seen that the data points for each plot are internally consistent in that they tend to lie along a smooth curve. As a measure of the reproducibility of the results, a standard deviation was calculated from the percent deviation of each point from a smooth-curve fit through all of the data points. The standard deviation (of an individual observation) computed in this manner for pressure was 11.9 percent and for impulse, 7.6 percent.

Also included in Figs. 4-11 and 4-12 are two curves (dashed lines) illustrating expected values for 18 lb of a standard high explosive[***] detonated under two conditions: one, in the absence of the target, the other with an infinite target. (The latter condition corresponds to 36 lb in the absence of the target.) It would be expected that the blast wave characteristics from the 18-lb pentolite spheres with the massive target would correspond to those from a 36-lb charge without the target at distances less than the minimum target dimensions, and that they would correspond to those from an 18-lb charge without the target at distances very much greater than the minimum target dimensions. Although there should be a gradual transition from one case to the other, the exact manner in which this occurs in not known.

---

[*] The terms "peak overpressure" and "overpressure" and "positive-phase-impulse" and "impulse" are used interchangeably throughout this report.

[**] These data as well as the propellant test data have not been corrected for the difference in ambient pressure between sea level (14.7 psi) and that existing at the test site (approximately 13.7 psi). The correction is small and unnecessary for later yield computations, because it is common to both the calibration and impact test data.

[***] For overpressure, these curves are based on data given in Ref. 4-2 for composition A charges (95% RDX - 5% wax) detonated over a flat surface with a scaled HOB of 0.94 ft/lb$^{1/3}$. (This is equivalent to a 3-ft HOB for a 36-lb charge.) These data were used since suitable pentolite data for the proper HOB were not readily available, and composition A has explosive characteristics very close to those of pentolite. For impulse, these curves are based on data given in Ref. 4-3 for a surface burst of TNT. These data were used since neither suitable pentolite nor composition A data were readily available. (It is estimated that the 18- and 36-lb TNT curves would be obtained with about 15 to 30 lb of pentolite, respectively.)

ANALYSIS OF DATA

The results obtained from the high-velocity test series were analyzed to
determine whether the observed variations in yield with the different test con-
ditions could be considered significant in a statistical sense.

An analysis of variance was first performed on all the high-velocity data
to test for significance of the scale and target geometry effects. This analy-
sis was performed on the basic data without transformation, with a square root
transformation, and with a $\log_{10}$ transformation. In the first case, the vari-
ance is assumed independent of the mean value; in the second case, the variance
is assumed to be proportional to the mean (or the standard deviation is propor-
tional to the square root of the mean); and in the third case, the variance is
assumed to be proportional to the mean squared (or the standard deviation is
proportional to the mean). These two transformations were used since it is be-
lieved that the uncertainty in yield value as expressed by the standard devia-
tion tends more to be proportional to the mean than independent of it. Except
for cases where the mean value is quite small, the $\log_{10}$ transformation seems
most appropriate.

The results of the analysis on both the original and transformed data
showed that:

1. The scale effect was not significant at the 10-percent level.[*]

2. The target geometry effect was significant at the 2.5-percent level,
    i.e., the deep-hole geometry gave significantly higher yields than
    the flat-wall target.

3. The interaction of the target geometry and scale effect was signifi-
    cant at the 10-percent level. In other words the effect of target
    geometry at the 200-lb scale tended to be somewhat greater than at
    the 1000-lb scale.

Because of the moderate interaction effect, the yield data were next

---

[*] Refers to level of significance used in the statistical test. A 10-percent
level means there is a 10 percent probability of erroneously rejecting a
valid null-hypothesis.
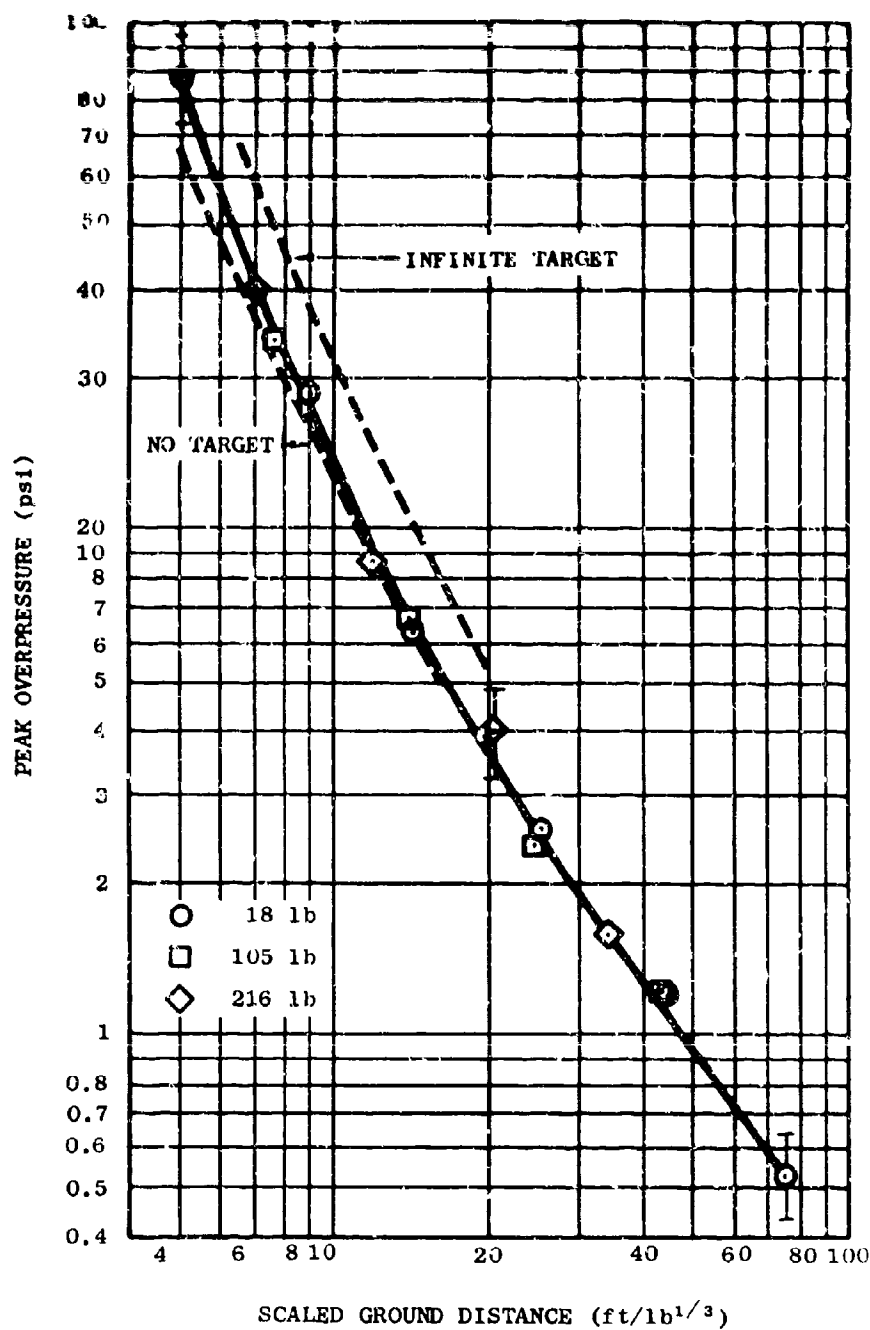
Fig. 4-11. Peak Overpressure vs Distance for Pentolite
(flat-wall target, 3-ft HOB)

analyzed for scale effect separately for each target geometry. Again the
original data and the two transformations were used. For both the flat-
wall and deep-hole targets the data exhibited no significant scale effect
(at the 10-percent level).

Next, an analysis was performed to determine whether there was a
significant effect of velocity between the mean of the six high-velocity
observations which had low-velocity counterparts and that of the three
lower velocity observations: Equality of population variance was not
assumed. The analysis was performed on both the original and transformed
data. No significant effects were detected at the 10-percent level.

In summary, those statistical analyses indicate that:

1. The deep-hole target gives significantly larger explosive yields
    than the flat-wall target.

2. A variation in impact velocity from approximately 340 to approxi-
    mately 570 ft/sec does not significantly affect the yield.

3. For the deep-hole target there is a small tendency for the yield
    to decrease with increasing propellant weight.

In addition an overall estimate of the experimental variability was computed
using the sets of duplicate data that were available and assuming that the stan-
dard deviation is proportional to the mean yield. For this computation both the
hypergolic and cryogenic high-velocity-impact data were used.[*] These computa-
tions indicated that the standard deviation in yield is approximately 25% of the
mean yield. The uncertainty was estimated to be equal to two standard deviations.

EXPLOSIVE-DONOR TESTS

Test Conditions

The explosive-donor case is similar in some respects to the high-velocity-

---

[*] The cryogenic high-velocity-impact data are described in detail in Section 5.
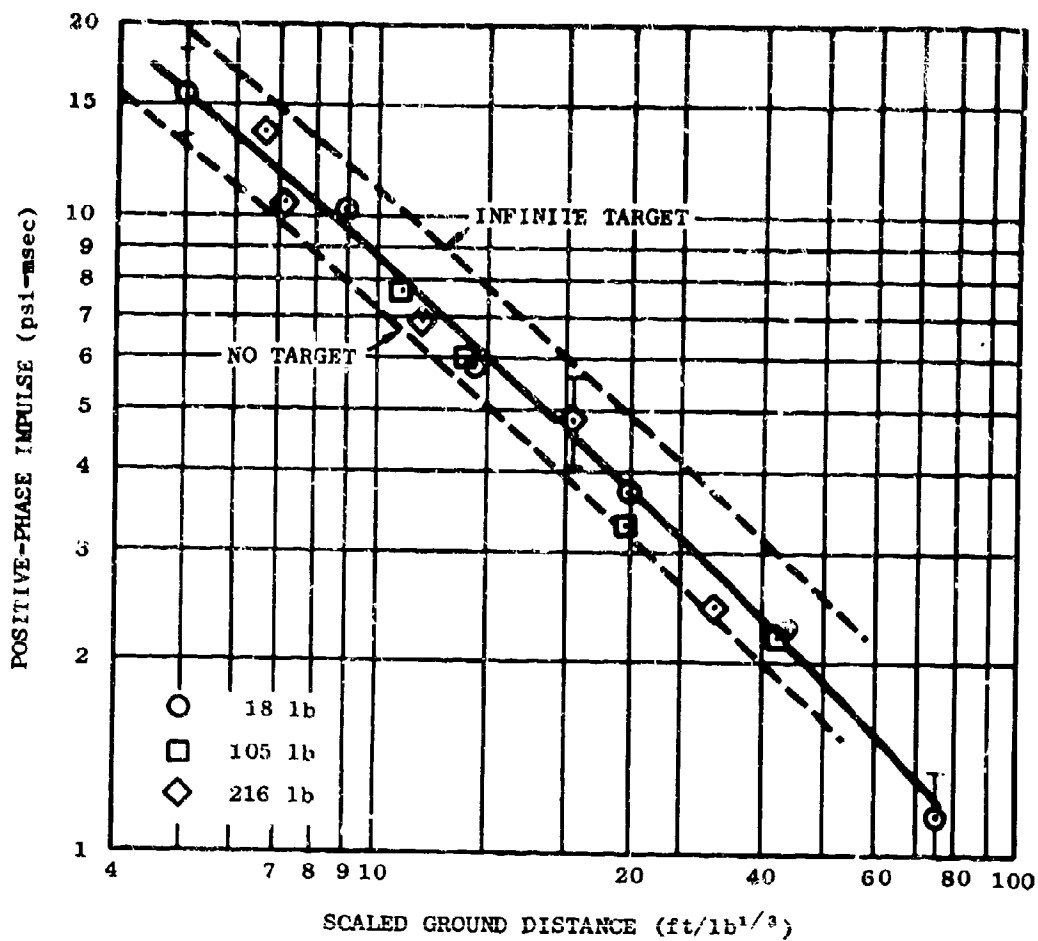
Fig. 4-12.   Positive-Phase Impulse vs Distance for Pentolite
(flat-wall target, 3-ft HOB)

impact case. The major difference is that in the explosive-donor case, the propellants are subjected to a short-duration, very-high-pressure loading rather than a longer duration, moderate-pressure loading, as in the high-velocity-impact case.

The parameters which appeared important for the explosive-donor situation were:

- Geometry of propellant tanks
- Weight of explosive donor
- Location of explosive donor
- Shape of explosive donor
- Geometry of neighboring surfaces

As in the impact tests, the most important geometry of the propellant tanks appeared to be that of a conventional vehicle, i.e., two cylindrical tanks, one on top of the other with the length-to-diameter ratio and tank strengths being the minimum values consistent with expected usage.

The weight of potential explosive donors could vary over wide limits. However, there are several factors which tend to narrow down the range of primary interest. First it can be shown that there is not too much concern with donors whose weight approaches that of the propellants. If a donor equal to the propellant weight is necessary to make the majority of the propellants react explosively, then the resulting explosion is not much worse than that given by the donor itself. (An increase in explosive weight by a factor of two only increases the distance at which a given peak pressure is obtained by a factor of $(2)^{1/3}$ or 1.26.)

On the other hand, too small a donor may not be able to cause the propellants to mix and explode (if in fact, they are capable of exploding under the action of an explosive donor). With this line of reasoning, it was concluded that the range of interest was from about 1 to 50 lb for 200 lb of propellant.

A variety of shapes and locations of donors were considered with regard to their ability to create extremely fast mixing. These included:

4-31

- A spherical charge on top of the tank

- A disk charge on top of the tank

- Longitudinal charges spaced at intervals around the tank sidewall

- A shaped charge on top of the tank with the jet directed along the axis of the tank.

With the assumption that rapid mixing can occur only with a rapid increase in interface area, it appeared that the spherical and disk charges would be more effective than the longitudinal charge. Furthermore, it did not appear that there would be much difference in effects between the spherical and disk charges, and since the former is simpler, the disk and longitudinal charges were dropped from further consideration.* For the spherical charge, it seemed appropriate to use a charge weight of 30 lb, which is near the upper end of the range of interest. The charge was placed on the top of the tank, and the tank was placed on the ground surface to take advantage of the confinement of the propellant between the explosion and the ground surface.

The shaped charge differs from the other types because it is a directed source of energy release. By vaporizing the propellants along the axis of the tank, a radial velocity should be given to the remaining propellants, which may lead to relatively fast mixing. Since the possibility of an actual shaped charge, particularly of large size, is relatively unlikely in an actual missile failure, it seemed appropriate in this case to use a charge weight of the order of a pound, which is at the lower end of the range of interest.

A 1-lb shaped RDX charge having a copper-lined reentrant cone, with a 60-deg apex angle, was selected for this purpose. Such a charge was reported to be capable of penetrating 14 in. of steel. This charge and its initiator were oriented so that a fan-shaped jet was directed down the axis of the propellant tanks.

---

* A command destruct test series using longitudinal charges was conducted later in the program,

For both types of tests, the tanks were approximately 29 in. long and 15
in. in diameter with 1/16-in.-thick aluminum walls. The oxidizer was in the up-
per part of the cylindrical tank and the fuel in the lower part, separated by a
tempered glass diaphragm. The total propellant weight was 200 ib. The propel-
lant length-to-diameter ratio was 1.8 and the oxidizer-to-fuel weight ratio 1.9.
A sketch of this type of tank is shown in Fig. 4-16.

This test series was conducted at AFRPL, and the blast environment was mea-
sured using the basic PYRO instrumentation system, which consisted of 15 piezo-
electric transducers distributed along 3 radial lines, 120 deg from each other,
over a ground distance of approximately 7 to 67 ft. A complete discussion of this
system is presented in Appendix A.

There were two propellant tests for each type of donor and one spherical
donor test with both propellants replaced by water. This latter test was conduc-
ted because it was suspected that the contribution of peak pressure and impulse
by this 30-lb donor charge might be large compared to the propellant. If this
occurred, separation of the yield (effective charge weight) of the propellant
from that of the donor would be extremely uncertain unless the results from the
donor charge itself were known quite well.

Test Results

The peak overpressure and impulse data and the propellant yields computed
from these data are presented in Volume 2. The computed terminal yield values
for these tests are presented in Table 4-4. For the spherical-charge tests, the
propellant yields were obtained by subtracting the yield values of the tests
with water from those of the tests with propellants. For the shaped-charge tests,
the propellant yields were obtained by subtracting the estimated yield of the
donor (0.5 percent) from the total yield. This estimate is believed to be com-
mensurate with the accuracy of the measurement for the outer measuring stations
but is relatively uncertain close to the explosion because of the shape of the
charge. For the spherical-donor tests, there is a large scatter in the yield
results from station to station because the propellant yield was small compared
to the donor yield. Accordingly, it was not practical to ascertain distance

4-33
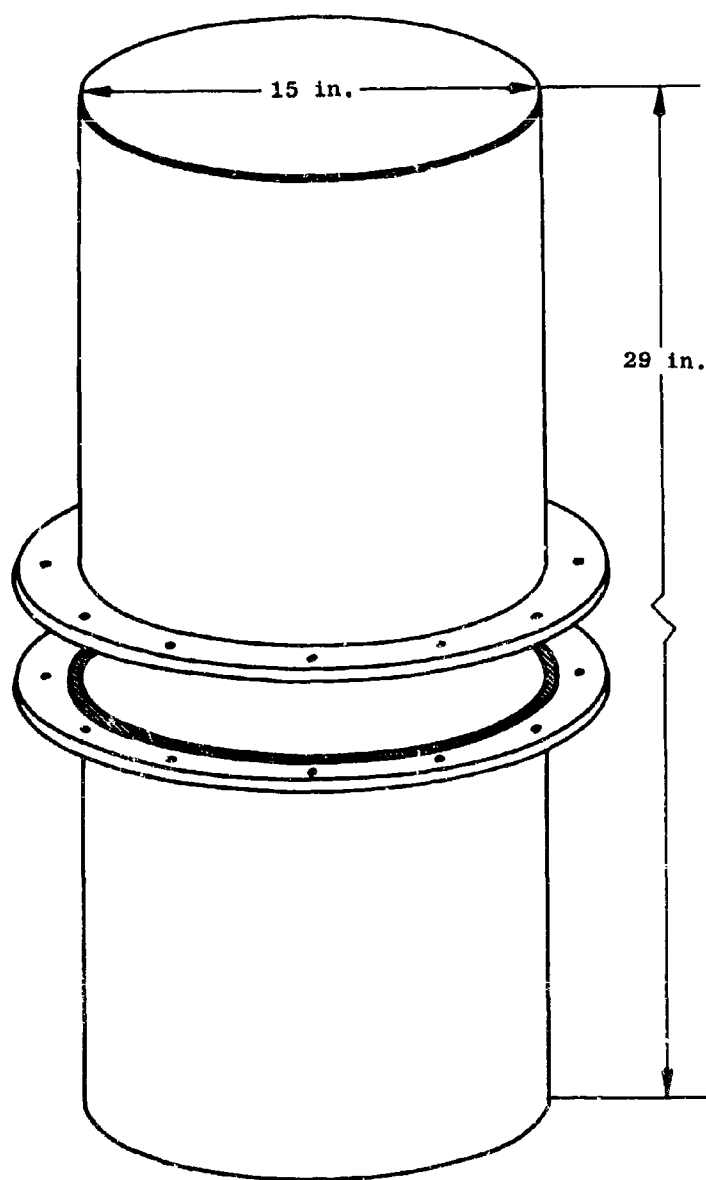
Fig. 4-16.   Explosive-Donor Tank

4-34

effect on yield, and terminal yield values were computed by averaging the over-
pressure and impulse yield values at all stations. Although the results from
the two tests showed remarkably good agreement, considering the variability in
individual station results, it is estimated that the average terminal yield value
of the two tests, 3.6 percent, is uncertain by a factor of about 2 to 3.

For the shaped-charge tests, both the overpressure and impulse yields are
roughly constant beyond 22.5 ft, so that terminal yields were computed by averag-
ing the pressure and impulse yields for the last three stations.

Considering the small estimated uncertainty in the instrumentation system
and the relatively good agreement between the two tests, it is estimated that
the average terminal yield, 1 percent, is uncertain to about a factor of 2.

The average terminal yield for the two tests with the 30-lb spherical donor
was 3.6 percent, and since this is equivalent to only 7.2 lb of TNT (0.036 x 200)
or about 25 percent of the donor weight, it is evident that this type of explo-
sive donor is not very effective in creating mixing of the propellants. Since
the uncertainty in the yield estimate for this test condition is about a factor
of 2 to 3, it cannot be concluded that the propellant yield is completely negli-
gible compared to the donor, but it represents a relatively small additional
contribution.

The average terminal yield for the two tests with the shaped charge was 1
percent, indicating that this arrangement of the explosive was also not very ef-
fective in creating propellant mixing, although per pound of donor charge, it
was more efficient than the spherical charge.

Table 4-4

TERMINAL YIELDS FROM EXPLOSIVE DONOR TESTS

Test No.	Donor Type	Terminal Yield
019	30-lb spherical donor	3.4
030	30-lb spherical donor	3.7
028	1-lb conical donor	1.2
029	1-lb conical donor	0.8

HYPERGOLIC CONFINEMENT-BY-THE-MISSILE TESTS

Test Conditions

In this test condition, an internal failure, such as bulkhead rupture, is assumed to occur, and one propellant falls down onto the other. As stated in the discussion of this failure mode (Section 3), the time of interest for the in-tank confinement case is limited to the time the propellants remain confined by the walls of the missile. This time is determined by the strength of the tankage, the rate of reaction of the propellants, the initial tank pressure, and the initial ullage space.

Thus the primary requirement on the tankage is to contain the propellants in the proper length-to-diameter ratio until the internal pressure created by the hypergolic reaction exceeds the normal missile tankage design burst pressure. From communications with AFRPL and various missile manufacturers, it was determined that most missile fuel tankage would fail at internal pressures below 100 psi. Accordingly, this value (100 psi) was chosen as the design burst pressure for the tank.

Although it was not anticipated that the exact manner in which the tank fails would have an important effect on the explosion and/or the burning geometry of the propellants, it appeared worthwhile to make some effort to control the failure mode as well as the burst pressure. The simplest way to accomplish this was by making the bolts holding the two flanges together the weak point in the system.

The tank designed with these criteria is sketched in Fig. 4-17. It is a cylindrical tank with 2:1 ellipsoidal domed ends and is divided into two separate propellant compartments by a tempered glass diaphragm. The top compartment contains N_2O_4 and the bottom 50% UDMH — 50% N_2H_4.

The shell of the tank was fabricated from 1/16-in.-thick aluminum. The domes were spun on hardwood molds from 1/16-in.-thick aluminum, and were heat-treated, after forming. Bolted flanges, 3/8-in. thick, were provided for the placement and sealing of the tempered glass diaphragm.
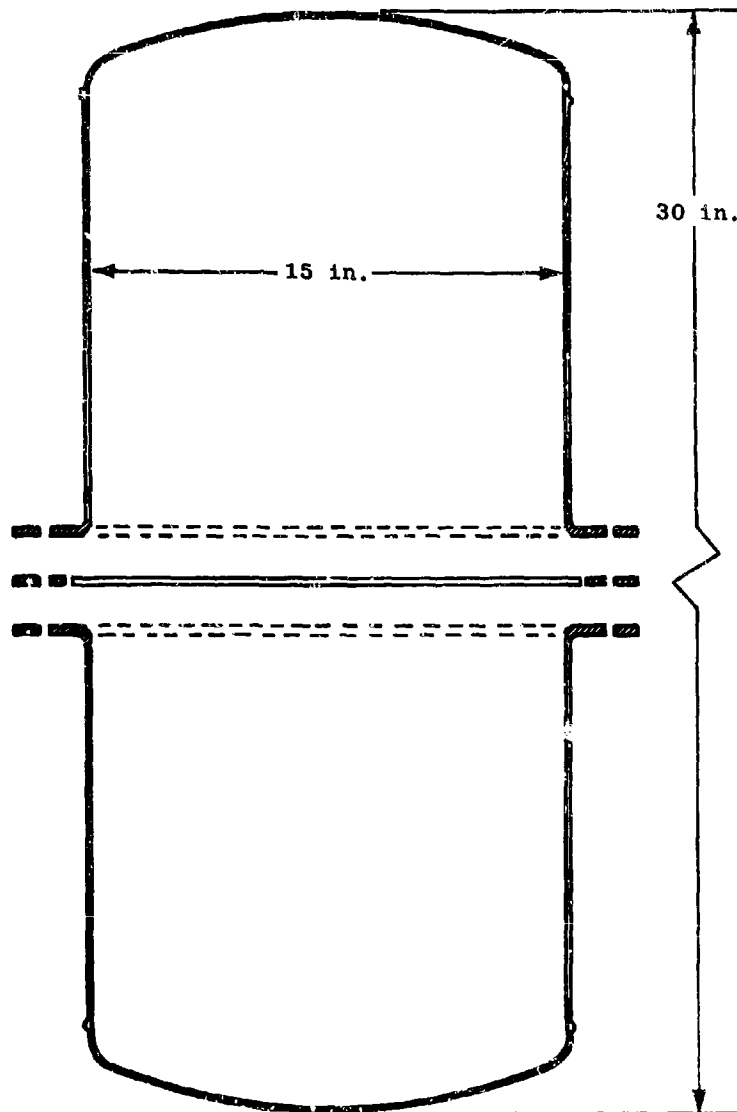
Fig. 4-17. Hypergolic Confinement-by-the-Missile Tank

This tempered glass diaphragm, 1/4 in. thick, was ruptured, by a six-bladed explosive-driven breaker ram, which is pictured in Fig. 4-18. This ram, which rests on the top surface of the tempered glass, is connected to a long drive shaft which extends up through the top of the tank through a gasket seal. An explosive charge (approximately 0.09 lb of C-4) is placed on a small plate affixed to the end of this drive shaft.

A total of three tests with 200 lb of total propellant were run. All tests had total propellant length-to-diameter ratios of 1.8 and oxidizer-to-fuel weight ratios of 1.9. The blast environment was measured using the basic PYRO instrumentation system, which is described in Appendix A.

Test Results

A total of three tests were conducted (Test Nos. 31, 32, and 35). The individual peak overpressure and positive-phase-impulse data, and the computed yield values from these data are presented in Volume 2. The computed terminal yield values were: Test No. 31 — 0.20 percent; Test No. 32 — 0.08 percent; and Test No. 35 — 0.15 percent.

Considering the relatively small uncertainty in individual read-ings obtained during the calibration tests of the instrumentation system (estimated to be 8 to 12 percent), it is clear that the major source of uncer-tainty in an average terminal yield value for this test condition arises from the variability in explosive yield from test to test. It is estimated that the average terminal yield for the three tests is uncertain by a factor of 2 to 3.

COMMAND DESTRUCT TESTS

Test Conditions

In this series of tests the propellants were contained in a cylindrical tank and separated by a tempered glass diaphragm. Failure of the tank was caused by two external linear-shaped charges (total weight of explosive 0.04 lb)
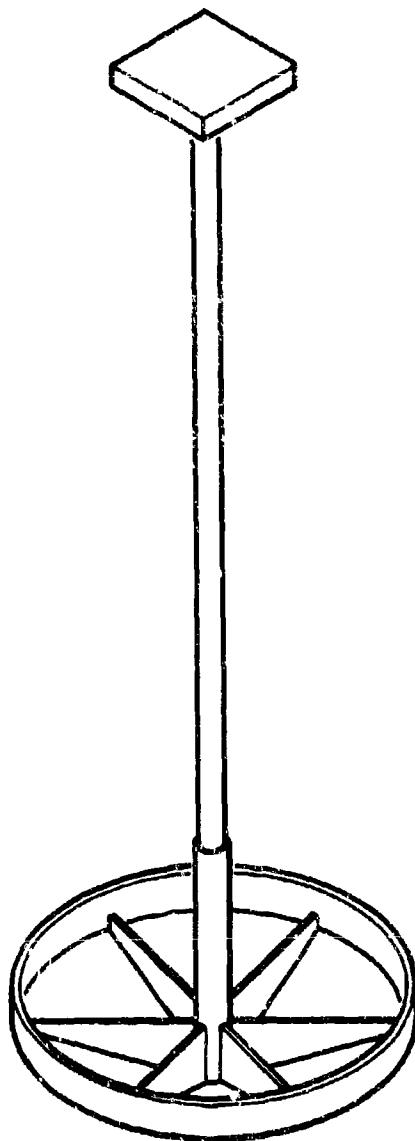
Fig. 4-18. Breaker Ram

vertically aligned against the tank wall. The charge on the lower tank was
oriented 180 deg from that on the upper tank so that the propellants would
spill simultaneously from openings on opposite sides of the container and
initial propellant contact would be at or near the ground surface. The con-
tainer was 29 in. in length and 15 in. in diameter with 1/16-in.-thick
aluminum walls, as shown in Fig. 4-16.

The blast environment was measured as described above under Explosive-
Donor Tests.

Two propellant tests were performed, each with a total propellant weight
of 200 lb, a total propellant length-to-diameter ratio of 1.8, and an oxidi-
zer-to-fuel weight ratio of 1.9.

Test Results

The individual peak overpressure and positive-phase-impulse data and the
computed explosive yields obtained from this data are presented in Volume 2.
The terminal yields from these tests were: Test No. 25 — 0.35 percent and
Test No. 36 — 0.30 percent with an estimated uncertainty of 1.5 to 2.

TOWER DROP TESTS

Test Condition

In this series of tests the propellants were dropped from a 100-ft drop
tower. This tower, which was designed and built for the PYRO Program, is shown
in Figs. 4-19 and 4-20. The first 30 ft of this tower was a tripod constructed
of 6-in.-diameter double-extra-strong pipes with cross bracing of high-strength
cable. The remaining 71 ft of the tower was a high-strength version of a
standard radio tower. The vertical members were fabricated from seamless
mechanical tubing, and high-strength bolts were used throughout.

A T-shaped track was affixed down one side of the tower to guide the test
tanks, which had thin walls and aluminum foil bottoms. These tanks were guided
and held to the T-shaped track by a "skate" which clamped around the track by
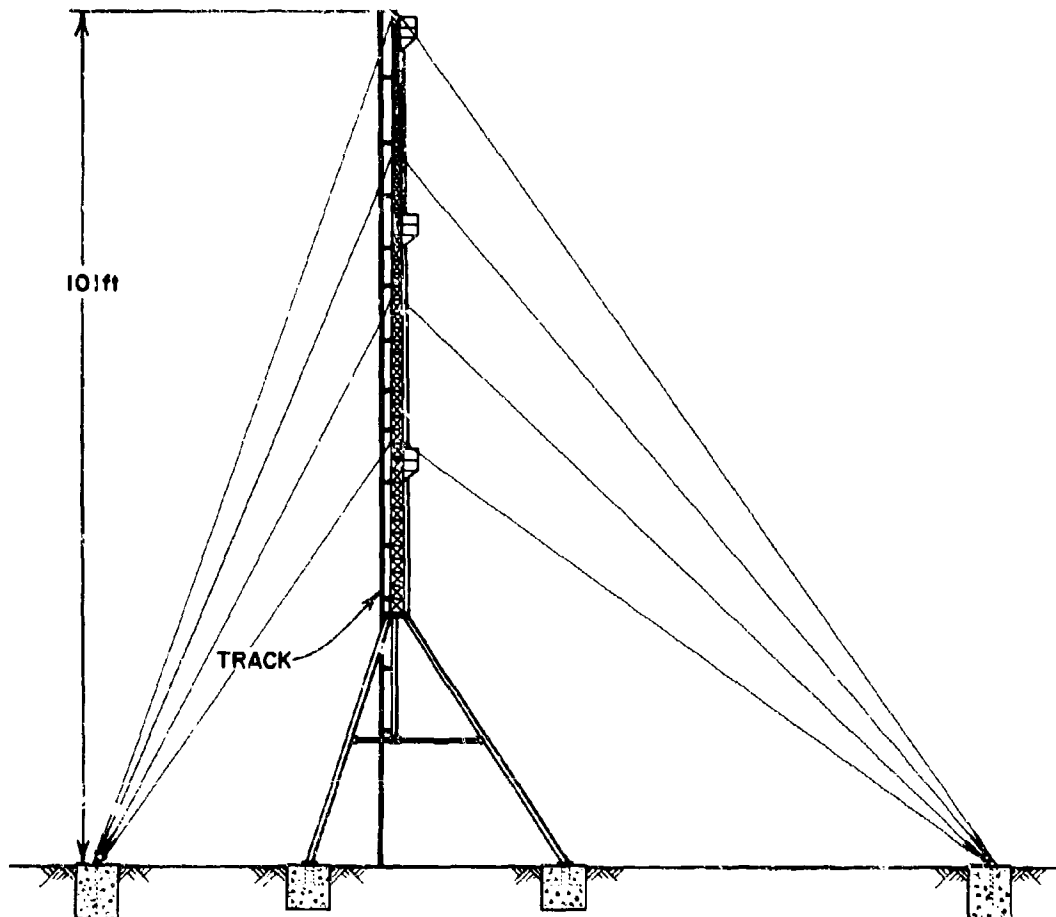
Fig. 4-19. Sketch of the Drop Tower
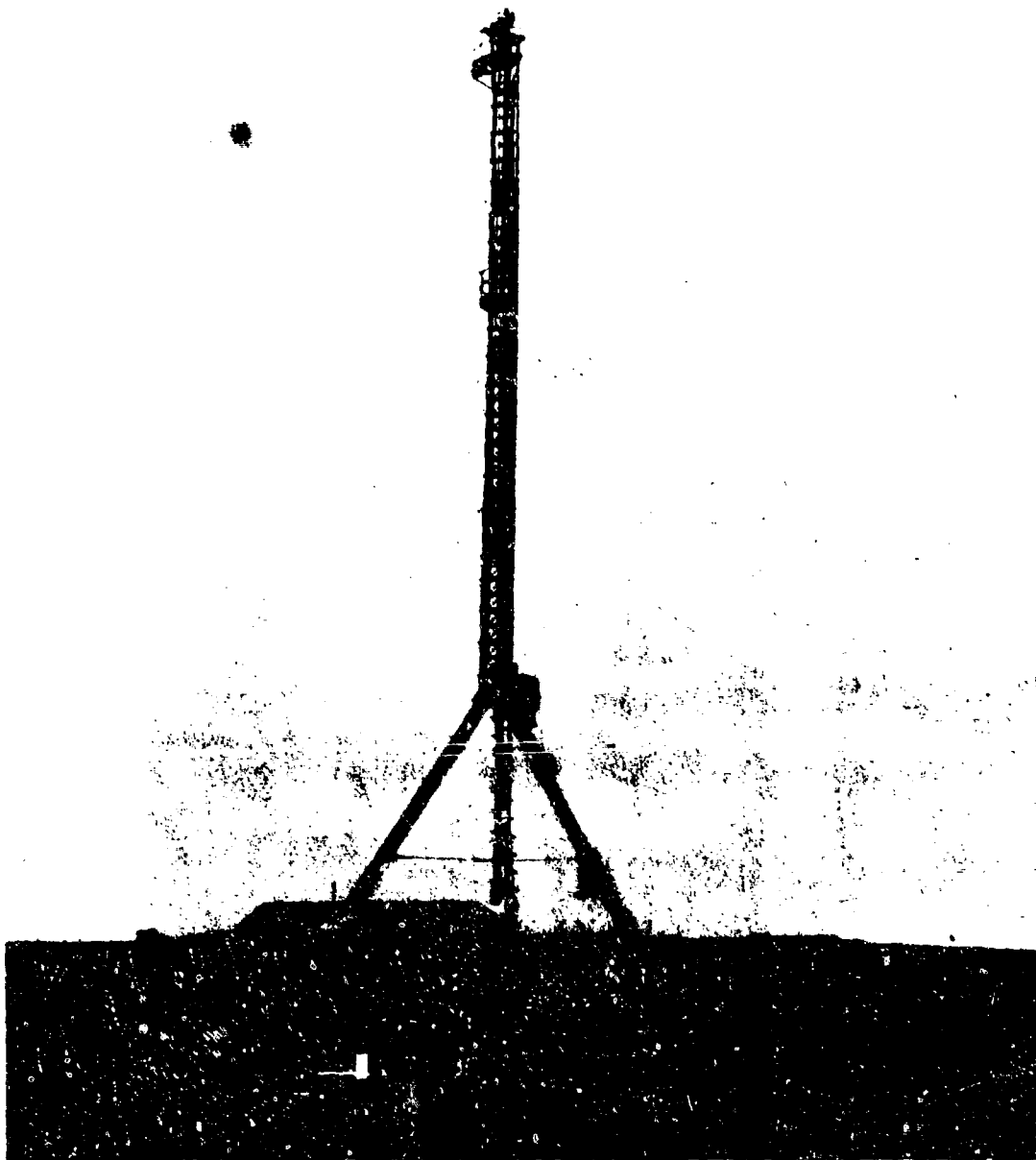
Fig. 4-20. Drop Tower

six roller-bearing wheels. Dropping of the tank was accomplished by an
explosive cable-cutting device. A typical drop tank and guide assembly is
shown in Fig. 4-21.

Diaphragm breaking was accomplished by a single six-pronged breaker
installed on the pad at GZ. Immediately after the diaphragm was pierced, the
tanks were abruptly stopped by a rigid frame at an elevation of approximat-ly
2 ft above the test pad and the propellants allowed to flow out.

Three tests were performed with a propellant weight of 200 lb and three
with a propellant weight of 1,000 lb. The propellant length-to-diameter
ratios were 1.8 and the oxidizer-to-fuel weight ratios were 1.9.

Test Results

The individual peak overpressure and positive-phase-impulse data and the
computed explosive yields obtained from these data are presented in Volume 2.
The terminal yields from these tests are presented in Table 4-5. The data
for these six tests was quite reproducible and there was no evidence of a
scale effect between the 200- and 1000-lb tests. The estimated uncertainty
for the case was estimated as 1.5 to 2.

COLD" PROPELLANT TESTS

The objective of this limited test series with hypergolic propellants was
to determine whether a simple mixing technique could be used to obtain signif-
icant explosive yields when the propellants are cooled sufficiently to be
nonhypergolic.

The oxidizer and fuel were cooled in separate open-topped containers by
adding liquid nitrogen (LN_2) to each container. After a suitable cooling
period the oxidizer and remaining LN_2 were poured into the fuel container.
The intention was to initiate the mixture with a 32-lb TNT donor charge after
the LN_2 had evaporated, approximately 2-1/2 min after the original mixing.
In only one of the three tests, however, was this condition obtained. Brief
descriptions of each test are given below:
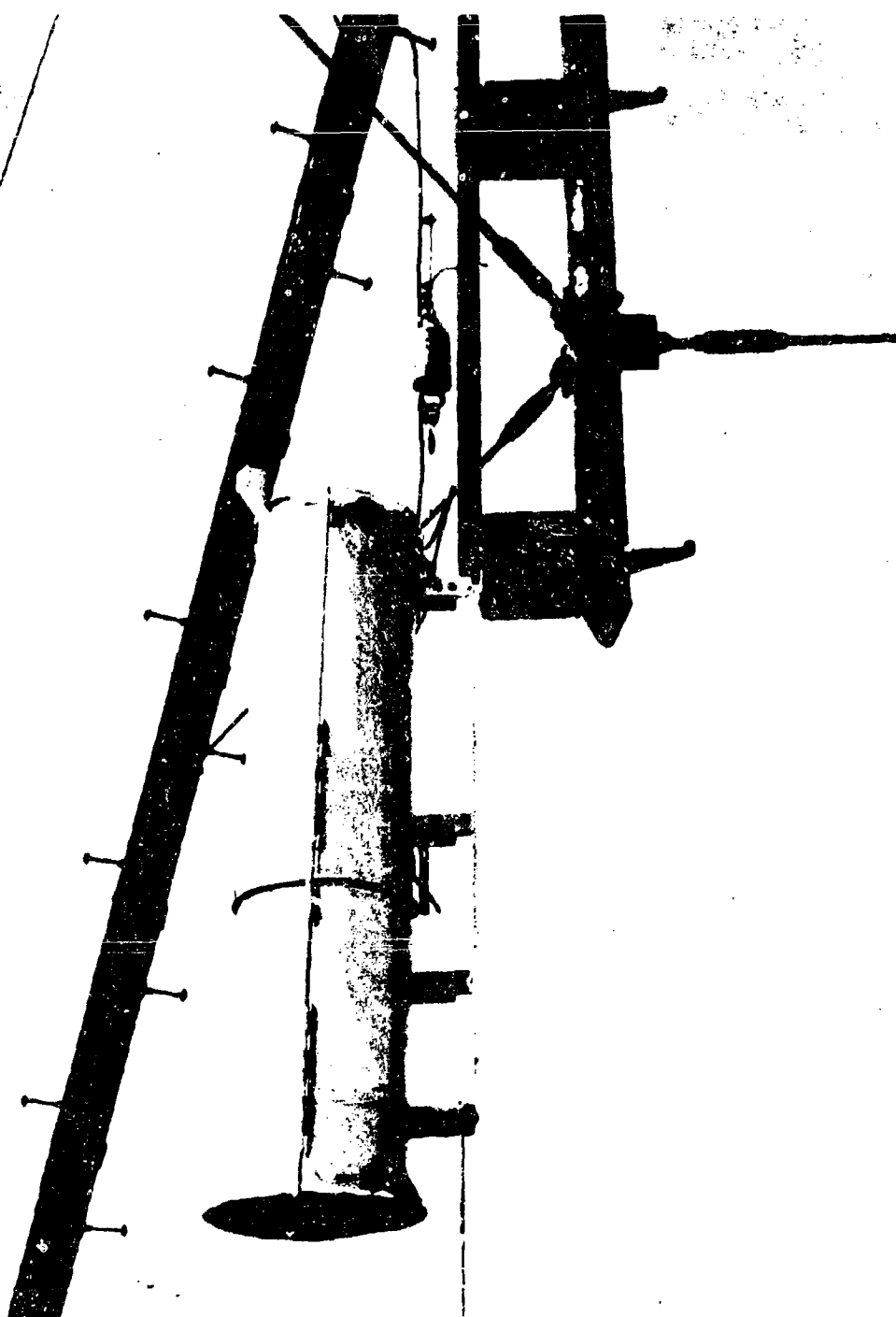
Fig. 4-21.   Typical Drop Tank and Guide Assembly

Table 4-5

TERMINAL YIELDS FOR HYPERGOLIC DROP TESTS

PROPELLANT WEIGHT (lb)	TEST NO.	TERMINAL YIELD (%)
	157	0.29
200	158	0.20
	159	0.30
	189	0.35
1000	257	0.30
	258	0.25

- **Test 033.** Explosion of the propellants occurred 5 sec after the propellants were united (and before the donor charge was initiated) due to a fire on the ground surface from spilled propellants. A posttest survey revealed sufficiently numerous TNT fragments to suggest that little, if any, of the explosive-donor charge detonated.

- **Test 034.** Failure of the oxidizer transfer system prevented mixing of the propellants, and the 32-lb charge was detonated to provide reference data for the other tests.

- **Test 037.** The frozen propellant mixture was initiated by detonating the 32-lb TNT donor charge 2-1/2 min after uniting the propellants.

In all tests the TNT charge, which was rectangularly shaped, was located on the ground just beneath the fuel tank. This tank was cylindrical with a diameter of 22 in. and was made of 1/16-in.-thick aluminum.

The blast environment was measured as described above under Explosive-Donor Tests.

The individual peak overpressure and positive-phase-impulse data and the computed explosive yields obtained from these data are presented in Volume 2.

The terminal yields for these tests were: Test 033, 8,8 percent; and Test 037, 13.7 percent. The terminal yield for Test 033 was computed by assuming that the donor charge did not contribute to the blast. The yield for Test 034 (donor charge only) agreed with the expected value for 32 lb. Thus the yield for Test 037 (donor charge and propellants) was obtained by subtracting 32 lb (the weight of the donor) from the total effective charge weight of the explosion. Since the two tests were not identical, the uncertainty in terminal yields for both test conditions was estimated, on the basis of the test-to-test reproducibility of other tests, to be about a factor of 2.

PART 2 - SUMMARY OF DATA FROM OTHER SOURCES

This part of the report presents the available information concerning the explosive potential of this hypergolic propellant combination as obtained from a number of experimental programs other than Project PYRO.

The various experimental programs can be divided into two general categories: those in which the propellant mixing generally simulated that which might occur from failure of full-scale vehicles and those special tests in which the propellant mixing mode did not correspond to any credible full-scale failure mode but rather was selected to study the influence of some particular parameter of the mixture on the explosive yield.[*]

The simulated failure mode tests can be further subdivided into two categories by the manner in which the propellants come into contact with each other:

1. **Diaphragm rupture.** In this case the propellants are initially in separate cylindrical tanks, one on top of the other, with either a common bulkhead or closely adjacent bulkheads. The failure is created by rapidly removing all or most of the bulkhead (or bulkheads) separating the two propellants, allowing reaction to occur within the remainder of the tankage. Two test programs have been conducted which fit in this category, one by Aerojet General (Ref. 4-4) and one by Martin Marietta (Ref. 4-5).

2. **Spill.** In this case the propellants are spilled from tanks, and interaction of propellants occurs external to the tank, generally on the underlying surface. The tanks initially are near the surface, so that the impact velocity of the fluids is generally low. Confinement of the spilled propellants varies from shallow basins on the ground to model silos. Five series of tests have been conducted which fit in this category, four by Rocketdyne (Ref. 4-6) and one by the U.S. Army Chemical Research and Development Laboratories (CRDL) (Refs. 4-7 and 8).

Three test series were conducted which were not intended to simulate any credible full-scale failure mode.[**] These are listed below:

a. **Aerojet high-interface-area tests (Ref. 4-9).** In this series the objective was to find the importance of interface area and oxidizer-to-fuel ratio on explosive yield.

---

[*] It should be noted that not all of the test series listed under the simulated failure mode category were specifically classified in that manner by the experimenters; however, it is the opinion of the authors of this report that they can be logically so considered.

[**] The initial interface area per unit volume of propellants used in series a and b is considered to be much greater than could be obtained in a credible full-scale failure and the quantities of propellants involved in series c were too small to be applicable.

b. <u>Aerojet detonation tests (Ref. 4-10)</u>. In this series, the objective
   was to determine whether steady-state detonation could be induced in
   well-mixed propellants.

c. <u>Atlantic Research Laboratory tests (Ref. 4-11)</u>. This series of tests
   was exploratory in nature and involved tests with milliliter quanti-
   ties of propellants.

SIMULATED FAILURE MODE TESTS

Diaphragm Rupture

Aerojet Diaphragm Rupture Tests* (Ref. 4-4)

This program consisted of two series of tests in which the propellants
were contained in a cylindrical tank separated by a diaphragm. The two sets
of tests differed basically in the mechanism employed to rupture the diaphragm
and in the propellant orientation.

For one set of tests, the propellant container was elevated to a height
of 15 ft. The upper section, which in this case contained the oxidizer, also
contained a vertically aligned rod or ram along the container axis. The entire
container was permitted to fall, and upon impact with the ground surface, the
impulse associated with the changing momentum of both the ram and the upper
propellant fractured the diaphragm (tempered glass). Near-total removal of
the diaphragm was achieved by a ring attached to the ram.

It is possible that continued motion of the ram influenced the propellant
reaction. Further, it is likely that the upper propellant retained some
fraction of its motion relative to the lower propellant upon diaphragm rupture.

For the other tests, in which the fuel was the upper propellant, dia-
phragm rupture was accomplished by the explosion of a linear charge that had
been formed into a circular loop and placed immediately above the diaphragm
(0.003-in. aluminum foil).

---

* In this disucssion only the basic overpressure and impulse data were obtained
from the original reference. All yield computations and error estimates were
made for this report.

The arc of the charge loop was just less than one complete circumference. Consequently a small arc remained uncut and acted as a diaphragm hinge, thereby insuring against propellant reaction influence by the diaphragm (the correctness of these statements was tested using water in the upper tank).

Flexible plastic tubing was placed over the linear charge in order to contain explosive fragments and prevent initiation of the fuel. The tubing permitted transfer of the shock wave in sufficient intensity to rupture the diaphragm without rupture of the tubing wall or damage to the tank walls.

For both test types, the container was 0.10-in.-thick aluminum with a diameter of 17-3/4 in.

The blast wave environment was measured by means of an array of 12 piezoelectric gauges located 10, 25, and 40 ft from ground zero along four radial lines at 90 deg to each other.

Calibration tests were conducted with cylindrical, 5-lb TNT and composition C-4 charges and 25-lb TNT charges, which were positioned near the ground surface. The authors of Ref. 4-4 stated that a comparison of the calibration test results with the data of Ref. 4-2 indicated a negligible difference a' all gauge distances.

Two tests for each failure mode were conducted, although for one of the linear charge tests, the results were of insufficient magnitude to record. All tests were with 300 lb total propellant, a propellant length-to-diameter ratio of 1.6:1, and an oxidizer-to-fuel weight ratio of 2:1.

Prop '' . . t . esults in terms of peak overpressure and positive phase impulse are given in Table 4-6. Explosive yields relative to a TNT surface burst were computed from the average overpressure and impulse at each distance for each test and a1   isted in Table 4-7.

For the two drop tests it is evident that there was a slight but fairly consistent tendency for yield to increase with distance over the range from 10 to 25 ft. Accordingly, terminal yield values for each test were computed

Table 4-6

PEAK OVERPRESSURE AND POSITIVE-PHASE-IMPULSE DATA
FROM AEROJET DIAPHRAGM RUPTURE TESTS

Test Type	Test No.	Gauge Line	Distance (ft)					
			10		25		40	
			Pressure (psi)	Impulse (psi-ms)	Pressure (psi)	Impulse (psi-ms)	Pressure (psi)	Impulse (psi-ms)
Drop	7	1	1.8	5.4	0.8	2.0	0.5	1.6
		2	9.7	12.1	2.1	3.6	1.0	2.1
		3	8.2	9.3	2.5	5.8	1.1	2.2
		4	2.0	6.2	1.0	2.1	0.6	1.3
		Avg	5.4	8.3	1.6	3.6	0.8	1.8
Drop	8	1	3.0	10.4	1.3	5.4	0.8	3.3
		2	10.1	13.0	3.6	6.6	1.9	4.2
		3	17.0	21.7	4.8	7.7	2.5	4.7
		4	5.0	10.2	2.8	5.0	1.5	2.9
		Avg	8.8	13.8	3.1	6.2	1.7	3.8
Linear Charge	4	1	0.5	*	0.3	*	0.4	*
		2	0.5	*	0.2	*	0.1	*
		3	0.5	*	0.2	*	0.1	*
		4	0.6	*	0.2	*	0.1	*
		Avg	0.5	*	0.2	*	0.2	*

* No impulse values were obtained due to low overpressure values.

Table 4-7

EXPLOSIVE YIELDS FROM
AEROJET DIAPHRAGM RUPTURE TESTS

Test Type	Test No.	Basis of Computation	Yield (%) at Indicated Distances (ft)			Terminal Yield (%)
			10	25	40	
Drop	7	Pressure	0.12	0.16	0.14	0.24
		Impulse	0.33	0.37	0.31	
Drop	8	Pressure	0.37	0.65	0.74	0.80
		Impulse	0.83	0.89	0.91	
Linear Charge	4	Pressure	0.001	0.002	0.007	0.007
		Impulse	-	-	-	

by averaging the overpressure and impulse data from the 25- and 40-ft stations. The resulting values were 0.24 percent for Test 7 and 0.80 percent for Test 8. It may be noted that the overpressure and impulse values for Test 8 were within about 25 percent of each other, while for Test 7 the overpressure yield was less than one-half of the impulse yield.

Although there was considerable variability in the four gauge readings at each distance for the drop tests, the major source of error in yield estimation for this test condition again appears to be the test-to-test reproducibility of the blast phenomena. Based on the difference in terminal yield between the two tests, a factor of 3.3, it is estimated that the mean terminal yield for the two shots, 0.52 percent, is uncertain to a factor of about 3 or 4.

For the one linear charge test there was a tendency for yield to increase with distance over the entire range so that the terminal yield was taken to be the yield of the last station. The resulting terminal yield for this test condition, 0.007 percent, is estimated to be uncertain by a factor of about 5.

One-Half-Scale Titan II First-Stage Destruct Test* (Ref. 4-5)

The half-scale model tanks used in this test were 5-ft-diameter cylinders with domed ends. The upper tank, containing 21,500 lb of oxidizer, was approximately 15 ft long and the lower tank, containing 11,200 lb of fuel, was approximately 13 ft long. The separation between tanks was about 2 ft.

Failure of the tankage was induced by simultaneously rupturing the bottom dome of the top tank and the top dome of the bottom tank with a linear-shaped charge containing approximately 0.5 lb of explosive. The linear charge was arranged to rupture a minimum of 75 percent of the tank domes.

The blast environment was measured with eight pressure transducers ranging from approximately 10 to 300 ft from the test tankage. Five of the transducers were mounted on a frame surrounding the test tankage and were

---

*In this discussion only the basic overpressure values were obtained from the original reference. All correction factors, yield computations, and error estimates were made for this report.

within 20 ft of the tankage. The remaining three transducers were mounted at a height of 23 ft above the ground on one radial line at ground distances of 61, 141.9, and 300.5 ft from the center of the tankage.

The propellant reaction following rupture of the tankage produced two separate explosions, both of which were stated to have occurred in the vapor phase. One occurred at approximately 3.1 sec after the initial destruct action, and the other occurred at approximately 4.3 sec after the destruct action. The position of the explosions could not be determined very accurately. The center of the 3.1-sec explosion was estimated to be at a height of about 28 ft and about 20 ft in a horizontal direction from the centerline of the tank, and that for the 4.3-sec explosion, at a height of about 40 ft and about 5 ft horizontally from the centerline of the tank.

Because of the uncertainty in the location of the centers of the two explosions, the pressure data obtained from the five close-in transducers was not suitable for estimating the yields of the two explosions. The low magnitudes of the peak pressure values obtained at these stations, however, which ranged from 3 to 10 psi, certainly support the postulate of a low-energy-density reaction.

The pressures measured at the three long-distance stations for each explosion are given in Table 4-8.

Since the pressure measurements were made well above the ground surface and since the height of the explosion was also well above the ground surface, it was necessary to use two special reference curves in computing yields. From the assumed geometry it is concluded that Station 6 was at a distance where Mach reflection was just starting, so that the gauge (23 ft above the ground) was well above the triple point and in the region where the incident and reflected wave fronts were separate. At the distance of Station 7 the triple point had increased in height but still should have been below the gauge. Station 8 was well in the Mach reflection region, and the triple point should have been significantly higher than the gauge.

Table 4-8

PEAK OVERPRESSURE DATA FROM ONE-HALF-SCALE
TITAN II FIRST-STAGE DESTRUCT TEST

Gauge Station	Nominal Ground Distance (ft)	Explosion[1]	Estimated Actual Distance[2] (ft)	Peak Over-Pressure (psi)	Yield (%)
6	61.0	3.1	48	3.0	0.1
		4.2	60	5.0	0.4
7	141.9	3.1	128	1.0	0.2
		4.2	140	1.1	0.3
8	300.5	3.1	287	0.5	0.1
		4.2	297	1.3	0.9

1. Refers to 3.1-sec or 4.2-sec explosion.

2. For stations 6 and 7, value is slant distance from the point of
    explosion to the gauge; for station 8, it is the ground distance
    from the point of explosion to the gauge.

It is assumed that the peak overpressure values reported for Stations 6 and 7 corresponded more nearly to the incident or free-air values rather than the reflected values seen at ground level. Accordingly in computing yields, which are also given in Table 3-8, a free-air pressure-distance TNT curve (Ref. 4-12) was used for the data from Stations 6 and 7.

Station 8 was well below the triple point, so that the pressures from this station should correspond fairly well to those at ground level. The explosions, however, were too far off the ground surface to allow use of the TNT surface burst reference curve. Actually the explosions in the two previous diaphragm rupture cases also were not truly surface bursts, but in most cases they were estimated to be at a height of burst of less than 1 or 2 $ft/lb^{1/3}$. In the present case the best estimate of the scaled height of burst is of the order of 5 to 6 $ft/lb^{1/3}$. To maintain consistency in the analysis of these data with the two previous sets, the yields for Station 8 were first computed using the same surface burst reference curve and then reduced by a factor of 2.3 to account for the difference between a 5-$ft/lb^{1/3}$ and a 1-$ft/lb^{1/3}$ height of burst. This correction factor was based on data given in Fig. 3.67b of Ref. 4-13 for the pressure region of 1 psi.

Prior to computing yields it was also necessary to correct the overpressures to their equivalent sea level values by means of Sachs' scaling law (Ref. 4-15). (These tests were conducted at an atmospheric pressure of 11.7 psi and the reference data are for 14.7 psi.)

Because of the data scatter, it is difficult to be sure whether there is any significant tendency for the yield to increase with distance or not. However, since primary interest is in the 4.2-sec explosion (the largest), which has some of this tendency, the estimated terminal yield value for this test, 0.6 percent, was obtained in a conservative (high) fashion by averaging only the values from the last two stations.

Considering the small number of useful gauge readings (2), the small yield values, the lack of impulse data, the variability in results from gauge to gauge (factor of 3), and the fact that only one test was conducted, it is estimated that the terminal yield value has an uncertainty of a factor of 2 or 3.

Spill Tests

Rocketdyne Small-Scale Spill Tests* (Ref. 4-6)

This test program consisted of two separate series of tests, the first using straight hydrazine and the second a 50/50 mix of UDMH-hydrazine. In general, the experimental arrangement was quite similar for both. Approximately 2.5 lb of propellant were fed through separate 1/2-in. lines under a pressure of 30 to 50 psi into a concrete spill basin 6 in. deep.

In the first series, the basin had a 2- by 2-ft cross section and the spill lines discharged the propellants from about 1 ft above the surface so that they impinged on the basin within a radius of 2 in. The parameters varied in the tests were the nature of the surface of the basin (concrete, asphalt, dirt, or water) and the order in which the propellant flows were started (simultaneous or lead of one propellant by the other by about 1 sec).

In the second series of tests, the concrete spill basin was 4 by 4 ft in cross section and the spill lines were 8 in. above the surface, arranged so that the propellants impinged on the basin within a radius of 2 to 4 in. The parameter variation included the nature of the surface of the basin (concrete, dirt, or water) and the order in which propellant flows started (simultaneous or lead of one propellant by the other by 0.5 - 1.0 sec).

In both series of tests, pressures were measured with two Photocon microphone pickups, at distances of 10 and 15 ft, mounted face-on to the center of the basin at a height of 1 ft.

The propellant combinations ignited within a few milliseconds after contact under all conditions tested. A series of explosions was recorded in most cases. The pressure values for the largest explosion on each test of the first series are given in Table 4-9 along with the corresponding yields computed by means of

---

* In this discussion only the basic overpressure data were obtained from the original reference. All yield computations, statistical analyses, and error estimates were made for this report.

Table 4-9

PEAK OVERPRESSURE AND EXPLOSIVE YIELD DATA FROM THE FIRST
SMALL-SCALE SPILL TEST SERIES

Test No.	Surface	Order of Spill	Propellant Wt (lb)[1]	Pressure (psi)[2]		Yield (%)		Terminal Yield (%)
				10 ft	15 ft	10 ft	15 ft	
55	Concrete	Simultaneous	1.5/1.0	0.82	0.33	0.06	0.03	0.04
56	Concrete	Fuel lead	1.5/1.3	2.0	1.81	0.38	1.0	0.69
57	Concrete	Oxidizer lead	2.0/1.0	1.0	0.67	0.07	0.11	0.09
58	Asphalt	Simultaneous	1.5/1.3	No detectable explosion				
59	Asphalt	Fuel lead	1.5/1.3	1.54	0.67	0.21	0.11	0.16
60	Asphalt	Oxidizer lead	2.0/1.0	1.23	0.71	0.12	0.12	0.12
61	Dirt	Simultaneous	1.5/1.0	1.46	0.76	0.21	0.17	0.19
62	Dirt	Fuel lead	1.5/1.3	1.91	1.62	0.34	0.80	0.57
63	Dirt	Oxidizer lead	2.0/1.0	1.73	1.24	0.23	0.41	0.33
64	Water	Simultaneous	1.5/1.9	1.82	1.23	0.35	0.53	0.44
65	Water	Fuel lead	1.5/1.3	1.23	0.62	0.13	0.10	0.12
66	Water	Oxidizer lead	4.0/2.0	1.05	0.43	0.04	0.02	0.03

1. First number refers to oxidizer weight, second number to fuel weight.

2. Pressures are peak reflected overpressures.

a surface-burst TNT reference curve.[*] The results of the second test series
are given in a similar fashion in Table 4-10. The investigators reported that
(based on examination of high-speed photography) all explosions occurred in
the vapor phase.

It is apparent from Tables 4-9 and 4-10 that there is no consistent trend
for yields to increase from 10 to 15 ft, although the average yield at 15 ft is
somewhat greater than that at 10 ft. Accordingly, terminal yield values were
obtained by averaging the two data points.

The data in Table 4-9 suggest that a fuel lead or dirt surface tends to
give the highest yields and that an oxidizer lead or asphalt surface tends to
give the lowest yield. However, since there were no repeat tests or calibration
data reported, it is difficult to be sure whether the observed differences are
significant. In an effort to estimate the significance of the effects and the
reproducibility of results, the data given in Table 4-9 were treated as a single
replicate factorial design, and an analysis of variance was performed (with the
type of surface and order of propellant release the two variables) on the
assumption of no interaction between variables. The results, which were computed
separately for each gauge station, indicated that statistically, with the above
assumptions, there was no significant effect of either the type of surface or
order of flow. The calculated remainder standard deviations (expressed as
percentages of the mean values) were 70 and 110 percent for the 10- and 15-ft
stations, respectively.

The data in Table 4-10 are consistent with those from Table 4-9 in regard
to the effect of the order of flow; however, they suggest that a concrete surface
gives higher yields than the dirt surface, which is in contrast to the trend
indicated by Table 4-9. Because of the similarity of test conditions in the two
test series, it is assumed that they both have the same uncertainty and that the

---

* The authors of Ref. 4-6 reported that photographic evidence indicated the
  explosions occurred from 2 to 4 ft off the surface. Thus the use of a surface
  burst reference curve may not be appropriate even though the liquid propellants
  were on the surface. It was used, however, to maintain consistency throughout
  all spill test series. (In the other series no comments were made regarding
  the explosion height of burst.)

Table 4-10

PEAK OVERPRESSURE AND EXPLOSIVE YIELD DATA FROM THE
SECOND SMALL-SCALE SPILL TEST SERIES

Test No.	Surface	Order of Spill	Propellant Wt (lb)[1]	Pressure (psi)[2] 10 ft	15 ft	Yield (%) 10 ft	15 ft	Terminal Yield (%)
1	Concrete	Simultaneous	1.5/1.0	1.67	-	0.28	-	0.28
2	Concrete	Simultaneous	1.5/1.0	1.63	0.67	0.27	0.13	0.20
3	Concrete	Oxidizer lead	2.0/0.5	No overpressures recorded		No overpressures recorded		
4	Concrete	Fuel lead	1.0/1.5	1.67	1.41	0.28	0.66	0.47
5	Dirt	Simultaneous	1.5/1.0	1.17	0.60	0.13	0.10	0.12
6	Dirt	Oxidizer lead	2.0/0.5	0.55	0.40	0.02	0.04	0.03
7	Dirt	Fuel lead	1.0/1.5	0.77	0.52	0.05	0.07	0.06
8	Water covered concrete	Simultaneous	1.5/1.0	0.87	0.44	0.07	0.05	0.06
9	Water covered concrete	Fuel lead	1.0/1.5	No overpressures recorded				

1. First number refers to oxidizer weight, second number to fuel weight.

2. Pressures are peak reflected overpressures.

observed differences in Table 4-10 are no more significant than those for
Table 4-9. Accordingly, an average terminal yield was computed for all data
for each test series. The result is 0.25 percent for Table 4-9 and 0.18 percent
for Table 4-10. Considering the fact that only two data points were available
for each test, that no calibration data were reported, and that no impulse
data were available, it is estimated that these average yield values are uncertain
to about a factor of 2 or 3.

CRDL Suppression Tests[*] (Refs. 4-7 and 4-8)

In this test series, the primary objective was to determine the effectiveness
of water deluge and water fog systems in suppressing the fire and fumes resulting
from "spilled" propellants. Blast data were of secondary concern, so that only
a single pressure transducer, located near the ground 50 ft from the center of
the reaction pan, was used.

The propellants were fed through separate 1-1/2-in. lines oriented 180
deg to each other, so that initial fuel and oxidizer contact occurred before
the propellants had an opportunity to disperse on the surface. The pipe
nozzles were slightly off the ground and 2 ft from the center of a 16- by
16- by 1-ft-deep reaction pan.

The water deluge system was located on the interior perimeter of the
reaction pan and consisted of a 2-in. feed pipe with twelve 1-in. outlets
equally spaced around the pan. These outlets could, for example, deliver
water at a rate of 415 gal/min at an outlet pressure of 48 psig.

The water fog system consisted of thirty-six 1-in. fog nozzles arranged
in three tiers at heights of 2, 10.5, and 17.5 ft above the outside perimeter
of the reaction pan, each tier having twelve equally spaced nozzles. This sytem
could, for example, deliver water at a rate of 800 gal/min at a nozzle pressure
of 48 psig.

---

* In this discussion only the basic overpressure data were obtained from the
 original reference. All yield computations, statistical analyses, and error
 estimates were made for this report.

Tests were conducted for a range of total propellant weights from 90 to 300 lb and with and without the water deluge and fog suppression. The propellant flow durations ranged from about 6 sec for the 90-lb tests to about 20 sec for the 300-lb tests. It should be noted that the suppression systems were usually started about 6 to 7 sec after the propellant flows started, so that for an appreciable portion of the flow duration, the propellants were actually unsuppressed.

Because of the long durations of flow in this test series, it did not seem appropriate to compute yields with the total propellant quantity. Instead, yields were calculated by means of the estimated amount of propellant delivered in a 1-sec period, a time corresponding approximately to that used for the other spill test series. The best estimate of the amount of propellant delivered in 1 sec is 15 lb; however, this value is uncertain to about a factor of 1.5 to 2.0.

Peak overpressures and explosive yields (in both pounds and percent) for each test are listed in Table 4-11.

In an effort to estimate the significance of the variables (i.e., propellant weight and degree of suppression), average yields were computed for each test condition. These average yields were then treated as a single replicate factorial design and an analysis of variance was performed on the assumption of no interaction between variables. The results indicated that statistically, with the above assumption, there was no significant effect of propellant weight or degree of suppression. The calculated remainder standard deviation (expressed as a percent of the mean value) was 50 percent.

Considering the fact that only one data point was available from each test, that no impulse data or calibration data were reported, and that the yields were very small, it is estimated that the average yield for these tests, 0.02 percent, is uncertain to a factor of about 4 to 5.

Table 4-11

PEAK OVERPRESSURE AND EXPLOSIVE YIELD DATA FROM CRDL SUPPRESSION TESTS

Prop Wt (lb)	Reaction Suppressed-Unsuppressed	Test No.	Pressure (psi)	Effective Charge Wt (10^{-3} lb)	Yield (%)
90	U	5	0.07	4.4	0.029
		15	0.05	2.2	0.015
	S	4	0.045	1.7	0.011
		6	0.045	1.7	0.011
120	U	7	No results		
		8	0.06	3.2	0.021
	S	9	0.065	3.8	0.025
150	U	10	Instrument Failure		
		11	0.04	1.3	0.009
	S	12	0.02	0.3	0.002
210	U	13	0.03	0.7	0.005
		16	0.09	7.4	0.049
		21	0.04	1.3	0.009
		22	0.05	2.2	0.015
	S	17	0.065	3.6	0.024
		18	0.035	1.0	0.007
		19	0.05	2.3	0.015
		20	0.035	1.1	0.007
		23	0.06	2.9	0.019
240	U	27	0.04	1.3	0.009
		31	0.06	3.2	0.021
	S	28	0.045	1.7	0.011
		29	0.08	5.7	0.038
		30	0.04	1.3	0.009
270	U	32	0.05	2.2	0.015
		33	0.06	3.2	0.021
		34	0.09	7.4	0.049
	S	35	0.045	1.7	0.011
300	U	36	0.06	3.2	0.021
		37	0.12	13.0	0.087
		38	0.05	2.2	0.015
	S	39	0.05	2.2	0.015
		40	0.045	1.7	0.011
		41	0.04	1.3	0.009
		42	0.03	1.1	0.007

Rocketdyne Model-Missile Spill Tests[*] (Ref. 4-6)

This program consisted of scale-model missile spills in which the propellants were initially contained in separate cylindrical tanks with the oxidizer on top and allowed to fall to the underlying surface by pneumatically removing the bottom plate of the tank. The tank sizes used corresponded to 1/18 and 1/10 linear scale models of the Titan II (scaled by volume only). The 1/18-scale tank, which was 8.5 in. in diameter and 14 in. high, contained 50 lb of propellant with an oxidizer-to-fuel weight ratio of 2:1 and the 1/10-scale tank, which was 12 in. in diameter and 36 in. high, contained 300 lb of propellant at the same oxidizer-to-fuel ratio. On the 1/18 scale the tanks were separated by approximately 28 in. and on the 1/10 scale by 24 in. Neglecting this spacing, the effective L/D of the 1/18-scale tanks is about 3.3:1 and that for the 1/10 scale about 6:1.

The spill tests were performed in 1/18- and 1/10-scale silo models and aboveground in a steel tray approximately 20 by 20 by 2 ft deep. The silo dimensions were 3 ft in diameter by 9 ft deep and 5 ft in diameter by 15 ft deep for the 1/18-scale and 1/10-scale silos, respectively.

Pressure measurements were made at ground level on one gauge line at distances of 25, 35, 50, and 75 ft from the center line of the tanks.

Other variables included in the testing were the order in which propellants were released from the tanks (simultaneous as well as oxidizer and fuel leads) and the silo environment prior to spill (burning fuel, light oxidizer and fuel vapors, and water in the bottom).

The pressure data obtained from these tests are given in Table 4-12. In cases where multiple explosions occurred, only the data from the largest are given. Only data from the 25- and 75-ft stations are included since the authors of Ref. 4-6 indicate that the data from the 35- and 50-ft stations could not be trusted. Yield values computed using a surface burst TNT curve are also given in this table.

---

[*] In this discussion only the basic overpressure data were obtained from the original reference. All yield computations and error estimates were made for this report.

It can be seen from Table 4-12 that in all cases yield values were
increasing up to the 75-ft station, so that the data from this station represent
the best estimate of the terminal yield values.

Several TNT calibration shots were also performed as part of this test
series. The overpressure values and yields computed by means of a surface
burst reference curve are included in Table 4-12. The results from the one
above-surface test indicate that the instrumentation system is reading high by
almost a factor of 2.

Only one repeat TNT calibration shot and one repeat propellant test were
available to estimate the reproducibility of the instrumentation system and
the test-to-test blast phenomena. The repeat calibration shot was for the
silo geometry. They showed a difference of 40 percent in yield. The repeat
propellant tests (12 and 15) were also for a silo geometry. They showed a
difference of about 15 percent in yield.

Considering that the terminal yield values are based on one gauge reading,
that the yields are very small, that the results from the calibration shots
differed by a factor of almost 2 from the standard curve, and that no impulse
data were available, it is estimated that the absolute values of the terminal
yields are uncertain to about a factor of 3 or 4. On a relative basis, the
results are probably uncertain to a factor of 2 or 3.

Rocketdyne Large-Scale Spill Tests[*] (Ref. 4-6)

In these two tests the propellants were contained in separate 150-gal
cylindrical tanks, 30 in. in diameter and approximately 60 in. in length. The
tanks were positioned adjacent to each other with their cylindrical axes tilted
20 deg from the vertical so that the propellants discharging from a 6-in. port
at the bottom of the tank would impinge in the center of 20- by 20- by 2-ft
deep spill tray.

---

[*] In this discussion only the basic overpressure data were obtained from the
original reference. All yield computations and error estimates were made for
this report.

Table 4-12

PEAK OVERPRESSURE AND EXPLOSIVE YIELD DATA
FROM THE MODEL-MISSILE TESTS

Test No.	Scale	Order of Spill	Overpressure (psi)		Yield (%)	
			25 ft	75 ft	25 ft	75 ft
ABOVEGROUND						
7	1/10	60-sec fuel lead		No explosion		
8	1/10	2-sec oxid lead	0.5	0.16	0.01	0.03
9	1/10	60-sec oxid lead		No explosion		
10	1/10	60-sec oxid lead		No explosion		
11	1/10	Simultaneous	1.0	0.36	0.05	0.15
		10 lb TNT	11.0	1.92	180	190
STEEL SILO						
12	1/18	Simultaneous	0.9	0.32	0.27	0.73
13	1/18	30-sec oxid lead	0.85	0.28	0.24	0.55
14	1/18	Simultaneous into burn fuel	0.8	-	0.20	-
15	1/18	Simultaneous	0.85	0.3	0.24	0.63
16	1/18	Simultaneous into 50 lb of water	0.6	0.15	0.11	0.14
17	1/10	1-sec oxid lead	2.0	2.0*	0.26	-
18	1/10	Simultaneous with light oxid vapor	2.5	0.65	0.43	0.56
19	1/10	180-sec fuel lead		No explosion		
20	1/10	Simultaneous with light fuel vapors	1.25	0.4	0.09	0.20
		1.5 lb TNT	2.70	0.6	98	93
		2.0 lb TNT	3.63	0.8	138	134

* Assumed to be spurious reading and not included in yield computation.

The propellants were released by rupturing a thin diaphragm in the 6-in. port. The tanks were pressured to 50 psia to assure rapid expulsion of the propellants.

Pressures were measured with gauges at ground level at distances of 25, 50, and 75 ft.

In the first test, 300 lb of fuel and 1300 lb of oxidizer were used. The diaphragms were ruptured simultaneously, and the fuel was emptied in less than 0.5 sec and the oxidizer in 1.5 sec. After 2 sec, a water deluge system was actuated which delivered 100 gal/min into the spill tray. Several weak explosions were audible at a distance of 1,000 ft; however, the blast instrumentation did not detect these small overpressures.

In the second test, 500 lb of fuel and 800 lb of oxidizer were used, and again the diaphragms were ruptured simultaneously. The fuel was emptied in approximately 0.625 sec and the oxidizer in 0.75 sec. Multiple explosions were obtained, the largest yielding peak overpressures of 2.2 and 0.67 psi at the 25- and 75-ft stations, respectively. These correspond to yields of 0.08 and 0.14, respectively. (The authors of Ref. 4-6 indicated that the data from the 50-ft station was not usable.)

As in the previous test series the data from the last station was taken as the best estimate of terminal yield. One 6-lb and one 12-lb TNT calibration shot were also performed as part of this test series. The pressure values for the 6-lb shot were 4.0 and 1.02 psi at the 25- and 75-ft stations, respectively, and those for the 12-lb shot, 6.0 and 1.2 psi. These pressure values correspond to yield values ranging from 53 to 77 percent computed by means of the surface-burst TNT reference curve.

Considering that the terminal yield estimate is based on one gauge reading, that the yields are very small, that the results for the calibration shots differed by almost a factor of 2 from the standard curve, and that no impulse data were available, it is estimated that the absolute value of the terminal yield is uncertain to a factor of about 3 or 4.

SPECIAL TESTS

Aerojet High-Interface-Area Tests[*] (Ref. 4-9)

The objective of this program was to determine the influence of the initial interface area between oxidizer and fuel and the oxidizer-to-fuel weight ratio on explosive yield.

In these tests the oxidizer was contained in a number of small cylindrical glass Dewars placed in an aluminum pan containing the fuel. Propellant mixing was accomplished by dropping the pan a distance of 10 to 15 ft onto a steel plate, thereby shattering the Dewars.

Use of various Dewar sizes permitted variation of oxidizer-to-fuel ratio and initial interface area (defined as that area obtained by using the mean radius of the double wall of the glass Dewars). Tests were performed using three different contact areas for each of three oxidizer-to-fuel weight ratios, 3:1, 2:1, and 1:1. The three contact areas were slightly different for each oxidizer-to-fuel ratio; however, in each case the three values were in the order of 1:2:4.

The blast environment was measured with an array of 12 piezo-electric gauges located at 10, 25, and 40 ft from ground zero along four radial lines at 90 deg to each other.

Calibration tests were conducted with cylindrical 5-lb TNT and composition C-4 charges and 25-lb TNT charges, which were positioned near the ground surface. The authors stated that a comparison of the calibration test results with the data of Ref. 4-2 indicated a negligible difference at all gauge distances.

Peak overpressures and positive-phase impulses from each of the propellant tests are given in Table 4-13 and the corresponding explosive yields computed by means of a surface-burst TNT reference curve in Table 4-14.

---

[*] In this discussion only the basic overpressure and impulse data were obtained from the original reference. All yield computations and error estimates were made for this report.

Table 4-13

PEAK OVERPRESSURE AND POSITIVE-PHASE-IMPULSE DATA
FROM AEROJET HIGH-INTERFACE-AREA STUDY
(Oxidizer-to-Fuel Weight Ratio = 1:1)

Interface Area (sq ft)	Gauge Line	Distance (ft)					
		10		25		40	
		P	I	P	I	P	I
8.88	1	4.2	25.6	2.1	12.3	1.5	10.5
	2	3.3	23.0	2.5	17.4	1.1	8.0
	3	3.6	20.7	2.2	12.3	1.6	9.7
	4	5.0	33.6	3.0	13.9	2.1	9.3
	Avg	4.0	25.7	2.5	14.0	1.6	9.4
18.0	1	11.9	67.3	8.0	43.2	4.6	27.3
	2	13.5	91.5	6.7	32.4	3.1	17.3
	3	12.2	62.3	7.1	37.3	4.6	22.1
	4	11.5	69.7	8.9	44.7	4.3	19.3
	Avg	12.3	72.7	7.7	39.4	4.2	21.5
35.9	1	52.8	144.0	24.9	73.9	11.5	55.4
	2	75.8	172.0	34.2	81.5	10.9	39.8
	3	56.5	131.0	22.2	62.9	11.4	43.6
	4	75.0	147.0	28.5	82.4	13.7	52.1
	Avg	65.0	148.3	27.5	75.2	11.9	47.7

P - Peak Overpressure, psi

I - Positive-Phase Impulse, psi-msec

Table 4-13 (Cont.)
(Oxidizer-to-Fuel Weight Ratio = 3:1)

Interface Area (sq ft)	Gauge Line	Distance (ft)					
		10		25		40	
		P	I	P	I	P	I
12.6	1	4.4	26.8	2.3	12.0	1.3	8.6
	2	*	*	2.5	12.0	1.4	7.3
	3	5.2	28.8	2.3	10.5	1.5	7.5
	4	5.0	26.9	2.5	14.0	1.8	7.5
	Avg	4.9	27.5	2.4	12.1	1.5	7.7
25.4	1	21.7	95.2	10.3	39.5	5.4	29.5
	2	16.3	85.5	13.2	52.5	4.9	23.1
	3	19.5	84.3	10.3	29.7	5.5	24.7
	4	———	———	11.0	34.5	6.7	25.5
	Avg	19.2	88.3	11.2	39.1	5.5	25.7
51.0	1	97.6	*	30.3	80.1	14.5	58.4
	2	85.0	186.0	36.0	89.9	10.8	43.7
	3	103.9	*	20.4	55.2	12.3	43.2
	4	103.1	147.0	26.3	72.2	15.0	51.6
	Avg	97.2	166.5	28.3	74.4	13.2	49.2

P - Peak Overpressure, psi

I - Positive-Phase Impulse, psi-msec

* - Gauge damaged by fragments

—— - No Gauge

Table 4-13 (Cont.)

(Oxidizer-to-Fuel Weight Ratio = 2:1)

Interface Area (sq ft)	Gauge Line	Distance (ft)					
		10		25		40	
		P	I	P	I	P	I
11.4	1	2.4	21.5	1.7	12.7	1.2	8.7
	2	3.2	29.3	2.2	16.6	1.0	6.6
	3	4.0	25.4	1.9	12.3	1.1	7.3
	4	3.2	26.1	2.0	12.2	1.4	8.4
	Avg	3.3	25.6	2.0	13.5	1.2	7.8
22.9	1	22.9	103.1	10.5	45.8	5.8	33.2
	2	20.2	92.5	13.7	58.1	5.4	26.2
	3	19.4	80.6	9.8	41.8	5.7	28.1
	4	*	*	10.1	40.6	6.7	29.7
	Avg	20.8	92.1	11.0	46.6	5.9	29.3
45.5	1	52.6	163.0	23.9	77.9	10.7	54.4
	2	52.9	104.0	35.7	106.0	10.0	49.4
	3	81.3	133.0	19.1	55.8	11.1	50.3
	4	70.7	*	23.9	*	14.5	47.6
	Avg	64.4	133.3	25.9	79.7	11.6	50.4

P - Peak Overpressure, psi

I - Positive-Phase Impulse, psi-msec

* - Gauge damaged by fragments

Table 4-14

EXPLOSIVE YIELDS FROM AEROJET HIGH-INTERFACE-AREA STUDY

Oxidizer-to-Fuel Weight Ratio	Oxidizer-Fuel Interface Area (ft²)	Basis of Computation	Yield (%) at Indicated Distance (ft)			Terminal Yield Estimate (%)
			10	25	40	
1:1	8.88	Pressure	0.07	0.42	0.65	2.0
		Impulse	2.5	2.9	3.4	
	18.0	Pressure	0.47	3.5	4.8	8.5
		Impulse	15.2	17.3	11.1	
	35.9	Pressure	5.0	25.0	29.3	34
		Impulse	52.7	53.0	42.3	
2:1	11.4	Pressure	0.05	0.27	0.34	1.6
		Impulse	2.5	2.6	2.5	
	22.9	Pressure	1.1	6.2	8.7	12.4
		Impulse	22.5	23.0	17.2	
	45.5	Pressure	4.9	22.6	27.3	36
		Impulse	43.7	56.6	47.4	
3:1	12.6	Pressure	0.10	0.39	0.56	1.5
		Impulse	2.9	2.4	2.5	
	25.4	Pressure	0.93	6.5	7.8	12.0
		Impulse	21.4	16.9	14.8	
	51.0	Pressure	8.2	25.2	33.0	40
		Impulse	63.3	51.0	45.4	

From Table 4-14 it can be seen that the pressure yields are increasing with distance over the entire distance range, that the impulse yields are generally decreasing with increasing distance (except for the smallest-interface-area cases), and that although the pressure and impulse yields are converging towards each other, the impulse yields at the farthest station are still considerably greater than the pressure yields. This yield-distance behavior is similar to that obtained in the AFRPL impact tests, and the terminal yields given in Table 4-14 were estimated in the same fashion as described for the impact tests.

The lack of duplicate tests in this test series makes it difficult to estimate the uncertainty in the results. The stated good agreement between the expected and measured results from the calibration shots and the generally good agreement between results from the four gauges at a given distance suggest that errors due to the instrumentation system or blast asymmetries are small. The fact that terminal yield conditions were not reached within the measuring range and had to be estimated by extrapolation introduces some uncertainty in the terminal yield values. This uncertainty is particularly large for the smallest interface-area tests, since the impulse yields at the greatest measuring distance were still about a factor of 5 to 7 greater than the pressure yields. For the intermediate- and high-interface-area cases, the differences were about factors of 2 and 1.5, respectively. Based on these differences and the test-to-test reproducibility obtained in other test series, it is estimated that the terminal yields for the highest-interface-area cases are uncertain to about a factor of 1.5, those for the intermediate-area cases to about a factor of 2, and those for the smallest areas about a factor of 3 to 4.

Aerojet Detonability Tests[*] (Ref. 4-10)

This test series consisted of 11 detonability tests using 130 to 140 lb of propellant. The test setup consisted of a vertical Plexiglas tube, 9-13/16 in. ID by 42 in. long with a 1/8-in.-thick wall, containing 11 test tubes approximately 45 in. long fabricated from 47-mm ID Pyrex tubing of 2-mm wall thickness. The Plexiglas tube was pressed onto a ring of Presstite putty on a

---

* In this discussion the basic overpressure and explosive yield values were obtained from the original reference. Only the terminal yield and error estimates were made for this report.

24-in.-square by 1/8-in.-thick Plexiglas sheet which was placed on a 9-1/2-in.-diameter by 9-in.-long cylinder (approximately 45 lb) of composition B explosive. The Plexiglas sheet served both as the bottom of the N_2O_4 vessel and as a blast shield to prevent detonation products from the booster from obscuring the detonation wave in the hypergolic mixtures. A sketch of the test configuration is presented in Fig. 4-22.

Primacord (Type A-5 mild detonating fuse) was suspended along the entire length of each test tube to provide the shock stimulus to shatter the tubes and initiate mixing of the fuel and oxidizer. In order to ensure the generation of a reasonably planar shockwave at the booster-propellant interface, the composition B booster was initiated simultaneously at seven points on its bottom surface (by seven commonly initiated lengths of Primacord which terminated in cylindrical charges of composition C-4 explosive in precast cavities in the bottom surface of the booster).

Immediately before testing, the Pyrex tubes were filled to a depth of 40 in. with fuel; then, the oxidizer was added remotely to the outer cylinder to the same depth, to give a total propellant weight of 130 to 140 lb, with an oxidizer-fuel weight ratio of about 2.4:1.

The blast yield of the system was measured by four Atlantic Research Corporation Model LC-33 piezoelectric-type blast gauges located 15.0, 21.9, 34.7, and 60.3 ft from the center of the charge. The TNT equivalence was determined by comparing the overpressure from the propellant system with a shock overpressure vs distance curve for the test area previously obtained with the same gauge array, using various weights of composition B and composition C-4 explosive.

The only parameter varied in these tests was the delay time between initiation of the mild detonating fuse (MDF) and initiation of the composition B booster.

The results of the tests are summarized in Table 4-15. It can be seen that in the majority of cases the pressure from the first station was significantly lower than those from the others. Accordingly, terminal yields were estimated by averaging the results from the last three stations. Duplicate

PYREX TUBE

PLEXIGLAS TUB

42" 45"

PRESSTITE PUTTY

PLEXIGLAS SHEET

9"

COMPOSITION B
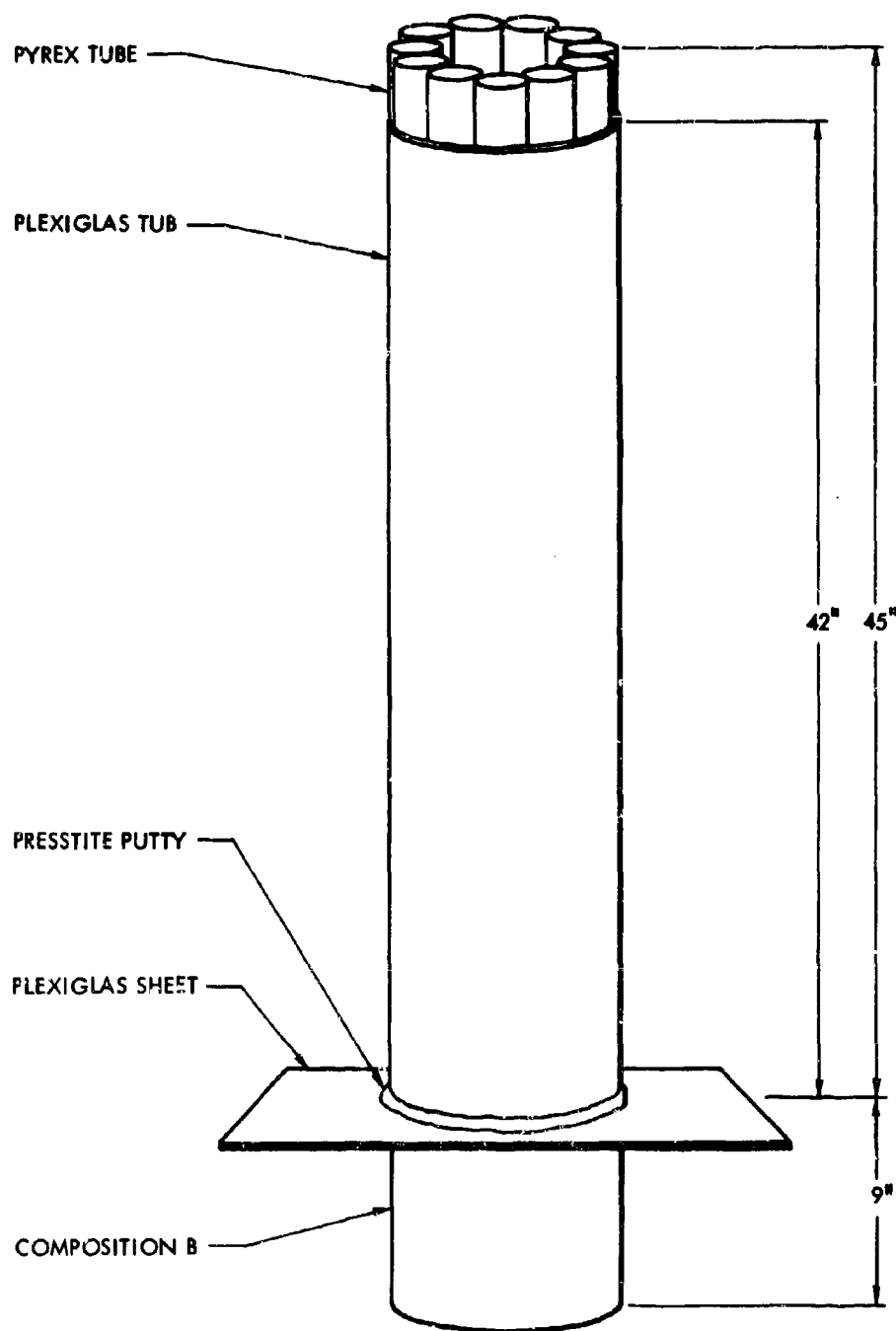
Fig. 4-22.   Aerojet Detonability Test Configuration

Table 4-15

PEAK OVERPRESSURE AND EXPLOSIVE YIELDS FROM AEROJET DETONABILITY TESTS

Test No.	Delay Time* (msec)	Gauge No.**	Overpressure (psi)	Yield (%)	Terminal Yield (%)
N/A-2	1	1	380	10.4	52
		2	65	43.3	
		3	29.1	66.8	
		4	8.1	46.4	
N/A-3	3	1	231	27.8	35
		2	57	28.1	
		3	23.4	34.7	
		4	7.9	42.9	
N/A-4	0.6	1	237	25.9	51
		2	74.8	56.1	
		3	No data	--	
		4	8.0	45.0	
N/A-5	0.3	1	135	<0	44
		2	No data	--	
		3	29.1	63.4	
		4	6.6	23.7	
N/A-6	0.1	1	113	<0	16
		2	48.5	12.6	
		3	20.8	24.2	
		4	5.8	11.1	
N/A-7	-	1	28.9	6.2	20
		2	14.6	9.9	
		3	8.0	15.8	
		4	3.3	23.5	
N/A-8	6	1***	23.9	5.5	16
		1	117	<0	
		2	50.7	19.2	
		3	17.1	11.0	
		4	5.8	17.1	
N/A-9	6	1***	26.4	6.3	14
		1	122	<0	
		2	49.6	18.0	
		3	12.3	<0	
		4	6.5	25.1	
N/A-10	0.6	1	226	29.9	41
		2	72.0	49.0	
		3	19.3	29.5	
		4	7.7	44.0	
N/A-11	0.1	1	151	0.3	28
		2	49.7	18.4	
		3	No data	-	
		4	7.5	38.6	
N/A-12	-	1	No data	-	18
		2	16.4	12.0	
		3	8.3	17.8	
		4	3.4	24.9	

* Delay time = time between initiation of MDF train and initiation of Composition B booster.

** Gauge 1, 2, 3, and 4 located 15.0, 21.9, 34.7, and 60.3 ft from the charge.

*** Initial shock of fireball engulfing Gauge No. 1 before initiation on booster.

tests were run in four of the test conditions. In two of these conditions the
two values agreed within a factor of 1.1 of each other; in one, a factor of
1.2; and in the last, a factor of about 1.5. Considering this degree of repro-
ducibility and the lack of impulse data, it is estimated that the terminal
yields listed are uncertain to about a factor of 1.5.

In addition to the instrumentation described above, pressure probes were
mounted on the Plexiglas cylinders, and streak-camera photographs were taken
to measure detonation velocity in the propellant mixture.

No evidence of a propagating detonation was noted in any of the tests;
however, rapidly fading shock waves were noted on tests N/A-4 and N/A-5. These
were attributed to the decaying shock from the booster with slight contribution
by the propellant mixture. The authors of Ref. 4-10 concluded that with this
configuration the propellant mixture is incapable of steady-state detonation.

Atlantic Research Laboratory Tests (Ref. 4-11)

This test series included several hundred experiments with milliliter
quantities of propellants and used a variety of test geometries. Because of
the small quantities of propellants used, no actual pressure measurements were
attempted. The tests were documented by high-speed photographs and visual ob-
servations. The number and variety of these tests makes it imp- ctical to sum-
marize the results in this report, and the reader is referred to the original
work for details. For the purpose of this report, perhaps the most important
conclusion of the experimenters was that the full body of their results is in-
consistent with the explosion being a hydrazine vapor-air explosion, as sugges-
ted in the small-scale spill test results of Ref. 4-6.

Part 3
SUMMARY OF DATA AND CONCLUSIONS

Parts 1 and 2 of this section presented the data from the 32 tests conducted during the basic PYRO program and an additional 100 tests conducted during recent years by a number of other agencies using the hypergolic propellant combination N_2O_4/50% UDMH - 50% N_2H_4.

From the results of these tests, it is clear that the explosive yield of the N_2O_4/50% UDMH - 50% N_2H_4 propellant combination is very dependent on the failure mode and tankage configuration as well as on the inherent properties of the propellants. Thus the process of selecting the maximum credible explosive yield for this propellant combination involves first establishing the failure modes and tankage configurations considered credible, then obtaining estimates of the explosive yields for each case, and finally selecting the largest of these explosive yields.

Since not all configurations using this propellant combination appear to have the same credible failure modes, use of a single explosive yield value (determined in the fashion described above) will be overly conservative for many cases. Accordingly, it seems desirable to use not one, but a number of explosive yield values for this propellant combination, each value corresponding to the worst credible failure mode for the designated configuration.

The following generalized configurations seem to provide a reasonable grouping for this purpose:

1. Static test stand

2. Launch pad
   a. Pre launch
   b. Launch

3. Post launch
   a. In flight
   b. Ground impact

Static Test Stand

For the static test stand case it is assumed that the tanks, and in
particular the tank support systems, are strong enough so that failure
modes which involve the entire tank structure falling off its supports are
not credible. It is further assumed that there will be no large explosive
sources in the vicinity that can act as explosive donors.[*] This leaves as
credible failure modes those involving bulkhead (diaphragm) ruptures. tank
wall failure (resulting in propellant spills) or possible small explosive
donors (e.g., rupture of high-pressure gas tanks). The scale-model tests
which correspond to those failure modes are the diaphragm rupture tests,
confinement by the missile tests, spill tests, 100-ft tower drop tests and
the small explosive donor tests.

The data presented in Parts 1 and 2 indicated that the range of terminal
explosive yields and the estimated upper limit yield for each of these modes
is as follows:

	Terminal Yield Range (%)	Estimated Upper Limit
Diaphragm rupture (confinement by the missile)	0.01 - 0.8	1.5
Spill	0.02 - 0.3	0.5
Small explosive donor	0.8 - 1.2	2.0
Tower drop	0.2 - 0.4	0.6

Based on the largest of these, the small explosive donor, the maximum
credible yield selected for the static test stand case is 2%. It is possible,
however, that in many static test stand situations an explosive donor will not
be present. For these cases, the next highest failure mode could be used,
i.e., diaphragm rupture, and the maximum credible yield would be 1.5%.

---

[*] The only source of large explosive yield considered credible for any
situation is another stage of the vehicle. In the static test stand case,
it is assumed that only one stage is tested at a time.

Section 5

CRYOGENIC PROPELLANT PROGRAM

Section 5

CRYOGENIC PROPELLANT PROGRAM

During the program a total of 212 tests using the cryogenic propellant combinations liquid oxygen-RP-1 $\left(LO_2/RP-1\right)$ and liquid oxygen—liquid hydrogen $\left(LO_2/LH_2\right)$ were conducted. For purposes of discussing and presenting the results from these tests, this section of the report has been organized as follows:

Part 1 - Confinement-by-the-Missile, Confinement-by-the-Ground-Surface, and High-Velocity-Impact test procedures and test hardware.

Part 2 - Test results from the basic program.

Part 3 - Discussion of results from the basic program.

Part 4 - Full-Scale Tests, includes a failure test of a Saturn S-IV with ~100,000 lb LO_2/LH_2 and a Titan with ~100,000 lb $LO_2/RP-1$.

Part 5 - Discussion of yield and ignition time scaling.

Launch Pad

This failure category has been divided into two sub-categories; pre-launch and launch.

The pre-launch category is very similar to the static test stand case and the same failure modes apply, i.e., diaphragm rupture, spill, small explosive donor, and tower drop. Thus, the maximum credible yield for the pre-launch category is 2%. The launch category includes the static test stand failure modes as well as command destruct and large explosive donor. This category, however, does not include the high-velocity-impact case (either from a high-altitude fallback or from turn-around and powered impact) since, in these cases, the point of impact on the ground surface is almost sure to be at a considerable distance from its launch pad.

Although the separation between low- and high-velocity impact is somewhat arbitrary, it is assumed that the low-velocity case is limited to a velocity on the order of 140 ft/sec (corresponding to free fall from a height of about 300 ft).[*] The high-velocity case is assumed to have an upper limit of about 600 ft/sec. It is also assumed that for a silo geometry, the maximum impact velocity would be significantly less than that for the flat-pad case (say by a factor of 2) because of the lower probability of the vehicle falling directly back into the silo from the greater heights.

The terminal explosive yields for each of the failure modes included under the launch pad failure category are as follows:

	TERMINAL YIELD RANGE (%)	ESTIMATED UPPER LIMIT
Diaphragm rupture (CBM)	0.01 - 0.8	1.5
Spill (CBGS)	0.02 - 0.3	0.5
Small explosive donor	0.8 - 1.2	2
Large explosive donor	3.4 - 3.7	5
Command destruct	0.3 - 0.35	0.5
310-ft drop (CBGS)	~1.5	3

---

[*] Assumption is based on premise that failure is much less likely to occur when the vehicle has traversed on its own length since by that time it will have cleared all launch support facilities. The maximum vehicle length has been taken as about 300 ft.

4-80

PART 1 - CONFINEMENT-BY-THE-MISSILE, CONFINEMENT-BY-THE-GROUND-SURFACE, AND
HIGH-VELOCITY-IMPACT TEST PROCEDURES AND TEST HARDWARE.

CONFINEMENT BY THE MISSILE

These tests were intended to investigate the interaction of the propellants
for the case where an internal failure occurs and one propellant falls down
onto the other. The duration of interest of this tank confinement case is
limited to the time that the propellants remain confined by the walls of the
missile. This time is determined by the strength of the tankage, the rate of
vaporization of the cryogenic propellants, the initial tank pressures, and the
initial ullage space.

Test Tanks

The primary requirement of the tankage for this test condition was to
contain the propellants in the proper length-to-diameter ratio until the
internal pressure created by the vaporization of the cryogenic propellants
exceeded the normal vehicle tankage design burst pressure. From communica-
tions with AFRPL and various vehicle manufacturers, it was determined that
most vehicle fuel tankage would fail at internal pressures well below 100 psi.
Accordingly, this value (100 psi) was chosen as the design burst pressure for
the tank.

A complete discussion of the rationale for this test series is presented
in Section 3. In this discussion a list of important parameters was presented.
These parameters which had a direct influence on the design of the tanks and
test hardware are repeated below:

- Propellant type: $LO_2/RP-1$, LO_2/LH_2
- L/D ratio: 5:1, 1.8:1 (considered to be the length-to-diameter
  ratio of the propellant masses)
- Propellant weight: 200, 1,000, 25,000 lb
- D_o/D_t ratio: 1:1 and 0.45:1 (where D_o is the diameter of the
  opening in the diaphragm and D_t is the vehicle diameter)
- Type of ignition: detonator or squib

5-2

The terminal yields for the first five failure modes were obtained from Parts 1 and 2 of this section. The yield for the 300 ft drop was obtained from Fig. 4-23, a plot of terminal yield vs impact velocity. For this estimate only the flat-pad data were used since it is assumed that the area immediately adjacent to the launch pad would most likely be paved or at least hard ground.

A best-fit curve through the flat-pad data indicates that a credible yield for this case would be approximately 1.5%, with an estimated uncertainty of 1.5 to 2.

It will be noted that the highest yields were obtained from the large explosive-donor case. It should be noted, however, that an explosive donor weighing 2 or 3 times the effective weight of the exploding propellant mass was required to achieve this large a yield. Thus, in any case where this situation occurs, there would be more concern about the blast from the donor than that from the propellant explosion. For this reason it seemed reasonable to present two yield values for this case; one with a large explosive donor and one without. The estimated maximum credible yield values for the launch category with a large explosive donor is 5% and without a large explosive donor 3%.

Estimation of a credible yield value for the silo case is slightly more uncertain than for the flat-pad case. A lower credible drop height of say 150 ft. would tend to reduce the yield a factor of 2 below the flat-pad value, however, confinement would tend to increase it. The model-missile tests discussed in Part 2 suggest that for the spill case, silo confinement increases yields by about a factor of 4. Since there is no reason to expect confinement effects to be less than this for low-velocity impact, it appears that confinement effects will more than counteract the effects due to a decrease in impact velocity. Thus the best estimate of a maximum credible terminal yield for the silo case would be 6% (assuming no large explosive donor).

Post Launch

Failures after launch have been divided into two subcategories, in-flight and ground impact. Although no data have been obtained for the in-flight case,

- Internal design operating pressure of the tankage: upper tank 30 psi, lower 0 psi (chosen to simulate the effects of the gravitational and pressure head of the top propellant)

- Tank rupture at approximately 100 psi

Aside from these general parameters, there were many other requirements which were considered to be important and were included in the design criteria for the tanks and test hardware. These were:

- Fuel volumes that were consistent with the oxidizer-to-fuel ratios in normal vehicle usage, i.e., $LO_2/RP-1 = 2.25:1$, $LO_2/LH_2 = 5:1$

- An ullage space consistent with normal vehicle usage

- Low total mass of tank so as to cause minimal interference with the explosion of the mixed propellants

- Tank materials compatible with the propellant combinations

- Fabrication techniques in general use throughout the industry to keep the lead time short and costs low

- A diaphragm removal system which would bring the two propellants together rapidly, reproducibly, and with minimal influence on the subsequent mixing process

With all these items taken into consideration, the basic design shown in Fig. 5-1 was chosen. This is a thin-walled right circular cylinder with 2·1 ellipsoidal domed ends. This design was the strongest, for the mass of the tank, which could be readily and inexpensively fabricated.

Fabrication

The 200- and 1,000-lb tanks were fabricated by URS. The cylindrical shells and flanges were shop-fabricated from tempered aluminum. The domed ends were spun on hardwood molds and then heat treated before assembly. The shell and dome thicknesses were 1/16 in. for the 200-lb tanks and 1/8 in. for the 1,000-lb tanks.

The 25,000-lb tanks were fabricated by the Marshall Space Flight Center, Huntsville, Alabama. The dome thicknesses were 5/16 in. for the $LO_2/RP-1$ and 3/16 in. for the LO_2/LH_2 tanks. The shell thicknesses were 3/16 in. for the $LO_2/RP-1$ and 1/4 in. for the LO_2/LH_2 tanks.
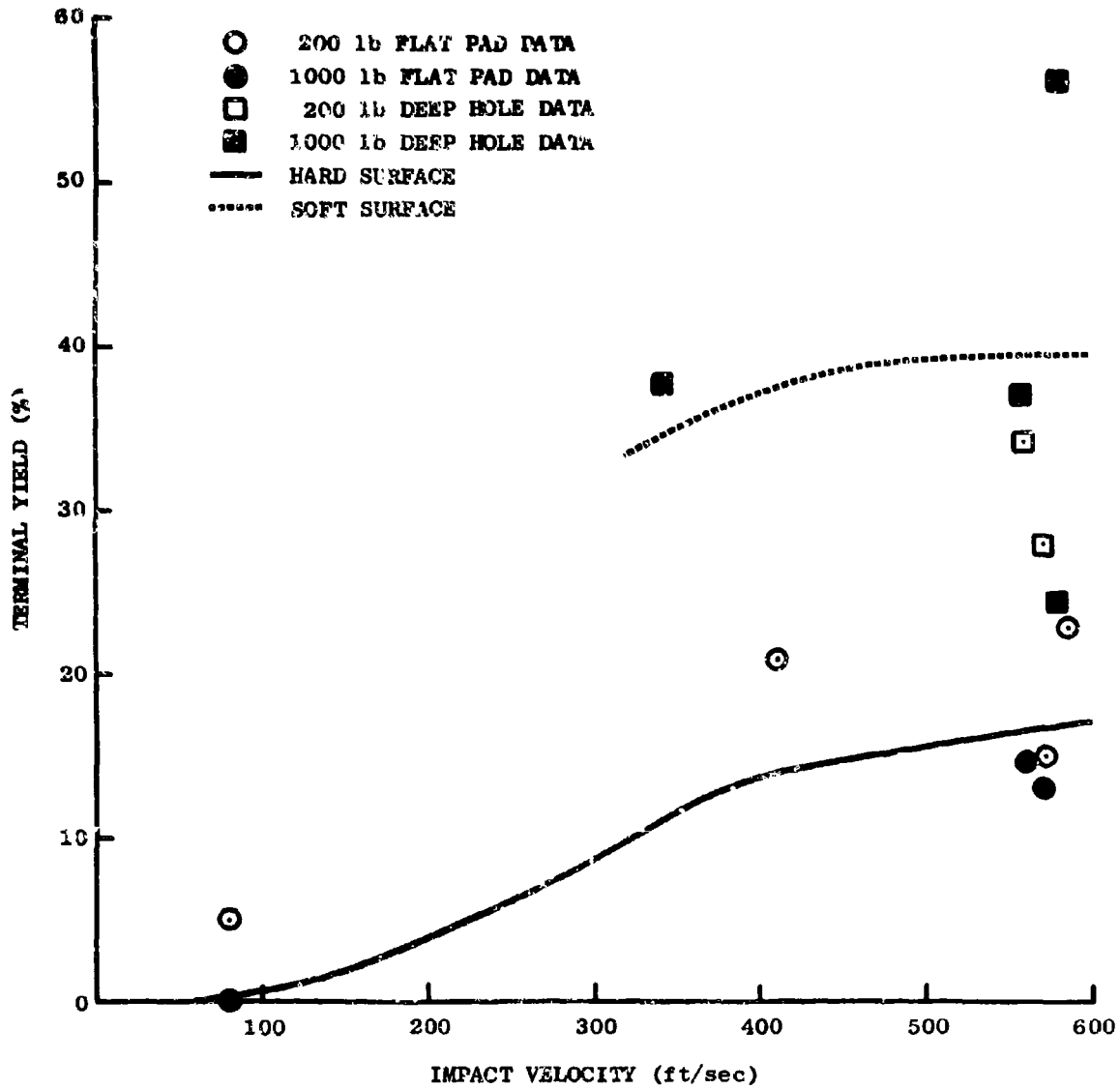
Fig. 4-23. Terminal Yield vs Impact Velocity for Hypergolic High-Velocity Impact

4-82
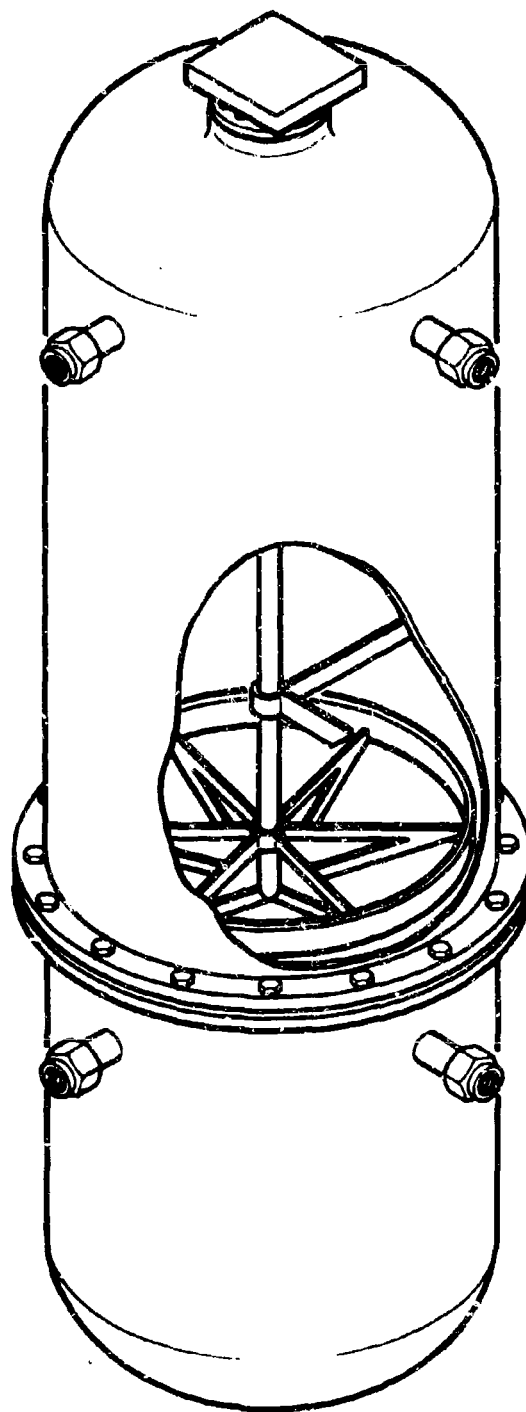
Fig. 5-1. Cryogenic Confinement-by-the-Missile Tank

in the absence of a spill surface there seems no possible way for the failure
mode to be more severe than for the launch pad case. Actually, the worst
credible failure mode for the in-flight case appears to be the large explosive
donor. The data presented earlier suggested that the explosive yield for
this case is about 5%.

The worst credible failure mode for the ground-impact case has been
assumed to be high-velocity impact. The data from the experimental tests,
(see Fig. 4-23) indicates that at the maximum impact velocity investigated,
about 570 ft/sec, the mean of the explosive yields varied from about 18
percent for impact on a flat surface up to well over 40 percent, depend-
ing on the degree of cratering, and therefore confinement, provided by the
target surface. The estimated upper limit for these two failure modes
is 25% for the flat surface case and 60% for the cratering case.

Although the ground-impact case gives large yield values, it is not
clear how this yield value can be used for design purposes or for establish-
ing safety distances because of the large uncertainty in the point of
impact.

Modifications to the Terminal Yield Values

The explosive yield values quoted for each of the failure mode categories
is the terminal yield, i.e., the yield obtained at long distances from the
explosion where both the pressure and impulse data values tended to reach a
constant value.

In order to use these data at locations other than at long distances, it
is necessary to examine the comparison between the shapes of propellant pres-
sure and impulse distance curves and those for TNT. These comparisons are
shown in Figs. 4-24 and 4-25, which are plots of the pressure or scaled
impulse ($I/W_T^{1/3}$) as a function of scaled distance ($D/W_T^{1/3}$). Each point
represents the average of the data from all gauges (usually two or three) at
a given distance for a given test.

The basic dimensions for the 200-, 1,000-, and 25,000-lb tanks are
presented in Fig. 5-2 and a photo of a 25,000-lb LO_2/RP-1 test tank is
presented in Fig. 5-3.

The Diaphragm and Diaphragm Removal Mechanism

The diaphragm system used for the CBM test series consisted of a sheet
of tempered glass which was broken by an explosively driven ram (the same
system used in the hypergolic program). The tempered glass was held in place
by a clamping ring and bolted flanges and was sealed using Teflon-impregnated
asbestos gasket material. The breaker used was a six-finned stainless steel
probe. To assure complete removal of the tempered glass, a clean-out ring
was attached to the tips of the fins. A sketch of a 200-lb test article
diaphragm breaker is shown in Fig. 5-4 and a photo of a diaphragm breaker
in place in a 25,000-lb test article is shown in Fig. 5-5.

The breaker was mounted on the end of a long rod extending through a
Wilson seal in the top of the tank and was capped by a flat, square plate.
This plate held a small explosive charge of C-4, which drove the breaker
through the tempered glass.

CONFINEMENT-BY-THE-GROUND-SURFACE

This test series was intended to investigate the interaction of pro-
pellants subsequent to tank rupture, when the propellants are impacting on a
flat, horizontal surface. A complete discussion of the rationale for this test
condition is presented in Section 3. In this discussion, a list of important
parameters was presented. Those parameters which have had an influence on the
design of the experimental hardware are presented below:

- Propellant type: LO_2/RP-1 - LO_2/LH_2

- Propellant length-to-diameter ratio: 1.8:1 to 5:1

- Propellant velocity: (low drop) 15 to 20 fps
  (medium drop) 40 to 50 fps
  (high drop) 70 to 80 fps
  High-Velocity Impact $\sim$ 600 fps

PEAK OVERPRESSURE (psi)

10

1.0

X HIGH-VELOCITY-IMPACT TESTS

° OTHER TESTS

10   100

SCALED DISTANCE (ft/lb$^{1/3}$)
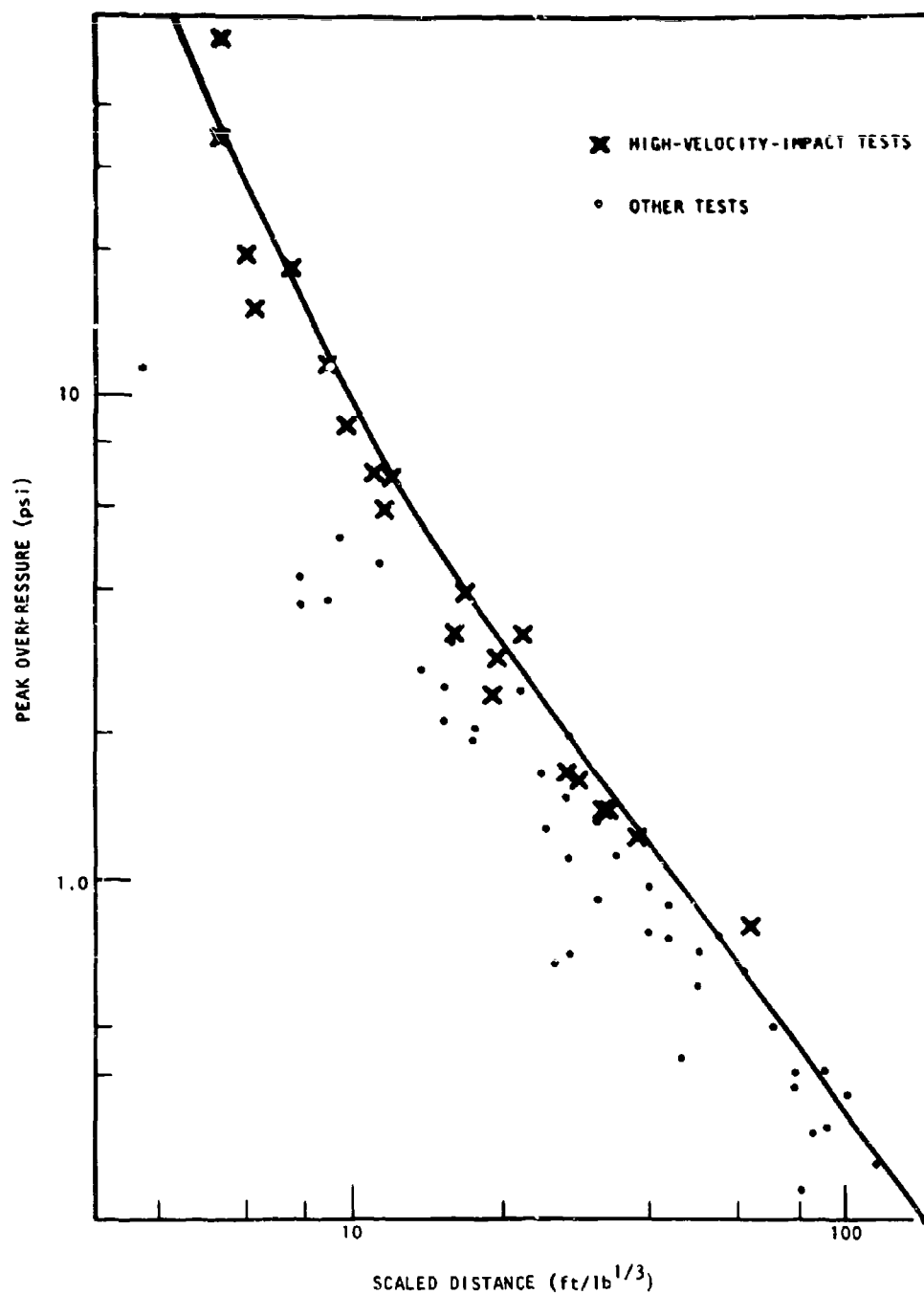
Fig. 4-24. Pressure vs Scaled Distance for Hypergolic Tests

4-84
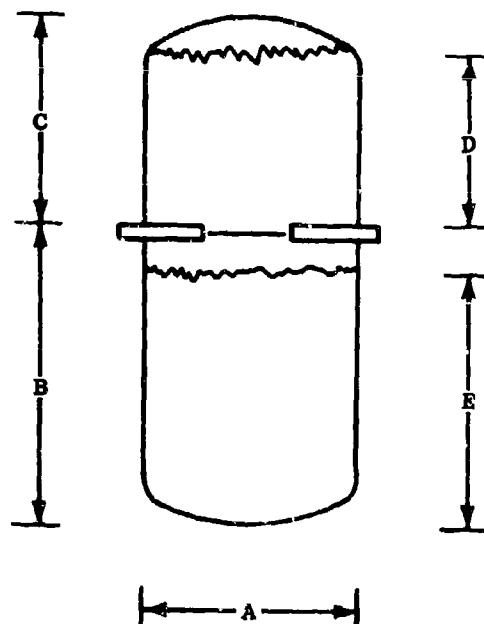
PROPELLANT WEIGHT (lb)	PROPELLANT TYPE	L/D	DIMENSIONS (in.)				
			A	B	C	D	E
200	LO_2/LH_2	1.8	23¼	13	36¼	31¼	11¾
		5	16¼	23¾	70½	62¾	21¼
	LO_2/RP_1	1.8	15¾	13½	20¼	17¼	12¼
		5	11¼	24½	39½	33¾	22½
1000	LO_2/RP_1	1.8	26¾	19¾	35¾	29¾	21¾
	LO_2/LH_2	1.8	39¼	20¼	61¼	52¼	18¾
25000	LO_2/RP_1	1.8	78	65½	101½	90¾	61
	LO_2/LH_2	1.8	114	63	183	164	57

Fig. 5-2.   Cryogenic Confinement-by-the-Missile Tanks
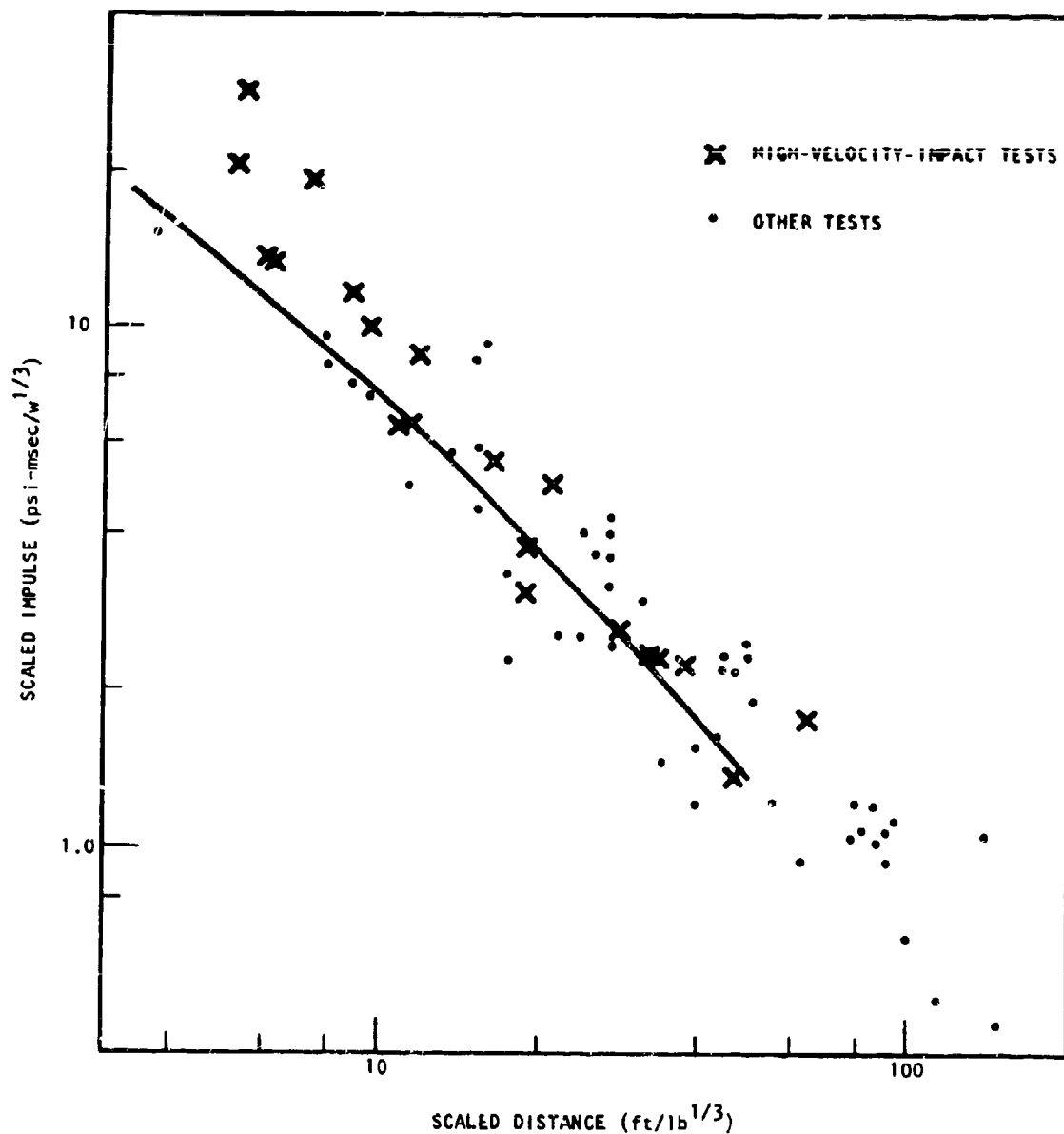
Fig. 4-25. Scaled Positive Impulse vs Scaled Distance for
            Hypergolic Tests
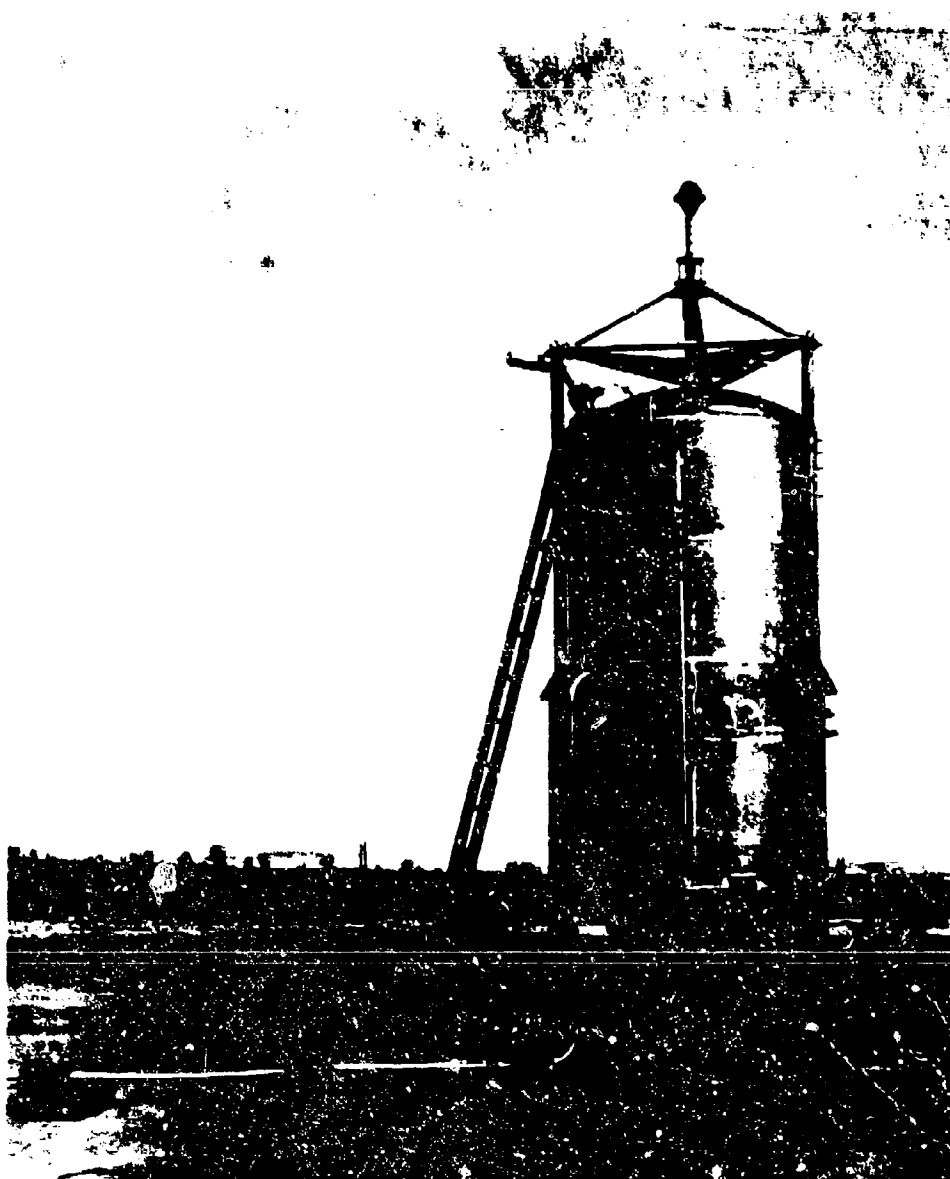
Fig. 5-3. 25,000 lb LO_2/RP-1 Confinement-by-the-Missile Tank

W_T is the TNT equivalent weight of the test (in pounds) and is equal to the product of the total propellant weight and the terminal yield. In Fig. 4-24, the pressure-distance curve, it can be seen that for all practical purposes the upper bound for the high-velocity-impact data is the TNT curve. For the other data, however, the upper bound tends to lie somewhat below the TNT curve at pressures above 4 psi (scaled distance of about 15 ft/lb$^{1/3}$).

In Fig. 4-25, the impulse data is compared with the TNT curve. In this case the data tend to lie generally above the TNT curve. In Fig. 4-26a and 4-26b, the peak overpressure and positive-phase impulse upper bounds are plotted as a ratio of the TNT curve. Conservative estimates of the pressure and impulse values to be expected from propellant explosions can be obtained by applying the pressure and impulse values obtained from the standard TNT reference curves by these ratios.
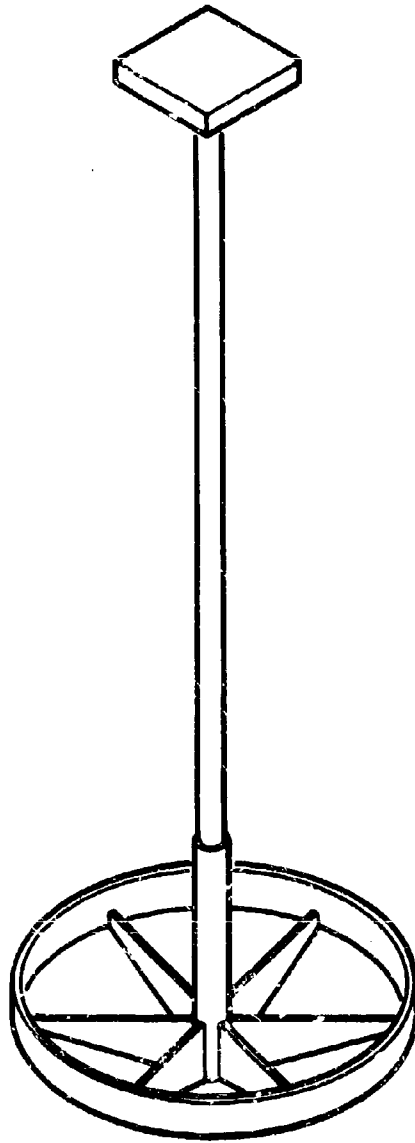
Fig. 5-4.   Breaker Ram
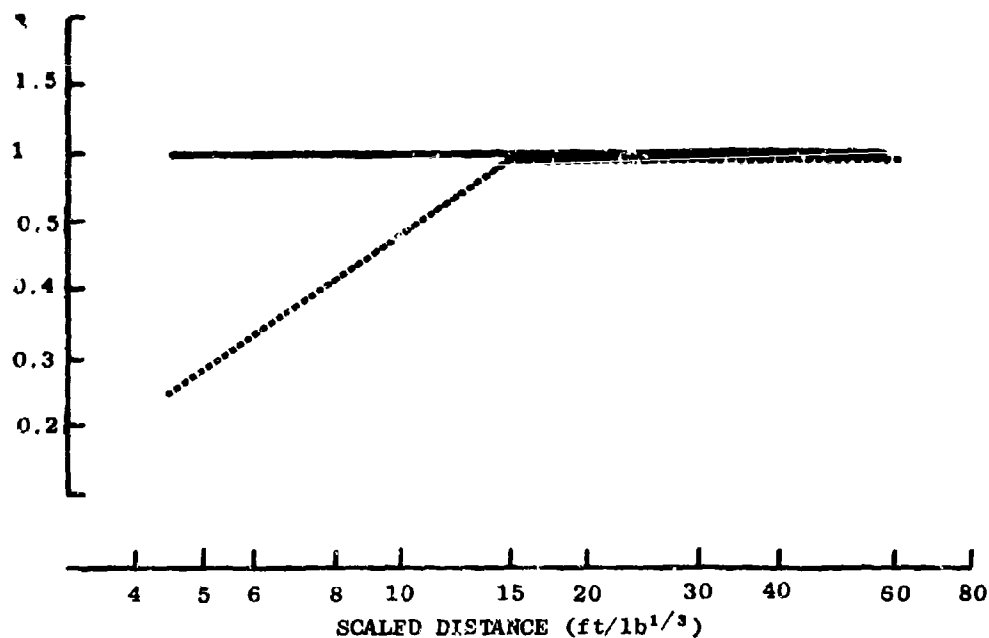
Fig. 4-26a. Ratio of Upper Bound of Propellant Pressure Data to Standard
TNT Curve (solid line: high-velocity-impact data; dashed
line: other test data)
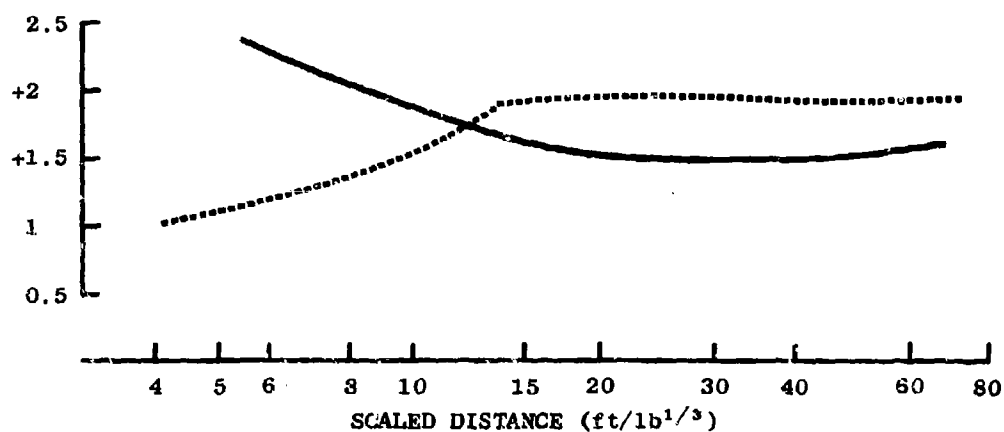
Fig. 4-26b. Ratio of Upper Bound of Propellant Impulse Data to Standard
TNT Curve (solid line: high-velocity-impact data; dashed
line: other test data)

4-87
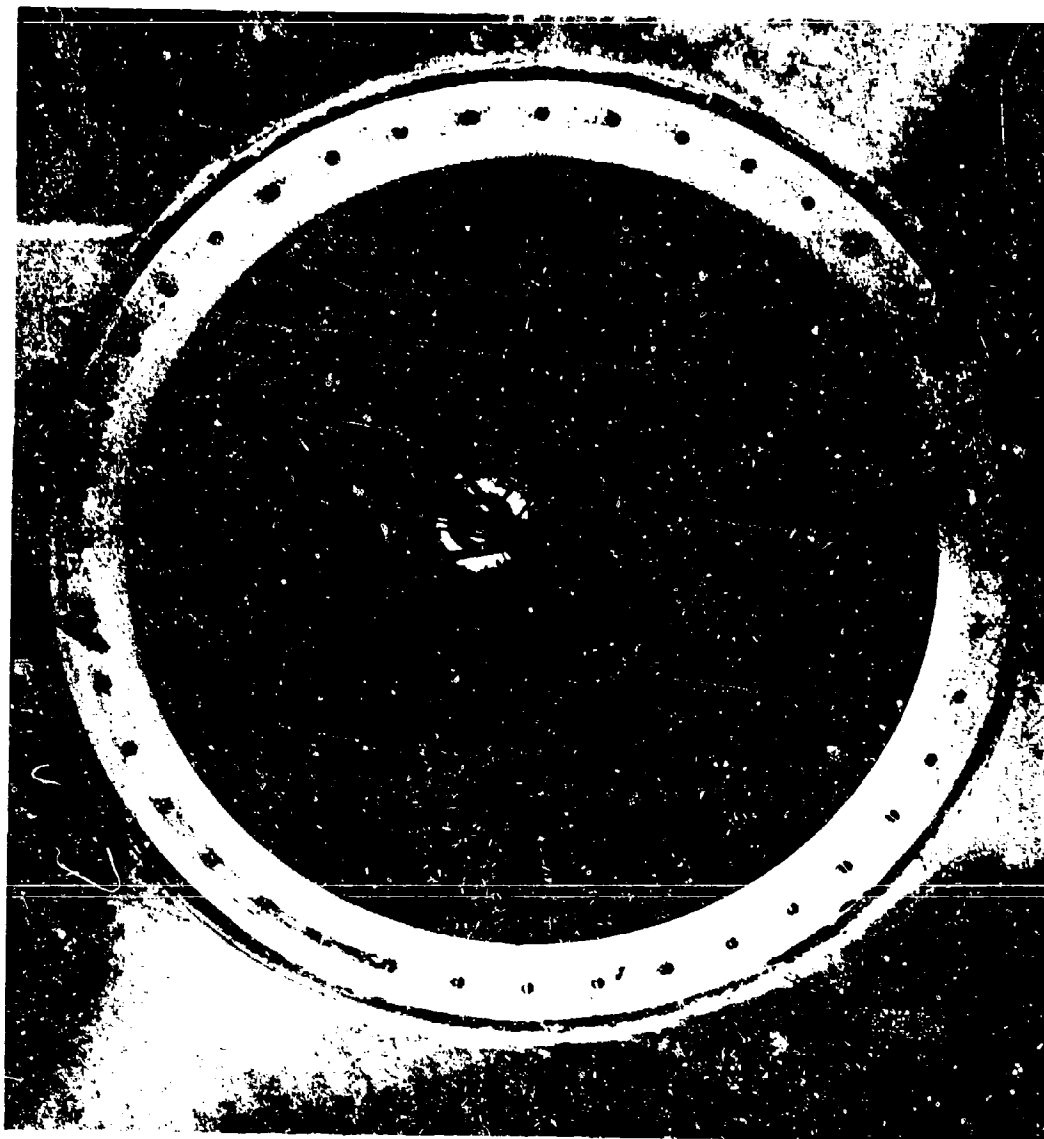
Fig. 5-5.   Diaphragm Breaker Ram for 25,000-lb Tank

Section 4

REFERENCES

4-1. American Society of Mechanical Engineers, Unfired Pressure Vessels, Section VIII - "Rules of Construction of Unfired Pressure Vessels," 1962 Edition, New York, New York*

4-2. Ingery, C. N. and B. F. Pannill, Peak Overpressure vs Scaled Distance for TNT Surface Bursts (Hemispherical Charges), BRL Memorandum Report No. 1518, Ballistic Research Laboratories, April 1964 (AD 443 102)*

4-3. Defense Atomic Support Agency, Operation SNOW BALL Project Descriptions, Volume 1 (U), DASA Data Center Special Report 24-1, DASA 1516-1 (AD 441 974)*

4-4. Pesante, R. E., R. D. Erickson, D. G. Frutchery, and W. J. Helm, Blast and Fireball Comparison of Cryogenic and Hypergolic Propellants with Simulated Tankage, Report No. 0822-01(02)FP, prepared for NASA by Aerojet-General Corporation, June 1964

4-5. Titan II - Dyna-Soar Destruct Test and Analysis Report, ER 12269, Martin Marietta Corporation, March 1962

4-6. Research on Hazard Classification of New Liquid Rocket Propellants, Vols. I and II, Rocketdyne for Rocket Test Annex, Space Systems Division, AF/SSD-TR-61-40, October 1961

4-7. Henderson, W. Paul, Technical Progress Report on CRDL Project Supported by USAF and NASA, Chemical Research and Development Laboratories, 13 April 1964

4-8. Henderson, W. Paul, Technical Progress Report on CRDL Project Supported by USAF and NASA, Chemical Research and Development Laboratories, 7 August 1964

4-9. Pesante, R. E., M. Nishibayashi, D. G. Frutchey, R. D. Erickson, W. J. Helm, Blast and Fireball Comparison of Cryogenic and Hypergolic Propellants, Report No. 0822-01(01)FP, prepared for NASA by Aerojet General Corporation, 26 June 1964

4-10. Irwin, O. R. and J. L. Waddell, Study of Detonation Induction in Solid Propellants by Liquid Propellant Explosions, Report No. 0797-01(09)QP, prepared for George C. Marshall Space Flight Center by Aerojet-General Corporation, 7 July 1964

---

* Reference curves from these documents are reproduced in Appendix F.

● Flow direction: vertical and horizontal

Aside from these general parameters, there were many other requirements which were considered to be important and were included in the design criteria for the experimental arrangement. These were as follows:

● Tankage should be light and frangible so as not to interfere with the expansion and subsequent measurement of the blast wave.

● Tankage should release the propellants rapidly and uniformly, and all tankage should be kept clear of the mixing area of the propellants.

● The two propellants should make first contact at or near the ground surface.

● The propellants should flow concentrically from GZ to minimize blast asymmetries.

o Tank material compatible with propellant combinations.

● Fabrication techniques in general use throughout industry.

Low Drop Tests (Impact velocity ~23 ft/sec)

In this test series, the tanks were suspended with the bottom of the tank 2 to 3 ft above the test pad, filled with propellant, and allowed to drop onto a breaker, which ripped open the bottoms of both propellant compartments. As soon as the bottom of the tank was broken, the tank was stopped by a rigid frame and the propellants allowed to spill out onto the test pad.

The basic experimental configuration for these tests (shown in Fig. 5-6) consisted of a lightweight, frangible frame and a thin-walled frangible tank assembly. The frame and tank were constructed of aluminum to minimize the size of the fragments produced.

The tankage assembly consisted of a right cylindrical tank, guide tubes, fueling ports, and for the tanks containing the cryogenic propellants, a remote liquid-level measuring system and lightweight tank insulation. The cylindrical tank was of welded aluminum construction with a wall thickness of 50 mils. The bottom was aluminum foil 5 mils thick. Equally spaced vertically around the tank were three lightweight aluminum pipes, which served as guides during the

5-10
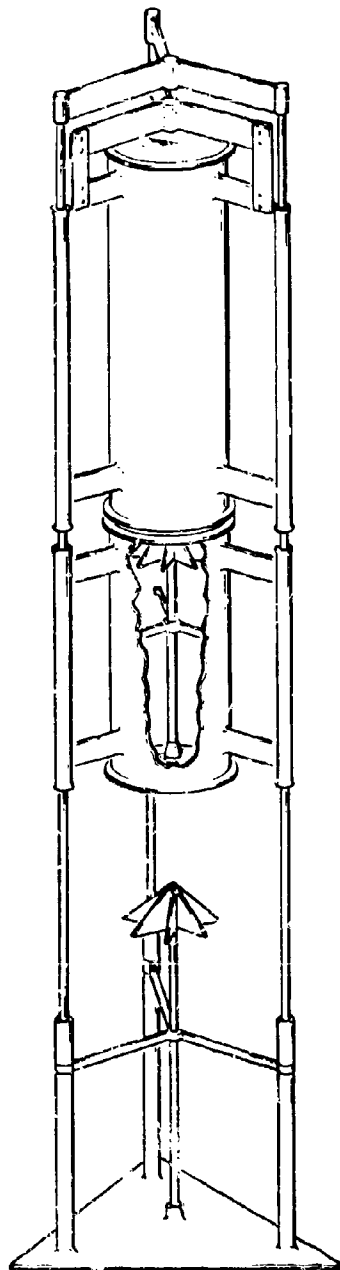
Fig. 5-6.   Sketch of Tank Assembly and Drop Frame for the Confinement-
by-the-Ground Surface Low Drop Test Series

5-11

4-11   Friedman, R., W. P. Barnes, Jr., and M. Markels, Jr., A Study
        of Explosions Induced by Contact of Hydrazine-Type Fuels with
        Nitrogen Tetroxide, TDR ASD-TDR-62-685, prepared for Aeronautical
        Systems Division by Atlantic Research Corporation, September 1962

4-12   Kingery, C. N. and B. F. Pannill, Peak Overpressure Vs. Scaled
        Distance for TNT Surface Burst (Hemispherical Charges), BRL
        Memorandum Report No. 1518, Ballistic Research Laboratories,
        April 1964 (AD 443 102)

4-13   Mills, R. R., Jr., F. J. Fisch, B. W. Jezek, and W. E. Baker,
        Self-Consistent Blast Wave Parameters, DASA-1559, prepared for
        Defense Atomic Support Agency by Aircraft Armanents, Inc.,
        October 1964

4-14   Glasstone, Samuel, editor, The Effects of Nuclear Weapons, prepared
        by the U.S. Department of Defense, published by U.S. Atomic Energy
        Commission, April 1962

4-15   Wallace, N. R. and A. B. Willoughby, Effects of Topography on
        Dynamic Pressure, BRC 170-7, prepared for Defense Atomic Support
        Agency by Broadview Research Corporation, October 1961

free-fall of the tank. The tank was suspended on a simple frame, which had three
slender (5/8 in.) aluminum-rod legs. These legs passed through the aluminum
pipes attached to the tanks. The tank assembly was suspended from the frame by
a 1/8-in. aircraft cable, which was passed through an explosive cable-cutting
device.

To rapidly remove the diaphragm, the tank was dropped onto a six-bladed
diaphragm breaker. This breaker was constructed of tempered aluminum blades
which had been filed razor sharp on the top or cutting edges. For the L/D
of 1.8 tests, a single breaker was fastened to the bottom of the frame.
For the somewhat longer tank in the L/D of 5 tests, a secondary breaker was
included in the lower tank. This secondary breaker, which broke the dia-
phragm on the top tank, was activated by the first breaker as it pushed
through the lower tank diaphragm.

Later in the program a 100-ft drop tower was installed for the high drop
test series. This tower, which is discussed in detail in Section 4, furnished
an excellent support for the remaining 200- and 1,000-lb low-velocity tests,
and the configuration shown in Fig. 5-7 was used. In this configuration,
the propellant tanks were essentially the same as before, but the tank was
guided on two taut aircraft cables attached between the tower and the ground
surface. The tanks were released by means of an explosive cable-cutting device
and dropped onto a six-bladed diaphragm breaker.

A limited number of tests were conducted using the horizontal
flow direction. For this test condition it was required that the lower pro-
pellant have as low a velocity as possible and the top propellant have a
velocity much higher than the lower propellant. Thus, for this test series,
the configuration shown in Fig. 5-8 was used. This configuration used two
breakers, one installed on the test pad to open the bottom tank diaphragm and
the second installed on the top of the bottom tank to open the top tank dia-
phragm. A photograph of an LO_2/RP-1 horizontal drop test article in place
on the test pad is shown in Fig. 5-9 and a close-up of the breaker on the top
of the bottom tank is shown in Fig. 5-10.
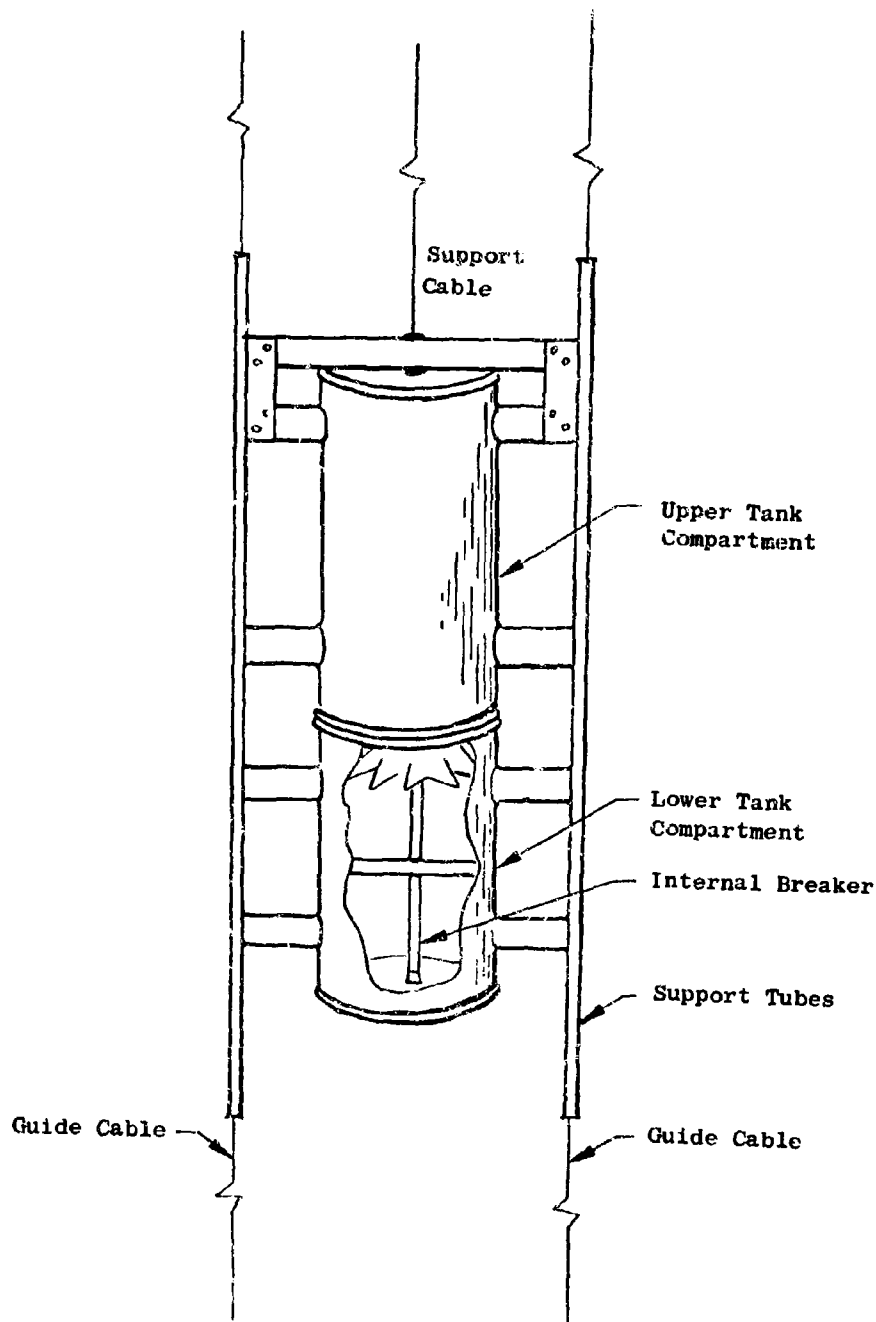
Fig. 5-7. Test Tank for the Confinement-by-the-Ground-Surface
           Low Drop Test Series

5-13
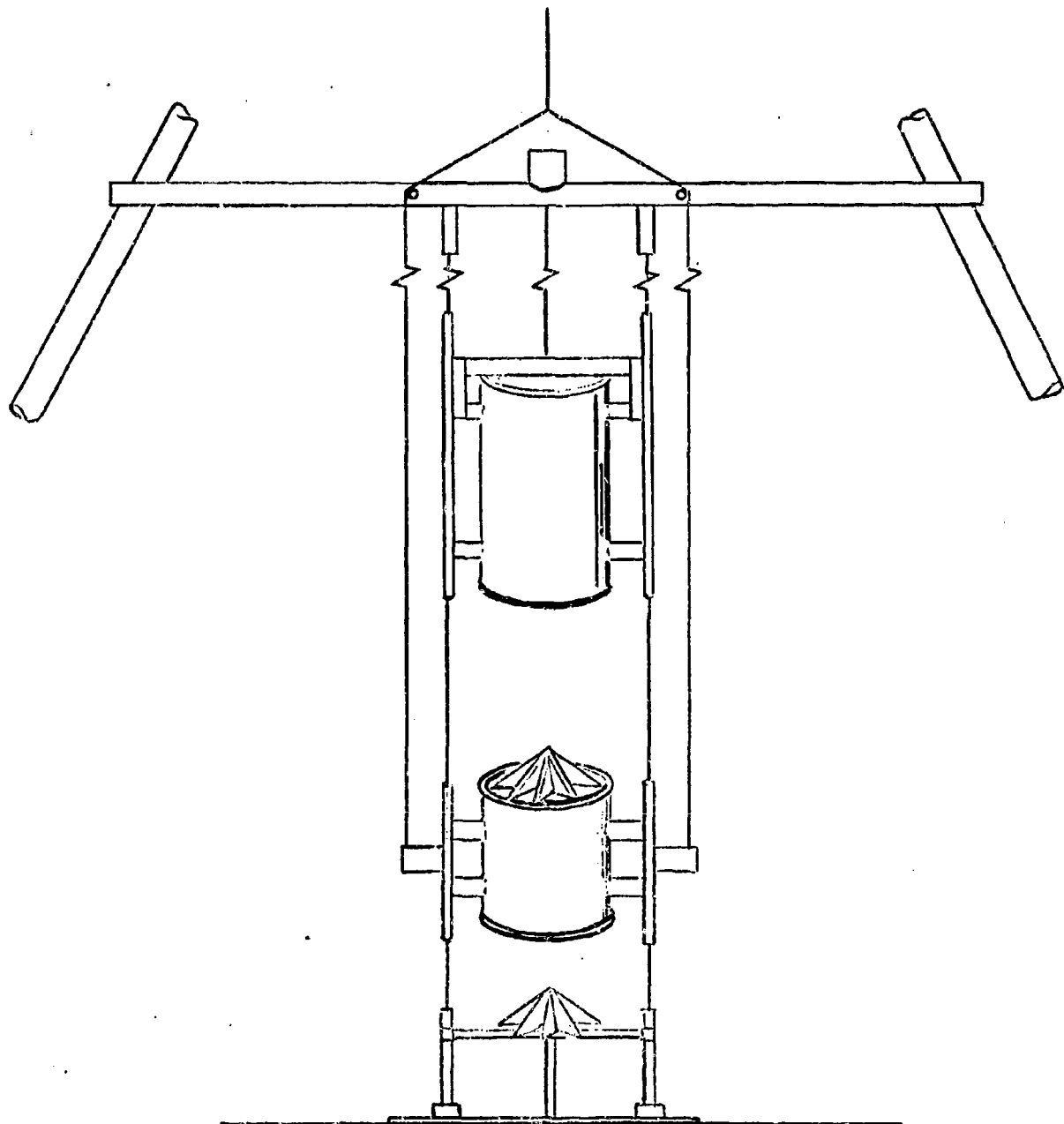
Fig. 5-8. Low-Drop Horizontal CBGS Test Article

Fig. 5-9.   200-lb-LO$_2$/RP-1 Horizontal CBGS Test Configuration
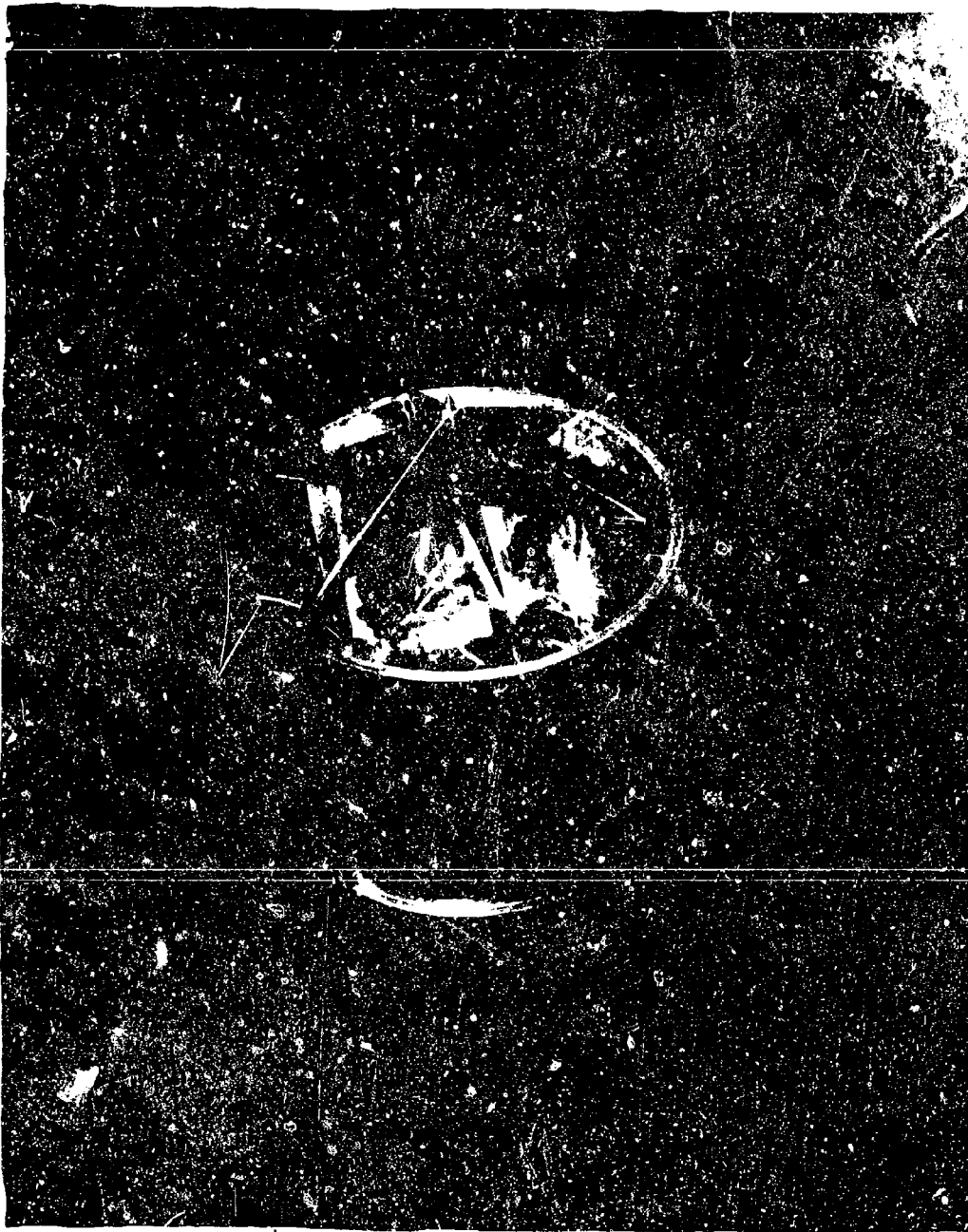
Fig. 5-10.　Diaphragm Breaker - Lower Tank of Horizontal
CBGS Tank

Medium Drop Tests (Impact Velocity ~ 44 ft/sec)

In this test series the tanks were suspended so that the bulkhead separating the two propellants was ~ 30 ft above the test pad. The 200- and 1,000-lb tests in this series were conducted using the lower portion of the 100-ft drop tower which is described in the previous section.

The tanks were essentially the same type used in the low-velocity drop test series (i.e., thin walls and an aluminum foil bottom). A typical tank and guide assembly is shown in Fig. 5-11.

For the 25,000-lb medium drop tests, a special 50-ft expendable drop tower was installed. This tower is shown with an LO_2/RP-1 test article in place in Fig. 5-12. The legs of this tower were fabricated of extra-strong 12-in.-diameter pipe. A trap door type release mechanism triggered by an explosive cable-cutting device released the tank. The tank was dropped onto a breaker ram and the tank stopped by a large hydraulic shock absorber. A photograph of the trap door mechanism is shown in Fig. 5-13.

High Drop Tests (Impact Velocity ~ 78 ft/sec)

In this test series the propellant tanks were suspended so that the bulk-head separating the two propellants was ~ 97 ft above the test pad on the 100-ft drop tower. The remaining test conditions were similar to those used for the medium drop test series.

Summary of Tank Dimensions

As noted throughout the discussion, the test tanks used for the confinement-by-the-ground surface test series were of light and frangible construction. For example the 200- and 1,000-lb LO_2/RP-1 tanks and the 200-lb LO_2/LH_2 tanks had sidewall thickness of 60-mil aluminum and the diaphragm was 6-mil aluminum foil. The LO_2/LH_2 1,000-lb tank had sidewalls of 60-mil and a diaphragm of 10-mil aluminum foil.

The 25,000-lb drop tank had sidewall thickness of 1/8-in. and diaphragm thickness of 32-mils. The basic dimensions for all tanks are presented in Fig. 5-14.
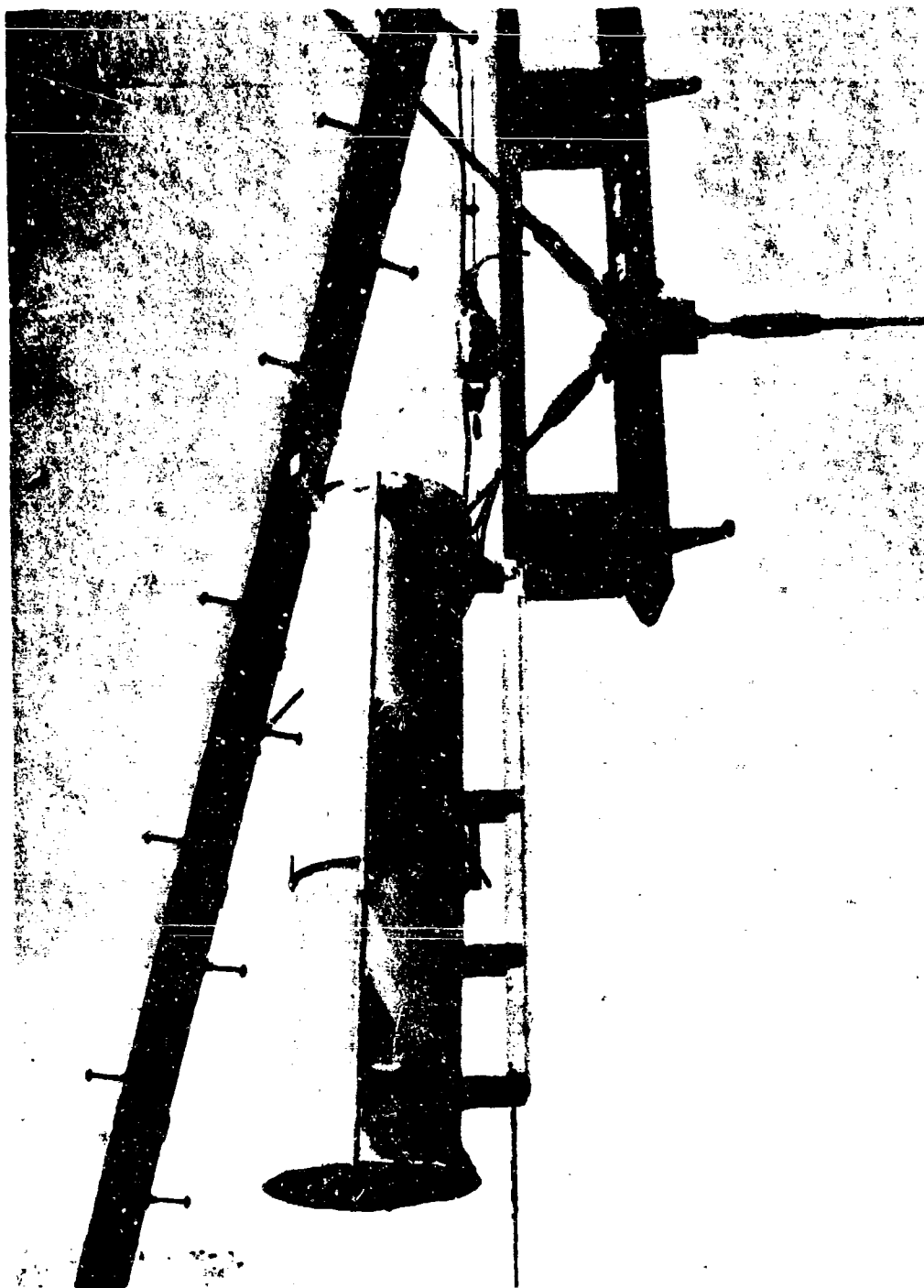
Fig. 5-11. Typical Drop Tank and Guide Assembly
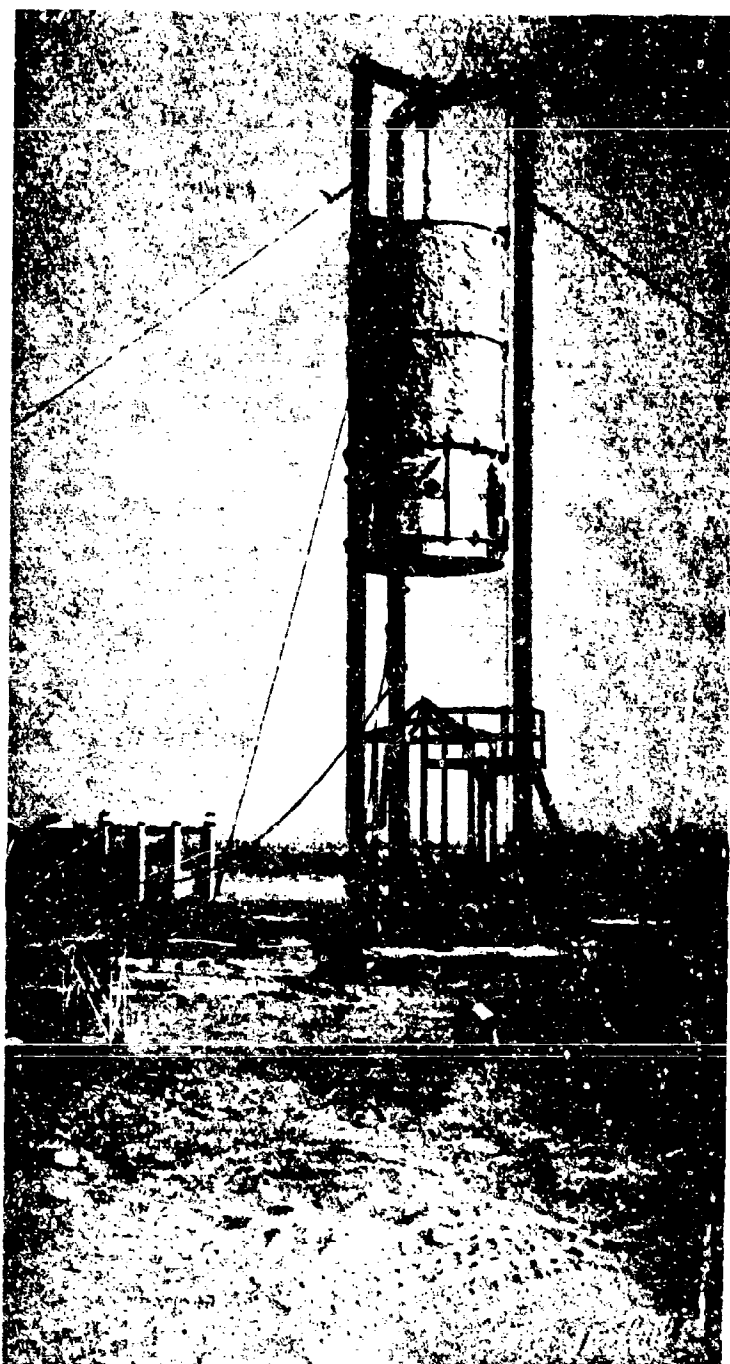
Fig. 5-12.   50-ft Drop Tower and 25,000-lb LO_2/RP-1 Test Article

Fig. 5-13.   Release Mechanism for 25,000-lb Drop Tests
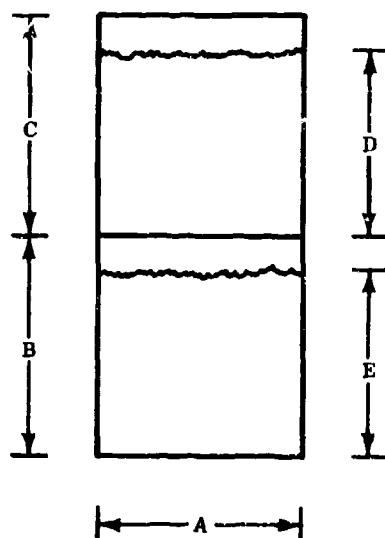
PROPELLANT WEIGHT (lb)	TEST TYPE	L/D	DIMENSIONS (in.)				
			A	B	C	D	E
200	LO_2/LH_2	1.8	23	$12\frac{1}{2}$	34	$31\frac{1}{4}$	$9\frac{3}{4}$
		5	$16\frac{1}{4}$	$22\frac{1}{2}$	$65\frac{3}{4}$	$62\frac{3}{4}$	$10\frac{1}{2}$
	LO_2/RP_1	1.8	$15\frac{3}{4}$	$13\frac{3}{4}$	20	$17\frac{1}{4}$	11
		5	$11\frac{1}{4}$	25	37	34	22
1000	LO_2/RP_1	1.8	$26\frac{3}{4}$	$21\frac{3}{4}$	$32\frac{3}{4}$	$29\frac{3}{4}$	$18\frac{3}{4}$
	LO_2/LH_2	1.8	$39\frac{1}{4}$	$19\frac{1}{4}$	$56\frac{1}{4}$	$53\frac{1}{2}$	$16\frac{1}{2}$
25000	LO_2/RP_1	1.8	78	$66\frac{3}{4}$	102	92	$58\frac{3}{4}$
	LO_2/LH_2	1.8	114	63	176	167	$55\frac{3}{4}$

Fig. 5-14   Cryogenic Confinement-by-the-Ground-Surface Tanks

HIGH-VELOCITY IMPACT

The cryogenic high-velocity test series consisted of six tests in which 200-lb quantities of the cryogenic propellant combinations, LO_2/RP-1 and LO_2/LH_2, were propelled down a sled track at speeds ranging from 500 to 600 ft/sec and allowed to impact into various target configurations.

The target configurations used were: (1) a flat-wall target simulating impact into a rigid flat surface, and (2) a deep-hole target simulating impact into a soft surface in which a crater would be formed.

The test series consisted of two LO_2/RP-1 and one LO_2/LH_2 propellant tests with the flat-wall target configuration and two LO_2-RP-1 and one LO_2/LH_2 propellant tests with the deep-hole target configuration.

While it was anticipated that ignition of the cryogenic propellants would occur upon impact and breakup of the tank, a supplemental ignition source in the form of a railroad flare was placed on the ground near the impact target for the first couple of tests. Upon analysis of the films of these tests, it became evident that ignition was indeed occurring upon impact and the flares were not used on the remaining tests.

High-Velocity-Impact Targets

To create the flat-wall targets, a massive concrete block was faced with 1-in.-thick steel plates, 8 ft high and 16 ft wide with a 1-ft splash shield around the edge. To create the deep-hole targets, the massive base was faced with concrete blocks containing preformed steel-lined cylindrical cavities. A sketch of this type of target is presented in Fig. 5-15.

High-Velocity-Impact Tanks

The tanks used for this test series are shown in Figs. 5-16 and 5-17. The general tank geometry and length-to-diameter ratios were similar to those used in the previous hypergolic tests. The tank shells and flanges were aluminum with a shell thickness of 1/16 to 1/8 in. A 1-in. air chamber was left between the tanks for insulation. This air chamber was

LO$_2$/RP-1:   72 IN. WIDE X 72 IN. HIGH X 62 IN. DEEP

LC$_2$/LH$_2$:   83 IN. WIDE X 85 IN. HIGH X 86 IN. DEEP

POINT OF
IMPACT

LO$_2$/RP-1:   32 IN. DIA. X 48 IN. DEEP

LO$_2$/LH$_2$:   48 IN. DIA. X 78 IN. DEEP
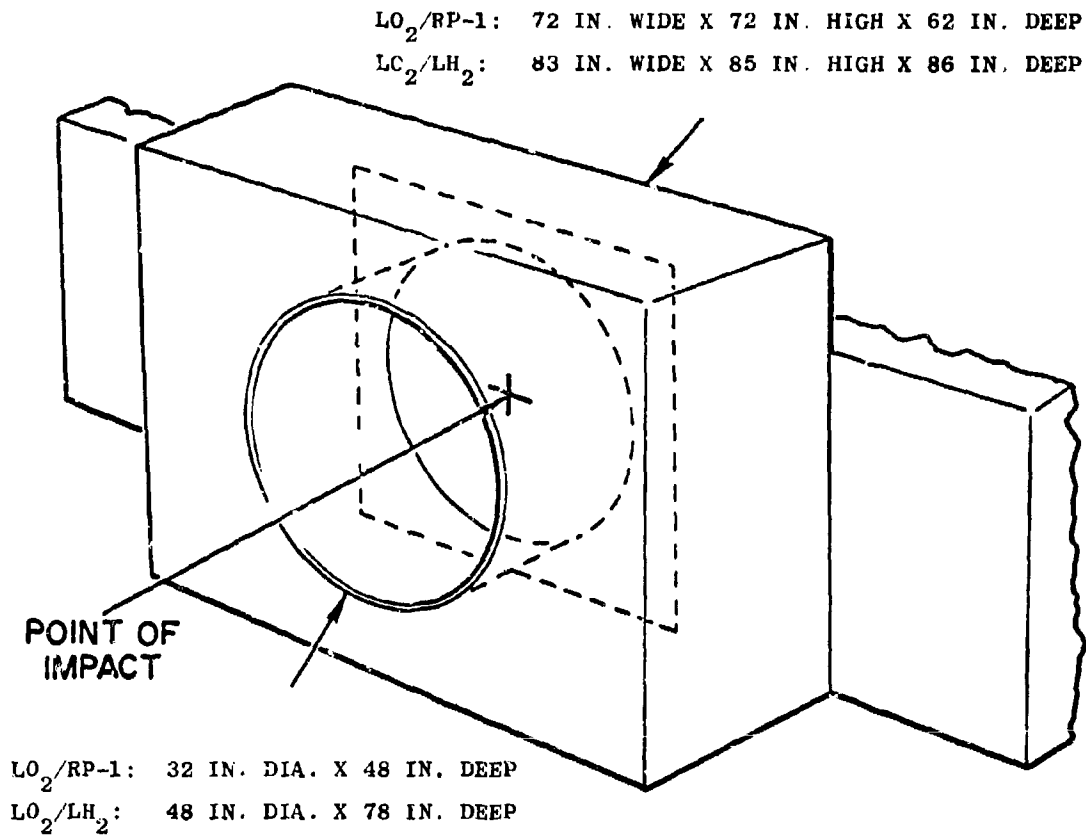
Fig. 5-15   Deep-Hole Target for the Cryogenic Impact Tests
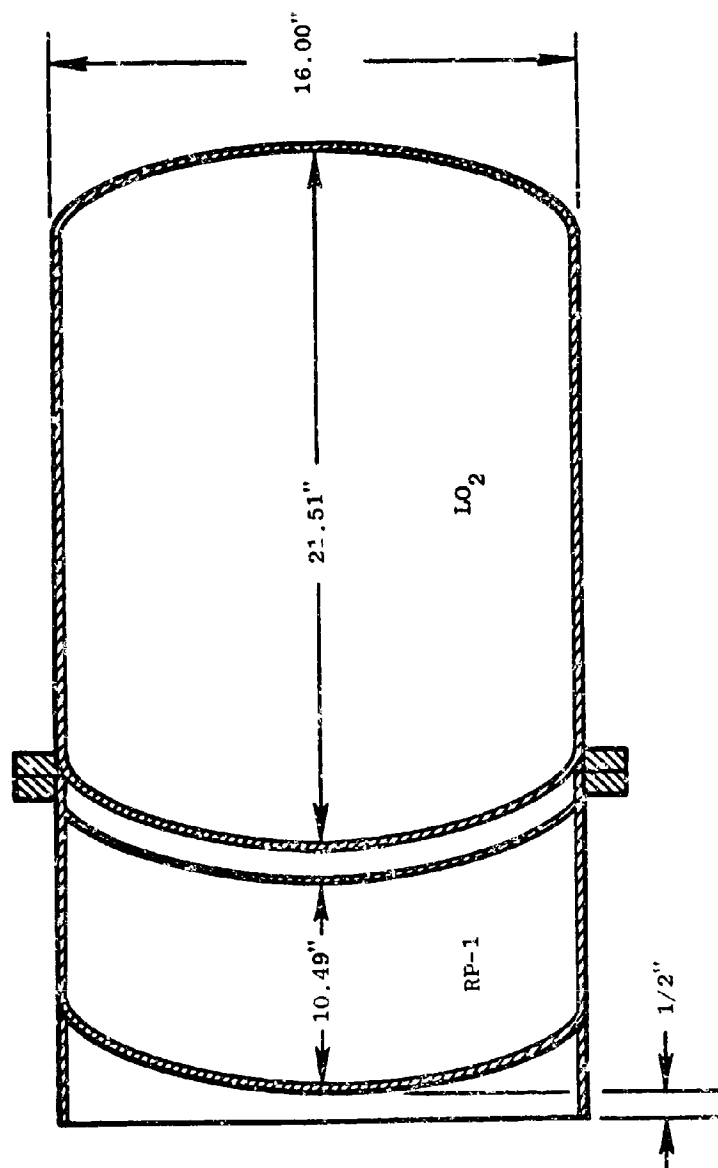
Fig. 5-16 200-lb LO$_2$/RP-1 Impact Tank

16.00"

21.51"

LO$_2$

10.49"

RP-1

1/2"
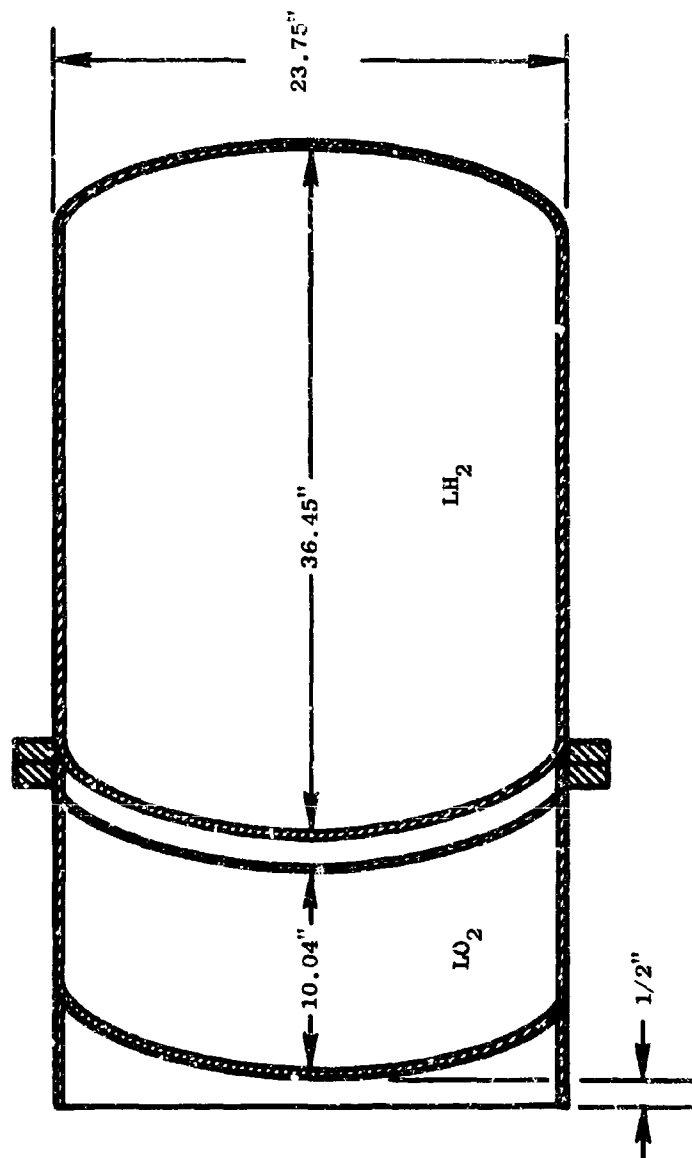
Fig. 5-17 200-lb LO_2/LH_2 Impact Tank

vented to the atmoshpere to prevent a possible negative pressure between
the bulkheads caused by the cooling of the air in this chamber by the
cryogenic propellants. All surfaces of the cryogenic compartments of these
tanks were covered with foamed-in-place polyurethane foam.

An enlarged d awing of the tank flange detail is shown in Fig. 5-18.
The flange labele No. 1 is securely welded to the rear tank and has bolt
holes of normal size. Flange No. 2 is securely welded to the forward
tank, has enlarged bolt holes, and is sandwiched between two Teflon gaskets
which are labeled in Fig. 5-18. The third flange is a loose clamping flange,
which was slipped on over the forward tank and has bolt holes of normal size.
The purpose of the Teflon and enlarged bolt holes in the forward tank flange
is to allow for thermal contraction of this tank, which always contained
the colder of the two propellants. A photograph of a LO_2/RP-1 tank in
place on the sled track is shown in Fig. 5-19.

The remaining test hardware, the test conditions, and the instrumentation
system were the same as that used in the second hypergolic high-velocity test
series discussed in Section 4.

Scale

2.2" = 1"

6 welds

1. 1" x 3/8" flange
2. 1" x 3/8" flange
3. 1" x 1/4" clamping flange
4. 1" x 1/8" Teflon gasket
5. 7/8"x 1/8" Teflon gasket
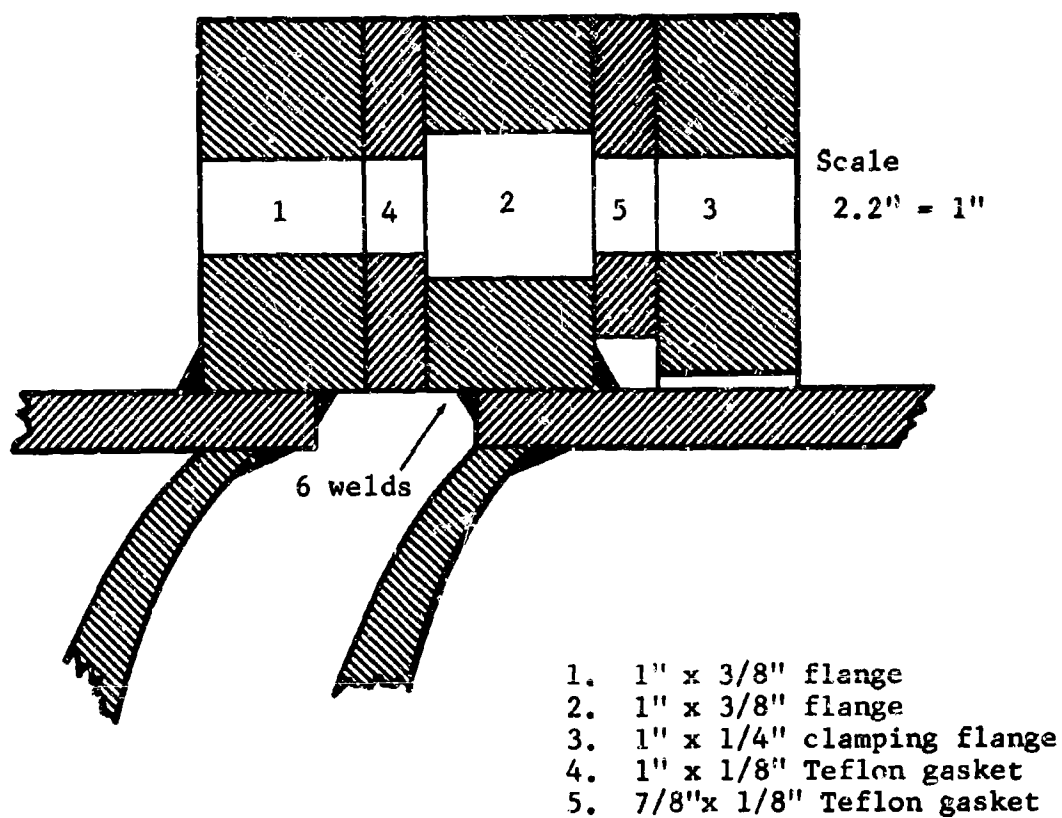
Fig. 5-18. Tank Flange Detail
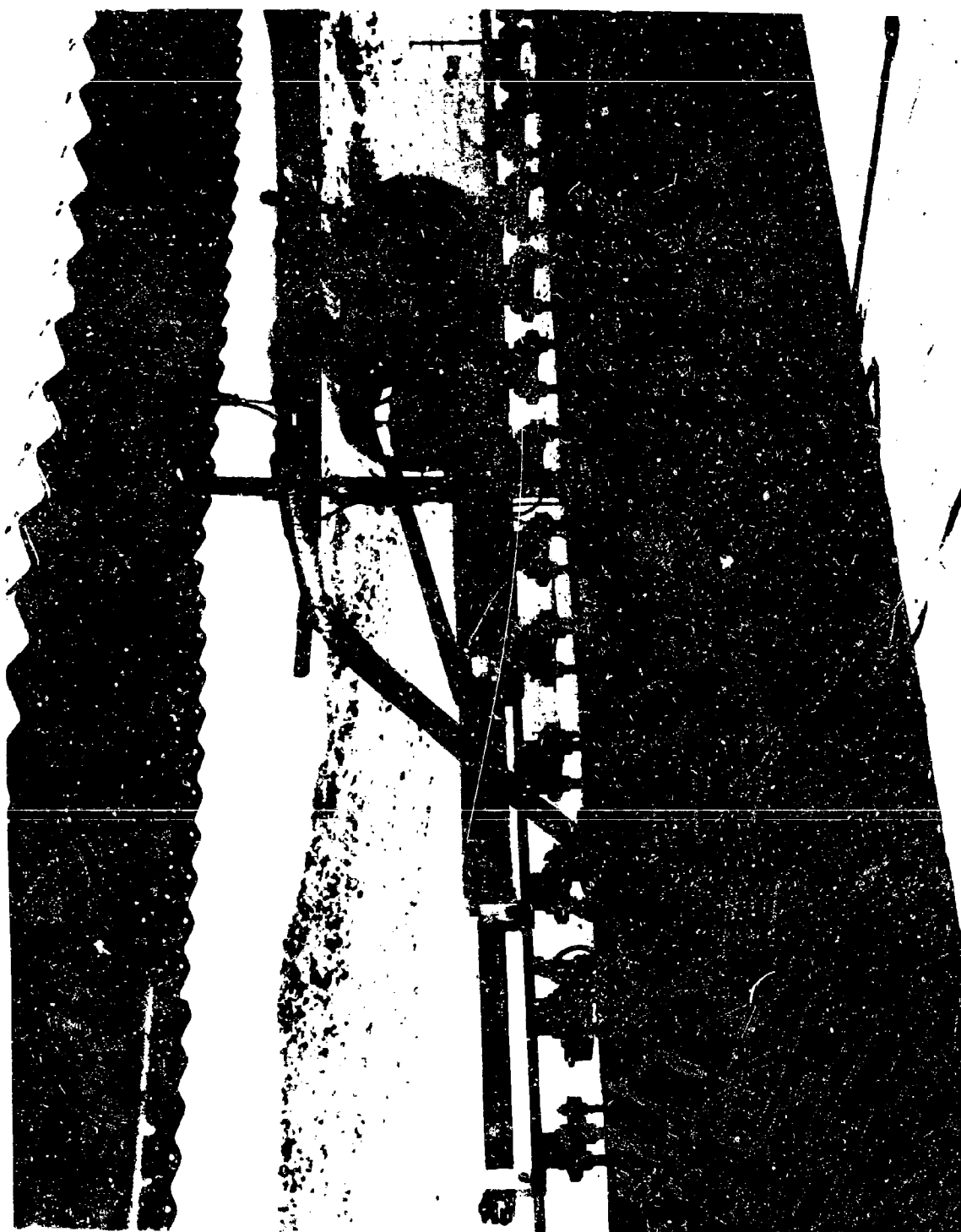
Fig. 5-19 Photo of Tank on Sled Track

Part 2 - TEST RESULTS FROM THE BASIC PROGRAM

General

    As noted in the beginning of this section, a total of 212 tests were con-
ducted using the cryogenic propellant combinations $LO_2/RP-1$ and LO_2/LH_2. Of
the total number, 152 were considered as valid tests, meeting the requirements
of the basic PYRO program discussed in Section 3. A summary of these tests is
presented in Table 5-1. These tests are discussed in Part 5 of this section.
Included in this part of the report are: a brief description of the instrumen-
tation system to indicate the overall scope of the data; a discussion of the
method used to obtain representative explosive yield values; a table of the
yield values for each valid test; and a discussion of the comparisons between
propellant peak overpressure[*] and positive-phase-impulse[*] distance curves and
those for TNT.

Instrumentation Systems

    The cryogenic CBM and CBGS tests were conducted at AFRPL, and the blast
environment was measured using the basic PYRO instrumentation system. This
system consisted of 15 piezoelectric transducers distributed along three radial
lines, 120 deg apart and at five distances from ground zero. A sketch of the
gauge layout is presented in Fig. 5-20. The system was designed to cover the
pressure range from 1 to 100 psi and to have a minimum of three gauges in the
region below about 15 psi, where the shock wave would be expected to be unsup-
ported, i.e., classical in nature for a 10 percent nominal explosive yield.

    To maintain these criteria, the gauge location distances were increased
with increasing propellant weight. This is illustrated in Table 5-2, which
lists typical blast instrumentation distances for tests with 200, 1000,

---

[*]   The terms peak overpressure and overpressure and positive-phase impulse and
     impulse are used interchangeably throughout this section.

Table 5-1

SUMMARY OF CRYOGENIC TESTS

Propellant Type	Test Configuration	Propellant Weight (lb)	Number of Tests
LO_2/RP-1	Confinement-by-the-Missile	133	2
		200	16
		1,000	4
		25,000	3
		100,000	1
	Confinement-by-the-Ground Surface	200	34
		1,000	7
		25,000	2
	High-Velocity Impact	200	4
LO_2/LH_2	Confinement-by-the-Missile	133	2
		200	16
		1,000	4
		25,000	3
		100,000	1
	Confinement-by-the-Ground Surface	200	40
		1,000	7
		25,000	3
	High-Velocity Impact	200	2
Combined LO_2/RP-1 and LO_2/LH_2	Confinement-by-the-Ground Surface	1,200	1

C

IX

VIII

VII

VI

SEE DETAIL A BELOW

V

V

VI

VI

VII

VII

VIII

VIII

IX

A　IX

B

IV

III

II

I

II

III

IV

I

II

III

IV

III

II

IV

DETAIL A

Fig. 5-20　Gauge Layout

Table 5-2
SUMMARY OF BLAST INSTRUMENTATION

No.	Gauge Line	Nominal Distance (ft)	200 lb P_s*	200 lb P_o**	1000 lb P_s	1000 lb P_o	25000 lb P_s	25000 lb P_o	100000 lb P_s	100000 lb P_o
I	A	2.8		X						
	B									
	C									
II	A	4.5	X	X		X				
	B									
	C									
III	A	7.5	X	X	X	X				
	B		X	X						
	C			X						
IV	A	13	X	X	X	X		X		X***
	B			X	X	X				
	C			X		X				X***
V	A	23		X	X	X	X	X		
	B			X		X				X
	C			X		X				X
VI	A	58		X		X	X	X		
	B			X		X	X	X		X
	C			X		X		X		X
VII	A	67		X		X	X	X		X
	B			X		X		X		X
	C			X		X		X		X
VIII	A	117				X		X		X
	B					X		X		X
	C					X		X		X
IX	A	200						X		X
	B							X		X
	C							X		X
X	A	335						X		X
	B							X		X
	C							X		X
XI	A	600						X		X
	B							X		X
	C							X		X

*   head-on-oriented stagnation pressure sensor

**   side-on-oriented overpressure sensor

***   a single gauge at the 13-ft distance was alternately located along gauge lines A and C

and 25,000 lb of propellant. To supplement the basic overpressure measure-
ment system, two overpressure gauges were installed as close to the explosion
as practical and stagnation pressure gauges spanning the range from near
ground zero to the 30-psi level were installed for many of the tests. A
complete description of the system and the methods of calibration and estimates
of the accuracy of the system are given in Appendix A.

The cryogenic high-velocity-impact tests were conducted at the Naval
Weapons Center, China Lake, California. The instrumentation layout used
for this series is the same as that used for the second hypergolic high-
velocity impact test series. A sketch of this system is shown in Figure
5-21. The propellant tanks in these tests were propelled along a track and
allowed to impact into a target. Piezoelectric overpressure gauges were
installed at four distances on a line 30 deg from this track, at three dis-
tances at 90 deg and at two distances in line with the track and behind the
target.

Test Results

The peak overpressure and positive-phase-impulse data for the CBM and
CBGS tests are presented in Volume 2. Also presented with these data
are the TNT equivalent yield values for each of the peak overpressure and
positive-phase-impulse numbers.

A study of these TNT equivalent yield values indicated that the explosive
behavior of the cryogenic propellant mixtures in many cases was somewhat
different from TNT, in that the explosive yield tends to be a function of
distance and in some cases a function of the parameter measured. This
behavior appeared to take two general forms. For low yields, it was commonly
observed that both pressure and impulse yields increased with increasing
distance from the explosion, with the yields tending toward a constant value
(the terminal yield) at long distances. In addition, the impulse yield was
usually higher than the pressure yield and changed more slowly with distance.
For higher yields, the pressure yield behaved in the same fashion, but the

K₂ TRACK

30° LINE

30°

C

B

A

90° LINE

D   C   B   ← TARGET

NOMINAL GZ-TO-STATION
DISTANCE (ft)

A	13
B	23
C	38
D	67

C

180° LINE

D
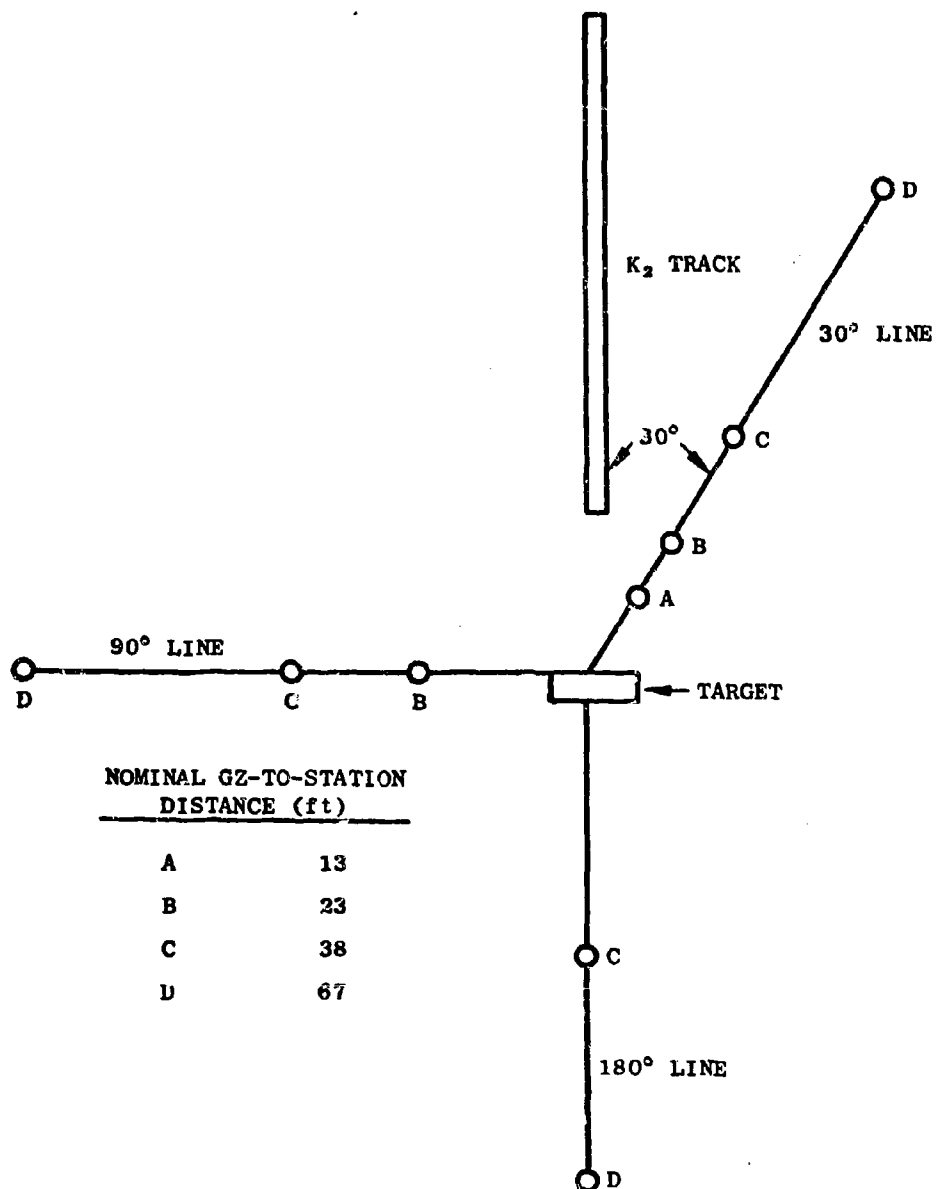
Fig. 5-21. Pressure Sensor Locations for Cryogenic High-Velocity
Impact Test Series

impulse yield at close distances was much greater than the pressure yield
and tended to decrease with increasing distance and ultimately approached
the pressure yield value. Two examples of this are shown in Figs. 5-22
and 5-23 which are plots of peak overpressure and positive-phase impulse
vs distance for two LO_2/LH_2 confinement-by-the-missile tests. Included
in these figures are curves (dotted lines) representing the peak over-
pressure and impulse that would be obtained if the various indicated percent-
ages of 200 lb of TNT were exploded on the ground surface (TNT overpressure
data were obtained from Ref. 5-1 and impulse data from Ref. 5-2).

Note in Figs. 5-22 and 5-23 that both the peak overpressure and positive-
phase-impulse data for the lower yield test, Number 091, tend to show an in-
crease in yield with an increase in distance. The peak overpressure data for
the higher yield test, Number 090, also show an increase in yield with distance
but the positive-phase-impulse data show a decrease with distance.

Because of this yield variation with distance and in some cases with
the shock wave parameter used in the computation, the explosive yield number
used in this report is the terminal yield, i.e., the yield obtained at long
distances from the explosion where both the pressure and impulse yields
tend to reach a constant value.

The terminal yields for the $LO_2/RP-1$ and LO_2/LH_2 confinement-by-the-missile
tests are presented in Tables 5-3 and 5-4 and for the $LO_2/RP-1$ and LO_2/LH_2 con-
finement-by-the-ground-surface tests in Tables 5-5a and b and 5-6a and b. The
terminal yields for both the $LO_2/RP-1$ and LO_2/LH_2 high-velocity-impact tests
and a combined $LO_2/RP-1- LO_2/LH_2$ CBGS test are presented in Tables 5-7a and b.

Pressure and Impulse – Distance Curves

A comparison between the shapes of the propellant pressure and impulse –
distance curves and those for TNT is shown in Figs. 5-24 through 5-31, which
are plots of the pressure or scaled impulse ($I/W_T^{1/3}$) as a function of
scaled distance ($D/W_T^{1/3}$). Each point represents the average pressure of
all gauges (usually two or three) at a given distance for a given test.
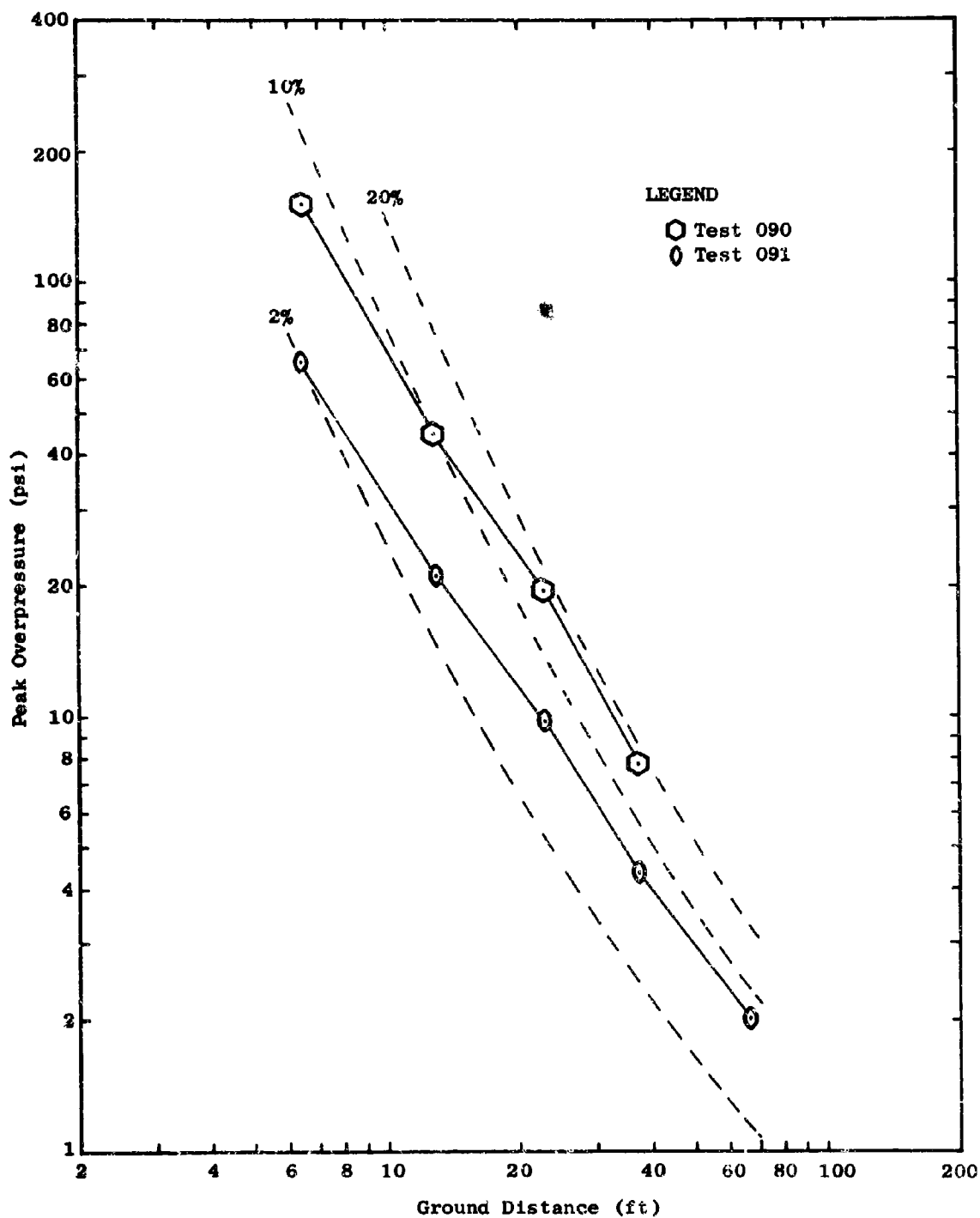
Fig. 5-22 Peak Overpressure vs Ground Distance for 200-lb LO_2/LH_2 Confinement-by-the-Missile Tests, $L/D = 1.8$, $D_o/D_t = 0.45$ (Dashed lines are TNT surface burst reference curves)
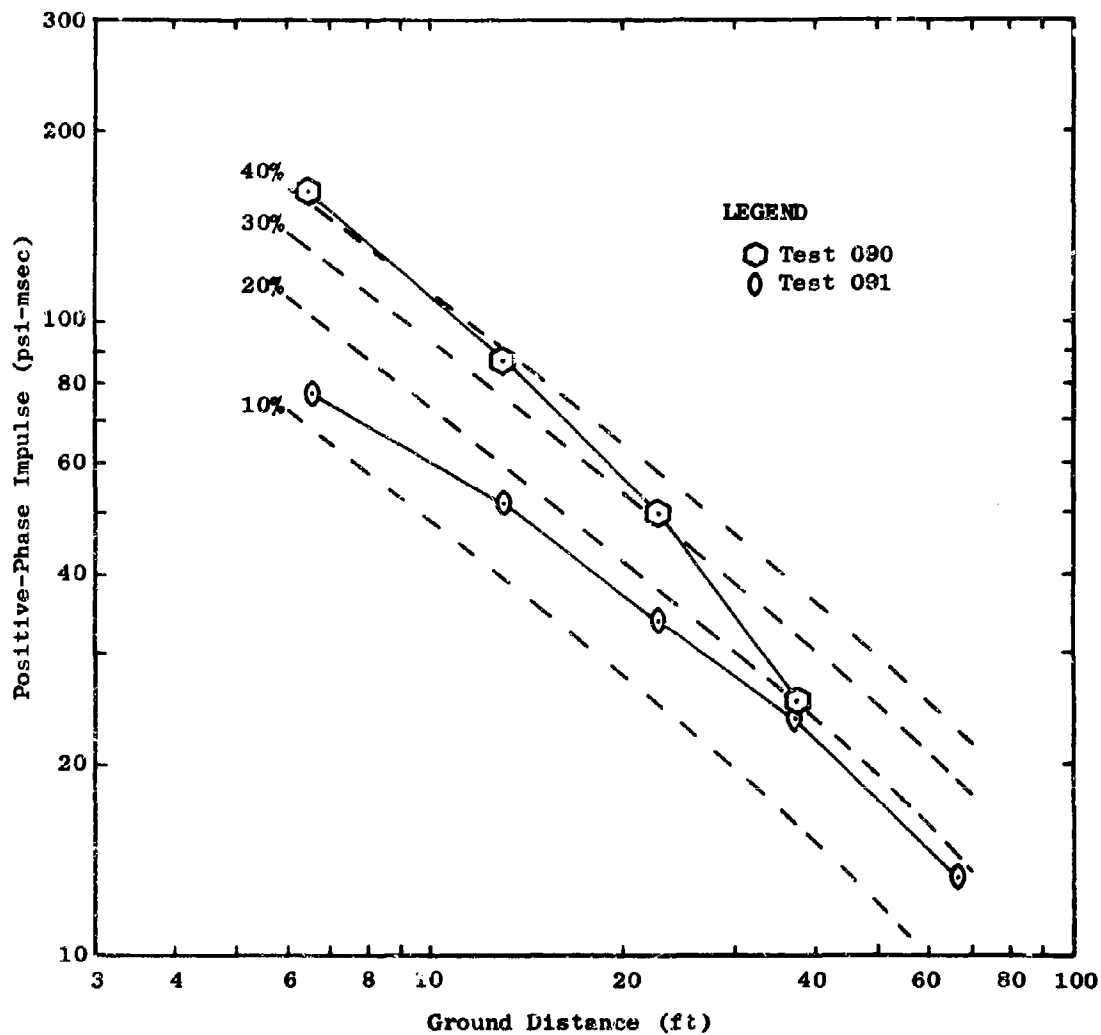
Fig. 5-23. Positive-Phase Impulse vs Ground Distance for 200-lb LO_2/LH_2 Confinement-by-the-Missile Tests, $L/D = 1.8$, $D_o/D_t = 0.45$ (Dashed lines are TNT surface burst reference curves)

Table 5-3

LC$_2$/RP-1 CONFINEMENT-BY-THE-MISSILE TESTS

L/D	D_o/D_t	PROPELLANT WEIGHT (lb)	TEST NO.	TERMINAL YIELD (%)	IGNITION TIME (msec)
1.8	1	200	042	48	290
			058	27	200
			086	14	100
	0.45	200	044	18	120
			087A	16	70
			095A	17	120
			101	35	145
			237	32	127
			238	19	85
			239	32	156
		Partial Full*	174	52	150
			240	60	156
	0.45	1000	192	14	216
			193	20	222
			209	10	121
			270A	13	225
	0.45	25000	275	4	515
			278	13	530
			282	13	540
5	1	200	047	10	120
			049	12	316
			085	12	380
5	0.45	200	046	17	143
			088	4	60
			100	23	220
4	0.1375	94000	301	4	840

* Tank contained ~133 lb propellant

Table 5-4

LO_2/LH_2 CONFINEMENT-BY-THE-MISSILE TESTS

L/D	D_o/D_t	PROPELLANT WEIGHT (lb)	TEST NO.	TERMINAL YIELD (%)	IGNITION TIME (msec)
1.8	1	200	050	86	180
			051	22	80
			093	34	147
	0.45	200	053	4	1
			090	29	35 sec
			091	13	0
			118	20	82
			199	8	816
			200	17	417
		Partial Full*	167	24	8.74 sec
			172	35	770
		1000	210	7	20
			212	27	1366
			213	35	708
			265	10	750
		25000	277	0.2	31
			279	0.2	33
			281	0.1	-
5.1	1	200	052	7	83
			057	1	12
			092	26	3 min
	0.45	200	054	6	17
			055	1	1
			094	25	329
			138	17	100

* Tank contained ~133 lb propellant.

Table 5-5a

LO$_2$/RP-1 CONFINEMENT-BY-THE-GROUND-SURFACE VERTICAL TESTS

L/D	PROPELLANT WEIGHT (lb)	VELOCITY RANGE	PROPELLANT ORIENTATION	TEST NO.	TERMINAL YIELD (%)	IGNITION TIME (msec)
1.8	200	Low 23 ft/sec	Normal	096	14	50
				144	24	190
				202	42	870
				248	25	210
			Reversed	097	32	240
		Medium 44 ft/sec	Normal	208	62	460
				232	30	1220
				249	50	710
				250	52	200
	1000	Medium 44 ft/sec	Normal	218	4	0
				219	14	1835
				220	96	525
				267	64	1770
				268	70	340
	25000	Medium 44 ft/sec	Normal	284	2	0
				285	37	465
	200	High 78 ft/sec	Normal	110	26	35
				141	5	0
				205	41	40
				206	85	350
				207	38	28
				236	74	720
	200	High 78 ft/sec	Reversed	107	29	42
				142	14	33
	1000	High 78 ft/sec	Normal	190	96	570
				269A	44	77
5	200	Low 23 ft/sec	Normal	098	14	300
				154	18	470
			Reversed	099	23	140
		High 78 ft/sec	Normal	109	10	40
			Reversed	108	31	60

Table 5-5b

LO$_2$/RP-1 CONFINEMENT-BY-THE-GROUND SURFACE HORIZONTAL TESTS

(All Tests 200 lb Propellant Weight)

PROPELLANT TYPE	VELOCITY RANGE*	PROPELLANT ORIENTATION	TEST NO.	TERMINAL YIELD (%)	1ST PROP. TO 2ND PROP. (msec)	2ND PROP. TO IGNITION (msec)
LO$_2$/RP-1	Low 23 ft/sec	Normal	121	30	**	184
			122	28	388	139
			123	25	362	53
			176	65	468	374
			177	30	111	203
		Reversed	155	55	314	202
			156	63	182	230
	High 78 ft/sec	Normal	124	5	238	0
			125	52	142	76
			127	42	510	55
			140	12	420	10
			179	12	787	23

*   Velocity shown for top propellant only.   Bottom propellant velocity ~12 ft/sec for all tests.

**   RP-1 on ground at start of film.

Table 5-6a

LO$_2$/LH$_2$ CONFINEMENT-BY-THE-GROUND-SURFACE VERTICAL TESTS

L/D	PROPELLANT WEIGHT (lb)	VELOCITY RANGE	PROPELLANT ORIENTATION	TEST NO.	TERMINAL YIELD (%)	IGNITION TIME (msec)
1.8	200	Low 23 ft/sec	Normal	105	7	0
				152	14	480
				153	14*	121
				184	17	810
				201	26	1524
				225	34	933
		Medium 44 ft/sec	Normal	197	19	500
				203	31	800
				204	42	317
				229	53	1374
				230	21	24
				231	24	525
				251	64	775
				252	38	325
				254	32	533
	1000	Medium 44 ft/sec	Normal	211	12	0
				217	33	1490
				262	42	900
				264	22	21
				266	14	0
	25000	Medium 44 ft/sec	Normal	288C	13	365
				289	4	166
				290	4	105
	200	High 78 ft/sec	Normal	114	54	74
				150	35	40
				151	46	167
				195	104	292
				226	51	283
	1000	High 78 ft/sec	Normal	215	20	20
				216	9	0
5	200	Low 23 ft/sec	Normal	104	6	258
				164	4	125
				165	8	325
			Reversed	103A	39	208
		High 78 ft/sec	Normal	116	10	18
				160	32	67
				161	5	0
			Reversed	113	52	77
				115	15	93

*   No impulse because of bad timing

Table 5-6b

LO_2/LH_2 CONFINEMENT-BY-THE-GROUND SURFACE HORIZONTAL TESTS

(All Tests 200 lb Propellant Weight)

PROPELLANT TYPE	VELOCITY RANGE*	PROPELLANT ORIENTATION	TEST NO.	TERMINAL YIELD (%)	1ST PROP. TO 2ND PROP. (msec)	2ND PROP. TO IGNITION (msec)
LO_2/LH_2	Low 23 ft/sec	Normal	131	6	441	125
			132	5	0	0
			133A	6	289	286
			185	8	469	0
			186	9	597	61
			223	18	708	157
			224	16	899	621
	High 78 ft/sec	Normal	183	15	448	0
			196	17	639	77
			228	34	560	42
			253	57	561	108

* Velocity shown for top propellant only. Bottom propellant velocity ~12 ft/sec for all tests.

Table 5-7a

CRYOGENIC HIGH-VELOCITY-IMPACT TESTS

Propellant Type	Test Number	Target Geometry	Impact (fps)	Terminal Yield (%)
LO_2/RP-1	75	Flat Wall	526	21
	77	Flat Wall	523	20
	76	Deep Hole	523	57
	78	Deep Hole	518	77
LO_2/LH_2	79	Flat Wall	597	121
	80	Deep Hole	569	163

Table 5-7b

COMBINED PROPELLANT TEST
(LO_2/RP-1 and LO_2/LH_2)

L/D	Propellant Weight	Velocity Range	Propellant Orientation	Test No.	Terminal Yield (%)	Ignition Time (msec)
1.8	1000 LO_2/RP-1 and 200 LO_2/LH_2	Medium 44 ft/sec	Normal	295	70	544
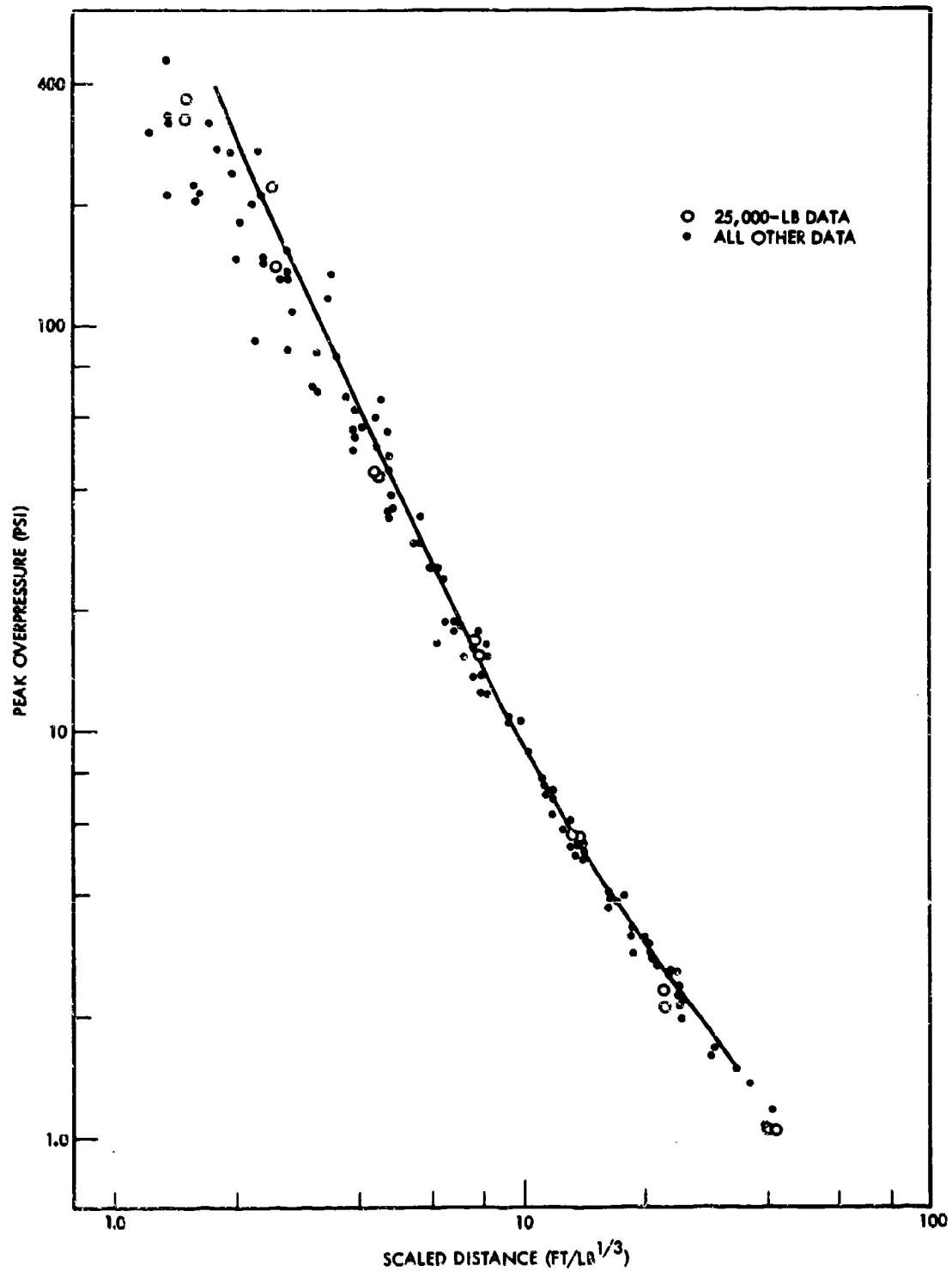
Fig. 5-24. Pressure vs Scaled Distance for $LO_2/RP-1$ CBM Case
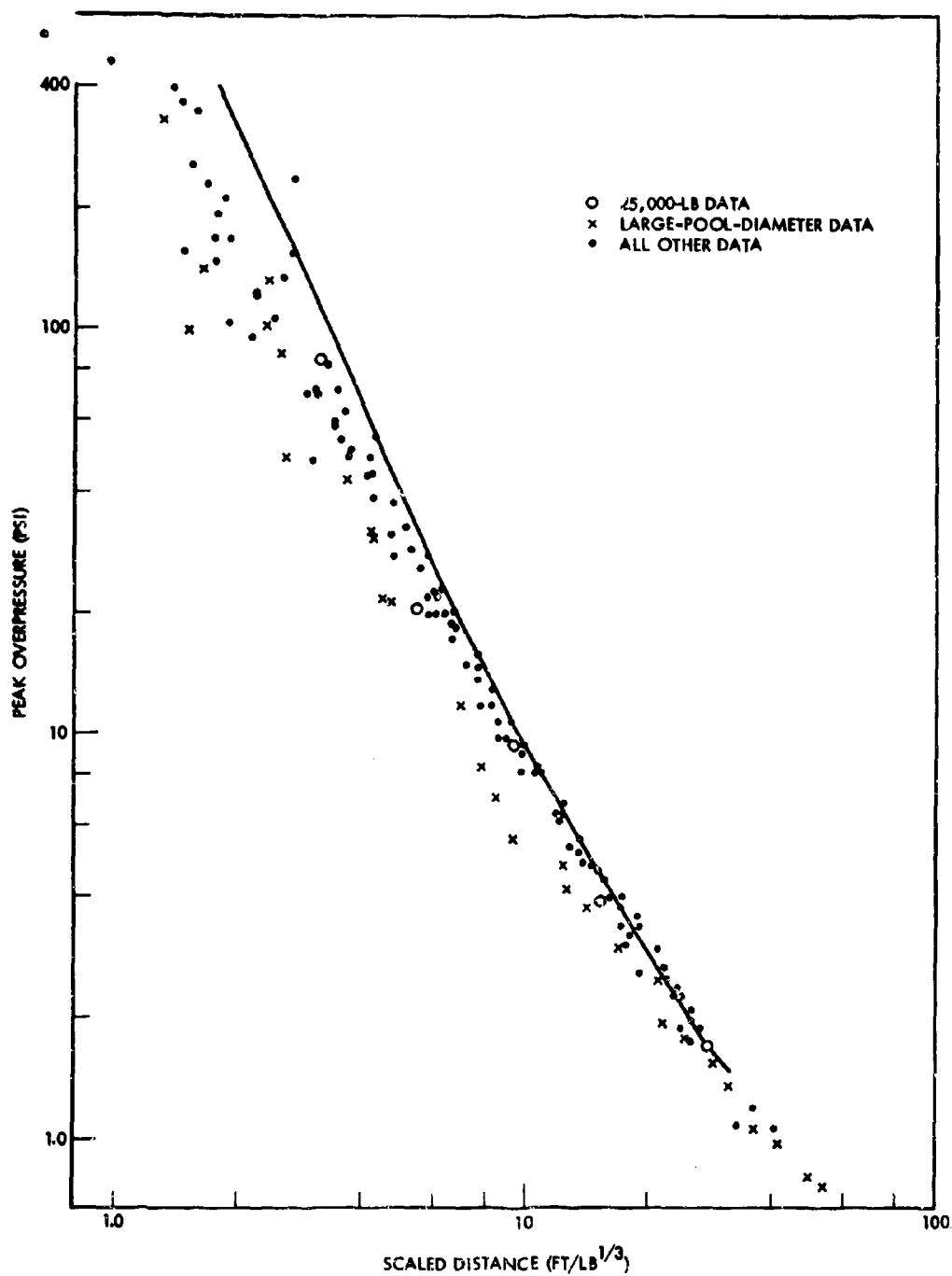
Fig. 5-25. Pressure vs Scaled Distance for LO_2/RP-1 CBGS-V Case
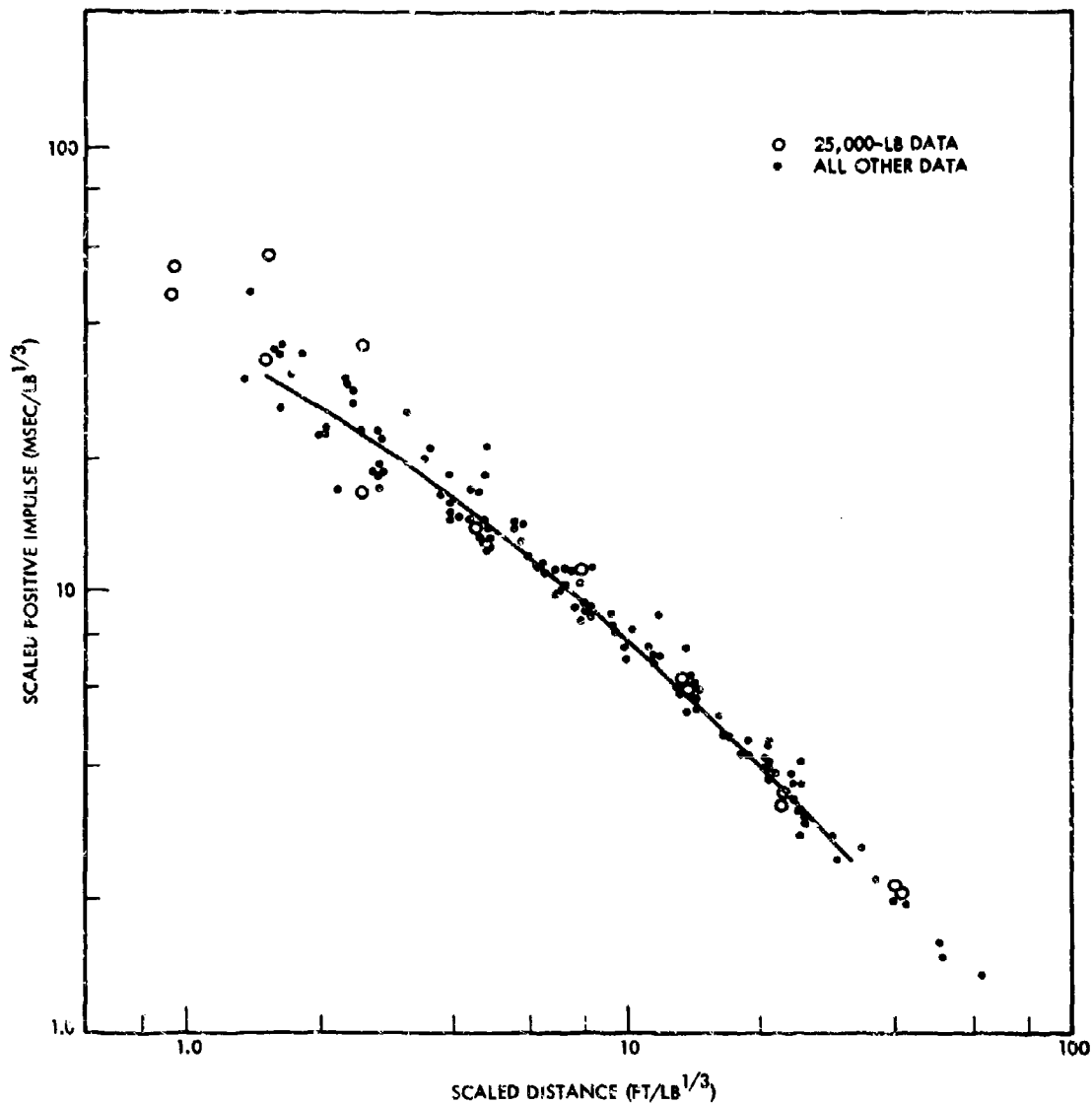
Fig. 5-26.   Scaled Positive Impulse vs Scaled Distance for LO_2/RP-1 CBM Case
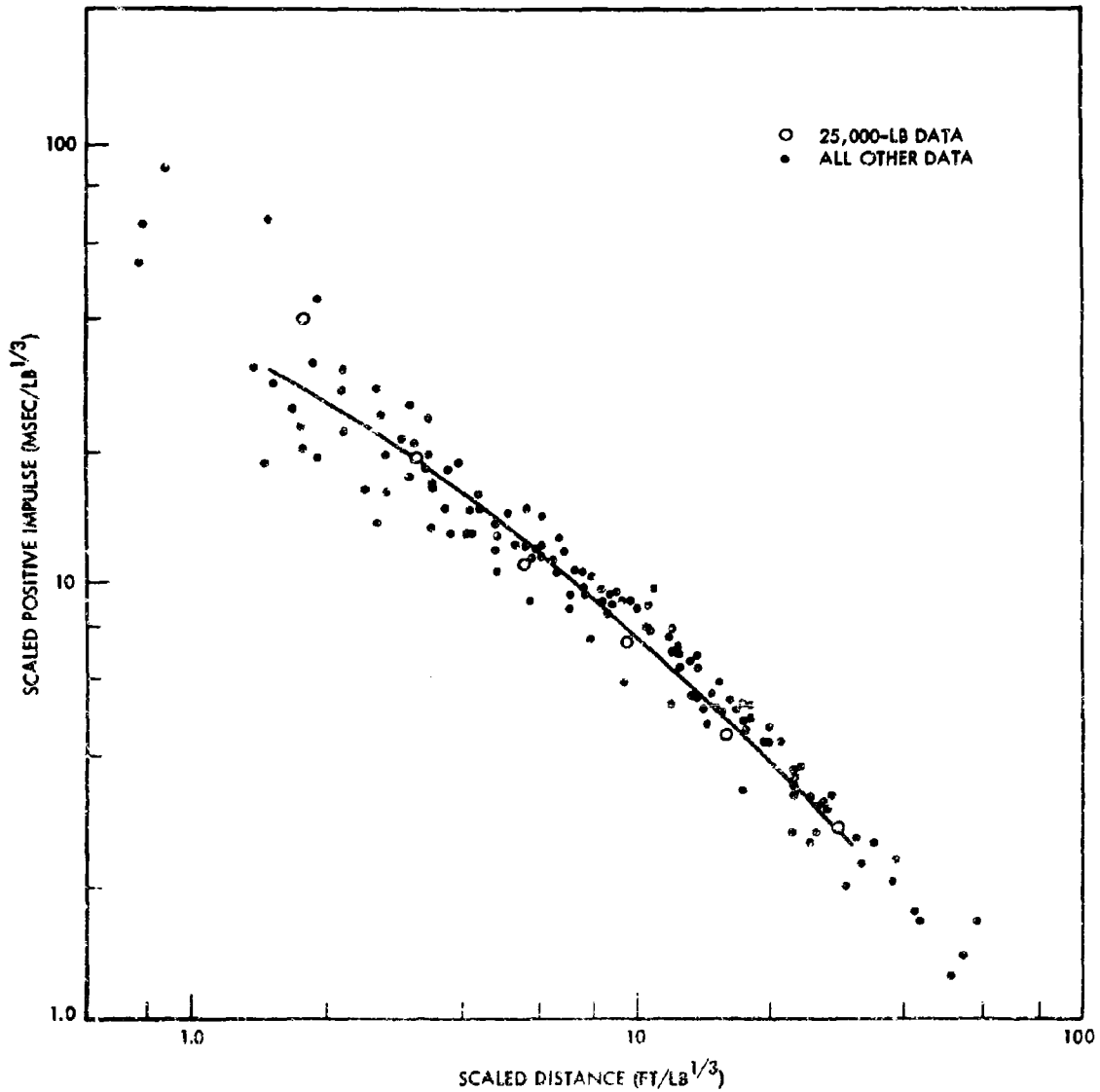
Fig. 5-27. Scaled Positive Impulse vs Scaled Distance for $LO_2/RP-1$ CBGS-V Case
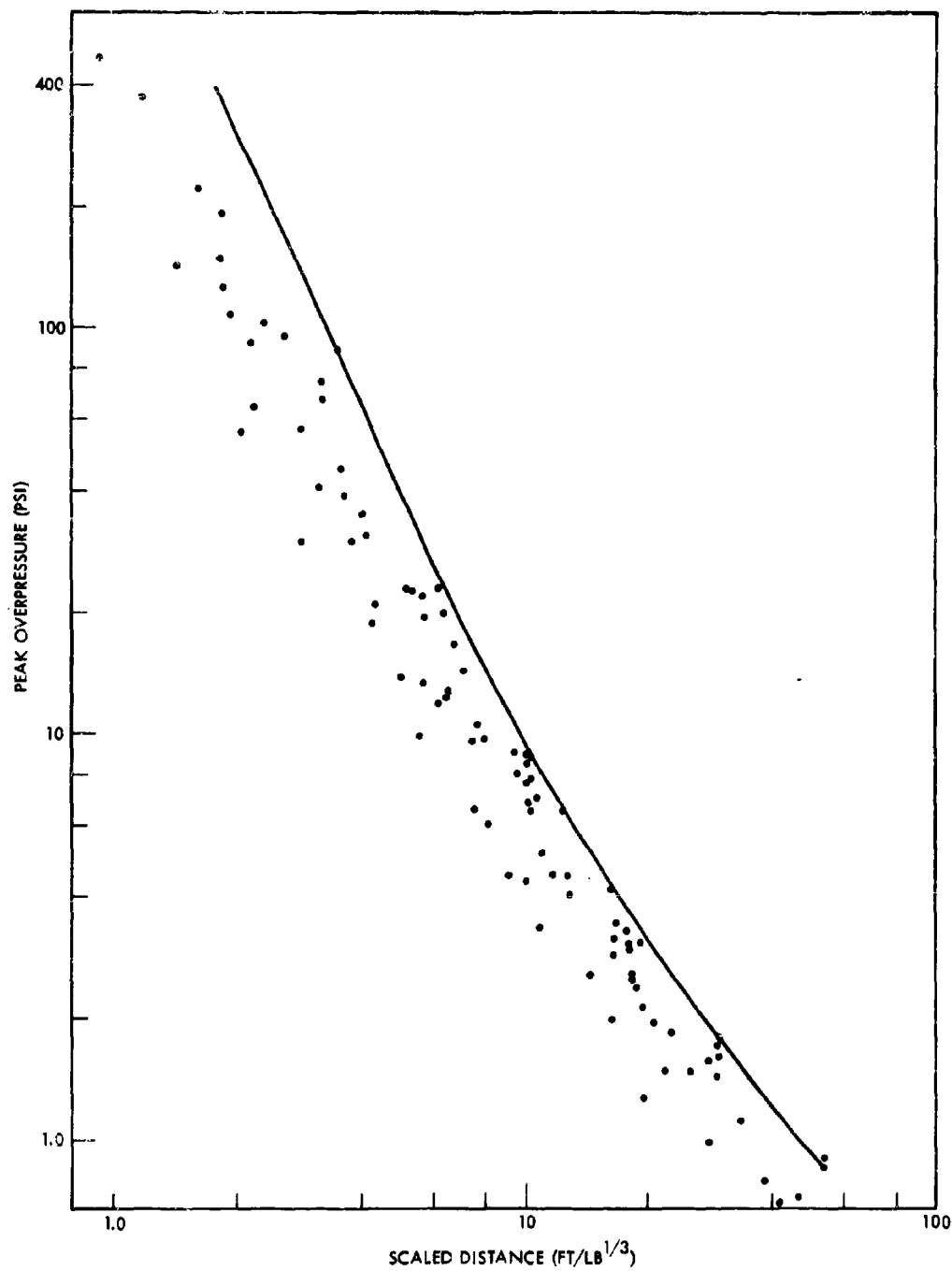
Fig. 5-28. Pressure vs Scaled Distance for LO_2/LH_2 CBM Case
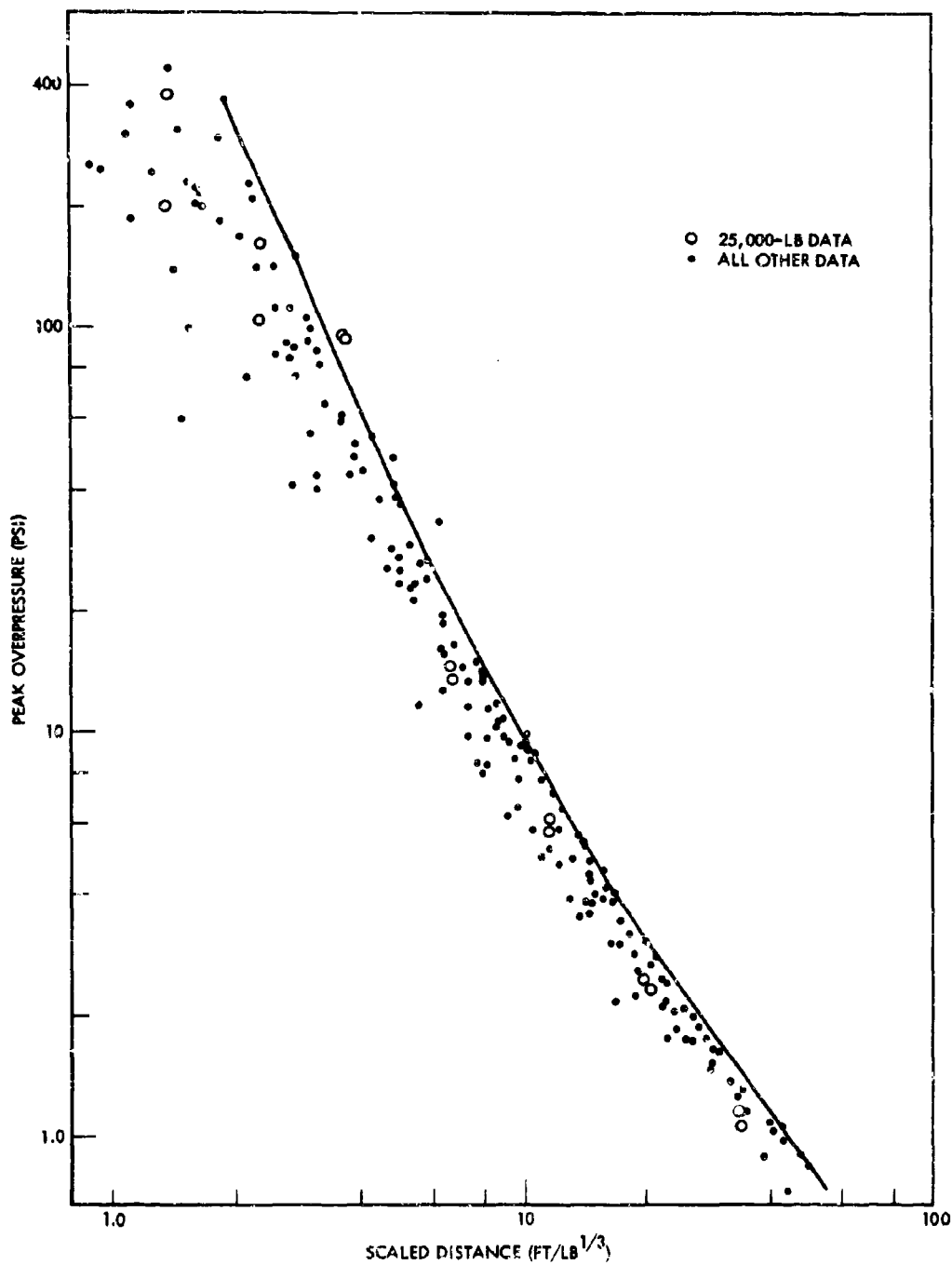
Fig. 5-29. Pressure vs Scaled Distance for LO_2/LH_2 CBGS-V Case
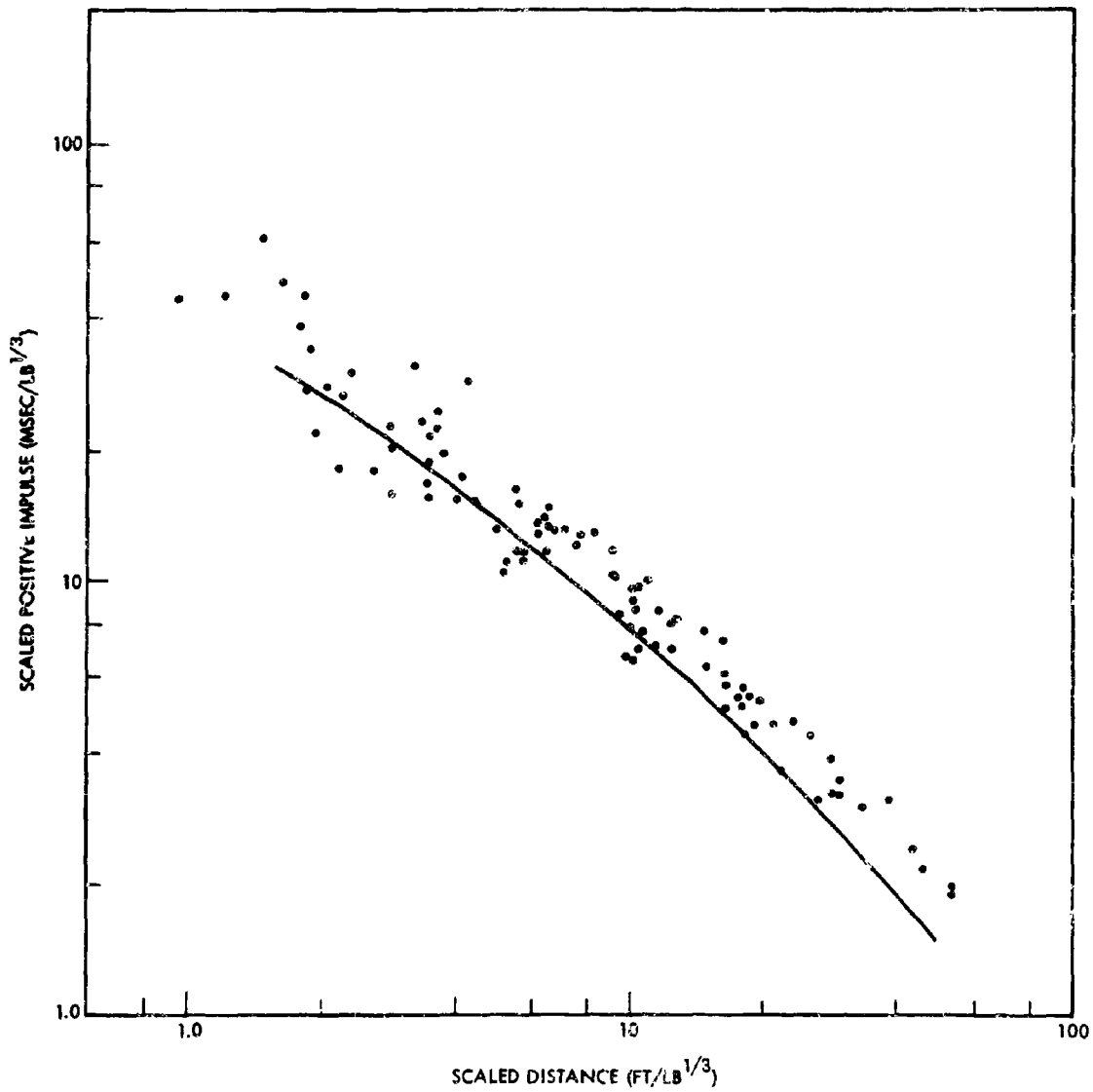
Fig. 5-30.　Scaled Positive Impulse vs Scaled Distance for LO_2/LH_2
　　　　　　CBM Case
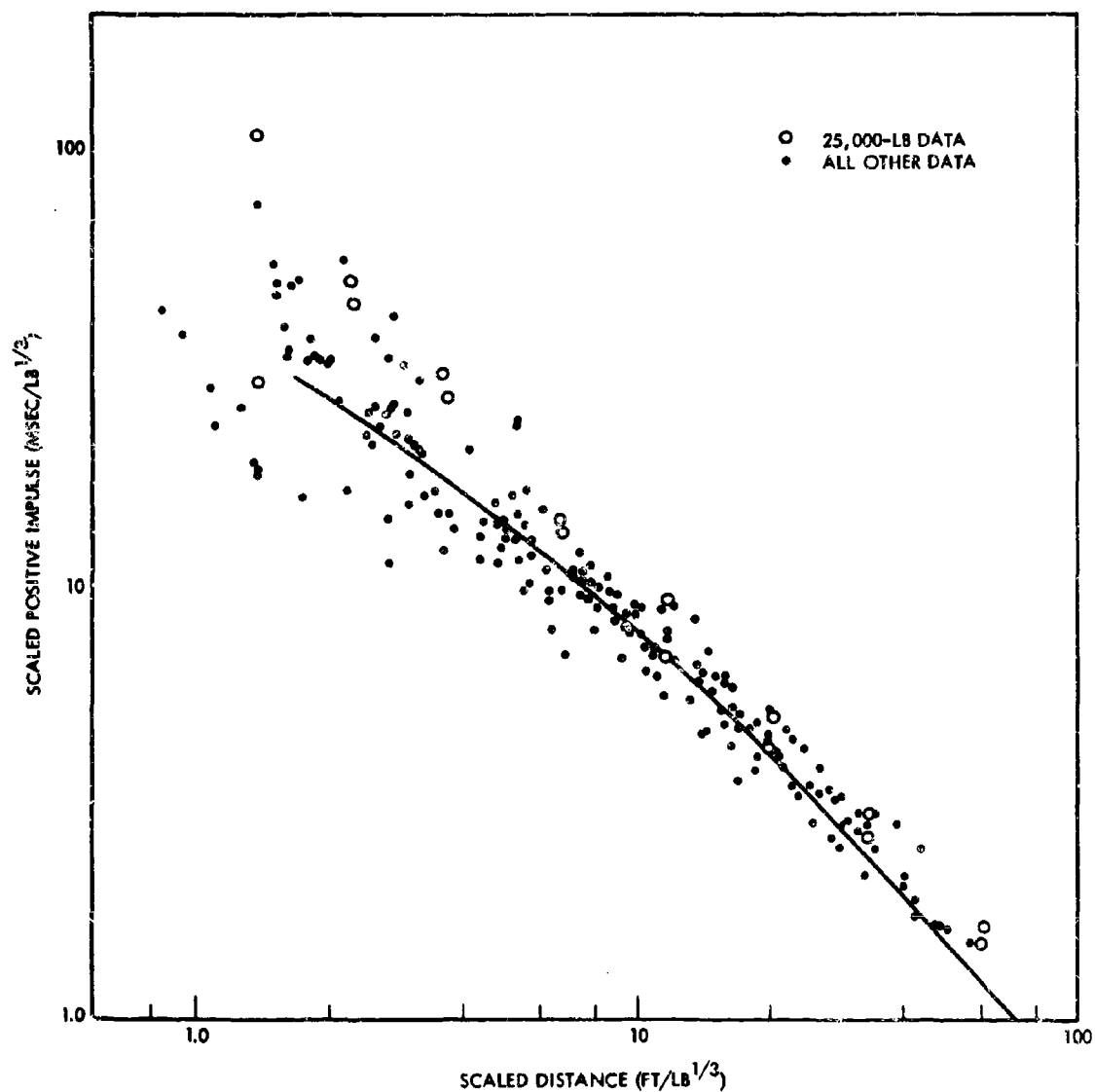
Fig. 5-31. Scaled Positive Impulse vs Scaled Distance for
LO$_2$/LH$_2$ CBGS-V Case

W_T is the TNT equivalent weight of the test (in pounds) and is equal to the product of the total propellant weight and the terminal yield. These plots include the data from more than 95 percent of all tests satisfying the CBM and CBGS-V cases. The CBGS-H data were much more limited and showed essentially the same trends as the CBGS-V results, so they were not included.

From Figs. 5-24 and 5-25, which are the pressure—distance curves for the LO_2/RP-1 CBM and CBGS cases, respectively, it can be seen that for all practical purposes the upper bound of the data is the TNT curve. It also can be seen that there is some spread below the reference curve. The spread tends to increase as the pressure increases. The bulk of the data, however, are within about 30 percent of the reference curve up to an over-pressure of about 50 psi (scaled distance of about 4.5 ft/lb$^{1/3}$). With only minor exceptions, the data points which are more than 30 percent below the reference curve in this region are for the CBGS case with long ignition times, where the propellants had spread to make large pools, greater than the critical size for maximum yield (noted as x points on graph).

Above about 100 psi (scaled distance of about 3.5 ft/lb$^{1/3}$), the spread increases rapidly and some of the data are as much as a factor of 4 or 5 below the reference curve, while others are still fairly close to the curve. Although there is some slight indication that the higher velocity impact points have a bigger deviation in this region, the data are not sufficient to clearly define any trends other than the one noted in the lower pressure region. Thus, although on the average the pressures in the region from 100 to 400 psi are about 60 to 70 percent of the TNT value, it would be difficult to guarantee that any particular test would do this.

Note that the data from the three 25,000-lb tests (included on these plots as O points) show essentially the same results as the smaller scale data. The one low yield value (CBM, 25,000-lb test, Number 275) which is not shown on these plots gave pressure data points which were about 60

percent of the reference curve and impulse data points a corresponding
amount above the reference curve.

The LO_2/RP-1 impulse data are compared with the TNT reference curves
in Figs. 5-26 and 5-27. In this case the spread of data is nearly
symmetrical about the reference curve and again the spread tends to get
larger as the scaled distance gets smaller. With only no exceptions the
data lie within about 30 percent of the curve down to a scaled distance of
about 4 (corresponding to an overpressure of about 70 psi). At smaller
scaled distances the spread increases to about 50 percent. There is some
indication that, on the average, the CBM data are slightly higher than the
CBGS data, but these differences are small compared to the spread.

The LO_2/LH_2 pressure data given in Figs. 5-28 and 5-29 again show
that the TNT reference curve is a good upper bound and that the spread
tends to get larger for increasing pressure. The magnitude of the spread,
however, is considerably greater than for LO_2/RP-1. Even at pressures as
low as 1 psi, some of the data, particularly for the CBM case, are as much
as a factor of 1.5 to 2 below the reference curve. There is some indication
that the higher yield values lie somewhat closer to the line than do the
lower yields values, but the trend is not entirely consistent. On the
average, the CBM data are about a factor of 2 below the reference curve up
to an overpressure of about 100 psi and a little more than that above
100 psi. The CBGS data have about the same spread above 100 psi but a
significantly smaller one below, decreasing to about a factor of 1.5 at
10 psi and 1.3 at 1 psi. The trends for the LO_2/LH_2 impulse data, which
are given in Figs. 5-30 and 5-31, are generally as expected from the pressure
data. At low pressures for the CBM case, where the pressures were well below
the curve, the impulses are correspondingly above the reference curve.
For both cases, on the average, the impulse data in the low-pressure region
lie above the reference curve, although the data scatter includes the curve.
In the higher pressure region the spread is more symmetrical about the curve.
An upper bound of 40 percent above the reference curve appears suitable
down to a scaled distance of about 5 and about 100 percent above the reference
curve for smaller scaled distances.

Table 5-8 summarizes the estimated upper bound information for the propellant curves in terms of their ratio to the TNT reference curves. Conservative estimates of the pressure and impulse values to be expected from propellant explosions can be obtained by multiplying the pressure and impulse values from the standard TNT reference curves by these ratios.

Table 5-8

Ratio of Estimated Upper Bound for
Propellant Data to TNT Reference Curves

PRESSURE

Propellant	Scaled Distance Range $(ft/lb^{1/3})$	R_1 *
$LO_2/RP-1$	all	1.0
LO_2/LH_2	all	1.0

IMPULSE

Propellant	Scaled Distance Range $(ft/lb^{1/3})$	R_1 *
$LO_2/RP-1$	≥ 3	1.3
	≤ 3	2.0
LO_2/LH_2	≥ 5	1.4
	≤ 5	2.0

* R_1 – estimated ratio of upper bound of propellant
data to TNT reference curve

Part 3 - DISCUSSION OF CRYOGENIC TEST RESULTS

General Analysis Approach

The general approach used in analyzing the results from each of the basic
test conditions in the cryogenic program was to first formulate trial general
relationships between explosive yield and the variables investigated for that
test condition. Statistical analyses were next performed using these relation-
ships to determine which of the alternate equation forms and parameter combina-
tions best explain the variations in observed yields and to derive values
for the constants of the selected equation form. Prediction intervals were
then developed which can be used with these functions to predict and bound
(with a high degree of certainty) the range of yield values expected to occur
for future tests in each condition.

A variety of statistical techniques was used to accomplish these steps,
the most important of which were regression analysis and prediction interval
estimation. The application of these techniques to the data is described in
detail in Appendix B and only the results of the analysis will be given here.

The trial general relationships or models relating explosive yield to
the parameters of interest were developed using all available information on
the propellant mixing and explosion process. These models have been of an
evolutionary nature; preliminary versions were formulated at the time of the
original planning of the test program in order to ma decisions about the
variables to be included in the test program and the relative effort to place on
the various phases. These models were based on the propellant explosion in-
formation existing at that time and on general hydrodynamic considerations.
The models have been modified and updated during the course of the program on
the basis of the experimental test data, high-speed photography of the tests,
and results from the transparent tank and laboratory test programs.

In the following material, the discussion of the analysis of results is
grouped first by the basic test condition (CBM, CBGS-V, CBGS-H, high-velocity
impact) and then by propellant type ($LO_2/RP-1$, LO_2/LH_2).

Confinement-by-the-Missile Case

Test Parameters

In the CBM case, the propellants are initially contained in a cylindrical tank divided into two compartments separated by a tempered-glass diaphragm. The ullage space in the upper propellant compartment is pressurized to about 20 psi, while that in the lower compartment is near ambient. On rupture of the diaphragm, the upper propellant is forced downward by the large pressure differential and impacts on the lower propellant.

The basic variables selected for testing in this condition were:

   t – the time between diaphragm rupture and ignition

   L/D – the length-to-diameter ratio of the propellants

   D_o/D_t – the ratio of the diameter of the diaphragm opening to the
           tank diameter

   W – the total propellant weight

In the majority of testing, the propellant compartments were fully loaded, which left approximately 10 percent of the volume of each tank for ullage space. In a few tests, however, a two-thirds-full propellant loading condition was used, which resulted in the ullage volume being about 40 percent of each compartment.

In all cases, the conventional propellant orientation was used, i.e., LO_2 over the RP-1 and LH_2 over the LO_2.

Descriptive Model for LO_2/RP-1 CBM Case

On rupture of the diaphragm, the LO_2 is forced downward by the approximately 20-psi pressure head and impacts on the RP-1, with the leading edge somewhat uneven and with some turbulance in the RP-1 created by the falling glass fragments. When the diaphragm opening is equal to the tank diameter ($D_o/D_t = 1$) the initial impact process tends to be relatively stable since the LO_2 mass has essentially the same cross-sectional area as the RP-1. Because the LO_2 density is 40 percent greater than that of the RP-1, however,

an instability should be created fairly rapidly, which may be augmented by
the localized differential pressures generated in the boiling heat transfer
process. In any case, there is a strong tendency for the LO_2 to penetrate
into the RP-1 pool. The details of the penetration process are uncertain,
although high-speed movies from a series of transparent tank tests (which
were unpressurized) suggest that penetration occurs on a scale much smaller
than the tank diameter and that it is not a simple overturning process of the
entire interface.

As the mixing process proceeds, increasing quantities of the RP-1 will
become partially or completely frozen, and it might be expected that this
frozen slush would tend to inhibit mixing and possibly cause it to ultimately
stop altogether. The experimental results suggest that some slowdown in
mixing may have occurred for the L/D of 5 case but that mixing is not basically
limited by such freezing, but rather by the pressure buildup in the tank
(produced by the evaporating LO_2) to a value greater than the bursting
pressure (approximately 100 psi).

From this model, it would be reasonable to expect that the rate of yield
buildup would be less as the L/D of the propellants increases, since this
results in an initially smaller interface and since the LO_2 has to penetrate
to a much greater absolute depth to involve the same fraction of the pro-
pellants. This need to penetrate to a greater absolute depth also suggests
the possibility that more of the LO_2 is evaporated in the process. If so,
it would not be surprising to find that the maximum yield obtainable (at
the time 100 psi was reached) also decreases somewhat with an increase in
L/D ratio.

The situation for the partially open diaphragm case ($D_o/D_t = 0.45$) is
expected to be somewhat different from that for the full-open case, since
the cross-sectional area of the impacting LO_2 stream is only about 20 percent
that of the RP-1 tank, thus permitting the LO_2 stream initially to penetrate
much more readily into the RP-1 pool. This plunging process is expected to
create a very rapid initial rate of mixing, and thus yield should be generated
more rapidly than for the fully open diaphragm case. This plunging process

would be expected to slow down greatly once sufficient LO_2 enters the RP-1 tank to fill its ullage space (approximately 10 percent of the total volume). For additional LO_2 to enter, some of the RP-1 must be forced into the upper tank. It is also anticipated that in the zone of mixing in the lower tank, there will likely be a larger surplus of RP-1 than in the fully open case. Thus, it would not be surprising that the amount of O_2 gas generated for a given amount of mixed propellant would be greater than for the fully open case. This would mean that the maximum yield reached before the tank bursts would be less.

As noted above, it is expected that the yield generation process is limited by tank rupture due to O_2 gas buildup rather than by any basic limitation on the mixing process itself. On this basis, it is evident that increasing the ullage volume would increase the amount of oxygen that could be vaporized before the tank ruptures, with a consequent increase in maximum yield. This raises the very likely prospect that partially filled tanks could lead to a larger total yield than completely filled tanks.

Because of the complexity of the LO_2 penetration processes as well as that of the subsequent mixing from the interfaces, there is uncertainty with regard to the specific nature of the expected scaling relations. With regard to time scaling, it can be argued that at least initially the mixing should tend to be proportional to the interface area. This would mean, for example, that an increase in linear scale by a factor of 2 (weight scale of a factor of 8) would give 4 times as much material mixed at a given absolute time, but this weight of mixed propellant would amount to only one-half as much of the original propellant weight.

Similarly, since the ullage volume would also be proportional to the cube of the linear scale factor, the pressure increase in the tank would be less at the same absolute time. Thus, as the scale increases, longer mixing times are expected to be required to give the same yield and pressure increase in the tank. To a first approximation, it seems reasonable to assume that time scaling is on a geometrical basis, i.e., that similar yield values (expressed as a fraction of the total propellant weight) would be obtained

at times divided by the linear scale factor (or cube root of the propellant weight).

Prediction Equation Development for LO_2/RP-1 CBM Case

Based on the above model the following general guidelines were obtained as the basis for formulating the trial equations to use in the statistical analyses.

1. Yield is expected to increase monotonically with time, and the yield value at zero ignition time is expected to be quite small (relative to the maximum value).

2. The most likely manner for time to scale is on the basis of geometrical scaling, which leads to the scaled-time term of $t* = t/W^{1/3}$.

3. There is no obvious reason to expect strong interactions between the effects of the variables.

The simplest equation which satisfies these guidelines has the following general form:

$$\frac{Y}{f(t*)} = g(L/D) + h(D_o/D_t) + j(W)$$

where f, g, h, and j denote functions of the variable in the parenthesis.

Trial plots of the data were then made to help determine the best specific form for the individual functions. These plots indicated that:

1. The rate of yield increase is nearly constant in time so that $f(t*) \approx t*$.

2. Simple first-power terms of L/D and D_o/D_t appeared to satisfactorily account for the effects of these variables, so that $g(L/D) \approx \alpha' + \gamma(L/D)$ and $h(D_o/D_t) \approx \alpha'' + \delta(D_o/D_t)$ where α', γ, α'', δ are constants.

3. There is a tendency for yield to decrease with an increase in scale (W); but the magnitude of the decrease also decreases with scale, so that $j(W) \approx \alpha''' + \beta/W$.

5-61

Thus the specific form of the first trial equation becomes

$$\frac{Y}{t^*} = \alpha + \beta/W - \gamma(L/D) - \delta(D_o/D_t)$$

Using this general form of the equation and the set of experimental data given in Table 5-3 (except for the partially full tests, Nos. 174 and 240), a stepwise regression analysis was then run which indicated that all of the parameter terms were significant. The result is given below:

$$\frac{Y}{t^*} = 1.07 + \frac{122}{W} - 0.175 \, L/D - 0.527 \, D_o/D_t$$

One disadvantage of this equation is that it treats the weight-scale effect as an additive term. Although it satisfactorily accounts for the change in yield with weight for the case studied at various weight scales (L/D of 1.8, D_o/D_t of 0.45), when used for larger scales with larger L/D values it gives unrealistically small yields. For example the equation gives negative yields for weights over about 4,000 lb for an L/D of 5 and a D_o/D_t of 0.45.

From the above it is clear that a more satisfactory form for the equation would involve the weight term as a multiplicative rather than additive factor despite the fact that this complicates the equation, particularly from the viewpoint of the statistical analysis procedures required.

The final form of the equation selected was

$$\frac{Y}{t^*} = (1 + \beta/W) \, (\beta_o + \beta_1 \, L/D + \beta_2 \, D_o/D_t)$$

The regression coefficients β_o, β_1, and β_2 were first determined using only the 200-lb data and letting the weight terms equal 1. These coefficients were then substituted back in the equation below and the values of α and β were determined using the data for all weights and for an L/D of 1.8 and a D_o/D_t of 0.45:

$$\frac{Y}{t^*} = (\alpha + \beta/W) \, (\beta_o + \beta_1 \, L/D + \beta_2 \, D_o/D_t)$$

By arithmetic manipulation, the coefficient values for the original equation were then determined (see Appendix B for details). The result is:

$$\frac{Y}{t^*} = (1 + \frac{217}{W}) (0.87 - 0.092 \, L/D - 0.28 \, D_o/D_t) \qquad (5.1)$$

This equation is compared with the experimental data in Fig. 5-32. To illustrate quantitatively the uncertainty in the prediction equation, the upper bounds to the 90-percent prediction intervals for the D_o/D_t of 0.45 curves are also shown in the figures. The meaning of these lines is that there is a 90-percent probability that the yield value obtained in a single future test will lie below the line.

It should be noted that the equation derived above is directly applicable to the following ranges of conditions

1. L/D ratios of the propellant between 1.8 and 5

2. D_o/D_t ratios from 0.45 to 1.0

3. Fully loaded propellant tankage having an ullage volume equal to 10 percent of the tank volume

4. Propellant tankage having a bursting strength of approximately 100 psi

5. All values of ignition time up to tank rupture

6. Propellant weights greater than 200 lb

The use of this equation for values of the parameters outside the ranges given above is considered below.

L/D Ratio. Values of this ratio less than 1.8 are not anticipated, so that the only concern is with values greater than 5. Although it is anticipated that the yield will continue to decrease with an increase in L/D, there is insufficient information available to know whether the rate of decrease would be the same as in the region where it was determined. Accordingly, it is recommended that a conservative approach be adopted by using an L/D value of 5 for all values greater than 5.
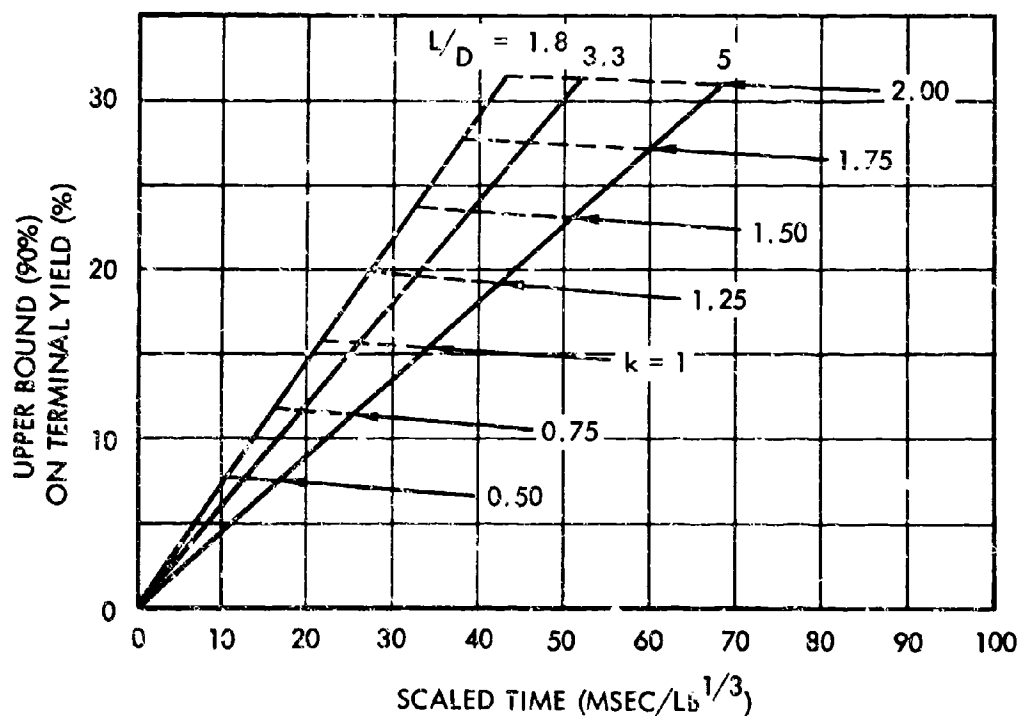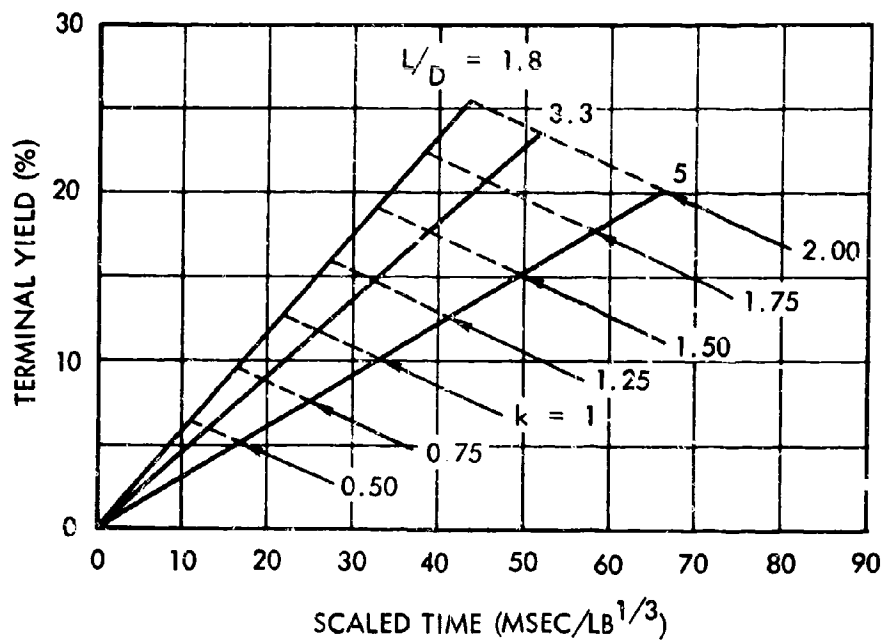
Fig. 5-36. Terminal Yield vs Scaled Time for LO_2/RP-1 CBM Case
as a Function of L/D and k Factor
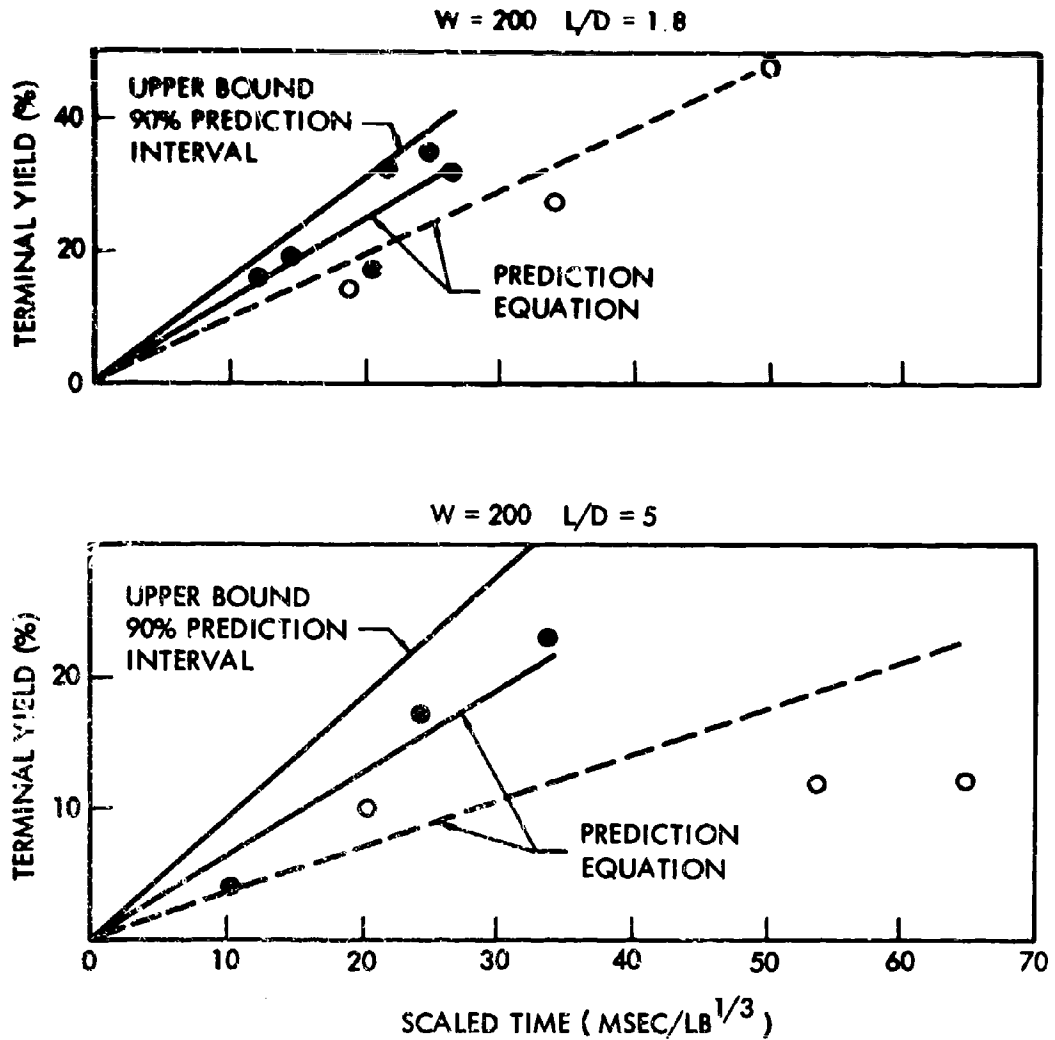
Fig. 5-32.   Comparison of Prediction Equation for $LO_2/RP-1$ CBM Case
with Experimental Data.   (Open circles and dashed lines
D_o/D_t of 1, solid circles and solid lines D_o/D_t of 0.45)
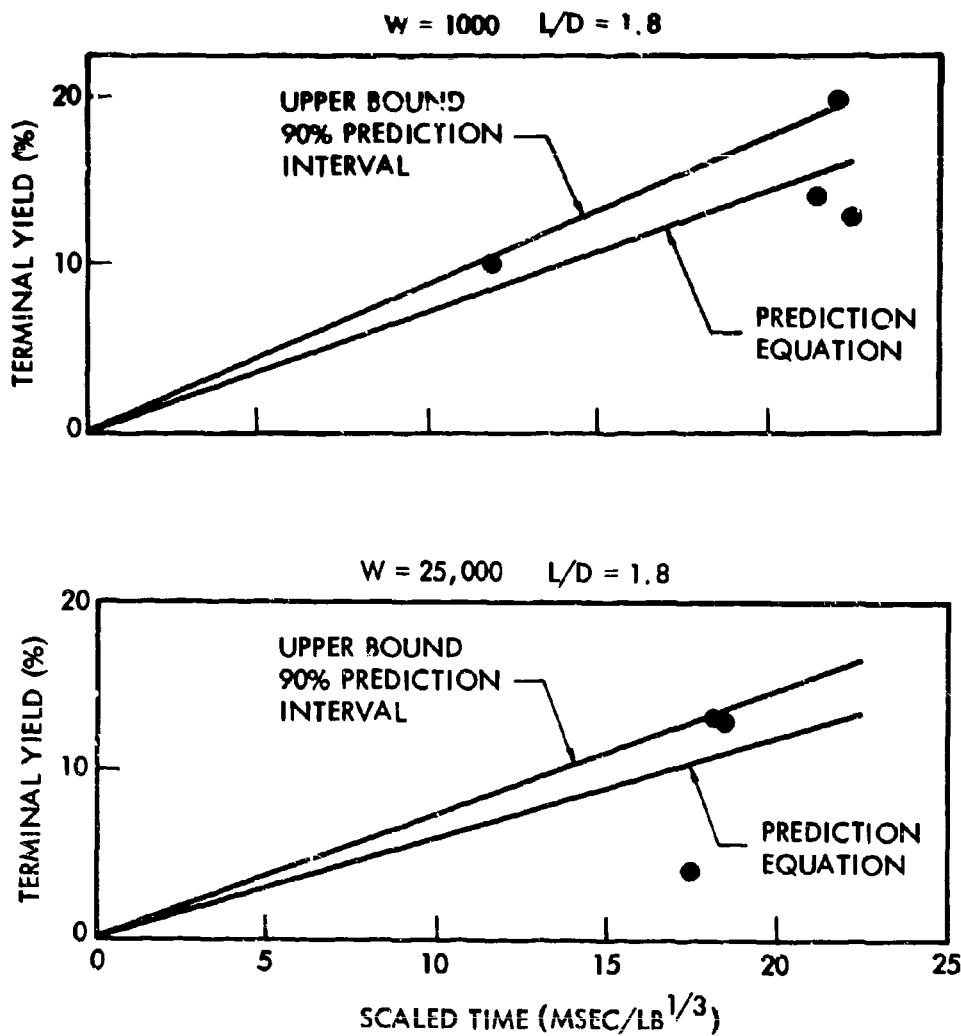
Fig. 5-32, cont. Comparison of Prediction Equation for $LO_2/RP-1$ CBM
Case with Experimental Data - D_o/D_t of 0.45

D_o/D_t Ratio. Over the range this parameter was studied, its effect was to cause changes in both the rate of yield buildup and in its maximum value. For both L/D ratios the partially open diaphragm caused a more rapid rate of yield buildup, and for the larger L/D ratio (5) the maximum value was also somewhat greater than for the full-open case. For the smaller L/D ratio (1.8), however, the maximum value was less. Apparently in the case of an L/D of 5 with the fully open diaphragm, mixing tends to be inhibited by the partially frozen RP-1, so that the additional penetration provided by the partially open diaphragm can lead to larger yields. Since the partially open diaphragm case used, D_o/D_t of 0.45, results in an opening that is only 20 percent of the RP-1 tank diameter, it seems reasonable to believe that further decreases in the size of the diaphragm opening will not cause much additional increase in mixing that can be ascribed to increased penetration; rather, it seems more likely that a smaller diaphragm opening will tend to result in a yield decrease because of the great excess of RP-1 in the mixing zone. The LO_2/LH_2 results (discussed later), in which the effects of D_o/D_t were investigated down to a value of 0.083 (approximately 0.7% open), tend to confirm this line of reasoning. It is recommended, therefore, that a value of D_o/D_t of 0.45 (approximately 20% open) be used for all smaller values of D_o/D_t.

Propellant Loading Fraction. The data given earlier in this section showed that higher explosive yields could be obtained for the LO/RP-1 propellant combination when the propellant tanks are partially full than when they are in their normal full-load condition. As discussed previously this result would be expected, provided that propellant mixing is terminated by tank rupture due to O_2 gas buildup — as is indicated by the available evidence. The reasoning is that as the propellant loading fraction is decreased, with a consequent increase in ullage volume, the propellants have a greater time to mix prior to generating sufficient gas to rupture the tank and thus should give a larger specific yield (yield per unit weight of propellant).

As the ullage volume gets very large, it would be expected that the specific yield would tend to approach the theoretical maximum of about 120 percent, a value almost an order of magnitude larger than that obtained for the fully loaded tank (ullage volume of 10 percent). Actually, however, the

yield of most concern is not the specific yield, but the yield relative to
the total amount of propellants in the tankage when it is fully loaded. This
actual terminal yield value (Y) which is equal to the product of the specific yield
(Y_s) and the propellant loading fraction (L), would not increase as much as
the specific yield since an increase in Y_s due to an increase in ullage
volume (V_u) is normally obtained by reducing L. If an L of 1 corresponds to an
ullage volume of 10 percent (such as in the present test program) then

$$L = \frac{1 - V_u}{0.9}$$

or
$$V_u = 1 - 0.9 L$$

and
$$Y = Y_s L = Y_s \frac{(1 - V_u)}{0.9}$$

Although only limited data are available for ullage volumes other than
the 10 percent used in the basic test program, a reasonable estimate of how
the actual yield value changes with ullage volume for the case of most in-
terest (L/D of 1.8, D_o/D_t of 0.45) can be obtained by using this equation and
the available experimental data regarding the change of Y_s with ullage volume
as illustrated in Fig. 5-33. Curve A is the experimentally derived relation
between Y_s and V_u. The experimental data shown for the ullage volumes of
10 and 40 percent are from the 200-lb test series for an L/D of 1.8 and a
D_o/D_t of 0.45. Because only 200-lb data were available for the 40-percent
ullage condition (Test Numbers 174 and 240) and because of the weight-scale
effect described earlier, only 200-lb test data (Test Numbers 101, 237, and
239) were used for the 10-percent ullage condition. For all of these tests,
ignition occurred at approximately the time of tank rupture, which corresponded
to a nominal 100 psi overpressure. The yield value used for 100-percent ullage
corresponds to the maximum possible yield value for perfectly mixed propellants
having an oxidizer-to-fuel ratio of 2.25 and was obtained from small-scale
experiments with ideal mixtures of the propellants (Fig. 7-2). Since precooled
fuel was used in these ideal mixtures, this yield value is expected to be some-
what on the high side.
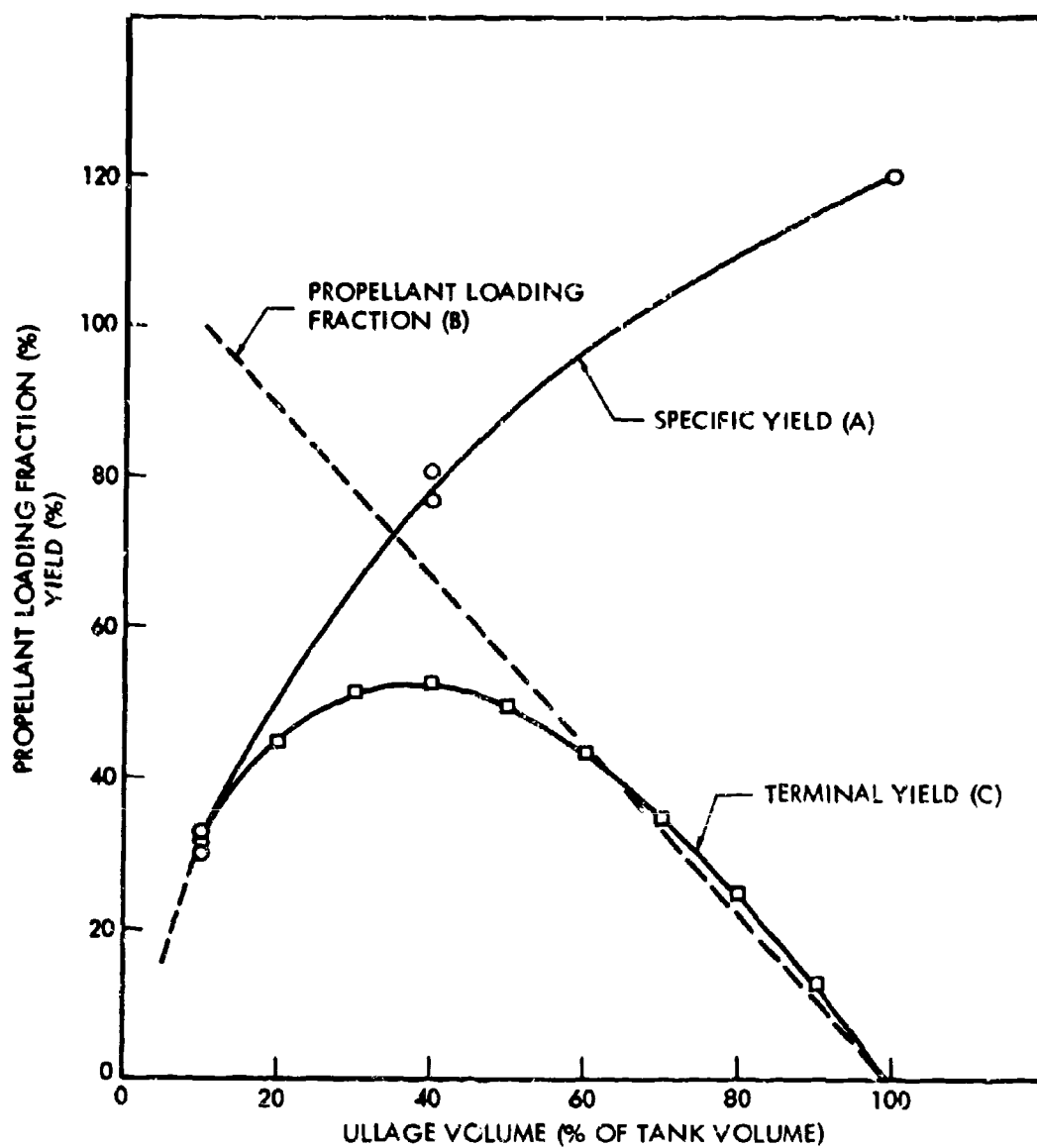
Fig. 5-33. Effect of Ullage Volume on Yield

Curve B is a plot of L versus V_u, and Curve C is the derived curve of Y
versus V_u obtained from the product of Curves A and B. One of the interest-
ing features of Curve C is that the maximum value occurs for an ullage volume
of about 40 percent, one of the values for which experimental data on Y_g were
available. This fact along with the relatively flat nature of Curve C in the
vicinity of the maximum is good evidence to indicate that there is not much
uncertainty in the magnitude of the maximum value of Y despite the fact that
experimental data on Y_g were only available for a few ullage values.

The most important feature of Curve C is that the maximum value is
about a factor of 1.7 times greater than the value for the standard fully
loaded test condition of 10 percent ullage. Note that the ratio of yields
is considered more pertinent here than the absolute values because of the
weight-scale effect mentioned earlier.

Curve C also indicates that the yield should decrease as the ullage
volume decreases below the standard 10 percent used in the basic test series,
and a linear extrapolation of the curve for at least a factor of two in
yield, as shown by the dashed line, seems reasonable.

Tank Rupture Pressure. The effects of varying the tank strength are
expected to be generally similar to the effect of varying the ullage volume
in that an increase in tank strength with all other conditions equal will
allow more O_2 gas to be generated prior to tank rupture and thus more pro-
pellant mixing and a higher yield. Similarly a decrease in tank strength
will result in less propellant mixing and a lower yield. Actually it is not
only the burst pressure but also the initial pressure which is of concern,
because the amount of O_2 gas which needs to be vaporized to rupture the tank
is dependent on the difference between these pressures. In the basic test
series, the initial pressure in the LO_2 tank was about 35 to 40 psia and that
in the RP-1 tank about 15 psia, for an effective average pressure of about
30 psia, while the burst pressure was about 115 psia. This pressure differ-
ential of approximately 85 psi is believed to be greater than any in actual
use, so that the yield values derived from these tests should be somewhat
conservative.

A quantitative estimate of how yield varies with changes in tank burst pressure can be obtained with the assumption that the specific explosive yield is a function of the number of moles of gas generated. This is a reasonable assumption as long as the same geometry and type of propellant mixing prevails. The reasoning is that to a reasonable approximation the number of moles of gas generated to reach a given final pressure is proportional to the product of the initial ullage volume and the pressure differential between the initial and final pressures, i.e., $\Delta N \: \alpha \: \Delta P_r \: V_u$ where ΔP_r = burst pressure - initial pressure. Thus the specific yield can be considered a function of $\Delta P_r \: V_u$, and Curve A of Fig. 5-33 can be used to generate a family of terminal yield curves (such as Curve C) for a range of ΔP_r values by using an effective value of ullage volume rather than the actual value to determine the specific yield where the effective ullage value is as given below:

$$V_{u-eff} = \frac{\Delta P_r}{85} V_u$$

Figure 5-34 shows the combined effects of ullage volume and pressure differential on the maximum terminal yield calculated in the manner indicated above. The yield changes are expressed by a factor k, which is the ratio of the yield for a given V_u and ΔP_r to that for the standard condition of V_u = 10% and ΔP_r = 85 psi.

Prediction Method Development for LO_2/RP-1 CBM Case

In developing a yield prediction method based on the information given in the previous section, it is convenient to consider two basic cases: one where the ignition time is not known and one where it is known. It is also desirable to treat separately certain ranges in values of some parameters which are of little interest or whose occurrence is extremely unlikely.

These excluded parameter ranges, which are listed below, are considered in a special section following the general prediction method development:

- Propellant Weight (W) <10,000 lb
- Diaphragm-Opening-to-Tank-Diameter Ratio $(D_o/D_t) \geq 0.45$
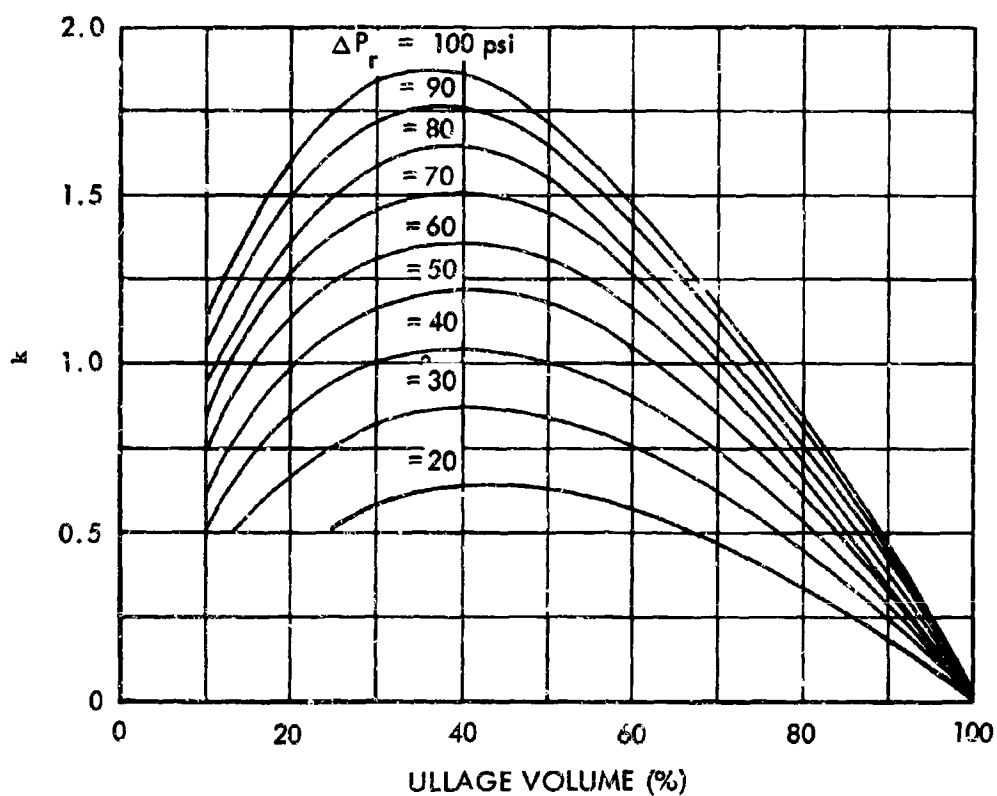
Fig. 5-34. Effects of Ullage Volume and Pressure Differential on
Terminal Yield for LO_2/RP-1 CBM Case

Case 1 - Unknown Ignition Time. To obtain a conservative estimate for
this case it must be assumed that the ignition time is the maximum possible,
i.e., the value at the time of tank rupture. Thus in this case we are in-
terested in predicting yield as a function of L/D, V_u, and ΔP_r, given that
$t^* = t^*_{max}$ and D_o/D_t - 0.45.

By excluding W's of 10,000 lb or less and D_o/D_t's greater than 0.45, Eq.
(5.1), the basic prediction equation for the standard conditions of V_u = 10% and
ΔP_r = 85 psi, becomes

$$\frac{Y_s}{t^*} = 0.76 - 0.092 \, L/D \tag{5.2}$$

The value of t^*_{max} for these same standard conditions can be obtained by
averaging the experimentally observed ignition times for the tests which are
considered to fit in this category. These results are given below

L/D	Test Number	Ignition Time (msec)	Propellant Weight (lb)		t^*_{max} (msec/lb$^{1/3}$)
1.8	237	127	200		21.7
1.8	101	145	200		24.8
1.8	239	156	200		26.6
				Average	24.4
1.8	192	216	1000		21.6
1.8	193	222	1000		22.2
1.8	270A	225	1000		22.5
				Average	22.1
1.8	275	515	25,000		17.6
1.8	278	530	25,000		18.1
1.8	282	540	25,000		18.5
				Average	18.1
				Grand Average	21.5
5.0	100	220	200		37.7

For an L/D of 1.8 these results indicate a slight decrease in t^*_{max} with increasing propellant weight. Although conceivably some credit could be taken for this in extrapolating to larger scales, the reductions would not be large, and considering the uncertainties in the burst strengths and tank pressure at rupture, it seems somewhat safer to not extrapolate this trend but to use the average value of all the data as a conservative estimate. For an L/D of 5, only one test at the 200-lb scale was conducted with ignition at tank rupture. The ignition time for this test was a factor of 1.55 times the average value of the ignition time for the 200-lb, L/D of 1.8 data. Thus the best estimate of t^*_{max} for an L/D of 5 was taken as 1.55 times the average value for an L/D of 1.8 or 1.55 times 21.5 = 33.2 msec/lb$^{1/3}$.

The yield values obtained from Eq. (5.2) for L/D ratios of 1.8 and 5.0 and the t^*_{max} values given above are plotted in Fig. 5-35. Also shown in the figure are the upper 90 percent prediction values for these two points. A linear interpolation, as indicated by the straight lines, is recommended for intermediate L/D values. As discussed earlier, the values for an L/D of 5.0 are recommended for larger L/D values.

To account for differences in V_u and ΔP_r from the standard values, the correction factor k has to be multiplied by the yield values given in this figure. The values of k can be obtained from Fig. 5-34.

Case 2 - Known Ignition Time. For this case t^* is retained as a variable and Eq. (5.2) would be used

$$Y = t^* (0.76 - 0.092 \, L/D)$$

This equation is valid for all t^* values which give yield values less than or equal to the maximum yield values computed for Case 1. The yield as given by this equation is plotted in the upper part of Fig. 5-36 as a function of t^* for various L/D and k values, where k is obtained from Fig. 5-34. The upper bounds for the 90-percent prediction interval for this equation are given in the lower part of Fig. 5-36.
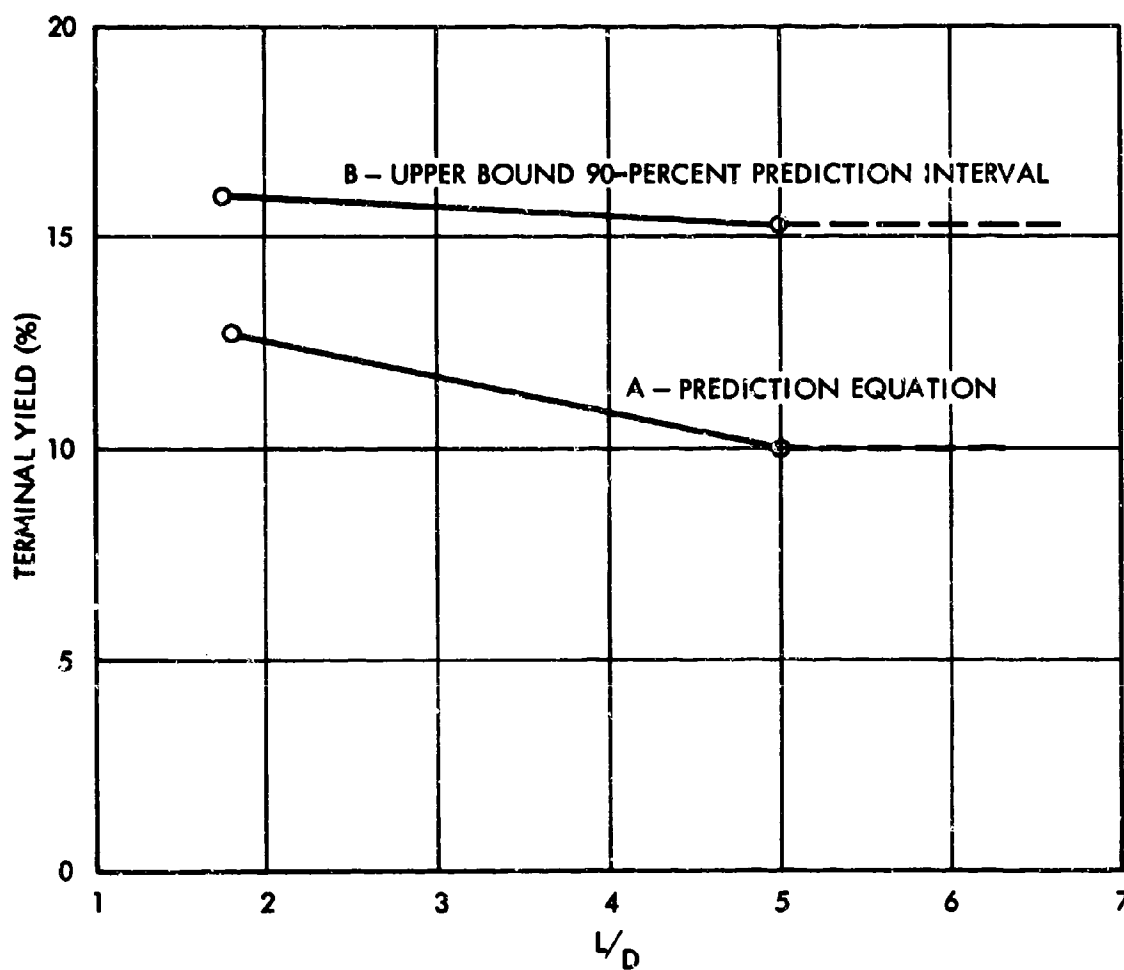
Fig. 5-35. Terminal Yield at Tank Rupture for LO_2/RP-1 CBM Case (V_u = 10%) Δp_r = 85 psi)

These plots are basically for the purpose of determining either the expected yield or the upper bound for the 90-percent prediction interval about the expected yield given the expected ignition time. The various constant k lines (dashed), however, also give the yield value corresponding to the maximum t^* value possible prior to tank rupture.

Note that a straight-line interpolation has been used between the L/D values of 1.0 and 5 for each of the constant k lines in the upper part of Fig. 5-36. Equation (5.2) actually gives a curved line which lies slightly below the straight line for intermediate L/D values but the differences are very small (less than 5 percent of the yield value), so they have been neglected.

Also note that the form of the selected equation leads to both the yield and the upper bound being zero for an ignition time of zero. Insufficient data were obtained at small scaled times to verify this point, however, so that a minimum time of 5 $msec/lb^{1/3}$ is recommended.

Special Cases.

(1) $W \leq 10,000$ lb

As shown by Eq. (5.1) the yield values for this condition can be obtained by multiplying the yield values obtained from the general prediction method by the factor

$$(1 + \frac{217}{W}), \text{ where W is in pounds}$$

(2) $D_o/D_t \geq 0.45$

Use Eq. (5.1) to determine yield values for the standard conditions $(V_u = 10\%, \Delta P_r = 85$ psi)
Estimated t^*_{max} values are given below:

D_o/D_t	L/D	t^*_{max}
1.0	1.8	43
1.0	5.0	57

To correct for differences in standard conditions, multiply t^*_{max} values by k factor given in Fig. 5-34.

Descriptive Model for LO_2/LH_2 CBM Case

Although some of the features of the descriptive model for the $LO_2/RP-1$ case are applicable to the LO_2/LH_2 case, there are some significant differences in behavior due primarily to the very low density of the LH_2. In this case, the LH_2 is on top, and since its density is very much less than that of the LO_2, there is little tendency for it to penetrate the LO_2 once the initial impact and plunging process is over.

Also, because of the very low density of the LH_2, it would be expected that the plunging of the LH_2 stream in the middle of the LO_2 pool for the partially open case should be much less pronounced. This suggests that there would not be as much difference in the rates of yield generation between the partial- and full-open cases as in the $LO_2/RP-1$ case. The low heat of vaporization of the LH_2 also would be expected to result in a relatively greater amount of gas generation, which would tend to keep the main masses of propellants apart, particularly for the larger L/D ratios.

The likely greater physical stability of this propellant combination suggests that frozen oxygen may have a much greater inhibiting effect on mixing than does frozen RP-1, and the experimental evidence tends to confirm that some such terminating process as this exists, since tank rupture due to LH_2 buildup occurred in only one of the four test configurations studied (L/D of 1.8, D_o/D_t of 1.0).

Because of the inherent characteristics of LH_2, there is some potential for a small explosive reaction between the LO_2 and LH_2 being enhanced by subsequent mixing and reaction of the LH_2 with the ambient air outside of the tankage. Thus the yield for small ignition times may be relatively much greater than for $LO_2/RP-1$.

Prediction Equation Development for LO_2/LH_2 CBM Case

The important guidelines obtained from the above model with regard to the formulation of trial equations are as follows:

1. Yield is expected to increase with time initially and then to level off and approach a constant value. In most cases, the leveling off point is expected to be reached prior to tank rupture.

2. In contrast to LO_2/RP-1, the yield value (if ignition occurs at zero time) may be large enough compared to the maximum value that the yield should not be zero at zero time in the mathematical model.

3. As with LO_2/RP-1 the most likely manner for time to scale is on the basis of geometrical scaling, which leads to the scaled-time term of $t/W^{1/3} = t^*$.

4. There is no obvious reason to expect strong interactions between the effects of the variables.

The simplest equation which satisfies these guidelines has the general form $Y = a + f(t^*) + b/W + C(L/D) + d(D_o/D_t)$, where f denotes a function of t^* and a, b, c, and d are constants.

Using various specific forms for $f(t^*)$ and the data given in Table 5-4, regression analyses were performed with yield as the dependent variable and the other parameters as the factors. The results of the analysis indicated that the L/D and t^* terms were significant, while the W and D_o/D_t terms were not significant. It was also noted that elimination of the case of an L/D of 1.8 and D_o/D_t of 1.0 rendered L/D as no longer significant and that the time effects were only evident in the first 100 msec (based on 200-lb data). Since D_o/D_t values of greater than 0.45 are considered highly unlikely, this case was dropped from the general analysis and considered separately. The final form of the trial equations then became:

$$Y = a + b\, t^* \qquad\qquad t^* \leq t^*_{crit}$$

$$Y = b'\, t^* \qquad\qquad t^* \geq t^*_{crit}$$

Values of the three constants were then obtained by a stepwise regression analysis and that for t^*_{crit} from the intersection of the two equations. The final form of the prediction equations is given below:

$$Y = 2.8 + 0.82\, t^* \qquad\qquad t^* \leq 21.1 \text{ msec/lb}^{1/3}$$

$$Y = 20 \qquad\qquad t^* \geq 21.1 \text{ msec/lb}^{1/3} \qquad (5.3)$$

This equation is plotted in Fig. 5-37 along with the experimental data points for comparison. Also shown in the figure is the upper bound for the 90-percent prediction interval.

The use of this equation for values of the parameter outside the range studied is considered below.

L/D Ratio. It is reasonable to expect that this equation is valid for all ranges of L/D of interest (i.e., all values greater than 1.8) and that it will be on the conservative side for L/D values greater than 5.

D_o/D_t Ratio. Several data points are available for D_o/D_t ratios less than 0.45. These are given below and compared with the values predicted from Eq. (5.2).

Test Number	D_o/D_t	Propellant Weight (lb)	t^* $(msec/lb^{1/3})$	Measured Yield (%)	Predicted Yield (%)
169	0.083*	200	54	15	20
173	0.083	200	10	15	11
S-IV	0.083	91,200	4	5	6

* Corresponds to a 0.7% area opening

The differences between the measured and predicted yields are well within the uncertainty range of the equation and thus the differences cannot be considered significant. It is concluded therefore that this equation is valid for all D_o/D_t values less than 0.45. This equation is also considered valid for D_o/D_t values between 0.45 and 1.0 providing the L/D value is 5 or greater.

Ullage Volume and Tank Pressure. Since the mixing process for this propellant combination appears to be terminated by some mechanism (most likely by a frozen or partially frozen LO_2 block) other than tank rupture due to propellant vaporization, changes in ullage volume and tank burst pressure are not expected to have the large effect found for $LO_2/RP-1$ (still excluding the case of $D_o/D_t > 0.45$). Two data points are available which verify this postulate.
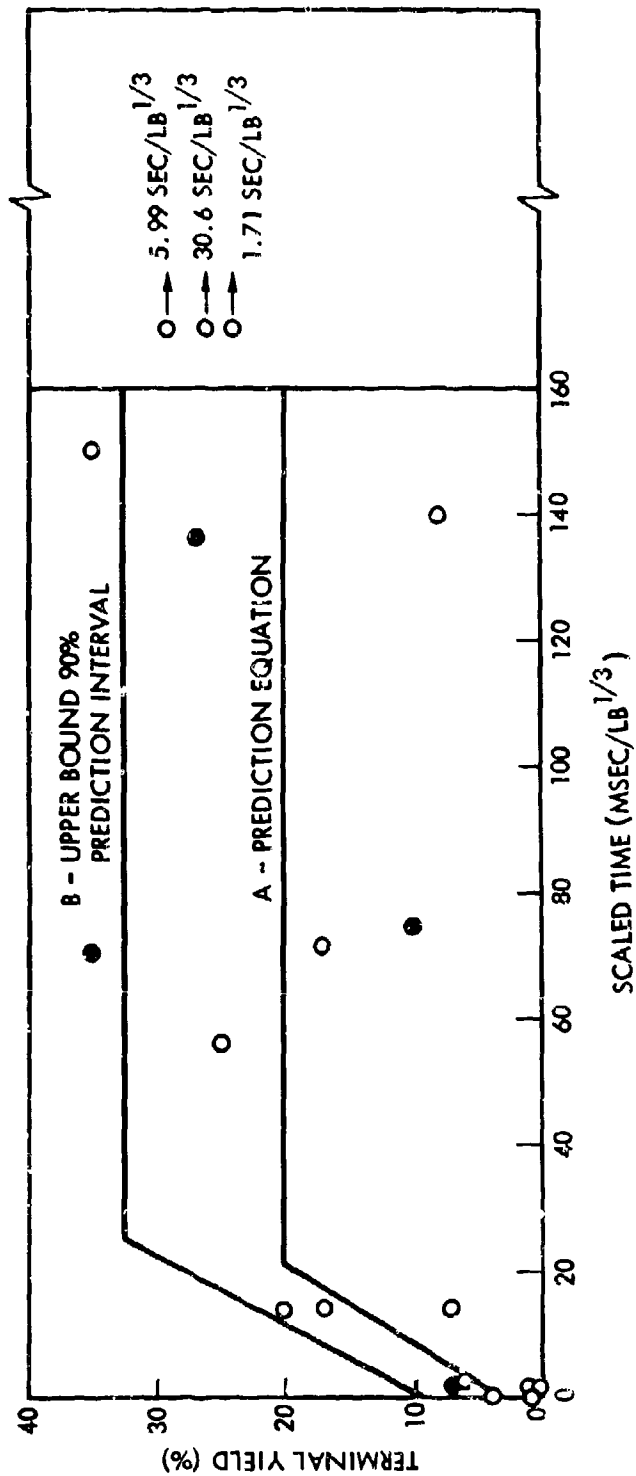
Fig. 5-37. Comparison of Prediction Equation for LO_2/LH_2 CBM Case with Experimental Data for All Cases but L/D of 1.6 and D_o/D_t of 1 (o – 200 lb, ● – 1,000 lb)

These are shown below and compared with the values predicted from Eq. (5.2).

Test Number	Ullage Volume (%)	Propellant Weight (lb)	t^* $(msec/lb^{1/3})$	Measured Yield (%)	Predicted Yield (%)
167	40	133	1490	24	20
172	40	133	132	35	20

Here the data are above the predicted values but not far enough above compared with the uncertainty, so that the differences can be considered insignificant. Thus it is concluded that the equation is valid for all reasonable ranges of ullage volumes and tank burst pressures.

Special Case: $D_o/D_t > 0.45$ and $L/D < 5.0$. The only data available for this case are for a D_o/D_t of 1 and an L/D of 1.8. The data are plotted in Fig. 5-38, and their use is recommended as a conservative estimate for all D_o/D_t values greater than 0.45 when the L/D ratio is less than 5. These data are insufficient in themselves to compute a 90-percent upper prediction interval curve. Accordingly the ratio between the equation and the upper bound in the flat region of the curve in Fig. 5-37 was used to estimate this bound.

Confinement-by-the-Ground-Surface Case

Test Parameters

In the confinement-by-the-ground-surface case, the propellants are initially contained in separate tanks with thin foil bottoms, one suspended above the other, on a drop tower. The tanks are released from their support cable and allowed to drop under essentially free-fall conditions, guided only by skates fastened to a rail on the side of the drop tower. The bottoms of the tanks are ruptured by a cutter ram when they near the ground surface and the tank proper is stopped about 1.5 tank diameters off the surface. Thus the propellants are permitted to impact and spread on the ground surface free of the tankage.
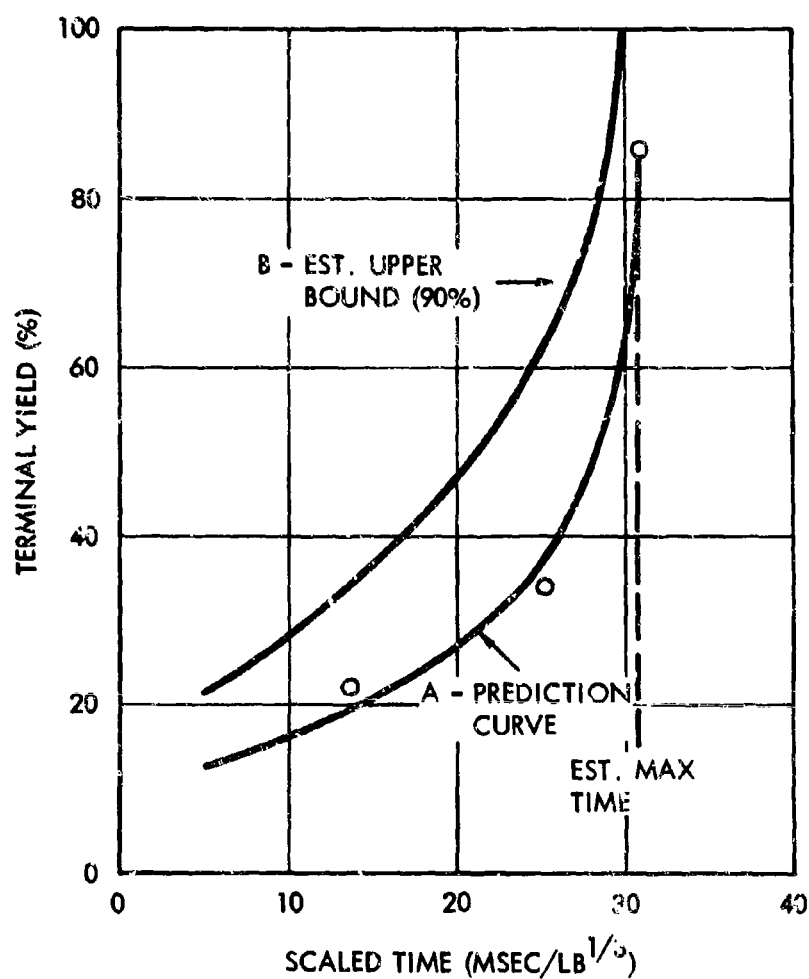
Fig. 5-38.   Terminal Yield vs Time for LO_2/LH_2 CBM Case with $D_o/D_t = 1$ and $L/D = 1.8$

The basic parameters selected for testing in this condition were:

t - Time

v - Impact velocity

F - Flow direction

L/D - Length-to-diameter ratio of propellants

PO - Propellant orientation

W - Propellant weight

Descriptive Model for LO$_2$/RP-1 CBCS-V Case

In the model developed for the vertical condition of the CBGS case, it is convenient to consider the time sequence of events as divided into four consecutive periods.

1. From the time of drop until the second (or top) propellant starts impacting the ground

2. From the time the second propellant starts impacting the ground until it is essentially all down

3. From the time the second propellant is all down until it overlaps the bottom propellant

4. From the time the second propellant overlaps the bottom propellant to the time it has spread to a pool of about three times the size of that of the bottom propellant

If ignition occurs during the first time period, relatively small yields would be expected, since the main masses of propellants have not yet contacted each other. The situation would be expected to be somewhat similar to that for the hypergolic propellant combination under similar impact conditions.

During the second time period, significant mixing can start to occur, because both propellants are in a favorable geometry for mixing, i.e., overlapping thin layers. Since only about 30 percent of the bottom propellant has been overlapped at the end of this time period, however, the yield at this time is still expected to be much below the maximum value. If it is assumed

that the yield is proportional to the fraction of the bottom pool overlapped, it would be about 30 percent of the maximum.

During the third time period, as the propellants continue to spread out on the ground surface, an increasingly larger percentage of the bottom propellant becomes overlapped, and if both propellants continued to spread indefinitely at the same velocity, the yield would tend to asymptotically approach some maximum value (assuming a negligible amount of boil-off). For the normal orientation, however, the RP-1, which is on the bottom, does not spread indefinitely at a constant velocity, but rather tends to slow down and stop rather abruptly at some maximum pool diameter. Thus, the LO_2, which has been lagging behind the RP-1, rapidly catches up and completely overlaps the RP-1. It is anticipated that the maximum yield value should occur at approximately this catch-up-time, since that portion of the liquid oxygen which is not trapped in the RP-1 pool can overrun it.

As long as the propellants are moving at constant velocity and geometrical scaling is assumed, it can be shown that the fraction of pool overlapped during the third time period, at least up until the time the RP-1 pool stops, remains invariant with a change in the scale of testing, provided that time and distance are scaled by the linear scale factor, i.e., the cube root of the weight. It also was noted in the films that the maximum diameter of the RP-1 pool increased as the velocity of impact increased. Thus, it would be expected that the pool diameter at which the maximum yield would be obtained would scale in the following fashion:

$$D/W^{1/3} f(v)$$

During the fourth time period, the LO_2 pool is overrunning the RP-1, and the yield will decrease until all the LO_2 which is not trapped with the RP-1 has left the vicinity. During this period, boiling of the oxygen will also contribute to the yield decrease; however, it is believed that this is a somewhat slower phenomenon than the overrunning and thus not a major factor in the time period of concern.

For the reversed propellant orientation, the LO_2 — which is on the bottom — would not stop, so that the RP-1 is unlikely to catch up completely with it. This indicates that the maximum yield for the reversed propellant orientation should be less than for the normal orientation.

This general model also suggests that the effects of increasing the L/D ratio of the impacting propellants would cause the rate of buildup of yield to be slower (because the LO_2 would initially lag farther behind the RP-1) but that it would likely reach the same maximum value at a slightly longer time (because the RP-1 would stop at approximately the same radius).

In addition to the velocity effect on the critical pool diameter, it also would not be surprising to find that throughout the entire time range the yield would be somewhat greater for the higher impact velocities because of the greater turbulence in the propellant flows.

Prediction Equation Development for LO_2/RP-1 CBGS-V Case

On the basis of this descriptive model of the process, the following guidance can be obtained with regard to the trial mathematical models:

1. Once the propellants are all down, the yield is expected to increase rather rapidly as the pools spread and to reach a maximum value when the LO_2 pool just overlaps the RP-1 pool. This overlap is expected to be reached at a pool diameter proportional to the product of $W^{1/3}$ and some function which increases with an increase in v. In other words, the overlap pool diameter is expected to be reached for a constant value of $D/W^{1/3}f(v)$.

2. As the LO_2 pool spreads beyond the overlap pool diameter, the yield is expected to decrease at a fairly rapid rate (but less rapidly than on the buildup side) and to asymptotically approach some relatively constant value (ignoring boil-off).

3. The yield values throughout the entire range of pool diameters are likely to increase with increasing impact velocity.

These points suggest that correlation of the results can be obtained by the following general type of equation

$$\frac{Y}{h(v)} = h\left(\frac{D*}{f(v)}\right)$$

5-85

where $D* = D/W^{1/3}$ and f, g, and h denote functions of the variables enclosed
in the parentheses. After some preliminary trials of various specific forms
of this general equation, it appeared that f(v) and h(v) could be adequately
expressed as simple positive powers of v. Thus the equation could be reduced
to

$$\frac{Y}{v^n} = g\left(\frac{D*}{v^m}\right)$$

where n and m are constants.

Because of the relatively complicated form anticipated for the function
$g(D*/v^m)$, i.e., a rapid increase to a maximum value followed by a somewhat
slower decrease approaching some constant value asymptotically, it seemed
desirable in the actual regression analysis to divide the equation into two
parts, one function to express the increase in yield to the maximum value,
the other to account for the decrease.

The final trial forms of the equation selected were as follows:

$$\frac{Y}{v^n} = a + \frac{bD*}{v^m} \quad \text{for } 0 \le \frac{D*}{v^m} \le \left(\frac{D*}{v^m}\right)_{crit}$$

$$\frac{Y}{v^n} = a' + b'\left(\frac{D*}{v^m}\right)^{-1} \quad \text{for } \frac{D*}{v^m} \ge \left(\frac{D*}{v^m}\right)_{crit}$$

It should be noted that the effects of L/D and propellant orientation
are not included in the trial equation. Only a small number of tests were
run using conditions other than the standard ones of the normal propellant
orientation and an L/D of 1.8, and it seemed better to consider variations of
those parameters after the equation development for the standard conditions.

The values of the constants (a,b,a',b',n and m) in these equations were
determined by a stepwise regression analysis using the set of data given in
Table 5-5. (See Appendix B for treatment of n and m.) The final form of
the prediction equation is given below:

$$\frac{Y}{v^{0.9}} = 0.22 + \frac{2.7D^*}{v^{0.2}} \quad \text{for } 0 \le \frac{D^*}{v^{0.2}} \le 1.1$$

$$(5.4)$$

$$\frac{Y}{v^{0.9}} = 0.33 + \frac{3.2v^{0.2}}{D^*} \quad \text{for } \frac{D^*}{v^{0.2}} \ge 1.1$$

This equation is plotted in Fig. 5-39 along with the experimental data for comparison. Also shown in this figure is the upper bound on the 90-percent prediction interval about this equation. Note that the 25,000-lb data point, which was not used in deriving the equation, fits the curve very well. Also note that the equation is based only on the data where all the propellants are out of the tankage and on the surface. (Corresponding to $\frac{D^*}{v^{0.2}}$ values greater than 0.1, and is expected to be conservative for earlier times when some of the propellants are still confined in the tankage.)

Another rather interesting check on the prediction equation in the vicinity of its maximum is Test Number 295, which simulated a two-stage missile in the CBGS-V test condition. The bottom stage consisted of the standard 1000-lb $LO_2/RP-1$ tankage with an L/D of 1.8, while the upper stage consisted of the standard 200-lb LO_2/LH_2 tankage with an L/D of 1.8. The impact velocity was 44 ft/sec, the time of ignition was 540 msec, and the terminal yield 70 percent.

The $LO_2/RP-1$ prediction equation gives a yield of 93 percent for 1000 lb or an equivalent TNT weight of 930 lb. The LO_2/LH_2 prediction equation [Eq. (5.5)], discussed later, gives a yield of 37 percent for the 200 lb of LO_2/LH_2 or an equivalent weight of 74 lb. The total equivalent weight for both stages is 1004 lb for an overall yield of about 84 percent. This compares very well with the measured value of 70 percent.

The test data for the reversed propellant orientation and for an L/D of 5 are compared with the prediction equation in Fig. 5-40. As expected, the data for the normal propellant orientation with an L/D of 5 lie below the prediction equation, reflecting the greater separation between the two spreading pools and thus the smaller fraction of the RP-1 pool overlapped by the LO_2 at a given time for this case compared with that for the L/D of 1.8 case. The arrows on each of the data points show the pool diameter for the L/D of 1.8 case which has the same percent overlap of the RP-1 by the LO_2
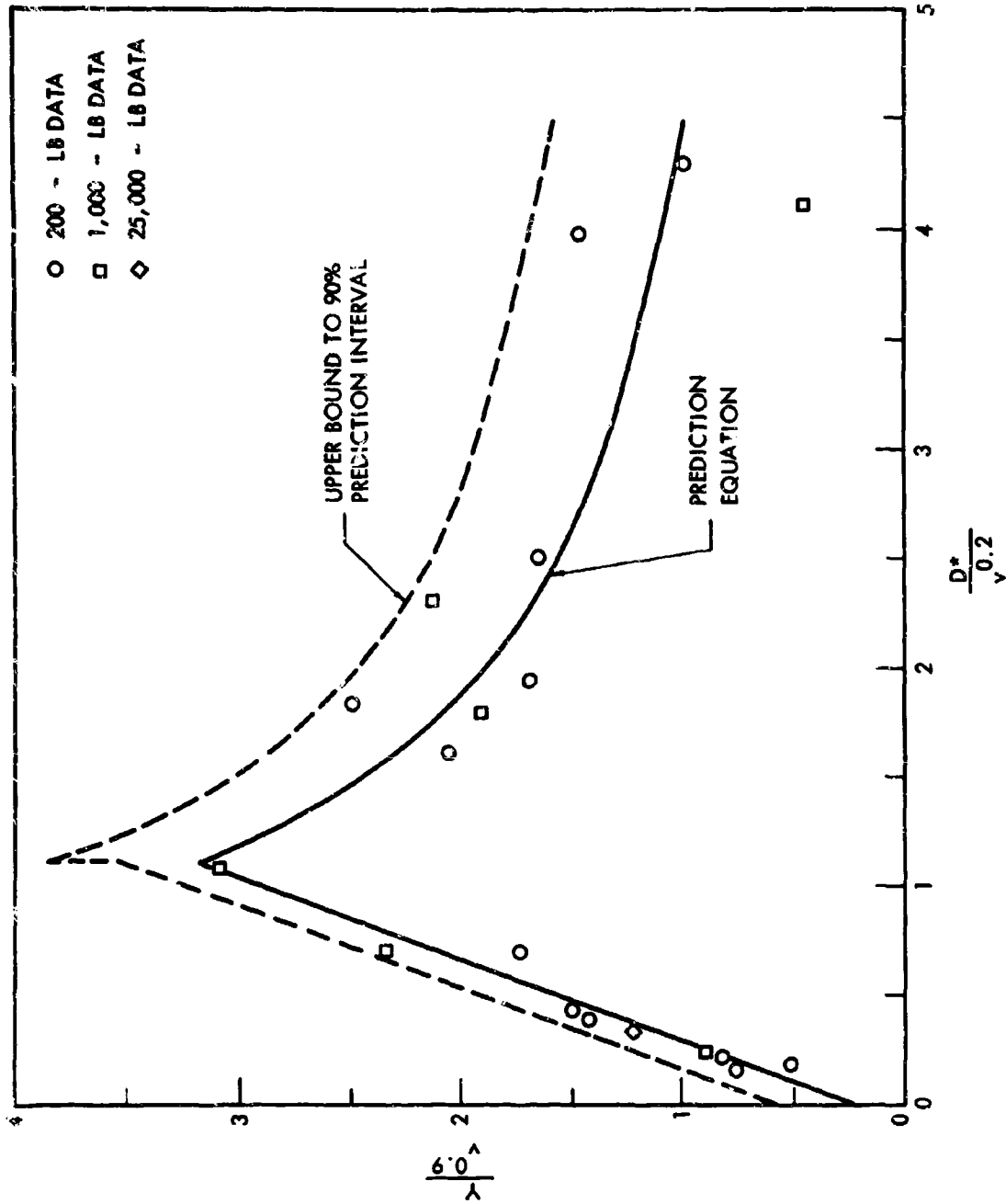
Fig. 5-39. Scaled Terminal Yield vs Scaled Pool Diameter $LO_2/RP-1$ CBGS Case
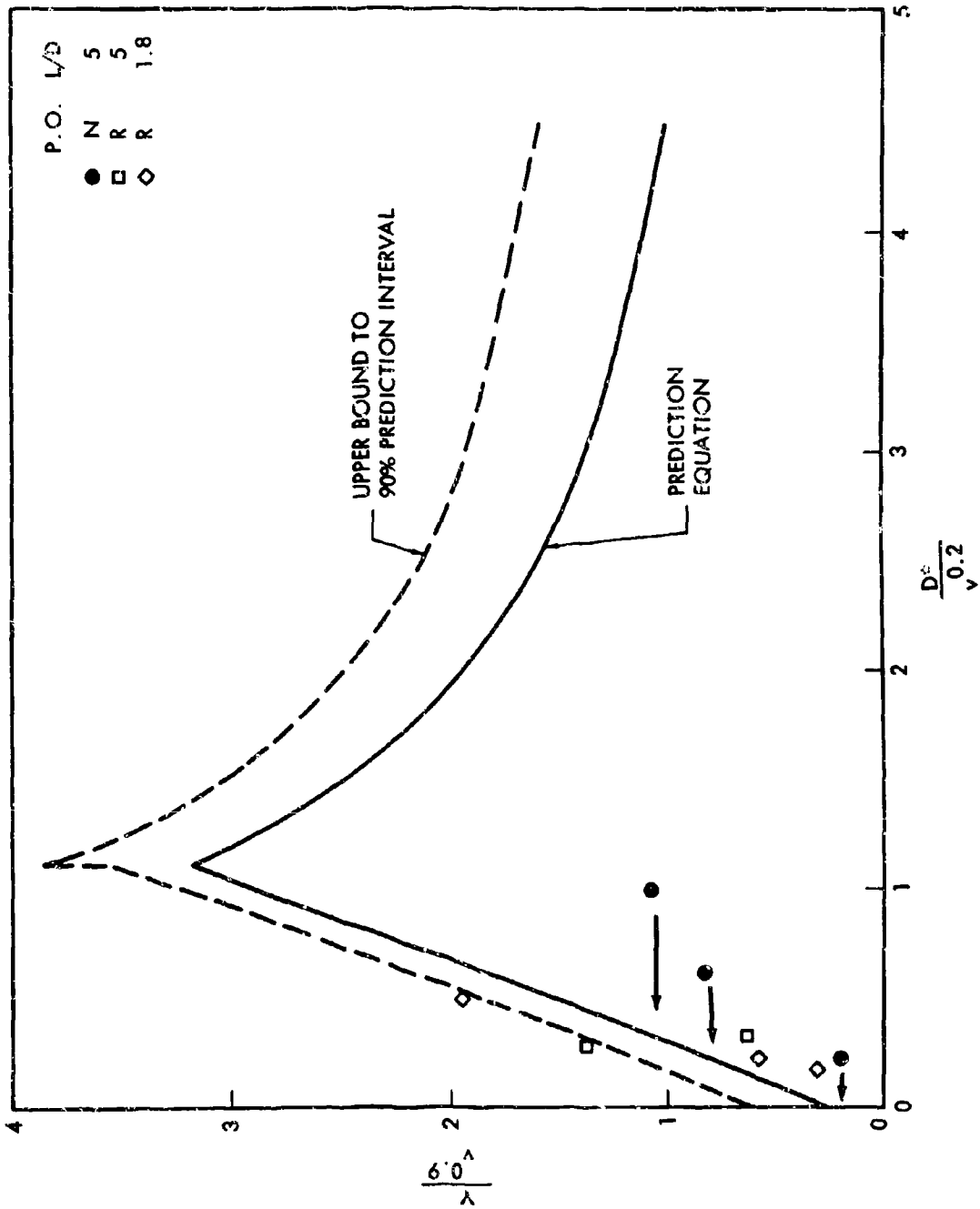
Fig. 5-40. Comparison of Data for Reversed Propellant Orientation and for an L/D of 5 with LO_2/RP-1 CBGS Prediction Equation

as for the L/D of 5 case (calculated on the assumption of a uniform thickness
pool). This comparison generally supports the postulated effect of L/D on
yield, although the data suggest the possibility that yield values for an L/D
of 5 might be somewhat lower than those for an L/D of 1.8. The data for an
L/D of 5, however, are too limited both in number and range of D^* values to
use in trying to derive a correction factor. Accordingly it is recommended
that the results for an L/D of 1.8 be used as a conservative estimate for all
larger L/D values; the estimate is conservative in the sense that on the in-
creasing portion of the curve, including the maximum value, the yield values
for larger L/D values will be less. Because of the expected shift in peak
position, the larger L/D values could give higher yields in the falling part
of the curve.

The data points for the reversed propellant orientation scatter around
the prediction equation and seem to fit it within the uncertainty in results
indicated by the difference between the equation and the 90-percent upper
prediction interval. Accordingly Eq. (5.4) is also considered valid for
the reversed propellant orientation.

Prediction Method Development LO$_2$/RP-1, CBGS-V Case

As with the CBM case, it is convenient to consider two basic cases, the
ignition time known or unknown. If the ignition time is unknown, it is
possible that ignition could occur at the time (or pool diameter) which gives
the maximum yield ($D^*/v^{0.2}$ = 1.1 from Fig. 5-39). Curve A of Fig. 5-41 is a
plot of this maximum yield as a function of impact velocity. This curve
indicates that yields over 100 percent are expected for velocities greater
than 50 ft/sec (corresponds to free fall from a height of about 38 ft).

Since the peak of the curve shown in Fig. 5-39 is rather narrow, it could
be argued that the probability of ignition at or near the peak is rather low
and that it is too conservative to use the peak value. Instead, one might
choose the yield value which is exceeded during only 10 percent of some
selected time interval. For example, if this were done for a time interval
up to a $D^*/v^{0.2}$ of 5, the maximum yield value as a function of impact velocity
would be Curve B shown in Fig. 5-41. It can be seen that this does not change

DROP HEIGHT (ft)
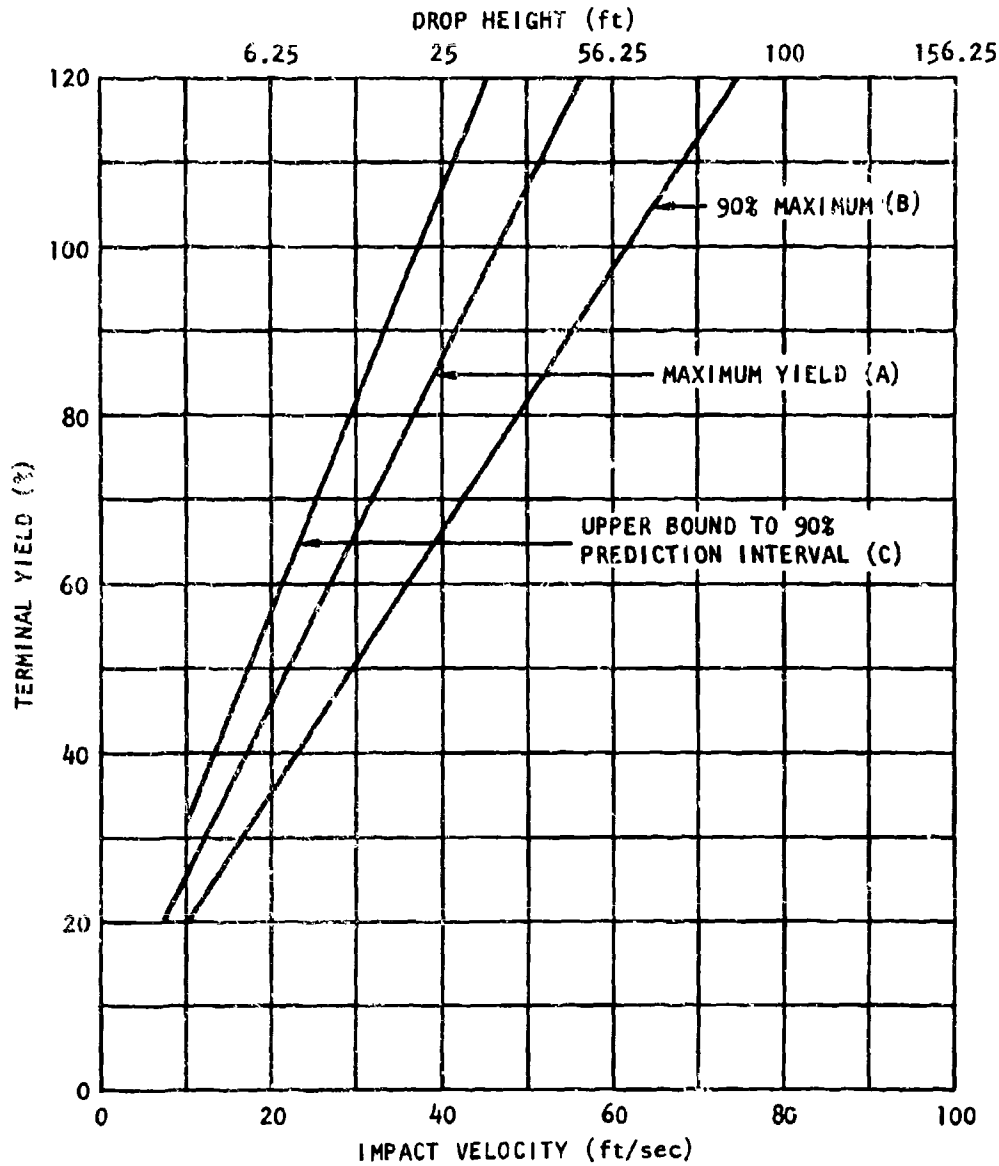
Fig. 5-41. Maximum Terminal Yield vs Impact Velocity for
LO$_2$/RP-1 CBGS Case

the overall picture significantly, since Curve B also indicates large yields
at relative low velocities. The upper bound to the 90-percent prediction
interval about Curve A is given in Fig. 5-41 as Curve C.

If the ignition time is known, the yield values can be obtained directly
from Eq. (5.4). Figure 5-42 is a plot of yield versus t^* for selected values
of velocity. Also shown are the drop heights which would lead to the veloc-
ity values. Figure 5-43 is a similar plot for the upper bound to the 90-percent
prediction interval.

Descriptive Model for LO_2/LH_2 CBGS-V Case

With one important exception, the descriptive model for the $LO_2/RP-1$
case is applicable to the LO_2/LH_2 case. This exception is that the LO_2, the
bottom propellant for this case, does not stop spreading, as does the RP-1.
Thus the yield is expected to asymptotically approach some maximum value, with
the only factor tending to eventually reduce the yield being the boil-off of the
propellants.

Prediction Equation Development for the LO_2/LH_2 CBGS-V Case

On the basis of the descriptive model of the process, the following
guidance can be obtained with regard to the mathematical models:

1. Once the propellants are all down, the yield is expected to in-
   crease rather rapidly as the pools spread and to asymptotically
   approach a maximum value.

2. The yield values are generally expected to increase with an in-
   crease in impact velocity.

These points suggest that correlation of the results can be obtained by
the general type of equation $Y = f(v)g(D^*)$, where f and g denote a function of
the variable in parenthesis. After some preliminary plots and trials of
various specific forms of this general equation, it appeared that each of
the two functions could be adequately represented by a simple power series.
Thus the equation reduced to

$$Y = (a + bv + cv^2 + \ldots)\quad(a' + b'D^* + c'D^{*2} + \ldots)$$
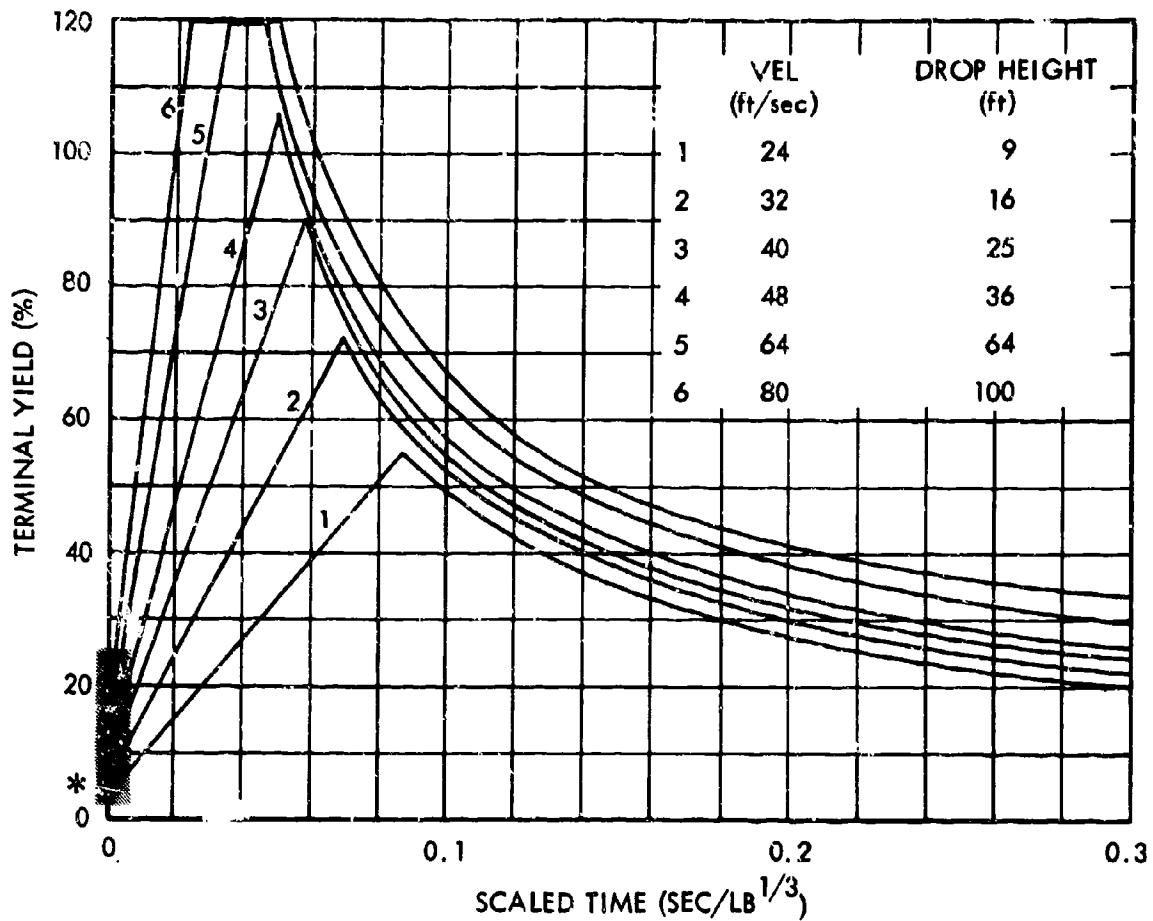
Fig. 5-42. Terminal Yield vs Scaled Time for LO_2/RP-1 CBGS Case
as a Function of Impact Velocity

* Yield for Scaled Time = 0

V = 24 ft/sec	Y = 4 %
32	5
40	6
48	7
64	9
80	12
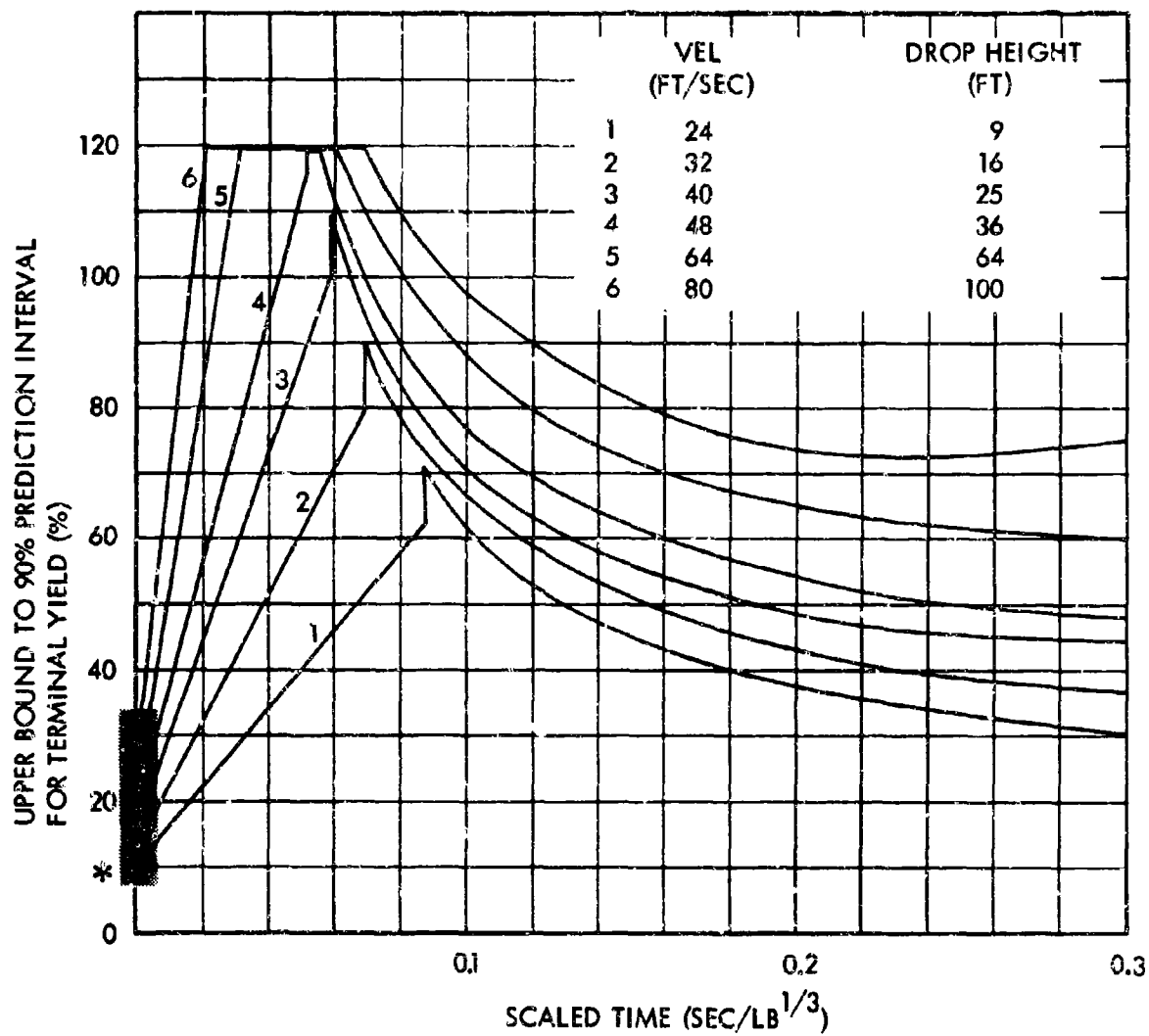
* Upper Bound Value for Scaled Time = 0

V = 24 ft/sec	Y = 10 %
32	13
40	15
48	18
64	24
80	29

Fig. 5-43. Upper Bound to 90% Prediction Interval for Terminal Yield
vs Scaled Time for LO$_2$/RP-1 CBGS Case

A stepwise regression analysis was then made using this form for the equation. The results indicate that the only terms of significance were aa', $v^2D^{*^+}$, and $v^2D^{*^2}$. Thus the final form of the equation becomes

$$Y = 18.4 + 0.0031v^2D^* - 0.00015v^2D^{*^2} \tag{5.5}$$

This equation is plotted in Fig. 5-44 along with the experimental data for comparison. Also shown is the upper bound to the 90-percent prediction interval.

Prediction Method Development For LO_2/LH_2 CBGS-V

As with the LO_2/RP-1 case, it is convenient to consider two basic cases, the ignition time known or unknown. If the ignition time is unknown, it is possible that ignition could occur at the time (or pool diameter) which gives the maximum yield [$D^* = 10.3$ from Eq. (5.5)]. Curve A of Fig. 5-45 is a plot of this maximum yield as a function of impact velocity. This curve indicates that yields over 100 percent are expected for velocities greater than about 70 ft/sec. Also shown as Curve B in Fig. 5-45 is the upper bound to the 90-percent prediction interval for this case.

If the ignition time is known, the yield values can be obtained directly from Eq. (5.5). Figure 5-46 is a plot of yield vs t^* for selected values of velocity. Also shown are the drop heights which would lead to these velocity values. Figure 5-47 is a similar plot for the upper bound to the 90-percent prediction interval.

Descriptive Model and Prediction Method Development for LO_2/RP-1 CBGS-H Case

In this case for the normal propellant orientation, the RP-1 was always dropped from the lowest practical height, which produced a velocity of about 12 ft/sec, while the LO_2 was dropped from various heights and resulted in impact velocities ranging from about 25 to 78 ft/sec. Various time delays between dropping the two tanks were used to obtain various sized pools of RP-1 at the instant the LO_2 impacted the ground.
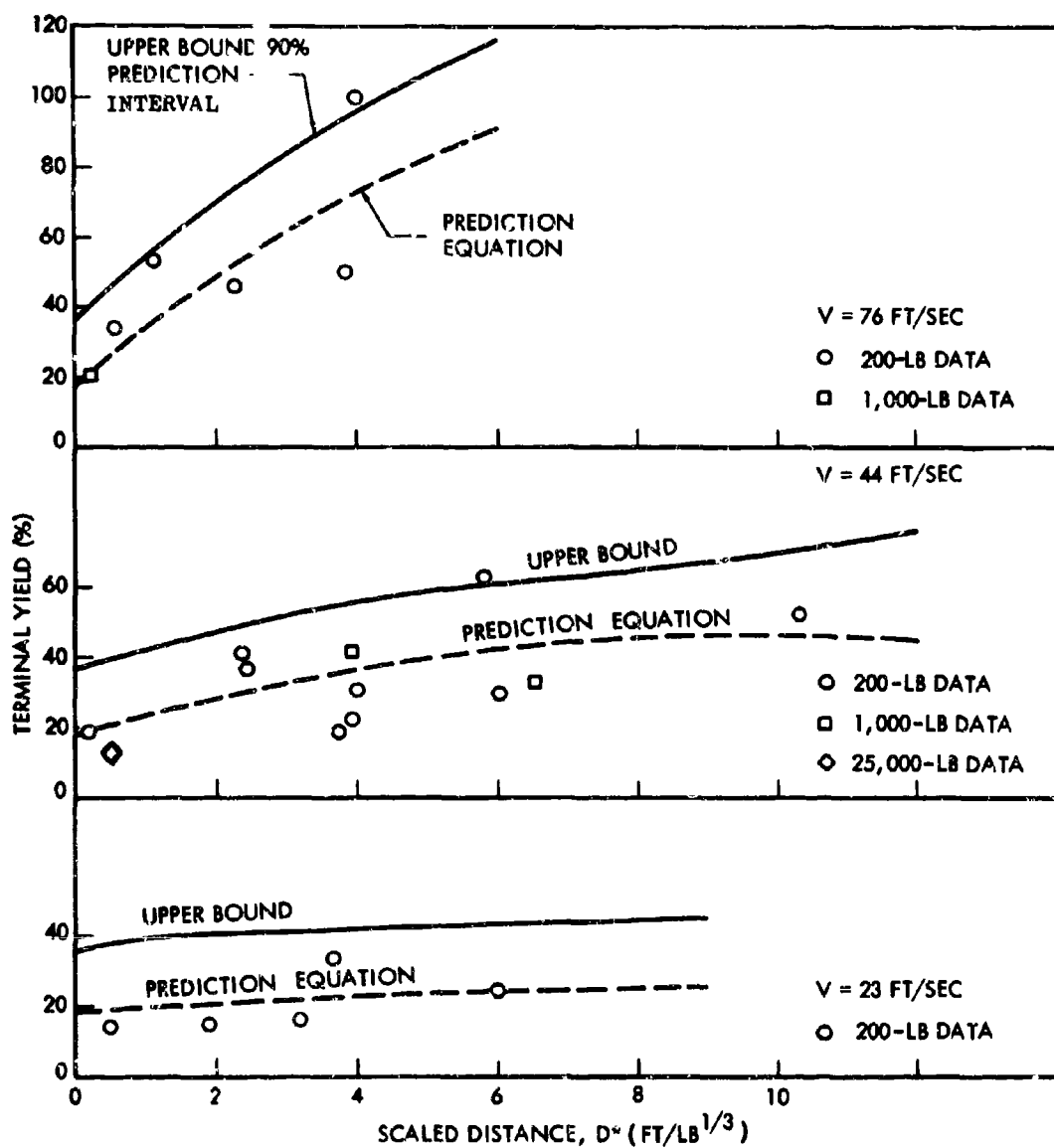
Fig. 5-44. Comparison of Experimental Data with Prediction Equation
for LO_2/LH_2 CBGS-V case (dashed line - prediction
equation; solid line upper bound to 90% Prediction Interval

DROP HEIGHT (FT)
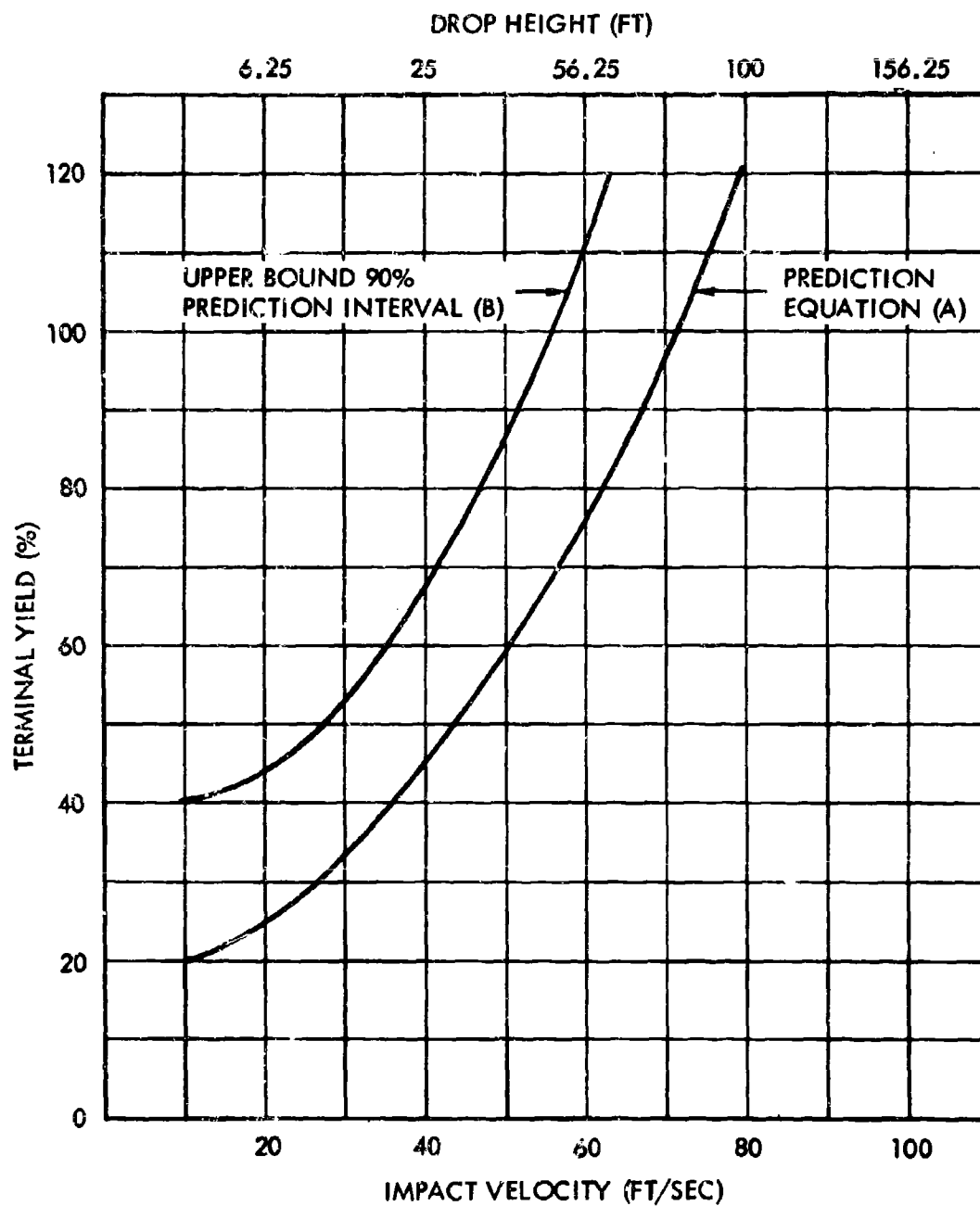
Fig. 5-45. Maximum Terminal Yield vs Impact Velocity for
LO$_2$/LH$_2$ CBGS Case
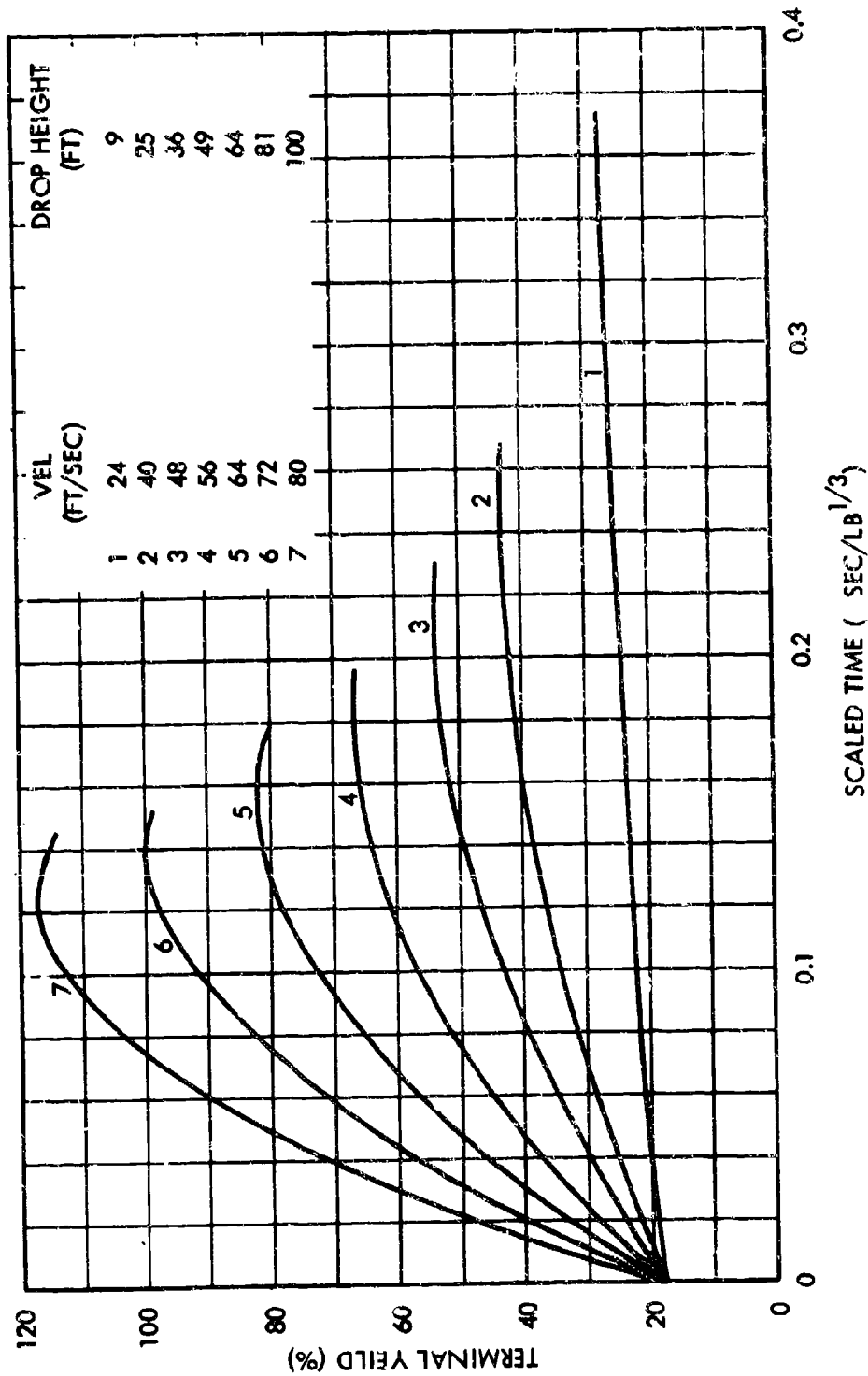
Fig. 5-46. Terminal Yield vs Scaled Time for LO_2/LH_2 CRGS Case as a Function of Impact Velocity
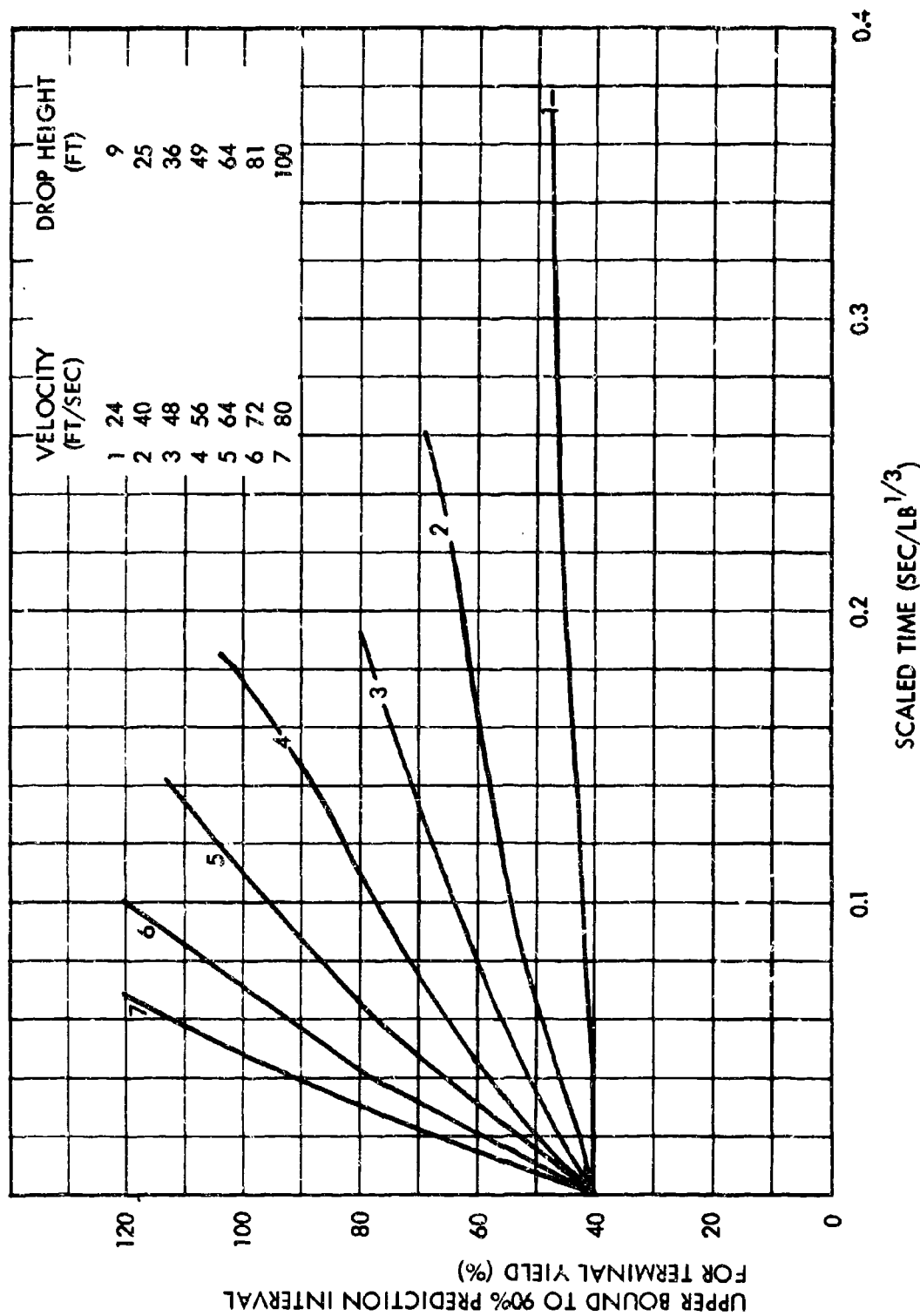
Fig. 5-47. Upper Bound to 90% Prediction Interval for Terminal Yield vs Scaled Time for LO_2/LH_2 CBGS Case

The propellant mixing behavior for this case is expected to be generally similar to that for the CBGS-V case, i.e., yield should increase rapidly as the LO_2 overlaps the RP-1 pool and reach a maximum at about the time the pools are completely overlapped and then decrease again as the LO_2 overruns the RP-1.

This similarity is illustrated in Fig. 5-48, which compares the basic prediction curve for the vertical case with the experimental data for the horizontal case. In plotting the experimental data for the normal propellant orientation, the velocity of the LO_2 was used in determining $Y/v^{0.9}$ and $D^*/v^{0.2}$, and the time used in computing D^* was the time after the LO_2 impacted the ground plus the time to travel the length of the RP-1 tank. In other words, the horizontal data were plotted such that the size of the LO_2 pool was the same as it would have been for the vertical case. For the reversed propellant orientation, the RP-1 velocity and time were used.

It would be expected that the horizontal data would generally be on or below the vertical prediction curve since the vertical case with both pro-pellants being dropped together and having the same velocity tends to create the maximum propellant overlap conditions. The horizontal case with the top propellant having a much higher velocity tends to minimize the overlap time. The experimental data confirm this point, since only one data point is above the upper prediction bound and the great majority lie well below the prediction curve. Note that the reversed propellant orientation data also follow the same pattern. The one high data point is for a very low impact velocity, about 19 ft/sec, and the actual yield was only 25 percent.

Since the vertical prediction curve provides a reasonable upper limit to the horizontal case, its use is recommended to obtain a conservative estimate for yields in the horizontal case. Its use may be somewhat overly conservative when the bottom propellant pool is very large at the time of impact of the second propellant and when ignition occurs soon after the second propellant impacts; but it is not expected to be so for longer times of ignition, since complete propellant overlap for the horizontal case can also occur.
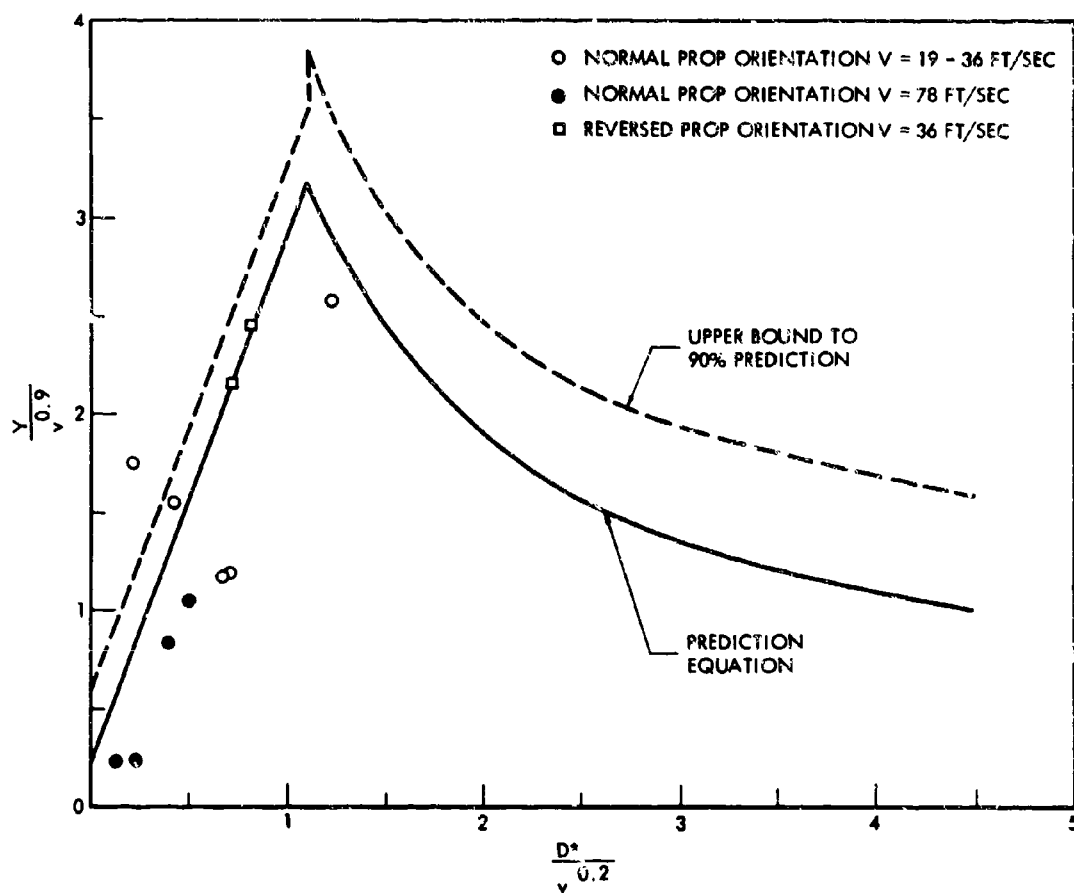
Fig. 5-48.   Comparison of Experimental Data for LO_2/RP-1 CBGS-H
            Case with Prediction Equation [Eq. (5.4)]

To minimize the degree of conservatism at early times of ignition for the large pool case, another upper limit in this region can be obtained by: first determining the quantity of bottom propellant overlapped at the time of ignition (W_b); second, computing a new effective total propellant weight ($W_b + W_t$) by adding W_b to the original top propellant weight (W_t); third, computing an effective oxidizer-to-fuel ratio (W_t/W_b); fourth, determining the maximum specific explosive yield (Y_s) in percent for this ratio (Fig. 7-2); and fifth, determining the total yield (in percent) by multiplying the specific yield by the ratio of the effective weight to the original total weight of propellant (W), i.e.,

$$Y = Y_s \left(\frac{W_t + W_b}{W} \right)$$

Because of uncertainties in propellant locations and the possibility of some reaction after ignition, a minimum yield value of 20 percent is recommended.

Descriptive Model and Prediction Method Development for LO$_2$/LH$_2$ CBGS-H Case

As with LO$_2$/RP-1, the horizontal case for LO$_2$/LH$_2$ is expected to be generally similar to the vertical case. This similarity is illustrated in Fig. 5-49, which compares the horizontal data with the vertical prediction equation. Because of this good agreement, it is again recommended that the vertical case be used as a conservative approximation for the horizontal case.

High-Velocity-Impact Case

Test Parameters

In the high-velocity-impact tests, the tanks were accelerated down a sled track to speeds ranging from 500 to 600 ft/sec and allowed to impact into a massive target having two basic configurations. This was a very limited test series and the target geometry was the only variable. One target configuration was a flat wall, which simulated a rigid ground surface, the other was a deep hole, which simulated impact into a soft surface in which a crater would be formed by the impact process.
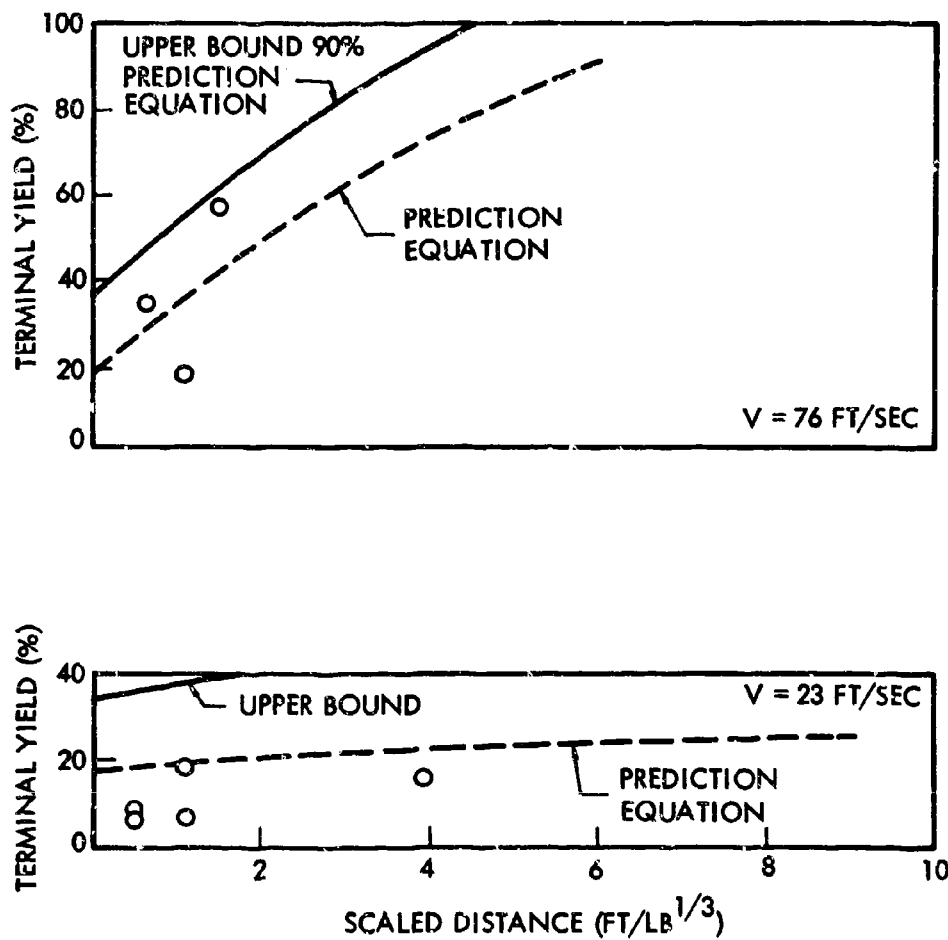
Fig. 5-49. Comparison of Experimental Data for LO_2/LH_2 CBGS-H Case
With Prediction Equation [Eq. (5.5)]

Descriptive Model and Prediction Method Development for High-Velocity-Impact Case for Both Propellant Combinations

Since ignition at or very soon after the time of impact is obtained for this case, there is little time for the type of mixing experienced in the CBM case or the much lower velocity CBGS case. The propellants, however, have a great deal of kinetic energy, and it is anticipated that significant mixing can occur after ignition. In general, the amount of mixing, and thus yield, would be expected to increase with increasing impact velocity. It also would be expected that the confinement offered by the deep-hole target would tend to contain the reacting propellants sufficiently to result in increased post-ignition mixing.

The experimental results for $LO_2/RP-1$ and LO_2/LH_2 are plotted in Figs. 5-50 and 5-51, respectively. Also shown on the figures are the CBGS results for an ignition time $t* = 0$. These results confirm the expected trends in the data, i.e., increase in yields with increase in impact velocity and higher yields for the deep-hole target.

For the $LO_2/RP-1$ flat-wall case, it would seem reasonable to use as the best estimate of the terminal yield vs impact velocity curve, the line given by the prediction equation [Eq. (5-4)] up to 150 ft/sec, and then the constant value of 21 percent. The data for velocities above 100 ft/sec are insufficient to rigorously establish an upper bound to the 90-percent prediction interval in this region. If the upper bound for Eq.(5-4) is extrapolated to 150 ft/sec, it would indicate an upper bound of about 40 percent. This seems somewhat on the conservative side, however, considering the good reproducibility of the 2 data points at approximately 520 ft/sec. Furthermore, the general repro-ducibility of the hypergolic high-velocity-impact tests also suggests less variability. Accordingly it is recommended that 30 percent be used as the estimated upper 90-percent bound. The two selected curves are shown in Fig. 5-52 (Curves A and B).

For the $LO_2/RP-1$ deep-hole case, the extension of the basic prediction equation [Eq. (5-4)] which fits the two-high-velocity points was selected as the best estimate. The upper bound was estimated by extending the upper bound
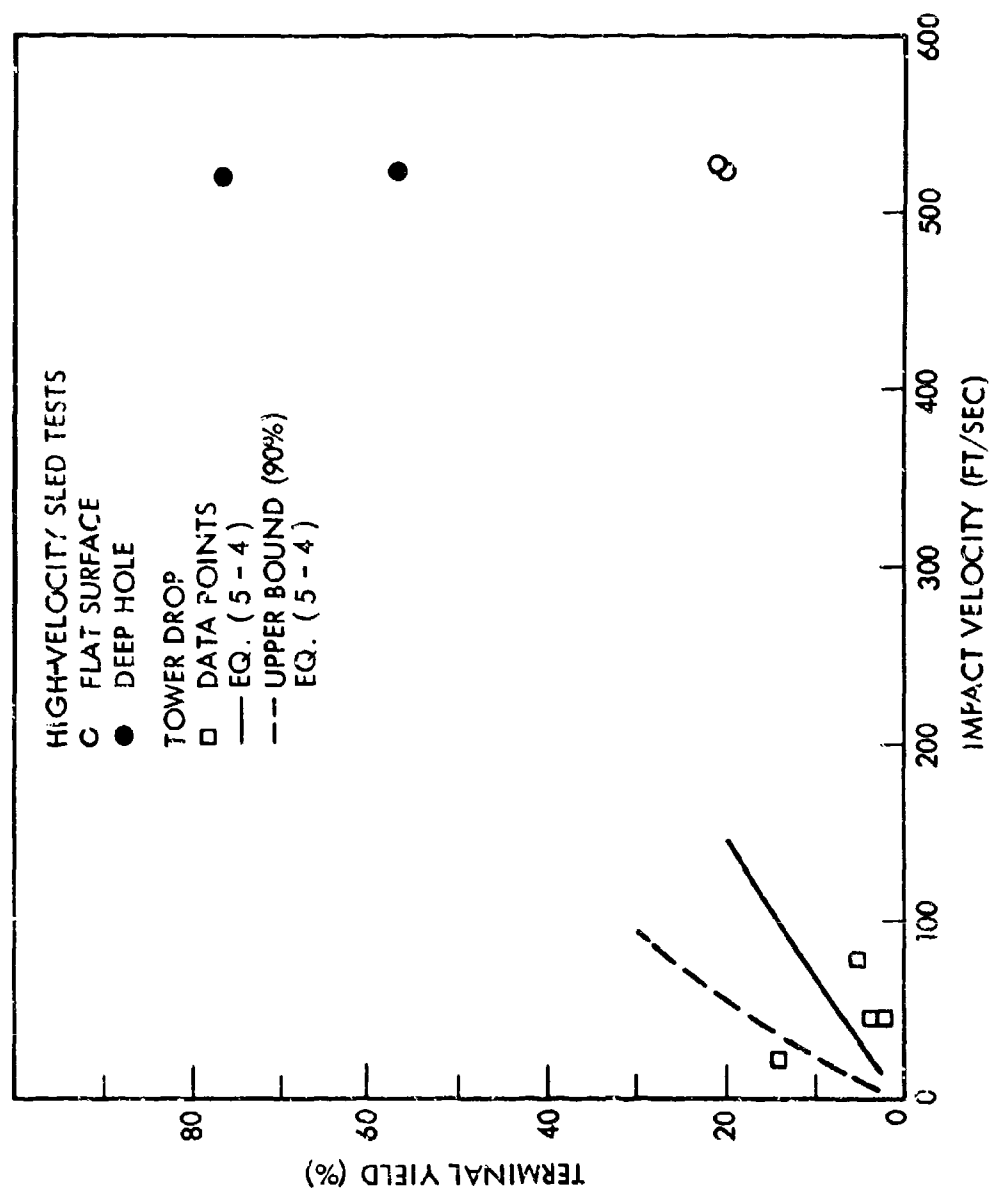
Fig. 5-30. Experimental Yield Data vs Impact Velocity for LO_2/RP-1 With Ignition at or about the time of Impact
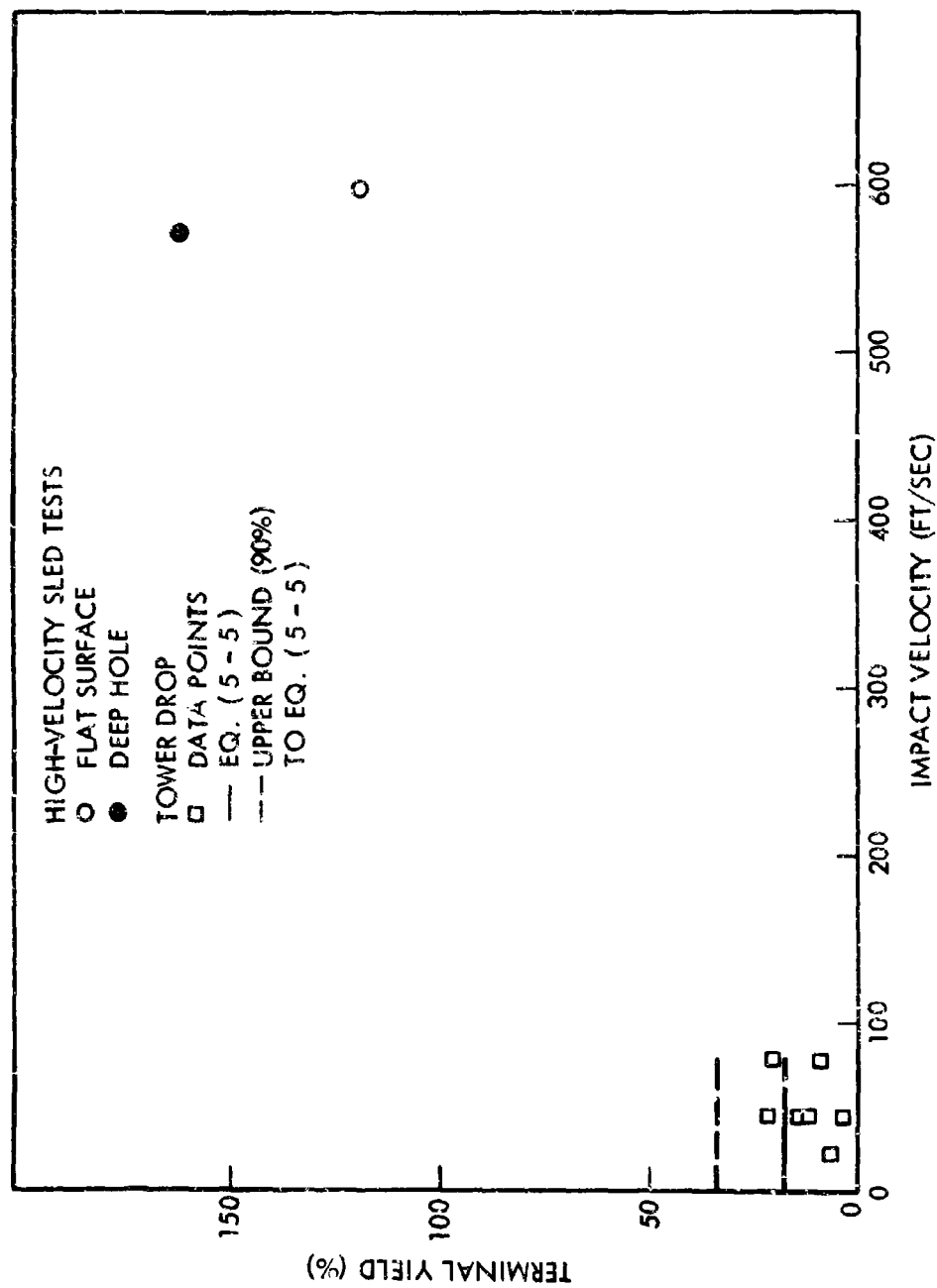
Fig. 5-51. Experimental Yield Data vs Impact Velocity for LO_2/LH_2 With Ignition at or about the time of Impact
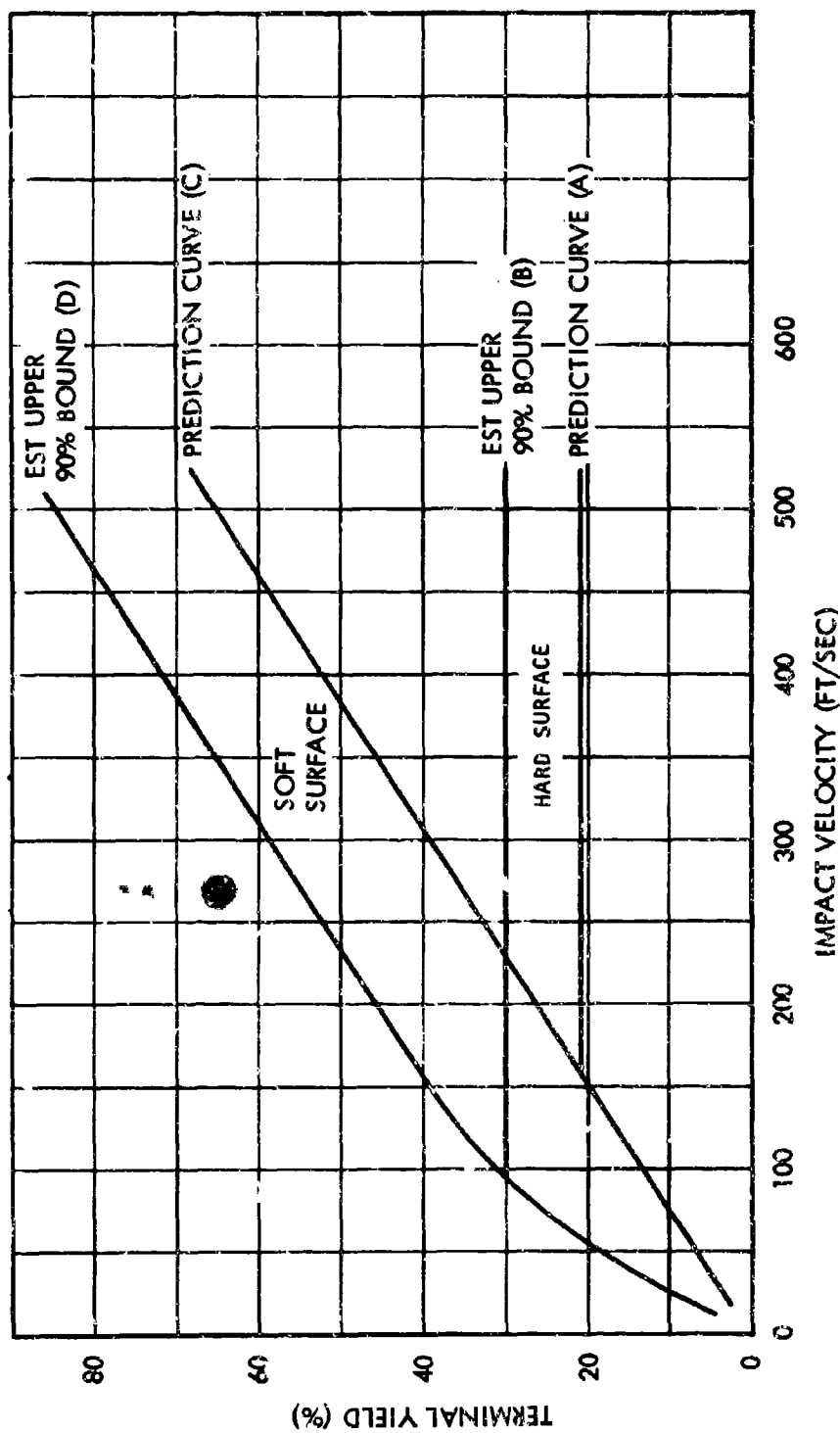
Fig. 5-52. Terminal Yield vs Impact Velocity for $LO_2/RP-1$

of Eq. (5.4) to 150 ft/sec and then extending it in a line parallel to the
basic prediction equation. Again this is not a derived value, but an esti-
mated one based on engineering judgment. The two selected curves are again
shown in Fig. 5-52 (Curves C and D).

Note that the similarity between the flat-wall and deep-hole curves
in the low-velocity region is reasonable because these impact velocities
are not sufficient to cause significant impact craters even in a soft
surface.

For the LO_2/LH_2 flat-wall case, the best estimate of the yield vs.
impact-velocity curve was obtained by a linear extrapolation between the
CBGS prediction equation [Eq. (5.5)] and the high-velocity data point. The
deep-hole case was estimated in a similar manner. The upper bounds to the
90-percent prediction intervals were estimated by assuming a 30-percent
uncertainty at a yield value of 100 percent and assuming a linear extrapola-
tion to the value determined in the low-velocity region. The selected
curves are shown in Fig. 5-53.

It should be emphasized that the two surface conditions used were
selected to bound the range of interest. The rigid or hard surface condition
corresponds to essentially no penetration of the surface by the impacting
tankage. Rock or concrete surfaces would satisfy this condition. The
soft surface condition means essentially complete penetration of the entire
tankage into the surface. A water surface would satisfy this condition.
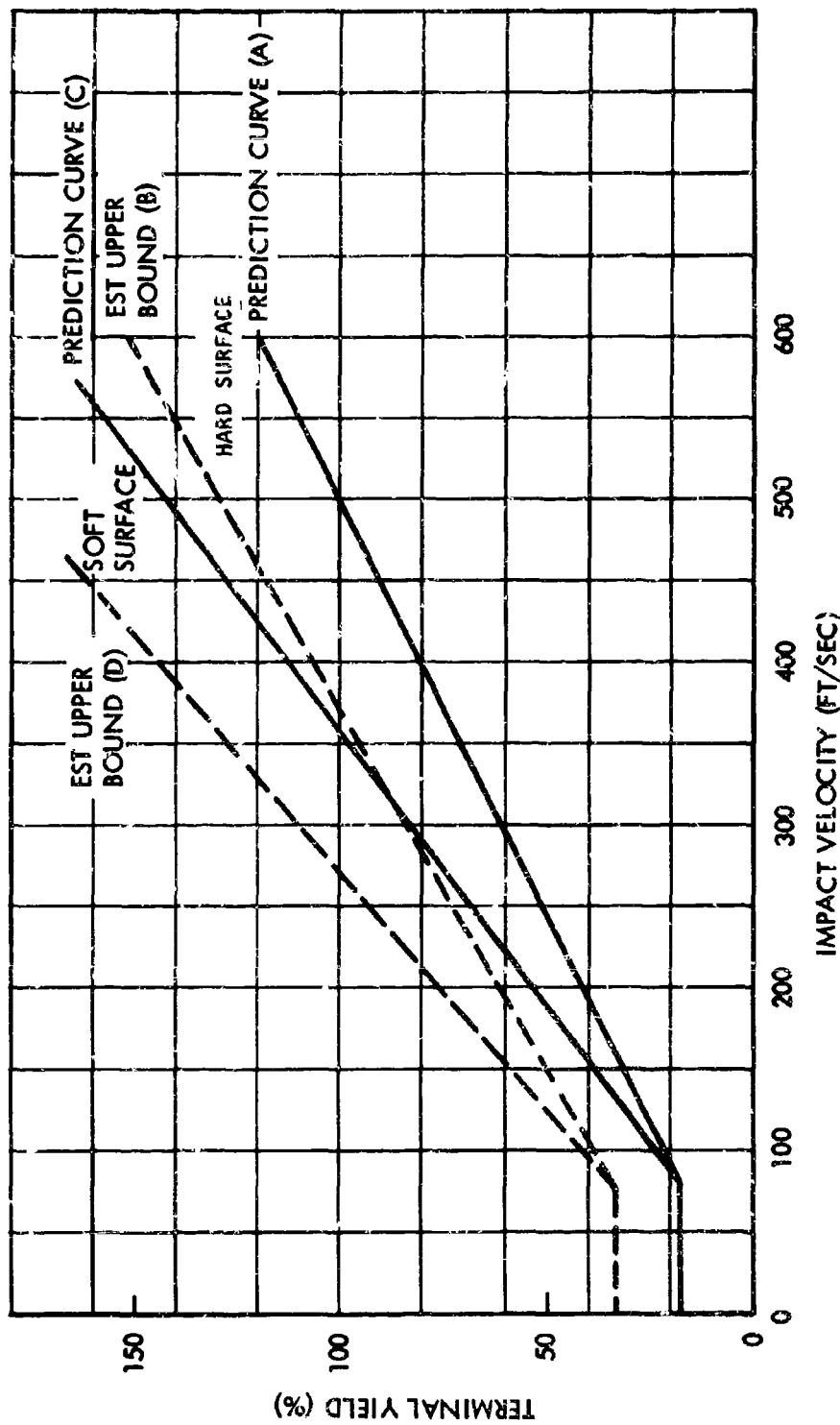
Fig. 5-53. Terminal Yield vs Impact Velocity for LO_2/LH_2

Part 4 — FULL-SCALE TESTS

During the program two valid data tests were performed using full-scale missile hardware. These were a Saturn S-IV stage containing approximately 91,000 lb of LO_2/LH_2 and a Titan I first stage containing approximately 100,000 lb of $LO_2/RP-1$. The objectives of these tests were to obtain full-scale data points regarding the blast, thermal, and fragmentation hazards of $LO_2/RP-1$ and LO_2/LH_2 propellant combinations.

Saturn S-IV

The planned failure conditions for this test were to rupture the common bulkhead, forcibly bring the two propellants together by having a pressure differential between the two propellant compartments, and to ignite the resulting propellant mixture at a known delay time. A photo of the S-IV test article is shown in Fig. 5-54.

The common bulkhead of the S-IV vehicle is an 18-ft-diameter dome constructed of two thin sheets of aluminum separated by an insulating layer of hexcell material. The overall thickness of this bulkhead is approximately 1 in.

This bulkhead was ruptured from the underside with an explosively driven segmented cutter, 18 in. in diameter. This cutter was designed to slice through the bulkhead, creating six small segments which could then be easily removed by fluid flow through the hole. A photo of this cutter ram assembly is shown in Fig. 5-55.

This cutter was attached to a drive rod and was installed in the LO_2 tank in the guide tube assembly as shown in Fig. 5-56. The lower end of the drive rod extends through the stopping tube and part way into the drive barrel.

To rupture the common bulkhead, the drive rod cutter assembly was pushed by detonating an explosive charge in the driver barrel. Once the
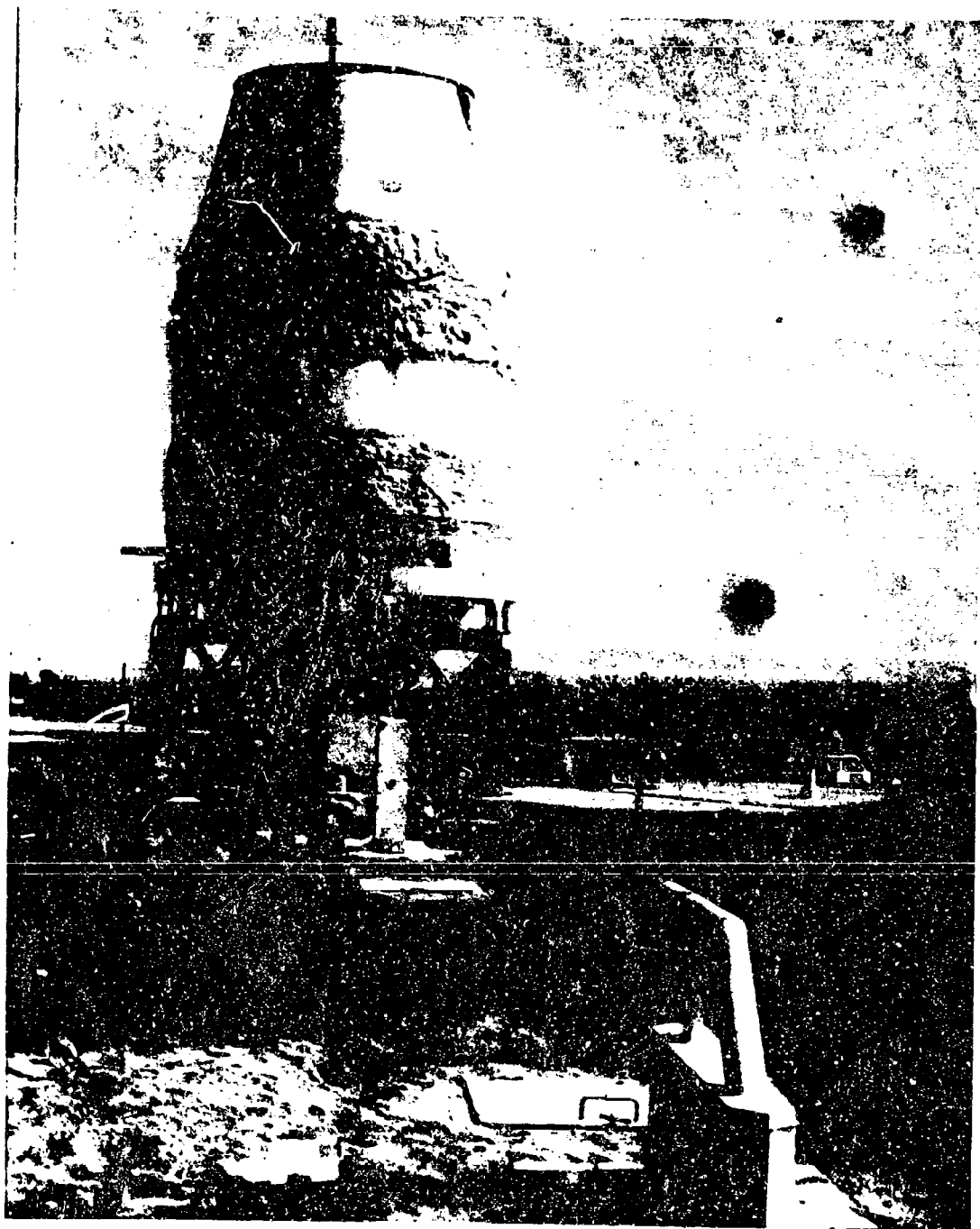
Fig. 5-54   Saturn S-IV

Fig. 5-55 Cutter for the Saturn S-IV Cutter Ram Assembly
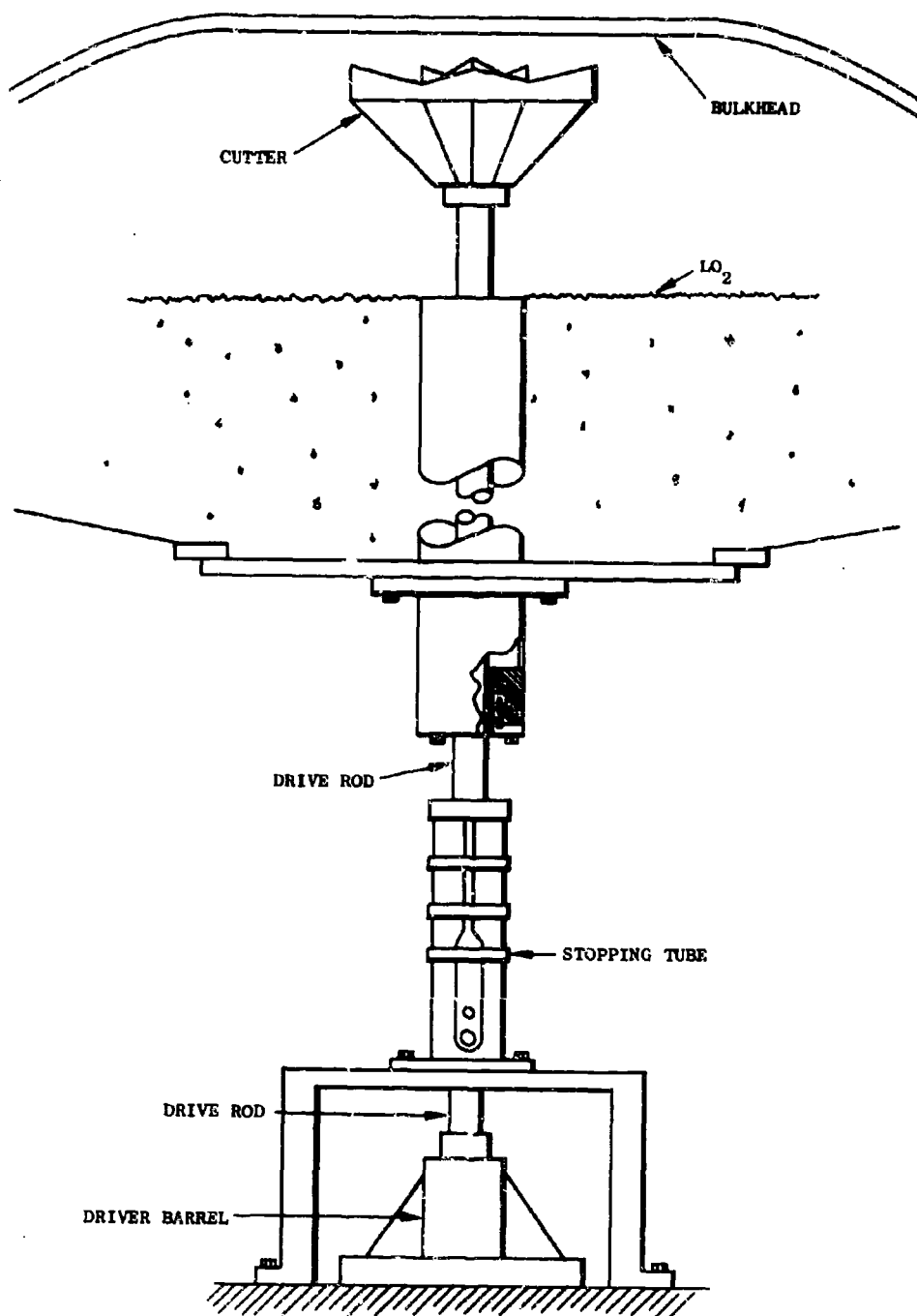
Fig. 5-56.   Saturn S-IV Cutter Ram Assembly

cutter ram penetrated the common bulkhead, a pin installed through the drive rod impacted a slot in the stopping tube. This brought the drive rod and cutter to a stop and prevented it from continuing on into the LH$_2$ tank and possibly damaging the top of that tank.

To aid in removing the small segments cut by the cutter assembly and to forcibly bring the two propellants together, the upper tank was pressurized to approximately 15 psi, while the lower tank was kept at ambient pressure. The ullage volume in the tanks was approximately 3 percent in the LH$_2$ tank and 10 percent in the LO$_2$ tank. The planned ignition time for this test was ~10 sec, although it was expected that the tank would reach burst pressure (~100 psi) much sooner than this and self-ignite.

Test Results

According to all available data, including direct observations, high-speed motion picture films, pressure records, etc., the failure mechanism hardware functioned as planned. Ignition, however, occurred 183 msec after rupture of the common bulkhead, which was much shorter than the planned ignition time and well before the internal pressure reached 100 psi.

The overpressure and positive-phase-impulse data obtained from this test are given in Table 5-9.

Average yield values at each distance have been calculated from the data in Table 5-9 and are presented in Table 5-10. Note that the pressure yield seems to level off at a value of about 3 to 3.5 percent and the impulse yield at a value of 6.5 to 7.0 percent.

Table 5-9

PEAK PRESSURE AND POSITIVE-PHASE IMPULSE FROM S-IV TEST

GROUND DISTANCE (ft)	GAUGE LINE	PEAK OVERPRESSURE (psi)	POSITIVE-PHASE IMPULSE (psi-msec)
38	A	96.0	440
67	C	26.42	231
117	A	12.1	192*
	B	12.4	**
200	A	4.57	***
	B	4.40	**
335	A	2.55	87.2
	B	2.55	73.3
600	A	1.02	**
	B	1.03	41.56
	C	1.15	44.5

---

*   Uncertain because of large correction.

**   Noise on traces.

*** Suspected base shift.

"A" refers to 11 o'clock leg, "B" refers to 7 o'clock leg, "G" refers to 3 o'clock leg.

Table 5-10

S-IV YIELDS

Distance (ft)	Yield Surface Burst Reference Curve	
	Pressure (%)	Impulse (%)
38	1.5	6.0
67	1.5	4.2
117	2.5	5.8
200	2.4	-
335	3.5	6.8
600	2.9	6.6

S-IV Fragmentation Survey

Following the S-IV test a complete fragmentation survey was conducted of the test area. This survey included locating, measuring, weighing, and describing each fragment from the S-IV vehicle weighing over 1 lb. The area covered was from 100 ft from ground zero to the outer limit of the fragment dispersion, which was approximately 900 ft.

The procedure used for this survey was to lay out on the ground surface a system of 16 radial lines marked off in 100-ft increments, thus dividing the area into 128 easily defined areas. Teams of URS and AFRPL personnel then searched each of these areas, and as each fragment was collected, its approximate location within the area was noted on a map and an identification number written on the fragment. The fragments were then loaded on a truck for transportation to a central point for weighing and measuring. The data obtained from this survey are presented in Volume 2. These data indicated that the majority of the fragments were within a radius of 800 ft from ground zero, with a few out to 1,000 ft.

Titan I Tests

The planned failure condition for this test was similar to that used for the Saturn S-IV in that a common diaphragm between the propellants was to be ruptured, differential pressure in the two tanks would force the propellants together, and ignition would be initiated after a known delay. A photo of the Titan 1 on the test pad is presented in Fig. 5-57. This missile normally contains approximately 170,000 lb LO_2/RP-1. The test conditions planned for these tests were to fill the propellant tanks two-thirds full, which would be 78,600 lb LO_2 and 35,000 lb RP-1, or a total propellant weight of 113,600 lb.

In a Titan I first stage, the two propellant tanks are separated by some 10 in. To allow the propellants to come together, a tubular conduit with an internal diameter of 16-1/2 in. was installed between the two propellant compartments and a tempered-glass diaphragm installed at the top of the conduit. This diaphragm was removed during the test by an explosively driven segmented cutter ram similar to those used in the small-scale CBM test series. This 16-1/2-in.-diameter hole is equal to approximately 2 percent of the tanks' cross-sectional area.

Test Results

Two tests of the Titan I were attempted. The first Test Number 300, produced no data because a structural failure in the missile resulted in ignition before instrumentation was scheduled to be turned on.

In the second test, Number 301, propellant filling difficulties resulted in the LO_2 tank being only one-half full rather than the two-thirds full originally planned. The failure mechanism hardware appears to have functioned properly, and pressure in the RP-1 tank rose smoothly from ambient to about 54 psi immediately before ignition, which occurred about 842 msec after rupture of the diaphragm.
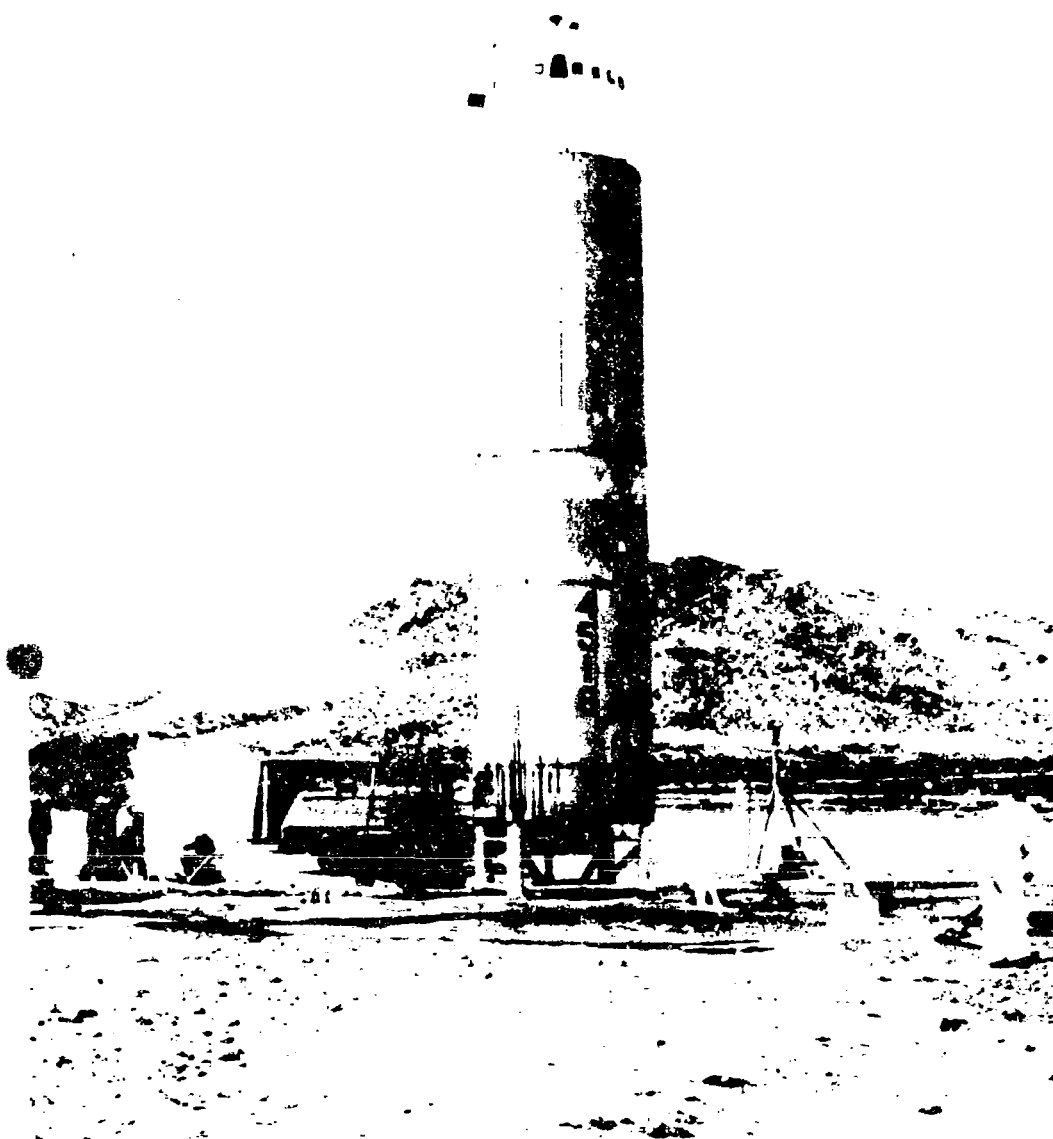
Fig. 5-57.   Titan I on Test Pad

The peak overpressure and positive-phase-impulse data for this test
appear in Table 5-11. The terminal yield for this test,based on the
estimated 94,000 lb of propellants on board, is 4 percent. A posttest photo
of this test appears as Fig. 5-58.

Table 5-11

Peak Overpressure and Positive-Phase-Impulse Data
for Titan 1 LO_2/RP-1 Test

Distance	Peak Overpressure		Positive-Phase-Impulse	
(ft)	psi/in.^{2}	yield (%)	psi/msec	yield (%)
37	45	0.5	310	3.0
67	39	2.5	218	3.6
117	12	2.5	158	4.3
200	5.6	3.2	78	3.0
233	2.3	2.7	*	*
600	1.1	3.0	34.2	4.6

* Impulse not readable because of noise
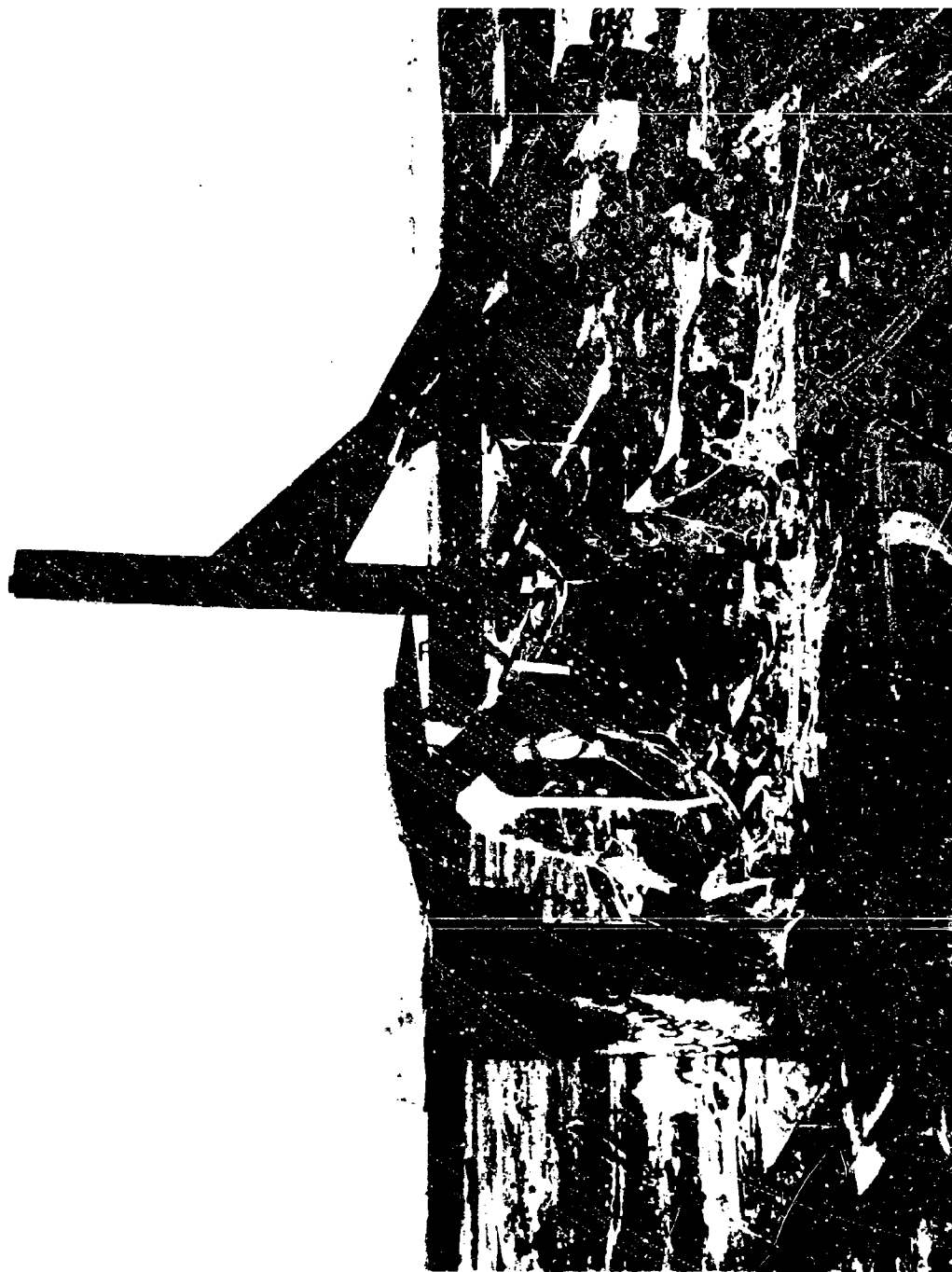
Fig. 5-58. Posttest Photo Titan I Test

Part 5 - DISCUSSION OF YIELD AND IGNITION TIME SCALING

Yield Scaling

The basic blast prediction equations presented in the previous sections were initially developed using data obtained from 200-lb weight scale and from postulated scaling relationships based on available information regarding the propellant mixing and explosion phenomena. Specifically, the initially postulated relationship was that the explosive yield (in percent of the total propellant weight) would be independent of the propellant quantity and that the time of ignition to obtain equal explosive yields would scale as the cube root of the propellant weight. In other words, $Y = f\ (t/W^{1/3})$. This relation is illustrated below for the LO_2/RP-1 CBM case and with L/D = 5 and a k = 1.

PROPELLANT WEIGHT (lb)	IGNITION TIME (msec)	SCALED IGNITION TIME ($msec/lb^{1/3}$)	YIELD (%)	YIELD (lb of TNT)
200	193	33	10	20
1,000	330	33	10	100
5,000	564	33	10	500
25,000	965	33	10	2,500
125,000	1,650	33	10	12,500
625,000	2,820	33	10	62,500
3,125,000	4,725	33	10	312,500

1,000-lb Scaling Tests

The validity of the postulated scaling was tested first using results from the 1,000-lb scale with the following results:

LO_2/RP-1 CBM. Comparison of the 200- and 1,000-lb data showed significant differences, which indicated a deviation from the postulated scaling. The magnitude of the effect could not be adequately evaluated without use of the 25,000-lb data.

LO_2/LH_2 CBM. Comparison of the 200- and 1,000-lb data showed no significant differences and all data were used in deriving the prediction equation (see Fig. 5-37).

LO_2/RP-1 CBGS. Comparison of the 200- and 1,000-lb data showed no significant differences, and all data were used in deriving the prediction equation (see Fig. 5-39).

LO_2/LH_2 CBGS. Comparison of the 200- and 1,000-lb data showed no significant differences and all data were used in deriving the prediction equation (see Fig. 5-44).

25,000- to 100,000-lb Scaling Tests

Further tests of the validity of the postulated scaling were made with tests using propellant quantities ranging from 25,000- to 100,000-lb scale with the following results:

LO_2/RP-1 CBM. Since the results from the 200- and 1,000-lb tests showed a scale effect and were not in themselves sufficient to establish its magnitude, the basic prediction equation was developed using all the 200-, 1,000-, and 25,000-lb data. The results showed that the yield tended to decrease with increasing weight but that the rate of decrease also tended to decrease with increasing weight so that the yield was essentially independent of weight for weights greater than 10,000 lb.

One 94,000-lb test was run which was considered consistent with this postulated scaling even though the measured yield value was below the predicted range as shown below:*

---

* A second similar test was run but the diaphragm failed early and no data were obtained.

         Measured Yield   4% for 94,000 lb, 2% for 170,000 lb

         Predicted Yield

            Best Estimate   6%

            Range[*]   4-8%

     The prediction method was based on results with intertank openings
equal to 20% of the tank cross-sectional area and thus would be expected
to be conservative (i.e., somewhat high) for this case because the inter-
tank bulkhead opening area was only 2%.

     LO_2/LH_2 CBM. Three 25,000-lb tests were run. In all three tests
ignition occurred very early and prior to the time the LH_2 could have
contacted the LO_2, the minimum time of interest for this case.[**] Since
these tests did not satisfy the basic criteria for this test case, they
are not suitable for a quantitative check of scaling. Their results, however,
which ranged from 0.1 to 0.2% are not inconsistent with the predicted zero
time yield value of 2.8% and range of 0-10% since they would be expected
to be smaller than the predicted value. One 91,200-lb test was run (S-IV)
which was consistent with the postulated scaling as shown below:

                          S-IV Yield

            Measured Yield   5%

            Predicted Yield

               Best Estimate   6%

               Range   0-13%

---

[*] Bounds of 80% two-sided prediction interval. (There is an 80% probability
     that a single test will fall within these bounds.)

[**] It is believed that in two of the cases, the initial reaction was between
      the LH_2 and frozen oxygen trapped in the LH_2 during the filling process.
      In the other case, the diaphragm did not break.

$LO_2/RP-1$ CBGS. Two 25,000-lb tests were run, one of which ignited prior to the second propellant reaching the ground surface (the minimum time of interest for this case) and thus was not suitable for a quantitative scaling check. The results from the other test were consistent with the postulated scaling as shown below:

> Measured Yield   37%
>
> Predicted Yield
>
>   Best Estimate   36%
>
>   Range   26-46%

The early time test was also in qualitative agreement with the predicted value. For a zero time of ignition, the equation gives a yield of about 6.5% with a range from 0-16.5%. The measured yield was 2%, which is in the lower part of the range, as would be expected since it ignited prior to the defined zero time.

LO_2/LH_2 CBGS. Three 25,000-lb tests were run, two of which ignited prior to the second propellant reaching the ground surface (the minimum time of interest for this case) and thus are not suitable for a quantitative scaling check. The results from the third test were consistent with the postulated scaling as shown below:

> Measured Yield   13%
>
> Predicted Yield
>
>   Best Estimate   22%
>
>   Range   2-42%

The two early ignition time tests are also qualitatively consistent with the predicted value. Both tests gave 4% yields, which compare with a predicted value of 18.1% and a range from 0-40%.

Ignition Time Scaling

Because the scope of Project PYRO did not include investigation of
ignition probabilities, the resulting data are not considered suitable
for quantitative estimates of credible ignition time or the manner in
which ignition times scale. This is primarily because the results of any
such analysis are more dependent on the assumptions involved in the analyses
than on the data themselves. The inherent limitations and assumptions in
using the PYRO results for this purpose are discussed below.

First of all it should be emphasized that the objective of Project PYRO
was to determine the yield as a function of time and other controlling
parameters, so that in the experimental design, time of ignition was selected
to be a controllable parameter rather than a random variable. In essentially
all cases (except for some of the high-velocity-impact tests) a controlled
time ignition source was provided and efforts were made, insofar as practical,
to eliminate other possible ignition sources. In the majority of the tests
conducted, ignition did occur from the planned ignition source, and clearly
these data are not very helpful in determining the probability of ignition.

The next major limitation in using the PYRO results to infer ignition
probabilities, particularly as a function of scale (i.e., propellant weight),
is that a decreasing number of tests were conducted as the propellant quantities
increased. The reason this complicates the analysis is that when spurious
ignitions were obtained on the initial tests for a given test mode and scale,
efforts were made to identify their source, and changes were made in the
experimental arrangement to try to minimize the spurious ignitions. In
some cases these efforts were reasonably successful, so that the probability
of obtaining a spurious ignition tended to decrease as the number of tests
for a particular testing mode and scale increased. This combination of an
experimental learning curve with regard to controlling ignition and a
decreasing number of tests with increasing propellant weight rather automati-
cally leads to an increasing percent of spurious ignitions with increasing

weight due solely to the experimental procedure used and not necessarily because of any inherent scale effect on ignition probability. Since the spurious ignitions generally occurred well before the planned ignition time, this in turn leads to lower average yields as the weight scale increases.

Another limitation in using the results from the spurious ignition tests for inferring ignition probability scaling (or yield scaling) is that many of the ignitions occurred so early in time that the resulting failure mode did not satisfy the basic criteria for the desired test case. In the CBM case, for example, the earliest time of ignition considered of interest was at the moment when the upper propellant first contacts the lower propellant. As noted earlier in all three 25,000-lb LO_2/LH_2 tests, ignition occurred well before this time, so that these tests could not be included in the standard CBM case. For the CBGS case, the major time regime of interest is after all the propellants are on the ground surface, and the earliest time of interest is when the top propellant reaches the ground surface. In a number of the spurious ignition tests, including two of the three 25,000-lb LO_2/LH_2 tests, ignition occurred prior to this time, so that these tests cannot be considered as part of the standard CBGS case.

The last major limitation in using the PYRO data for inferring ignition probabilities is that the test tankage and failure modes used in the experiments at the 200-, 1,000- and 25,000-lb scales were designed to create certain generalized types of propellant interactions (i.e., ways in which the propellants come together and mix) that could occur in failure of full-scale vehicles, but no attempt was made to directly model actual full-scale tankage with regard to strength, detailed failure mechanisms, or inherent ignition characteristics. Even between the various scales of testing in PYRO, no considerations were given to duplicating these characteristics. Thus any similarity between the basic characteristics which control ignition probability in full-scale accidents and those of PYRO would be fortuitous.

Section 5
REFERENCES

5-1. Kingery, C. N. and B. F. Pannill, Peak Overpressure vs Scaled Distance
for TNT Surface Bursts (Hemispherical Charges), BRL Memorandum Report No.
1518, Ballistic Research Laboratories, April 1964 (AD 443 102)[*]

5-2. Defense Atomic Support Agency, Operation SNOW BALL Project Descriptions,
Volume 1 (U), DASA Data Center Special Report 24-1, DASA 1516-1 (AD 441
974)[*]

---

[*] Reference curves from these documents are reproduced in Appendix F.

Section 6

THERMAL ENVIRONMENT

OBJECTIVES

The objective of the thermal portion of the study was to make measurements
which enable "reasonable" bounds to be placed on, or which substantiate theor-
etical predictions of, the heat transfer to objects in and about the "fireball"
created by the explosion of liquid propellant mixtures. Residual fires are not
included.[*]

GENERAL ORGANIZATION

The thermal hazard portion of the study is located in four separate sec-
tions of the report. The contents of these sections are as follows:

- Section 6 of Volume 1 commences with a general discussion which de-
  scribes the fireball characteristics, the nature of the heat transfer
  within the fireball, and the general experimental approach that has
  been taken. This is followed by a brief summary of the thermal instru-
  mentation, and finally the results from the 25,000-lb and Titan tests
  are presented.

- Appendix C of Volume 1 consists of a detailed description of the ther-
  mal instruments, their mounting and location, and the errors of the
  associated measurements.

- Section 2 of Volume 2 contains the basic thermal data records. Data
  are given regarding the.

  (1) Heat flux density into slabs immersed in the fireball for the
      25,000-lb and Titan tests

  (2) Radiant flux density within the fireball for the 25,000-lb tests

  (3) Radiant flux density outside the fireball from the 25,000-lb and
      Titan tests

  (4) Temperature of thermocouple probes selected from the 25,000-lb
      test data

---

[*] For thermal hazards of residual fires see, for example, Ref. 6-1.

Heat flux vs time at "large" propellant weight scales is then considered.
A recommended scaling relationship for heat flux vs time is given, along with
a listing of the experimental evidence upon which the relationship is based.
The Titan I heat flux data are then compared with the $LO_2/RP-1$ bounding heat
flux-time curve that has been scaled, using the recommended scaling, to the
100,000-lb level.

Finally, the radiant flux density measurements from outside the fireball
are considered. The results of the 25,000-lb tests are presented only in terms
of summary data plots indicating the data mean and range. A single measurement
from the Titan I test is given.

Results of the 25,000-lb Tests

Gas Temperature from the Photo-Recording Pyrometer

A summary of the pyrometric gas temperature measurements for the 25,000-
lb tests is presented in Fig. 6-1 for both the $LO_2/RP-1$ and the LO_2/LH_2 tests.
(No equivalent Titan data are currently available.) The plots include a curve
of the mean temperature and an indication of the highest and lowest measured
temperature, where the plotted values are time averages over, in most cases,
100- and 200-msec time intervals for the $LO_2/RP-1$ and LO_2/LH_2 tests, respec-
tively. The number of data curves from which the summary plots are constructed
changes with time because the fireballs have a range of durations, and this
number is indicated just beneath the plot. It should be remarked also that the
temperature range of the pyrometer for these tests was such that temperatures
below about $1900°K$ could not be measured. For two tests (Tests 279 and 282),
the temperature during the fireball duration fell temporarily to levels at or
somewhat below $1900°K$, and for this time and these two tests, a value of $1900°K$
was used in obtaining the temperature average over the tests.

A most evident feature of the gas temperature values is their consistency
from test to test. The variation appears to be somewhat larger for LO_2/LH_2
than for $LO_2/RP-1$ with — for instance — the greatest deviation of a single
measurement from the mean of the measurements being about $300°K$. There is a
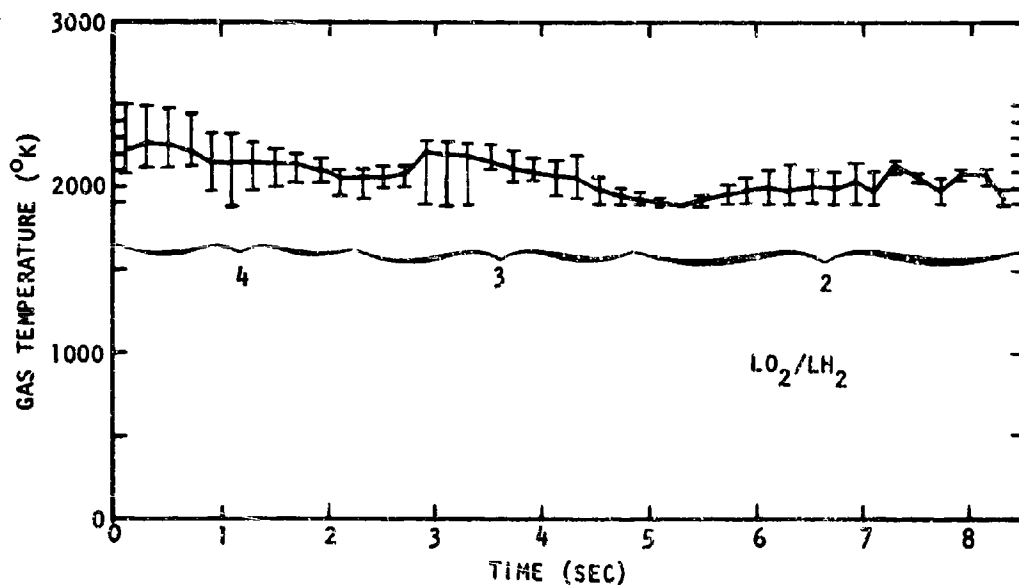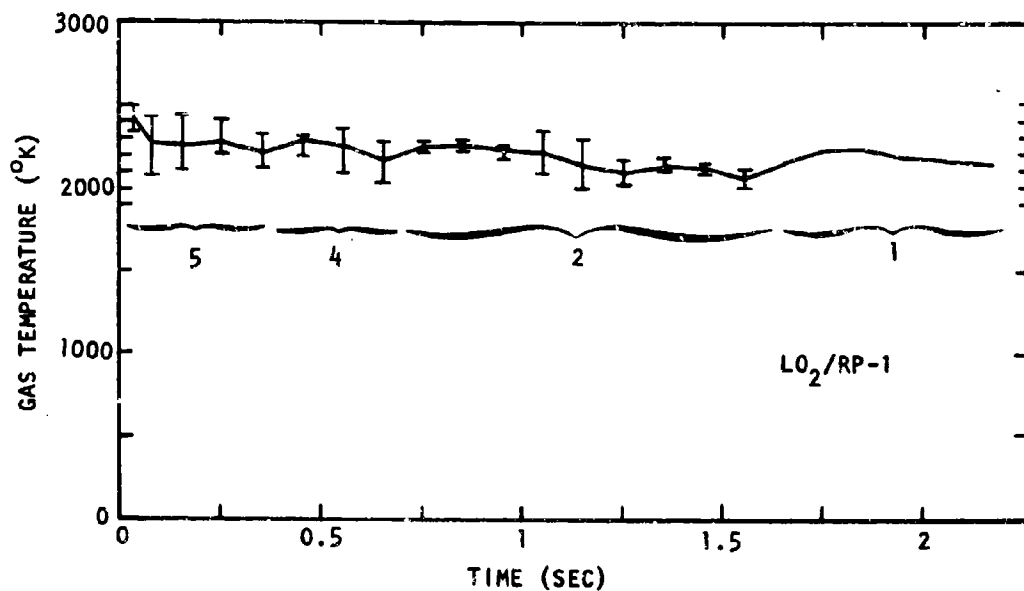
Fig. 6-1.   Pyrometric Gas Temperature Measurement Summary for the
25,000-lb Tests

- Section 6 of Volume 3 consists of a summary of the heat flux density
  —time vs propellant weight prediction.

It should be acknowledged that certain of the thermal measurements were planned and conducted, and the data reduced, by the Sandia Corporation, and the Sandia instruments are designated as such in the description of instruments in Appendix C of Volume 1.

PREFATORY REMARKS

The expressions "heat flux density, " "total heat flux density," "heat flux," and "flux density" are used interchangeably and represent the energy per unit area per unit time transported through a material surface due to both the radiant and convective modes of heat transfer. Similarly, the expressions "radiant flux density" and "radiant flux" represent the energy in radiant form per unit area per unit time.

GENERAL DISCUSSION

Characteristics of the Fireball

The size, duration and gross motion of the propellant fireball depends on the total quantity of propellants. During its growth and the early stages thereafter, the fireball from a propellant mixture on or near the ground surface is more or less hemispherical, reaching a maximum diameter that is approximately proportional to the cube root of the propellant weight. More specifically, an empirically derived expression relating the maximum diameter D in feet to the total propellant weight W in pounds is given by[*]

$$D = 9.56^{0.325} \qquad (6.1)$$

---

[*] Equation (6.1) along with Eq. (6.2) below, have been extracted from Ref. 6-2. The equations were obtained through the statistical analysis of data from either the literature or by reduction of photographic records from a total of 71 tests or incidents with the propellant combinations of $LO_2/RP-1$ or LO_2/LH_2 and which ranged in propellant weight from 10 to 250,000-lb.

notably short duration for the LO_2/RP-1 compared with both the LO_2/LH_2 gas temperature duration and, more importantly, with the measured LO_2/RP-1 heat flux durations that will be considered below. Substantial temperatures appear to have persisted within the fireball for significantly longer periods than could be measured by the remote temperature instruments, evidently due to obscuration by "cooler" gases and/or particulate matter along the surface of the fireball.

A feature of the temperature data that does not appear in Fig. 6-1 is the frequent occurence of a comparatively high but abruptly decreasing temperature in the initial stage of fireball expansion; these temperature "pulses" are not resolved in Fig. 6-1 since their duration is generally a small fraction of the 100- and 200-msec time intervals of Fig. 6-1. A listing of the highest magnitude and the duration of the pulses is given in Table 6-2, where the duration is defined as the time from ignition for the temperature to decay to (and remain below) $2450°K$; a radiant flux density of 200 watt/cm^2 corresponds to a temperature of $2450°K$ for an emissivity of one. Also included in the table are maximum values of the radiant flux density during this time for an emissivity of 1.

While comparatively large temperatures or corresponding magnitudes of heat flux frequently occur, the damaging response of most structures or objects to these pulses is small compared with the response from the remaining or subsequent heat transfer.

An indication of the spatial variation of gas temperature over the fireball is given in Fig. 6-2, where the temperature over three separate regions of the fireball from Test 283 is given. A crude indication of the size of each region of measurement relative to the fireball dimensions and the location of each region is given in the upper right hand corner of the figure.

It can be seen that spatial differences of the temperature at given times are commonly of the order of $200°K$, and it should be remarked that comparative examination of film coverage of the various 25,000-lb tests suggests that the fireball from Test 288 was relatively uniform. Temperature variations of this

where the estimated standard error of the diameter is 30 percent. Thus, diameters, for instance, for 1,000 and 1,000,000 lb are about 93 and 850 ft, respectively. It is emphasized, however, that Eq. (6.1) does not always indicate maximum fireball dimensions, in part because it was derived on the basis that "in those instances where the fireballs were markedly asymmetrical, attempts were made to estimate equivalent spherical diameters."[*] Moreover, in the tests from which Eq. (6.1) was obtained, there was a tendency for the spatial dispersal of propellants prior to their ignition to be less extensive than can practically occur, and comparatively extensive dispersal can lead to correspondingly large maximum dimensions; larger fireballs would tend to result from propellant spills, for instance, if the propellants spread sufficiently along the ground surface prior to their ignition. The Titan test (involving about 100,000 lb of LO_2/RP-1) provides an illustration, first, of the departure of the maximum dimensions that can occur from the diameter given by Eq. (6.1), and second, of still another mechanism of propellant dispersal. In this test, a fraction of the propellants was intentionally allowed to mix and subsequently ignite while within the confines of the missile tankage. However, the forces of the explosion evidently caused part of the remaining unmixed propellants to be displaced in such a manner that they did not mix and react until they had been substantially displaced laterally from the center of explosion. The maximum dimension of the resultant fireball was estimated to be from 800 to 1000 ft, while the diameter as given by Eq. (6.1) is approximately 400 ft.

Fireball durations, i.e., the period over which visible radiation exists, also increase approximately with the cube root of propellant weight as given by

$$\tau = 0.196 \ W^{0.349} \tag{6.2}$$

where the duration, τ, is in seconds for a weight in pounds, with a standard error of 84 percent; 1,000- and 1,000,000-lb durations are 2.2 and 24 sec,

---

[*] Ref. 6-2.

6-3

Table 6-2

FIREBALL TEMPERATURE DURING INITIAL STAGE
OF FIREBALL EXPANSION FROM PHOTO-RECORD PYROMETER

PROPELLANT TYPE	TEST NO.	TIME FOR TEMPERATURE TO DECREASE TO 2450°K (msec)	MAXIMUM TEMPERATURE (°K)	MAXIMUM RADIANT FLUX FOR AN EMISSIVITY OF 1 (watts/cm²)
LO$_2$/RP-1	275	30	>2650	>270
	278	25	>2500	>210
	282	15	>2600	>250
	284	10	2560	235
	285	10	2860	360
LO$_2$/LH$_2$	277	0	2380	175
	279	0	2320	160
	281	0	2250	140
	286	25	2900	285

respectively. For large enough propellant quantities, the duration is suffi-
cient for the fireball to rise to heights of the order of a few fireball diam-
eters, the rise occurring with accompanying modifications of the shape of the
fireball, first to that resembling a sphere, and finally approaching, should
it continue to persist, the characteristic toroidal geometry. Vertical motion
is, for practical purposes, generally nonexistent at the 1,000-lb (or less)
level, while significant heights are generally attained with quantities of
25,000 lb or more. A significant rise is accompanied also by the formation
of a vertical and temporarily rising column, generally referred to as the stem,
which extends from the lower region of the fireball to the ground surface.
While this column may become heated due to its proximity to the fireball, it
essentially does not consist of the products of explosion, but rather of gases
and particulate matter that have been swept from regions lateral to the initial
fireball.

Velocities that accompany fireball growth are at first supersonic but
rapidly decay to subsonic levels. From film coverage of 25,000-lb tests, radial
expansions of 60 ft (about one-half maximum dimension) typically occur in about
50 msec, giving an average velocity during that time of 1200 ft/sec. While the
growth velocities thereafter rapidly subside, randomly directed local motion
persists throughout the duration of the fireball.

Temperatures that prevail in the fireball are typically of the order of
2,500°K ($\sim$ 4,000°F), with spatial variations tending to occur particularly after
the period of fireball growth. Unlike explosions of high explosives or "well-
mixed" propellants, there is evidence suggesting that the process of fuel-oxi-
dizer mixing and subsequent chemical reaction continues during and perhaps some-
what after fireball growth. Since the rate of chemical reaction in, and the
consequent energy emitted from, an elemental region depends on the quantities
of fuels and oxidants in the region that are in sufficient proximity to interact,
and since the spatial distribution of these potential reactants can easily be
nonuniform, there is no guarantee of thermodynamic equilibrium; and radiation
from any such region is therefore not necessarily governed by the Planck radia-
tion laws. With time, of course, uniformity throughout any given elemental

magnitude result in comparatively large spatial variations in heat flux, par-
ticularly since the radiant flux varies with the fourth power of the tempera-
ture. For an emissivity of 1, the radiant flux computed from the temperatures
of about 2320 and 2520°K at 0.5 sec in Fig. 6-2, for example, are 160 and 220
watt/cm², respectively. Similarly, temperatures of 2090° and 2320°K at 1.3
sec correspond to flux densities of 100 and 160 watt/cm². In addition to spa-
tial variations in heat flux of this magnitude, temporal variations (at a sta--
tionary point) of the same magnitude can be expected to occur in small frac-
tions of a second, as evidenced, first, by the abrupt temperature changes in
Fig. 6-2, and more vividly through high-speed film coverage of the apparent
motion of high- or low-temperature regions about the fireball.
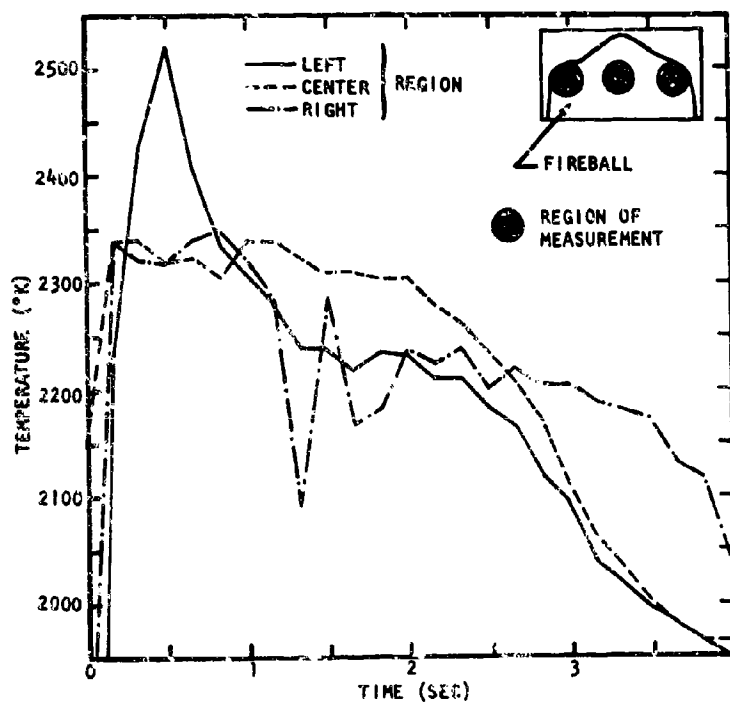
Fig. 6-2. Spatial Variation in Gas Temperature for Test 288

region will be approached. thermal... making it... ible to consider Planckian
radiation and its associated laws. When laws such as Stefan's radiation law
are applied, however, there remains the uncertainty of the emissivity, an un-
certainty stemming primarily from ignorance of the fireball constituents at a
given instant.

Heat Transfer within the Fireball

The transfer of energy to material surfaces immersed in and moving rela-
tive to a "high-temperature" gas is effected through some combination of the
mechanisms of radiation and forced convection. An object whose surface is ev-
erywhere convex or planar will be uniformly irradiated, provided the mean free
photon distance, the mean distance that a photon travels through the fireball
before being absorbed, is significantly less than the distance to either the
edge of the fireball or some other object that can obstruct its irradiance.
With the quantities of carbon that are present in the LO_2/RP-1 fireballs, this
mean distance is evidently small compared with the dimensions of the fireball,
so that for most circumstances there would be uniform irradiance. This is less
clear for fireballs from the LO_2/LH_2 propellant combination

For the LO_2/RP-1 propellant combination, particulate carbon is present in
sufficient quantities to suggest that the emissivity of a layer of the fireball
would approach that of carbon for a thickness that is small compared with the
fireball diameter. If this is assumed, along with a gas temperature of 2,500°K,
a radiant flux density of about 215 watts/cm^2 (190 Btu/ft^2-sec) is obtained.

Convective transfer from ordinary gases at these temperatures tends to be
small compared to the radiant transfer mentioned above except as flow velocities
approach supersonic levels. As noted previously, the velocities that accompany
the fireball growth commence at supersonic levels, but the growth approaches
completion within tens or hundreds of milliseconds. Consequently, while
convective transfer rates can be comparable to expected radiative rates during
this time, the short duration renders their contribution negligible compared
with the total transfer. However, high-speed motion does not cease with the
completion of growth. Local and randomly directed "swirling" motion continues

Heat Flux Density

All heat flux density data from the 25,000-lb tests are presented in Figs.
2-1 through 2-28 of Section 2, Vol. 2.   Included in the present section are
discussions of the results and comparisons of the data with other data. More
importantly, however, it is desirable to use the heat flux density data to ob-
tain a "conservative yet realistic" bound to the heat flux that a structure or
object immersed in the fireball can receive, and this section commences with
the presentation and discussion of this upper bound.

Two complications occur in acquiring the upper bound. First, the flux
instruments are not continuously in the most severe region of the fireball,
and second, because the test design was based on blast rather than thermal
considerations, there are some difficulties with regard to identifying thermal
test conditions.

Regarding the first complication, the fireball parameters of potential
importance to heat transfer, such as the gas temperature, are not generally
uniform throughout the fireball. This is particularly evident from film cov-
erage of the tests, and was illustrated for gas temperature specifically in
Fig. 6-2. It would be expected, therefore, that a direct flux density measure-
ment from a stationary instrument would approach or attain the maximum possible
value only occasionally, that is, for some times for some tests. It is an ob-
served characteristic of the measured flux density-time curves to exhibit
periodic "surges" or maxima, evidently reflecting the variations in the gas
parameters as the gas flows past the instrument, and statistically, some of
these maxima will be, or will approach, the highest value possible at that
time for the fireball in question. Provided there is a sufficiently large
number of measurements per test and a sufficiently large group of tests having
identical test conditions, the upper bound to the heat flux density for this
set of test conditions will be revealed by superimposing the flux density pul-
ses having the higher maxima on a single flux density-time graph; or more
specifically, a smooth curve fitted to the highest maxima of this graph will
represent an upper bound. This approach of estimating an upper bound, or a

throughout the duration of the fireball, with velocities, as photographically
indicated, typically ranging from 100 to 400 ft/sec. An immersed object, there-
fore, will tend to receive "surges" of convectively transferred energy at lev-
els that are not negligible compared with radian, transfer, and the object may
experience several such surges from more or less random directions. It is
again emphasized that this discussion pertainc to ordinary gases.

There is a difference of potential importance between a gas and the so-
called fireball "gas" in that the fireball contains particulate matter, a fact
which can greatly affect energy transfer. To illustrate the possible extent of
the effect, consider a flow of high-temperature gas within which are particles
that have the same temperature and velocity as the gas. On approaching an ob-
ject, the comparatively large momentum of the particles will tend to permit
their impingement on the object, and during the time of contact, energy will be
conducted from the particles to the object. As an example, a 500-μ carbon par-
ticle at 2,500°K has about 3 joules of internal energy that can be transferred
to a room-temperature heat sink, and if the particle is assumed to temporarily
deform on impact in such a way that a circular area of diameter equal to the
particle is in contact for 0.01 sec, approximately 1 joule of energy will be
transferred from the particle. The continual bombardment from the flow of a
concentration of particles will, of course, result in a heat flux to the object,
as illustrated in Table 6-1, where the heat flux density associated with ranges
of particle size, particle concentration, and duration of contact are considered
for a velocity of 200 ft/sec.

Table 6-1

ESTIMATES OF HEAT FLUX DENSITY (in watts/cm^2) BY PARTICLE IMPINGEMENT

		DIAMETER (μ)			
		50		250	
		CONCENTRATION (particles/cm^3)		CONCENTRATION (particles/cm^3)	
		10^{-2}	1	10^{-2}	1
Duration of Contact (ms)	0.1	0.01	1.2	0.5	50
	10	0.01	1.5	1.8	180

bounding curve, has been applied, and the results obtained from it, along with indications of the limitations associated with the approach, are presented below.

With this approach, it is essential that the data that are combined to obtain an upper bound are from tests which have identical test conditions. The discussion in the following paragraphs serves primarily to indicate how closely we are able to comply with this requirement. It will be seen that a practical choice of separating the tests into thermal test condition categories is made without complete technical justification for the choice. The discussion commences with a brief description of test conditions.

There were variations of the propellant test tankage, propellant ignition time, etc., which were introduced to determine their effect on blast wave hazards, and these will be referred to as blast wave test conditions. These conditions may or may not influence the thermal hazard, and thus, may or may not constitute a thermal test condition. There were three blast wave test conditions for the 25,000-lb tests. The first is the propellant type, and is specified by indicating either the $LO_2/RP-1$ or the LO_2/LH_2 combination. A second condition, which we will refer to as the propellant configuration, separates the tests on the basis of whether they were of the so-called confinement-by-the-missile condition (CBM) or the confinement-by-the-ground-surface condition (CBGS). For the CBM condition, the propellants were permitted to mix within the propellant tankage by the abrupt creation of an opening in the diaphragm that originally separated the two propellants. For the CBGS condition, the propellants were permitted to spill from the tankage and to spread (and mix) along the ground surface. For each of the several tests conducted for each of these conditions the propellants were permitted to mix for varying lengths of time prior to their ignition, and "ignition time" constitutes a third condition. In order to describe a test, then, it is necessary to specify the propellant type, propellant configuration, and the ignition time. The blast wave test conditions for each 25,000-lb test (for which there are heat flux data) are indicated in Table 6-3 for reference in the discussion to follow.

While it is difficult to obtain clearly realistic assumptions, the results
of Table 6-1 suggest that energy transfer by particle bombardment can not eas-
ily be ignored. At the outset, the assumption that the contact of all of the
impinging particles is temporary may be unrealistic, since the explosions are
accompanied by a permanent deposition of particles, a case in which a greater
fraction of the internal energy of a particle will be conducted to the object.
It thus becomes important whether some permanent particle adherence occurs dur-
ing the heating pulse or whether the deposition is confined to a later settling
of cooled particles.

Experimental Approach

A completely general experimental approach would require measurement of all
properties and variables of the fireball which are necessary to evaluate heat
transfer to any object, and while ideal, it is prohibitive, aside from the dif-
ficulty of evaluation, in terms of the required instrumentation. Diminishing
the scope of this approach by measuring only the most essential or dominant
variables, such as the gas temperature, introduces an uncertainty in evaluating
the heat flux density, of course, since assumptions about the fireball are re-
quired; a case in point is that of the effect of heat transfer through particle
impingement mentioned above, a case which is difficult to evaluate realistically.
However, an approximate gas temperature, a most critical variable, can be meas-
ured remotely, which permits selecting the fireball region to be measured, and
thus enables a measurement of the highest apparent temperature region of the
fireball. This is important because an upper bound of the heat flux density is
sought. Indeed, remote gas temperature measurements of this kind have been
made throughout the program by the Sandia Corporation, using a photographic re-
cording pyrometer.

A less general though more direct approach is that of simply measuring the
heat flux into various immersed objects, the distinct advantage being that no
assumptions regarding the fireball are required. The most serious disadvantage
of measurements of this sort within the fireball is that the instrument is not
always in the most severe environment, the environment of primary interest.

Table 6-3

BLAST WAVE TEST CONDITIONS FOR THE 25,000-LB TESTS

TEST NUMBER	PROPELLANT TYPE	PROPELLANT CONFIGURATION	IGNITION TIME (sec)
275 278	LO$_2$/RP-1	CBM	0.51 0.53
284 285		CBGS	0.00 0.46
279	LO$_2$/LH$_2$	CBM	0.03
288 289 290		CBGS	0.36 0.17 0.11

Since the approach used to construct the bounding curves requires a num-
ber of individual flux–time curves for each test condition, it is desirable to
combine all tests whose blast wave test conditions do not differ in ways that
are of importance to heat transfer. To the extent that it is practical then,
we will con ider the effect of blast wave test conditions on the heat flux den-
sity and on the heating duration. Commencing with the effect on heat flux,
the photo-recording pyrometer measurements were first considered, and it was
found that the gas temperature in the fireball region where the temperature was
maximum does not, for practical purposes, depend on blast wave test conditions
other than propellant type. (The consistency of gas temperature for all condi-
tions for a given propellant was indicated in Fig. 6-1.) Gas temperature,
moreover, is expected to be the most critical parameter; that is, it will have
the greatest influence on the magnitude of the heat flux.

The test conditions of propellant configuration and ignition time can af-
fect the flow velocity (and pattern) and so, in turn, can affect the heat flux.
For "ordinary" gases, however, estimates of the flux contribution from convec-
tive heat transfer at the most extreme flow velocities (except during the

early fireball growth stages) are small compared to the radiant transfer. The
possible presence of particulate matter in the explosive products of the
LO_2/RP-1 tests, however, makes it mandatory that test conditions influencing
flow velocity be considered as a possible thermal test condition. Since par-
ticulate matter is present, any condition which affects either the flow veloc-
ity or particle concentration may constitute a thermal test condition. The
only practical means of attempting to establish the dependence or independence
of the heat flux on particulate concentration is through analysis of the heat
flux density data themselves. The assortment of test conditions that existed
for the 25,000-lb tests, as indicated in Table 6-3, is not readily amenable to
analysis, and we resort to the following method. We first compared the mean
value of the time average of each flux trace from Test 285 with the correspond-
ing mean of the combined test data from Tests 275 and 278, where the test con-
ditions of these two test groups differ only in propellant configuration. It
was concluded that there is no reason to believe that the two mean values are
different. That is, there is no reason to believe the flux depends on propel-
lant configuration, and the probability that this analysis has failed to reveal
a difference that really exists is about 0.01. Next, with the assumption that
this conclusion also applies to the LO_2/LH_2 propellant combination, the analy-
sis of the flux data from several tests may be used to determine the effect of
propellant type on the time average of the flux. Specifically, the mean of the
time average of each flux trace from Tests 275, 278 and 285 was compared with
the corresponding mean from Tests 286 and 289, and it is concluded that the
flux does not depend on propellant type, and the probability that this part of
the analysis has failed to reveal an existing difference is about 0.30. Since
the ignition time for Test 289 is substantially less than that of the other
four tests, as can be seen in Table 6-3, the analysis was also performed with
the data from Test 289 excluded, and the conclusion was the same. If there is
no significant effect of propellant type on heat flux, as the analysis suggests,
the presence of particulate matter evidently has no pronounced effect; the flow
velocity, then, should not have a pronounced effect; and finally, there should
be no pronounced effect of either propellant configuration (which was already
concluded from the crude data analysis above) or ignition time. Regarding

Thus, a statistical sampling of measurements must be obtained, and several di-
rect measurements of heat flux density were made per test at locations distri-
buted throughout the fireball.

Two additional types of measurements were made that pertain to heat trans-
fer within the fireball, in particular, the radiant flux density and the
thermocouple probe measurement, although there is a tendency to regard them as
secondary measurements with respect to the two measurements mentioned above, in
part because of certain experimental uncertainties associated with these meas-
urements. The associated inaccuracies do not necessarily exist; rather, it is
difficult without further, and perhaps unwarranted, effort to firmly establish
that they are negligible or to determine a suitable correction. The problems
are discussed in the instrument and error analysis sections, although, in sum-
mary, it can be said that for most circumstances, the radiant flux density
errors are not expected to be "excessive" nor are those of the thermocouple
probe, except as they approach their melting temperature.

These two measurements are also considered secondary in that they cannot
satisfactorily accomplish by themselves the primary objectives of the thermal
program; rather, they tend to support (or depreciate) the heat flux density and
pyrometric gas temperature measurements discussed above. It should be recog-
nized, however, that supporting measurements are relatively important in light
of the ease with which a substantial error can occur with any one type of
measurement.

In summary, the experimental approach intended to accomplish the more im-
portant objective of determining a bound to the heat flux density within the fire-
ball consists of a combination of the general and the direct approach, supple-
mented by supporting measurements.

SUMMARY OF THERMAL INSTRUMENTATION

This summary of instrumentation permits comprehensive reading of the presen-
tation of results without requiring reference to the detailed description given
in Appendix C of this volume.

The heat flux density is measured near the surface of various slabs located within the fireball. The dimensions of the slabs are of the order of 1.5 inches in thickness (normal to their exposed surface) and range from 1 to 3 inches laterally; over the heating duration, however, the slabs are thermally representative of semi-infinite slabs, that is, they effectively occupy half of space. The heat flux density is evaluated by measuring the temperature with time just beneath the exposed surface of the slab and applying this temperature data to the computation of the heat flux density through the following relation (or its equivalent):

$$q(t) = K' \int_0^t \frac{\frac{\partial T_s(\tau)}{\partial \tau}}{\sqrt{t - \tau}} \, d\tau \tag{6.3}$$

where q is the heat flux density; $K' = (K\rho c/\pi)^{1/2}$; K, ρ, and c are the conductivity, density, and specific heat, respectively, of the slabs; T_s is the slab surface temperature; and t is time. The slab temperature is measured by means of a thermocouple junction embedded just beneath the slab surface.

Radiant flux density is measured with a "Gardon" type radiometer. The energy-sensitive element of the radiometer consists of a circular metallic foil whose circumferential edge is joined to a heat sink. Irradiance of the foil induces a temperature differential between the center and edge of the foil that is proportional to the incident radiant flux density. The temperature differential is measured with a differential thermocouple whose output, then, is a measure of radiant flux density.

Heat flux density measurements were obtained at instrument stations H, S, and P, two each at stations H and S and five at station P, and up to four radiant flux density measurements were obtained at station H. Station H is approximately __ ft from the test pad center along gauge line A,[*] and about 52 in. above the

---

[*]   Radial gauge lines designated gauge lines A, B and C are 120-deg from each
      other.

6-9

ignition time, a crude analysis was performed with the data from Tests 288 and
289, which differ only in ignition time, and it indicated that the average
heat flux does increase with increasing ignition time, in contradiction to the
conclusion above. In searching for a way to account for the contradiction, it
was noticed that the pyrometric gas temperature for Test 288 was somewhat
higher during the time of interest than for the other LO_2/LH_2 tests, although
there are no pyrometric data available from Test 289 with which to make a dir-
ect comparison. If the abnormally high temperature for Test 288 was the cause
of the influence of ignition time on average heat flux, this tends to detract
from the first conclusion above, namely, that the gas temperature is, for prac-
tical purposes, independent of these test conditions. This conflicting result
illustrates the limitations of separating the tests into distinct test condition
categories. In the case above, for purposes of estimating upper bounds of the
heat flux, we have chosen to disregard propellant configuration and ignition
time as test conditions, although we were unable to establish a firm basis for
the choice.

In order to consider the effect of test conditions on heating duration,
the time from propellant ignition for the fireball to lift from the ground sur-
face was obtained from film coverage of the tests, this time being a measure
of the potential heating duration at the location of the instruments. These
durations are listed in Table 6-4.[*] In this case, there appears to be a de-
cidedly longer duration for LO /RP-1 tests than for LO_2/LH_2 tests, and analysis
(using all data given) supports this. The suggestion from a comparison of
Tests 284 and 285 that duration decreases with increasing ignition time is off-
set by the opposite trend suggested by a corresponding comparison of Tests 288
and 290. (It should be noted that the duration of 3.4 sec for Test 285 is
particularly uncertain.) There appears to be no reasonable means to ascertain
the effect of propellant configuration. As a practical choice, propellant
type is treated as the only test condition affecting heating duration (or heat
flux magnitude), and the flux data will be combined on this basis.

---

[*] The details of these durations are described in a later discussion.

Table 6-4

HEATING DURATIONS FROM THE 25,000-LB TESTS

PROPELLANT TYPE	TEST NUMBER	HEATING DURATION (sec)
LO$_2$/RP-1	275	4.7
	278	4.0
	282	5.2
	284	6.8
	285	3.4
	LO$_2$/RP-1 Average	4.8
LO$_2$/LH$_2$	281	3.7
	288	3.8
	290	3.5
	LO$_2$/LH$_2$ Average	3.7

Heat flux density maxima plots are presented for LO$_2$/RP-1 and LO$_2$/LH$_2$ tests in Figs. 6-3 and 6-4, respectively. Each flux density "pulse" is label- ed with the letter H, S, or P to indicate the instrument station (as designa- ted in Appendix C) from which it was obtained, and the test number is identi- fied by the type of curve as indicated in the legend. The numbers "1" through "5" adjacent to the station letter "P" on Fig. 6-4 designate the instrument position at that station. Bounding curves, or curves which are estimates of the upper bound, are also indicated in the figures.

Regarding these graphs, a high concentration of maxima near the bounding curve tends to support the firmness of the curve, and, of course, suggests that it would not be unusual to obtain values that approach the curve in a subse- quent test. A reasonably large concentration near the curve is in fact re- quired for the construction of a bounding curve to be a sensible endeavor. This requirement is clearly satisfied for the LO$_2$/RP-1 test condition. Examin- ation of Fig. 6-3 indicates, for instance, that the absence of any measurement would not require marked revision of the bounding curve, perhaps the worst case being a minor modification in the 3- to 5-sec region associated with the

ground surface The two slabs of station M are adjacent and arranged so that
the flow of gas along each is similar. Station S, consisting of two slabs, is
located 13 ft above the ground surface and as near to the center of the explo-
sion as practical. In Tests 275 through 285, it was located at a ground dis-
tance of 23 ft along gauge line A, and thereafter was 32 ft from the test pad
cen r at a point approximately intersecting gauge lines A and B. Station P,
installed after Test 285, consists of a series of five instrumented slabs
(designated as being at positions "1" through "5") distributed at 60-deg inter-
vals along the circumference of a 12-in.-diameter, vertically oriented pipe.
The station is 11 ft above the ground surface and is part of the support struc-
ture of station S.

The primary gas temperature measurement was obtained from a photographic
recording pyrometer. This measurement technique consists of matching, over a
portion of the visible spectrum, the intensity of an image of a region of the
fireball with the intensity of a similar image of one of several tungsten fila-
ments, each of which is at a known and preset temperature. Since the intensity
from the tungsten in the optical spectrum approximates that of a blackbody, the
measured fireball temperature is near the blackbody equivalent temperature. It
was the policy to measure the fireball region having the highest intensity or
temperature. The pyrometer was located about 450 ft from the test pad along
gauge line A.

The secondary gas temperature measurement was obtained with a thermocouple
probe, which consists of a metallically sheathed thermocouple junction, with the
thermocouple leads insulated from the sheath except at the junction. One or
more thermocouple probes per test were mounted on the Sandia instrument station,
located 13 ft above the ground surface about 30 ft from the test pad center at
a point approximately intersecting gauge lines A and C.

Radiant flux density was also measured at locations external to the fire-
ball by means of the Gardon-type radiometer described above. Generally, three
radiometers were used per test, two at the same distance (335 ft) from ground
zero along radial gauge lines (A and B) 120 deg from each other, with the third
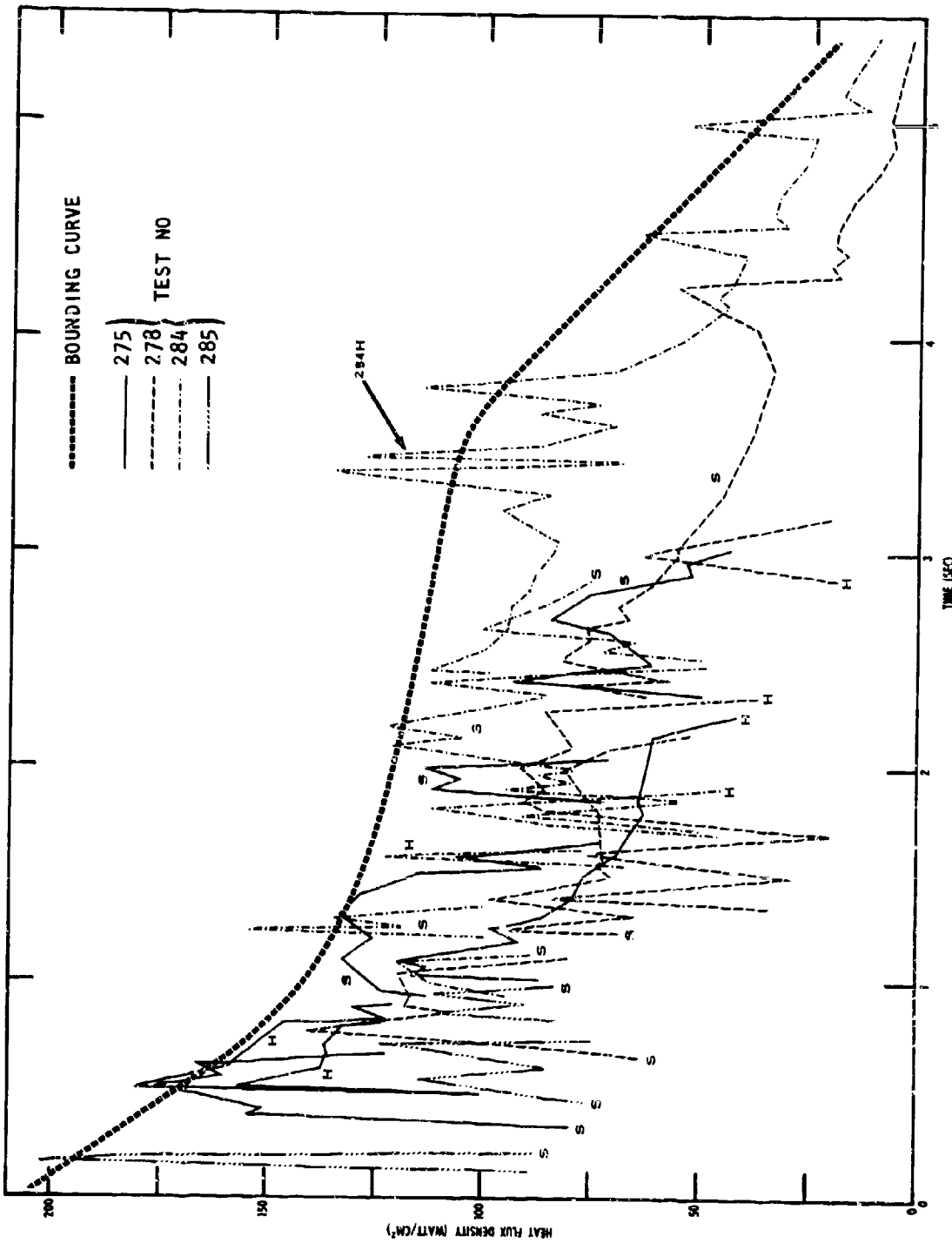
Fig. 6-3. Heat Flux Density Pulses from the 25,000-lb LO_2/RP-1 Test

more remotely located (600 ft) along gauge line A. These distances are such
that with the existing field-of-view of the instruments, radiant energy orig-
inating in any region of the fireball prior to its rise is not restricted from
falling incident on the sensitive foil of the instrument.

PRESENTATION OF RESULTS

General Organization

Results of the primary measurements of slab heat flux density and pyro-
metric gas temperature are presented first. This commences with a graphical
summary of the pyrometric temperature that shows the range and mean value of
the measurements for each propellant type (LO_2/RP-1 and LO_2/LH_2) for the
25,000-lb tests. (No Titan I data are currently available.) In addition, a
graph is presented which indicates the spatial variation of temperature over
the fireball from a single test.

The results of the heat flux density measurements are presented next, in-
cluding curves which represent the upper bound of this parameter (bounding
curves) and curves which represent values of this parameter that are suitable
to anticipated applications (recommended curves). Indications of the basis and
limitations of both the bounding and recommended curves are also given. The
correspondence between the heat flux density measurements and the pyrometric
gas temperature measurements is given next by comparing the radiant flux den-
sity computed from the gas temperature measurements with the heat flux density
measurements.

The secondary measurements from the 25,000-lb tests are then considered,
commencing with illustrations of the degree that the radiant flux-density
measurements within the fireball support the primary measurements (the corre-
sponding measurements for the Titan I test were unsuccessful). This is followed
by similar illustrations of support from the temperature measurements obtained
from the thermocouple probes (no equivalent Titan I data are currently avail-
able).
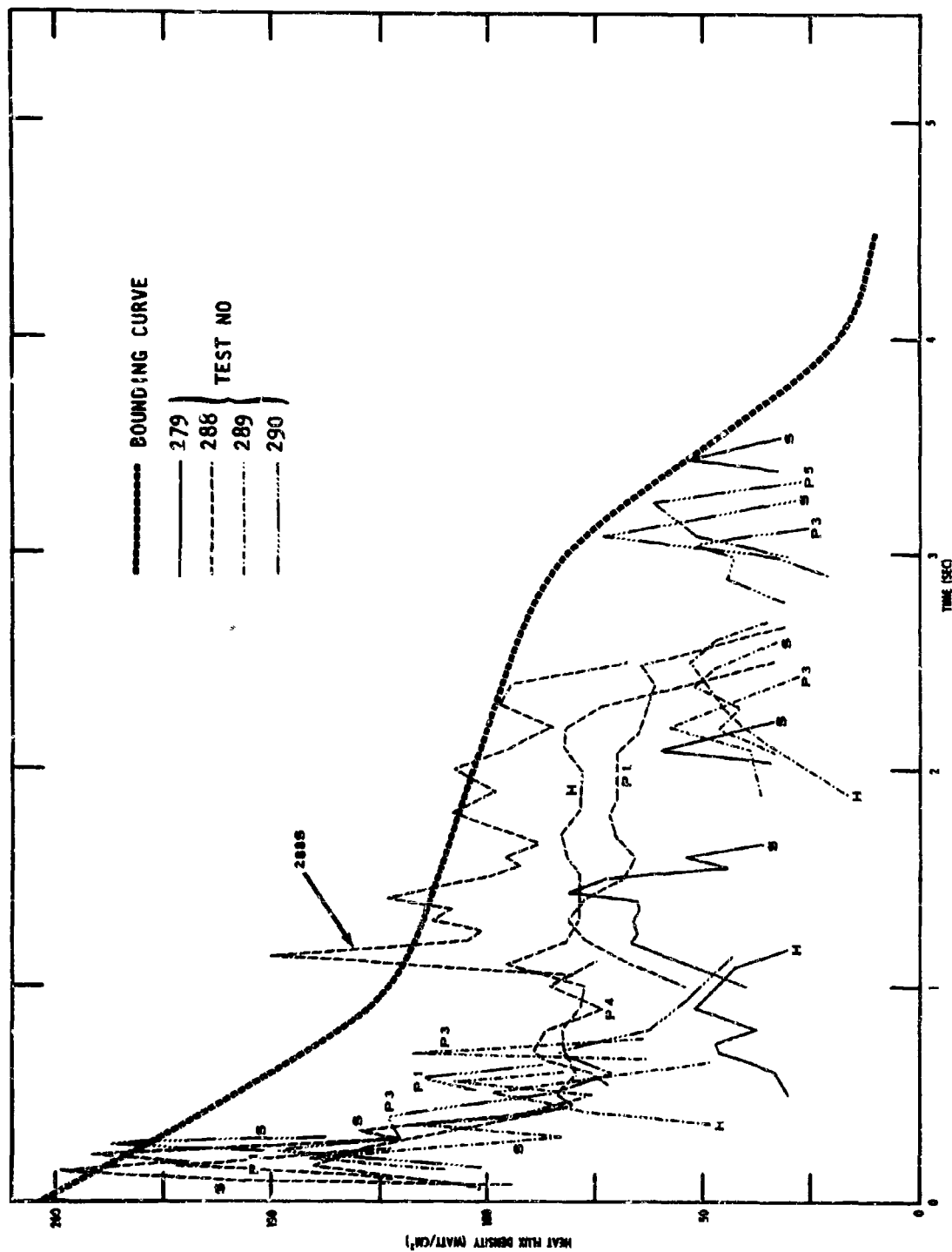
Fig. 6-4. Heat Flux Density Pulses from the 25,000-lb LO_2/LH_2 Tests

elimination of the pulse labeled "284H." For the LO_2/LH_2 plots, the distribution of maxima does not as firmly support the position of the curve. It can be seen on Fig. 6-4 that the elimination of the particular pulse labeled "288S," for example, would result in a substantial modification of the curve and would reduce the associated accumulative flux by approximately 10 percent. With the statistical sampling at this limited level, it is not clear if this particular measurement is unusual or reasonably typical, and the position of the bounding curve is evidently somewhat less certain than the previous LO_2/RP-1 case. It would be expected that the addition of further measurements would more substantially alter the LO_2/LH_2 curve than that of the LO_2/RP-1. The LO_2/LH_2 curve is included, however, since it represents the best (and evidently a reasonable) approximation to the bound for this test condition that can be made with the available data.

As noted above, the flux density associated with the bounding curves is indicative of the energy that an immersed object <u>can</u> receive and is, for most applications, a reasonably conservative condition to impose, both in terms of the magnitudes and, particularly, in terms of the length of time that such magnitudes would be sustained. No object tested, for instance, received a cumulative flux density in excess of 60 percent of that associated with the bounding curve. Since the bounding curve is evidently somewhat conservative, it is desirable both to investigate the degree of conservatism, and to provide a curve which is more suitable to anticipated applications. Both of these require statistical investigations and several associated points should be emphasized. The first is, simply, that the quantity of data is sufficiently limited that the analysis will provide only a reasonable approximation to the numerical results. Secondly, as noted above, an assumption has been made with regard to what constitutes a test condition, so that some of the data scatter is probably attributable to unrecognized test conditions. Finally, it is not clear how extensive would be the variation of heat transfer with test condition outside the range that has been tested; for instance, failures leading to more thoroughly mixed propellants at ignition may, in turn, lead to somewhat higher temperatures and heat transfer rates. Thus, the restricted range of test conditions over which these data were obtained should be considered in any application.

The conservatism of the bounding curve is illustrated in Table 6-5, which lists the ratio of the energy accumulated in 5.4 sec at each instrument station to that of the bounding curve for the same time, the latter being 590 and 420 watt-sec/cm^2 for the $LO_2/RP-1$ and LO_2/LH_2 curves, respectively. Also included in the table are the magnitudes of the cumulative flux density for 5.4 sec. The measured cumulative flux density can be seen to range from 9 to 60 percent of that associated with the bounding curve. If one assumes that the measured values conform to a Gaussian distribution, the probability of obtaining, for instance, 75 percent of the cumulative bounding flux is 0.02 and 0.002 for $LO_2/RP-1$ and LO_2/LH_2, respectively, and the corresponding figures for 65 percent are 0.07 and 0.02.

In obtaining a curve which is more suitable to application (than the bounding curve), a difficulty arises in that a recommended curve depends on the particular application (e.g., on the degree of conservatism the application calls for, on the materials and geometry that the structure whose response to the environment is desired, and so on). It is not possible then to provide a curve that is applicable to all situations, and one is given which is suitable to many anticipated applications. The criteria upon which this curve, hereafter referred to as the recommended curve, is based are discussed below.

The first criterion is that the cumulative flux density associated with the recommended curve, that is, the area under the recommended flux density-time plot, is such that the probability of exceeding this cumulative flux density is 0.01. With this criterion, analysis of the cumulative flux distributions in Table 6-5 (again assuming a Gaussian distribution) indicates that the cumulative flux densities of the recommended curve are approximately 450 and 300 watt-sec/cm^2 for $LO_2/RP-1$ and LO_2/LH_2, respectively.

Several difficulties arise when consideration is subsequently given to time distributions of flux density which are appropriate and consistent with these cumulative flux values. It is typical for the measured flux density surges to approach and temporarily remain near the bounding curve and for the heating activity during the time periods separating these surges to be comparatively moderate or negligible. (This is perhaps most easily observed by

Table 6-5

CUMULATIVE FLUX DENSITY FOR 25,000-LB TESTS

| PROPELLANT TYPE | TEST NO. | INSTRUMENT STATION | | | | | |
| | | H | | S | | P | |
		CUMULATIVE FLUX (watt-sec/cm^2)	FRACTION OF BOUNDING CURVE	CUMULATIVE FLUX (watt-sec/cm^2)	FRACTION OF BOUNDING CURVE	CUMULATIVE FLUX (watt-sec/cm^2)	FRACTION OF BOUNDING CURVE
LO$_2$/RP-1	275	249	0.44	334	0.60	-	-
	278	165	0.29	280	0.50	-	-
	284	304	0.54	265*	0.47*	-	-
	285	49	0.09	140	0.25	-	-
LO$_2$/LH$_2$	279	89	0.20	163	0.37	-	-
	288	234	0.53	259	0.58	242	0.54
	289	135	0.30	145	0.33	116	0.26
	290	98*	0.22*	139	0.31	177	0.40

---

* The cumulative flux values for Station S, Test 284 and for Station H, Test 290 are to a time of 2.8 and 2.6 sec, respectively, and these two values were not used in the analyses.

scanning the individual flux-data curves in Figs. 2-1 through 2-28 given in
Section 2, Vol. 2.) This suggests that the recommended curves should be super-
imposed on the corresponding bounding curves and that the reduced cumulative
flux values of 450 and 300 watt-sec/cm^2 be obtained by imposing flux voids (or
more moderate flux values) over one or more time periods, and the remaining
question, in that case, would be in regard to a suitable selection of voids
and their distribution. No evident pattern in this distribution is suggested
by examination of the individual flux—time measurements. However, it is not
uncommon for the flux to remain uninterruptedly near the bounding curve for
large fractions of the heating duration. This is illustrated by the example
data presented in Figs. 6-5 and 6-6. The flux shown in Fig. 6-5 from Test 288,
for instance, remains near the bounding curve from about 1 to 2.5 sec, and
similarly for Test 284 on Fig. 6-6 from about 2.5 to 5.5 sec. It is important
to recognize that most of the energy transfer for these examples is associated
with a single pulse, that the flux during these pulses is near the bounding
curve, and that this is evidently not a rare event. This coupled with the
factors previously mentioned suggests that the recommended curves should be as
follows: That they should uninterruptedly superimpose the bounding curves and
that their cumulative flux density should be reduced from that of the bounding
curves to approximately 450 and 300 watt-sec/cm^2 for LO$_2$/RP-1 and LO$_2$/LH$_2$, re-
spectively. Recommended curves as such are presented in Figs. 6-7 and 6-8,
where the deletion of the cumulative flux density from that of the bounding
curve is conservatively located at the late end of the heating period.

For some applications, the recommended curves may be slightly conserva-
tive, and the stringency may be reduced, for instance, by modifying from 0.01
the probability of exceeding the cumulative flux-density. Other possible means
may be justified and suitable under given circumstances, as described in the
following example. For purposes of illustration, the measured flux density
for Test 275 is given in Fig. 6-9, and it can be seen that the flux is near
the bounding curve from about 0.5 to 3 sec, although there is periodic but
short-lived relief in the flux level during this time (at about 0.8, 1.75, and
2.1 sec). Intermittent relief such as this can significantly affect the re-
sponse of some structures, and such flux density—time patterns are not uncommon.
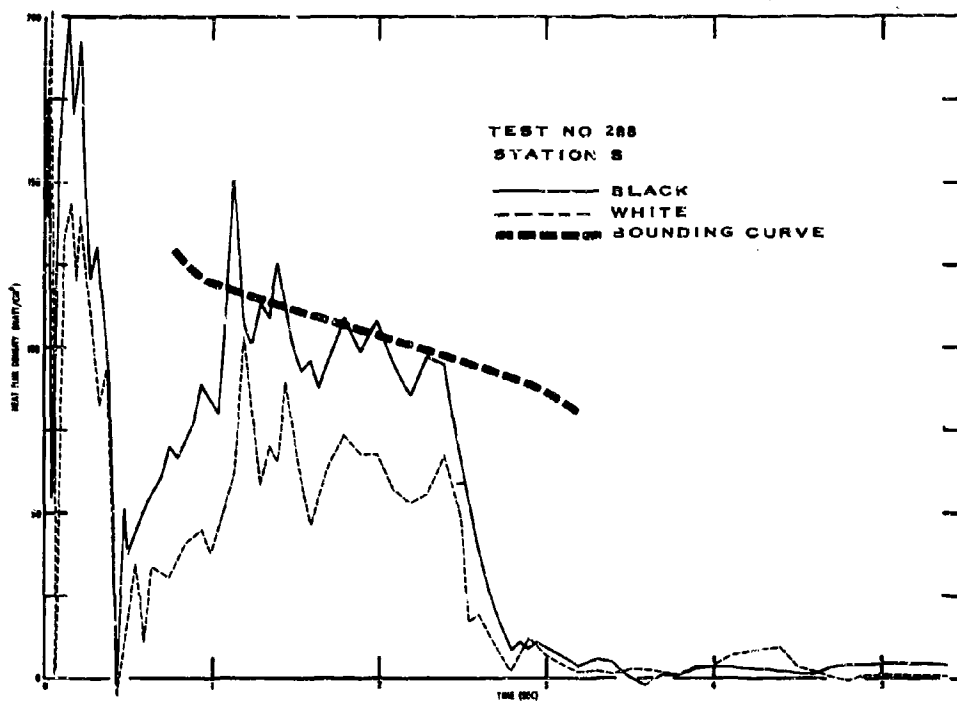
Fig. 6-5.   Heat Flux Density at Station S from Test 288
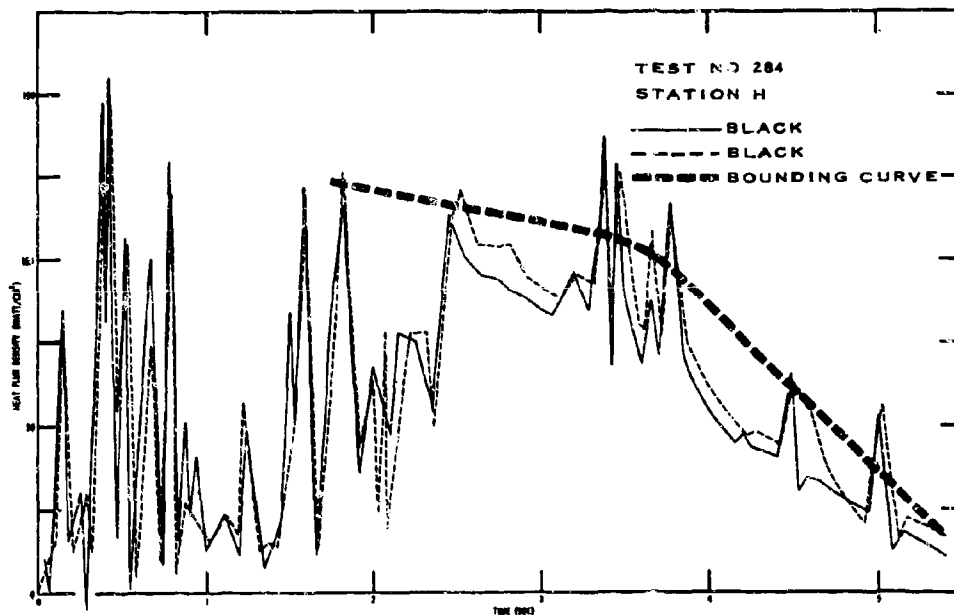
Fig. 6-6.   Heat Flux Density at Station H from Test 284
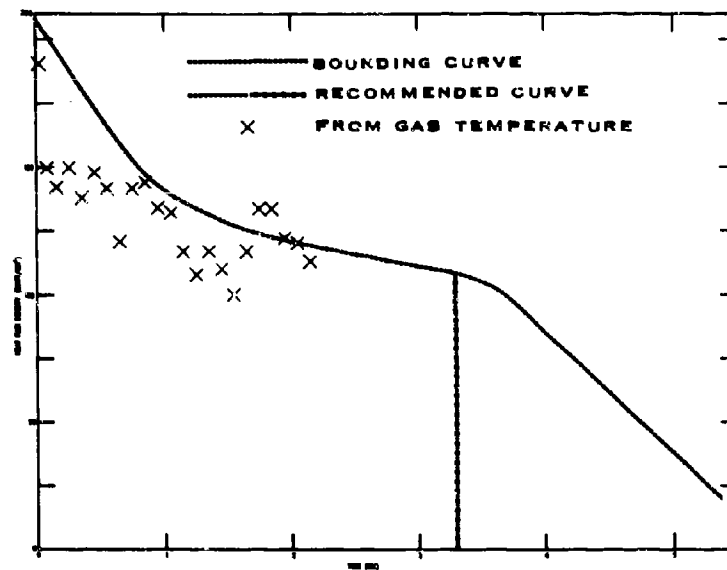
Fig. 6-7.   Bounding and Recommended Heat Flux Density Curves for
            25,000-lb LO_2/RP-1 Tests
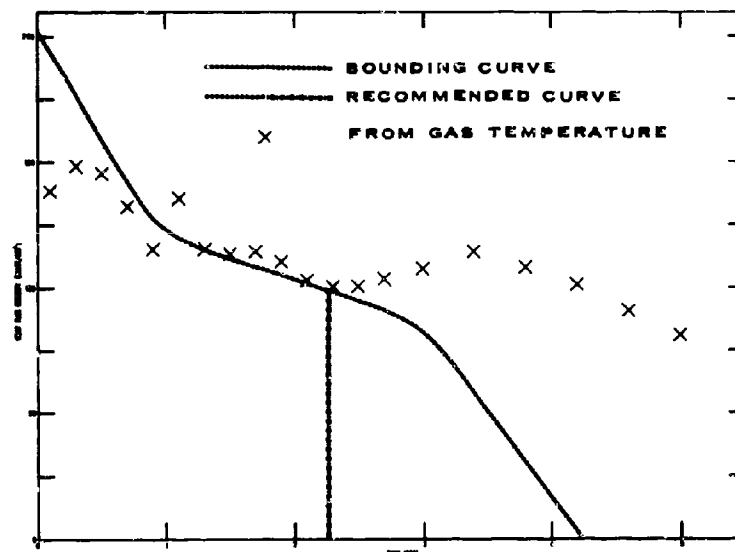
Fig. 6-8.   Bounding and Recommended Heat Flux Density Curves for
            25,000-lb LO_2/LH_2 Tests

This relief, for instance, can afford an opportunity for energy to be conducted
through the structure from high- to low-temperature regions, thus reducing the
maximum temperature that the high-temperature regions of concern will sustain
compared with that for an uninterrupted heat pulse having the same energy. If,
in applying the recommended curve, the structural response is found to reach,
but not greatly exceed, damaging proportions, one may be justified in introduc-
ing an appropriate region of reduced flux. Justification of such a modifica-
tion would, of course, require statistical analysis of the durations, magni-
tudes and time distributions of the energy pulses, and such an analysis is not
given here.
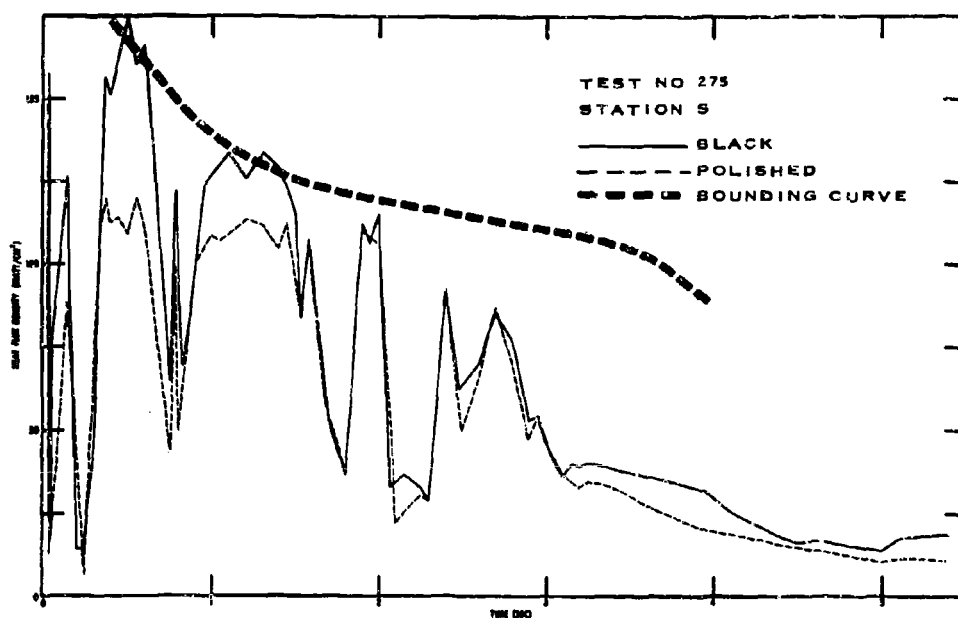
Fig. 6-9. Heat Flux Density at Station S from Test 275

Information computed from the pyrometric gas temperature measurements are
included on Figs. 6-7 and 6-8 in order that the rather important comparison

can be made between these measurements and the bounding curve. It has been
previously mentioned that the gas temperature measurements are of the fireball
region having the highest apparent temperature. It has also been implied above
that the bounding flux curve approaches the flux that would be sustained in the
region(s) of highest temperature. Thus, there should be a correspondence be-
tween (not necessarily an equality of) the bounding flux curve and the flux
implied by the gas temperature measurement. To this end, the radiant flux den-
sity values were computed from the gas temperature (on the assumption of a con-
servative emissivity of unity) and the results plotted (X's) on Figs. 6-7 and
6-8. The correspondence is remarkable. Consider first the LO_2/LH_2 case in
Fig. 6-8. During the early fireball stages, when the gas flow velocities can
be sufficient for significant convective transfer to occur, it is reasonable
to expect that the total heat flux measurements will exceed the remote measure-
ment implications, since the latter account for radiative transfer alone, and
Fig. 6-8 is compatible with this notion. As the more extreme velocities
subside, it is reasonable to expect that the two curves will converge, with the
radiative mode of energy transfer predominating; and the curves are also con-
sistent with this supposition, at least to approximately 2.5 sec, where the
two values commence to diverge, the "pyrometric" flux thereafter exceeding the
directly measured values. This divergence is accounted for through film cov-
erage of these tests. In particular, it is at this time that the fireball
lifts from the ground surface or from the direct heat flux instruments. For
the $LO_2/RP-1$ data given in Fig. 6-7, the pyrometric gas temperature measure-
ments are restricted to about 2 sec so that a comparison is only possible dur-
ing this time.[*] It can be seen that the results are consistent with expecta-
tions in the same manner as described for the LO_2/LH_2 case.

The results of this comparison are rather significant in that two totally
independent means of evaluating heat transfer indicate similar magnitudes in
the region where a similarity should exist. Moreover, in other regions, the
comparative magnitudes of the two measurements are qualitatively correct.

---

[*] This apparent difference in duration was discussed above in the section "Gas
Temperature from the Photo-Recording Pyrometer."

A common feature of the heat flux data that is not indicated either in the
data figures presented in this section or in those presented in Section 2 of
Vol. 2 is the presence of a comparatively high-magnitude but very short-lived
pulse at the beginning of the heating period. When this pulse occurs, it com-
mences with a magnitude in the vicinity of 400 watts/cm^2 and decays to below
200 watts/cm^2 within, for the 25,000-lb tests, about 20 msec. It can be re-
called that pulses of the same magnitude and duration were inferred from the
pyrometric gas temperature measurements. The pulse was present in the heat
flux measurements for Tests 278, 285, and 288; for the pyrometric measurements,
it was present for Tests 275, 278, 282, 284, 285, and 288. A more detailed
comparison will not be made for the following reason. In computing the heat
flux from the slab temperature data, two comparatively large errors occur in
the first few computational time intervals (that is, over the first 10 or 20
msec), and these errors become increasingly large as the time approaches the
first (or earliest) computational interval. One of the errors is systematic
and correctable, but a substantial effort is required. Since the pulse is of
such small duration, the effort appeared to be clearly unjustified. It should
be noted that the pulse was also present in the heat flux data from the Titan
I Test, although its duration was approximately 50 msec.

One further characteristic of the heat flux density data should be men-
tioned. The flux density data from instrument stations S and H given in Sec-
tion 2 of Volume 2 are presented in pairs, one pair for each station, corres-
ponding to the adjacent slab pairs of those stations. Usually the exposed
surface of one of each pair was coated with a black deposit, and the companion
slab was either coated with a "white" deposit or the surface was polished.
The comparative data trends for these companion slabs with dissimilar radia-
tion absorption properties (as given approximately in Appendix C) are as fol-
lows. For the LO$_2$/LH$_2$ data, the ratios of the energy of the black slab to that
of the white range from just over 1 to about 1.5, with the ratio for a given
slab pair remaining approximately the same throughout the heating duration.
For the LO$_2$/RP-1 tests, the data trends are somewhat different, with two pat-
terns appearing. For some cases, the energy into each slab is essentially the
same, while for others, the energy into the black slab is initially substantially

larger than that into the white, but they become equal by about 1.5 sec. (See,
for example, the data at Station S for Test 275 on Fig. 6-9 above and Test 284
on Fig. 2-6 of Section 2, Vol. 2.)   This combination of data trends for both
propellant types _suggests_ that modification of the radiation-absorbing proper-
ties of the slabs for LO_2/RP-1 tests through deposition of particulate carbon
— always found in posttest examination and at thicknesses ranging to about
0.03 or 0.04 in. — occurs during the heating duration, and the deposition is,
in some instances, immediate. It appears advisable, therefore, to use radia-
tion absorptance values near unity for structural surfaces immersed in LO_2/RP-1
fireballs regardless of their initial value.

One of the primary reasons for the installation of instrument Station P
(heat flux density measurements at locations distributed around the circumfer-
ence of a vertically oriented cylinder) was to reveal any consistent, signifi-
cant differences in the heat transfer at different locations on the surface of
an immersed object, with particular reference to the orientation and location
of the instrument with respect to the gas flow direction of the initially ex-
panding fireball. Data were obtained at this station from three 25,000-lb
tests, and no marked trends with respect to instrument location were obtained.
(Individual heat flux density records from these tests for this station are
given in Figs. 2-15 through 2-17, 2-20 through 2-22, and 2-26 through 2-28 of
Section 2, Vol. 2, for Tests 288, 289, and 290, respectively.)

Radiant Flux Density within the Fireball

Radiometer data within the fireball are presented in Figs. 6-10 through
6-12 for the 25,000-lb tests. (No equivalent Titan data were obtained.) These
data are presented primarily to indicate the degree that they support the to-
tal heat flux density and gas temperature measurements above; and since the
radiometers were always mounted near a slab heat-flux meter, as described in
Appendix C, the radiant flux data are plotted with the heat flux curve that is
evaluated from the adjacent black-coated slab.

The variation among the radiometer data is somewhat larger than is desir-
able, although some of the scatter can be attributed to the difference in time
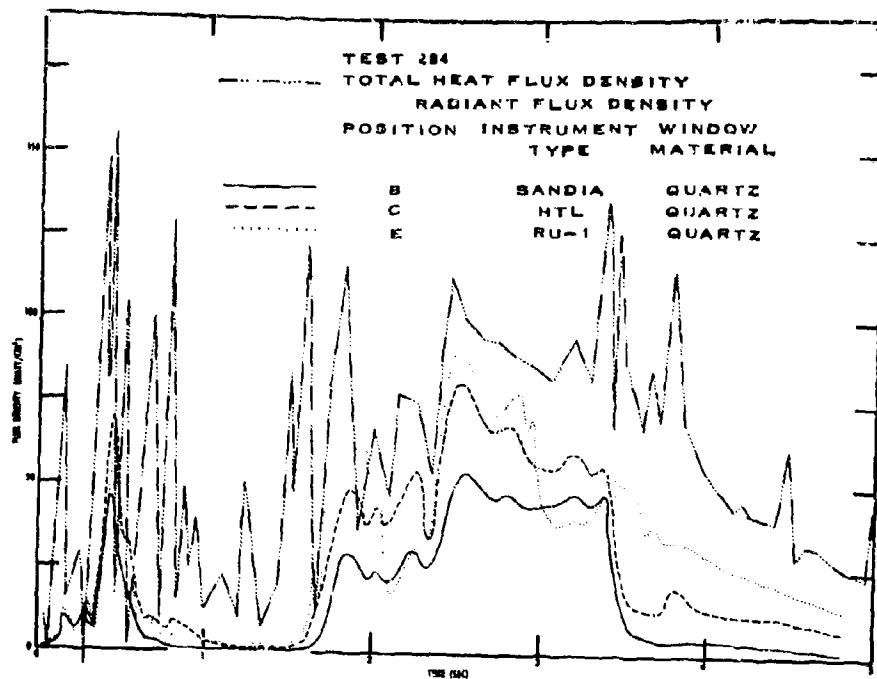
Fig. 6-10. Total and Radiant Flux Density for Test 284
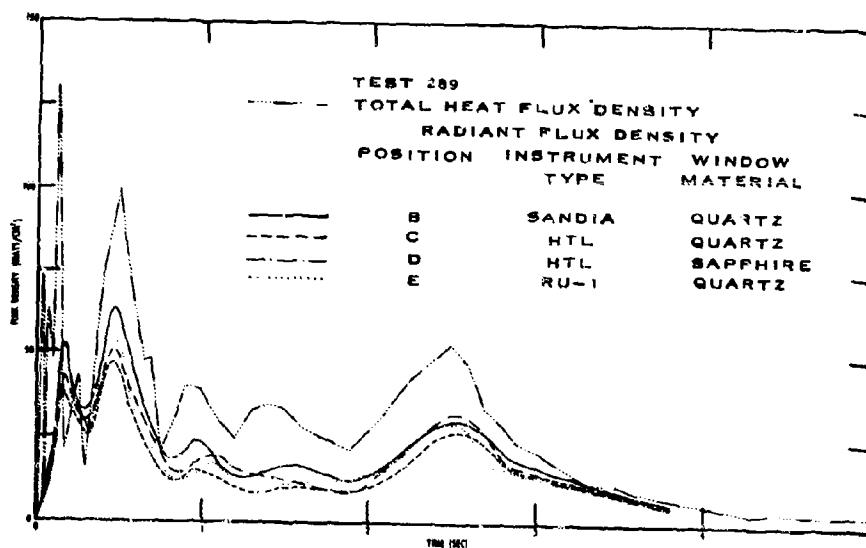
Fig. 6-11. Total and Radiant Flux Density for Test 289

response of the various instruments. For instance, during the sharp pulses that occur within the first second for Tests 284 and 289, the more rapidly responding radiometers at Positions B and E more nearly follow the total flux. Large differences among the radiometer data were also obtained for Test 284, for instance, from about 1.5 to 4.5 sec, but this difference is not attributable to instrument response. Test 284 was a $LO_2/RP-1$ test (the only 25,000-lb $LO_2/RP-1$ test for which radiometer data within the fireball were obtained), which requires purging of the radiometer windows to prevent deposition of the products of the explosion. Posttest examination indicated a clean window at Position E and partially coated windows at Positions B and C, and this appears to account for the differences. The flux for Position B is significantly low throughout this time and, along with the flux from C, does not respond between 3.5 and 4 sec to the energy transfer that is indicated both by the radiometer at Position E and by the total flux measurement.
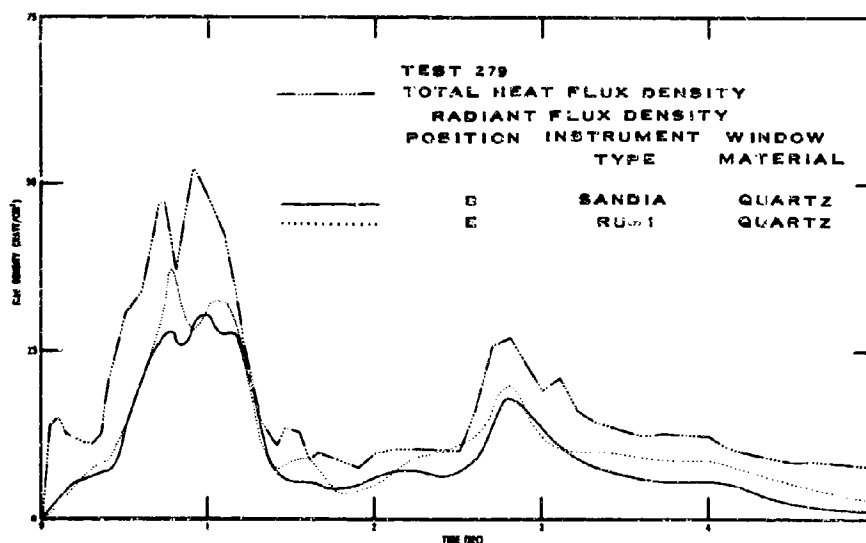
Fig. 6-12. Total and Radiant Flux Density for Test 279

In comparing the radiant with the total flux density, several factors should be considered. First, a correction factor has been applied to the radiometer data to account for energy losses by absorption within and reflection at the surfaces of the windows, and, as indicated in Appendix C, the correction is based on a fireball at about 2200°K. Thus, only during times when there are indications of comparatively high-level energy transfer corresponding to such gas temperatures is the estimated correction applicable. For lower temperatures, the radiant flux density measurement will tend to be lower than the actual flux density. In addition, due to the comparatively slow response of the radiometers, the radiometer data are not expected to closely follow the total flux for "sharp" energy pulses, such as those during the early times of the three tests given in Figs. 6-10 through 6-12. Circumstances in which a reasonable comparison can be made are found between 2.5 and 4 sec for Test 284. In light of a relatively small convective component that should exist, the radiometer data, to the extent that their accuracy permits, clearly support or lend confidence to the total flux measurements.

Temperature of Thermocouple Probes

Measurements of gas temperature as indicated by thermocouple probes at one or two locations within the fireball were obtained by the Sandia Corporation throughout the program. The two measurements from Test 288 are given in Fig. 6-13, and example dat' from a few other tests are given in Section 2 of Volume 2.

The data of Fig. 6-13 may be compared with the gas temperatures for Test 288 from the remote photo-record pyrometer given in Fig. 6-8. The "peak" values of the thermocouple temperatures are somewhat higher than the pyrometric temperatures. However, an error is not implied by this difference in temperatures; since the pyrometer measures a blackbody equivalent temperature and the thermocouple probe, with some reservation regarding its accuracy, measures the true gas temperature, the pyrometric temperature will depending on the fireball emissivity, tend to be lower than, but at most equal to, the thermocouple temperature. Due to the uncertainty in the fireball emissivity, exacting comparison between the measurements is not possible.
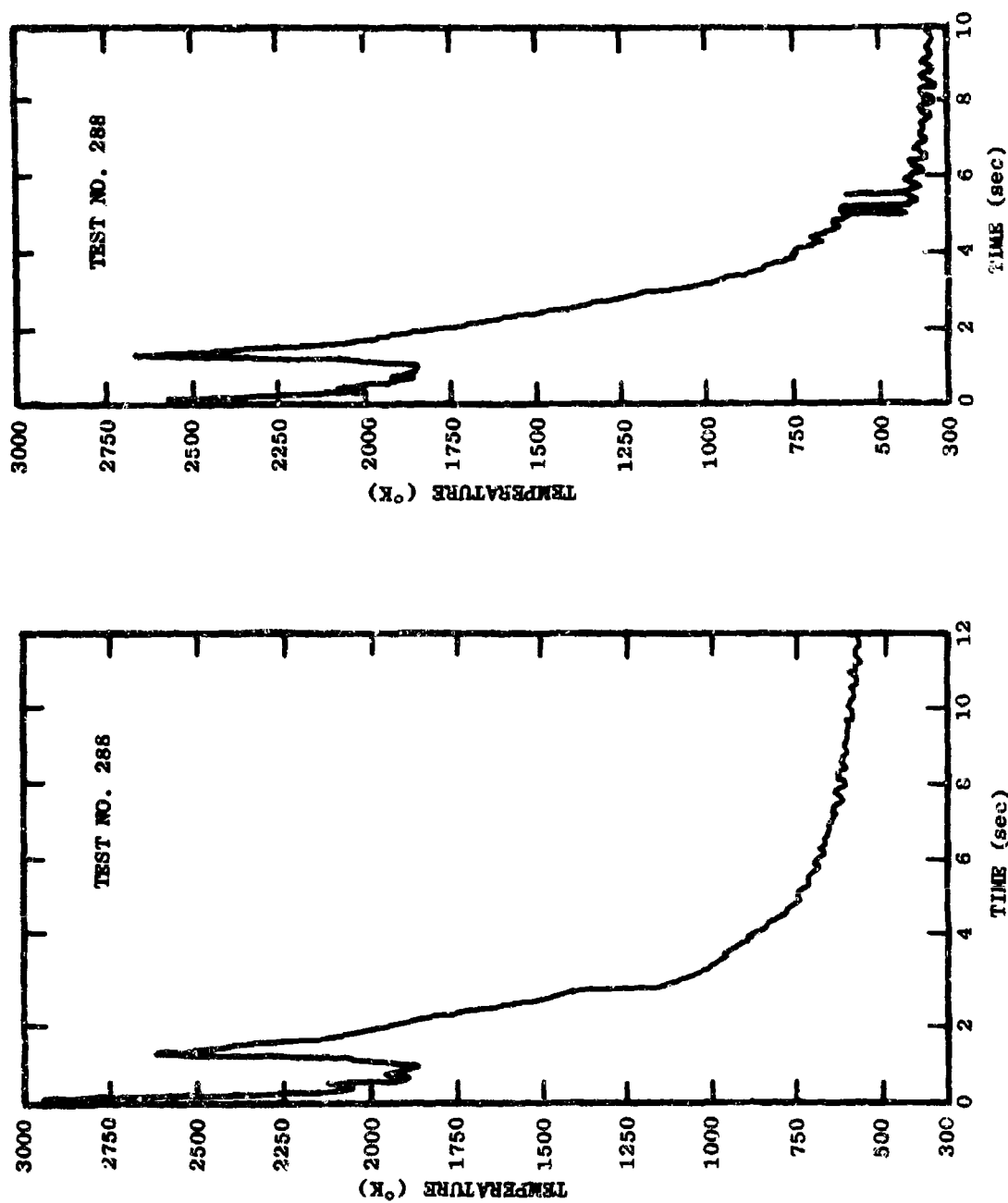
Fig. 6-13. Thermocouple Probe Temperatures from Test 288

A crude comparison can also be made between the thermocouple data and the heat flux density data. For example, the thermocouple temperature in Fig. 6-13 can be compared to the heat flux density for the same test (Test 288) in Fig. 6-5 (pg. 6-29). A similarity can be seen first with regard to the presence of first and second "peaks" at similar times. However, the radiant flux densities computed from the thermocouple temperature values (for an emissivity of 1) for both data traces are 380 and 250 watts/cm^2 for the first peaks and 250 and 280 watts/cm^2 for the second peaks, and this is substantially higher than the measured heat flux density at corresponding times in Fig. 6-5, which are in the vicinity of 200 and 150 watts/cm^2 for the first and second peak, respectively. In this case, the direct heat flux density measurements should be equal to or higher than the flux computed from the pyrometric temperatures for any possible emissivity; thus the thermocouple probe measurements do not support the direct heat flux measurements.

Heat Flux at "Large" Propellant Weight Levels

Heat flux data from explosions of propellant quantities in excess of 25,000-lb are available from only a single test — the Titan I Test involving approximately 100,000-lb of the LO_2/RP-1 propellant combination — and reliable scaling relationships from which the bounding and recommended curves may be extended from the 25,000-lb level cannot therefore be obtained on the basis of heat flux data. Scaling relationships are described in the following paragraphs for curves that are instead based on fireball temperature data obtained from the photo-recording pyrometer measurements and on heating duration data obtained from film coverage. This is followed by a comparison between the bounding curve scaled to the 100,000-lb level and the heat flux data from the Titan I Test.

Scaling of Bounding and Recommended Curves

Fireball temperature measurements from the photo-recording pyrometer are available from more than 200 propellant tests, which range in propellant weight from 200 to 25,000 lb. (Only a summary of the 25,000-lb data is presented in this report.) It is found that the fireball temperature, for practical

purposes, is invariant with propellant weight over this weight range. The
weights of interest extend well above this range, however, and in the ab-
sence of experimental data on weights of interest or of suitable analytical
relationships between temperature and weight, it is assumed that temperature
remains invariant with weight. The uncertainty of this assumption in regard
to weights of the order of a million pounds is clearly greater than is desir-
able. The assumption is, however, not entirely without support; the rough in-
dications of temperature derived from the fireball "color" on the film cover-
age of comparatively large explosions suggests that the assumption is not
grossly unrealistic.

In considering the effect of a temperature invariance on heat flux, it was
seen in Figs. 6-7 and 6-8 that the bounding curve and radiant flux computed
from the pyrometric gas temperature measurements were similar except at early
times. An emissivity of 1 was used in this computation, which should be a
close approximation at least for the fireballs from $LO_2/RP-1$ explosions. The
transfer of energy was therefore almost entirely through radiant transfer; and
since the radiant transfer depends on the fireball temperature, the magnitude
of the heat flux density should also be invariant with propellant weight.

The scaling relationships for the heating duration are based primarily on
film coverage of tests that range to 100,000 lb of propellant. The heating
duration as observed in the films is defined as the time from ignition for the
fireball to rise from the ground surface, and this duration is nearly identi-
cal with the potential heating duration of the heat flux instruments. The
heating duration of a structure, of course, may easily be smaller because of
its ejection from the fireball. While it may also be larger, it is difficult
to hypothesize a set of circumstances which would cause a structure to follow
the motion of the fireball. A heating duration given as the time to fireball
"lift-off" is chosen because it is the longest that a structure is likely to
experience.

It is found experimentally that for explosions of 200-lb quantities of
propellant, the fireball temperature subsides before appreciable rising motion

occurs, and the heating duration is thus synonymous with the fireball duration.
For quantities of 25,000 lb and more, the fireball will rise substantially,
and it appears that the ratio of the heating duration to the fireball duration
may be some decreasing function of propellant weight. Since the bounding and
recommended curves are based on 25,000-lb heat flux measurements and since
most applications are for propellant quantities in excess of 25,000 lb, it is
of particular interest to determine the dependence of heating duration on pro-
pellant weight for these larger quantities. Heating durations obtained from
all the large-scale-test film available are given in Table 6-6, along with the
fireball durations and the ratios of these two durations. In addition, estim-
ates of heating durations from the heat flux measurements are included for
data traces for the cases in which the duration can be readily identified.
These latter durations, which are included to indicate the extent to which they
support the film data, should be somewhat less than or equal to the heating
durations derived from the film.

There are t o uncertainties associated with the magnitudes of the heating
duration that have been obtained from the film. First, events such as the
fireball lift-off are not always distinct and are subject to interpretation.
For tests where it is appropriate, therefore, qualifying remarks will be made.
For instance, for several tests, and particularly for Tests 277, 281, and 284,
a substantial region of burning remained near the ground after the original
fireball lifted from ground surface. Lift-off time for these cases, however,
was taken to be the time that the original fireball lifted from the ground sur-
face because the remaining region of burning was much less extensive than the
original fireball, e.g., this region did not include the instruments. The
fireball for Test 285 was particularly lacking in definition, and the lift-off
time is especially uncertain. Regarding the second uncertainty, while accu-
rate timing marks were superimposed on the test film, for very few cases were
useful indications provided on films that were otherwise useful for evaluating
the lift-off time. It was consequently necessary to evaluate most of the times
on the basis of frame rate settings of the cameras, and this results in a larger
error than is desirable. It was observed that the scatter tended to increase
as the frame rate increased. Consequently the data were obtained from the

films with the slowest rates (usually 64 frames per second). Nevertheless, the standard deviation associated with the lift-off times (and total fireball durations), which are listed in Table 6-6, are probably of the order of 20 percent.

Consideration of the heating durations in Table 6-6 suggests that the heating duration does not increase as rapidly with weight as does the fireball duration, i.e., does not scale to the one-third power. With the one-third power law, the average heating duration of 4.9 seconds for $LO_2/RP-1$ at 25,000-lb would result in a heating duration of 7.8 seconds at 100,000-lb, while a value of 6.7 seconds was obtained for the Titan I Test. Similarly for LO_2/LH_2, a heating duration of 4.5 seconds was obtained for the Saturn IV Test, while a value of 5.7 seconds would be expected at 92,000-lb ror an average of 3.7 seconds at 25,000-lb.

Consider next the ratios of the heating durations to the fireball durations given in Table 6-6. The errors that are contained in the durations which are due to the uncertainties in film speed mentioned above are not contained in these ratios. Once again, the evidence indicates that the heating duration has a somewhat weaker dependence on propellant weight than the fireball duration. For instance, the average ratio from the 25,000-lb $LO_2/RP-1$ tests is 0.85, while the ratio lies between 0.82 and 0.56 for the Titan I Test. Similarly for LO_2/LH_2, the average ratio for the 25,000-lb tests is 0.39, while for the Saturn IV Test, the ratio is 0.28. Since it was established in Ref. 6-2 that the fireball duration increases with the cube root of propellant weight, ratios which decrease with weight suggest a weaker dependence of heating duration on weight.

The conservative assumption that the heating duration increases with the cube root of the propellant weight for weights in excess of 25,000-lb is recommended even though the film data suggest a somewhat weaker dependence. The data are clearly too few and uncertain to recommend the reduction of durations from this rule at comparatively large propellant weights.

Table 6-6

MEASURED HEATING DURATIONS

PROPELLANT TYPE	TEST NO.	FROM FILM COVERAGE			FLUX DENSITY HEATING DURATIONS (sec) FOR STATION		
		HEATING DURATION (sec)	FIREBALL DURATION (sec)	RATIO OF HEATING DURATION TO FIREBALL DURATION	H	S	P
LO₂/RP-1	275	4.7	5.7	0.82	4	4.5	–
	278	4.0	4.5	0.89	–	4.5	–
	282	5.2	6.1	0.85	–	–	–
	284	6.8	7.6	0.90	5.5	–	–
	285	3.4	4.8	0.71	–	–	–
	25,000-lb Average	4.8	5.7	0.83	–	–	–
	Titan I	6.7	8.2(12)*	0.82(0.56)*	–	–	–
LO₂/LH₂	281	3.7	9.5	0.39	–	–	–
	288	3.8	11.7	0.33	3	3	3
	290	3.5	6.7	0.52	–	3.5	3.5
	25,000-lb Average	3.7	9.3	0.41	–	–	–
	Saturn IV**	4.5	16	0.28	–	–	–

---

* There is some difficulty obtaining a distinct fireball duration for the Titan I Test. It may be as short as 8.2 sec, but probably extends to about 12 sec.

** About 92,000 lb of LO₂/LH₂ were involved in the Saturn IV Test.

In summary, it has been assumed that the heat flux magnitudes will remain invariant with propellant weight, while the heating duration will increase with the cube root of propellant weight. In order to obtain a bounding or recommended curve at a scale in excess of 25,000 lb, that the curves given in Figs. 6-7 or 6-8 be used, with the times in these figures multiplied by $(W/25,000)^{1/3}$, where W is the propellant weight of interest in pounds.

In the section that follows, the heat flux data from the Titan I test are compared to the bounding curve scaled to the 100,000-lb level, applying the above scaling rule.

Titan I Data

The instruments and their locations for the Titan I test, with one exception, were the same as for the 25,000-lb test series. The only modification was the replacement of copper slabs by iron slabs at Positions 1 and 5 of instrument Station P. In anticipation of the relatively long durations of this test, some of the copper slabs were replaced by iron slabs to avoid an error that would be encountered toward the end of the heating pulse if 1.4-in. thick copper slabs were used. The flux curves from the copper slabs will gradually become larger than the correct value. It should also be noted that the thermocouple junction depth for the iron slabs is comparatively small (0.0002 in. compared with 0.005 in. for copper), with the consequence that slab temperature data and heat flux data will tend to be more erratic since the thermocouple junction can more readily sense minor and comparatively short-lived heating activity.

The heat flux density data are given in Figs. 6-14 through 6-16. Two of the data curves from Station P (Fig. 6-16) have somewhat larger-than-ordinary errors over certain time regions due to noise in the corresponding temperature records, and the details of these errors are noted in the data presentation section (Section 2, Vol. 2).

Included on Figs. 6-14 through 6-16 are scaled versions of the "bounding curve" that was given for the 25,000-lb LO_2/RP-1 test series in Fig. 6-3, applying the scaling rule described in the previous section.
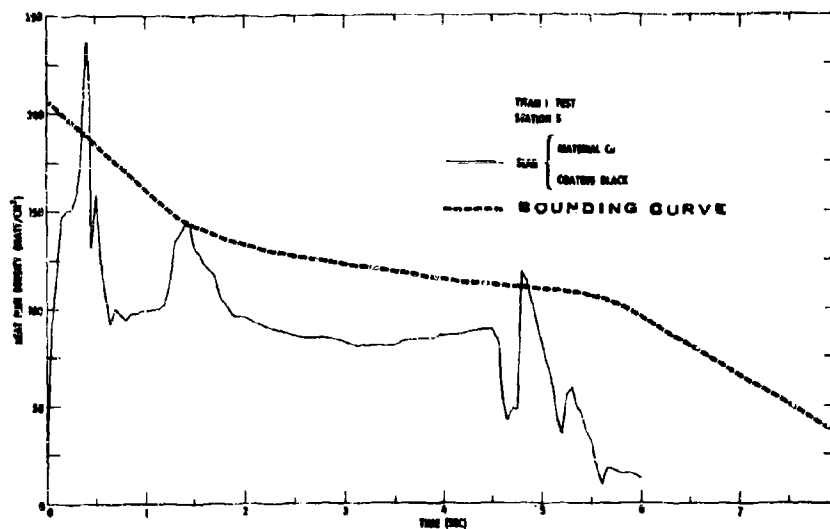
Fig. 6-14.   Heat Flux Density at Station S for the Titan Test
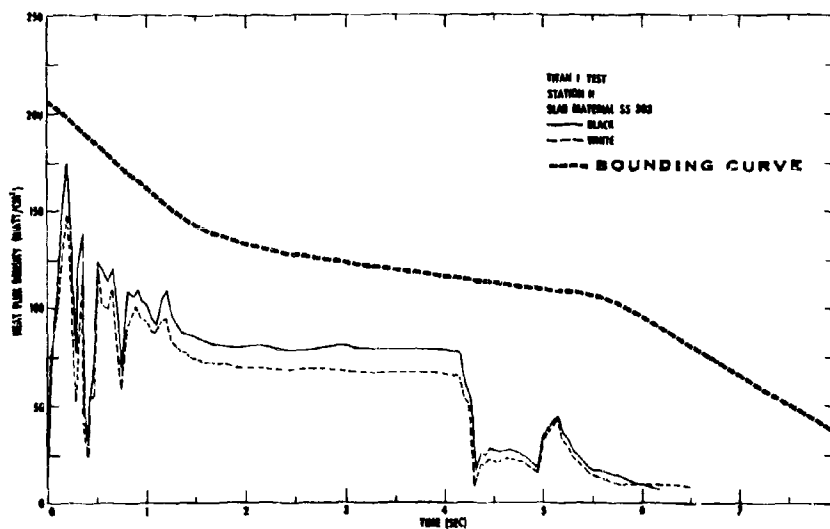
Fig. 6-15.   Heat Flux Density at Station H for the Titan Test
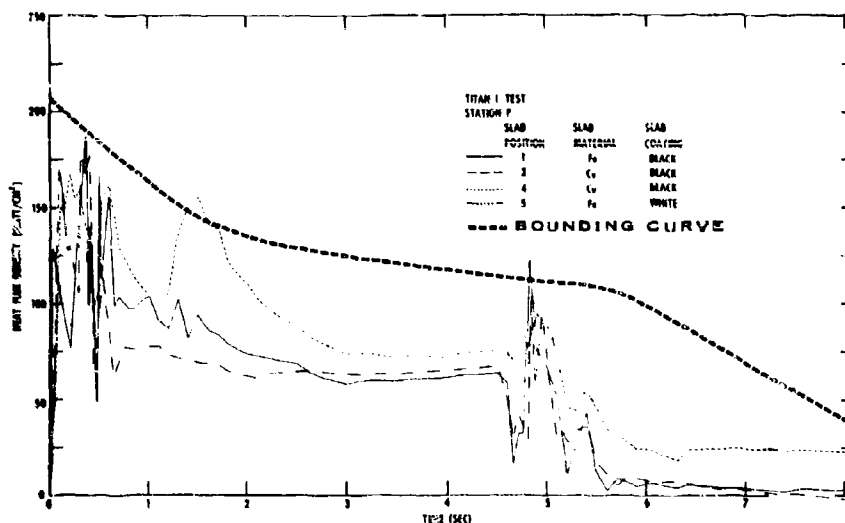
Fig. 6-16. Heat Flux Density at Station P for the Titan Test

Although the data from a single test can not validate the scaling that has been applied, it can be seen that the flux data are clearly not inconsistent with the scaled curve.

The cumulative or time-integrated flux to 8 sec for each flux curve is listed in Table 6-7, along with the ratio of each to the time-integrated flux of the _scaled_ bounding curve, the latter being approximately 1075 watt-sec/cm^2.

The ratios of the measured accumulative flux density to that of the bounding curve are similar to those obtained throughout the 25,000-lb LO_2/RP-1 tests (Table 6-5). There is a similarity also between the ratios of cumulative flux density from black-coated slabs to those of white-coated slabs, suggesting again that there is a rapid deposition of explosive products. The actual deposit was not as thick as had been obtained for the 25,000-lb test, although it was sufficiently thick to be opaque both on upper horizontal surfaces, and on side (vertical) and face-down surfaces.

6-46

Table 6-7

CUMULATIVE FLUX DENSITY FROM THE TITAN I TEST

INSTRUMENT STATION	SLAB MATERIAL[1]	SURFACE COATING	CUMULATIVE FLUX DENSITY (watt-sec/cm^2)	FRACTION OF THE SCALED BOUNDING CURVE
P	Fe	Black	416	0.35
	Cu	Black	588[2]	0.50[2]
	Fe	W_te	390	0.33
	Cu	Black	535[2]	0.45[2]
S	Cu	Black	555[2]	0.47[2]
H	SS	Black	418	0.36
	SS	White	371	0.32

1. SS refers to Stainless Steel 309.

2. Cumulative Flux Value slightly larger than correct value.

Radiant Flux Density Outside the Fireball

25,000-lb and Titan Tests

Summary plots of radiant flux measurements at locations outside of the fireball are presented in Figs. 6-17 and 6-18 for the 25,000-lb LO_2/RP-1 and LO_2/LH_2 tests, respectively. Information presented in these plots is limited to a curve representing the data mean for all tests (the measurements from each test rather than each measurement being weighted equally) along with an indication of the data range (shaded area). Other than adding a few qualifying remarks, the Presentation of Results subsection does not consider these data in any greater detail than is found in the summary plots. However, all of the available data (from both the 25,000-lb and Titan tests) are presented in Section 2 of Vol. 2 in order that the data may be examined in greater detail.
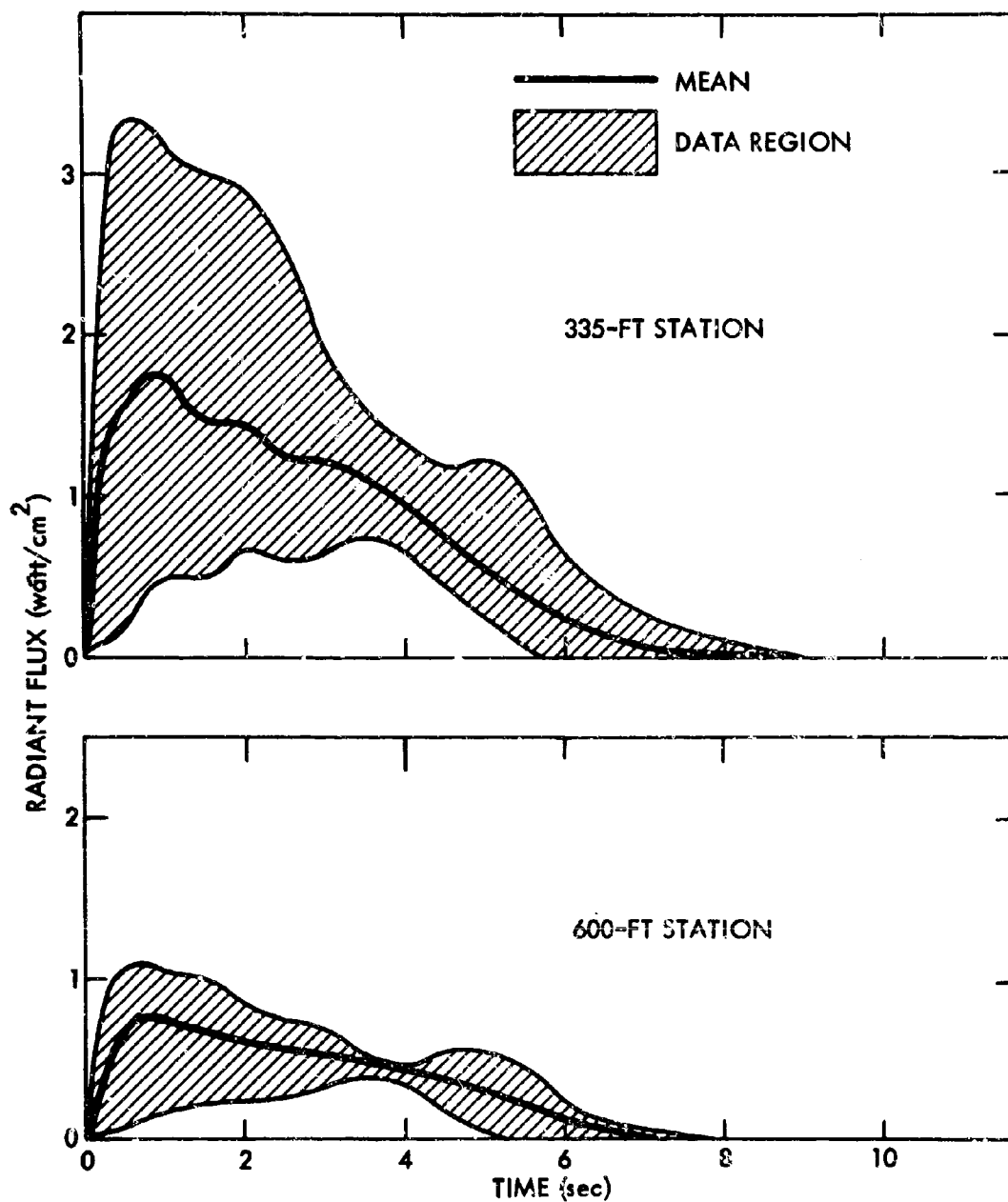
Fig. 6-17. Summary Plots of Radiant Flux Density Outside the Fireball
            for the 25,000-lb LO$_2$/RP-1 Tests
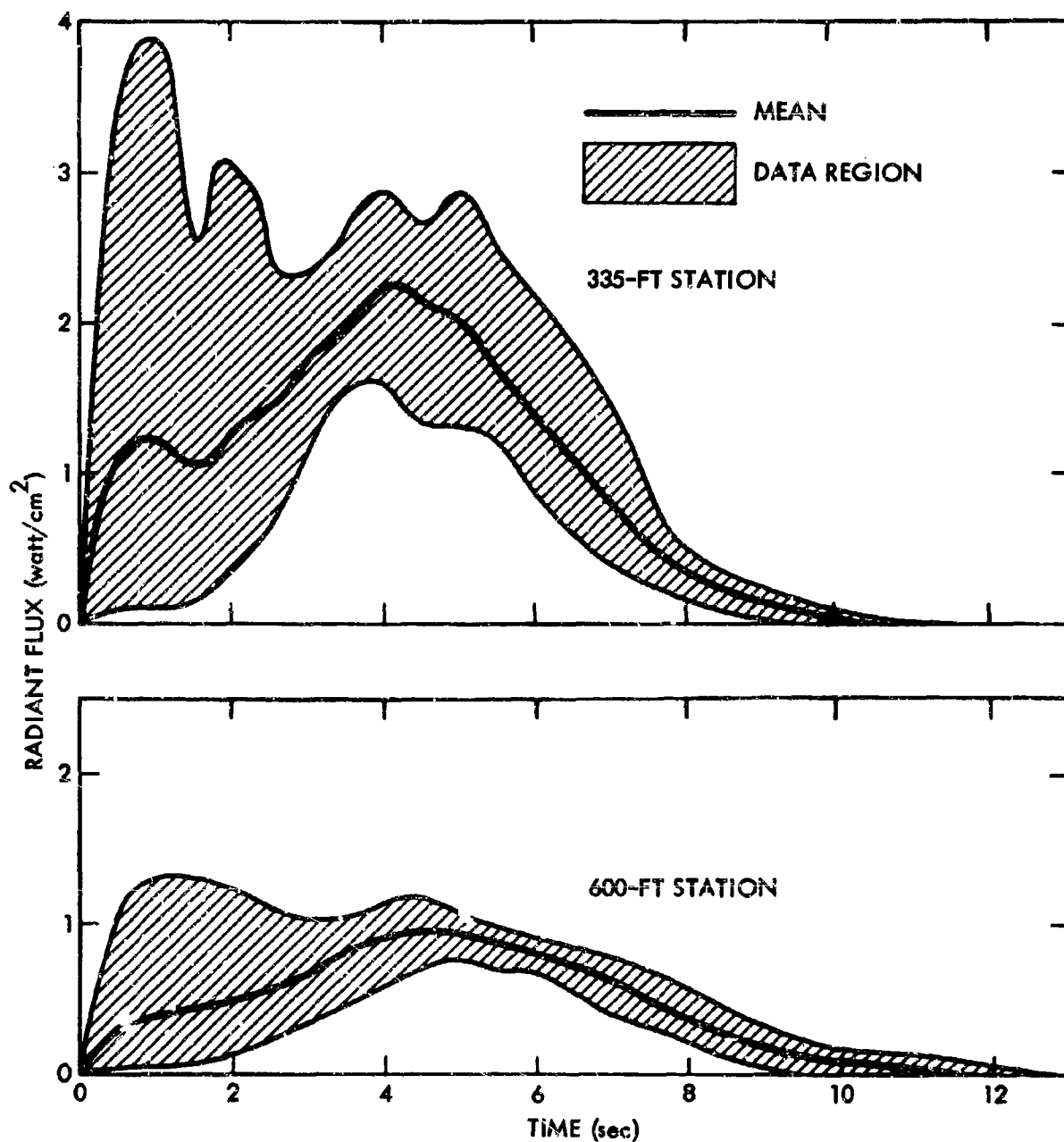
Fig. 6-18.   Summary Plots of Radiant Flux Density Outside the Fireball
             for 25,000-lb LO_2/LH_2 Tests

Generally, three radiometers were used per test, two at 335 ft from ground
zero along radial gauge lines 120 deg from each other (gauge lines A and B),
with the third at 600 ft from ground zero along one of these gauge lines (along
gauge line A). For only two tests, however, were satisfactory data acquired
from both radiometers at 335 ft. For one of these two tests, Test 278, the
flux at 335 ft along gauge line B rose during the later stages of the heating
pulse to a value significantly larger than that from the corresponding 335-ft
gauge line A station, as seen in Fig. 6-19. Photographic coverage indicates
that the fireball drifted toward the gauge line B station, thereby accounting
for the inflated value. Gauge line B data from this test were consequently
not used in the construction of the summary plot of Fig. 6-17. The data from
gauge line A, even though somewhat deflated for the same reason, were used,
however, since their deflation will tend to be less pronounced. This compara-
tively extreme example has been mentioned primarily to illustrate the "coarse
nature" of these data, because such physical occurences, but of lesser degree,
were present in the other tests. Moreover, these measurements are comparative-
ly inaccurate, ranging, it is estimated, between 10 and 20 percent, depending
on the quality of a given raw data trace; and as fireball temperatures subside,
these errors tend to increase due to energy absorption within the radiometer
window.

One further qualification of the data should be noted. The "field of
view" of the external radiometers is inherently restricted to 90 deg (45 deg
in any direction from the instrument "line of sight"), and the instruments are
directed approximately 10 deg above the horizontal. It is thus possible for
the fireball to rise sufficiently to escape view of the radiometers, first
from those at 335 ft and later at 600 ft, before its temperature or radiant
output has entirely subsided. This occurred noticeably for Test 288, as can
be seen by comparing the 335 and 600 ft gauge line A flux traces in Fig. 6-20.
During the early stages, the flux at 600 ft should be, and is to the first ap-
proximation, one-third of that at 335 ft, while at later stages this ratio
changes, and eventually the flux is greater from the 600-ft instrument. While
this has not occurred while any significant flux levels persisted it cannot be
concluded that the emitted energy from the fireball has subsided, since much

of the decrease at the instrument is due to increase in distance between the fireball and the instrument produced by the elevation of the fireball. Thus fireball durations are not accurately reflected in the flux-time curves. It is of interest, however, to compare the duration for 25,000 lb as given by Eq. (6.2), which is approximately 6 sec, with the somewhat larger durations suggested by Figs. 6-17 and 6-18, the latter averaging approximately 7 and 11 sec for $LO_2/RP-1$ and LO_2/LH_2, respectively. While the difference in duration for LO_2/LH_2 is nearly a factor of two, it will be recalled that the estimated standard error of Eq. (6.2) is 34 percent.
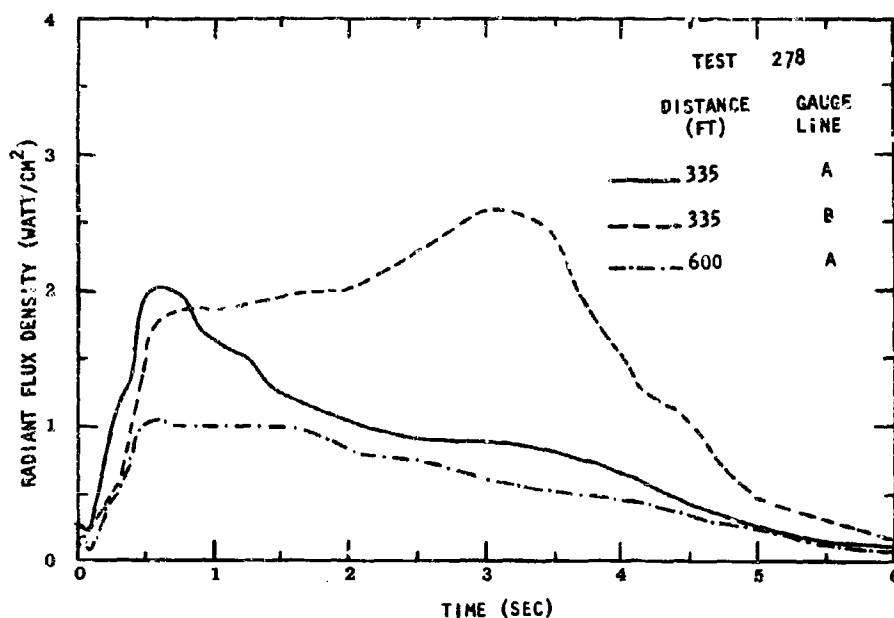
Fig. 6-19.   Radiant Flux Density Outside the Fireball from Test 278

Radiant flux density at the 600-ft station for the Titan test is given in Fig. 6-21. The fireball dimensions and their uncertainty prevented interpretation of the radiometer data at the 335-ft stations; the fireball expanded

6-51
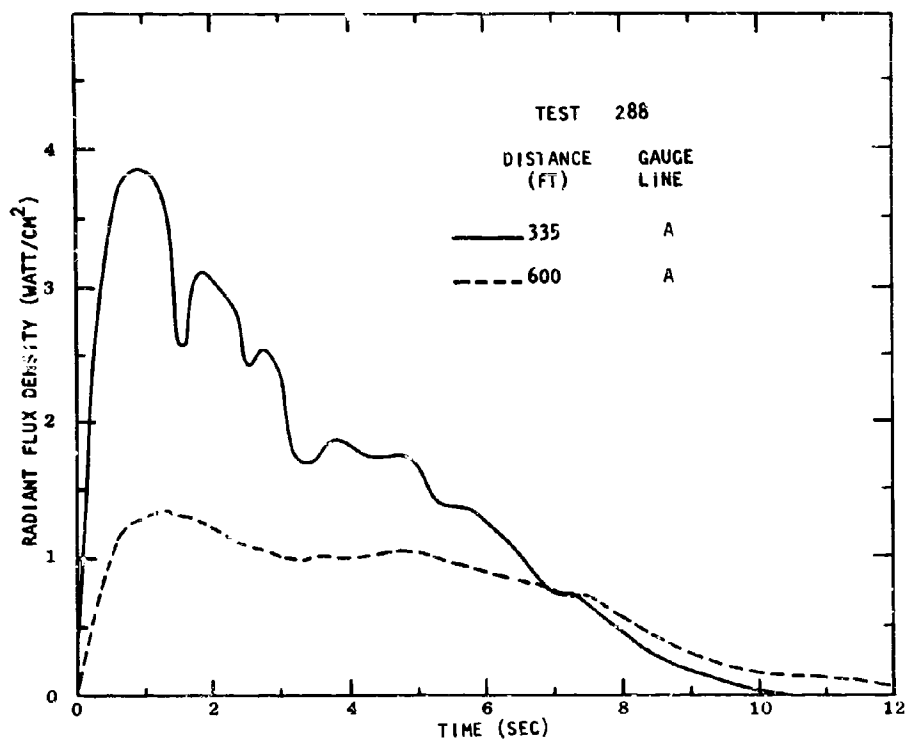
Fig. 6-20.   Radiant Flux Density Outside the Fireball from Test 288
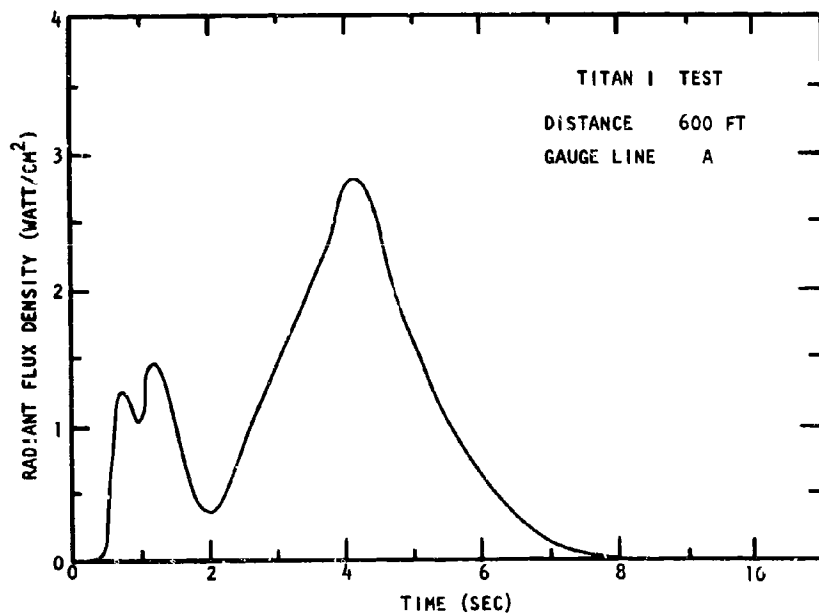
Fig. 6-21.   Radiant Flux Density Outside the Fireball from the Titan I Test

beyond the field of view of all photographic coverage, but diameters along the
horizontal near the ground surface were estimated to be from about 800 to 1000
ft. The uncertainty in diameter also prevents exact interpretation of the data
at 600 ft.

Section 6

REFERENCES

6-1. Bader, B. E., Heat Transfer in Liquid Hydrocarbon Fuel Fires, paper pre-
       sented at the symposium on Shipment of Radioactive Materials, Fifty-
       seventh Annual Meeting, Boston, Massachusetts, Dec. 6-10 1964

6-2. Gayle, J. B. and J. W. Bransford, Size and Duration of Fireballs from
       Propellant Explosions, NASA TM X-53314, George C. Marshall Space Flight
       Center, Huntsville, Alabama, 4 Aug 1965

Section 7
SUPPORT STUDIES

Several auxiliary studies involving analytical or small-scale experimental work were initiated in support of the PYRO hot-test program. These include:

- Particle-size studies: an investigation of the effect of particle size on explosive yield

- Heat transfer studies: inquiry into the rate of cooling of small fuel drops in LO_2

- Mixing studies: an investigation of possible methods for assessing the relative importance of mechanical and thermodynamic forces in the mixing process

- Small-scale H.E. tests: a test series to obtain data on the effects of detonation conditions on blast characteristics

These studies were conducted as the initial phase of an overall program to investigate the basic phenomena involved in propellant mixing and explosion processes. This program was initiated because a better understanding of the basic phenomena would assist in the overall design of the hot-test program, in the interpretation of the results from the program, and in the extrapolation of the results to propellant types and conditions other than those tested. It would also provide theoretical justification for the largely empirical scaling relationship derived from the main hot-test program.

The major goals of the overall program were to establish what properties of a propellant mixture determine or control the explosive characteristics of that mixture and to find the predominant mechanisms by which these definitive properties develop during the propellant mixing process.

The particle-size, heat transfer, and small-scale H.E. tests were all directed towards the first of the above goals, the identification of the definitive properties of a propellant mixture.

The specific objective of the particle-size study was to find the
variation of the explosive yield of LO_2/RP-1 charges with fuel particle size,
total propellant weight, and oxidizer-to-fuel ratio. Previous investigations
(Ref. 7-1) had indicated that the particle size of the dispersed fuel was
one of the most important properties of a propellant mixture with regard to
its explosive potential. These previous studies, however, were limited to
only one oxidizer-to-fuel ratio and one charge size, and to further under-
stand the particle-size effect required further investigation of oxidizer-
to-fuel ratio and charge-size effects.

The heat transfer study was the first step towards finding the effect,
if any, that oxygen gas films, which are prevalent during the film boiling
of LO_2 over fuel surface, may have on explosive yield of the LO_2/RP-1 pro-
pellant mixture. The importance of this situation, if, in fact, it does
occur, is that charges composed of particles with gaseous envelopes (due to
boiling at the particle surface) might have explosive properties different
from those of charges in which the fuel-particle surfaces are in contact with
oxygen in the liquid phase. A charge composed of particles of fuel enveloped
in gaseous oxygen would necessarily be reduced in charge density because of
the presence of boiling films on the fuel-particle surfaces. It might also
develop lower explosive yield, owing to the lower concentration of oxygen
in the gaseous film at the fuel surface and the consequently less favorable
conditions for rapid reaction, which would support the detonation wave.

The specific objective of the heat transfer study was to determine the
time required to cool RP-1 fuel particles below the temperature at which film
boiling prevails. If the cooling times were an order of magnitude (or more)
less than the time required for breakup of major propellant masses, it could
be concluded that only an insignificant proportion of fuel drops capable of
contributing to explosive yield could be in the cooling process at any given
point in time; and hence, the problem of the possible effect of the film
layer on the yield could be ignored.

7-2

The mixing study was directed towards the second long-range goal, finding the predominant mechanisms by which spilled propellants form explosive mixtures. The specific objective was to formulate an experimental approach for determining the relative importance of the two major mechanisms postulated for mixing of cryogenic propellants.

- the kinetic energy of the flowing fluids

- turbulence created by the effects of boiling heat transfer

The method considered depends on using a simulant for RP-1 which can be precooled to the approximate temperature of LO_2 and have essentially the same properties at this temperature that RP-1 has at room temperature. Mixing of the precooled simulant fuel and LO_2 would thus be solely due to flow processes while LO_2/RP-1 mixing under the same conditions would be due to both heat transfer and flow processes. The relative explosive yields measured for the two kinds of fuel in the same mixing geometry would thus reveal the relative importance of each mixing process.

Because of the relatively limited effort available in the PYRO program for these types of basic studies, it was not possible to pursue any of them very far. The progress which was made on each study, however, is covered in the following subsections along with a brief description of the recommended follow-on work. Also included is an outline of additional areas which warrant study as part of the overall program to investigate propellant mixing and explosion processes.

PARTICLE-SIZE STUDY

It has been hypothesized that the following properties of a mixture of LO_2/RP-1 might uniquely determine its explosive yield:

* Interface area of the two propellants per unit volume of mixture

* Uniformity of distribution of interface area within the mixture

* Total weight of propellants in the mixture and its geometrical
  configuration

In the case of LO_2 and LH_2 mixtures, it would likely be necessary to
include factors influencing the contribution of gas-phase detonation to the
over-all explosive yield.

The particle-size studies were started to investigate the effects of
each of the hypothesized definitive properties listed above on the explosive
properties of mixtures of LO_2/hydrocarbon fuel, using charges composed of
paraffin particles of known uniform size in LO_2. It has been shown in
previous work (Ref. 7-1) that perfectly mixed or adsorbed-fuel[*] charges
composed of paraffin in LO_2 produce the same yield as perfectly mixed LO_2/
RP-1 charges of the same weight ratio of oxidant and fuel. Paraffin can,
therefore, be used as an excellant simulant for RP-1 in test charges, with
the advantage that properties such as interface area per unit volume, etc.,
can be controlled by the use of preformed and sized particles in the test
charges.

Particle size, at a given ratio of oxidizer to fuel, determines the in-
terface area of the propellants per unit volume. It has been demonstrated
in previous work (Refs. 7-1, 2) that the explosive yield of small test
charges (27 gm) decreases as particle size of the fuel is increased; however,
these experiments involved only one size of charge and one ratio of oxidizer
to fuel (3:1). In exploring the effect of particle size on explosive yield,
it is necessary to include the effects of varying charge size and the ratio
of propellant weights, because it has been determined that this ratio affects
yield, and it may be expected that particles of the same size would produce
different yields in different charge diameters, just as in the case of con-
ventional explosives.

---

* These are charges that were constructed by adsorbing hydrocarbon fuels,
  such as kerosene, RP-1, JP-4, and paraffin, while in a liquid state, onto
  an inert structural material like diatomaceous earth, thus providing a
  uniformly dispersed distribution of fuel with, in effect, a particle size
  that is a minimum.

With the relatively little effort available for this study, it has not
been possible to complete the investigation of all three of these parameters,
i.e., particle size, charge size, and oxidizer-to-fuel ratio; the effect
of charge size, for example, has not yet been explored at all. Nevertheless,
from tests completed so far, a number of significant observations were made
and some insights gained. The general approach, experimental effort, and
results are described below.

Approach

The experimental result mentioned previously, in which it was observed
that for a given charge size the explosive yield decreased with increasing
particle size, suggested that the reaction may have been limited by trans-
port phenomena, e.g., the reaction rate may not have been sufficient to
completely burn up the larger particles during the time in which the re-
action could contribute its energy to the formation of the blast wave. These
results gave no information on whether or not all of the oxidizer enters
the reaction. As the first trial hypothesis, however, it was assumed that
all of the oxidizer did enter the reaction.

The previous experimental results also indicated that for fuel particle
sizes small enough to completely react, the explosive yield was dependent
on the oxidizer-to-fuel ratio. For particle sizes large enough that all
the fuel does not enter the reaction, it would also be expected that the
oxidizer-to-fuel ratio would be important. In this case, however, there is
not a unique oxidizer-to-fuel ratio, since the initial ratio differs from
the end-point ratio (the ratio of oxidizer to fuel actually reacted). Since,
with the hypothesis discussed above, the unreacted kernel of each particle
could be replaced with inert material, it was assumed for the initial
hypothesis that it was the end-point ratio that was most important.[*] In

---

[*] In actuality, the use of a simple parameter to characterize the reaction
process for incomplete reactions, such as either the initial or end-point
oxidizer-to-fuel ratio for the case of large particles, may not provide a
complete explanation, since the effects of this parameter no doubt enter
in complex ways. At this time, however, consideration was limited to
defining this parameter only in terms of these two ratios, since they are
the only values that can be determined experimentally without making
additional assumptions.

applying the above concept, end-point ratios would be determined from know-
ledge of the initial ratio and from a ratio of reacted to unreacted fuel.
Any selection of the latter ratio uniquely fixes both the total mass of re-
actants relative to the initial mass and the end-point ratio.

The fuel-limited-reaction concept is seen to lead to two sources of
change in explosive yield associated with increase in fuel particle size, one
acting always to reduce the charge yield, because of reduced charge weight
due to unreacted fuel, and the other acting to either decrease or increase the
charge yield in accordance with the end-point, or effective, reaction ratio of
oxidizer to fuel. The net of both of these effects determines the explosive
yield in a given charge. This simplified fuel-limited version of the transport-
limited concept obviously lacks the sophistication of a method for excluding
any LO_2 in the transport process, but the nature of the observations should
provide further insights into the processes. The experimental information
required is discussed below.

By conducting additional tests with adsorbed-fuel charges in the current
program, a more complete spectrum of explosive yields, as a function of the
end-point ratio of oxidizer to fuel, has been obtained. With this more complete
set of data, an iterative process may be used to determine, from subsequent
experimentally measured yields on particulate-fuel charges, an effective end-
point LO_2-to-fuel ratio and hence a corrected charge weight. Repetition of the
process finally results in fixing the weight of fuel unreacted. The spherical
fuel-particle geometry used makes it possible to calculate, from the inferred
weight of fuel unreacted, a value for the depth of the layer of fuel burned
off the surface. Thus, it is possible to plot layer thickness consumed as a
function of particle size.

Several other concepts aid in drawing inferences from the available
information. It would seem reasonably to expect, for a given charge weight,
that at each initial ratio of oxidizer to fuel there will be a different upper
limit to the fuel particle size effectively completely reacted, i.e., the size
which will give the same yield as the ideal adsorbed-fuel charges. It may be
further expected that this size will increase with increases in the initial
ratio of oxidizer to fuel because of a higher probability of unreacted material
coming together during the time available for such to still contribute to the

main reaction. There may also exist some particle size and, as previously
mentioned, some initial LO_2-to-fuel ratio above which reaction rates are LO_2-
transport limited. This would of course affect the yield and, further, could
act to alter the nature of peak pressure fall-off with distance.

Finally, the qualitative effect of an increase in charge size is anti-
cipated to operate, as in a conventional explosive, to provide an increase in
the time for the reaction to occur. Thus, as charge size increases, it is
anticipated that the size of the fuel particle that is effectively completely
reacted at each LO_2-to-fuel ratio will increase also. With sufficient data of
this sort, the postulated concept of an effective burning or reaction rate
might be examined experimentally.

Experimental Method

The paraffin particles used in the experiments were produced by atom-
ization of liquid paraffin. The particles solidify while settling a distance
of about 8 ft through the air. The solidified particles pass through an
opening in the upper wall of a horizontal duct of rectangular cross section.
Air flow velocity in the duct was regulated so that particles of different
sizes in the range of experimental interest (10 to 400 μ diameter) were sepa-
rated owing to their differing fall rates within the duct. The sized particles
were collected from appropriate areas of the floor of the duct. The particles
were further graded accurately to narrow size ranges by sieving them while
they were bathed in LN_2.

The uniformly sized particles were dispersed in kieselguhr, from which
test charges were formed. The proportion of kieselguhr and its compaction
in the charge was adjusted so that it would absorb an amount of LO_2 corres-
ponding to the desired LO_2-to-fuel weight ratio when immersed in LO_2. It has
been shown in previous experimental work that the amount of kieselguhr required
does not significantly affect the explosive yield (Ref. 7-3).

After a charge was constructed, it was frozen and then introduced into
a lightweight wire-mesh basket constructed of household screening material.
The basket prevents erosion of the charge when it is finally introduced into

the LO_2 bath prior to detonation and holds the Primacord securely in place.
A typical charge can be seen in Fig. 7-1. (For purposes of the photograph,
the wire tabs that secure the Primacord have been bent aside.)

After the charge had soaked in the bath long enough to assure complete
penetration of the LO_2 it was rapidly withdrawn by means of a manually operated
pulley arrangement and detonated by an explosive cap attached to the Primacord.
Side-on pressure —time measurements of the resulting blast wave were made with
a series of four Kistler 605 piezoelectric pressure gauges mounted at various
distances from the charge. The pressure gauges were calibrated before and
after each test series in a shock tube, and standard high-explosive charges
were used for field calibration and for establishing the reference peak-
overpressure-versus-distance curves used in computing explosive yield values.

Experimental Results

The primary objectives of the experimental program have been to test
the validity of portions of the concepts discussed earlier and to gain in-
sights into controlling processes.

The first experimental effort consisted of extending the quantitative
relationship of maximum explosive yield versus the ratio of oxidizer to fuel
to higher ratios by means of adsorbed-fuel (kerosene) charges of 27 gm total
weight. A plot of these data appears in Fig. 7-2. This particular quantitative
relationship may be considered to be invariant with charge size, since all the
material reacts in time to contribute to explosive yield. This is supported
by the fact that the theoretical calculations (Ref. 7-4), based on all material
reacting, agree with the experimentally measured values and that the maximum
experimentally measured yield is seen to occur at a ratio of 3:1, where the
theoretical maximum is expected. Ratios greater or less than 3:1 result in
reduced yields.

In addition to measurements of explosive yields at higher ratios of
oxidizer to fuel, tests were conducted with the initiator only and with standard,
oxygen-soaked adsorbed charges, in which water was substituted for the
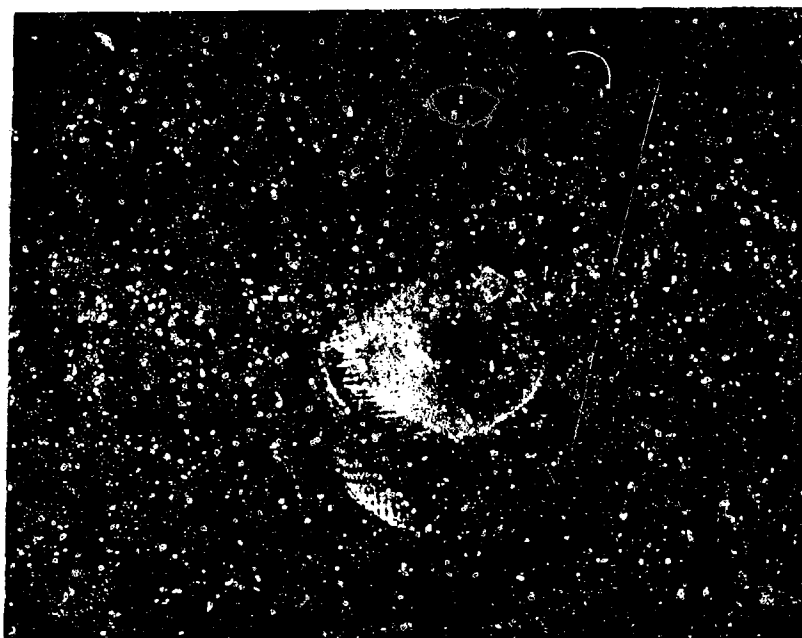
Fig. 7-1. Photograph of Test Charge
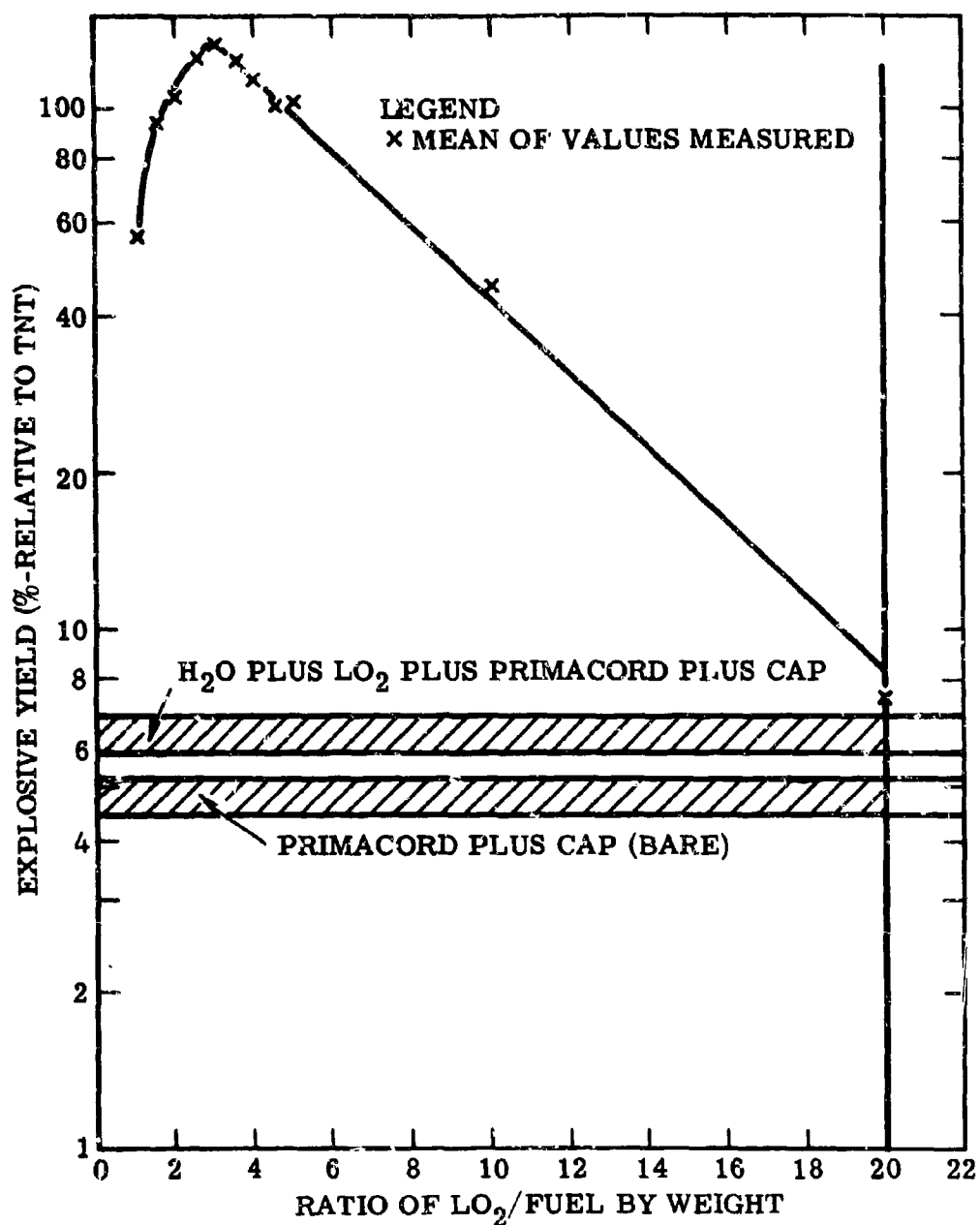
Fig. 7-2. Explosive Yield vs Ratio of LO$_2$-to-Fuel for Maximum
Surface Area of Fuel in Contact with LO$_2$

hydrocarbon fuel.* The objective of these tests was to set a lower limit to
yields and an upper limit to ratios of oxidizer to fuel that would be meaning-
ful. It is seen in Fig. 7-2 that no specific conclusions can be drawn where
oxidizer-to-fuel ratios are above, say, about 20:1 or where yields are below
7 percent TNT equivalent.

The second experimental effort was aimed at determining the effect of
particle size on explosive yield for an initial LO_2-to-fuel ratio other than
the previously studied ratio of 3:1, where maximum yield occurs. Figure 7-3
shows a plot of yield versus particle size at the ratio of 3:1, obtained from
data in Refs. 7-1 and 7-2. Figure 7-4 shows the results obtained in the present
study for an oxidizer-to-fuel ratio of 5:1, plotted in the same manner. In
both Figs. 7-3 and 7-4 the vertical lines indicate the yield for the case where
the initial and end-point ratios are the same, i.e., for adsorbed fuel charges.
Thus, it may be inferred that the point of intersection of these lines with
the yield-versus-particle-size line indicates the maximum particle diameter
effectively completely reacted. This would be 2 μ at 3:1 and 28 μ at 5:1. In
addition, the two plots indicate an exponential decrease in yield with in-
creasing particle size, approaching the yield of the initiator asymptotically.
The rate of decrease has an apparent dependence on the initial ratio of oxidizer
to fuel; but as noted earlier, it was assumed that the correct view is to
consider it on the basis of the final effective LO_2-to-fuel ratio, which
ultimately depends on the weight of fuel actually burned off the particle
surfaces.

Reconsider, in the light of the previous paragraph, the information con-
tained in Fig. 7-2. Since all the fuel is apparently consumed** these data can
also be interpreted as indicating the yield to be expected for any reaction

---

* It was anticipated that some of the organic composition of the Primacord
would react with the liquid oxygen to give a slightly increased yield.

** These data are for adsorbed-fuel charges, where no transport problems
are considered to exist, i.e., the subdivision and distribution of fuel
and oxidant is considered to be such that every molecule of fuel has in
its immediate vicinity all the oxidant necessary for a complete reaction
at the ratio indicated.
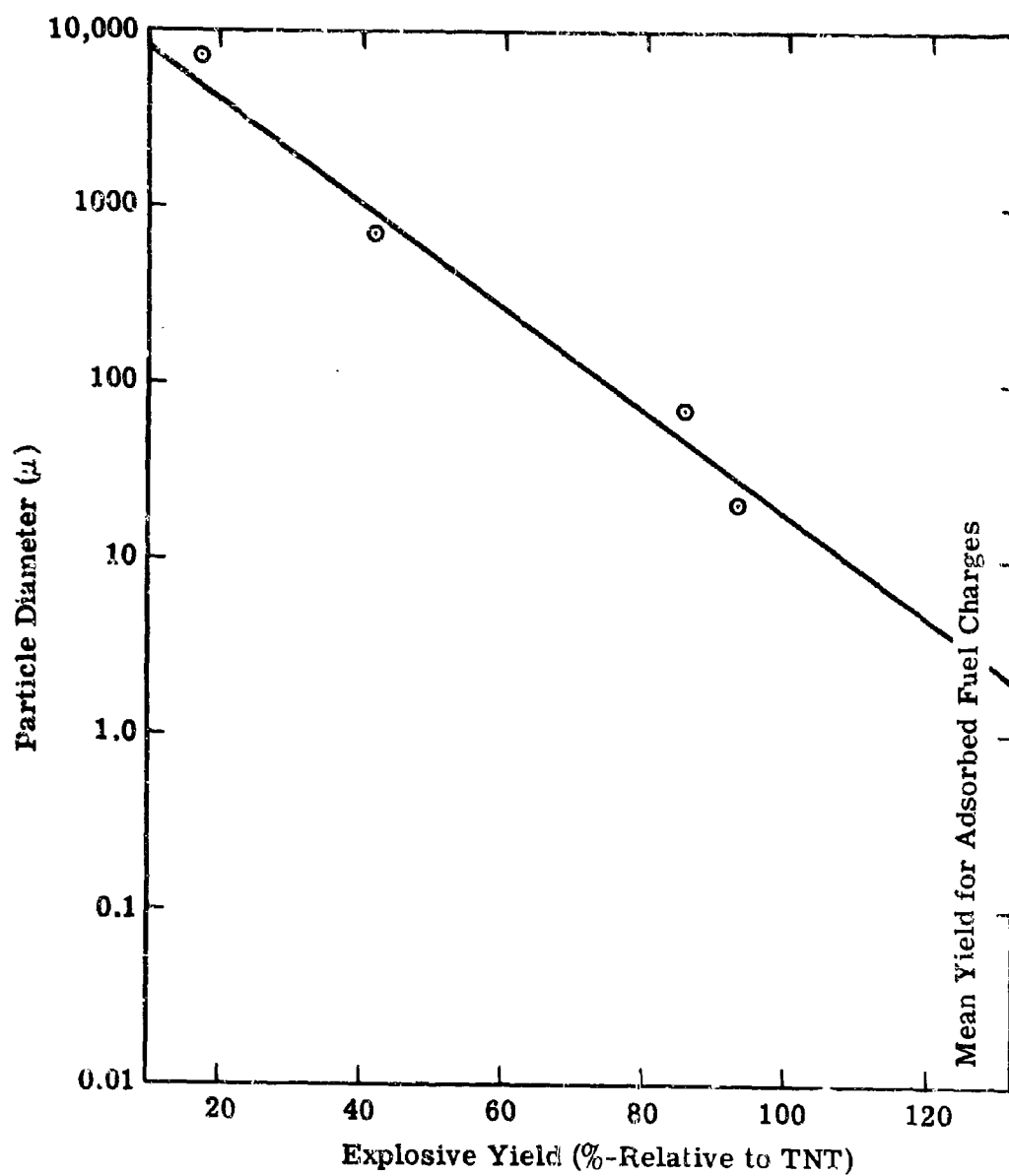
Fig. 7-3. Explosive Yield vs Fuel Particle Diameter for 3:1 Ratio
of LO_2-to-Fuel
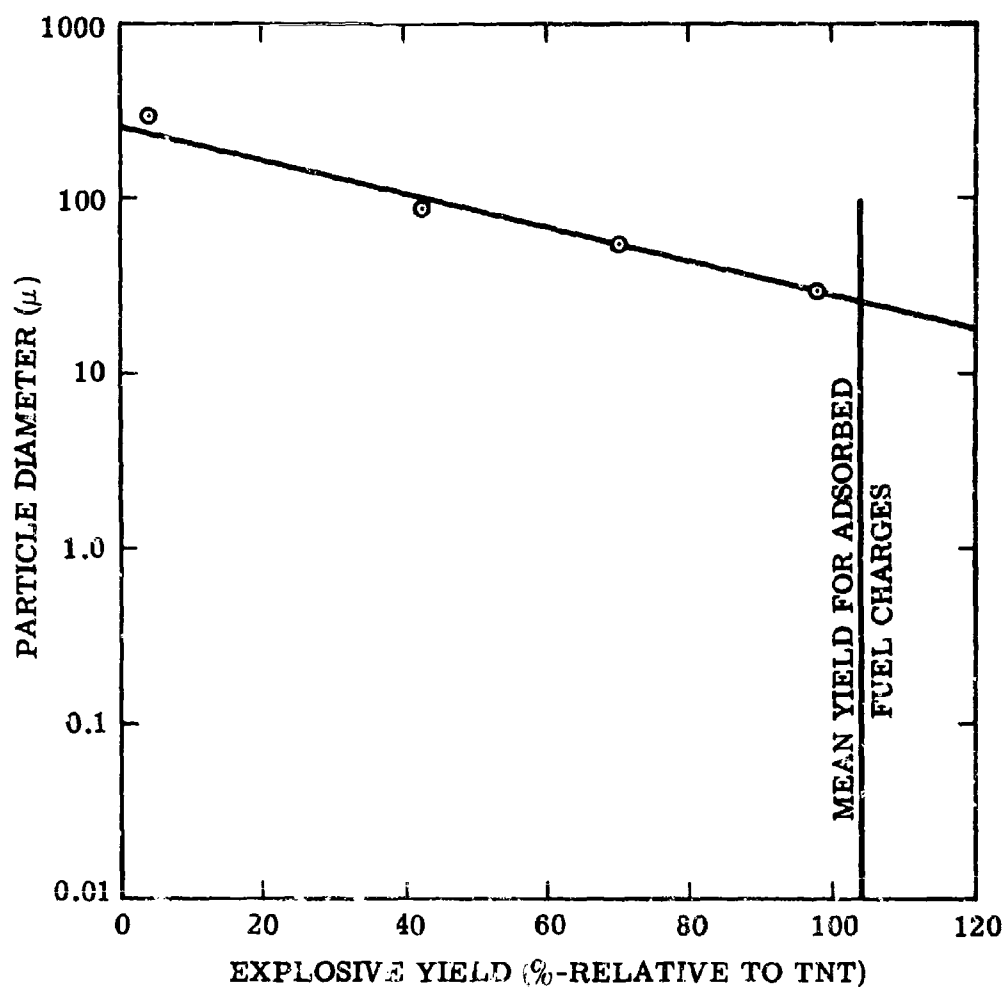
Fig. 7-4. Explosive Yield vs Fuel Particle Diameter for 5:1 Ratio
of LO$_2$-to-Fuel

in terms of its ultimate end-point LO_2-to-fuel ratio. As an example, let this concept be applied directly to calculate the yield, as a function of various end-point LO_2-to-fuel ratios, that is to be expected from a charge initially composed of 13.5 gm each of LO_2 and fuel. In this computation, selection of an end-point ratio fixes the amount of fuel that does not enter the reaction. Table 7-1 indicates the net effect on explosive yield for such a situation. The data in Table 7-1 are summarized in the plot in Figure 7-5, which also shows the net effect of the change in ratio and the corresponding loss in active charge weight on yield. It is evident from both the table and the plot that the postulate of yield dependence on end-point LO_2-to-fuel ratio results in an expected higher absolute yield if some of the fuel fails to enter the reaction. In fact, if anywhere up to four-fifths of all the fuel is, for some reason, unreacted, the yield is seen to be either equal to or higher than the case where 100 percent of the fuel reacts. At an end-point ratio between 2.5:1 and 3:1, the plot demonstrates that the mean yield has increased to its peak value, or about 88 percent TNT versus the 51 percent at 1:1.

Additional experiments were conducted at an initial LO_2-to-fuel ratio of 1:1, using fuel particles in the 74- to 104-μ range (mean size by volume of 87 μ) and the 256-to 420-μ range (mean size by volume of 333 μ). Both sets of tests resulted, as postulated above, in mean yields higher than 57 percent TNT equivalence. The smaller, 87-μ, size produced a mean yield of 84 percent, and the 333-μ size produced a mean yield of 61 percent. Each of these yields could correspond to two different end-point ratios, as seen in Fig. 7-5. Nevertheless, it may be inferred that if the 333-μ size shows the lower mean yield of the two, it must therefore be at the higher of the two end-point ratios possible. This would correspond to an LO_2-to-fuel ratio of 4.-:1 and 21 percent of the fuel reacted by volume. Hence, the surface layer burned off the radius would be about 7 percent or 11.7 μ. Consequently, it might be further inferred that a 23.4-μ particle (2 x 11.7 μ layer burned off) must surely have the same end-point ratio if the initial ratio is 4.8:1, i.e., that a particle size at least 23.4 μ in diameter would be completely consumed if incorporated in a charge with an initial ratio of 4.8:1.[*] Examination of

---

[*] Actually a larger size should react completely at this initial ratio since at every stage of the reaction the effective ratio will be higher than for an initial ratio of 1:1 with the end-point ratio of 4.8:1.

Table 7-1

CALCULATED EXPLOSIVE YIELDS (RELATIVE TO TNT) AS A FUNCTION OF THE END-POINT LO_2-TO-FUEL RATIO FOR A 27-GM CHARGE INITIALLY AT A 1:1 RATIO (COMPOSED OF 13.5 GM LO_2 AND 13.5 GM OF PARAFFIN SPHERES)

1	2	3	4	5	6
End Point LO_2-to-Fuel Ratio	Portion of Fuel Unreacted	Weight of Fuel Reacted(a) (gm)	Effective Charge Weight(b) (gm)	Yield per Gram of Reacting Material(c) (%)	Total Yield of Charge(d) (%)
1.0	0	13.5	27.0	57	57
1.5	1/3	9.0	22.5	93	78
2.0	1/2	6.75	20.25	113	85
2.5	3/5	5.4	18.9	126	88
3.0	2/3	4.5	18.0	132	88
3.5	5/7	3.9	17.4	123	79
4.0	3/4	3.4	16.9	115	72
4.5	7/9	3.	16.5	105	64
5.0	4/5	2.7	16.2	96	58
6.0	5/6	2.25	15.8	83	49
7.0	6/7	1.9	15.4	70	40
8.0	7/8	1.7	15.2	59	33

Notes:

(a) 13.5 divided by column 1
(b) 13.5 plus column 3
(c) From Fig. 7-2
(d) Product of columns 4 and 5 divided by 27
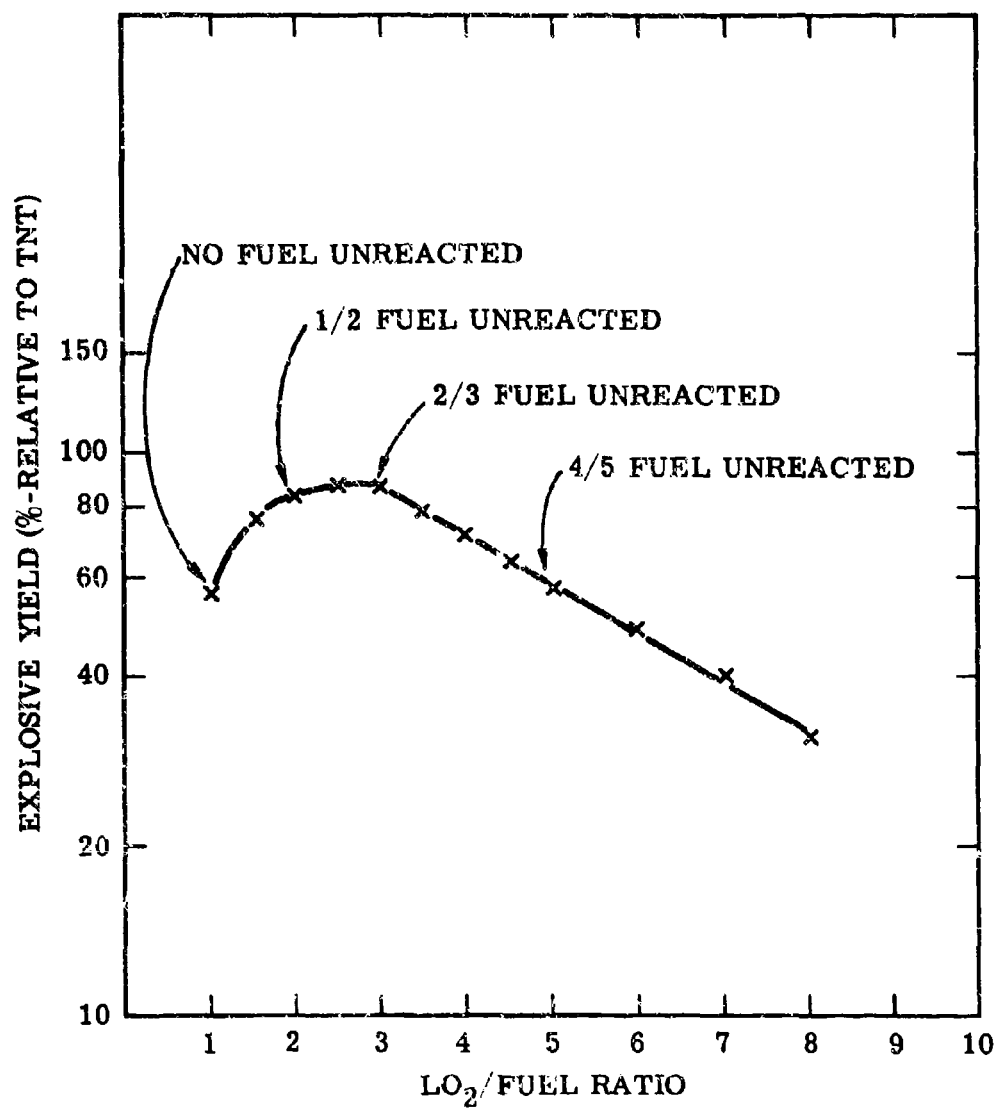
Fig. 7-5. Explosive Yield as a Function of End-Point LO_2-to-Fuel Ratio for an Initial LO_2-to-Fuel Ratio of 1:1

Fig. 7-4 shows that 28 μ is the largest particle size at an initial ratio of 5:1 that is expected to have an end-point ratio of 5:1. Thus, the hypotheses and inferences are, so far, consistent.

For initial LO_2-to-fuel ratios of 3:1 and 5:1, Table 7-2 presents layer thicknesses inferred to have reacted off the outside of the spherical fuel particles. The information was calculated on the basis of the fuel-limited-reaction concept by using information of the type presented in Table 7-1. Implicit in Table 7-1 is a relationship between yield (the information in Column 6) and reacted layer thickness as computed from the portion of fuel reacted (which can be determined from information on the amount of fuel unreacted, given in Column 2). Thus, the experimentally measured relationships between yield and particle size allows layer thickness reacted to be related to particle size for a given initial LO_2-to-fuel ratio. It is rather surprising that within experimental limits of error, there appears to be a constant layer thickness reacted (i.e., completely independent of particle size) for the case where the initial LO_2-to-fuel ratio is 5:1, but when the initial ratio is 3:1 (i.e., slightly less than stoichiometric), there appears to be an ever-increasing layer thickness reacting as particle size is increased. The apparent explanation for what appears at this time to be "anomalous" behavior in the fuel-limited-reaction concept is simply that the more sophisticated transport-limited concept involving limitations on the LO_2 transport seems to be required. The existence of an absolute limit on LO_2 transport would be more compatible with observations that indicate a constant layer thickness of fuel consumed when much excess LO_2 is available, as at the 5:1 initial-ratio condition.

Summary

A summary plot incorporating most of the available data and hypotheses and based on the various inferences discussed appears in Fig. 7-6 which is a plot of explosive yield vs initial LO_2-to-fuel ratio for a range of fuel particle sizes. From it, rough predictions can be made with regard to test results anticipated from particulate-fuel charges in regions where extrapolation, rather than interpolation, is required (for example, at higher initial LO_2-to-fuel ratios).
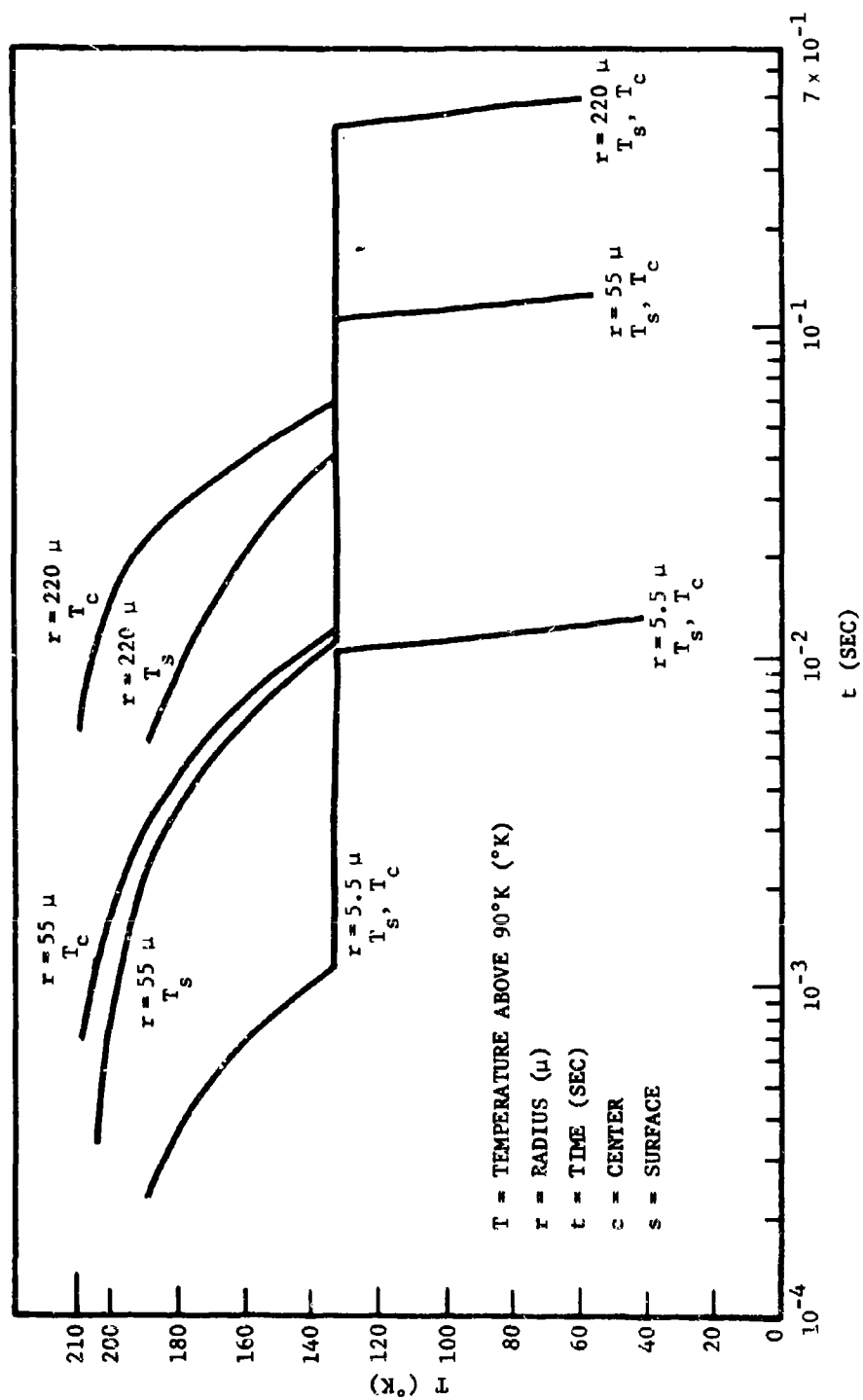
Fig. 7-8 Temperatures of the Surfaces and Centers of RP-1 Spheres as a
Function of Time for Various Radii

transfer coefficient appropriate to the successive boiling regimes prevalent
in the cryogenic at the particle surface. Boiling heat transfer coefficients
reported in the literature have been measured under nontransient conditions
at the surface of solid metal heaters immersed in cryogenic. These coefficients
have varied in different investigations by factors of 2 to 5. In our cal-
culation of particle cooling curves, the heat transfer surface (a spherical
RP-1 droplet) is liquid during part of the cooling process, and the heat
transfer process is transient rather than steady, so that the heat transfer
coefficient assumed to prevail at the particle surface was even more uncertain
than the reported experimental values.

To place the cooling curve calculations on a more secure basis, it was
decided to obtain an experimental measurement of the boundary heat transfer
coefficient under conditions directly applicable to the calculations, i.e.,
at the boundary of a cooling RP-1 fuel particle in cryogenic. The experimental
method sought was the least sophisticated one capable of providing the desired
measurement. The precision desired was only that required to determine whether
the heat transfer coefficient at the boundary of cooling particles was within
the range reported for steady boiling heat transfer from a solid heater in
cryogenics or whether it was significantly outside this range.

Basically the measurement consisted of obtaining an approximation to the
heat transfer rate by measuring the rate of vaporization of liquid cryogenic[*]
surrounding an initially liquid RP-1 particle that was injected under the
cryogenic surface. Measurement of the bubble volume in time, together with
the diameter of the responsible particle, was accomplished through photographic
recording of the region.

While the particle density is greater than that of the cryogenic, the
vapor formation surrounding the particle results in the ascension of both to
the surface during film boiling. In order to maintain the particle's position
below the surface and within camera view throughout a sufficient portion of
the cooling period, an arrangement permitting an adjustable, downward fluid
flow was used. This consisted of a vertical glass tube (1/2 in. in diameter)
dilated at the upper end to form a reservoir and a coneshaped rod, which was

---

* Liquid nitrogen was used in place of liquid oxygen.

Table 7-2

CALCULATION OF LAYER THICKNESSES REACTED AS FUNCTIONS OF PARTICLE SIZE
FOR TWO INITIAL RATIOS OF LO_2/FUEL

Part 1: Initial LO_2-to-Fuel Ratio of 3:1

1 REACTED WEIGHTS W_r (%)	2 LAYER* (% D)	3 END-POINT** LO_2/FUEL	4 TNT YIELD AT END-POINT RATIO† (%)	5 CHARGE WEIGHT REACTED†† (%)	6 TNT YIELD FOR CHARGE‡ (%)	7 PARTICLE SIZE D‡‡ (μ)	8 LAYER THICKNESS□ (μ)
100	100	3	132	100	132	2	1
80	41.5	3.75	122	95	116	5.2	1.07
64	28.8	4.7	102	91	93	27	3.7
51	21	5.9	80	97	70	130	13.7
40	15.7	7.5	59	85	50	520	41
32	12.2	9.4	42	83	35	1,400	85
25	9.2	12.0	25	81	20.4	3,900	180
20	7.3	15.0	15	80	12	7,100	260
16	5.7	18.75	8.3	79	6.5		

NOTE: Both parts of table based on charge weight of 27 gm.

* $1 - (1 - W_r)^{1/3}$

** $\dfrac{(3/W_r)}{1}$

† From Fig. 7-2

†† $(3 + W_r)^{1/4}$

‡ Col. 4 x 5

‡‡ From Fig. 7-3

□ $\dfrac{(Col.\ 2 \times 7)}{2}$

inserted in the lower end of the tube and which provided a means of controlling
the flow rate. (Particles entering the nucleate boiling region proceeded
downward even though the flow was stopped.)

Vapor generation through heat transfer to the liquid by other than the
particles required minimization to the extent that particle-generated bubbles
could be distinguished. To this end, heat conduction was minimized by
vacuum-jacketing the tube, including the reservoir, and immersing the lower
portion of the tube in cryogenic. Radiation was minimized by suitably cover-
ing all but the camera viewing region.

Energy from the RP-1 particles is not entirely consumed in the nitrogen
phase change. For example, volume changes of the gaseous envelope of a
particle cause changes in the height of the center of mass of the liquid
above it as well as causing changes in the liquid surface energy at the liquid —
gas interface. Temperature rises of the gaseous envelope above the liquid
nitrogen temperature also account for some energy. Estimates of the relative
magnitudes of energy, however, indicate that most of the energy is consumed
in the phase change.

To that approximation, then, the heat transfer rate is given as

$$q = \frac{Ln}{\pi D_p^2 \Delta t}$$

where q is the average heat per unit area per unit time over a time Δt from a
particle of diameter D_p, n is the number of moles of liquid nitrogen that are
vaporized in Δt (commencing at the beginning of bubble formation), and L is the
heat of vaporization of nitrogen (1,330 cal/mole). Then n is

$$n = \frac{p \pi D_b^3}{6RT}$$

where D_b is the bubble diameter (assuming $D_b \gg D_p$) and p and T are the pressure
and temperature of the gas. Thus

$$q = \frac{Lp D_b^3}{6RT \Delta t D_p^2}$$

7-30
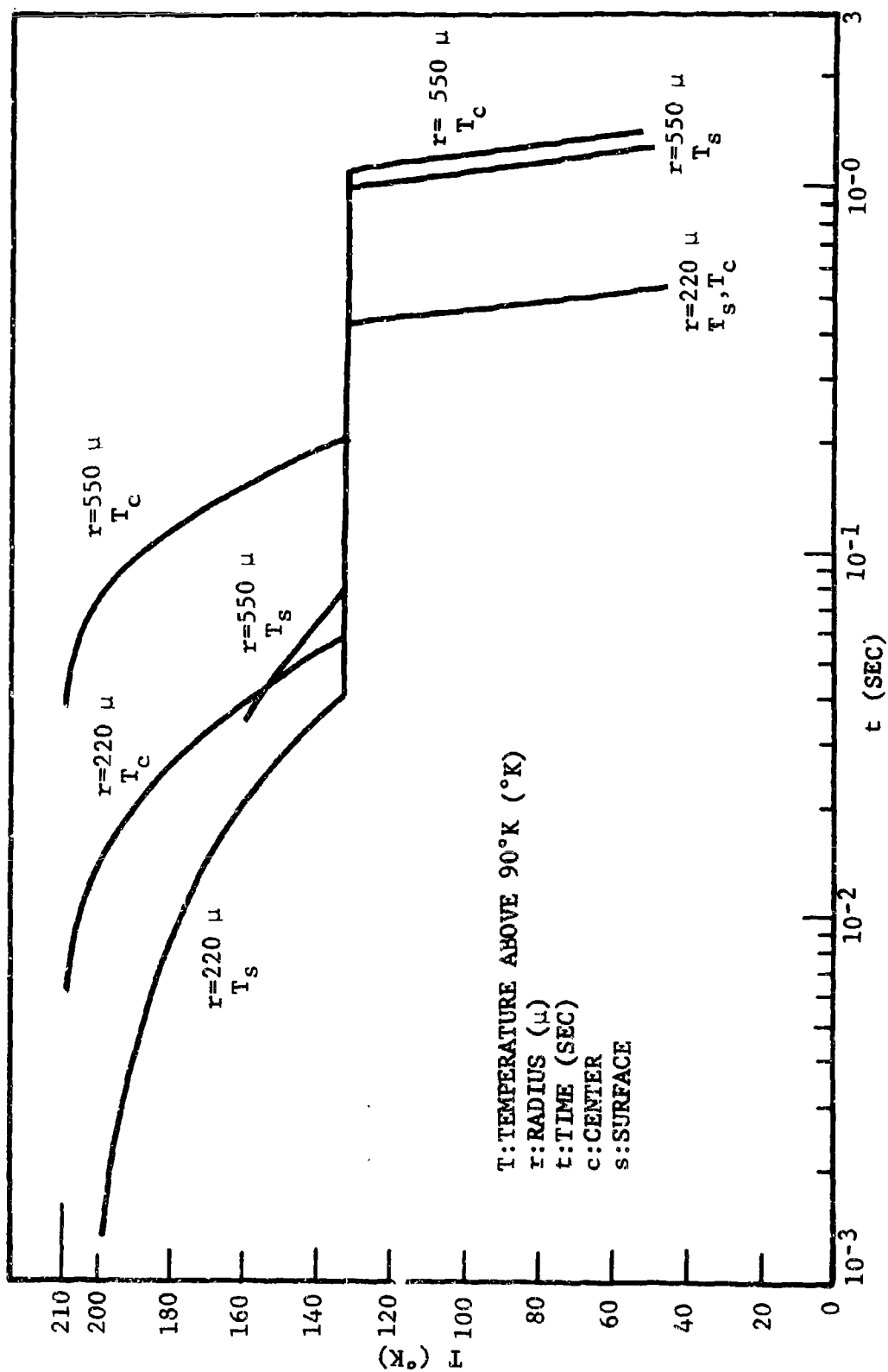
Fig. 7-9 Temperatures of the Surfaces and Centers of RP-1 Spheres as a Function of Time for Various Radii

Table 7-2, (cont.)

Part 2: Initial LO_2-to-Fuel Ratio of 5:1

1 REACTED WEIGHTS w_r (%)	2 LAYER* (% D)	9 END POINT LO_2/FUEL**	10 TNT YIELD AT END-POINT RATIO† (%)	11 CHARGE WEIGHT REACTED†† (%)	12 TNT YIELD FOR CHARGE‡ (%)	13 PARTICLE SIZE D‡‡ (μ)	14 LAYER THICKNESS□ (μ)
100	100	5	96	100	96	28	14
80	41.5	6.25	72	97	69	55	11.4
64	28.8	7.8	52	94	49	88	12.7
51	21	9.8	35	92	32	130	13.7
40	15.7	12.5	21	90	19	175	13.7
32	12.2	15.6	12	89	10.6	210	12.8
25	9.2						
20	7.3						
16	5.7						

NOTE: Both parts of table based on charge weight of 27 gm.

* $1 - \left(1 - w_r\right)^{1/3}$

** $\dfrac{\left(5/w_r\right)}{1}$

† From Fig. 7-2

†† $\left(5 + w_r\right)^{1/6}$

‡ Col. 10 x 11

‡‡ From F   7-4

□ $\dfrac{(Col. 2 \times 13)}{2}$
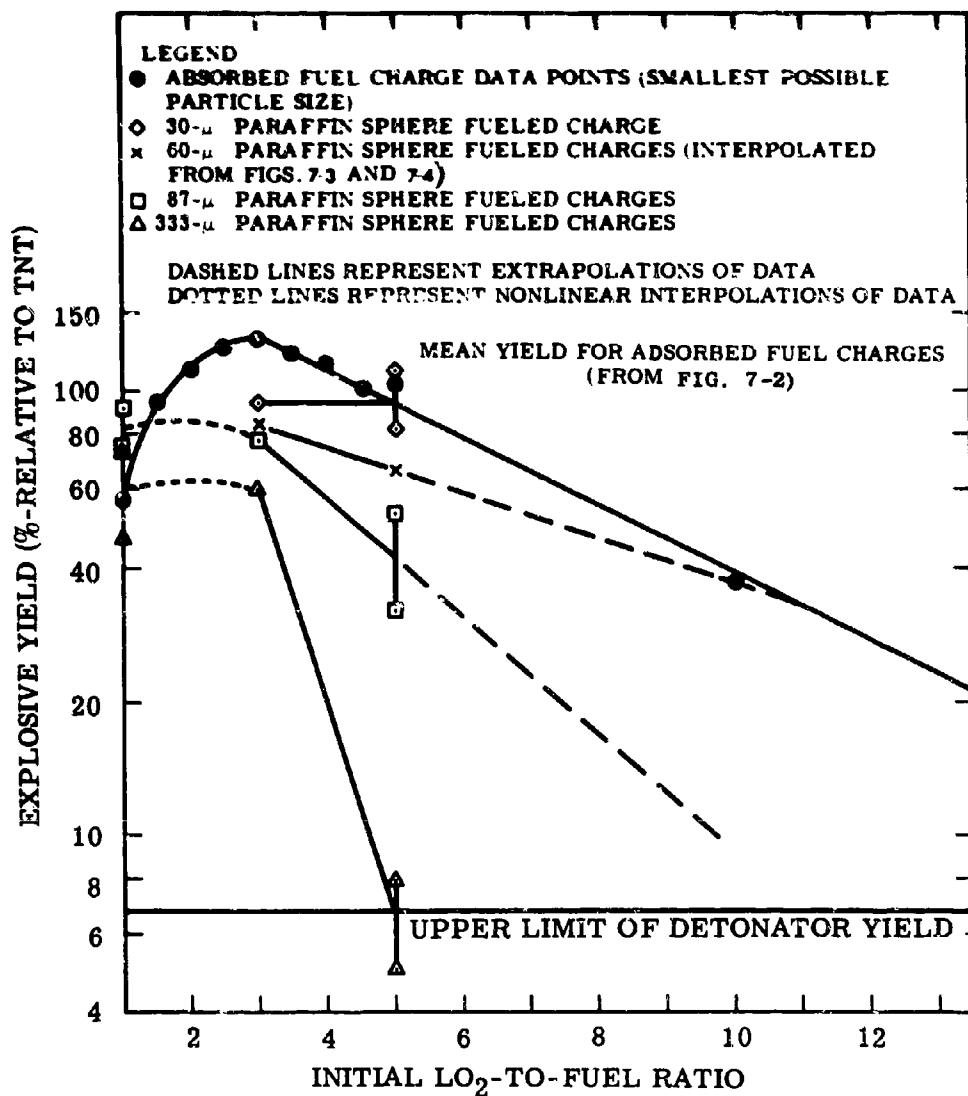
Fig. 7-6. Summary of Current Data and Hypotheses Regarding Yield
           Dependence on Fuel Particle Size

or if more than one bubble is generated,

$$q = \frac{L_p}{6RTD_p^2 \Delta t} \sum D_b^3$$

The experimental results are indicated in Table 7-3 and a comparison is made in Fig. 7-10 of the measured heat transfer rates with those of the pool boiling region of the characteristic curves for LN_2 and LO_2 taken from Ref. 7-7, p. 157. The measurements were average heat transfer rates over an interval of time, which implies that they were average rates over a temperature interval (confined to the film boiling region). However, during the phase change of an RP-1 particle, the particle temperature remains relatively constant (the RP-1 freezing temperature) throughout a larger portion of the cooling

Table 7-3

EXPERIMENTAL HEAT TRANSFER COEFFICIENTS

Particle Radius (μ)	q (cal/cm^2-sec)	Duration of Measurement (sec)	Number of Bubbles Generated
250	2.8	0.05	3
425	3.1	0.09	5
500	0.15[*]	0.12	2
500	8.4	0.05	6
500	8.8	0.05	10
680	3.8	0.04	4
680	5.0	0.05	5
1,100	1.9	0.07	6

[*]The generation of only two bubbles over a relatively long period resulted in an unusually low heat transfer rate from this particle. This was apparently due to the particle having less motion through the fluid than others. Determining if such rates are common would require more extensive observations.

Ultimately, tests with a charge size 8 times larger by weight (8 oz),
or 2 times larger in all linear dimensions than the 27-gm charges, are
required to provide a preliminary verification of the hypothesis that particles
twice as large will then be consumed to the same degree. If this hypothesis
is verified at the 8-oz charge size, it would be desirable to determine if
it can weather an additional factor of 5 in linear dimension scaling, or a
total linear scaling range of 20 to 30.

HEAT TRANSFER STUDY

The explosive yield of LO_2/RP-1 mixtures is known to depend on the
particle size or interface area per unit volume of the propellants. Break-
up of RP-1 is assumed to proceed by small drops being separated from the
larger mass of fuel that is in contact with LO_2. The small drops of RP-1
freeze rapidly in the LO_2 to form a fine-grained mixture capable of large
explosive yield. The question arises as to whether a major proportion of
the fuel particles in a fine-grained mixture in LO_2 could, at any time in
the breakup process, be in that stage of their cooling process in which they
are individually enclosed in gaseous oxygen envelopes. The possibility of
such a situation developing will obviously depend on the cooling times of
small RP-1 particles in LO_2 being of the same order of magnitude as the time
required for the entire fuel mass to break up into drops. The importance of
the situation, if it does, in fact, occur, is that charges composed of
particles with gaseous envelopes (due to boiling at the particle surface)
might have explosive properties different from those of charges in which the
fuel-particle surfaces are in contact with oxygen in the liquid phase. A
charge composed of particles of fuel enveloped in gaseous oxygen would
necessarily be reduced in charge density because of the presence of the boiling
films on the fuel-particle surfaces. It might also develop lower explosive
yield, owing to the lower concentration of oxygen in the gaseous film at the
fuel surface and the consequently less favorable conditions for a rapid
reaction to support the detonation wave.

The cooling rates of small RP-1 particles in LO_2 have been calculated
as a part of the study of this phenomenon. The objective was to determine
whether the time required for small RP-1 particles to cool in LO_2 is of the
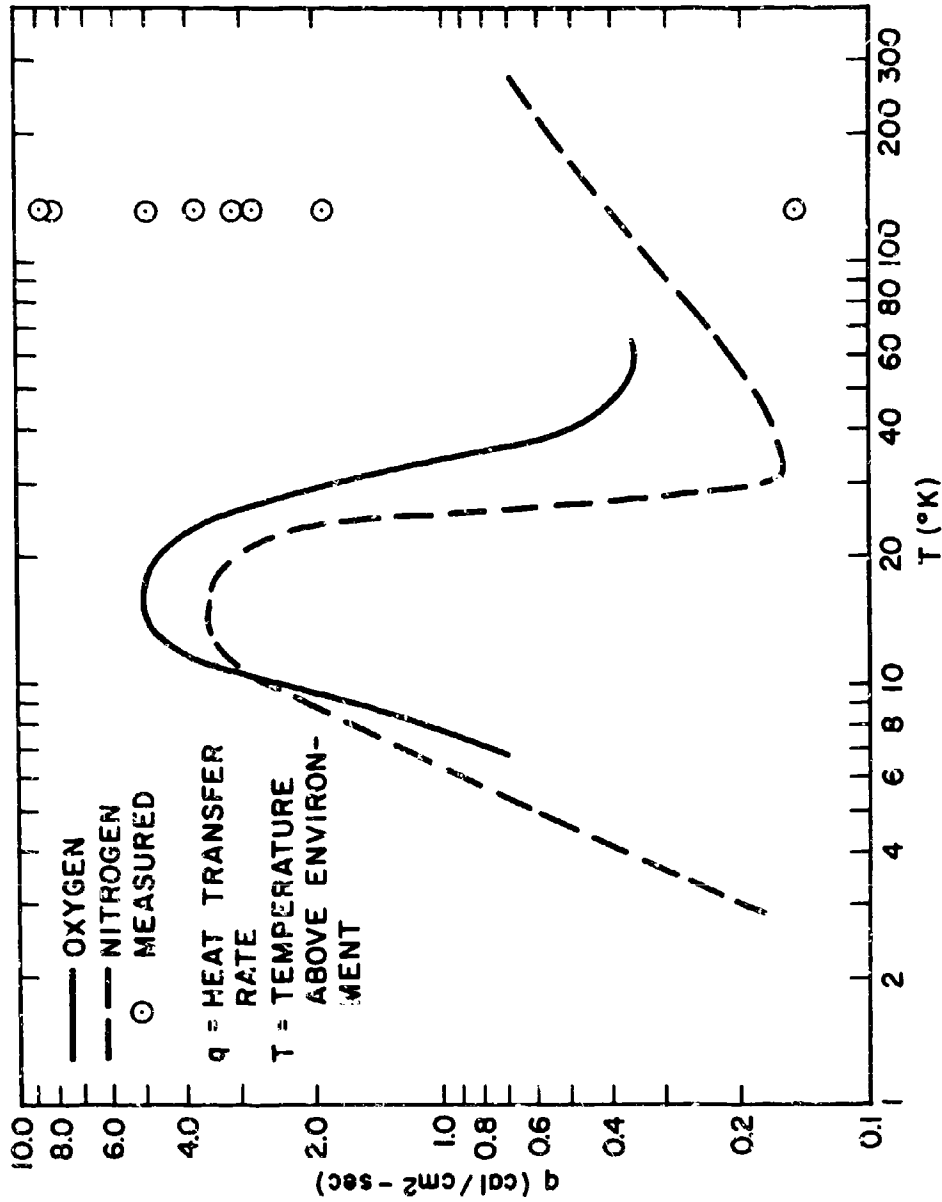
Fig. 7-10. Comparison of Measured Heat Transfer Rates and Typical Pool Boiling Curves

same order of magnitude or much less than the time required for large masses
of propellants to break up into explosive mixtures. If the cooling times
were an order of magnitude (or more) less than the time required for breakup
of major propellant masses, it could be concluded that only an insignificant
proportion of fuel drops capable of contributing to explosive yield could be
in the cooling process at a given point in time, and hence, the problem of
their possible effect on the yield could be ignored.

In addition to providing this insight, the cooling rate of small par-
ticles of RP-1 fuel in LO_2 is of interest because it is one aspect of the
overall heat transfer process between RP-1 fuel and LO_2. It is thought
that the boiling heat transfer between the fuel and LO_2 may be the major
source of agitation causing mixing of the two propellants in most cases.

The fuel-particle size range of interest was that capable of producing
substantial explosive yields when charges so constituted were detonated
when mixed with LO_2. The determination of this range of fuel-particle size
and its variation with charge size was the objective of our program, described
elsewhere in this section, to study the effect of fuel-particle size on the
explosive yield of charges composed of LO_2 and paraffin particles. The latter
investigation was not continued beyond the smaller charge size, so that no
information was obtained as to what fuel-particle sizes could be expected to
produce large explosive yields at the larger scale sizes.

The size of the largest particles of interest in the investigation of
fuel-particle cooling rates is, therefore, not presently known. Owing to
this fact, the calculation of particle cooling rates was limited to particles
not larger than about 1 mm in diameter for the present.

In the course of calculating the particle cooling rates, it was found
that the weakest point in the calculation was the value to be assigned to
the boiling heat transfer coefficient for LO_2 boiling on the surface of RP-1
fuel particles. To strengthen this part of the work, an experimental measure-
ment was made of this heat transfer coefficient.

period and also throughout most of the measurements. In Fig. 7-10, therefore, the measured values are plotted at the RP-1 freezing temperature. The RP-1 heat transfer rates are seen to be in the neighborhood of, but slightly higher than, those for other cases.

Complete agreement of the data is not to be expected, owing to the large number of variables known to affect boiling heat transfer and the fact that the RP-1 fuel particles constitute a heat transfer surface different from any for which heat transfer rates have been reported heretofore. A systematic presentation of the effect of variables affecting boiling heat transfer has been made by J. W. Westwater (Ref. 7-8), in which data are presented to show that a factor of two in boiling heat transfer coefficient can result from a change of material composing the heat transfer surface alone. Comparable effects attend changes in other significant variables.

Since the measurements were made in an effort to decrease the uncertainty of calculations of cooling times based on heat transfer coefficients reported for fixed, solid heater surfaces and since the results suggest that somewhat higher coefficients are more appropriate for RP-1 spheres, the effect of applying higher values on cooling times (ranging from 2.5 to 10 times) for particles having radii of 5.5 and 220 μ has been illustrated in Figs. 7-11 and 7-12. A relationship closely approximating an inverse is seen to exist between increase of heat transfer coefficient and time to reduce temperature difference between particle surface and LO_2 to a small value, say, 40°K. That is, increasing the heat transfer coefficient by a factor of ten requires one-tenth the time to reach $\Delta T = 90$°K.

Throughout the experiment, there occasionally were particles observed in which the manner of bubble generation was distinctly different in that relatively small bubbles left the particle but at a relatively high rate. Further, the particle had no observable gaseous envelope, and on all occasions such particles descended through the liquid, suggesting that there was probably little or no gaseous envelope. These particles had radii less than about 450 μ (however, only four such particles were observed) and were observed at times greater than about 0.15 sec. They had apparently extended into the nucleate boiling region. In particular, two of the particles had radii of 425 and 340 μ

Calculation of Particle Cooling Rates

In the computation of the particle cooling rate, it is assumed that
the particles remain spherical in shape. This assumption is valid for
particles sufficiently small that forces due to surface tension greatly
exceed those due to gravity and inertia. In the case of larger masses of
fuel, for which gravity and inertial forces predominate, the agitation of
the fluids due to boiling heat transfer between RP-1 and LO_2 can be expected
to act on the mass of fuel, continuously deforming its shape, and temper-
ature gradients within the mass at any time must also be a function of the
changing shape of the mass of fuel. Any analytical approach to the cal-
culation of the cooling rates of the larger masses of fuel in LO_2 would
need to consider the changing shape of the fluid mass and its effect on
the temperature gradients within the mass.

Within the particle of fuel, heat is transferred by conduction (molec-
ular diffusion of heat) and possibly by convection as long as the fuel
remains liquid within the particle. Similarity of systems undergoing free
convection is measured in terms of Grashof's number:

$$G = \frac{\beta \Theta_g L^3 \rho^2}{\mu}$$

where

β = thermal coefficient of expansion

Θ = temperature

g = acceleration of gravity

L = a characteristic linear dimension of the system

ρ = density of the fluid

μ = fluid viscosity

The appearance of L to the third power in Grashof's number indicates
that free convection within otherwise similar particles of fuel must decrease
very rapidly as their diameter is reduced. It has therefore been assumed,

7-23

AFRPL-TR-68-92

RADIUS = 5.5 μ

T = TEMPERATURE OF THE RP-1 SURFACE
ABOVE 90°K (°K)

t = TIME FROM IMMERSION (SEC)

h, USING A HEAT TRANSFER COEFFICIENT OF
h = 6.0 ×10⁻³ CAL/CM²-SEC-°K FOR
FIXED, SOLID SURFACES

4h, 10h, USING HEAT TRANSFER COEFFICIENTS
OF 4 AND 10 TIMES h
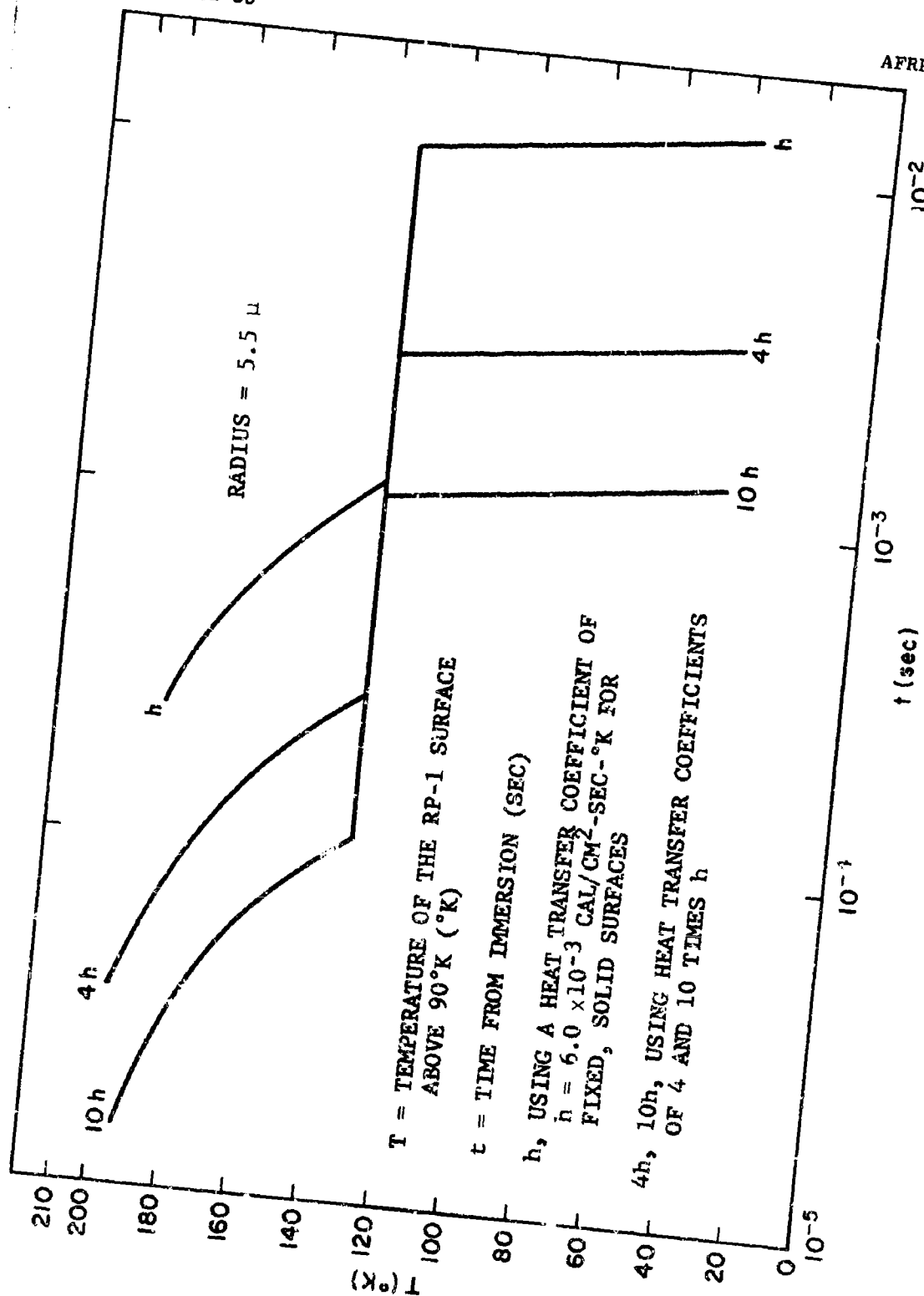
Fig. 7-11. Cooling Curves of 5.5-μ RP-1 Spheres in Liquid Oxygen

7-35
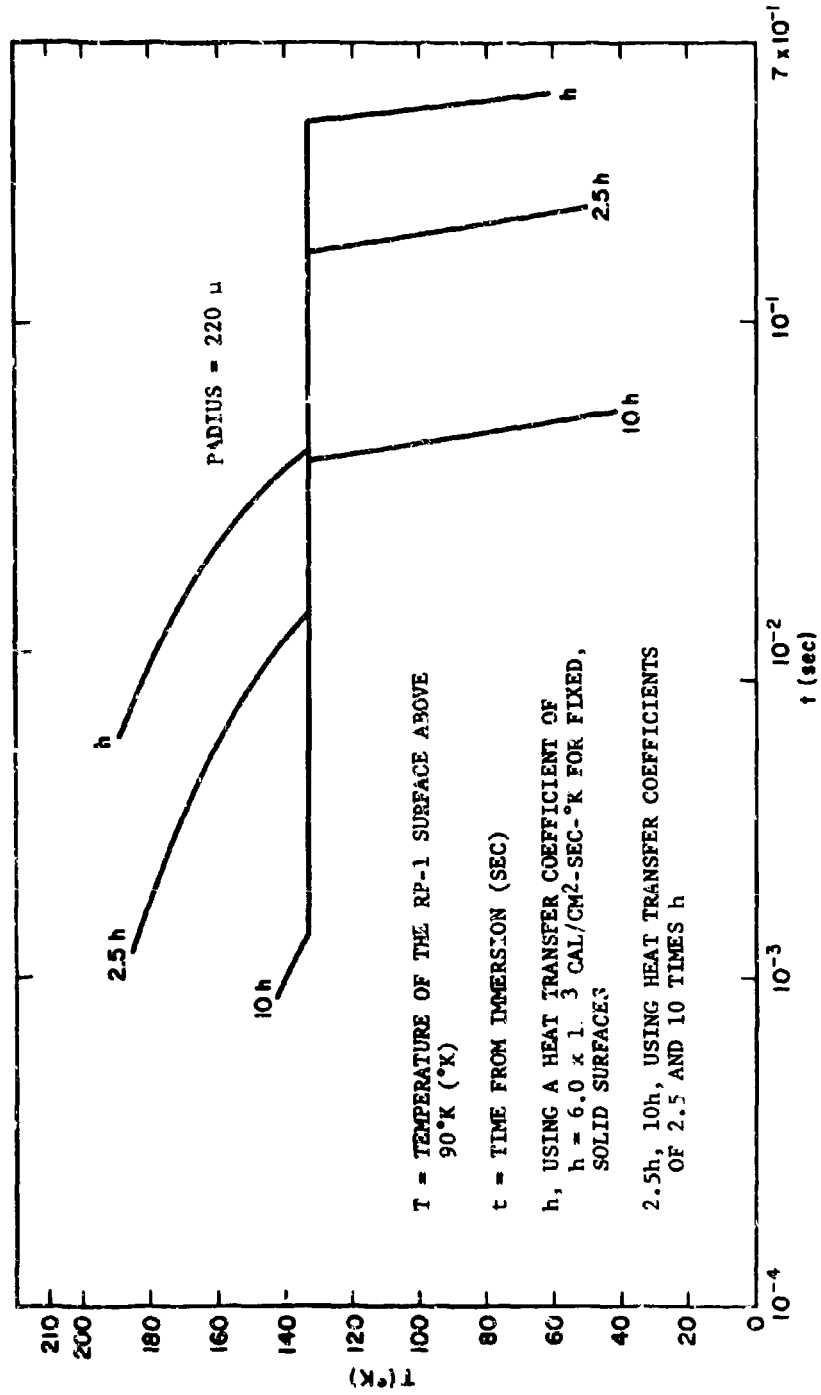
Fig. 7-12. Cooling Curves of 220μ RP-1 Spheres in Liquid Oxygen

that fuel particles small enough to maintain their shape approximately
constant will support negligible internal convection.

For these particles, the cooling process can be represented as conduc-
tion of heat within a sphere with a variable flux at the boundary. The
boundary flux is that corresponding to the LC_2 boiling regime prevalent at
the particle surface.

No satisfactory theoretical derivation of the flux obtained in boiling
heat transfer is available, so that it is best to use experimentally deter-
mined values. Representative curves are shown in Fig. 7-7, in which the
heat flux is plotted against the difference in temperature of the heat
transfer surface and the saturation temperature of the boiling liquid. The
curves are not single-valued, i.e, the same heat flux can be obtained at
more than one value of temperature difference.

This effect is attributed to the existence of two different regimes
of boiling heat transfer, nucleate and film boiling, with a third transi-
tion regime between them. It is worth noting that the boiling heat flux
changes by a factor of 10 to 20 in passing from the nucleate boiling maximum
to the minimum at the start of the film boiling region.

The heat transfer fluxes corresponding to the same value of tempera-
ture difference have varied in different investigations by factors of 2
to 5. The cause of this variation is not known, but is thought to be due
to variations in the condition of the heat transfer surface. Richards,
Steward, and Jacobs in National Bureau of Standards Technical Note No. 122,
dated October 1961, have surveyed the literature on heat transfer from
solid surfaces to cryogenic fluids. Their conclusion states, in part, "The
existing experimental data on heat transfer between solid surfaces and
cryogenic liquids (helium, hydrogen, nitrogen, and oxygen) vary appreciably
between experimenters, even when heater geometries and orientations, pressures,
etc. are comparable. The variations are both in the magnitude of the heat
flux and in the shape of the heat-flux-versus-temperature-difference curves,
and are possibly due to uncontrolled parameters such as surface roughness and
contamination."
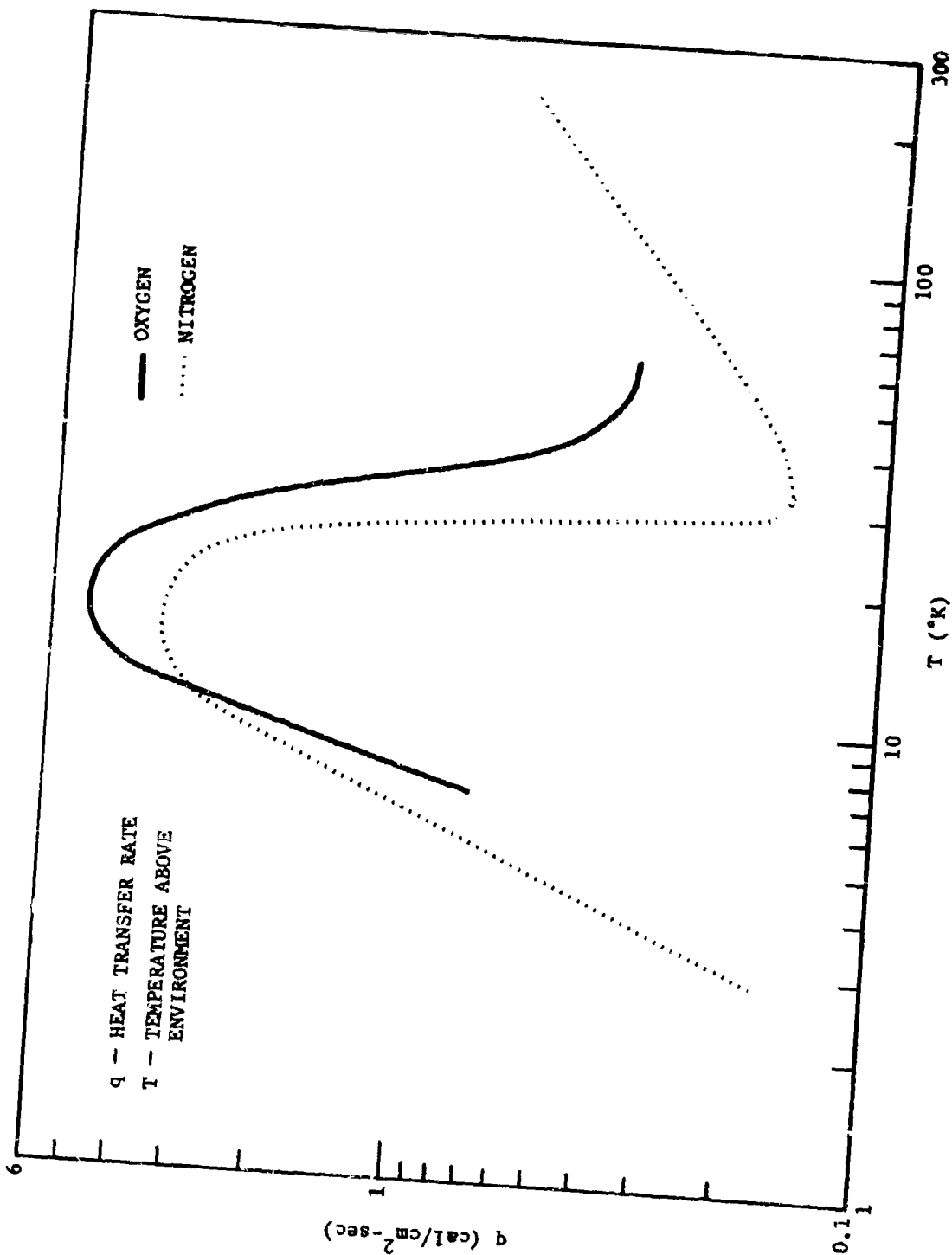
Fig. 7-7 Representative Curves Relating the Flux Obtained as a Function of the Difference in Temperature Between the Heat Transfer Surface and the Saturated Liquid for LO_2 and LN_2

OXYGEN

NITROGEN

q — HEAT TRANSFER RATE

T — TEMPERATURE ABOVE ENVIRONMENT

T (°K)

q (cal/cm²-sec)

and were observed beginning 0.27 and 0.54 sec after injection. Two other
particles, too small to resolve, left bubble trails commencing at 0.16 and 0.21
sec.

Another phenomenon clearly observed only once was the sudden disintegration
of a particle. This was accompanied by the rapid generation of a large bubble
apparently due to "new" surfaces at relatively high temperatures (for
sufficiently large particles) suddenly being exposed to the cryogenic, with a
consequent increase in area and heat transfer coefficient.

Summary

Application of the results of the fuel-particle cooling rate calculations
to deciding the question of whether a significant fraction of the fuel part-
icles composing a high-yield LO_2/RP-1 mixture can be in the film boiling,
regime at any instant of time is not presently possible because it is not yet
known what fuel particle sizes contribute to large explosive yield in charge
sizes greater than 27 gm. Until this information is available and the cooling
rate calculations are applied it is not known whether this study needs to be
pursued further. If it is found that film boiling can occur simultaneously
on a major fraction of the fuel particles capable of contributing to explosive
yield, development of a test charge of known LO_2/RP-1 ratio and particle size
will be needed that would be capable of being formed with or without a boiling
regime present at its LO_2 — fuel interfaces. The relative explosive yield in
these two conditions would then be indicative of the importance of film
boiling in affecting explosive yield.

MIXING STUDY

It is generally recognized that the mixing of propellants after a pro-
pellant spillage is an important process affecting the explosive yield of
the mixture. The specific properties of such mixtures that determine their
explosive yield are not yet well established, so that the term "mixing" can
not presently be defined and quantified, but must instead simply be synonymous
with potential explosive yield.

At present, the mechanism by which spilled propellants form explosive mixtures is not understood. In the case of cryogenic propellants, it is not known to what extent, and under what conditions, the mixing of the propellants is due to flow phenomena, such as turbulence and spattering on impact, or to the effects of boiling heat transfer, whereby the agitation due to boiling of the cryogenic may break up the warmer propellant of the combination to produce a larger heat transfer interface and, hence, more violent boiling.

The importance of understanding the mechanism by which mixing proceeds in various circumstances stems from the fact that the variables affecting the mixing process can not be deduced without some knowledge of the mechanism involved. Thus, if one sought to assess the effect on its explosive potential of changing one of the variables of the propellant spillage process, it would be necessary to know the principal mechanism by which mixing was proceeding in order to deduce the effect of that variable on the process and on explosive yield. In addition it is necessary to know the important variables affecting the mixing process in each of the configurations in which explosive testing is conducted so that correlation of yield data between scale sizes may be accomplished.

The following proposes a method by which effects of mixing due to flow conditions can be separated from those due to heat transfer effects. The method would apply only to the study of these effects in the LO_2/RP-1 propellant combination; however, the results should, by analogy, aid in understanding the mixing process in other cryogenic combinations.

The method depends on the use of a simulant for RP-1 capable of forming explosive mixtures with LO_2 to give the same yield as RP-1, but differing from RP-1 by remaining liquid at 90.1°K, the normal boiling point of LO_2. The explosive yield of spillage explosions using the simulant fuel, precooled to 90.1°K, would be compared with those of RP-1/LO_2 spillages under otherwise identical conditions, but with the RP-1 initially at room temperature. The simulant fuel, having been cooled to 90.1°K before the spill, would transfer no heat to the LO_2, so that any mixing would be due to phenomena other than heat transfer, such as flow or impact conditions. The RP-1/LO_2 spillage in the same conditions could mix by both a heat transfer and/or flow mechanism.

7-38

No experimental data on the film boiling of liquid oxygen under free convection were found. It was assumed that the curve for liquid oxygen in the film boiling region would parallel that for liquid nitrogen in this region. All of the experimental measurements of boiling heat transfer appear to have employed solid heat transfer surfaces, whereas fuel particles are liquid in part of the cooling process.

In the case of small fuel particles in LO_2, the uncertainties in the boiling heat flux (indicated above) are increased because the heat flux at the particle surface changes rapidly in time, whereas the experimental measurements of boiling heat transfer referred to above have been made under nontransient conditions.

The uncertainties in the boiling heat transfer rate limit the precision it is profitable to seek in calculating the cooling rate of fuel particles. Inspection of the curve for liquid nitrogen in Fig. 7-7 indicates that the boiling heat transfer coefficient, defined as the boiling heat flux divided by the corresponding difference in temperature between particle surface and saturated liquid, changes by about 50 percent as the particle surface cools from room temperature to the lower end of the film boiling regime. Within this film boiling region, therefore, a constant heat transfer coefficient, taken as the average over the region, represents the boiling heat transfer coefficient as well as it is known. A constant heat transfer coefficient was, therefore, assumed for LO_2 within the film boiling region.

In obtaining the heat flow within the particle, it is necessary to account for the freezing of the RP-1 during the cooling process. Analytical solutions of the diffusion of heat with change of phase do not include the case of constant flux or constant heat transfer coefficient at the boundary for spherical geometry (Ref. 7-5, p. 291) A solution is available, however, for diffusion of heat in a sphere with constant heat transfer coefficient at the boundary if no change of phase occurs (Ref. 7-5, p. 237). This solution has been presented as a chart by P. J. Schneider (Ref. 7-6, p. 97). In applying this solution to the case of RP-1 fuel particles in the period prior to the onset of freezing in the particle, it was found that within particles of diameter up to about 1 mm, the temperature gradients were very

The relative explosive yields measured for the two kinds of fuels in the same spillage geometry would constitute a measure of the fraction of total mixing due to flow conditions alone for that geometry. One would expect this fraction to be a maximum under violent flow conditions, such as impact, and very low for in-tank mixing.

Butene-1 ($CH_3-CH_2-CH = CH_2$) appears to be an optimum RP-1 simulant for the method outlined above. Some properties of butene-1 are tabulated below along with those of RP-1.

Fuel	Hydrogen Carbon Ratio	Heat of Combustion (Kcal/gm) (H_2O liq., CO_2 gas)	Freezing Point (°C)	Boiling Point (°C)
RP-1	1.9	10,370	-40 max.	185 to 274
Butene-1	2.0	11,490	-185.35	-6.25

The hydrogen-to-carbon ratio and heat of combustion, which largely determine the explosive yield of hydrocarbons in perfect mixtures with LO_2, differ by 5 and 11 percent, respectively. The explosive yield does not change linearly with these variables, however, so that the difference in explosive yield between charges of otherwise identical composition containing RP-1 and butene-1 should be much less than 11 percent. This question can be resolved experimentally by comparing the explosive yield of kieselguhr charges containing butene-1 with that of charges containing RP-1.

Because the butene-1 would be cooled to the close vicinity of 90.1°K (normal LO_2 boiling point) before being spilled to form the mixture with LO_2, its viscosity in this temperature range is of importance with respect to its simulation of the flow properties of RP-1 at room temperature and slightly below when spilled in the same geometry.

Some preliminary measurements have been made of the viscosity of butene-1 near the boiling temperature of LO_2. These measurements are tabulated below.

flat, i.e., at any time after the start of cooling, the centers of the spheres
differed by only a few degrees from the temperatures of their surfaces.
Thus, all parts of the spheres reached the freezing temperature of the fuel
nearly simultaneously. For this range of sizes, negligible error resulted
if the cooling of the particle to the bottom of the film boiling regime of
LO_2 was calculated in three separate stages. In the first stage, the cooling
curve of the liquid particle was obtained from room temperature to the freezing
point of RP-1 fuel, by means of the solution for constant boundary heat transfer
coefficient. In the second stage, the time for the latent heat of fusion of
the fuel contained in the particle to be removed was computed by means of the
rate corresponding to the boiling heat flux prevalent at the particle surface
at the fuel freezing temperature. In the third stage, the cooling curve for
the solid particle was obtained from the fuel freezing point to the bottom of
the film boiling regime of LO_2 by the same method used in the first stage.

The results[*] are presented in Figs. 7-8 and 7-9, in which the tempera-
tures at the surfaces and centers of spheres of RP-1 fuel of various sizes
up to about 1 mm diameter are shown as a function of time after immersion
in LO_2. The time difference between the cooling curve for the surface and
center of each particle becomes greater as particle size increases, indicating
steepening of the temperature gradients within the particle as diameter in-
creases. The error of the method of calculation should be negligible as long
as the time difference between the cooling curves for the center and surface
of the particle is small compared with the time the particle temperature remains
at the RP-1 freezing temperature.

Experimental Measurement of Boiling Heat Transfer Coefficients of LN_2 on
RP-1 Particles

As indicated in the foregoing, the major uncertainty in the calculation
of the cooling curves by any method is in specifying the magnitude of heat

---

[*] Values of heat transfer coefficient and RP-1 thermal properties used in the
calculation are: heat transfer coefficient = 6.0×10^3 cal/cm^2-sec-°K
heat of fusion = 50 cal/gm; thermal conductivity = 3.32×10^{-4} cal/cm^2-
sec-°K; density = 0.8 gm/cm^3; and heat capacity = 0.2 cal/gm-°K.

Temp (°C)	Viscosity (cp)	
-182	620	
-180	200	99% pure butene-1
-169	6.3	
-180	116	
-170	10.7	95% pure butene-1

Boiling Point LO_2 = -183.0°C

The viscosity of RP-1 is specified as not greater than 13.2 cp at -34.4°C, and is about 3 cp at room temperature.

Summary

It appears that butene-1, precooled near 90.1°K, can be made to simulate the flow of RP-1 to a satisfactory approximation for spillages in the range of 40 lb or greater. A positive statement in this regard is not easy to make, because it must be expected that the viscosity of RP-1 increases during the course of its flow due to its being cooled by LO_2, while the viscosity of precooled butene-1 should either remain constant or decrease during the flow. Much light could be shed on this question by examining high-speed photos of butene-1 and RP-1 in the same flow condition. If the flow velocities and patterns at the same time after spillage were substantially the same for the two cases, it could be assumed that viscosity differences had negligible effect on the flow.

The logical next steps in pursuing this portion of the mixing study are listed below.

   a. Conduct tests of butene-1 with LO_2 in kieselguhr charges to confirm its explosive equivalence to LO_2/RP-1 charges when perfectly mixed.

   b. Photograph spill tests of cold butene-1 and of RP-1 at room temperature to establish similarity of flow of the two fuels.

   c. Conduct scaled explosive tests in appropriate mixing modes with cold butene-1 as fuel simulant for comparison with otherwise identical tests using RP-1 at room temperature.

(i)   Choose at least one mixing mode having low kinetic
        energy in fluid flow, but having easily measurable yield
        with RP-1 as fuel.

(ii)   Choose at least one mixing mode having high kinetic energy
        in fluid flow, but with measurable yield with RP-1 as fuel.

RECOMMENDED ADDITIONAL WORK

As discussed in the introduction to this section the studies described
above constituted the initial phase of an overall program to investigate
the basic phenomena involved in propellant mixing and explosion processes.
To properly pursue this program requires proceeding as indicated with the
above areas of work and initiating certain additional studies as described
below.

For determining the properties of the propellant mixture that determine
its explosive characteristics, two additional study areas are of prime concern:

● **Uniformity of Mix.** Another aspect of spatial distribution
  besides charge geometry proposed as a possible definitive
  property of propellant spillages is nonuniformity of $LO_2/RP-1$
  ratio and particle size through the mixture. If the explosive
  yield of propellant mixtures as a function of their particle
  size and $LO_2/RP-1$ ratio is known from the particle size studies,
  the effect of nonuniformity of $LO_2/RP-1$ ratio or particle size
  on explosive yield could be estimated by adding up the yield
  contributions from each part of the nonhomogeneous charge according
  to its local $LO_2/RP-1$ ratio and particle size. Measurement of
  the explosive yields of charges having known nonuniform dis-
  tributions of paraffin particles can then be made in several
  charge sizes to test the accuracy of the estimated yields.

● **Gross Interface Geometry (Layered-Charge Study).** The possibility
  that distributions of the two propellants may commonly occur
  in which the explosion of well-mixed portions of the spillage
  could provide the impulse to force the mixing of adjacent
  volumes of bulk propellant in time for these previously un-
  mixed propellants to contribute to the explosive effects has
  been suggested. It has been tacitly assumed heretofore that
  any development of interface between the two propellants,
  to be capable of affecting the explosive yield of the mixture,
  must occur prior to ignition. This assumption was based on
  the premise that explosive reaction occuring at propellant
  interfaces would generally drive the two propellants apart,
  thus terminating any further development of interface between
  them.

In certain mixing modes tested in Project PYRO, viz., the diaphragm-rupture tests with hypergolic propellants and the early-ignition diaphragm-rupture tests with cryogenic propellants, such an explosively driven termination of the mixing process does indeed appear to prevail, as evidenced by the very low yields obtained.

For mixing modes which lead to highly convoluted or multilayered boundaries, however, the available evidence suggests that significant additional mixing can occur after ignition. Presumably this would occur because reaction at one interface, although tending to separate the propellants in that region, can force them together at another interface.

Examples of mixing modes in this category included the Aerojet high-interface-area, low-velocity drop tests (Ref. 7-9) and the hypergolic high-velocity impact tests conducted under the PYRO program at NOTS.

The definitive properties of propellant mixtures of concern in regard to post-ignition mixing should be relatively easy to identify, and it should be relatively straightforward to determine their effects experimentally. Such a phenomenon, if it occurs, would probably be found in convoluted, interlayered or multiply connected spatial distributions of the propellants. A series of tests have, therefore, been planned in which the explosive yields of such charges can be measured. The charges would be composed of alternate masses of fuel and LO_2, with conventional explosive in the form of sheets intervening.

The explosive sheets will provide a convenient simulation of explosive propellant mixtures at the interface between the bulk propellant masses, with the advantage that the explosive yield of the sheet explosive will be accurately known. Any measured explosive yield of such charges that is significantly greater than the known yield of the sheet explosive will be evidence of a contribution by the propellants due to post-ignition mixing.

The future course of the investigations of mechanisms leading to the development of the definitive properties in a propellant spillage will depend to some extent on the results obtained from the cold-fuel mixing study outlined earlier and thus cannot be defined in detail. However, the work would generally be directed toward study of fuel break up and study of more general flow processes.

In the fuel breakup study, once it has been determined what mechanism supplies the energy to break up RP-1 fuel in spillages with LO_2, it should be possible to deduce the variables likely to be important in the process. Thus, if the breakup was due only to fluid friction, variables such as fluid viscosity, velocity, and characteristic length would be dominant. If boiling heat transfer supplied the breakup energy, variables such as thermal conductivity, heat transfer coefficient, interface area, etc. would be important. In any case, the tentative identification of controlling variables depends on the construction of a simplified theoretical model of the breakup process, in which the interactions of the various forces leading to breakup of the fuel are developed conceptually.

Following the development of a simplified theoretical model (or models) of the breakup process in the more important mixing modes tested in Project PYRO, a series of experimental tests would be conducted to find the dependence of fuel breakup on each of the hypothetical controlling variables predicted by the simplified theoretical model.

These experiments would employ a method by which the final surface area and other particulate properties of the fuel can be measured after the fuel breakup process is complete. The problem of representative sampling can be disposed of by collecting all of the fuel in each test for surface area measurement. The planned experimental approach involves use of a model regime in which the temperatures of all important processes would be about 75 to 100°C higher than in the actual event, but the temperature differences and the heat transfer phenomena would, as nearly as possible, be maintained the same as in the actual process. In this kind of model, all the heat transfer phenomena and the turbulence leading to fuel breakup should be substantially the same as in the actual process, but the melting point of the fuel would be slightly

above room temperature so that the examination and measurement of its part-
iculate properties would be greatly facilitated. Molten wax, at an initial
temperature about 65 to 75°C above its melting point, would simulate the fuel
in the model. A mixture of two Freon compounds (Freon 14; CF_4; b.p. 145°K
and Freon 23; CHF_3; b.p. 191°K) having a ̲iling point of about 165 to 180°K
could be used to simulate LO_2. The use of this simulant for LO_2 would provide
for the initial temperature difference — as well as the temperature difference
at the fuel freezing point between fuel surface and cryogenic — to be the
same as the corresponding quantities in the LO_2/RP-1 interaction being modeled.
The heat of vaporization per unit weight of the LO_2 simulant would be nearly
the same as that of LO_2, so that the boiling heat transfer and the turbulence
thereby produced should simulate the LO_2/RP-1 interaction very well, assuming
that the boiling heat transfer rate as a function of the temperature difference
between fuel and cryogenic is the same for the Freon as for LO_2.

The first use of the Molten wax results would be to establish whether
the hypothetical controlling variables do, in fact, exert a major influence
on the breakup of the fuel and, hence, to test the theoretical model from
which they were deduced. The test results would ultimately form the basis
of a correlation formula expressing the fuel particle size (or whatever
aspect of particle size had previously been found to be definitive with respect
to explosive yield) as ̲ function of its controlling variables in dimensionless
form, from which the fuel breakup scaling relationship would be obtainable.

The following steps are anticipated.

a. Develop simplified theoretical models of fuel breakup in various
    mixing modes.

b. Conduct measurements of interface area developed in chosen mixing
    modes by means of molten wax techniques, varying parameters suspected
    as controlling variables from simple theoretical models developed
    ̲u item (a).

c. Develop correlation formulae from data obtained in (b), expressing
    interface per unit volume as a function of controlling variables
    in dimensionless form.

The additional flow process study would primarily be concerned with those
processes leading to propellant contact. The objective would be to find

whether the fraction of propellants that arrive in sufficiently close
juxtaposition to one another to participate in the development of potential
explosive yield change with scale and – if such a change is found – to
correlate the fractions of propellants so engaged with the variables con-
trolling their change.

The approach to be followed would be to develop sir 'ified theoretical
hydrodynamic models that best represent the major features of the fluid flow
in each mixing mode, using as a guide, appropriate photography (taken at
several scale sizes) of flow in the more important mixing modes tested in
Project PYRO. From these theoretical models, expressions relating the
fraction of each propellant to its maximum distance from an $LO_2/RP-1$ inter-
face as a function of time will be derived. The effect of scale changes on
these relationships will be deduced.

In some geometries, the flow instabilities either due to fluid friction
or boiling heat transfer may play a dominant role in determining the total
fraction of propellants that participate in development of potential explosive
yield. In such cases, it will be necessary to investigate the effect of scale
changes on these processes.

Section 7

REFERENCES

7-1. Broadview Research and Development, Laboratory Micro-Scale Tests, High Risk Program (U), Monthly Progress Report, BRD-56-9A1, August 1956 (Conf)

7-2. Broadview Research and Development, Laboratory Micro-Scale Tests, High Risk Program (U), Monthly Progress Report, BRD-56-11A1, September 1956 (Conf)

7-3. Condit, R. I., Explosive Potential of "ATLAS" Propellants (U), Final Report, BRC-57-6A1, Broadview Research Corporation, Burlingame, California, June 1957 (Conf)

7-4. Goodale, T. C., The Theoretical Heats of Explosion of Perfect Liquid Oxygen — JP-4 Fuel Mixtures and Their Probable Explosive Capabilities, Broadview Research and Development, July 1956

7-5. Carslaw, H. S. and J. C. Jaeger, Conduction of Heat in Solids, Second Edition, Oxford at The Clarendon Press, 1959

7-6. Schneider, P. J., Temperature Response Charts, John Wiley and Sons, Inc., New York, 1963

7-7. Vance, Robert W., ed., Cryogenic Technology, John Wiley and Sons, Inc., New York, 1963

7-8. Drew, Thomas B. and John W. Hoopes, Jr., eds., Advances in Chemical Engineering, Vol 1, Academic Press, Inc., New York, 1956

7-9. Pesante, R. E., M. Nishibayashi, D. G. Frutchey, R. D. Erickson, and W. J. Helm, Blast and Fireball Comparison of Cryogenic and Hypergolic Propellants, Report No. 0822-01(01)FP, prepared for NASA by Aerojet-General Corporation, 26 June 1964

Section 8
SUMMARY AND CONCLUSIONS

PURPOSE

The objective of Project PYRO was to develop a reliable philosophy for predicting the credible damage potential which may be experienced from the accidental explosion of liquid propellants during launch or test operations of missiles or space vehicles.

Such information is required for the siting of static test stands and launch facilities, for vehicle and payload design, for launch operations, etc. The propellant combinations of $N_2O_4/50\%$ UDMH - 50% N_2H_4, LO_2/RP-1, and LO_2/LH_2 were investigated.

METHOD OF APPROACH

The PYRO program included experimental determination of the blast and thermal environments resulting from various types of propellant mixtures for these liquid propellant combinations. Propellant weights up to about 100,000 lb were used for the cryogenic combinations and up to 1,000 lb for the hypergolic combination.

The generalized test conditions were selected to simulate the important classes of propellant interaction, i.e., the manner in which the two propellants come into contact with each other and mix during an accidental failure. The ways in which the propellants can mechanically interact with each other are dependent on the initial conditions of the propellants at the start of the interaction and on the nature of the boundary conditions which control or confine the flow of propellants during the spillage and mixing process. The two major boundary conditions selected for testing were confinement-by-the-missile (CBM) and confinement-by-the-ground-surface (CBGS).

The CBM condition is intended to simulate the general case where failure occurs in the intertank bulkhead and propellant mixing is confined within the tankage. The parameters of primary concern for this case are the ignition time, the size of the opening in the intertank bulkhead, the length-to-diameter ratio of the tankage, the ullage volume, and the pressure rise to cause tank rupture.

The CBGS condition simulates the situation where the propellants spill out of the tankage and mix on the ground surface (such as could occur in fallback of a vehicle on the launch pad). Major emphasis in the program has been placed on a flat ground surface, although a limited amount of data was obtained for other conditions. The parameters of primary concern for this boundary condition are the ignition time and the velocities, shapes, and relative orientation of the propellant masses at the start of their interaction.

Conceptually, propellant mixing can also occur without confinement, i.e., after the propellants spill out of the tankage but before they reach the ground, (such as could occur with a flight destruct system). Such free-fall mixing was not included in the program, however, because of the small amount of mixing anticipated. Unless there is a large velocity difference between the two propellants (which is unlikely for massive failures near the ground), there are no significant forces holding the two masses together, and even a small pressure generated by vaporization or reaction at the interface between the two masses will be sufficient to separate them and minimize mixing.

Although the generalized test conditions used resemble some actual failure modes, the intent in the program was not to investigate all credible combinations of tankage configuration, failure mode, and site geometry. There is an almost infinite number of such combinations. Rather, it was reasoned that many of these combinations would lead to similar propellant interactions and that study of several basic propellant interaction modes would be sufficient to provide a basis for evaluation or prediction under a variety of failure conditions.

The basic blast data obtained from these tests were peak overpressure and positive-phase impulse, both as a function of distance from the propellant explosion. Equivalent explosive weights at each measurement distance were

determined separately for peak overpressure and positive-phase impulse by means of standard TNT surface burst reference curves. Thermal data obtained from the tests included total heat flux, gas temperatures, and radiant heat flux.

SUMMARY OF TECHNICAL FINDINGS

The overall results obtained from the PYRO program are far too extensive in scope to fully summarize in this section, and the reader is referred to the main body of the report and the prediction method in Volume 3 for complete information. Certain of the findings, however, are sufficiently important to be emphasized here, and are discussed below.

Blast and Thermal Environment Prediction Method

The major result of Project PYRO was the development of a scientific method for predicting the blast wave and fireball characteristics of liquid propellant explosions. This method is based on the results of the basic test program in conjunction with the analytical studies and prior information regarding liquid propellant explosive behavior. The method can be applied to any given missile or space vehicle system for a wide range of specified failure modes.

In the prediction method, the thermal environment is given only as a function of propellant type and weight, while the blast environment is given as a function of a number of controlling parameters, including time of ignition for the cryogenic propellant combinations. The selection of appropriate values of the parameters needed to predict the blast environment for a specific system is considered to be the responsibility of the users of the information and in general requires a failure mode analysis of the system.

The derivation of the blast prediction method for the hypergolic propellant combination is given in Section 4 and for the cryogenic combinations in Section 5. The thermal prediction method for all propellant combinations appears in Section 6. The detailed procedures for using all prediction methods are given in Volume 3 of this report.

In general, the blast yields from hypergolic propellants are less than 2%.
Exceptions to this occur for the high-velocity impact condition, or when an ex-
plosive donor weighing more than 15% of the propellant quantity is employed.
With cryogenic propellants (LO_2/RP-1 or LO_2/LH_2) the yields will vary widely
as a function of the failure mode, ignition delay time, and several other fac-
tors. Thus, use of a single TNT equivalent yield value (such as the current
20% for LO_2/RP-1; 60% for LO_2/LH_2) may actually be far too high or too low, de-
pending on the particular system and failure conditions under consideration.

Liquid Propellant Blast Phenomena

Characteristically, the TNT equivalent weights computed from the measured
data vary both as a function of the shock wave parameter used (peak overpressure
or positive-phase impulse) and the distance from the explosion. At long dis-
tances, however, the equivalent weights tend to approach an equal and constant
value, which has been defined as the terminal equivalent weight (when expressed
as a percent of the total propellant weight).

The differences between the blast waves from liquid propellants and con-
ventional high explosives tend to get larger as the distance from the explosion
decreases. Characteristically the peak pressures from propellant explosions
tend to get smaller and impulses larger than for a similar quantity of TNT.
These differences can be large enough to significantly affect damage prediction.
Methods of modifying the blast characteristics to account for these differences
are included in the prediction method.

Effects of Factors

Ignition Time. In general, for the cryogenic combinations, the most cri-
tical parameter is the time of ignition. TNT equivalent yield values can vary
by as much as a factor of 5 between the conditions under which ignition occurs
early in the failure process and when it occurs at later times. This clearly
points out the desirability of establishing, whenever possible, that ignition
will occur at or near the earliest possible time.

Impact Velocity. Impact velocity was found to be a very significant fac-
tor in determining the yields of propellants impacting and mixing on the ground
surface (CBGS and high-velocity-impact mixing modes). Even with the storable
propellants, yields can become very high if the impact velocity exceeds several
hundred feet per second. With the cryogenic propellants, yields increase very
rapidly at much lower impact velocities, and very high yields can be obtained
from only a 100-ft drop height.

Geometry. The geometry of the tankage (L/D ratio) is a moderately signifi-
cant factor for the cryogenic combinations and must be considered in the CBM
failure condition. However, the yield does not vary over a wide range in going
from an L/D of 1.8 to 5.

Bulkhead Opening Size. The size of the bulkhead opening relative to the
tank diameter $\left(D_o/D_t \text{ ratio}\right)$ also is important in the CBM failure condition.
However, so long as the opening is less than 20% of the tank cross-sectional
area, the effect is relatively small. The maximum yield values for the 100%
open case are significantly larger than those for the 20% case, but obtaining
openings larger than 20% seems somewhat unlikely.

Ullage Volume. The large effect of ullage volume on yield was one of the
interesting results obtained from the LO_2/RP-1 CBM case. For this case it was
shown that the maximum yield (in pounds of TNT) expected from a given vehicle
when it was fully fueled was significantly less than that expected when it was
about one-half to three-fourths full. The explanation is that the much larger
ullage volume for the partially full case leads to a longer time for propellant
mixing (and thus more complete mixing) prior to tank rupture caused by the pres-
sure buildup resulting from vaporization of the LO_2. (The time of tank rupture
is considered to be the maximum credible ignition time.)

Tank Rupture Pressure Differential. The tank rupture pressure differential
(difference between tank burst pressure and initial pressure) was also found to
be significant for essentially the same reason that the initial ullage volume
was important. The larger the rupture pressure differential, the longer the
maximum available mixing time and, thus, the larger the maximum yield.

Quantity. The basic blast prediction method for full-scale quantities of cryogenic propellants was initially developed using data obtained from the 200-lb weight scale and from postulated scaling relationships based on available information regarding the propellant mixing and explosion phenomena. Specifically, the initially postulated scaling relationship was that the explosive yield (in percent of the total propellant weight) would be independent of the propellant quantity and that the time of ignition to obtain equal explosive yields would scale as the cube root of the propellant weight. The validity of the postulated scaling for the cryogenic propellant combination was tested first on the 1,000-lb weight scale and later by using propellant quantities in the range of 25,000 to 100,000 lb. In only one case did these larger scale tests result in a modification to the scaling relationships, and that was for the LO_2/RP-1 CBM condition. The results for this case showed that the yield tended to decrease with increasing weight but that the rate of decrease also tended to decrease with increasing weight, so that the yield was roughly constant above 10,000 lb and only a factor of 1.2 greater at 1,000 lb.

PROBLEM AREAS

The major problem area still remaining in regard to predicting the blast environment from liquid propellant explosions is in establishing credible ignition times for the cryogenic propellant combinations. As noted previously, very much smaller yield values can be used if it can be demonstrated that ignition will occur very early in the failure process.

Although early ignition is generally believed to be reasonably likely, at the present time no generally applicable method exists for quantitatively predicting the credible ignition time. The scope of Project PYRO did not include an investigation of the probability of ignition; and the fact that it was possible to get long times of ignitions for most of the test conditions in the PYRO program tends to make it even more difficult, without further study, to justify the assumption of early ignition. Admittedly, special precautions were taken in the test program to minimize the probability of accidental ignition and to obtain a wide range of ignition delay times. The real question is, what is the

probability of ignition as a function of time for full-scale missile and space vehicle systems? Because of the large yield reductions possible with early ignition, it is clear that this question deserves study by those responsible for design of missile and space vehicle systems.

Two basic approaches are possible to capitalize on the relatively low yields obtained from early ignition:

1. Develop a generally applicable method for predicting ignition times in the hope that the intuitive belief that it is likely to occur early will be verified.

2. Develop automated ignition systems that will ensure early ignition.

The first approach has the advantage that if it turns out as postulated, early ignition can be assured without development of new hardware. It may turn out, however, that early ignition cannot be assured in all cases, and then it would still be necessary to use the second approach for these cases. The second approach clearly offers greater assurance of providing the desired result, but it is likely to be significantly more expensive in the long run.

Since there is no clear-cut advantage within the present state of knowledge for one approach over the other, it is recommended that a two-phase program be conducted, with the first phase a preliminary study of both approaches in order to evaluate their relative potential, and the second phase the development of the approach showing the greatest potential.

Section 9

GLOSSARY AND SYMBOLS

GLOSSARY

Blast Scaling Laws: Scaling laws formulated from the general laws of similitude relating blast and environmental parameters. The most common blast scaling laws (termed "cube root scaling") relate blast wave parameters (e.g., blast pressure, P, positive-phase impulse, I, and positive-phase duration, t^+) to distance from an explosion d, and explosion weight W, as follows:

$$P = f(d/W^{1/3}) = f(\lambda)$$

$$I/W^{1/3} = h(d/W^{1/3}) = h(\lambda)$$

$$t^+/W^{1/3} = g(d/W^{1/3}) = g(\lambda)$$

The quantities $d/W^{1/3}$ and $t^+/W^{1/3}$ are commonly referred to as scaled distance and scaled time, respectively. (See SACHS SCALING LAW.)

Blast Wave: A pressure pulse (or wave) in air, propagated continuously from an explosion and characterized by an initial generally rapid rise of pressure above ambient values. The air within a blast wave moves in the direction of propagation, causing winds. (See SHOCK WAVE.)

Confinement-by-the-Missile (CBM): Condition in which an internal failure occurs and one propellant falls down onto the other. Duration of case is limited to the time the propellants are confined within the walls of the missile.

Confinement-by-the-Ground-Surface (CBGS): Test condition in which propellants interact subsequent to tank rupture, when propellants are impacting on flat horizontal surface. Both vertical and horizontal flow directions were investigated.

Vertical Flow Test Condition: Propellants impact the ground surface together.

Horizontal Flow Test Condition: Lower propellant is allowed to impact on ground surface, creating a pool prior to impact of top propellant.

Explosive Yield: The explosive potential of propellants is usually expressed in terms of their TNT equivalent yield, i.e., the amount of TNT which if put at the position of the propellant explosion would produce the same value of a particular shock wave parameter at the same distance as for the propellant explosion. The explosive yield of a given propellant explosion can be given in equivalent pounds

of TNT, although it is more common to express it in terms of the percent of the
total weight of propellants involved. The term explosive yield is usually modi-
fied by the shock wave parameter used in the calculation, e.g., peak overpressure
yield or positive-phase impulse yield.

Free-Air Overpressure (or Free-Field Overpressure): The unreflected pressure,
in excess of the ambient atmospheric pressure, created in the air by the blast
wave from an explosion.

Impulse (per unit area): The integral, with respect to time, of the overpressure
in a blast wave at a given point, the integration being carried out between the
time of arrival of the blast wave and that at which the overpressure returns to
zero at the given point. Impulse dimensions are the product of overpressure and
time, e.g., psi-seconds.

Overpressure: The transient pressure, usually expressed in pounds per square
inch, exceeding the ambient pressure, manifested in the shock (or blast) wave
from an explosion. The variation of overpressure with time depends on the energy
yield of the explosion, the type of explosive or propellant, the distance from
the point of burst, and the medium in which the explosive propellants are detona-
ted. The peak overpressure is the maximum value of the overpressure at a given
location and is generally experienced at the instant the shock (or blast) wave
reaches that location. (See SHOCK WAVE.)

Sachs Scaling Law: Scaling laws relating blast and environmental parameters
that include the effects of changes of ambient pressures. These scaling laws
are summarized below:

$$P/P_o = f'\left[d/\left(W/P_o\right)^{1/3}\right] = f'(\lambda')$$

$$I/\left(W/P_o\right)^{1/3} = h'\left[d/\left(W/P_o\right)^{1/3}\right] = h'(\lambda')$$

$$t^+/\left(W/P_o\right)^{1/3} = g'\left[d/\left(W/P_o\right)^{1/3}\right] = g'(\lambda')$$

where P = shock pressure

P_o = ambient pressure

d = distance from the charge

W = charge weight

t^+ = duration of the positive-pressure phase

I = positive-phase impulse

$$\lambda' = d/\left(W/P_o\right)^{1/3}$$

The quantities $d/\left(W/P_o\right)^{1/3}$ and $t^+/\left(W/P_o\right)^{1/3}$ are commonly referred to as Sachs scaled distance and Sachs scaled time, respectively.

Shock Front (or Pressure Front): The fairly sharp boundary between the pressure disturbance created by an explosion (in air, water, or earth) and the ambient atmosphere, water, or earth, respectively. It constitutes the front of the shock (or blast) wave.

Shock Wave: A continuously propagated pressure pulse (or wave) in the surrounding medium, which may be air, water, or earth, initiated by the expansion of the hot gases produced in an explosion. A shock wave in air is often referred to as a blast wave. The duration of a shock (or blast) wave is distinguished by two phases. First there is the positive (or compression) phase, during which the pressure rises very sharply to a value that is higher than ambient and then decreases to the ambient pressure. The duration of the positive phase increases and the maximum (peak) pressure decreases with increasing distance from an explosion of a given energy yield. In the second phase, the negative (or rarefaction) phase, the pressure falls below ambient and then returns to the ambient value. Deviations from the ambient pressure during the negative phase are never large. (See OVERPRESSURE.)

Terminal Yield: The value of the explosive yield in the region where the explosive yield becomes independent of distance from the explosion or the shock wave parameter used in the calculation. (See EXPLOSIVE YIELD.)

BLAST SYMBOLS

D = Ground distance from point of explosion (ft)

$D^* = D/W^{1/3}$ = Scaled ground distance

D_o/D_t = Intertank bulkhead opening ratio (ratio of effective circular diameter of opening in intertank bulkhead to tank diameter)

I = Positive-phase impulse (psi/msec)

$I/W^{1/3}$ = Scaled positive-phase impulse

k = Ratio of the terminal yield for a given V_u and ΔP_r to that for the standard condition of $V_u = 10\%$ and $\Delta P_r = 85$ psi

L = Propellant loading fraction (fraction of propellant tanks filled with fuel — assumes that $L = 1$ corresponds to a $V_u = 10\%$)

9-3

L/D = Propellant length-to-diameter ratio

P = Peak overpressure (psi)

ΔP_r = Difference between the tank burst pressure and the initial tank pressure

t = Propellant mixing time (for CBM case corresponds to time from initial propellant contact to ignition — for CBGS case corresponds to time from initial propellant contact on ground surface to ignition)

$t^* = t/W^{1/3}$ = Scaled propellant mixing time

t^*_{max} = Maximum scaled propellant mixing time (applicable to CBM case — corresponds to time from initial propellant contact to time for the tanks to burst due to pressure buildup from vaporization of cryogenic propellants)

t^*_{crit} = Critical scaled propellant mixing time (applicable to LO_2/RP-1 and LO_2/LH_2 CBGS case — corresponds to time from initial propellant contact on ground surface to time of maximum yield)

v = Propellant impact velocity on ground surface (or other target)

V_u = Tank ullage volume in percent of total tank volume

$V_{u\text{-eff}} = \dfrac{\Delta P_r}{85} V_u$ = Effective ullage volume for constant ΔP_r

W = Total propellant weight (lb)

W_t = Propellant weight in top tank

W_b = Propellant weight in bottom tank

Y = Explosive yield (percent of total propellant weight which acts like TNT, assuming surface burst conditions)

Y_I = Explosive yield computed from impulse data

Y_p = Explosive yield computed from peak overpressure data

Y_s = specific explosive yield (yield per pound of propellants)

Other Notation

Empirically derived constants (a, a', b, b', c, c', n, m, α, α', α'', α''', β, β_o, β_1, β_2, δ_1, γ)

Functions of variables $[f(\ ),\ g(\ ),\ h(\ )\ .\ .\ .\ ]$

THERMAL SYMBOLS

c = Specific heat (watt-sec/gm-°C)

D = Diameter (ft)

K = Thermal conductivity (watt/cm-°C)

$K' = (K\rho c/\pi)^{1/2}$

q = Heat flux density (watt/cm^2)

T_s = Temperature change (°K)

t = Time (seconds)

W = Total propellant weight (lb)

ρ = Mass density (gm/cm^3)

τ = Fireball duration (seconds)

Appendix A
BLAST INSTRUMENTATION SYSTEM

This section describes the blast instrumentation system installed at test pad 1-91, AFRPL, for the main portion of the PYRO test series. (Thermal instrumentation is described in Appendix C.) Included are a discussion of the rationale for the design of the system, the layout of the measuring stations, description of the blast sensors and mounts, and a description of the test program conducted to evaluate the blast instrumentation. Descriptions of the instrumentation systems installed at the Naval Ordnance Test Station for the high-velocity impact tests are presented in the section discussing the results from those tests.

EXPERIMENTAL ARRANGEMENT

Gauge Station Array

To provide adequate documentation of the explosive characteristics of propellant explosions, it is desirable to measure the pertinent blast characteristics as a function of both distance and azimuth. To provide this capability, the blast gauges were placed on three radial lines passing through ground zero and oriented 120 deg with respect to each other.

The basic blast-gauge system consisted of overpressure sensors on each line at several radii for each propellant weight. Since the peak overpressure decreases approximately as the negative 1.8 power of the distance over the pressure range of primary concern, 1 to 100 psi, it was convenient to space the stations at distances differing by a factor of approximately 1.8. This resulted in pressures differing by a factor of 2.5 from station to station, or a total difference in pressure over five stations of a factor of about 40. This arrangement not only provides a reasonable spacing of stations over the pressure range of interest, but also permits use of most of the same stations when the propellant weight used in the testing is increased. At the time the system was

designed, the planned propellant weights were 200, 1000, 5000, and 25,000 lb, each size differing from the previous one by a factor of 5. Since the pressure depends on the ratio of the distance to the cube root of the charge weight and since the pressure decreases approximately as the negative 1.8 power of the distance, the pressure at a given distance will vary approximately as the 0.6 power of the charge weight, i.e., it will increase by a factor of about 2.5 with an increase of charge weight by a factor of 5. Since this is the same as the difference in pressure from station to station, the same pressure range can be covered for a change in propellant weight by a factor of 5 by deleting the closest station and adding one new station at a distance of approximately 1.8 times the distance of the last station. The actual propellant weights used during the program were 200, 1000, 25,000 and 100,000 lb. To accomodate the 100,000 lb propellant weight, an additional ring of gauges was installed using the same 1.8 distance factor.

Since a variety of explosive yields was expected for each scale of testing, ranging from as low as 1 percent to nearly 100 percent, an intermediate yield level of 10 percent was selected for establishing the specific station location. (A 100-percent yield would give pressures about a factor of 4 higher than those for a 10-percent yield, while a 1-percent yield would give pressures about a factor of 4 lower.)

In addition to the foregoing considerations, selection of the actual pressure values for the stations was guided by the following: the pressure region of primary interest is between 1 and 100 psi, and a minimum of three of the stations should be in the region below about 15 psi, where the shock wave would be expected to be unsupported, i.e., classical in nature, for a 10-percent explosive yield situation.

To supplement the basic overpressure measurement system, the following additional measurements were also installed:

- Two overpressure-time measurements as close to the explosion as practical.

● Four measurements of stagnation pressure, spanning the range from near ground zero to the 32-psi level. (These gauges were also used as time-of-arrival gauges.)

Additional details of the instrumentation and station layout are given in Fig. A-1 and Table A-1.

Transducers and Amplifying and Recording System

The basic factors which were considered in the choice of an overpressure sensor for the primary blast-measuring system for project PYRO were:

● Gauges which would be unaffected by the ambient environment expected at the test site over the several-year test period. The most important factor to consider here is probably temperature stability.

● Gauges which would be small in diameter (< 1/2 in.) to fit in the thin probe required for the head-on overpressure measurements and also to have a very short air-shock travel time (rise time) for the side-on overpressure measurements. The gauge and preamp system should also have a high natural frequency (≥ 20 kHz) to accurately measure the air blasts from the smaller scale tests.

● Gauges which would survive the thermal and blast environment, which could be in excess of 3,000°K and 3,000 psi at the close-in stations.

● A gauge and preamp system which had been used in a similar environment and preferably one which we and other investigators had used in the field.

The system selected to satisfy all of the above requirements was manufactured by the Kistler Instruments Corporation and consisted of natural quartz piezoelectric transducers (Models 601A, 601H, 603A, 606A, and 701A) combined with a charge-amplifier-type preamp (Model 566M109). These transducers are small, approximately 1/4 in. in diameter, with a 1/8-in. sensitive area. They were enclosed in a stainless steel housing, had a flush-mounted stainless steel diaphragm, and were available with overpressure ranges in excess of 15,000 psi. The frequency response of the sensor-preamplifier system was rated from near DC to approximately 70 kHz. The sensors had good temperature stability and, with a protective thermal covering of silicone grease, had been used successfully in a similar propellant-blast environment by URS and by other investigators.
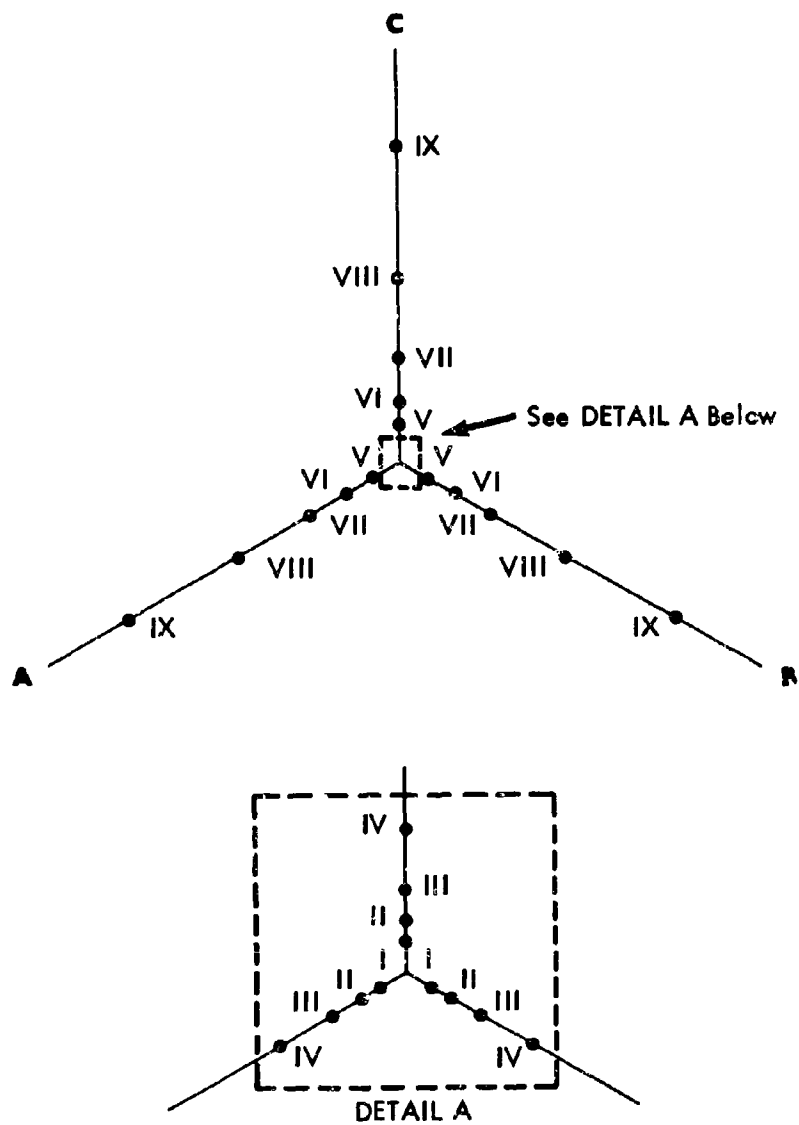
Fig. A-1. Instrumentation Layout

Table A-1

SUMMARY OF BLAST INSTRUMENTATION

NO.	GAUGE LINE	NOMINAL DISTANCE (ft)	200 LB		1000 LB		25000 LB		100,000 LB	
			P_s*	P_o**	P_s	P_o	P_s	P_o	P_s	P_o
I	A B C	2.8		X						
II	A B C	4.5	X	X		X				
III	A B C	7.5	X X	X X X	X	X				
IV	A B C	13	X	X X X	X X	X X X		X		X*** X***
V	A B C	23		X X X	X	X X X	X	X		 X X
VI	A B C	38		X X X		X X X	X X	X X X		 X X
VII	A B C	67		X X X		X X X	X	X X X		X X X
IX	A B C	200						X X X		X X X
X	A B C	335						X X X		X X X
XI	A B C	600						X X X		X X X

*   Head-on-oriented stagnation pressure sensor.

**   Side-on-oriented overpressure sensor.

***   A single gauge at the 13-ft distance was alternately located along gauge lines A and C.

A-5

The charge amplifiers for each sensor were mounted in protective junction boxes located 20 to 50 ft further away from ground zero than the sensors. These separation distances between the sensors and the amplifiers were necessary to eliminate any possible air-induced ground shock from affecting the amplifiers during the time of interest. In all cases the air shock pulse would have passed over the sensor before the shock front reached the location of the amplifier junction boxes.

The control and recording equipment was located in a "blockhouse" approximately 1000 ft from the test pad. The recording system consisted of three Model FR-1200 and three Model FR-100, 14-track Ampex instrumentation tape recorders.

All pressure channels were recorded on the three FR-1200's, which were run at 120 ips. The bandwidth of these records was DC to 20 kHz. The thermal instrumentation was recorded on the FR-100's, which had a bandwidth of DC to 10 kHz. Tape speed for the FR-100's was 60 ips.

Mounting of Transducers

The three basic sensor mount designs used for the blast instrumentation are shown in Figs. A-2 through A-4. The type A mounts, Fig. A-2, were fabricated from 3-in.-thick steel and were used in the close-in environment. The configuration shown, located 4.5 ft* from ground zero, contains a side-on overpressure sensor and a stagnation pressure sensor. Another version of this sensor mount, with the same basic design and containing only a single overpressure sensor, was located at 2.8 ft from ground zero.

The type B mount, Fig. A-3, located 7.5 ft from ground zero, was fabricated from 3-in.-diameter heavy-wall stainless steel tubing. The front nose of this mount was removable to allow use of either the pointed nose containing the

---

* In this discussion, the distances quoted refer to the 200-lb test series, as described in the discussion of blast instrumentation design. These distances were increased by a factor of approximately 1.8 for each increase in propellant weight of a factor of 5.

A-6
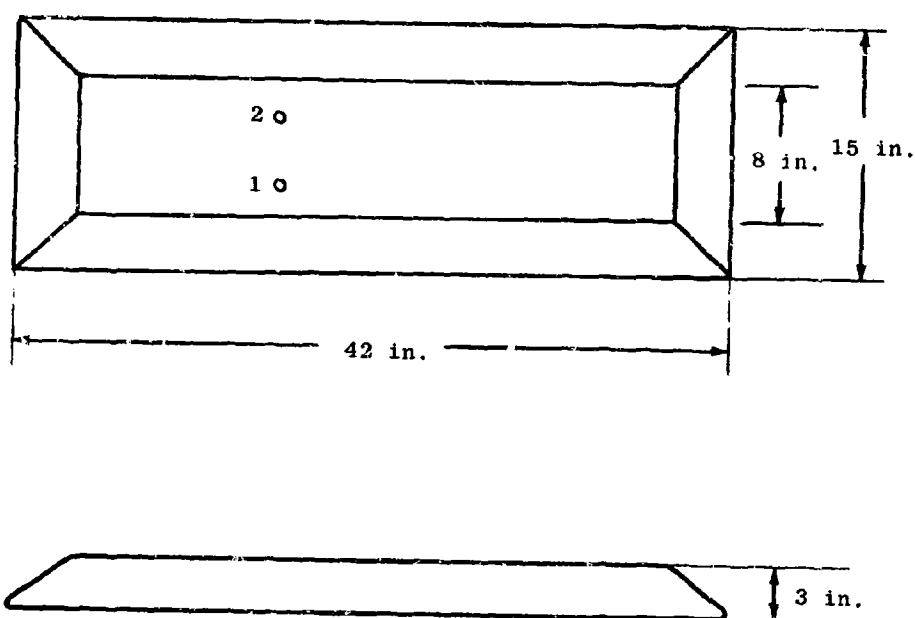
1. Side-on overpressure gauge

2. Stagnation gauge

Fig. A-2. Type A Sensor Mount
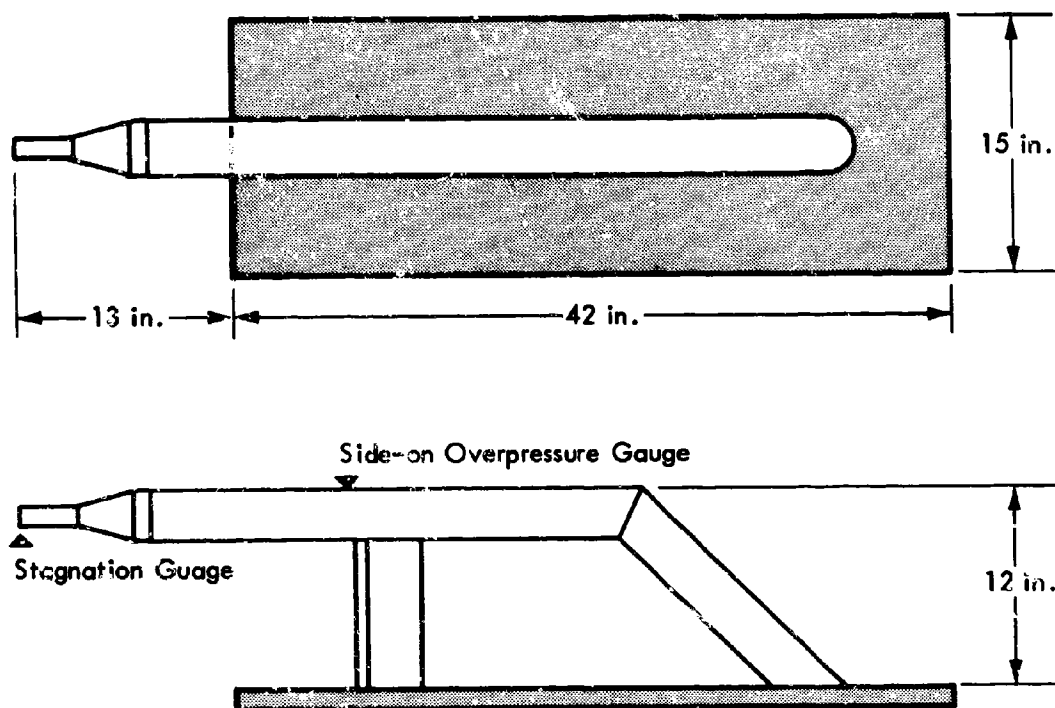
Fig. A-3. Type B Sensor Mount
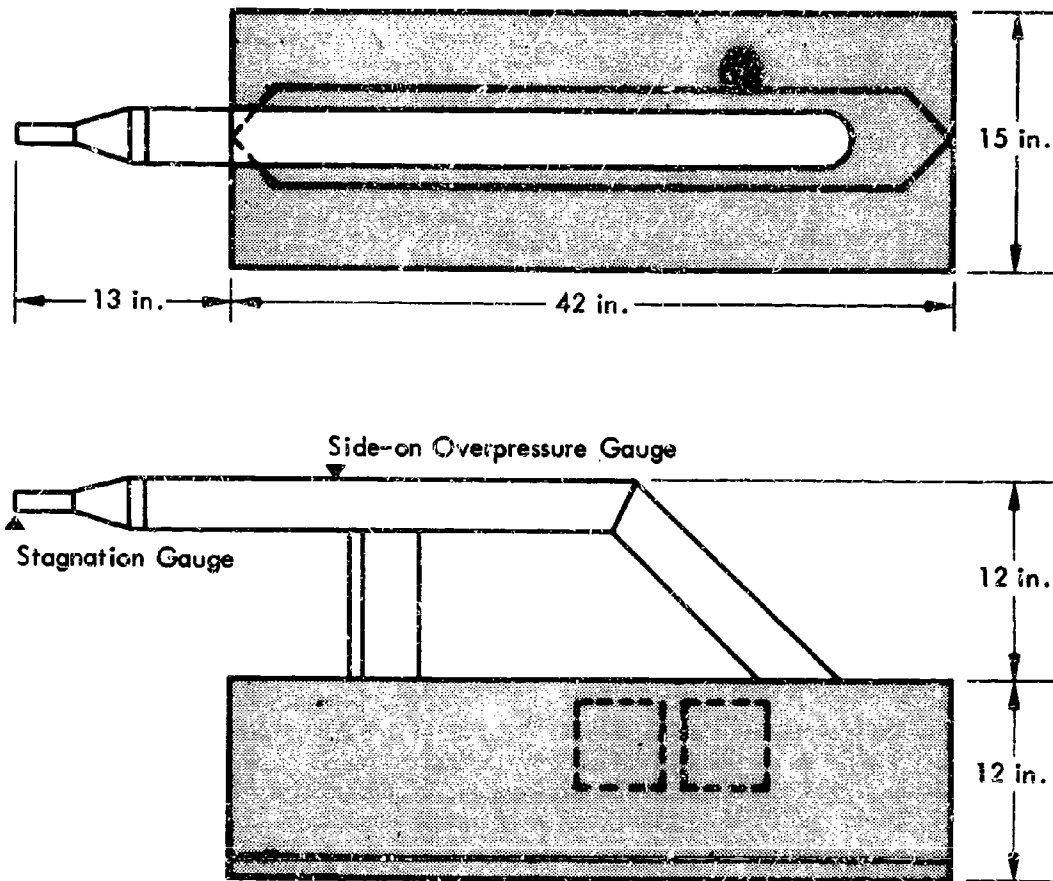
Fig. A-4. Type C Sensor Mount

stagnation sensor or a blunt protective nose. A side-on-pressure sensor was
located on top of the mount, as noted in the figure.

The type C mount, Fig. A-4, combined the type B with a 12-in.-high raised
pedestal. At the stations off the test pad, the additional height of the
raised pedestal helped to prevent ground surface irregularities and the dust
created by the explosions from influencing the overpressure readings.

CALIBRATION

The blast instrumentation system was calibrated by a variety of methods,
including periodic laboratory calibration of individual components, a calibra-
tion of electrical components during the countdown that proceded each propellant
and high-explosive (H.E.) test, a periodic end-to-end field calibration of
individual channels, and complete system calibrations using standard H.E.
charges.

Calibration by Other Than High Explosives

The laboratory calibrations of electrical components and piezoelectric
pressure transducers were periodically conducted by standard procedures, the
latter by standard shock tube techniques.

Calibration of the charge amplifiers in the field preceding each propel-
lant test was conducted by applying a measured charge signal to the input and
measuring the output voltage for the test gain setting, thus obtaining the
gain ultimately required for test data evaluation.

An end-to-end calibration of all blast instrumentation channels was con-
ducted by dynamically applying a known pressure step to each pressure gauge in
its field position by means of a small portable shock tube.

The calibration procedure for the amplifiers used with the thermal instru-
ments was somewhat less involved, since only the external feedback circuits
needed to be measured. These circuits were constructed on printed circuit cards

for easy removal from the test area to the control station for calibration. For
calibration, these circuits are inserted into a special calibration panel which
simulates the test configuration.

It should be mentioned also that AFRPL instrumentation personnel conducted
an accuracy study of the laboratory and electrical calibration procedures used
during the program. This study is reported in Ref. A-1.

High-Explosive (H.E.) Calibration Tests

General Description

Calibration of the instrumentation system was performed throughout the pro-
gram by detonating spherical charges of high explosives whose explosive proper-
ties are well known (TNT and Pentolite). The purpose of these tests was to
verify the correct overall operation of the blast instrumentation system, both
initially and throughout the program, and to provide information on the system
reproducibility.

A summary of the calibration tests is given in Table A-2 showing their di-
vision into test series, the first series being conducted to test the system
initially, and each of the remaining series being associated with a given set
of propellant tests.

The spherical charges were detonated at a scaled height of burst (HOB) of
about 1 ft/lb$^{1/3}$ for all tests. This charge height was selected because it was
high enough to minimize cratering and the subsequent hazard to instrumentation
from flying debris and still low enough to ensure a well-developed shock front
at the closest above-surface transducer. Furthermore, this charge height is
high enough so that the particular nature of the ground surface would not sig-
nificantly influence the results. (Much of the available reference data are
for natural ground surfaces, such as hard-packed clay, while the surface in the
vicinity of the explosion for the PYRO tests is concrete.)

Table A-2

SUMMARY OF H.E. CALIBRATION TESTS

NUMBER OF TESTS	CHARGE		TEST SERIES DESCRIPTION
	WEIGHT (lb)	TYPE	
6	18	Pentolite	Initial series; conducted prior to propellant testing.
18	18	Pentolite	Conducted periodically throughout the propellant testing at the 200- and 1,000-lb levels.
3	500	Pentolite	Conducted in conjunction with the 25,000-lb tests and the Titan I test.
2	1,000	TNT	Conducted in conjunction with the S-IV test.

Calibration Data

The individual gauge readings of peak overpressure and impulse for each of the four test series listed in Table A-2 are given in Tables A-3 through A-6.[*] It can be seen from the tables that various gauge changes were implemented, usually between test series. For instance, subsequent to the initial six tests one of the three gauges at both the 6.6- and 12.8-ft distances was deleted. In addition, starting with Test 221, three gauges were added at both 117 and 200 ft. The system was modified for the 500-lb pentolite tests (see Table A-5) as follows: three gauges (one for each gauge line) were added at both the 335- and 600-ft distances, two gauges were deleted at 13 ft, leaving one gauge at this distance along either gauge line A or C; and at both the 23- and 37-ft distances, a gauge was deleted along gauge line A, leaving seven gauges along gauge lines B and C.

---

[*] These data have not been corrected for the difference in ambient pressure between the test pad (about 13.4 psi) and sea level (14.7 psi), since the net effect of the correction (which has to be made in both the overpressure and scaled distance) is so small as not to influence any of the conclusions drawn from the data.

A-12

Table A-3

PEAK OVERPRESSURE (PSI) AND POSITIVE-PHASE IMPULSE
(PSI-MSEC) FROM 18-LB PENTOLITE SPHERES

Shot No.	Pressure-Impulse	Gauge Line	Distance (ft)				
			6.56	12.8	22.5	37.1	66.6
018	P	A	-	59.0	20.0	-	2.92
		B	-	46.2	18.3	7.4	2.66
		C	220	65.0	16.0	6.0	3.30
	I	A	-	13.8	12.4	--	4.06
		B	-	-	19.7	7.61	3.72
		C	-	14.8	10.7	6.78	4.43
021	P	A	-	54.0	17.6	6.00	3.08
		B	-	42.0	16.8	6.85	-
		C	300	57.6	12.0	4.95	2.92
	I	A	-	13.5	10.9	6.17	4.27
		B	-	-	10.1	6.55	-
		C	27.5	13.2	9.11	5.20	4.24
023	P	A	-	56.8	18.0	6.20	3.20
		B	350	66.4	15.0	6.20	2.92
		C	292	54.4	14.2	5.28	-
	I	A	23.5	13.5	11.1	6.00	4.32
		B	28.4	-	9.43	6.48	-
		C	27.6	13.1	9.85	5.93	4.03
024	P	A	333	55.0	17.2	6.32	3.12
		B	230	59.0	15.4	5.70	-
		C	274	54.0	13.0	4.96	2.58
	I	A	26.9	13.9	10.8	6.16	4.22
		B	30.1	-	9.78	6.02	-
		C	26.6	13.4	9.27	5.33	3.72
026	P	A	320	56.0	15.8	6.0	2.64
		B	236	44.17	16.5	5.4	-
		C	260	52.8	11.8	-	2.90
	I	A	24.3	12.0	10.9	5.81	3.69
		B	31.1	-	9.23	6.10	-
		C	26.7	13.3	7.76	-	4.23
027	P	A	-	-	-	6.1	2.72
		B	-	-	-	5.84	-
		C	-	-	-	-	3.00
	I	A	-	-	-	6.18	3.88
		B	-	-	-	6.21	-
		C	-	-	-	-	4.26

Table A-4

PEAK OVERPRESSURE (PSI) AND POSITIVE-PHASE IMPULSE
(PSI-MSEC) FROM 18-LB PENTOLITE SPHERES

Shot No.	Pressure-Impulse	Gauge Line	Distance (ft)						
			6.5	12.8	23	37	67	117	200
082	P	A	-	57.4	-	6.80	2.44	-	-
		B	226	68.3	17.5	6.24	2.38	-	-
		C	268	63.2	15.6	6.40	2.51	-	-
	I	A	-	42.8	-	18.7	9.22	-	-
		B	74.7	42.7	26.0	15.9	8.97	-	-
		C	81.3	45.2	25.9	15.8	9.09	-	-
083	P	A	-	59.8	-	6.81	2.58	-	-
		B	206	65.0	-	6.29	2.34	-	-
		C	281	59.8	16.2	6.14	2.40	-	-
	I	A	-	42.9	-	18.8	9.42	-	-
		B	73.0	42.8	-	16.2	9.19	-	-
		C	80.7	43.7	26.0	15.5	9.10	-	-
089	P	A	-	58.8	17.5	6.20	2.97	-	-
		B	197	57.1	13.1	5.96	2.19	-	-
		C	232	65.6	16.3	5.63	2.65	-	-
	I	A	-	39.6	24.1	17.8	10.4	-	-
		B	95.2	37.6	21.7	16.4	8.96	-	-
		C	76.4	43.8	26.4	14.9	9.32	-	-
111	P	A	-	71.7	17.6	6.41	2.88	-	-
		B	187	70.5	17.9	6.69	2.57	-	-
		C	-	76.0	17.5	6.99	2.56	-	-
	I	A	-	42.4	29.4	19.2	11.6	-	-
		B	81.7	45.1	28.3	19.3	10.7	-	-
		C	76.2	43.1	26.6	18.5	10.4	-	-
112	P	A	-	55.7	-	6.37	2.96	-	-
		B	159	67.5	15.6	6.52	2.47	-	-
		C	261	73.9	16.9	7.12	2.62	-	-
	I	A	-	41.2	-	20.3	11.8	-	-
		B	94.7	46.9	28.2	13.4	9.81	-	-
		C	93.4	44.8	29.2	18.4	10.4	-	-

Table A-4 (Cont.)

PEAK OVERPRESSURE (PSI) AND POSITIVE-PHASE IMPULSE
(PSI-MSEC) FROM 18-LB PENTOLITE SPHERES

Shot No.	Pressure-Impulse	Gauge Line	Distance (ft)						
			6.5	12.8	23	37	67	117	200
128	P	A	–	–	15.6	6.03	2.37	–	–
		B	237	–	16.5	6.52	2.56	–	–
		C	242	73.2	16.3	–	2.53	–	–
	I	A	–	–	22.2	18.7	9.59	–	–
		B	96.5	–	22.9	18.9	9.89	–	–
		C	79.4	38.7	28.9	–	9.53	–	–
129	P	A	–	–	16.5	6.19	2.44	–	–
		B	–	77.4	15.0	6.57	2.60	–	–
		C	211	73.4	16.0	–	2.57	–	–
	I	A	–	–	23.1	18.2	9.62	–	–
		B	–	47.2	24.6	18.0	9.97	–	–
		C	100	41.1	27.9	–	9.76	–	–
149	P	A	–	–	16.5	6.25	2.52	–	–
		B	255	64.4	18.0	6.54	2.71	–	–
		C	245	65.1	16.4	6.43	2.63	–	–
	I	A	–	–	26.3	19.0	9.06	–	–
		B	71.9	39.6	31.5	16.9	9.28	–	–
		C	68.7	44.9	27.4	16.5	9.17	–	–
187	P	A	–	–	16.9	6.88	2.78	–	–
		B	255	78.9	19.0	6.27	2.86	–	–
		C	282	59.0	17.0	7.03	2.79	–	–
	I	A	–	–	26.2	20.1	9.79	–	–
		B	77.8	38.8	28.8	18.1	10.8	–	–
		C	76.2	40.8	26.3	19.0	10.5	–	–
188	P	A	–	–	13.2	6.93	2.67	–	–
		B	251	77.4	18.3	6.11	2.78	–	–
		C	263	58.9	15.7	6.62	2.57	–	–
	I	A	–	–	22.9	18.7	9.32	–	–
		B	83.7	39.7	29.1	17.8	10.4	–	–
		C	65.1	39.0	26.5	19.4	9.40	–	–

Table A-4 (Cont.)

PEAK OVERPRESSURE (PSI) AND POSITIVE-PHASE IMPULSE
(PSI-MSEC) FROM 18-LB PENTOLITE SPHERES

Shot No.	Pressure-Impulse	Gauge Line	Distance (ft)						
			6.5	12.8	23	37	67	117	200
221	P	A	-	-	16.8	6.32	3.02	1.15	.535
		B	250	80.3	20.4	5.66	2.23	1.45	.608
		C	259	67.2	18.9	6.50	2.52	1.30	.684
	I	A	-	-	23.3	19.7	11.1	5.91	3.30
		B	90.6	31.4	28.7	17.0	9.24	7.24	3.23
		C	63.6	49.6	27.0	16.2	9.75	6.47	3.53
222	P	A	-	-	17.1	6.11	-	1.11	.622
		B	311	74.4	18.5	6.50	2.35	1.34	.652
		C	330	76.3	17.8	6.56	2.57	1.25	.575
	I	A	-	-	24.0	20.1	-	5.53	3.35
		B	73.8	38.2	27.9	17.0	9.62	5.72	3.24
		C	95.2	38.6	22.9	16.3	10.1	6.24	3.73
234	P	A	-	-	13.8	6.59	2.30	1.17	.625
		B	248	-	18.3	6.40	2.41	1.47	.655
		C	231	67.0	23.1	7.09	2.67	1.25	.683
	I	A	-	-	20.1	18.7	10.6	5.61	3.41
		B	-	-	22.8	17.7	9.37	6.50	3.56
		C	86.1	40.9	33.2	16.8	9.64	5.87	3.89
235	P	A	-	-	16.4	6.25	2.80	1.19	.639
		B	169	-	21.5	6.34	2.43	1.39	.688
		C	223	62.9	24.0	7.39	2.73	1.26	.737
	I	A	-	-	26.8	19.4	10.5	6.13	3.61
		B	-	-	30.3	17.9	9.95	5.92	3.53
		C	93.0	39.2	31.1	18.7	11.0	6.43	3.60
246	P	A	-	-	18.1	5.91	2.77	1.04	.606
		B	148	60.4	17.8	6.90	2.44	1.21	.729
		C	250	64.2	18.9	6.76	2.55	1.21	.518
	I	A	-	-	27.0	15.4	9.99	5.49	3.24
		B	43.1	33.0	27.4	17.8	9.48	5.37	3.48
		C	96.3	40.4	28.5	18.1	10.2	6.11	3.52

Table A-4 (Cont.)

PEAK OVERPRESSURE (PSI) AND POSITIVE-PHASE IMPULSE
(PSI-MSEC) FROM 18-LB PENTOLITE SPHERES

Shot No.	Pressure-Impulse	Gauge Line	Distance (ft)								
			6.5	12.8	23	37	67	117	200
	P	A	-	-	18.3	5.67	2.81	1.10	.596
		B	-	88.7	19.1	5.68	2.41	1.13	.691
247		C	221	85.6	17.8	5.88	2.48	1.28	.697
	I	A	-	-	25.5	18.2	10.1	5.67	3.74
		B	-	40.8	28.0	18.0	9.30	5.23	3.41
		C	67.1	46.2	28.9	16.5	10.6	6.20	3.92
	P	A	-	-	18.8	5.57	1.09	1.15	.571
		B	236	76.6	21.2	7.21	2.13	1.19	.674
255		C	289	72.1	21.3	7.08	2.61	1.28	.670
	I	A	-	-	28.4	17.6	4.26	6.08	3.35
		B	115	44.9	30.9	18.3	9.99	5.62	3.43
		C	89.9	44.5	35.1	18.1	10.8	6.11	4.02
	P	A	-	-	18.8	5.87	1.01	1.16	.578
		B	214	68.7	23.1	7.00	2.50	1.22	.693
256		C	278	72.8	20.2	6.71	2.63	1.27	.710
	I	A	-	-	28.3	18.7	3.74	5.91	3.15
		B	93.6	39.7	27.8	18.5	9.75	5.23	3.45
		C	89.2	40.1	31.2	17.0	10.8	6.23	3.52

Table A-5

PEAK OVERPRESSURE (PSI) AND POSITIVE-PHASE IMPULSE
(PSI-MSEC) FROM 500-LB PENTOLITE SPHERES

Shot No.	Pressure-Impulse	Gauge Line	Distance (ft)							
			13	23	37	67	117	200	335	600
274	P	A	694	-	-	14.5	5.14	2.38	0.995	0.563
		B	-	178	81.2	19.9	8.08	2.45	1.19	0.679
		C	-	-	47.9	17.0	6.69	2.35	0.901	-
	I	A	233	-	-	64.8	53.7	34.2	16.5	10.2
		B	-	173	109	65.0	63.1	32.1	16.0	11.3
		C	-	115	83.9	82.7	61.8	29.9	21.3	10.2
276	P	A	-	-	-	13.2	5.19	2.12	1.02	0.532
		B	-	210	53.0	20.1	5.52	2.41	1.26	0.654
		C	345	269	69.5	-	-	2.33	1.05	0.522
	I	A	-	-	-	51.3	57.0	30.0	16.7	9.69
		B	-	175	115	96.5	46.4	28.6	16.7	9.64
		C	258	209	142	-	32.2	30.4	18.3	10.5
280	P	A	-	-	-	16.6	5.10	2.39	1.01	0.561
		B	-	212	-	15.8	5.31	2.29	0.958	0.451
		C	479	259	64.9	16.2	5.80	1.79	1.03	0.520
	I	A	-	-	-	65.3	48.7	28.6	17.3	9.20
		B	-	189	131	70.1	49.8	24.1	17.4	8.65
		C	178	203	93.7	81.4	49.7	20.4	15.3	10.1

Table A-6

PEAK OVERPRESSURE (PSI) AND POSITIVE-PHASE IMPULSE (PSI-MSEC)
FROM 1,000-LB TNT SPHERES

Shot No.	Pressure-Impulse	Gauge Line	Distance (ft)						
			22.5	37.1	66.6	117	200	335	600
063	P	1	-	-	25.9	-	3.4	1.5	0.6
		2	-	-	-	8.7	3.2	2.2	0.6
		3	284.3	82.2	-	7.7	-	-	0.6
	I	1	-	-	112.0	-	42.5	23.6	13.3
		2	-	-	-	64.9	43.8	31.6	14.0
		3	327.5	186.6	-	61.3	54.5	-	14.9
064	P	1	-	-	28.6	-	4.4	1.8	0.6
		2	-	-	-	8.8	3.7	1.6	0.7
		3	300.9	91.4	-	6.9	-	-	0.6
	I	1	-	-	129.6	71.5	53.4	28.0	14.1
		2	-	-	-	68.7	48.8	33.1	13.0
		3	371.3	206.8	-	63.6	-	-	15.9

For the system as it existed for the Saturn S-IV test, two 1000-lb TNT spheres were detonated immediately after the propellant test at the usual 1-ft/lb$^{1/3}$ scaled height of burst. It can be seen from Table A-6 that the gauge array for these tests was much like that for the 25,000-lb and Titan I tests, although there were no 13-ft gauges and only one each at the 22.5-, 37.1- and 66.6-ft distances. It can also be seen from the table that the agreement between the pressure and impulse results from gauges at the same distance and for each particular test is quite good, but that the close-in data for test 064 are generally higher than the data for shot 063. While this difference is not unlike the normal test-to-test reproducibility at those distances, it is unusual for all the data to have the same trend. A possible explanation for this is that the detonation conditions for the two tests were not the same. The charge for Test 063 was detonated at the top surface, using a C4 booster, and the charge for Test 064 was detonated at the center, using the internally cast pentolite booster. While very little is known about the effect of point of initiation on blast-wave parameters measured close to a charge, it appears reasonable to assume that at least some of the data spread can be attributed to this change in detonation conditions.

Results of High-Explosive Calibration Tests

The calibration test data are presented in this section in terms of peak pressure and positive-phase impulse versus scaled distance graphs; for purposes of comparison, standard reference curves are included. Also presented are the results of statistical analysis of both the initial 18-lb pentolite tests and the subsequent series of eighteen 18-lb pentolite tests; no comparable analyses were performed for the 500- and 1000-lb series due to the small number of tests conducted.

The surface burst reference curves included with the calibration data plots are based on TNT surface burst data given in Refs. A-2 and A-3 for pressure and impulse, respectively. For use in these plots, these reference curves have been adjusted to a pentolite base. This adjustment entails the assumption that 1.18 lb of TNT is equivalent to 1 lb of pentolite.

Also included on some of the calibration data figures are reference curves based on spherical charges of Composition A detonated at a scaled HOB of 1.4 $ft/lb^{1/3}$ (from Ref. A-4). As would be expected, the surface burst data tend to lie somewhat below the calibration data collected at a scaled HOB of 1 $ft/lb^{1/3}$ and closer to the Composition A data collected at a scaled HOB of 1.4 ft/ $lb^{1/3}$.

18-lb Pentolite Tests. Plots indicating the results of the twenty-four 18-lb pentolite tests are given for peak pressure and scaled impulse on Figs. A-5 and A-6, respectively. The plotted points represent the mean pressure or impulse averaged over all three gauge lines and all 24 tests; data are occasionally missing for one or more of the three gauges at a given distance, and the data from each test -- rather than each gauge — were weighted equally. The brackets associated with each plotted point indicate the estimated standard deviation of the measurements, where the standard deviation is of the distribution of pressure or scaled impulse means over the gauge lines; thus, for pressure (or impulse) at 67 ft, the distribution consists of 24 pressure (or 24 scaled impulse) values, and since gauges were installed for the last eight tests only at the 117- and 200-ft distances, the distribution at these distances consists of eight pressure (or eight scaled impulse) values.

One of the major purposes of the calibrations tests was to obtain statistical information that would be useful in the analysis of the propellant test data, e.g., estimates of the standard deviation which can be attributed to the instrumentation system. The desired statistical information was obtained from the results of the tests by means of analysis of variance techniques. Separate analyses were made for the pressure and impulse data at each distance; a two-way classification was used, the factors being the shot (test) and the gauge, and interactions were assumed negligible.

The results of the analysis for the initial six tests are given in Table A-7. For this test series a 5-percent level of significance was used. Under the column labeled "effect," a "yes" (or "no") indicates that there was (or was not) a statistically significant difference between the mean values for that
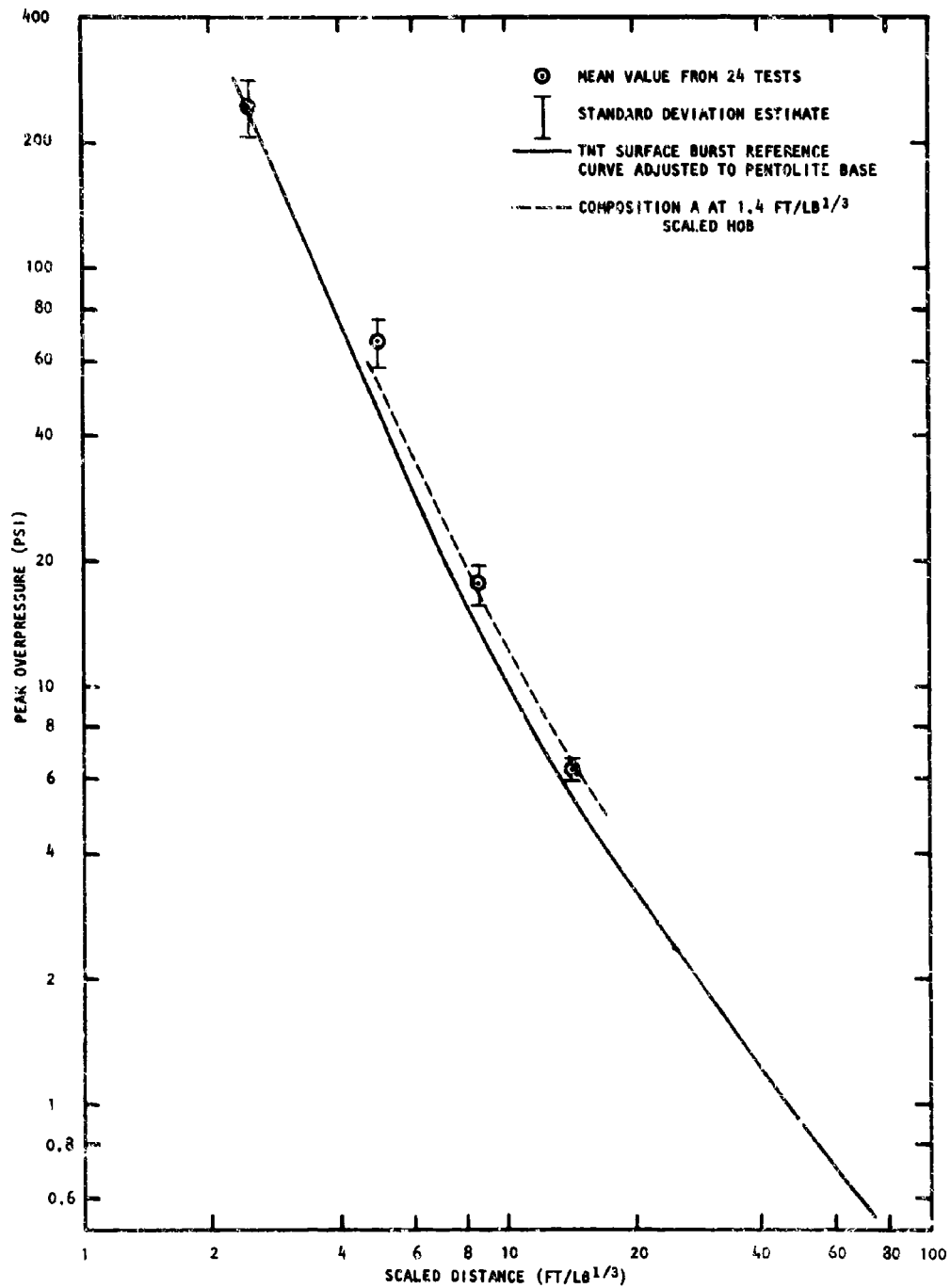
Fig. A-5. Peak Overpressure vs Scaled Distance from Twenty-four
Pentolite Spheres at a Scaled HOB of 1.0 ft/lb$^{1/3}$
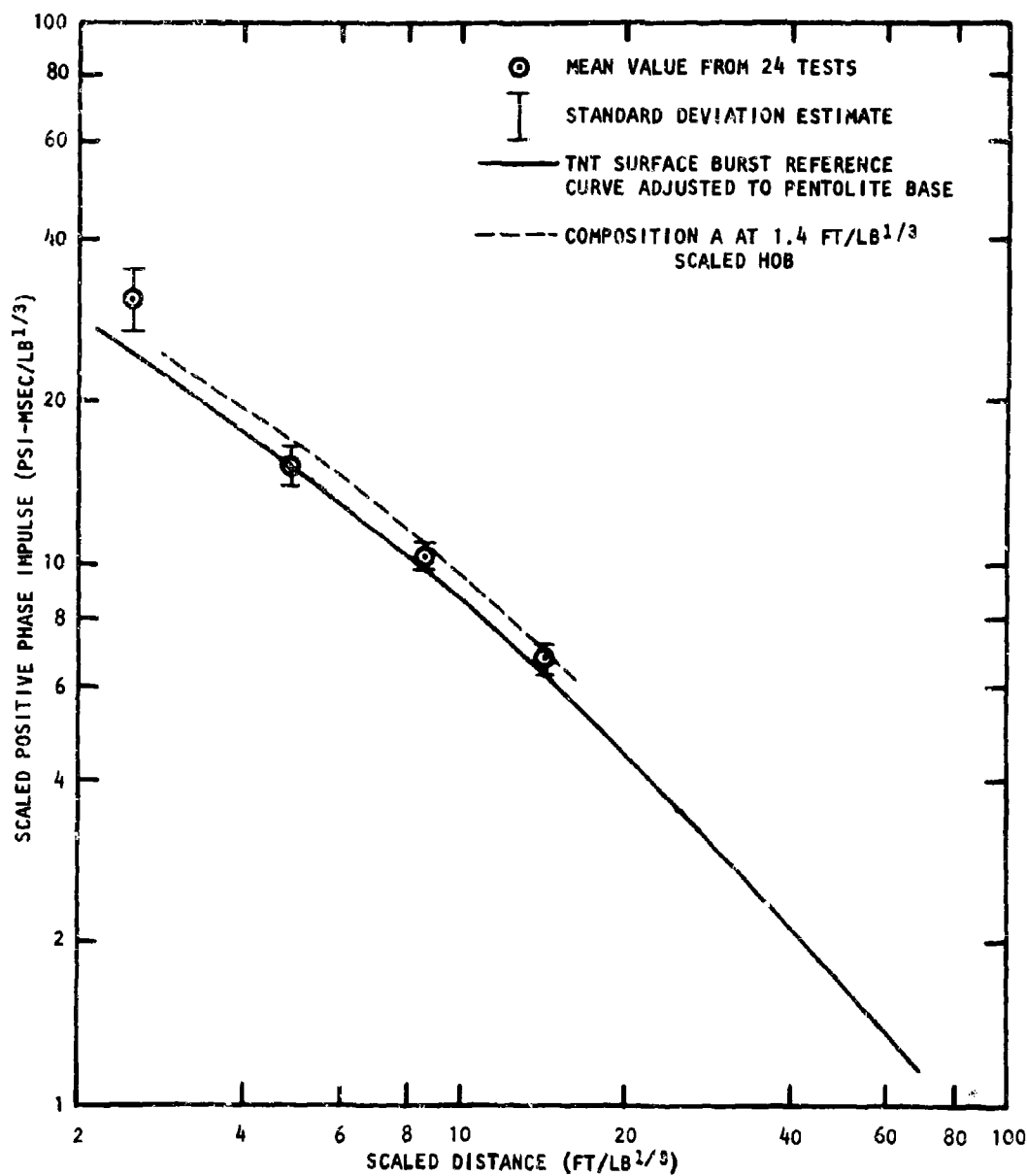
Fig. A-6. Scaled Positive-Phase Impulse vs Scaled Distance from Twenty-four
           18-lb Pentolite Spheres at a Scaled HOB of 1.0 ft/lb$^{1/3}$

parameter. For example, a "yes" under the gauge column indicates that the mean
values from the various gauges (averaged over all shots) were significantly dif-
ferent. Similarly a "no" under the shot column indicates that the mean values
from the various shots (averaged over all gauges) were not significantly differ-
ent. Also given in Table A-7 is an estimate of the standard deviation of an
individual reading computed from all the data. This standard deviation includes
shot and/or gauge effects, if they are present.

Table A-7

RESULTS OF STATISTICAL ANALYSIS OF THE INITIAL SIX 18-1b PENTOLITE TESTS

PARAMETER	DISTANCE (ft)	EFFECT		ESTIMATE OF % STANDARD DEVIATION OF INDIVIDUAL READING
		SHOT	GAUGE	
Pressure	6.6	No	Yes	15.5
	12.8	No	No	12.2
	22.5	Yes	Yes	14.8
	22.5*	No	Yes	13.9
	37.1	No	Yes	11.2
	66.6	No	No	7.4
Impulse	6.6	No	Yes	9.0
	12.8	No	No	5.4
	22.5	Yes	Yes	10.8
	22.5*	No	Yes	9.9
	37.1	No	No	7.7
	66.6	No	No	5.7

* Eliminating Shot 018

From Table A-7 it can be seen that, except at the 22.5-ft station, there
are no significant shot effects for either pressure or impulse. Furthermore,
it may be seen that if shot 18 is eliminated from consideration, the shot ef-
fect at the 22.5-ft station disappears. Since shot 18 was the first of the six
calibration shots and testing procedures were still being developed, it is be-
lieved that its results should not be weighted very heavily. Accordingly, it
is concluded that the inevitable shot-to-shot variations in the actual blast

wave from the high-explosive charges do not significantly inflate the total standard deviations over and above those that are attributable to the instrumentation system alone.

The analyses, however, did indicate significant gauge effects at the 6.6- and 22.5-ft stations for both pressure and impulse and for pressure at the 37.1-ft station.

The results given in Table A-7 indicate that the system as initially installed typically gave a pressure standard deviation value of about 12 to 13 percent and an impulse deviation of about 8 to 9 percent.

An analysis of variance similar to that for the initial six tests was also performed for the eighteen remaining 18-lb calibration tests, the latter differing only in that a 2.5-percent (rather than 5-percent) level of significance was used due to the increased quantity of data. The results are quite similar to those from the initial test series; for instance, shot effect was present only for impulse at 23 ft, and gauge effects were present in 9 of 14 cases, as opposed to 5 of 10 for the initial series. Gauge line effects, however, are ordinarily of little consequence in evaluating terminal yield as described above, since gauge line averages are used. In the infrequent instances of missing data at the outer distances, adjustments to the data in order to compensate for gauge effects are sometimes necessary. Any investigation of azimuthal variations in the blast wave would of course, require consideration of gauge line effects. However, blast wave asymmetries for the propellant tests (at the AFRPL test site) are not pronounced. Therefore such an investigation, beyond that required to establish the extent of blast asymmetries, is not included in this program. In the interests of indicating the general magnitude of the gauge line effects that are present in the instrumentation system, however, Table A-8 is presented to enable ready comparison of the gauge line mean values of pressure and impulse with the total mean value at each distance for the 18 calibration tests. Where the analysis of variance has indicated that the gauge line differences are significant, the total mean value is followed by an asterisk (*). It can be seen from the table that the mean value for a given gauge line is not grossly different from the corresponding total mean value.

Table A-8

GAUGE LINE COMPARISONS

PRESSURE-IMPULSE	DISTANCE (ft)	MEAN VALUE OVER GAUGE LINE			MEAN VALUE OF ALL MEASUREMENTS
		A	B	C	
Pressure	6.6	-	224	262	243
	12.8	-	71.7	68.9	70.3
	23	17.1	18.5	18.5	18.0*
	37	6.31	6.44	6.63	6.46*
	67	2.72	2.49	2.59	2.60*
	117	1.13	1.30	1.26	1.23*
	200	0.596	0.674	0.659	0.643*
Impulse	6.6	-	83.2	80.8	82.0
	12.8	-	40.6	43.0	41.8
	23	25.2	27.4	26.8	26.4
	37	19.0	17.6	17.2	18.0*
	67	10.1	9.69	9.68	9.89*
	117	5.79	5.85	6.21	5.95
	200	3.39	3.42	3.72	3.51*

The analysis of variance of these eighteen tests indicated that the pressure standard deviation was about 8.7 percent, and the impulse deviation about 8.7 percent. These numbers are similar to those obtained in the analysis of the initial series of six 18-lb tests, and as before, these values are inflated somewhat due to gauge line and, to a lesser extent, shot effects.

Series of Three 500-lb Pentolite Tests. Overpressure and scaled impulse versus distance plots for the three 500-lb pentolite tests are presented in Fig. A-7. In this case, each point represents the average of three gauge readings (one for each gauge line) at a given distance for a given test. As for the previous test series, the TNT surface burst curves adjusted to the pentolite base are included in the figure (continuous line), along with the curves from Composition A detonated at a scaled HOB of 1.4 $ft/lb^{1/3}$.

Due to the limited number of tests in the 500-lb series, the analysis of variance was not performed.
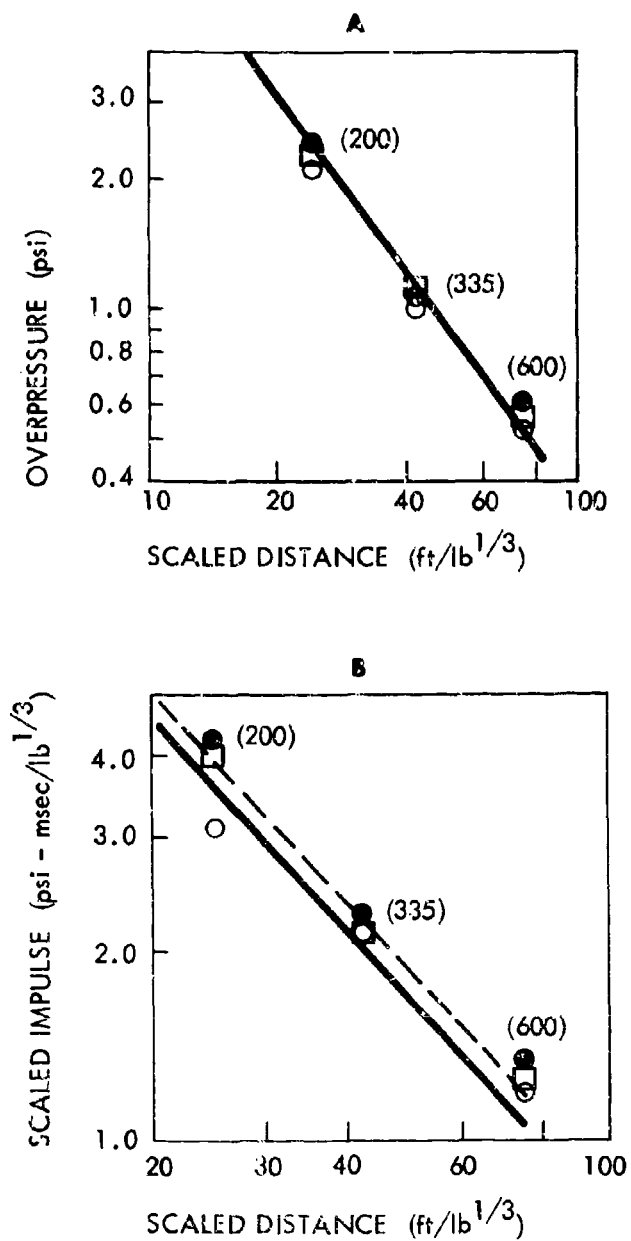
Fig. A-7. Peak Overpressure and Scaled Impulse at Outer Gauge Distances from 500-lb Pentolite Calibration Tests

SUMMARY TABLE

STEP NUMBER	VARIABLE		MULTIPLE		INCREASE
	ENTERED	REMOVED	R	RSQ	IN RSQ
1	DV^2		0.7272	0.5288 (3)	0.5288
2	D^2V^2		0.7564	0.5721 (4)	0.0433

Fig. B-1b.   Partial Output from Computer Program BMD 02 R

Note that contribution of the second variable was 4 percent. If in our
judgment this increase in explained variation was too small, then that varia-
ble was omitted from the final form of the regression equation. Such an elim-
ination of terms enabled us to simplify the starting equation given in Section
5 to that used in this section.

The coefficients of the best fitting yield relationships are given in Fig.
B-1a (10) and thus

$$\tilde{Y} = 18.4 + 0.0031 \ D^* v^2 - 0.00015 \ D^{*2} v^2 \qquad (B.1)$$

The residual variance which is needed to estimate the upper prediction in-
terval is 206.4 (8).

Prediction Interval Estimation

To obtain a "reasonable" bound for a future yield observation, an upper
prediction interval was computed. For $0 < \alpha < 1$, an upper prediction interval
is an interval bounded above which will bracket a single future observation
with probability $1-\alpha$. The decision to consider only an upper limit was based
on interest in maximum credible yields, rather than minimum. The α level up-
per prediction interval for an observation Y resulting from a choice of indepen-
dent variables $(Z_1, Z_2, \ldots, Z_{p-1})$ is given by the equation

$$Y_u = \tilde{Y} + \left(t^{\alpha}_{n-p}\right) S \left(1 + \sum_{i=0}^{p-1} \sum_{j=0}^{p-1} A^{ij} Z_i Z_j \right)^{1/2} \qquad (B.2)$$

Where the symbols have the following definitions

$\tilde{Y}$ is the value of the regression equation computed at the point
$(Z_1, Z_2, \ldots, Z_{p-1})$

t^{α}_{n-p} is a constant obtained from a table of Students t distribution with
n-p degrees of freedom

n is the number of sample points and p is the number of parameters. The quantity n-p can be found easily in Fig. B-1a (9).

S is the square root of S^2, the residual variance identified earlier

A^{ij} is the ij^{th} element in the inverse to the matrix (A_{ij}) whose ij^{th} element is:

$$\sum_{\ell = 1}^{n} X_{i\ell} X_{j\ell}$$

where

X_{ij} is the i (i = 1, ..., p - 1)th element of the jth observation of the vector X and for all j X_{oj} = 1.

For the LO_2/LH_2 CBGS-V case, we can make the following identifications:

$\tilde{Y}$ is given by Eq. (B.1)

α was chosen to be 0.1 for all cases

n = 20, p = 3, and n-p = 17

t^{α}_{n-p} = 1.33

$S = \sqrt{206.4}$

$$\left(A_{ij}\right) = \begin{pmatrix} 20 & 1.705445 \times 10^5 & 8.101516 \times 10^5 \\ 1.705445 \times 10^5 & 2.346231 \times 10^9 & 1.214744 \times 10^{10} \\ 8.101516 \times 10^5 & 1.214744 \times 10^{10} & 7.912697 \times 10^{10} \end{pmatrix}$$

This matrix, when inverted, yields

$$A^{ij} = \begin{pmatrix} 1.374266 \times 10^{-1} & -1.318130 \times 10^{-5} & 6.165114 \times 10^{-7} \\ -1.318130 \times 10^{-5} & 3.341659 \times 10^{-9} & -3.780473 \times 10^{-10} \\ 6.165114 \times 10^{-7} & -3.780473 \times 10^{-10} & 6.436284 \times 10^{-11} \end{pmatrix}$$

Series of Two 1,000-lb TNT Tests. Pressure and impulse data from the two
1,000-lb TNT tests that followed the S-IV propellant test are plotted in Figs.
A-8 and A-9, respectively. Each data point represents the gauge line average
at that distance for a particular test. The TNT surface burst reference curves
from Refs. A-2 and A-3 are included in the figures (continuous line); these
curves are thus identical with those used to evaluate yields. The Composi-
tion A curves at the scaled HOB are also included (dashed line), although in
this case they have been adjusted to a TNT base by the assumption that 1.18 lb
of TNT is equivalent to 1.0 lb of Composition A.

It can be seen from the figures that the data once again tend to lie be-
tween the surface burst and scaled HOB curves.

Due to the small number of tests, no statistical analysis of the data was
conducted.

Upon identifying

$$Z_o = 1$$

$$Z_1 = D^* v^2$$

$$Z_2 = D^{*2} v^2$$

Eq. (B.2) can be rewritten as

$$Y_u = 18.4 + 0.0031\ D^* v^2 - 0.00015\ D^{*2} v^2 + 1.33\ \sqrt{206.4}\ (1 + 1.374266 \times 10^{-1}$$
$$+ 3.541659 \times 10^{-9}\ D^{*2} v^4 + 6.436284 \times 10^{-11}\ D^{*4} v^4 - 2.636260 \times 10^{-5}$$
$$D^* v^2 + 12.330228 \times 10^{-7}\ D^{*2} v^2 - 7.560946 \times 10^{-10}\ D^{*3} v^4)^{1/2}$$

LO$_2$/RP-1 CBGS - VERTICAL

The form of the generalized equation selected for the regression analysis of this case was

$$\frac{Y}{v^n} = a + \frac{bD^*}{v^m} \quad \text{for } 0 \le \frac{D^*}{v^m} \le \left(\frac{D^*}{v^n}\right)_{crit}$$

$$\frac{Y}{v^n} = a' + b'\left(\frac{D^*}{v^m}\right)^{-1} \quad \text{for } \frac{D^*}{v^m} > \left(\frac{D^*}{v^m}\right)_{crit}$$

where a, b, a', b', n, and m are constants.

In this analysis the data (given in Table B-2) were divided into two sets, set number 1 consisting of those having D^*/vm values less than the critical and set 2 consisting of those values of D^*/vm greater than critical. Various trial plots of the data using a range of n and m values were used to make the initial grouping of data. Regression analyses were then made using the above equations and the data in Table B-2 for all combinations of n and m ranging from 0.1 to 1.0 in 0.1 increments.

Although the minimum residual error for each part of the equation did not occur for the identical set of r and m values, the two minimums were quite close
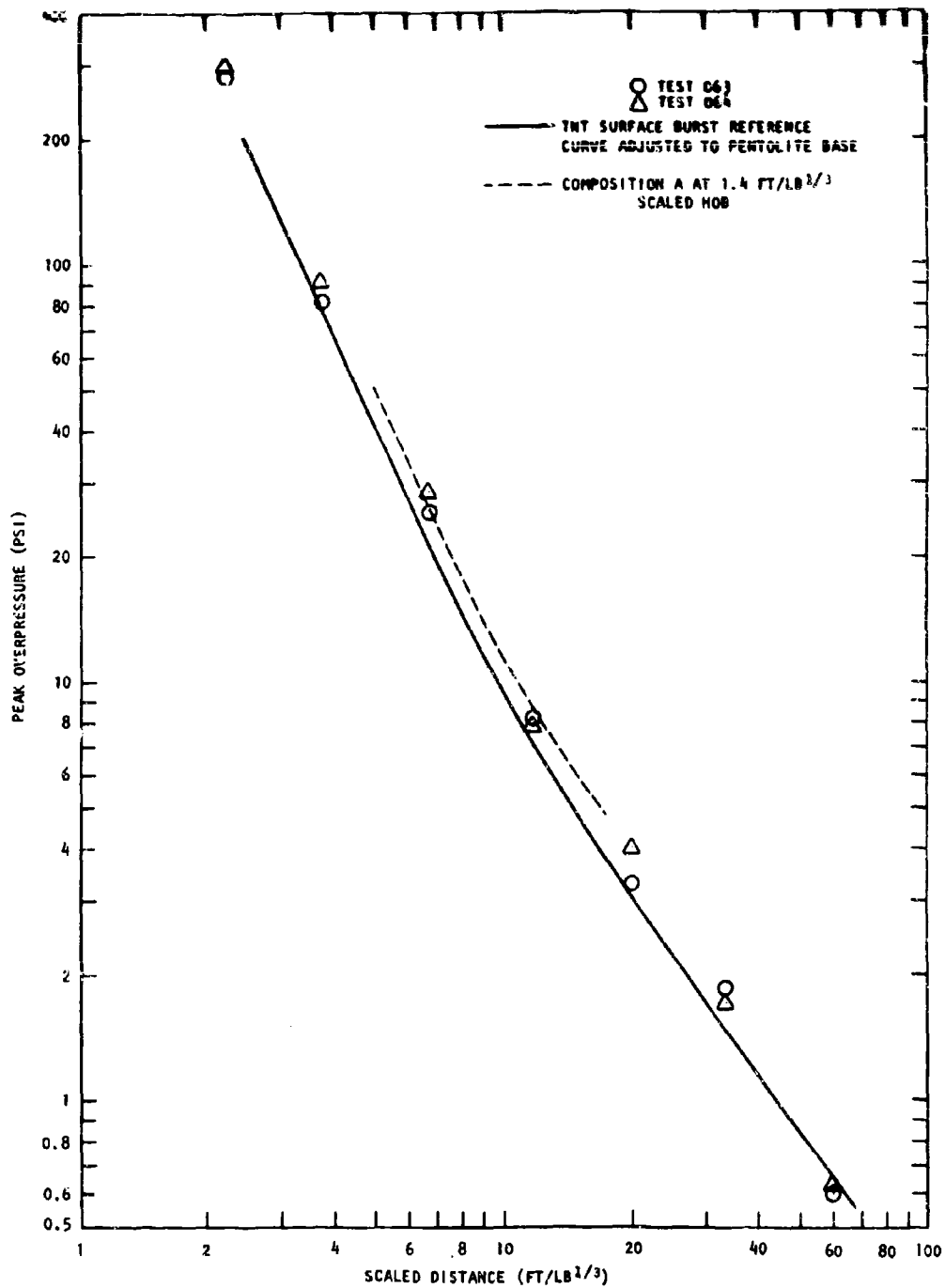
Fig. A-8. Peak Overpressure vs Scaled Distance from 1000-lb TNT Spheres at a Scaled HOB of 1.0 ft/lb$^{1/3}$

A-29

Table B-2

LO$_2$/RP-1 CBGS - VERTICAL DATA USED IN ANALYSIS

L/D	Weight (lb)	Velocity (ft/sec)	Test Number	Terminal Yield (%)	Ignition Time (msec)
1.8	200	23	144	24	190
1.8	200	23	202	42	870
1.8	200	23	248	25	210
1.8	200	44	208	62	460
1.8	200	44	232	30	1220
1.8	200	44	249	50	710
1.8	200	44	250	52	200
1.8	1000	44	267	64	1170
1.8	1000	44	268	70	340
1.8	1000	44	220	96	525
1.8	1000	44	219	14	1835
1.8	200	77	110	26	35
1.8	200	77	205	41	40
1.8	200	77	206	85	350
1.8	200	77	207	38	28
1.8	200	77	236	74	720
1.8	1000	77	190	96	570
1.8	1000	77	269A	44	77
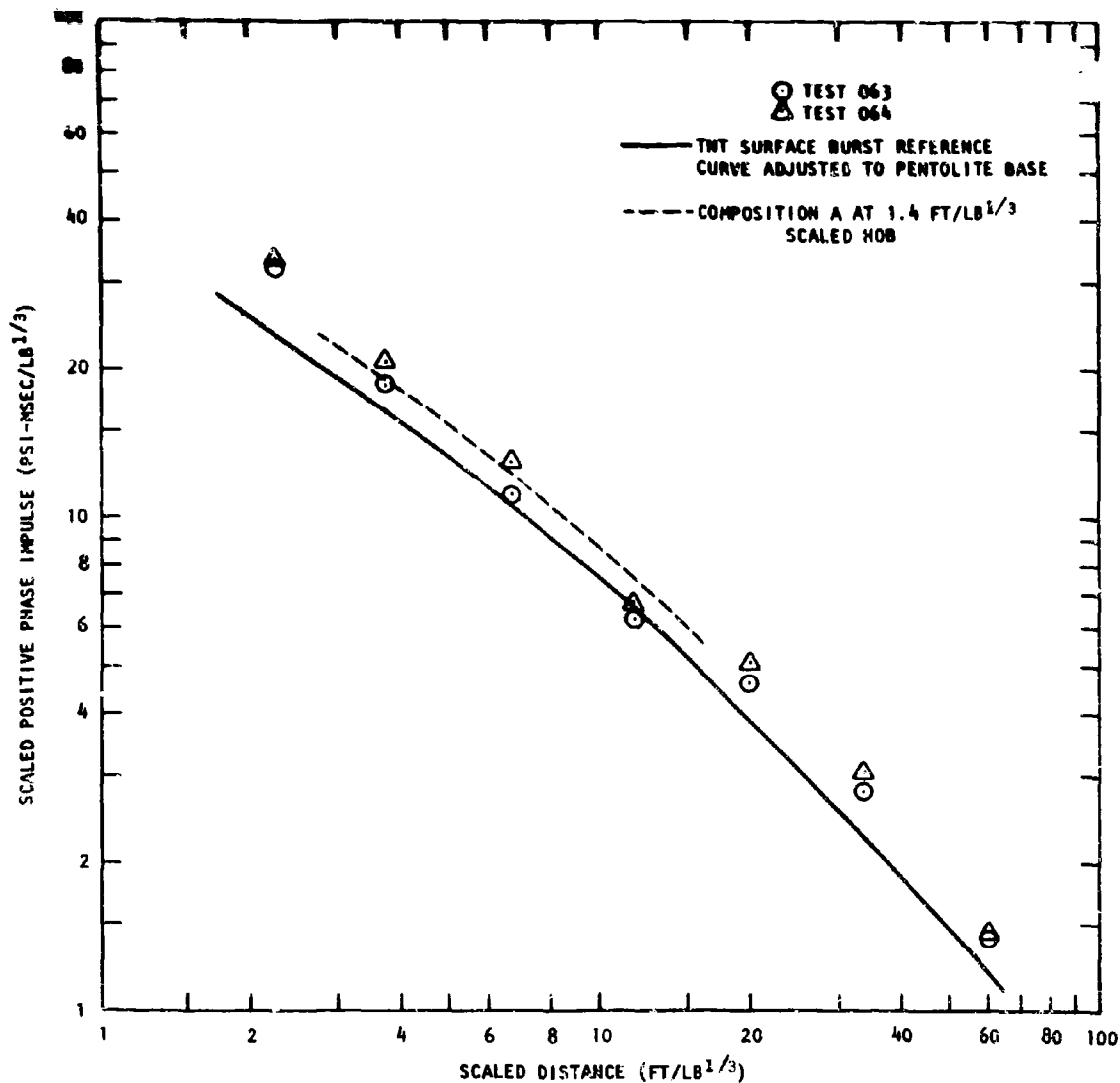
Fig. A-9. Scaled Positive-Phase-Impulse vs Scaled Distance from 1000-lb
TNT Spheres at a Scaled HOB of 1.0 ft/lb$^{1/3}$

Appendix A
REFERENCES

A-1. AFRPL-TR-68-111, A Report of an Instrumentation Accuracy Study Con-
ducted by AFRPL on the Basic PYRO Instrumentation System (in press)

A-2. Kingery, C.N. and B.F. Pannill, Peak Overpressure Vs. Scaled Distance
for TNT Surface Bursts (Hemispherical Charges), BRL Memorandum Report
No. 1518, Ballistic Research Laboratories, April 1964 (AD 443 102)

A-3. Defense Atomic Support Agency, Operation SNOW BALL Project Descrip-
tions, Volume 1 (U), DASA Data Center Special Report 24-1, DASA
1516-1 (AD 441 974)

A-4. Wilton, C., K. Kaplan, and N. Wallace, Study of Channeling of Air
Blast Waves Final Report, URS 170-19, DASA-1605, URS Corporation for
the Defense Atomic Support Agency, Burlingame, California, December
1964

together and the errors in the vicinity were changing rather slowly. The general region of the minimums for both parts of the equation occurred for n values of 0.8 and 0.9, and m values of 0.1 to 0.3.

The specific values of n = 0.9 and m equal to 0.2 were selected as suitable values near the minimum of each part of the equations and used in determining the following final form of the equations:

$$\left(\widetilde{\frac{Y}{V^{0.9}}}\right) = 0.22 + 2.7 \frac{D^*}{V^{0.2}}$$

$$\text{for } \frac{D^*}{V^{0.2}} \leq 1.1$$

$$\left(\widetilde{\frac{Y}{V^{0.9}}}\right) = 0.33 + 3.2 \frac{V^{0.2}}{D^*}$$

$$\text{for } \frac{D^*}{V^{0.2}} > 1.1$$

The upper prediction intervals calculated for these equations are:

$$\left(\frac{Y}{V^{0.9}}\right)_u = \left(\widetilde{\frac{Y}{V^{0.9}}}\right) + (0.20)(1.42)\left(1.38 - 1.18 \frac{D^*}{V^{0.2}} + 1.28 \frac{D^{*2}}{V^{0.4}}\right)^{1/2}$$

$$\text{for } \frac{D^*}{V^{0.2}} \leq 1.1$$

$$\left(\frac{Y}{V^{0.9}}\right)_u = \left(\widetilde{\frac{Y}{V^{0.9}}}\right) + (0.37)(1.46)\left(1.64 - 2.33 \frac{V^{0.2}}{D^*} + 2.49 \frac{V^{0.4}}{D^{*2}}\right)^{1/2}$$

$$\text{for } \frac{D^*}{V^{0.2}} > 1.1$$

LO_2/LH_2 CBM

The generalized form of the equation selected for the regression analysis was

$$Y = a + bt^* + \frac{c}{W} + d(L/D) + e(D_o/D_t)$$

where a, b, c, d, and e are constants and $t^* = t/W^{1/3}$.

The data for the D_o/D_t of 1.0 and L/D of 1.8 condition were excluded from the general analysis because their general pattern was significantly different from that of the remainder of the data, and the condition is of little interest, because D_o/D_t values greater than 0.45 are consi red highly unlikely.

The remainder of the data indicated that the yield increased with time up to a scaled time of about 17 msec/lb$^{1/3}$ and then became independent of time. Accordingly, the data shown in Table B-3 were divided into two groups for analysis with this equation.

Set 1 consists of 9 points corresponding to time values less than or equal to 100 msec. Set 2 consists of 11 points for which the ignition time was greater than or equal to 82 msec.

For set 1, the regression equation was

$$\widetilde{Y} = 2.75 + 0.82 \ t^* \tag{B.3}$$

The other independent variables, L/D and D_o/D_t, do not explain any appreciable amount of variability and hence were not included in the regression equation.

For set 2, the regression equation was computed to be

$$\widetilde{Y} = 20.0 + 0.00034 \ t^* \tag{B.4}$$

Appendix B
STATISTICAL ANALYSIS PROCEDURES

Data collected in the basic cryogenic test program were analyzed using the methodology described in this section. The two propellant combinations, $LO_2/$ RP-1 and LO_2/LH_2, and the two basic test configurations (CBM and CBGS) used gave rise to the four cases described in Section 5. To simplify the presentation of the statistical procedures, the analysis of the data arising in each of the four cases is presented in the following order:

1. LO_2/LH_2 CBGS - Vertical

2. $LO_2/RP-1$ CBGS - Vertical

3. LO_2/LH_2 CBM

4. $LO_2/RP-1$ CBM

The analysis was accomplished in two steps. In the first, regression techniques[*] were employed to obtain a relationship between yield and factors affecting yield. The process of establishing the form of the yield equation is described for each case in Section 5. Regression techniques were used to compare alternative forms for the yield equation, to select factors which could best explain observed variation in yield, and to determine values for the unknown parameters in the final equation.

In the second step, prediction interval estimation[*] techniques were used to determine an upper bound on a future yield observation.

These two steps will be described in detail and illustrated with the data from the LO_2/LH_2 CBGS-Vertical test series. For the other cases, the two steps are described briefly and variations in the analysis procedure are noted.

---

[*] See R. G. Miller, Simultaneous Statistical Inference, McGraw Hill, 1966, New York, for description of these techniques.

Table B-3

TEST DATA FOR LH_2/LO_2 CBM

L/D	D_o/D_t	Weight (lb)	Test Number	Ignition Time (msec)	Terminal Yield (%)	Set Number
1.8	0.45	200	053	1	4	1
1.8	0.45	200	090	35 sec	29	2
1.8	0.45	200	118	82	20	1,2
1.8	0.45	200	199	816	8	2
1.8	0.45	200	200	417	17	2
1.8	0.45	1000	210	20	7	1
1.8	0.45	1000	212	1366	27	2
1.8	0.45	1000	213	708	35	2
1.8	0.45	1000	265	750	10	2
1.8	0.083	200	169	318	15	2
1.8	0.083	200	173	56	13	1
5	1	200	052	83	7	1
5	1	200	057	12	1	1
5	1	200	092	3 min	26	2
5	0.45	200	054	17	6	1
5	0.45	200	055	1	1	1
5	0.45	200	094	329	25	2
5	0.45	200	138	100	17	1,2

LO$_2$/LH$_2$ CBGS - VERTICAL

<u>Yield Estimation by Regression Analysis</u>

In <u>simple regression</u>, one has a dependent variable, Y, and an independent variable, X. A set of observation pairs collected on Y and X is used to fit a line relating Y to X. In <u>multiple regression</u>, one has a dependent variable, Y, and several independent variables, X$_1$, X$_2$, . . ., X$_p$. Sets of data consisting of p + 1 numbers are collected from which is obtained a set of coefficients β_o, β_1, . . ., β_p enabling the yield to be expressed in terms of the independent variables according to the equation

$$Y = \beta_o + \beta_1 X_1 + \beta_2 X_2 \ldots + \beta_p X_p$$

The relationship, though seemingly linear, can be made nonlinear by replacing an independent or dependent variable with some nonlinear function of that variable. Thus, for example, Y can be replaced by Y$^{1/2}$ or X$_1$ can be replaced by X$_1^2$, etc. Thus, many different functional forms of the regression equation can be examined to find that one which does the best job in explaining the variation.

For the LO$_2$/LH$_2$ CBGS-Vertical case, the final form of the regression equation was found (Section 5) to be of the form

$$Y = \beta_o + \beta_1 D^* v^2 + \beta^{*2} v^2$$

where

$$D^* = \frac{Tv}{W^{1/3}}$$

and the symbols are defined as follows:

v denotes velocity (fps)

T denotes ignition time (sec)

W denotes weight (lb)

which for all intents and purposes can be considered independent of t.

The regression relation for yield was then taken to be Eq. (B.3) up to the time, t_c, at which this relation intersected the constant 20.0 and constant thereafter.

Thus,

$$\tilde{Y} = \begin{cases} 2.75 + 0.82\ t^* & t^* \leq 21.1 \\ 20.0 & t^* > 21.1 \end{cases}$$

An upper prediction interval for Eq. (B.3) was computed to be $Y_u = 2.75 + 0.82\ t^* + (1.415)\ (4.10)\ (1.24 - 0.00374\ t^* + 0.00270\ t^{*2})^{1/2}$, where 1.415 is the value of the t distribution of $\alpha = 0.1$ and seven degrees of freedom, and 4.10 is the residual standard deviation, S.

An upper prediction interval for Eq. (B.4) is

$$Y_u = 20.0 + (1.33)\ (8.46)\ (1.10)^{1/2}$$

It is possible to join the two upper prediction intervals by finding the point in which they intersect in the same manner as described for the regression equations.

LO_2/RP-1 CBM

The data for this case consist of the 23 tests described in Table B-4. The data can be observed to divide into two overlapping sets. One set consists of the sixteen 200-lb tests in which the parameter L/D assumes the values of 1.8 and 5 and the parameter D_o/D_t assumes the values 0.45 and 1. The other set consists of the 13 tests for which L/D = 1.8 and D_o/D_t = 0.45. In these 13 tests, the propellant weight parameter takes on the values of 200, 1,000 and 25,000 lb.

For each test the data consisted of yield, ignition time, impact velocity, and propellant weight. For the 20 tests used in the analysis, these data are shown in Table B-1.

Computations were done on a CDC 3800 computer system using a stepwise regression program, BMD 02 R, developed as part of the biomedical programs package by the UCLA Health Sciences Computing Facility. A partial output from this program is shown in Fig. B-1a.[†]

Note that the regression equation is developed stepwise. The contribution of each variable in reducing the unexplained variation in the data is computed and the variable showing the greatest reduction is entered first.

In this case D^*v^2 was the first variable entered (1)[††] and $D^{*2}v^2$ followed (2) in Step 2 as the remaining variable.

In Fig. B-1b, also obtained as output from the computer program, the contribution of each variable in reducing the variation is observable. The entry of D^*v^2 explained 53 percent (3) of the original variation, leaving 47 percent yet unexplained. Variable $D^{*2}v^2$ explained an additional 4 percent (4), increasing the explained variation to 57 percent and leaving an unexplained variation of 43 percent of the original variation in the data.

In Fig. B-1a, the total variation is 8199, (5), and the unexplained variation is 3863 (6), leaving an explained variation of 4336 (7). The ratio

$$\frac{4366}{8199} = 53\%$$

is the percentage of variation explained in the variable entered in the first step.

[†] Note the actual output has been retyped and edited to improve its clarity.

[††] The numbers in parentheses are keyed to the corresponding points of interest in the figures. The figure has been reproduced in upper case. Thus v appears in the figure as cap V. Also D^* appears as D.

Table B-4

SUMMARY OF TEST CONDITIONS AND TERMINAL YIELDS
FOR LO_2/RP-1 CONFINEMENT BY THE MISSILE TESTS

L/D	D_o/D_t	Propellant Weight (lb)	Test Number	Ignition Time (msec)	Terminal Yield (%)
1.8	1	200	042	290	48
1.8	1	200	058	200	27
1.8	1	200	086	100	14
1.8	0.45	200	044	120	18
1.8	0.45	200	087a	70	16
1.8	0.45	200	095a	120	17
1.8	0.45	200	101	145	35
1.8	0.45	200	237	127	32
1.8	0.45	200	238	85	19
1.8	0.45	200	239	156	32
1.8	0.45	1000	192	216	14
1.8	0.45	1000	193	222	20
1.8	0.45	1000	209	121	10
1.8	0.45	1000	270a	225	13
5	1	200	047	120	10
5	1	200	049	316	12
5	1	200	085	380	12
5	0.45	200	046	143	17
5	0.45	200	088	60	4
5	0.45	200	100	220	23
1.8	0.45	25000	275	515	4
1.8	0.45	25000	278	530	13
1.8	0.45	25000	282	540	13

Table B-1

LO$_2$/LH$_2$ CBGS - VERTICAL DATA USED IN ANALYSIS

L/D	Weight (lb)	Velocity (ft/sec)	Test Number	Terminal Yield (%)	Ignition Time (msec)
1.8	200	23	152	14	480
1.8	200	23	184	17	810
1.8	200	23	201	26	1524
1.8	200	23	225	34	933
1.8	200	23	153	14	121
1.8	200	44	254	32	533
1.8	200	44	197	19	500
1.8	200	44	231	24	525
1.8	200	4.	203	31	800
1.8	200	44	251	64	775
1.8	200	44	204	42	317
1.8	200	44	252	38	325
1.8	200	44	229	53	1374
1.8	1000	44	217	33	1490
1.8	1000	44	262	42	900
1.8	200	77	114	54	74
1.8	200	77	150	35	40
1.8	200	77	151	46	167
1.8	200	77	195	104	292
1.8	200	77	226	51	283

The final form of the yield equation of interest is

$$\frac{Y}{t^*} = (1 + \beta/W)\ (\beta_o + \beta_1\ L/D + \beta_2\ D_o/D_t)$$

where $t^* = t/W^{1/3}$ and t is time in milliseconds.

Yield Estimation by Regression Analysis

The regression coefficients β, β_o, β_1, and β_2 were obtained in three steps.

Step 1

Starting with the equation

$$\left(\frac{Y}{t^*}\right) = \beta_o + \beta_1\ (L/D) + \beta_2\ (D_o/D_t)$$

the 200-lb data were used to estimate β_o, β_1, and β_2. The resulting estimates were

$$\hat{\beta}_o = 1.792$$

$$\hat{\beta}_1 = 0.190$$

$$\hat{\beta}_2 = 0.570$$

Step 2

The estimates for β_o, β_1, and β_2 were then substituted into the equation

$$\frac{Y}{t^*} = (\alpha + \beta/W)\ \left[\beta_o + \beta_1\ (L/D) + \beta_2\ (D_o/D_t)\right]$$

Using the data for which $L/D = 1.8$ and $D_o/D_t = 0.45$, the factor

DEPENDENT VARIABLE   Y

STEP NUMBER   1

VARIABLE ENTERED DV^2 (1)

MULTIPLE R   0.7272

STD.ERROR OF EST.   14.6496

ANALYSIS OF VARIANCE

	DF	SUM OF SQUARES	MEAN SQUARE
REGRESSION	1	4335.561 (7)	4335.561
RESIDUAL	18	3862.989 (6)	214.610
TOTAL	19	8198.550 (5)	

VARIABLES IN EQUATION

VARIABLE	COEFFICIENT
CONSTANT	19.85061
DV^2	.00221

STEP NUMBER   2

VARIABLE ENTERED D^2V^2 (2)

MULTIPLE R   0.7564

STD.ERROR OF EST.   14.3667

ANALYSIS OF VARIANCE

	DF	SUM OF SQUARES	MEAN SQUARE
REGRESSION	2	4690.220	2345.110
RESIDUAL	17 (9)	3508.330	206.372 (8)
TOTAL	19	8198.550	

VARIABLES IN EQUATION

VARIABLE	COEFFICIENT
CONSTANT	18.40333 (10)
DV^2	.00310 (10)
D^2V^2	-.00015 (10)

Fig. B-1a. Partial Output from Computer Program BMD 02 R

$$\left[\beta_o + \beta_1 \ (L/D) + \beta_2 \ (D_o/D_t)\right]$$

is constant, and estimates $\hat{\alpha}$ and $\hat{\beta}$ can be computed for α and β. This computation yielded

$$\hat{\alpha} = 0.4850$$

$$\hat{\beta} = 105.236$$

Step 3

An equation of the desired form can now be obtained by dividing the first factor, $(\alpha + \beta/W)$ by α and simultaneously multiplying the second factor, $\beta_o + \beta_1 \ (L/D) + \beta_2 \ (D_o/D_t)$, by α. This computation yields the final equation:

$$\widetilde{\left(\frac{Y}{t^*}\right)} = \left(1 + \frac{217.0}{W}\right)\left[0.8693 + 0.0919 \ (L/D) + 0.2763 \ (D_o/D_t)\right] \qquad (B.5)$$

It is recognized that this is not a standard regression computation and the slight overlap in the data will produce some error in the equation. It is felt, however, that the error is not as large as might be the result of using some less desirable form of the equation.

Upper Prediction Interval Estimation

By restricting our interest to large weights, the above equation is approximately

$$\widetilde{\left(\frac{Y}{t^*}\right)} \approx 0.8693 + 0.0919 \ (L/D) + 0.2763 \ (D_o/D_t)$$

We can then use all the data to set up the matrix (A_{ij}) and obtain the confidence interval. The value for S^2 was obtained by taking the sum of the squared deviation of each data point from the value of Eq. (B.5) and dividing by 23 minus 3, to adjust for the effect of the number of parameters estimated.

B-17

This yielded the upper prediction interval

$$\left(\frac{Y}{t^*}\right)_u = \left(1 + \frac{217.0}{W}\right)\left[0.8693 + 0.0919 \; (L/D) + 0.2763 \; (D_o/D_t)\right]$$

$$+ 1.33 \left(\frac{217.0}{W}\right) 0.29 \left[1 + 0.3627 + 0.02459 \; (L/D)^2\right.$$

$$+ 0.8326 \; (D_o/D_t)^2 - 0.07466 \; (L/D) - 0.7442 \; (D_o/D_t)$$

$$\left. - 0.09258 \; (L/D) \; (D_o/D_t)\right]^{1/2}$$

Appendix C

THERMAL INSTRUMENTATION

Appendix C consists of discussions of the thermal instruments, the errors of the corresponding measurements, and the experimental arrangement and instrument mounting. The following list of measurements and the associated instruments are considered:

- Heat flux density computed from measurements of the surface temperature of slabs

- Fireball temperature from a photographic recording Pyrometer (a Sandia Corporation instrument)

- Radiant flux density within and external to the fireball from Gardon-type radiometers

- Gas temperature from thermocouple probes (Sandia Corporation instruments)

The general organization of Appendix C is given in the following paragraphs.

The measurement of heat flux density is considered first, starting with a description of the method of its evaluation from the surface temperature records. This is followed by an analysis of errors that are uniquely associated with this method and that are not related to the errors in heat flux density which are a consequence of errors in slab temperature measurements. The slab temperature transducers or instruments are then considered, and this is followed by a discussion of heat flux density errors that result from errors in the slab temperature measurements.

A brief description is then given of the photographic recording pyrometer. This instrument indicates blackbody equivalent temperatures through a radiation intensity comparison of an image of the fireball with corresponding images of several tungsten filaments, each of which is at a different temperature.

C-i

The radiometers are next described, and this is followed by an analysis of radiometer data correction factors, including an indication of their uncertainties, which are required in conjunction with intrafireball measurements.

A brief description of the thermocouple probes is then given. Finally, the experimental arrangement and instrument mounting is described.

Appendix C

THERMAL INSTRUMENTATION

HEAT FLUX DENSITY: METHOD OF EVALUATION, INSTRUMENTS, AND ERRORS

Computational Method of Evaluating Heat Flux Density from Surface-Temperature
Data

The basic relationship from which the heat flux density history at the
surface of a slab is evaluated from the slab surface-temperature history is[*]

$$q(t) = K' \int_0^t \frac{\frac{\partial T_s(\tau)}{\partial \tau}}{\sqrt{t - \tau}} \, d\tau \qquad (C.1)$$

where q is the heat flux density; $K' = (K\rho c/\pi)^{1/2}$; K, ρ, and c are the con-
ductivity, density, and specific heat, respectively, of the slabs; T_s is the
slab surface temperature; and t is time. This relationship is valid provided
the heat flux density is uniform over the surface of the slab, the thermal
properties, K, ρ, and c, are constant, and the slab is semi-infinite, that is,
it occupies, or effectively occupies, half of space.

The evaluation of q(t) from the surface temperature in data-trace form
through application of Eq. (C.1) may be accomplished by any of numerous pro-
cedures. For convenience, we have chosen to modify Eq. (C.1) to a form which
particularly accommodates temperature data in digital form, and this modifica-
tion is described in the following paragraph.

Integration of Eq. (C.1) over the time range t = o to t = t is first
divided into arbitrary intervals, so that for t in the interval $t_{i-1} \leq t \leq t_i$,
q(t) is given by

---

[*] A derivation of Eq. (C.1) is given starting p. 132 in Ref. C-1.

C-1

$$\frac{q(t)}{K'} = \sum_{n=1}^{n=i-1} \int_{t_{n-1}}^{t_n} \frac{\frac{\partial T_s(\tau)}{\partial \tau}}{(t - \tau)^{1/2}} d\tau + \int_{t_{i-1}}^{t} \frac{\frac{\partial T_s(\tau)}{\partial \tau}}{(t - \tau)^{1/2}} d\tau, \quad (t_0 = 0) \quad (C.2)$$

Then an expression representing the temperature in the nth interval $t_{n-1} \le t \le t_n$ is assumed and substituted into Eq. (C.2); in particular, the linear expression $T_{ns}(t) = a_n + b_n t$ has been chosen. Equation (C.2) then reduces to

$$\frac{q(t)}{K'} = 2 \left[b_1 t^{1/2} + \sum_{n=1}^{n=i-1} (b_{n+1} - b_n)(t - t_n)^{1/2} \right] \quad \text{for } t_{i-1} \le t \le t_i \quad (C.3)$$

Eq. (C.3) is further modified by writing the constants b_n in terms of the temperatures and corresponding times at the ends of the time intervals, that is, by $b_n = (T_n - T_{n-1})/(t_n - t_{n-1})$, giving

$$\frac{q(t)}{K'} = 2 \left[\frac{T_1}{t_1} t^{1/2} + \sum_{n=1}^{n=i-1} \left(\frac{T_{n+1} - T_n}{t_{n+1} - t_n} - \frac{T_n - T_{n-1}}{t_n - t_{n-1}} \right) \left(t - t_n \right)^{1/2} \right]$$

(C.4)

$$\text{for } t_{i-1} \le t \le t_i$$

Eq. (C.4) is, finally, the working equation, that is, q is evaluated at t by the substitution of appropriate temperature values (T_{n+1}, T_n, ..., T_1) and corresponding times (t_{n+1}, t_n, ..., t_1) that are evaluated from the data records.

Errors Associated with the Heat Flux Density Computational Method

Errors that are encountered in evaluating the heat flux density are, for convenience, separated into those associated with the instrumentation (that is, those due to errors in the thermal properties of the slabs [K' in Eq. (C.1)] and to errors in the surface temperature – time record due to the transducer, amplifier,

and recording system) and into those that are not associated with the instru-
ments. Those related to the instruments are considered later. The remaining
errors, which concern the application of Eq. (C.4), are considered in the pres-
ent section. This discussion commences with the assumption that a true or cor-
rect surface temperature-time record (trace form) is available. Under this
circumstance, there are two types of errors encountered in the evaluation of
the heat flux.

The first error type is that which results from the misrepresentation of
the true surface temperature-time curve which occurs when this curve is replaced,
in effect, by a sequence of line segments. By itself, this error can, of course,
be minimized to any desired degree by decreasing the time interval over which
the temperatures are evaluated; however, its elimination is precluded by the
fact that errors of the second type tend to increase with decreasing interval
sizes.

Errors of the second type result from the inability to exactly evaluate
the "true" temperatures at the ends of the intervals, there being the natural
tendency for the measured values to scatter above and below the true values.
The effect of these temperature errors on the computed heat flux density is il-
lustrated on Fig. C-1. On Fig. C-1a is a portion of a true temperature curve
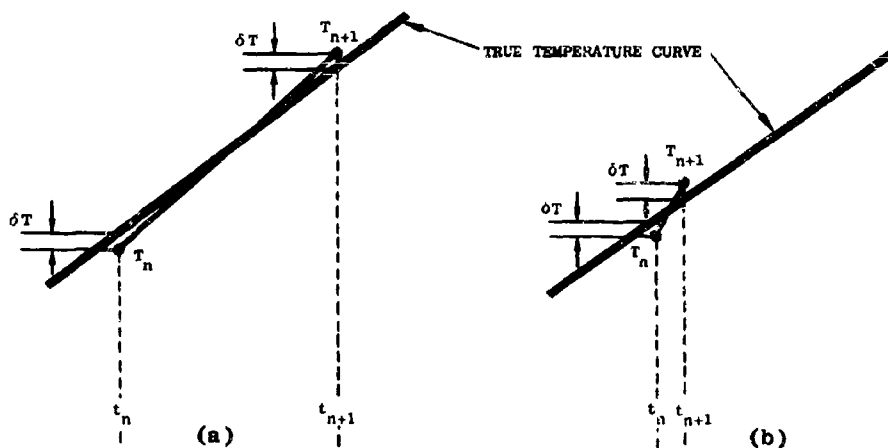
Fig. C-1. Illustration of Origin of Errors of Second Type

along with a line segment representing the curve over a single interval, where there is a temperature error, indicated as δT, at both ends of the interval, the evaluation being less than the true value at the early end and greater at the late end. For the same set of temperature errors over a smaller interval, as shown in Fig. C-1b, the error in the slope of the temperature—time curve is larger. From Eq. (C.4), the heat flux density is seen to depend on the slope over the interval (and all preceding intervals), and thus the flux density error due to temperature errors of this type will tend to increase as the size of the interval is decreased, as implied above.

Thus, with the first type error decreasing and the second type increasing with decreasing interval size, there is an optimum interval length, although the optimum length will vary along a given temperature curve, for instance, as the curvature of the temperature curve varies. A more complicating circumstance, however, is that an error in the heat flux evaluated within a given interval depends not only on the temperature—time slope error in the interval, but in all preceding intervals, as examination of Eq. (C.4) indicates. Because of this latter circumstance and the fact that there is a great variation in the temperature—time records obtained, a general and analytical error analysis is prohibitive and, in light of the objectives, unnecessary. In consequence, the analysis is confined to the evaluation of errors for temperature curves that resemble typical temperature data forms that have been obtained. In addition, because the maximum values of the heat flux that are obtained during heat transfer surges are given relative importance in the presentation of results, errors of the maximum values are emphasized in the error analysis.

The method of evaluating errors consists of comparing an exact heat flux density—time solution for a given surface—temperature—time function (equation) with the solution when Eq. (C.4) is applied to the same temperature function but with, in some cases, the insertion of deliberate and likely temperature errors in Eq. (C.4). The exact solutions are obtained in two ways, the first being simply to utilize existing solutions that are appropriate. When suitable solutions are not available, they are obtained by applying the basic relationship, Eq. (C.1), to temperature—time functions which both resemble typical data forms and which render Eq. (C.1) readily integrable. Examples of the heat flux

errors of both kinds that are encountered for various temperature curves are presented in the following paragraphs.

An example of a temperature-time function which is representative of "early time" data that are obtained is presented in Fig. C-2, along with the "true" flux density-time curve corresponding to that temperature for a K' [Eq. (C.1)] of 0.455 watt/$°C$-cm^2-$sec^{1/2}$, corresponding approximately to some of the stainless steels. The heat flux was evaluated "exactly" through Eq. (C.1), and the flux computed numerically by applying Eq. (C.4). This example is presented primarily as an illustration of concepts and certain features of the two error types, but the associated magnitudes are also useful since the temperature curve is representative of data obtained.

It is convenient to introduce a "pseudo-curvature," hereafter referred to as simply as the curvature, which is defined as
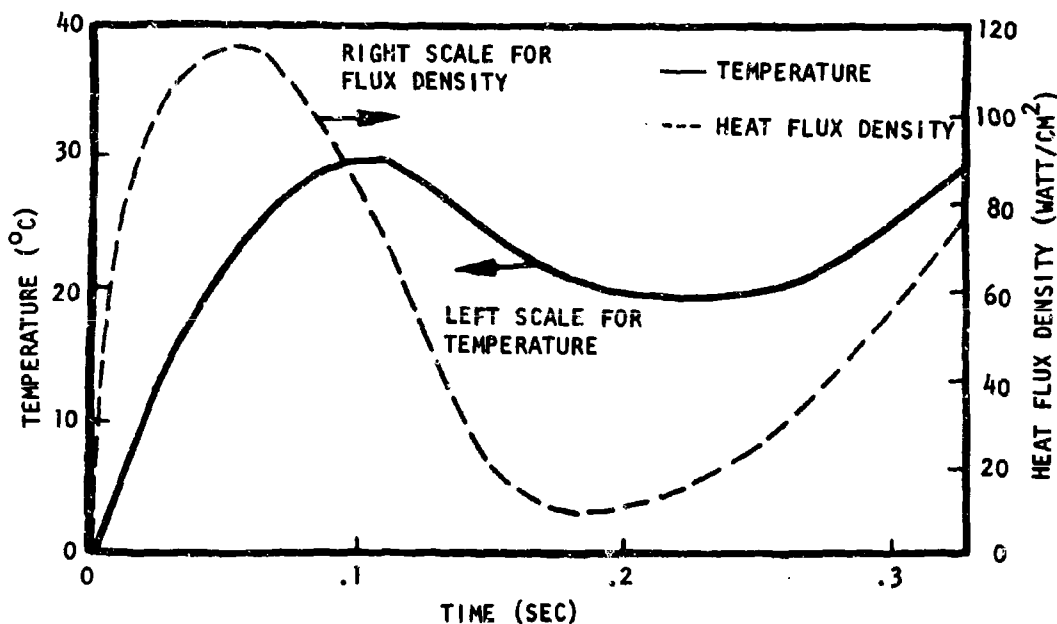
Fig. C-2. Heat Flux Density from Example Temperature-Time Trace

$$C = \frac{d^2T}{dt^2} \bigg/ \left[1 + \left(\frac{dT}{dt}\right)^2\right]^{3/2}$$

where C is the curvature, T is the temperature, and t is time. This is an extension of the ordinary or geometric curvature in that space or dimensional variables have been replaced by those representing temperature and time.

Errors of the first type have been evaluated for this temperature curve by applying Eq. (C.4) with a specific and uniform time interval for each computation, with the correct values of the temperature being used. This computation has been done for various computational time intervals, and the resultant error is plotted with the time interval on Fig. C-3 (continuous curve). Errors of this type tend to increase with increasing curvature of the temperature curve, and errors for other ranges of curvature will be presented later.
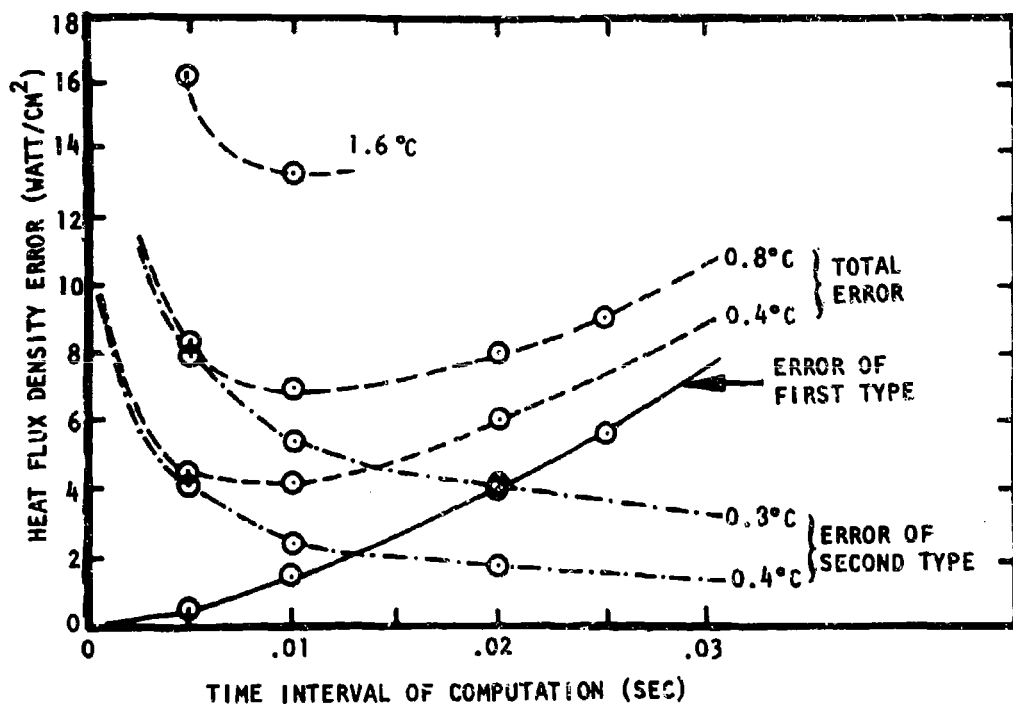
Fig. C-3. Heat Flux Density Errors for a Representative Temperature—Time Curve

C-6

Equation (C.4) was subsequently applied to the same temperature curve
using the same time intervals, but with deliberate sequences of errors in
the temperature values, therby revealing the total flux error, that is,
the error which includes errors of both types.[*] The temperature errors
used correspond to those that are likely to have occurred with the data
processing procedures that have been used. The temperature error distribu-
tion used consists of temperatures at the ends of time intervals that are
alternately above and below the correct value by a fixed magnitude. Thus,
the slope of the temperature curve over a time interval is alternately (from
time interval to time interval) above and below the correct slope, an' while
this particular distribution of errors is highly improbable, it is diagnos-
tically useful. Total errors obtained from this computation are plotted on
Fig. C-3 (dashed line) for a range of time intervals of computation and for
various magnitudes of temperature errors. A temperature of 0.4, 0.8, or
1.6 °C is listed adjacent to a curve to indicate the total temperature error
inserted at the ends of each interval, that is, the magnitude that the temp-
erature is above the true value at one end of a given time interval plus the
magnitude that it is below at the other end. As before, the curves are
plotted for errors obtained at 0.1 sec, and also as before, the error is
for practical purposes invariant for the range of curvatures present in the
temperature curve of Fig. C-2. It can be seen that the total error curves
reach minimum values for time intervals in the vicinity of 10 msec, with
least total errors of about 4, 7, and 13 watts/cm^2 for temperature errors
of 0.4, 0.8, and 1.6 °C, respectively. At the peak of the flux curve,
where the magnitude is approximately 114 watts/cm^2 (at about 0.05 sec on
Fig. C-2), errors of 4, 7, and 13 watts/cm^2 correspond to 3.5, 6, and 10
percent. From estimates of the standard deviation of the temperature
evaluation, the error curve that most nearly corresponds to actual errors
is the curve labeled "0.8 °C," thus indicating that a flux error of about 6
percent can be expected for this circumstance. It should be noted, however
that this will vary somewhat with the quality of the temperature data. More

---

[*] Errors of the second type may be isolated through certain applications of
Eq. (C.1). However, the effort is more extensive than is felt to be justified.

C-7

importantly, it should be understood that the value of 0.8 °C for a typical
temperature error is the result of both the techniques used for measuring
the displacement (or height) of the data trace and the particular scale
of the data trace. Regarding the latter, a temperature-time trace with a
different number of degrees (temperature) per inch on the paper would result
in typical temperature errors other than 0.8 °C, and perhaps well outside
the 0.4 to 1.6 °C range mentioned above. For a given scale, improving the
accuracy of the trace displacement measurement would of course decrease the
temperature error. The value of 0.8 °C is an estimate for the methods of
displacement measurement used with the data at the graphical scale that was
available. Referring once again to the typical flux error of 7 watts/cm^2,
for periods during which the flux is comparatively low, the _percentage_
error can be exceedingly large; for instance, in the vicinity of 0.2 sec
where the flux is approximately 12 watts/cm^2, the error is about 60 per-
cent. It is not correct, however, that all relatively small flux values
have percentage errors of this order. Roughly speaking, low but steady flux
magnitudes will be comparatively accurate, and the larger errors in flux
(on a _percentage_ basis) are associated with the minimum value of a sharp
depression or trough in a flux curve.

Estimates and trends of errors of the second type are also given on
Fig. C-3 (dash-dot curve), which were obtained by subtraction of the error
of the first type (continuous curve) from the errors which are due to errors of
both types (dashed curve).[*] With this additional curve, Fig. C-3 serves as a
useful guide. It is known, for instance, that for temperature curves having
less curvature than the curve of Fig. C-2 at 0.1 sec, the errors of the first
kind will not increase as rapidly with time interval as the curve presented

---

[*] For convenience, the errors of the first and second type are treated as
though their sum always represents the total error. For approximately
one-half of the intervals, however, the first and second error types are
in opposing directions, that is, the error of one type tends to negate
the error of the other type. Thus, the plots indicate worst or bounding
case errors.

on Fig. C-3, and therefore, the flux error for a given temperature error
can be greatly reduced by increasing the time interval of the computation
from 10 msec. If, however, it is necessary to maintain or improve the
accuracy for conditions of greater curvature, the only recourse is to im-
prove the temperature-data-evaluating procedure.

The effect of variation in the curvature of the temperature curves on
errors of the first type is given to a limited extent in Fig. C-4, where
the error is plotted vs time interval of computation for three values of
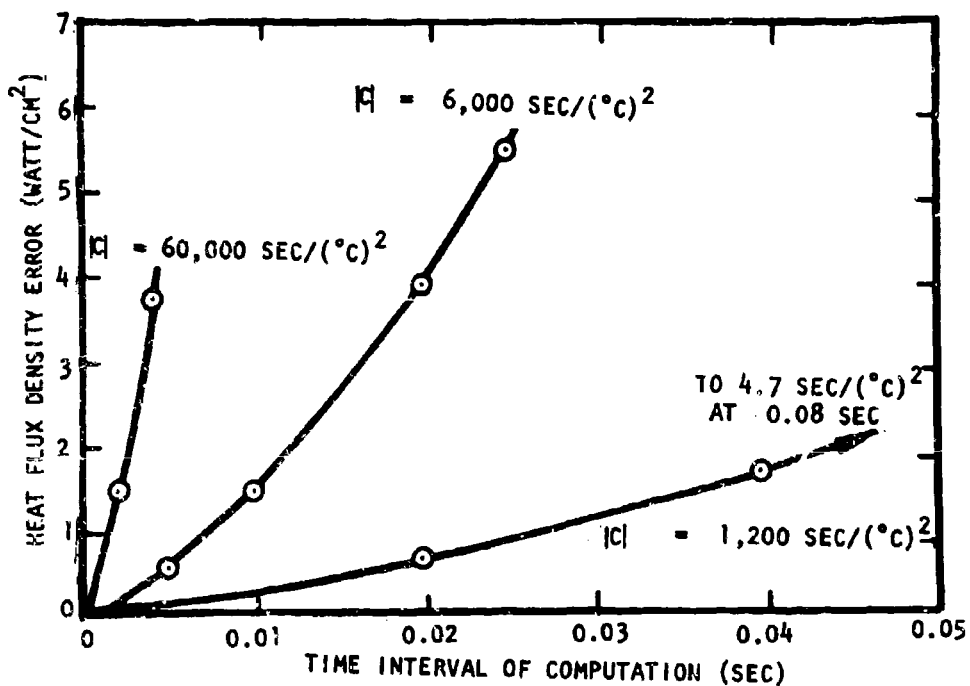
Fig. C-4. Heat Flux Density Errors of the First Type

curvature. Since errors of the second type depend only on the time interval
of computation and temperature evaluation error, that is, they are independent
of curvature[*], the curves for errors of the second type on Fig. C-3 and
those for the first type on Fig. C-4 may be combined so as to reveal curves
representing the total error for a range of curvatures. A family of curves
obtained from this process for the anticipated temperature errors of 0.8 °C
are given on Fig. C-5.[**]   These curves provide guidance in selecting the
computational interval that will minimize the errors, and provide an indi-
cation of the errors that can be expected for a given set of conditions.

It should be recognized that the error within a given interval depends
not only on the error in the slope of the temperature curve for that interval
but in the corresponding errors for all preceding intervals, and that the
sequence of temperature errors that has thus far been considered has con-
sisted of errors of a fixed magnitude that are alternately (from interval
to interval) above and below the true value. The error curves that have
been presented are, then, representative of this particular distribution of
temperature errors, while the actual distributions are, of course, infinite
in their variety. The effect of modifying the distribution was investigated
by imposing several different and intuitively probable temperature error
distributions on the same temperature function. The variation in the errors
for a given interval from among the various distributions was never in excess

---

[*] The independence of errors of the second type with curvature can be proven
analytically by applying Eq. (C.4) to two dissimilar but mathematically
arbitrary temperature functions which have identical but arbitrary temp-
erature error distributions imposed on them.

[**] Since the values of the errors of the second type on Fig. C-3 are very
uncertain at times less than 0.04 sec and these values are required over
this time range for the construction of total error curves for curvatures
of 60,000 sec/(°C)^2, an estimate of the error curve of the first type for
a curvature of 12,000 sec/(°C)^2 was obtained and the total error curve
corresponding to this curvature is given in Fig. C-5.
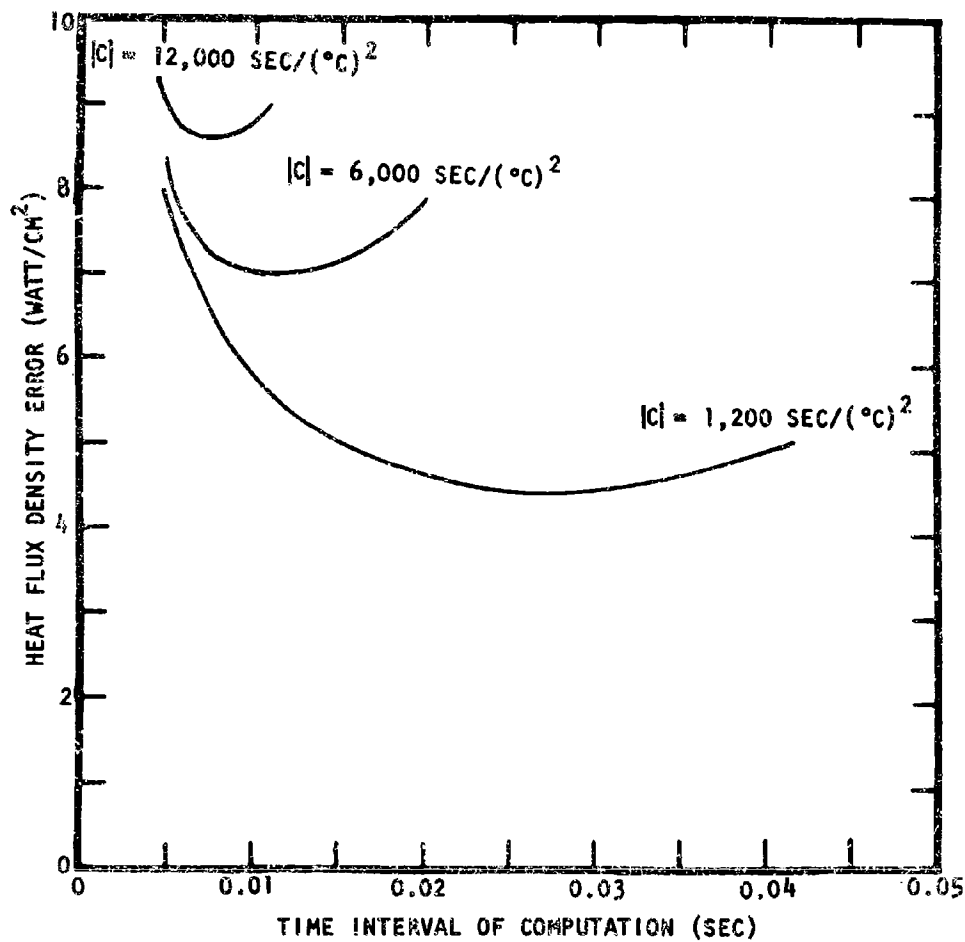
Fig. C-5. Heat Flux Density Error with Curvature and Time
           Interval of Computation

of 5 percent, and the error curves given for the special-case distribution in the figures above are representative of the errors for these distributions. The distributions that were considered by no means represent a thorough sampling, however, and distributions which result in variations in excess of 5 percent may occur.

The general errors as illustrated on Fig. C-5 have been generally verified for numerous conditions, and the results from a further example are presented primarily in the interest of illustrating certain points. One of the conditions of error that is of particular interest is that associated with the peak values for comparatively short-duration heating pulses. This was investigated by analytically imposing various short-duration heating pulses at various times on an otherwise constant and comparatively low-magnitude heating cycle. In the usual way, exact solutions were obtained and compared with numerical evaluations for which various appropriate errors had been introduced into the temperature values. For the example presented, a heating pulse of 40 msec duration centered about 0.1 sec* was superimposed on a constant heat flux density of 40 watts/cm^2, with the pulse maximum reaching approximately 132 watts/cm^2. Temperature errors covering their expected range were introduced <u>at approximately the time corresponding to the peak of the heating pulse</u>. The errors for this case are presented (in terms of percentage) on Fig. C-6. For a temperature error of 0.8°C corresponding to the most likely magnitude, the error from Fig. C-6 is about 15 percent, which corresponds to an error of about) watts/cm^2. This error is substantially greater than the minimal error (about 8.6 watts/cm^2) given for this curvature [about 12,000 sec/(°C)^2] on Fig. C-5 because a time interval of computation of 0.004 sec rather than the optimum interval of approximately 0.007 sec was used. However, since the 'dip or trough' in the total error curves of Fig. C-5 is comparatively 'sharp' for curvatures of this and larger magnitudes, this minimal error (cited above) is perhaps common for this curvature unless inordinately refined data analysis procedures are

---

* Precisely, the corresponding temperature 'pulse' rather the heating pulse was centered about 0.1 sec, the peak of the heating pulse slightly preceding this time.
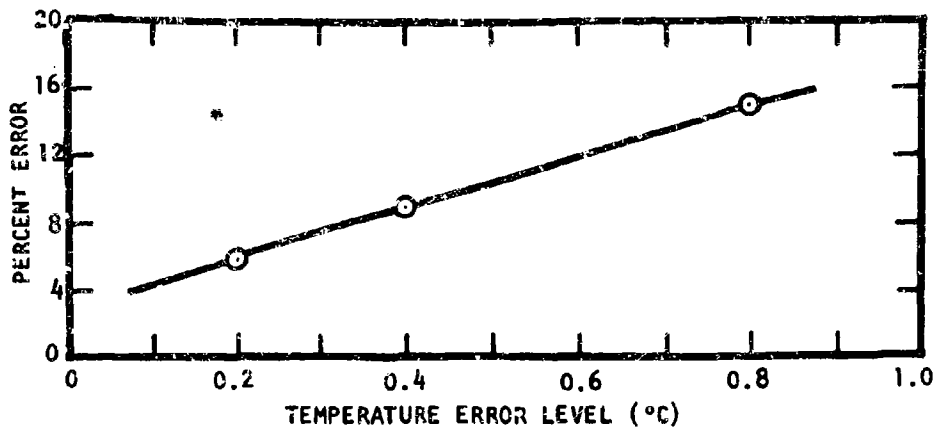
Fig. C-6. Error at the Peak of Heat Flux Density Pulse

adhered to. Moreover, misjudgments of a given magnitude would tend to more substantially inflate the error in this case compared to cases where the curvature of the temperature curve is smaller.

Finally, it is important to recognize that the errors presented above are representative of those associated with a __single__ computational interval, and that they will tend to scatter from interval to interval above and below the true value by such magnitudes. In the case above, ten computational intervals would be associated with the 40-msec pulse. An erroneously high value over a given interval will tend to be compensated by a correspondingly low value in the subsequent interval. Thus, a smooth curve through the computed values over the 40-msec pulse will be substantially more certain than indicated by the errors plotted on Fig. C-6 above. By way of illustration, the exact and computed cumulative flux density values over, say, 20 to 30 computational intervals for typical temperature curves and errors, never differ by more than 0.5 percent.

Surface-Temperature Transducers

The method employed to measure the temperature within a solid material, hereafter referred to as the parent material, is standard and described or referred to in several articles, for example in Refs. C-2, C-3, and C-4. Briefly, the transducer, illustrated in Fig. C-7, consists of a fine wire which is contained within a cavity in the parent material and which is electrically insulated from the walls of the cavity except at an end, where it is joined (welded) to form a thermocouple junction just below one exterior surface of the parent material. Thus, any change of temperature of the junction will introduce a corresponding change in the electrical potential difference between the wire and parent material.
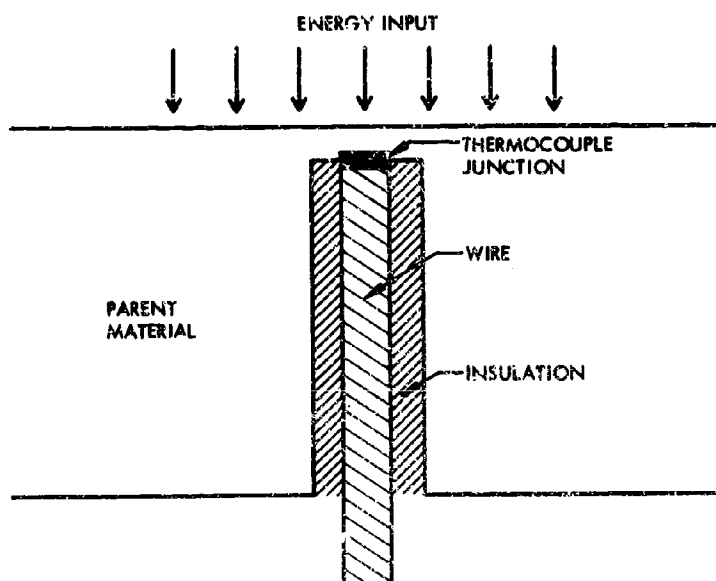
Fig. C-7. Generalized Configuration of a Surface-Temperature transducer

Instruments of two somewhat different designs are used. The details of the first type,[*] the transducer that was predominantly employed, are presented in a cross-sectional cutaway view, along with an enlargement of the thermocouple junction region, in Fig. C-8.[**] This transducer incorporates two wires so that only the molecular composition of the wires, not the parent material, enters into the electromotive force per unit temperature rise characteristic of the transducer.

Three slightly different versions of the transducer type shown on Fig. C-8 were used, differing only in the parent material and a single dimension. The parent material of the instrument presented in Fig. C-8 is copper, and the depths of the thermocouple junctions are 0.005 in. For the other two, the parent material is stainless steel 303 and 309, with junction depths for each of 0.002 in. The three versions are otherwise identical, including the thermocouple wire combination of chromel and alumel.

The important features of the second type of transducer[***] are presented on Fig. C-9, which is a cross-sectional view of just the thermocouple junction region, analogous to the region that was enlarged on Fig. C-8. This is a single-cavity (and wire) system, so that the parent material, in this case iron, enters into the electromotive force per unit temperature change characteristic. The depth of the thermocouple junction is 0.0002 in., and unlike the previous example, the material between the junction and the exposed surface does not match the parent material, the thin exposed layer being a copper deposit on an iron surface, as illustrated on Fig. C-9. The particular application planned for this transducer called for the parent material to be a comparatively poor heat conductor, more specifically, that the thermal diffusivity be low, in order to minimize the distance that a spatial non-uniformity in heat input along the surface of the parent material can effect

---

  [*] Manufactured by Advanced Technology Laboratories, Mountain View, California.

[**] Unless tolerances are noted on the figures, the distances shown were obtained by measurement of one transducer that has been cross-sectionally sliced and are uncertain to perhaps 0.003 in.

[***] Manufactured by Heat Technology Laboratories, Huntsville, Alabama.

ENLARGED VIEW
OF JUNCTION
REGION BELOW

|← 0.25" →|

DEPOSITED COPPER LAYER
THICKNESS 0.005" ± 0.0005"

CHROMEL WIRE

ALUMEL WIRE

Cu   Cu   Cu

LEADS (TO COLD JUNCTION)

COPPER   0.005" ± 0.0005

COPPER

ALUMEL
WIRE

CHROMEL
WIRE

COPPER

COPPER

COPPER

INSULATION

0.012"

0.020"

0.062"
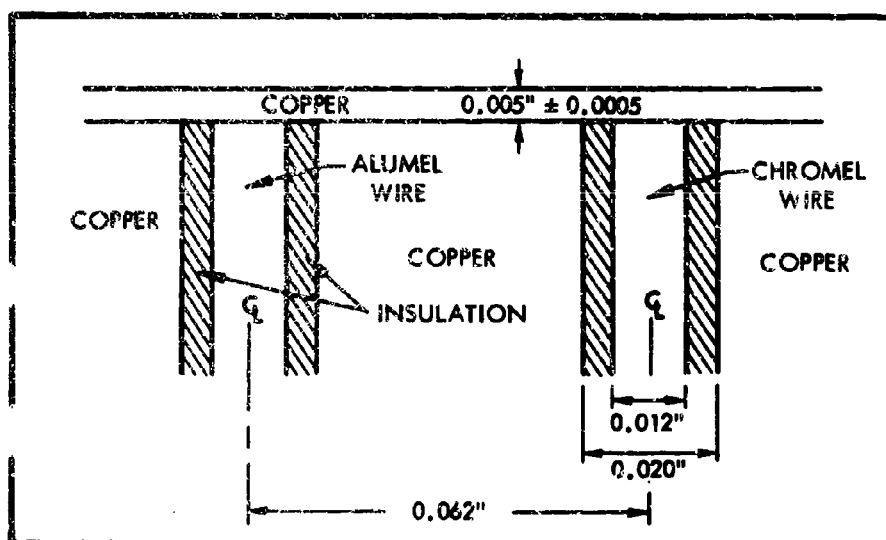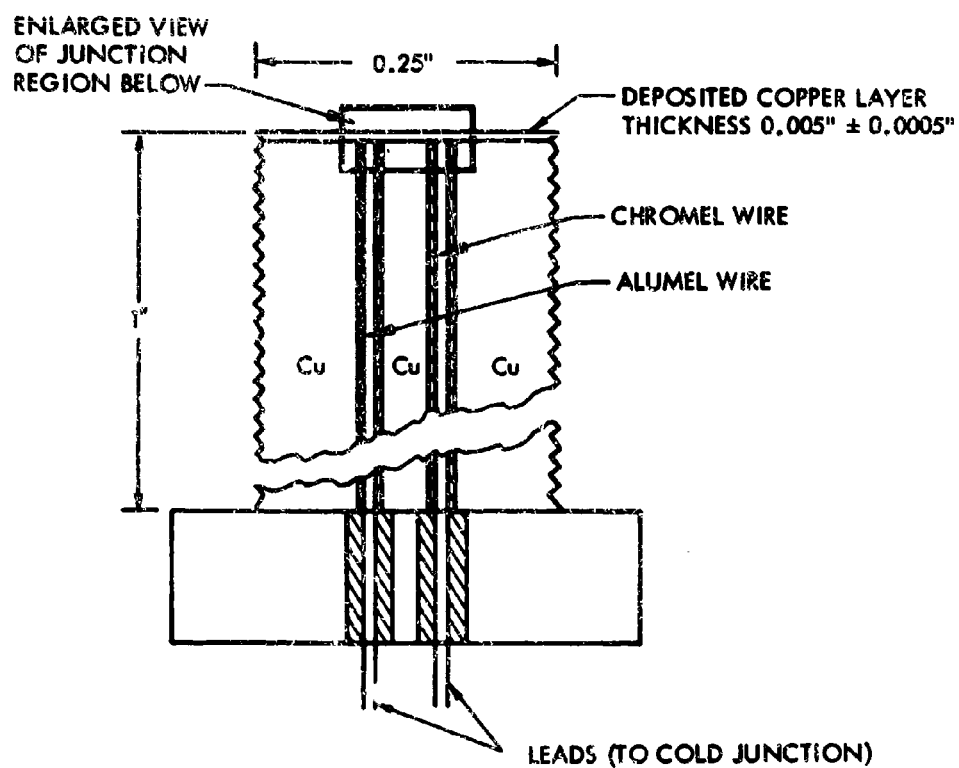
Fig. C-3. ATL Surface-Temperature Transducer

C-16
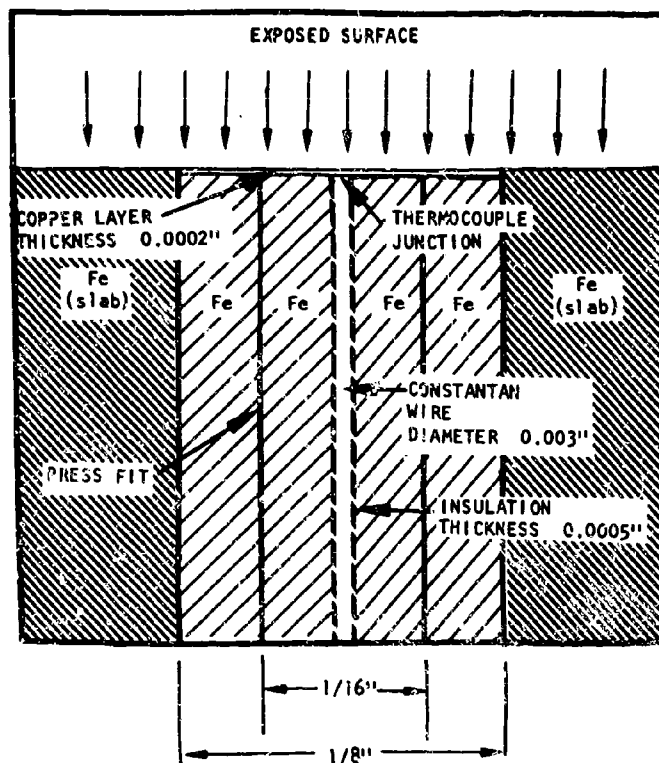
Fig. C-9. Thermocouple Junction Region of HTL Surface-Temperature Transducer

the temperature of the thermocouple junction in a given time interval. Of the
materials immediately available at that time, iron had the best thermal proper-
ties. Because of the pronounced tendency of pure iron to oxidize in a high
temperature oxidant atmosphere, thereby changing the thermal properties, the
layer was made of copper. The replacement of this thin iron region with a cop-
per layer, however, does not for practical purposes, alter the temperature
measurement for a given energy input.

The surface temperature instruments as thus far described are inserted in-
to larger objects, hereafter called slabs since for a time period they are
thermally representative of semi-infinite slabs, which match the parent material
of the given transducer. The surface of the transducer that is exposed to the

fireball, the surface nearest the thermocouple junction, is always flush with the surface of the slab it is inserted into. The exposed surface of the slab in most instances is planar, with the exception of a few measurements, described in more detail below, taken on a surface having some curvature, e.g., a radius of curvature of 6 in.

The thickness and lateral dimensions of the slabs are given below in the section on Instrument Mounting. These dimensions are of importance in that they govern the length of time that the slabs are thermally representative of semi-infinite slabs, or consequently, the time throughout which Eq. (C.1) may be properly applied.

The thermal properties of the slabs that have been applied in evaluating the heat flux are given in Table C-1 below, where the column on the extreme right is the value of the constant, $K' = (K\rho c/\pi)^{1/2}$, required in Eq. (C.1). These values were obtained from several sources including, for instance, Ref. C-5. The values listed for copper and iron are comparatively accurate since pure grades were used (see error analysis) whereas lot to lot variations can be expected for the stainless steels.

Table C-1

SLAB THERMAL PROPERTIES USED IN HEAT FLUX COMPUTATION

Slab Material	Conductivity (watt/cm-°C)	Mass Density (gm/cm^3)	Specific Heat (watt-sec/gm-°C)	K' of Eq. (C.1) (watt-sec$^{1/2}$/cm^2-°C)
Copper	3.81	8.94	0.389	2.05
Iron	0.652	7.85	0.418	0.825
Stainless Steel 303	0.147	7.8	0.503	0.437
Stainless Steel 309	0.155	7.8	0.586	0.475

Heat Flux Density Errors That Are Due to Instrument Errors

Heat flux density errors associated with the method of its computation
from the surface-temperature of slabs were discussed above, starting with the
assumption that a true temperature curve was available. There are, of course,
errors in the temperature -time traces, and errors that are propagated to the
heat flux density evaluation from these temperature errors are considered in
this section, along with the error that depends on the error in the properties
of the slab, i.e., on K' of Eq. (C.1). Consideration is given first to the
four sources of systematic errors, that is, errors that can be corrected, and
then to random errors.

The equation through which the heat flux density is evaluated from the
slab temperature [Eq. (C.4)] is applicable to the surface temperature, while
the slab thermocouple junctions are slightly below the surface. In order to
evaluate the effect of this on heat flux density, temperature – time functions
were first evaluated at the surface and then at depths corresponding to the
thermocouples for various heating pulses applied to the surface of the slabs,
and a comparison was then made of the heat flux densities from the two
temperature functions. The heating pulses or the slab boundary conditions
applied to both copper and stainless steel slabs were the so called radiation
boundary conditions using a gas temperature of $2,000°K$ and heat transfer
coefficients of both 0.34 and 0.042 watt/cm^2-°K. The resultant fractional
errors are presented on Fig. C-10. The curves indicate that large initial
errors rapidly converge to tractable values. The curves are somewhat mis-
leading in the following manner. Roughly speaking, the temperature slightly
below the surface tends to follow the surface temperature but with a small
time delay. Thus, in the analysis, there is a time period when the embedded
temperature is essentially zero while the surface temperature is rising
appreciably, with the consequence that infinitely large fractional errors are
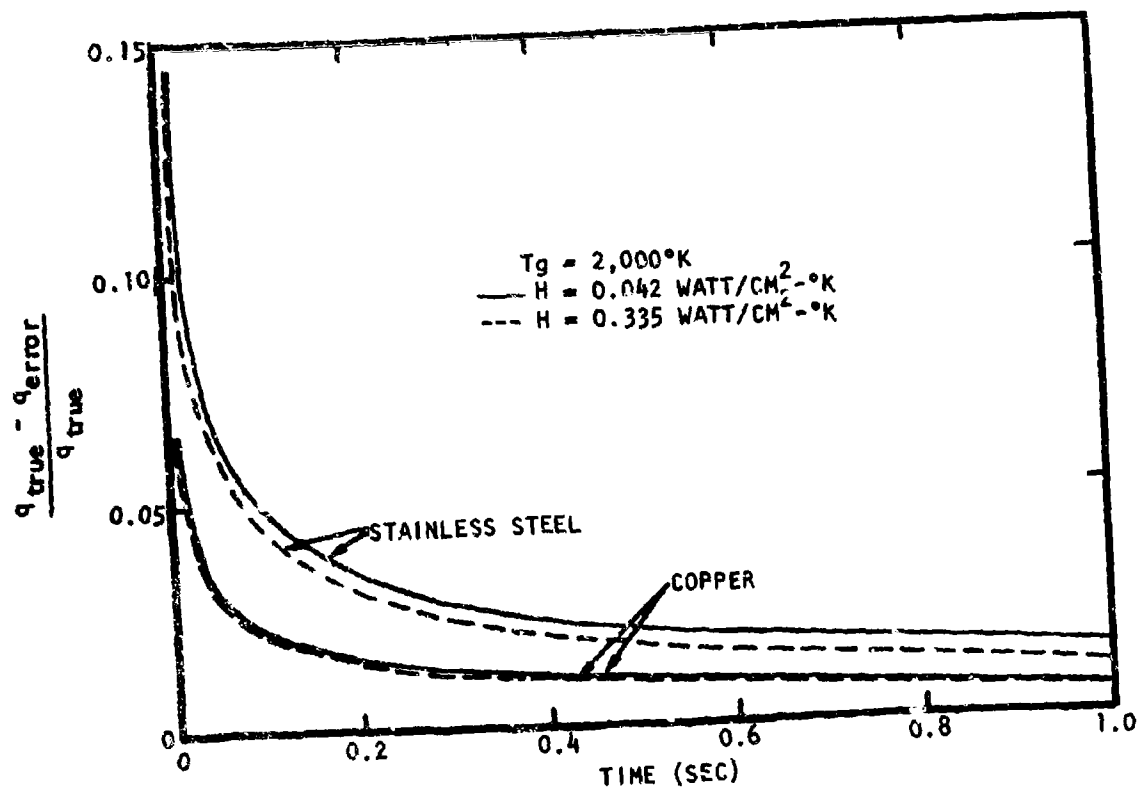
Fig. C-10. Heat Flux Density Errors which Result from Using Temperatures at Depths which Correspond to Those of the Thermocouple Junctions

indicated at early times. In actuality, zero time for an embedded measure-
ment would be designated as the instant the temperature commences to rise,
thus tending to minimize the magnitude of the initial error. The curves of
Fig. C-10 tend, in this sense, to bound the errors. However, the curves
are also misleading in another sense. The heating pulses applied to obtain
these curves vary gradually with time, while the corresponding pulses for
propellant tests are often comparatively erratic. Consequently, erratic
behavior in the heating pulse can occur before the errors indicated in
Fig. C-10 have decreased sufficiently. T' effect here is perhaps best
summarized as follows. Sharp or erratic behavior of a surface temperature
will tend to 'smooth' slightly at the thermocouple depth, with the result
that the measured heat flux density is also a slightly 'smoothed' version
of the true input. To an extent, this is desirable. Extremely high resolu-
tion is not required, and the expense of the heat flux computation for pre-
cise representations of the surface temperature would be unjustifiably in-
creased.

The second systematic error pertains to the effect on the temperature
within the slab due to the presence of the thermocouple (including leads) and
the cavity which contains the thermocouple. The analysis of this error is
extremely involved, and evidently as a consequence few thorough analyses
appear in the literature even though this is a standard instrument. While
the ultimate errors in heat flux density are not expected to be of particular
concern, it is difficult to numerically specify the uncertainty for a given
circumstance. A series of analytical studies* for slab and transducer con-
ditions, i.e., depth to thermocouple, cavity dimensions, properties of both
the slab and thermocouple leads, etc., that differ in some respects from the
cases of interest suggest minor errors can be expected. For instance, the
effect of heat conduction down the thermocouple lead for comparatively large
diameter leads and for lead to slab conductivity ratios of ten indicate correc-
tions of the order of 25 percent. With comparatively high conducting leads,

---

* A relevant part of this study is given in Ref. C-4.

it is not surprizing that errors of this magnitude would be attained. For
the instruments used, however, the conductivity ratios were no greater than
20 percent, and the errors from this effect would be substantially less. An
experimental study[*] in which known heat pulses were applied to slabs with very
similar instruments was conducted and a comparison made between the measured
temperature and that which should result from the heating pulse. In such a
study, the effects of all the systematic errors are inherently in the tempera-
ture differences observed, and it is not clear which individual error(s) are
predominantly responsible. Yet the systematic error in question is the only
one that cannot be readily estimated, so that conclusions can be drawn with
regard to this error. In any case, errors obtained were of the order of a
5 percent or less, thereby suggesting that the effect of the systematic error
in question was not grossly in excess of this figure.

While it does not appear that the effects of the presence of the cavity
and thermocouple leads are of serious concern, being perhaps no larger than a
few percent, these effects are the least certain of the systematic errors
leading to errors in heat flux density measurements.

The third and fourth types of systematic errors result from the non-
linearity of the amplifying and recording systems and the nonlinearity
between the thermocouple emf and the temperature of the junction. These
errors are similar and relatively simple to estimate or correct.

The deviation from linearity of the amplifying and recording systems
was determined by applying a sequence of step voltages to the amplifier,
where the ratios of steps are accurately known (0.5 percent), and measur-
ing the magnitudes of the corresponding step deflections on the final data
record. Such measurements were taken for all thermal data channels over
several tests. Then for each channel, fractions of various step deflections
to the highest step deflection on the final data record were obtained and
compared with the corresponding fractions of the input step voltages. The

---

* Ref. C-6.

deviation, in each case, of the fraction on the final record from the fraction
of the input is equal to the deviation, or error, of the temperature evalua-
tion along the trace from zero to maximum temperature. An erroneous tempera-
ture curve that is representative of the error indicated by the fractions was
constructed, and the heat flux was computed for the erroneous curve and a
corresponding true temperature curve. The representative erroneous tempera-
ture curve was constructed using the criterion that, at each step, two-thirds
of the deviations from linearity mentioned above were between the true and
erroneous curves, with the remaining one-third outside this range. The
resultant fractional error in heat flux density is presented on Fig. C-11,
and as can be noted, the effect of nonlinearity in the amplifying and
recording system tends to be minor.

Consideration of the nonlinearity of the appropriate emf vs temperature
curves indicates that the associated errors are negligible over typical tempera-
ture ranges of the slabs (50 and 200°C for copper and stainless steel, res-
pectively).
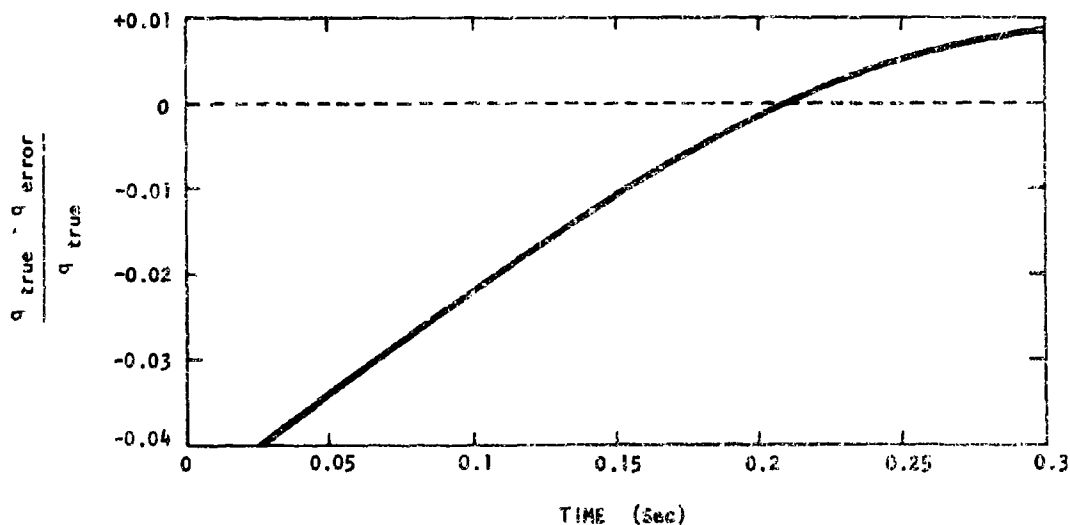
Fig. C-11.   Heat Flux Density Error Due to the Nonlinearity of the
             Amplifying and Recording System

Random errors in the slab temperature measurements will be separated
into two different types. The first type has a fixed value for a given data
trace, while the second type fluctuates with time over the course of ac-
quiring a data trace. Errors of the first type are considered first.

The slab temperatures are, in effect, evaluated using the equation

$$T(t) = \frac{Vd(t)}{EG}$$

where T is the temperatue above ambient at any time t, E is the emf (volts)
generated by the temperature transducer per unit temperature rise, G is the
amplifier gain, V is the voltage applied to the recording system per unit
deflection on the final data record, and d is the trace deflection on the final
record. The uncertainty in E is specified by the manufacturer to be 0.5 percent,
and G is periodically measured to within an accuracy of 1 percent. V is obtained
by measuring the step calibration voltage applied to the recording system
immediately before each test and dividing this voltage by the measurement of
the corresponding deflection on the final record. It is estimated that the
step deflection, preset to approximately match the maximum expected trace
deflection, can be evaluated to about 0.5 percent, while the voltage is evaluated
to about 5 percent; the uncertainty in the quotient V is then approximately
5 percent. This error, or its component errors, remain constant over the
entire data trace for a given channel. It can be seen from Eq. (C.4) that
the error in heat flux due to a pa icular error in temperature of this kind
are equal to the temperature error, so that the flux and temperature un-
certainties are about 5 percent.

Fluctuations of the measured temperature about the true value that
occur throughout the duration of the data traces (noise) are introduced by
the transducer, amplifier, recording system, playback system, and so on.
Some of these fluctuations are cyclic, while others vary in a randomlike
fashion with time. The cyclic fluctuations can be readily identified as

noise because of their presence on the constant value voltage input to each
data channel immediately prior to each test. The random fluctuations are
evidently comparatively negligible; they are imperceptible during the
constant-value voltage input (due account being made for the superimposed
cyclic fluctuations).

Regarding the uncertainty in K', the uncertainty in measurements of the
dependent parameters K and C (assuming the uncertainty in ρ is relatively small)
is typically 5 percent, so that the uncertainty in a measurement of K' would be

$$\frac{\Delta K'}{K'} = \frac{\sqrt{2}}{2} \times 0.05 = 0.035$$

Since the copper and iron slabs are of comparatively pure grade material (99.9-
percent pure for copper), the uncertainty in the properties specified for these
materials should be about equal to the typical measurement uncertainty. It is
likely to be somewhat higher for the stainless steel slabs (specified as stain-
less steel 303 and 309) since there is a greater lot-to-lot variability in the
constituents of stainless steels.

A further but temporary source of error occasionally arises due to a some-
what sinusoidal high-frequency oscillation in the initial portion of the surface
temperature – time data trace, which evidently results from passage of the shock
wave and/or the impact of high-speed fragments of the tankage hardware on the
instrument or its mounting. This signal attenuates rapidly with time and
generally decays to negligible proportions in less than 0.1 sec, and the amplitude
for the most extreme and rare cases is about 25 percent of the true signal.
Since the period of vibration is usually orders of magnitude smaller than the
period of typical changes of the true signal, "smoothing" the initial portion
of the trace to eliminate the vibration induced noise can usually be accomplished
with reasonable accuracy.

One additional systematic error should also be considered. The relationship
from which the heat flux density is computed from the slab surface temperatures
Eq. (C.1) assumes that the slab is effectively semi-infinite (occupies half

of space), while the instrumented slabs are finite. The surface temperature --
time curve from a finite slab will eventually commence to diverge from that of
a corresponding semi-infinte slab, and thus, an error will be introduced into
the computed heat flux unless Eq. (C.1) is modified to accommodate a finite slab.
This modification is somewhat involved, however, and the alternate approach
was taken of selecting the slab materials and dimensions such that the errors in
applying Eq. (C.1) are minor. The worst case was in connection with copper slabs
having thicknesses of about 1-1/2 in. (detailed slab dimensions are given below
in the discussion of instrument mounting). Comparative examination of
first time derivatives of the temperature - time curves for copper slabs of
this thickness and corresponding semi-infinite slabs indicate, for instance,
that errors in heat flux density as large as 10 percent can occur at 5 sec, but
that they are negligible at 2.5 sec. Iron slabs of similar thickness and stain-
less steel slabs 1 in. thick were also used, although the corresponding errors
are comparatively small.

PHOTO-RECORD PYROMETER

Blackbody equivalent temperature measurements using a photographic
recording pyrometer at a remote location were made by the Sandia Corporation.
This instrument is shown in Fig. C-12. Basically, the measurement consists of
matching in the visible spectrum the intensity of an image of a region of the
fireball with the intensity of a similar image of one of several tungsten
filaments, each of which is at a known and preset temperature. Since the
intensity of the tungsten in the optical spectrum approximates that of a black-
body, the measured fireball temperature is near the blackbody equivalent
temperature.

A more specific description is as follows. A camera is positioned to
photograph a region of the fireball to be measured. A lamp box containing
several tungsten lamps is placed so that the lamp filaments are in the lower
portion of the camera field of view and are in focus at the film plane. The
lamps are then adjusted to temperatures bracketing the expected temperature of
the fireball. The lamp temperatures are read with an optical pyrometer. A

Fig. C-2. Photographic Recording Pyrometer

Wratten 29 filter is placed in front of the camera lens, and the exposure set
so that the lamp filament images will give a maximum density on the film of
about 1.8. The lamps are burning during the operation, so that each data frame,
when processed, contains an image of the fireball, and the images of the lamp
filaments, each of the latter at a different calibrated temperature. The den-
sity of the calibration lamps is plotted against temperature, and the tempera-
ture of the fireball taken from this curve.

RADIANT FLUX: INSTRUMENTS, CORRECTION FACTORS AND ERROR ANALYSIS

Basic Description of Radiometers

The radiant flux measurements are made with an instrument ordinarily re-
ferred to as the Gardon-type radiometer. Detailed descriptions of the princi-
ples of operation of this instrument are given in Refs. C-7 and C-8. The fol-
lowing is a brief summary from these references.

The basic radiant-energy-receiving element of the instrument is a circular
metallic foil, as illustrated in Fig. C-13. If energy is absorbed at a constant
rate uniformly[*] over the surface of a sufficiently thin circular foil (or heat
is generated at a constant rate uniformly within the foil) whose circumferen-
tial edge is maintained at its initial temperature, a steady-state temperature
field is such that the temperature differential between the center and circum-
ferential edge of the foil is, to an approximation, proportional to the rate
of radiant energy absorption by the foil[**] or rate of heat generation within
the foil). Specifically, an approximate equation relating the temperature dif-
ferential to the constant heat flux (watt/cm^2) is

$$q = 4K\delta \ \Delta T/R^2 \tag{C.5}$$

---

[*] Uniform irradiance of the foil may not be a necessary condition for the flux
to be proportional to the temperature differential upon reaching steady
state, but it is known to be a sufficient condition, and thus we have made
efforts to maintain uniform irradiance.

[**] Some of these statements are subject to conditions too complex to consider
in this brief summary.

where K, δ, and R are the thermal conductivity, thickness and radius of the foil, q is the heat flux, and ΔT is the temperature difference between the center and edge of the foil.
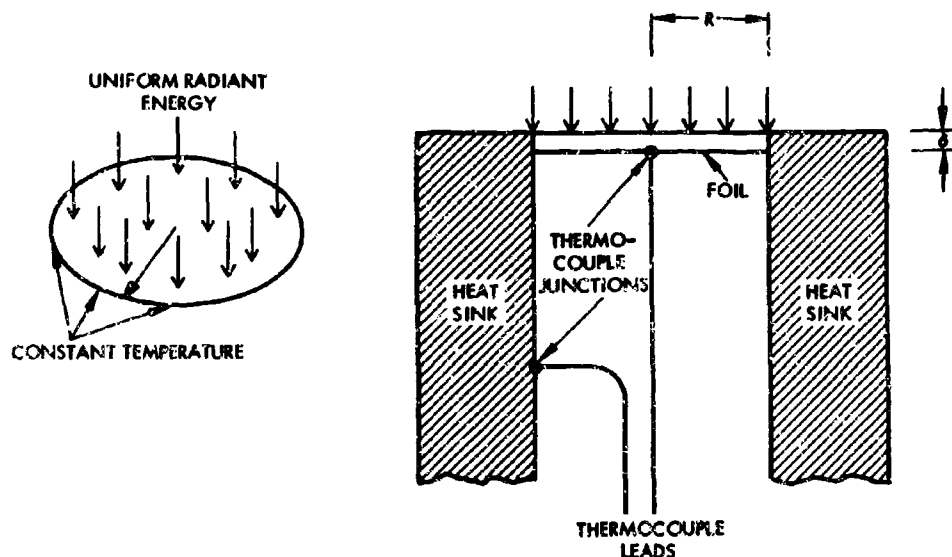
Fig. C-13. Configuration of Gardon-Type Radiometer

In practice, the condition that the temperature at the edge of the foil be maintained constant is approximately met by welding the foil to a highly con-ducting heat sink, as illustrated in cross section in Fig. C-13. Finally a differential thermocouple, whose voltage output is proportional to ΔT, is made by welding wires of the same material (but different from that of the foil) to the center and edge of the foil (the latter wire may be joined at any region of the heat sink). Then in terms of the electrical potential difference ΔV across the thermocouple leads, Eq. (C.5) becomes

$$q = 4K e \delta \, \Delta V / R^2$$

where e is the voltage difference per unit temperature difference across the thermocouple junctions.

C-29

An order of time τ for steady state to be approached after initiating the constant flux is given by

$$\tau = R^2/4\kappa$$

where κ is the thermal diffusivity of the foil.

Description of Radiometers

Radiometers of three slightly different types were used for measurements within the fireball designated as the Sandia, RU-1, and HTL[*] radiometers, and a fourth type for all remote measurements, designated the external radiometer. All four, however, are Gardon-type radiometers and function as in the basic description above. The differences are primarily in the materials used, for instance, for the sensitive foil and heat sink, and in dimensions, such as the foil diameter and thickness and the thickness of the windows.

A cross-sectional sketch of the HTL radiometer is given in Fig. C-14, with an enlargement of the aperture and foil region in the lower portion of the figure. The foil for this particular radiometer is 0.001-in.-thick constantan with a diameter of 0.89 in. The thermocouple junction wires are copper, and with this combination of materials and dimensions, the instrument has a time response of 50 msec and a sensitivity of 10 watts/cm^2/mV.

A feature of the HTL instrument that is not present in the other intra-fireball radiometers is an annular disc which restricts the aperture to approximately the diameter of the foil, as illustrated in the lower portion of Fig. C-14. The upper surface of the disc is coated with a thin, light-absorbing layer to minimize reflection, and energy that is absorbed by the disc is conducted to a region of the heat sink that is remote from the foil. This disc, along with an external annular ring illustrated on the upper sketch of Fig. C-14,

---

[*] The basic energy-sensing element of the radiometer was manufactured by Heat Technology Laboratories, Huntsville, Alabama. Fabrication of the supplementary hardware and assembly was done at the AFRPL shop, Edwards Air Force Base, California.
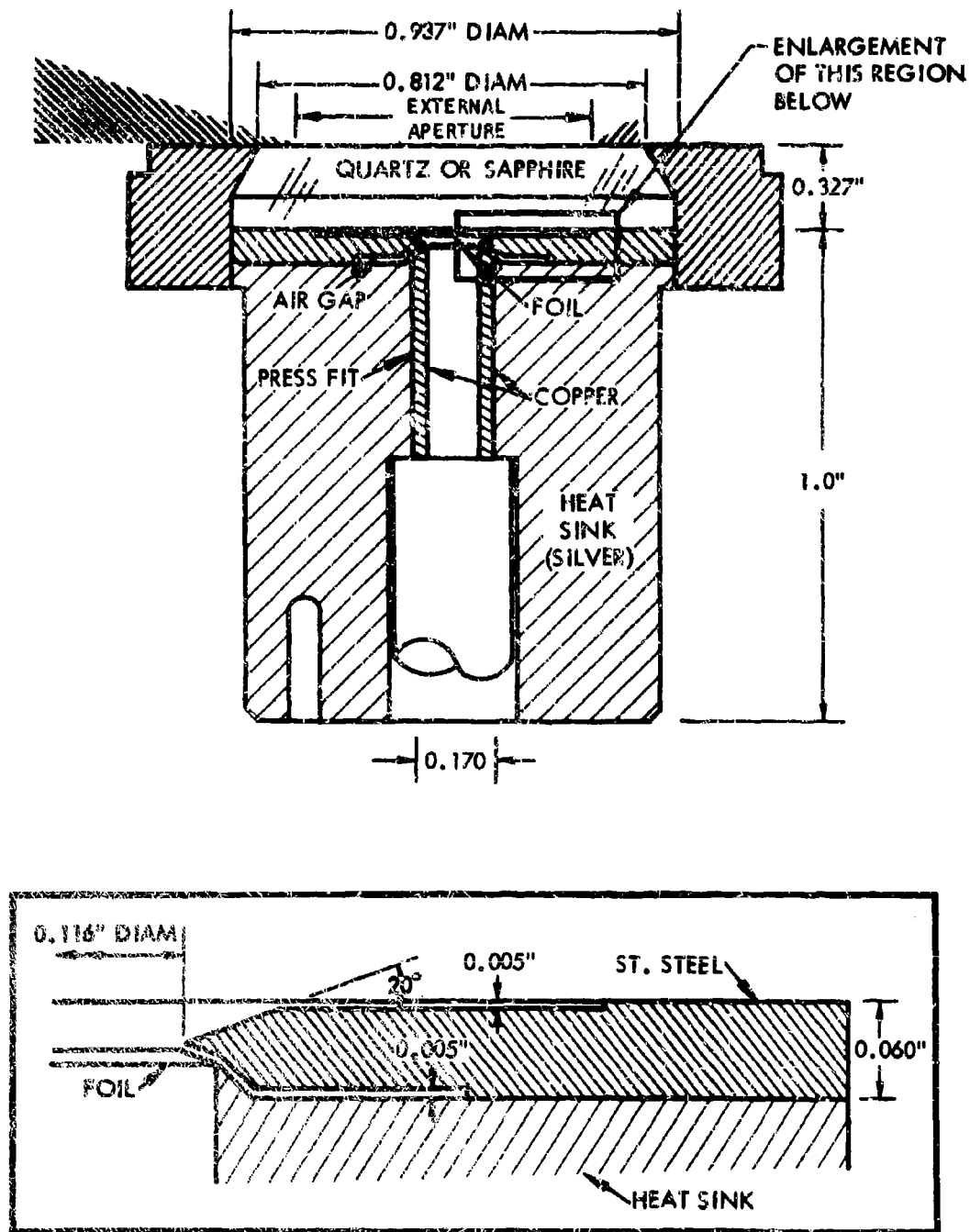
Fig. C-14. HTL Radiometer

restricts energy having angles of incidence between 70 and 90 deg from arriving
at the foil. The diameter of the external aperture is just sufficient, account-
ing for refraction at the window surfaces, to restrict energy incident between
70 and 90 deg from arriving at the foil. No such restriction, either internal-
ly or externally, existed for the remaining two intrafireball radiometers.

The relevant data and characteristics of all four radiometers are listed
in Table C-2.

Table C-2

DIMENSIONS AND CHARACTERISTICS OF THE RADIOMETERS

		HTL	SANDIA	RU-1	EXTERNAL
FOIL	Thickness (in.)	0.001	0.005	0.001	0.001
	Diameter (in.)	0.089	0.25	0.25	0.25
	Material	Constantan	Silver	Silver	Silver
Thermocouple Junction Wire Material		Copper	Constantan	Constantan	Constantan
WINDOW	Thickness (in.)	3/16	3/8	3/16	1/4
	Diameter (in.)	0.94	3.2	0.94	1.75
	Material	Quartz or Sapphire	Quartz	Quartz or Sapphire	Quartz
Field-of-View (deg)		70	90	90	45
Time Response (msec)		50	60	60	60
Sensitivity (watt/cm²/mV)		10	50	8	10

Correction Factors for Radiometer Measurements Within the Fireball

Questions for interpreting radiometer data that are obtained within the
fireball arise, and a correction factor permitting proper interpretation must
be obtained. Evaluation of the correction factor is necessary because the
intention is to evaluate the radiant energy incident on an immersed object

while the energy-detecting element of the radiometers is behind a window. Energy is lost enroute to the element by reflection at both surfaces of the window and by absorption within the window, and adjustment of the measured flux requires knowledge of the relationship between the flux at an exposed surface to that at the sensitive elements.

As will be described below, rather significant uncertainties exist regarding two properties of the fireball that are used in evaluating the radiometer-data correction factor. While these properties can be measured, a rather substantial effort is required, and in light of the secondary nature of the measurements, as mentioned in the general discussion, an effort to lessen these uncertainties did not appear to be warranted, nor was any made. In addition, no thorough analysis which would indicate the level of the uncertainty has been performed, although limited consideration suggests uncertainties of perhaps 20 or 30 percent. The data, however, are considered of value in supporting, at this level of uncertainty, the general magnitudes of other measurements, and consequently estimates of the correction factors based on the best available information have been evaluated. The origin and nature of the uncertainties will become more evident in the following paragraphs, which describe the process of evaluating the correction factors. The correction factor consists of the ratio of the radiant energy incident on an exposed surface area to that on the same area which is separated from the gas by a window, and the discussion commences with the evaluation of the energy on the exposed area.

Consider in Fig. C-15 the energy emitted from an elemental volume ΔV of gas which intersects the elemental area ΔA. Letting the energy emitted per unit volume of gas be e_1, the energy emitted from ΔV in all directions is $e_1 \Delta V$, and the fraction emitted in a direction so as to intersect the area ΔA is $(\Delta A \cos \theta)/4\pi r^2$, where r is the distance between ΔA and ΔV and θ is the angle between the line intersecting ΔV and ΔA and the normal to ΔA. Some of this energy is absorbed by the gas. In particular, the fraction of the energy not absorbed is e^{-kr}, where k is an absorption coefficient. The energy emitted by ΔV that arrives on ΔA then is

$$\frac{e_1 \Delta A}{4\pi} \sin \theta \cos \theta \ e^{-kr} \ d\theta dr d\varphi \tag{C.6}$$

$$\Delta V = r^2 \sin \Theta \, dr d\Theta d\varphi$$
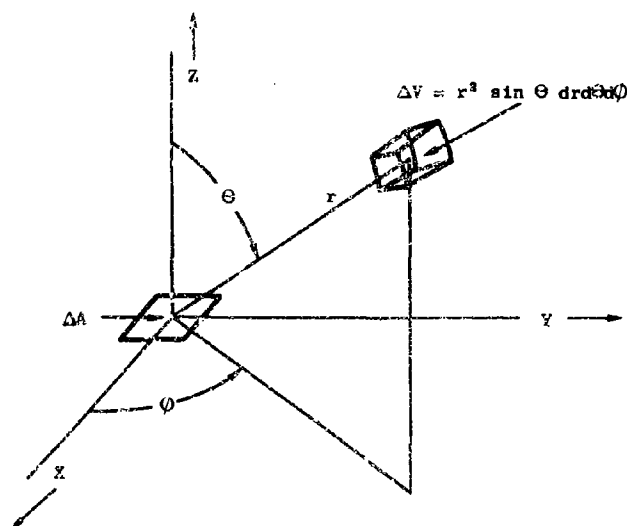
Fig. C-15.   Basic Geometry for Computation of Radiant Flux
            Density Correction Factor

In summing the contributions of energy from the entire gas, where it is
assumed that the gas extends indefinitely in both the lateral (X and Y) and
vertical (Z) directions, it is convenient to identify for later use the angular
energy distribution on ΔA by summing first over the ranges of the variables r
and φ giving

$$e_\theta = \frac{e_1 \Delta A}{2k} \sin \theta \cos \theta \, d\theta \qquad (C.7)$$

C-34

Thus e_θ is the total energy arriving at ΔA with an angle of incidence between θ and $\theta+d\theta$. Continuing the summation over the range of the angle θ, the total energy arriving on ΔA is

$$e = \frac{e_1 \Delta A}{4k} \qquad\qquad (C.8)$$

It is this quantity that must be compared with the energy on ΔA when a window is inserted between the radiating gas and ΔA.

For the case where a window separates ΔA from the radiating gas, it is convenient to first evaluate the energy incident on ΔA for a window having infinite lateral dimensions and to subsequently show that the energy is approximately the same for windows that are appropriately finite laterally.

Commencing with the assumed laterally infinite window and assuming that the radiating gas occupies all of the space on one side of the window, the angular distribution of energy on the upper exposed surface of the window is given by Eq. (C.7) (now interpreting the angle θ as simply the angle of incidence) and the energy is uniformly distributed over this surface since the gas extends indefinitely. Since the irradiance of the upper surface is uniform, the energy emerging from the lower surface of the windows is also uniform, although the angular distribution of the emerging energy will not be described by Eq. (C.7) since energy is lost by reflection at both the upper and lower surfaces of the window (absorption within the window is momentarily ignored) and the fraction of the energy reflected depends on the angle of incidence. However, since the radiant energy emerging from the lower surface of the window is uniform, evaluating the emergent radiant flux density (or the energy on ΔA below the window) is simply a matter of evaluating the energy that is transmitted through the window for an angular distribution of incident energy given by Eq. (C.7). That is, the complexities of computation that arise for cases where the emergent energy is not uniform can be avoided. The reflected energy at the exposed window surface depends on the angular distribution of energy at that surface and on the index of refraction of the window material relative to the radiating gas. (The fundamental relationships permitting evaluation of reflected energy are given, for instance, in Chapter 1 of Ref. C-9 and Chapter 25 of

Ref. C-10). At the lower or unexposed surface, the reflected energy depends
on the index of refraction of the window material relative to air and on the
angular distribution of energy at the lower surface. This distribution is
different from the above distribution due both to refraction (or bending) at the
upper surface and to the different quantities of energy that were reflected at
each angle at the upper surface. The index of refraction associated with the
upper surface is comparatively uncertain due to the uncertainty that exists in
the properties of the radiating gas, and this lack of knowledge represents one
of two significant weaknesses of the intrafireball radiometer measurements. In
order to provide an approximation to the correction factor, however, computations
were made for the single case where the index of refraction of the window relative
to the radiating gas is the same as that of the window relative to air (the same
as the index associated with the lower window surface). For this case, the
fraction of energy with an angle of incidence of θ that is transmitted through
both surfaces, ignoring multiple reflections at a given surface, is given by

$$T(\theta) = 8(n \cos \theta \cos \theta')^2 \left\{ \frac{1}{(\cos \theta + n \cos \theta')^4} + \frac{1}{(n \cos \theta + \cos \theta')^4} \right\} \quad (C.9)$$

where n is index refraction of window relative to surrounding gas and θ is
related to θ' by $\sin \theta = n \sin \theta'$. The angular distribution of energy on ΔA
beneath the window is then

$$e_\theta = \frac{e_1 \Delta A}{2k} \ T(\theta) \sin \theta \cos \theta \ d\theta \quad (C.10)$$

The summation of Eq. (C.10) gives the energy on ΔA and, as will be shown below,
has been computed for quartz and sapphire over various appropriate ranges of θ.
Finally, the data correction factor (thus far excluding the correction for absorbed
energy) is given by

$$F = \frac{e_1 \Delta A}{4k} \bigg/ \frac{e_1 \Delta A}{2k} \cdot \int_0^{\theta_1} T(\theta) \sin \theta \cos \theta \ d\theta \quad (C.11)$$

$$= 1/2 \cdot \int_0^{\theta_1} T(\theta) \sin \theta \cos \theta \ d\theta$$

where θ_1 is the maximum angle of incidence permitted in the particular instru-
ment. Eq. (C.11) is the ratio of energy incident on ΔA without a window Eq.
(C.8) to that with a window, so that the measured radiant flux density should
be multiplied by F in order to determine the radiant flux density on an exposed
surface. For the RU-1 and Sandia radiometers, θ_1 was 90 deg. whereas it was
usually 70 deg for the HTL radiometer due to presence of an aperture arrange-
ment both on the exposed and underneath side of the window.

Thus far, a laterally infinite window has been assumed. Consideration of
the path of light "beams" which arrive on ΔA from any possible direction, as
illustrated in cross section with incident beams at 0, 45, 90 deg on Fig. C-16a,
indicates that because of refraction, only a window section of finite diameter
D is involved. That is, the window, except for the disk of diameter D, could
be removed without any effect on the energy at ΔA. For the radiometers, ΔA,
the sensitive element of the radiometer, is slightly below the lower window sur-
face, and for radiation at a given angle, the diameter must be increased, as
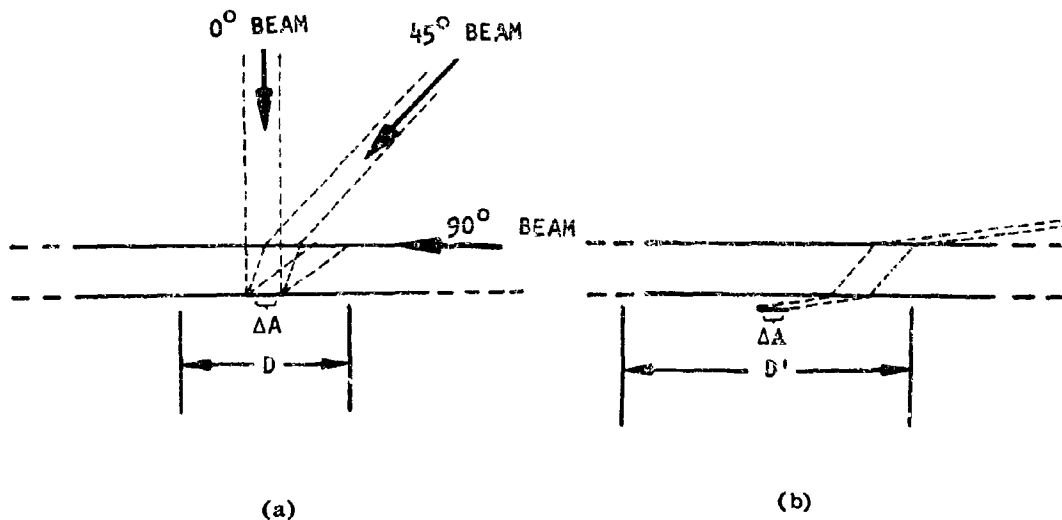
Fig. C-16. Illustration of the Useful Dimensions of Radiometer Windows

illustrated in Fig. C-16b, to D'. In addition, energy incident at and approach-
ing 90 deg is restricted from arriving at ΔA for a finite window. For the ra-
diometer dimensions used, however, this energy loss is negligible; for instance,
for the HTL radiometers where 3/16-in.-thick windows with an effective diameter
of 0.81 in. were used and the sensitive element was 0.003 in. below the window
surface, the fraction of the energy lost due to its finite diameter is estima-
ted to be about 1/10,000 for quartz, and similar numbers occur for other ma-
terials and radiometers.

Evaluating the energy absorbed within the window requires knowledge of the
wavelength and angular distribution of the incident radiant energy and the
absorption coefficient of the window material as a function of wavelength. The
wavelength distribution is not precisely known, although the general form for
black or grey bodies is known, given the temperature. The distribution for
fireballs from LO_2/RP-1 explosions probably reasonably approximates that from
a blackbody. This uncertain wavelength distribution, however, does create an
uncertainty in the evaluation of the absorbed energy, although it is not parti-
cularly serious at the expected temperature levels. The window materials have
been chosen so that for temperatures obtained, the absorbed energy will be minor
for any probable wavelength distribution. For instance, special grades of fuzed
quartz[*] are used which are excellant transmitters beyond (at greater wavelength
than) the 2.7-μ water band region to about 3.5 μ, along with sapphire,[**] which
transmits to the 4.5-μ region. To illustrate, the fraction of the energy from a
blackbody at 2300°K that is beyond 3.5 and 4.5 μ is about 14 and 8 percent,
respectively. This percentage can be somewhat higher for probable wavelength
distributions of the fireball, however. In addition, as the gas temperature
decreases, the fraction of the energy that is in the wavelength region beyond
the transmission cutoff increases, that is, the fraction absorbed increases, and
the error in the estimated energy loss tends to have a more serious effect on

---

[*]   A grade referred to as "Infrasil" from Englehard Industries, Inc., Amersil
      Quartz Division, Hillsdale, N.Y., and grade G-105 from General Electric
      Comp., Lamp Glass Dept., Cleveland, Ohio.

[**] Optical grade synthetic sapphire from Linde Division, Union Carbide Corp.,
      Torrance, California.

the total correction factor. In addition to the energy absorbed that is beyond
transmission cutoff at 3.5 and 4.5 μ, some energy is also absorbed in the trans-
mission region of quartz and sapphire. For the window thicknesses involved,
this represents a small fraction of the energy, and evaluating the energy in
this case does not depend critically on the wavelength distribution since the
absorption properties of quartz and sapphire are for practical purposes constant
over this portion of the spectrum. The absorption properties are more uncertain
here and increase in uncertainty as the absorption coefficients become negli-
gibly small; however, since this entails a large error of the negligible energy
loss, the correction factor is not seriously effected by the error.

An estimate of the fraction of the energy absorbed for the various window
thicknesses and materials and radiometer fields-of-view was obtained, and the
corresponding correction factors associated with absorption alone (as well as
those associated with the combined effect of reflection and absorption) are pre-
sented below. For the absorption estimate, the wavelength distribution from a
2200°K blackbody was assumed, and the absorption properties used were those
specified by the manufacturer of the windows, supplemented by data from the
technical literature.[*] Also, while the distance a given beam of energy tra-
verses through the window varies with the angle of incidence, the estimate was
based on an averaged distance. The absorption losses should properly have been
evaluated in conjunction with reflection losses. However, the error resulting
from their separate treatment is comparatively insignificant.

The final correction factors are listed in Table C-3. In order to indi-
cate the relative influence of reflection and absorption, the factors due to
reflection alone and absorption alone have been included along with the results
from their combined effect. It should be noted that these factors will tend to
become larger as the gas temperature decreases from 2200°K.

---

[*] Absorption properties of sapphire are given in Refs. C-11 and C-12. The
properties of fuzed quartz silica (SiO_2) are available in numerous hand-
books and infrared reference books.

Table C-3

RADIOMETER CORRECTION FACTORS

INSTRUMENT DESIGNATION	WINDOW MATERIAL	FIELD-OF-VIEW (deg)	CORRECTION TO:		
			DUE TO REFLECTION ONLY	DUE TO ABSORPTION ONLY	DUE TO REFLECTION AND ABSORPTION
Sandia	Quartz	90	1.19	1.19	1.43
RU-1	Quartz	90	1.19	1.18	1.41
HTL	Quartz	70	1.28*	1.18	1.51
HTL	Sapphire	70	1.37*	1.18	1.60

THERMOCOUPLE PROBE

Measurements of the fireball gas temperature at instrument locations within the fireball were made by the Sandia Corporation with a metallically sheathed thermocouple junction, or thermocouple probe. The probe consists of a 1-mil-wire-thickness tungsten/tungsten 26% rhenium thermocouple sheathed with 16-mil-O.D. molybdenum disulfate-coated tantulum. The thermocouple wires are insulated from the sheath and, except at the junction, from each other by beryllium oxide.

While the thermocouple probe is a standard instrument, for the temperatures and molecular constituents that occur in the fireball, a comparatively large uncertainty in the indicated temperature of its environment occurs. Upon immersion in the fireball, the temperature of the instrument commences to increase rapidly toward that of its environment, and at temperatures well below the melting temperature of the sheath, a chemical reaction between the sheath material and the nearby oxidants of the fireball gas commences. The energy from the reaction can contribute substantially to the temperature elevation of the probe and its ultimate temperature can exceed that of its environment. The rate of

---

* Includes loss due to field-of-view restriction.

reaction depends, of course, on the type and concentration of available oxidants, the flow velocities, and the sheath material, and it is difficult to establish whether the reaction is or is not inducing a false indication of significance. The resultant data, however, should be used with caution.

Passive Sensor

A piece of test hardware inadvertently became a passive thermal sensor for Test 285. This sensor consists of a solid aluminum cone, as illustrated in Fig. C-17. At the time of ignition, it was located at or within a few feet of the point of initial propellant ignition, and after the test was located within a few feet of its initial location. Approximately 0.1 to 0.2 in. of material had been uniformly ablated from the surface of the sensor. No thorough analysis of the possible heating pulses that could have induced such an ablation has been performed, nor is it clear if chemical reaction was involved in the process of ablating the surface.
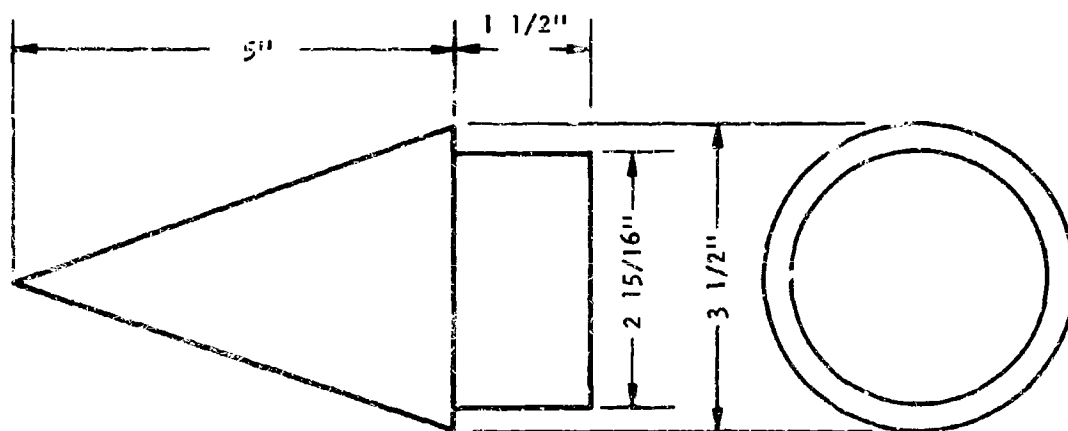
SCALE = 1/2
MATERIAL = 6061 - T6 Aluminum

Fig. C-17.   Dimensions of Aluminum Cone

INSTRUMENT MOUNTING

Within the Fireball

There are four intrafireball instrument mounts which are designated as
the H, S, P, and Sandia Stations. This section contains a description of these
stations, their location, and the position of the instruments on the stations.

A sketch of station "H" is given in Fig. C-18, showing the location of two
slabs and four radiometer positions along the upper surface of the mount. Also
along the upper surface is a "wing-like" projection (or wing), which extends
beyond the main body of the mount both laterally and toward the center of the
explosion. The wing is 1 in. thick (steel), with two adjacent slabs (3-by 3-by
1-in.-thick stainless steel 303) mounted with their exposed surface flush with
the upper surface of the wing. The upper wing surface is entirely planar, and
the leading edge and wing tips are tapered in toward the main body from the
perimeter of the upper surface at an angle of 30 deg from the horizontal. The
function of the wing is to induce similarity of gas flow along the surface of
the two slabs even though the flow direction may be somewhat askew of the vertical
plane of symmetry of the mount and/or of the horizontal plane.

Positions for four radiometers were included in order that gross differences
could be detected between simultaneous measurements from dissimilar instruments,
similar instruments with dissimilar window materials, etc., although differences
exceeding the measurement uncertainty were not obtained. The radiometers of this
station are provided, starting with test No. 279, with a helium purge (apparatus
not included in sketch) along the exposed surface of their windows, the purpose
being to minimize particle deposition and window heating, the latter because it
tends to alter the reflection and absorption properties of the window. Through
appropriate shaping of the purge-gas orifice and control of the velocity of the
purge gas at the orifice, the purge-gas flow along the upper surface of the
window was confined to a thickness of about a millimeter, and thus did not tend
to repel the fireball gas from the window surface to an undesirable extent. The

RADIOMETERS

SLABS
(STAINLESS
STEEL 309)

FLOW
DIRECTION

ALL DIMENSIONS ARE
IN INCHES
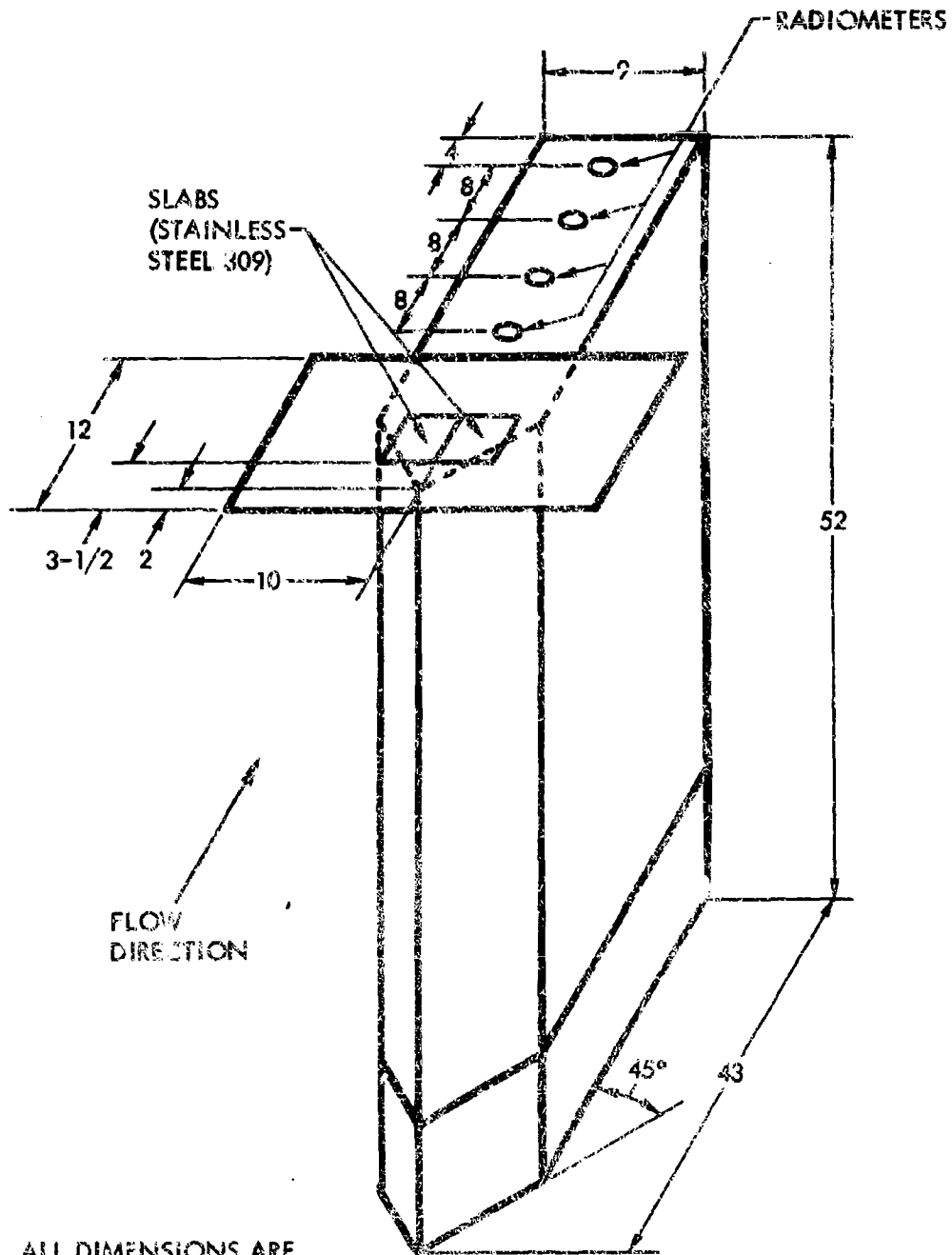
Fig. C-18. Intrafireball Thermal Instrument Station H

purge, however, did successfully eliminate deposition, although difficulty was experienced in maintaining the required purge-orifice alignment.

A sketch of station S is given on Fig. C-19, showing locations of two slabs, two thermocouple probes, and a radiometer, although no radiometer data were successfully acquired at this station. Station S was generally located approximately 13 ft above the ground surface and as near to the center of the explosion as practical. During Tests 275 through 285 it was located at a ground distance from the center of the test pad of about 23 ft approximately along gauge line A. Due to the difficulty of maintaining the station at this distance, it was relocated for the remaining tests to a ground distance of 32 ft along a radial line about half way between gauge lines A and B. A sketch of the station and its final support structure is given in Fig. C-20.
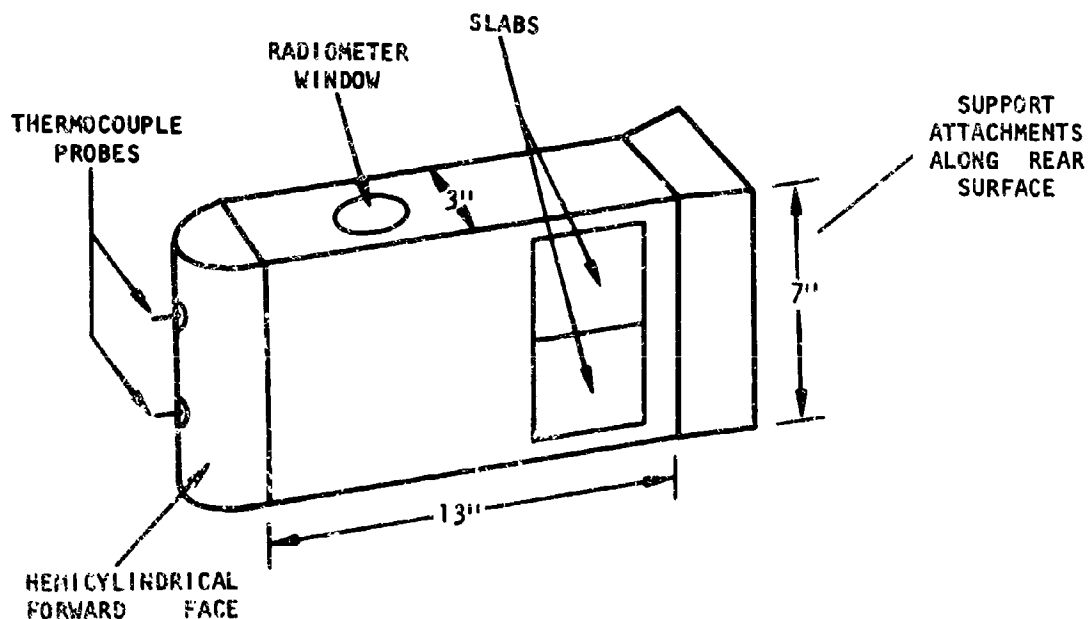
Fig. C-19. Intrafireball Thermal Instrument Station S

STATION S

12" DIAMETER

STATION P

SLABS

13'

10'
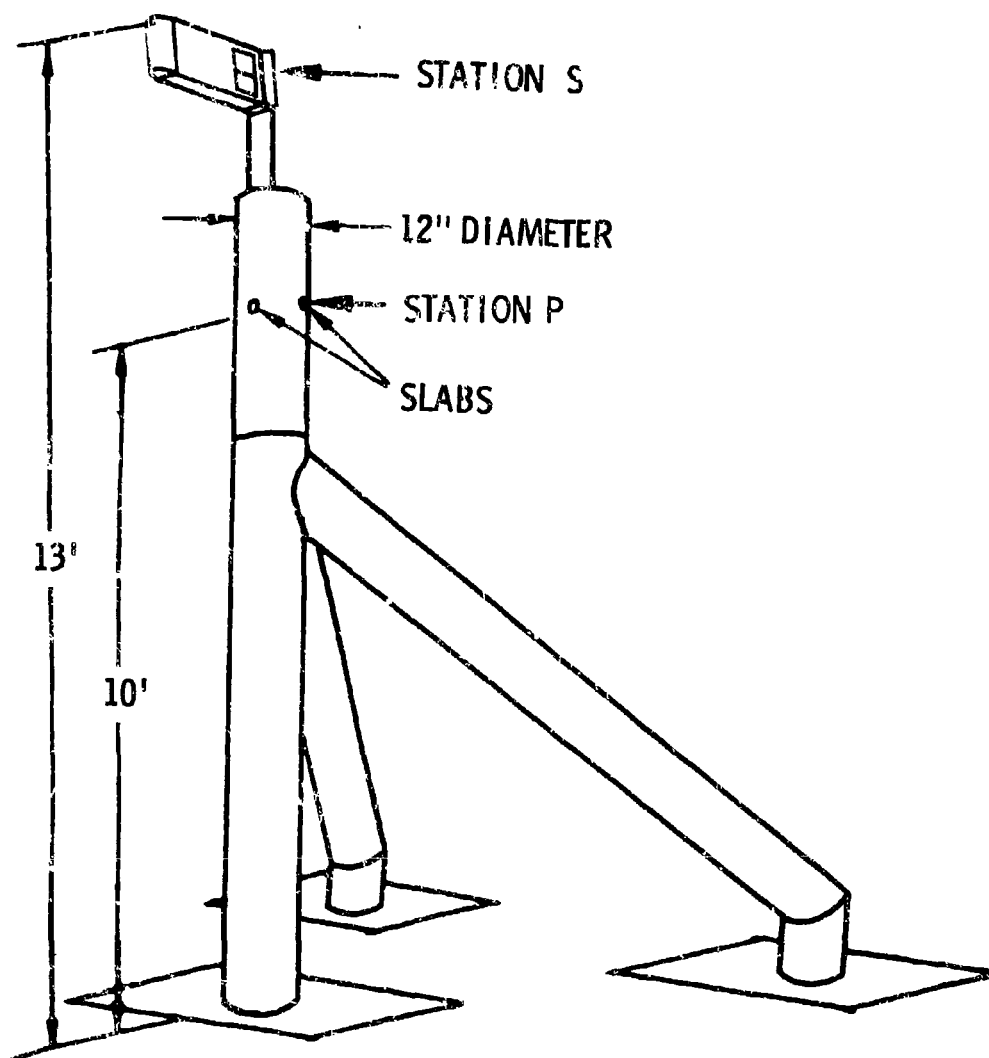
Fig. C-20. Thermal Instrument Stations P and S
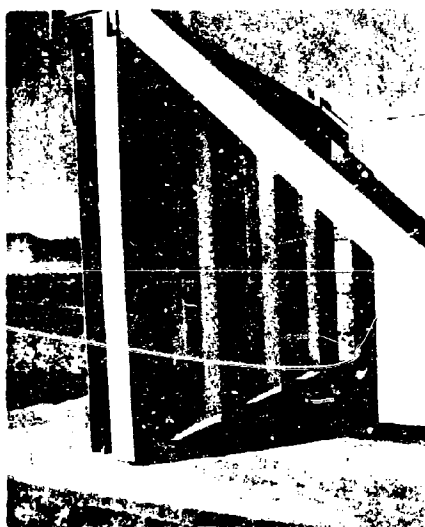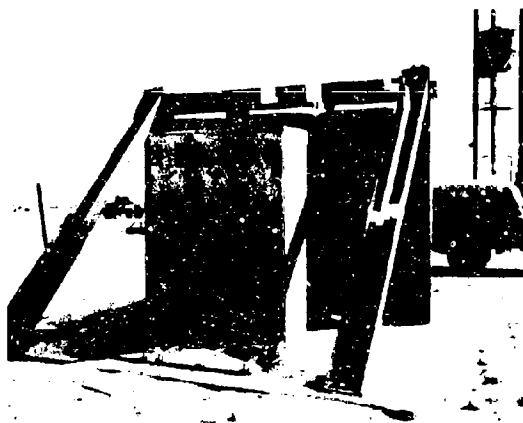
Fig. D-3.   NASA/MSFC Blast Shields

Fig. D-4. Typical Fireball Cloud

D- ⁄

The slabs on the 3 station from Tests 275 through 279 were 3 by 3 by 1-in.-thick stainless steel 309. While slabs having comparatively small thermal diffusivities such as stainless steel are preferable for the longer duration tests, the loss of several temperature transducers during the first few 25,000-lb tests required their replacement with transducers and slabs of copper. In order to increase the time during which negligible errors occur in the evaluation of heat flux, slabs having a thickness of 1-1/2 in. were installed, where as usual, the exposed slab surface was flush with the external surface of the mount.

The location of station P is shown in Fig. C-20 just below station S, station P being actually part of the support structure for station S. Station P, installed after test 285, consists of a series of instrumented slabs distributed at 60-deg-angle intervals along the circumference of a 12-in.-diameter, vertically oriented pipe. A more detailed cross-sectional cutaway view showing the slab arrangement is given in Fig. C-21, along with a dimensional sketch of an individual slab in the lower right hand corner of the figure. The primary purpose of the station was to determine if there are pronounced and consistent variations of flux density with position on such an object.

It was planned to use iron transducers and slabs in station P. However, iron transducers were not available until the Titan I test (Test 301) and copper transducers and slabs were substituted. The use of copper with these comparatively small slab dimensions will result in small errors in the evaluation of heat flux toward the end of the heating pulse as noted in the discussion of errors above. Iron slabs were installed for the Titan I test at station P positions 1, 3, and 5 (position is designated by numbers in parentheses on Fig. 21.

The Sandia station was elevated above the ground surface approximately 10 ft and supported by a structure similar to that for station S shown on Fig. C-20. It was located about 30 ft from the test pad center at a point approximately intersecting gauge lines A and C.

D-5a
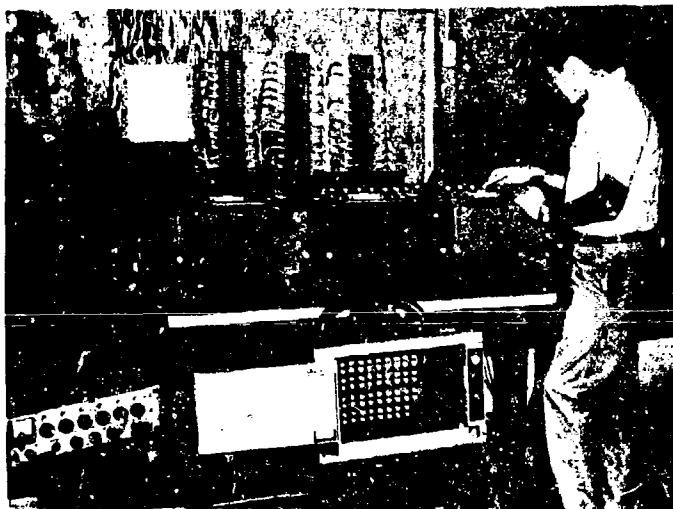
D-5b

Fig. D-5.　University of Florida Experiment
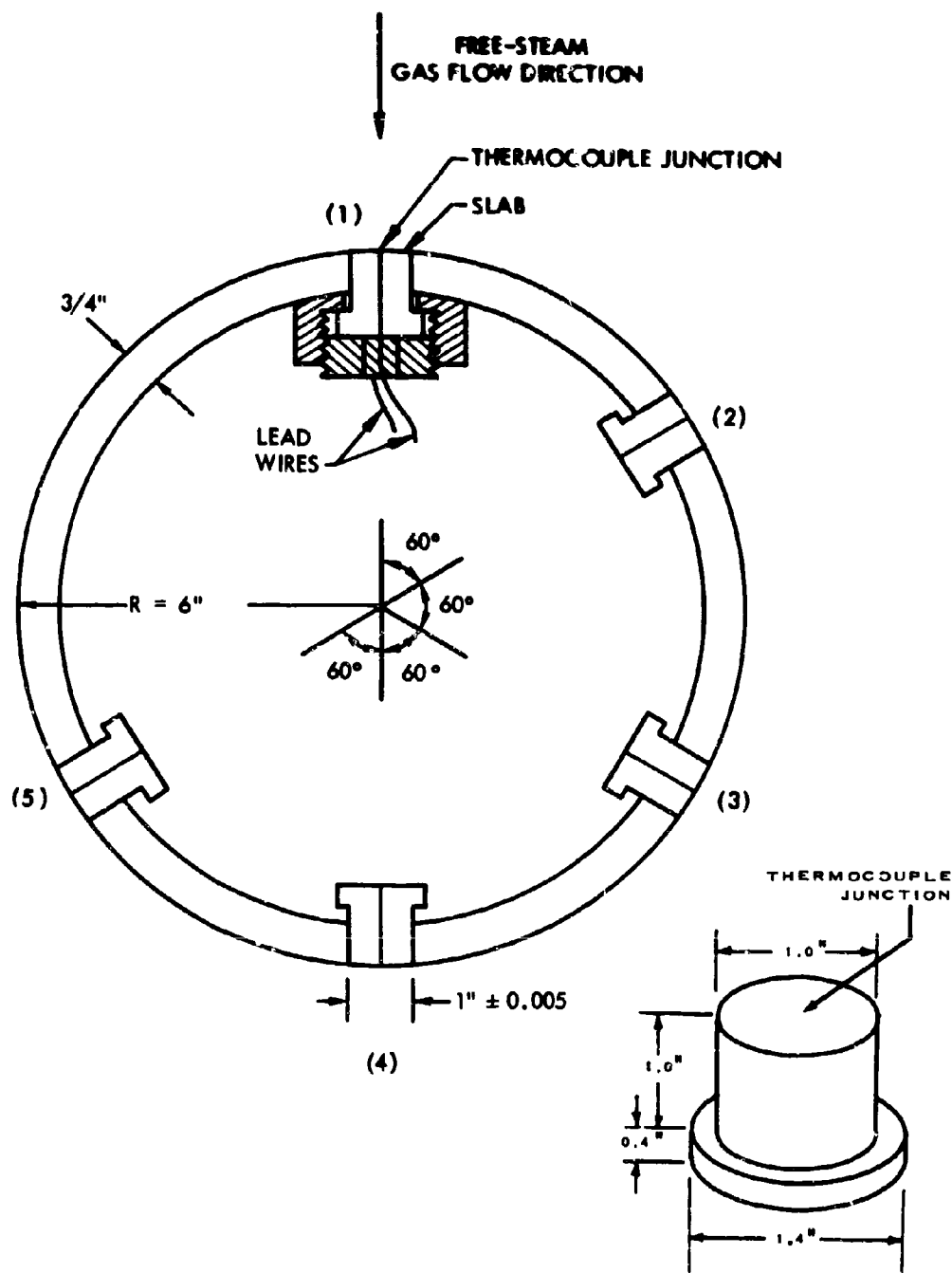
Fig. C-21. Cross-sectional Cutaway View of Thermal Instrument Station P
           and a Perspective View of the Associated Slabs
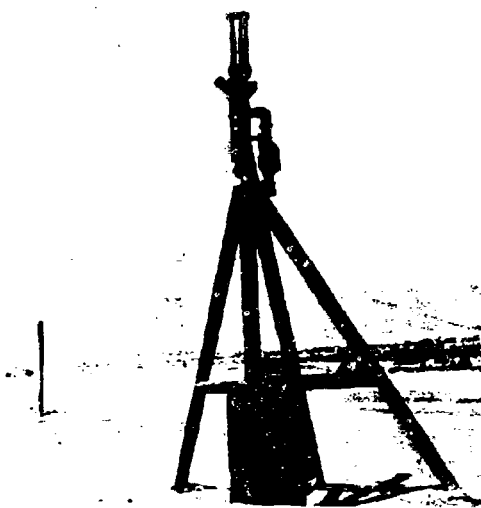
Fig. D-6.   Sandia Snap 27, Heat Transfer Experiment

Outside the Fireball

Measurements of radiant flux density and fireball temperature are made from remote locations. Generally three radiometers were used per test, two at the same distance (335 ft) from ground zero along radial gauge lines (A and B) 120 deg from each other, with the third more remotely located (600 ft) along gauge line A. Those distances are such that with the existing field-of-view of the instruments, radiant energy originating in any region of the fireball prior to its rise is not restricted from falling incident on the sensitive foil of the instrument.

The photo-recording pyrometer (a Sandia Corporation instrument) was located about 450 ft from the test pad along gauge line A.

Fig. D-7.　Pan American Cinespectrograph System

REFERENCES, Appendix C

C-1. Churchill, R. V., *Operational Mathematics*, McGraw-Hill Book Company, Inc., New York, New York, 1958

C-2. Kendall, D. N. and W. P. Dixon, "Heat Transfer Measurements in a Hot Shot Wind Tunnel," IEEE Aerospace Systems Conference, Seattle, Washington, 11-15 July 1966

C-3. Robertson, S. J., *Theory and Application of Long Duration Heat Flux Sensors*, HTL-TR-15, Contract NAS 8-11558, Heat Technology Laboratory, Inc., Huntsville, Alabama, 21 September 1964

C-4. RAD, Beck, J. V., Correction of Transient Thermocouple Temperature Measurements in Heat-Conducting Solids, Part I, Procedures of Thermo-Couple Temperature Correction in Solids Possessing Constant Thermal Properties, Technical Report, RAD-TR-60-38, Contract AF04(647)-258, 8 February 1961 (AD 269354)

C-5. Goldsmith, A., T. E. Waterman, and H. J. Hirschhorn, *Handbook of Thermo-Physical Properties of Solid Materials*, The Macmillan Company, New York, New York, 1961

C-6. Marchi, Vito V., Advanced Technology Division of American-Standard, Mountain View, California, Private Communication, 29 November 1965

C-7. Gardon, R., "An Instrument for the Direct Measurement of Intense Thermal Radiation," *The Review of Scientific Instruments*, Vol. 24, No. 5, May 1953

C-8. Ferris, H. G., *Theoretical Analysis of Radiometer Performance*, R & D Technical Report USNRDL-TR-311, AFSWP-1119, U.S. Naval Radiological Defense Laboratory, San Francisco, California, 13 January 1959

C-9. Born, M. and E. Wolf, *Principles of Optics — Electromagnetic Theory of Propagation, Interference and Diffraction of Light*, Pergamon Press, New York, New York, 1959
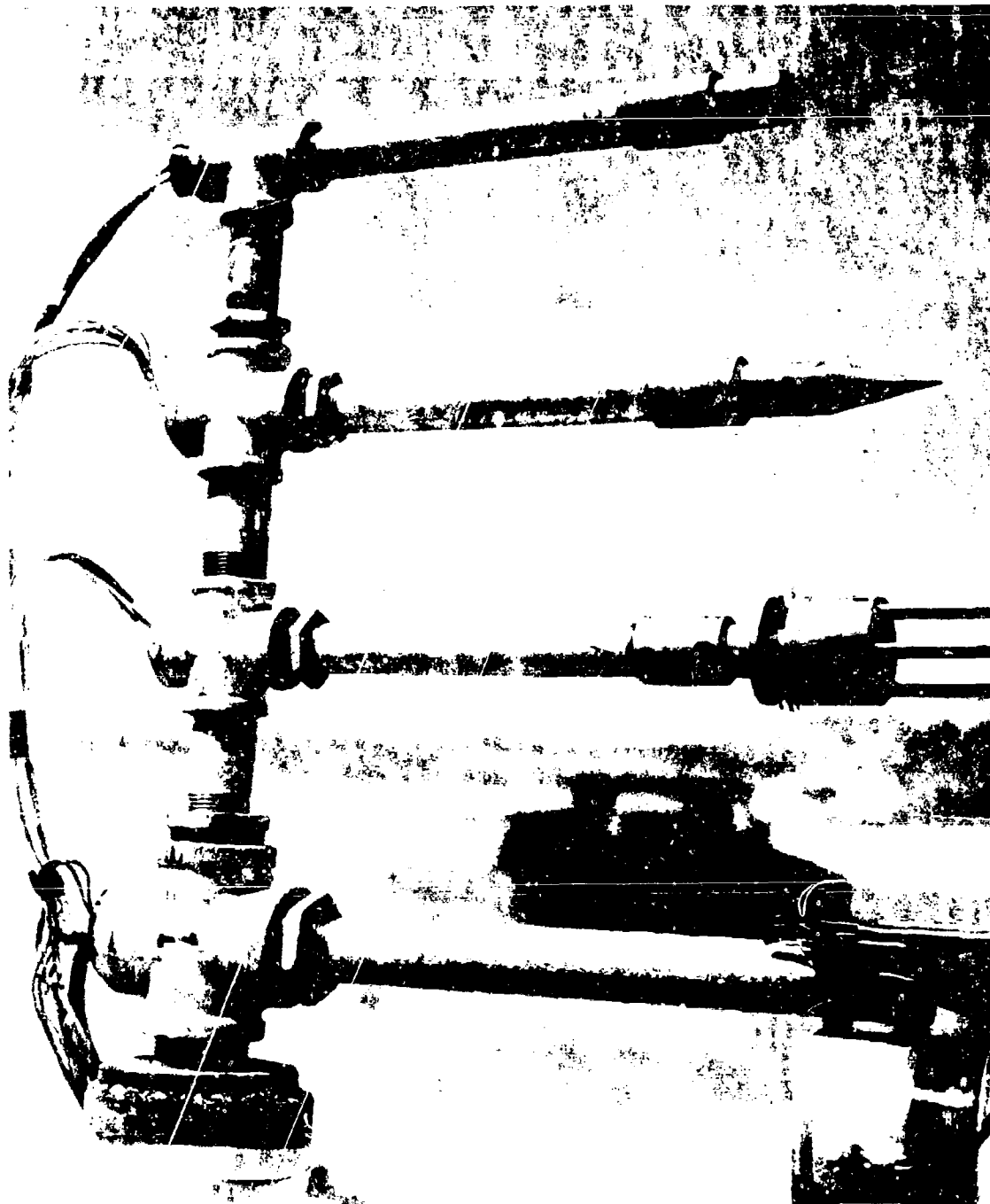
Fig. D-8. Midwest Research Institute Thermocouples

C-10.   Jenkins, F. A. and H. E. White, <u>Fundamentals of Optics</u>, McGraw-Hill
        Book Company, Inc. New York, New York, 1957

C-11.   Oppenheim, U. P. and U. Even, "Infrared Properties of Sapphire at
        Elevated Temperatures," <u>Journal Optical Society of America</u>, Vol. 52,
        No. 9, September 1962 pp. 1078-1079

C-12.   Gryvnak, D. A. and D. E. Burch, "Optical and Infrared Properties of
        Al_2O_3 at Elevated Temperatures," <u>Journal Optical Society of America</u>,
        Vol. 53, No. 6, June 1965 pp 625-630

Appendix D

"Ride-Along" Programs[*]

Included in the test phase of Project PYRO were several experiments
conducted by outside agencies which utilized the thermal and blast environ-
ment provided by the liquid propellant explosions. The data generated
in these experiments will be reported by the conducting agency. The follow-
ing is a summary description of each experiment and the technical contact.

The U.S. Army Corps of Engineers built and installed aluminum structures
in the PYRO test area (see Figure D-1) to measure structural response to
the liquid propellant blast wave. Figure D-2 shows the damage received
by a structure during a test. The technical contact for this program was
Mr. M. J. Rosenfield, Ohio River Division Laboratories, 5851 Mariement Avenue,
Cincinnati, Ohio 45227.

NASA/MSFC installed a series of blast shields 100 ft from ground zero
during the 25,000-lb test series to evaluate these shields for use on test
stands and launch pads to protect ground support equipment. Figure D-3,
shows typical blast shields as installed for the tests. The technical
contact for this program was Mr. Walter V. Medenica, NASA/MSFC (R-Test-B)
Huntsville, Alabama 35812.

BSD in conjunction with TRW Corporation tracked the fireball cloud
of three 25,000-lb tests to determine the feasibility of measuring the
turbulence velocity in and near the cloud. Figure D-4 shows a typical
fireball cloud. The technical contact for this program was Dr. Chris Bush,
1 Spruce Park, Building R-4, Room 1166, Redondo Beach, California 90278.

---

[*] This portion of the report was authored by Mr. R. Thomas, AFRPL.

Appendix E

EXPERIMENTAL TESTS

Presented in this appendix is a chronological listing of all the experimental tests conducted under this program. Included in this listing is the following information:

- Test Number

- Description of test conditions, including: <u>Propellant or explosive type</u>; LO_2/RP-1 (liquid oxygen/RP-1). LO_2/LH_2 (liquid hydrogen), hypergolic (nitrogen tetroxide/50% unsymmetrical dimethylhydrazine — 50% hydrazine), <u>High-Explosive Calibration Test</u> (a pentolite charge unless otherwise noted); <u>Flow direction</u> V - (vertical), H - (horizontal); <u>Impact Velocity</u>, LV - low velocity, MV - medium velocity, HV - high velocity; <u>Propellant orientation</u> normal, i.e., LO_2 on top of RP-1, LH_2 on top of LO_2, N_2O_4 on top of 50-50 unless marked RPO (reversed propellant orientation). All propellant weights are 200 lb unless otherwise noted.

- Yield - in percent TNT

- Ignition time in milliseconds

- Data Bank - indicates that the data are or are not in Volume 2, the data bank. A "no" in this column usually indicates that no data were recorded or that the data couldn't be reduced.

- Prediction method - indicates the data which were used either in the development of the prediction method or as large-scale confirmation of the method.

E-1

The University of Florida, under contract to NASA KSC, installed a thermo-
couple grid in the fuel tank of one 200-lb and two 25,000-lb LO_2/RP-1 CBM
tests to relate explosive yield to propellant mixing as measured by the
thermocouple grid. Figure D-5-A shows the grid as installed, and Figure D-5-B
shows the oscillograph recording equipment used. The technical contact
for this program is Dr. Farber of the University of Florida, Gainsville,
Florida 32603.

Sandia Corporation installed two thermal experiments during the 25,000-lb
test series. The PAMS (Pad Abort Measuring System), which is used at
Cape Kennedy, was evaluated by comparison with the basic PYRO thermal data.
The second instrument installed by Sandia, shown in Figure D-6, was the
SNAP-27 Heat Transfer Experiment. The data obtained from the SNAP-27 was
used to evaluate the thermal model employed in the design of the SNAP-27
power reactor capsule. The technical contact for these experiments is
Mr. F. D. Kite of Sandia Corporation, P.O. Box 5800, Albuquerque,
New Mexico 32925.

Pan American, under contract to AFETR, installed a cine-spectrograph
system, shown in Figure D-7, to provide data regarding the products of
the fireball and to measure the fireball temperature. The technical contact
for this project is Mr. Cy Golub of Pan American Airways, Mail Unit 706,
Building 989, Patrick AFB, Florida 32925.

The Midwest Research Institute, under contract to NASA/MSC, installed
pre-heated thermocouples of various designs (see Figure D-8) to determine
their survivability under blast wave loading. The purpose of these pre-
heated thermocouples is to measure directly the peak temperature of the
fireball. The technical contact for this experiment is Mr. R. F. Fletcher
of NASA/MSC (STED), Houston, Texas 77001.

NOTES FOR TEST TABLE

1. Propellant spilled to 20-ft diameter from rupture in bottom of tank.

2. Pressure reached 95 psi, 25 msec after diaphragm break. At this point, the top of the tank blew out, and a fire at the top of the tank was observed.

3. Detonator blew hole in tank, which tipped over. Propellant spilled on pad and spread until ignition.

4. Test similar to 087 except tank did not tip over.

5. Top part of tank flew to about the height of the apex of the tower before falling back on the pad. Ignition occurred after it had essentially come to rest.

6. Ignition at impact of top tank.

7. Comparison of tank pressure for test 275 with those for tests 278 and 282, which had very similar ignition time but considerably larger yield, showed a much slower and more linear pressure rise for 275 than for either 278 or 282.

8. Fire visible at bottom of tank about 12 msec before ignition.

9. Propellants not in contact at time of ignition.

The U.S. Coast and Geodetic Survey Agency installed ground shock
instrumentation for several 25,000-lb tests to relate ground shock data
from nuclear explosions to liquid propellant explosions. The technical
contact for this work is Mr. W. B. Mickey, U.S. Coast and Geodetic - ESSA,
Washington Science Center, Rockville, Maryland 20852.
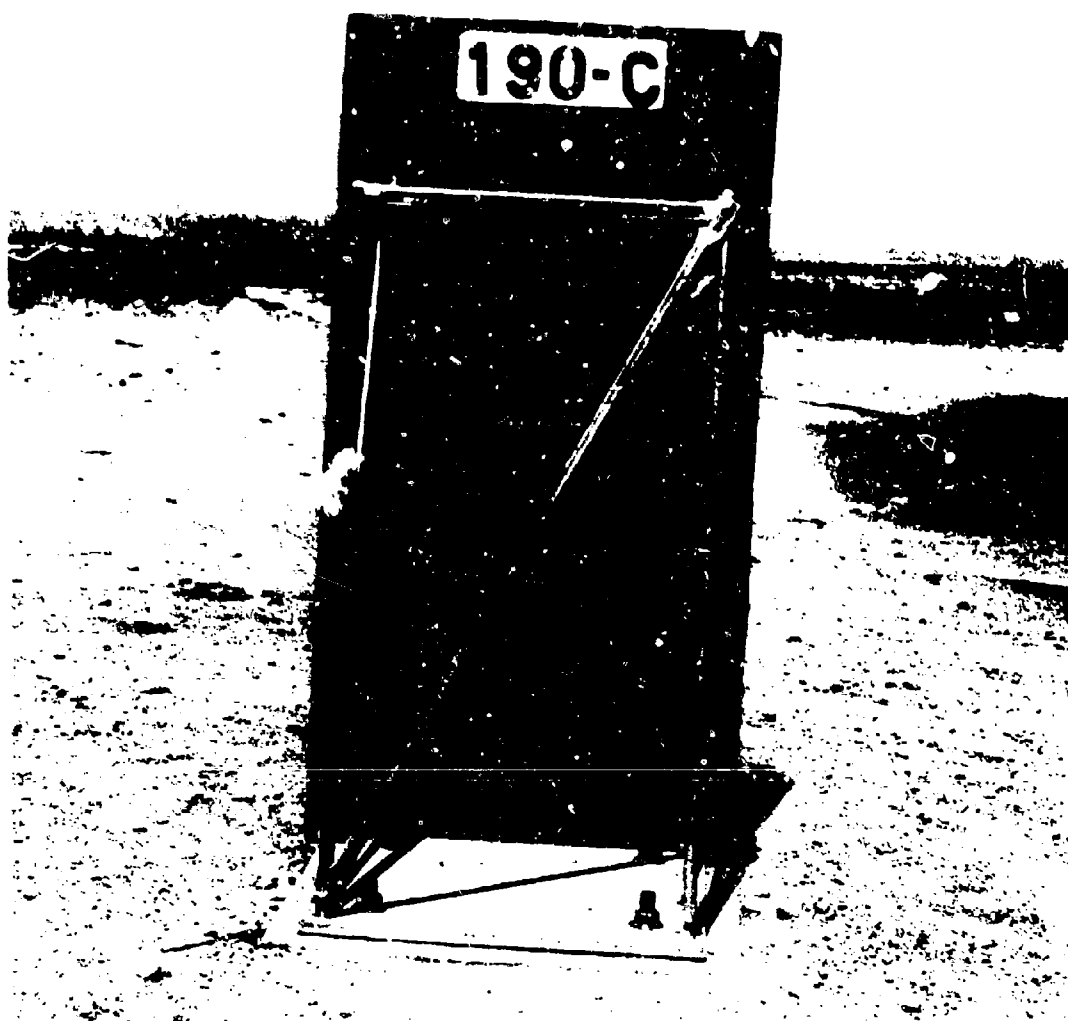
Fig. D-1. Pretest Photo, U.S. Army Corps of Engineers Structure
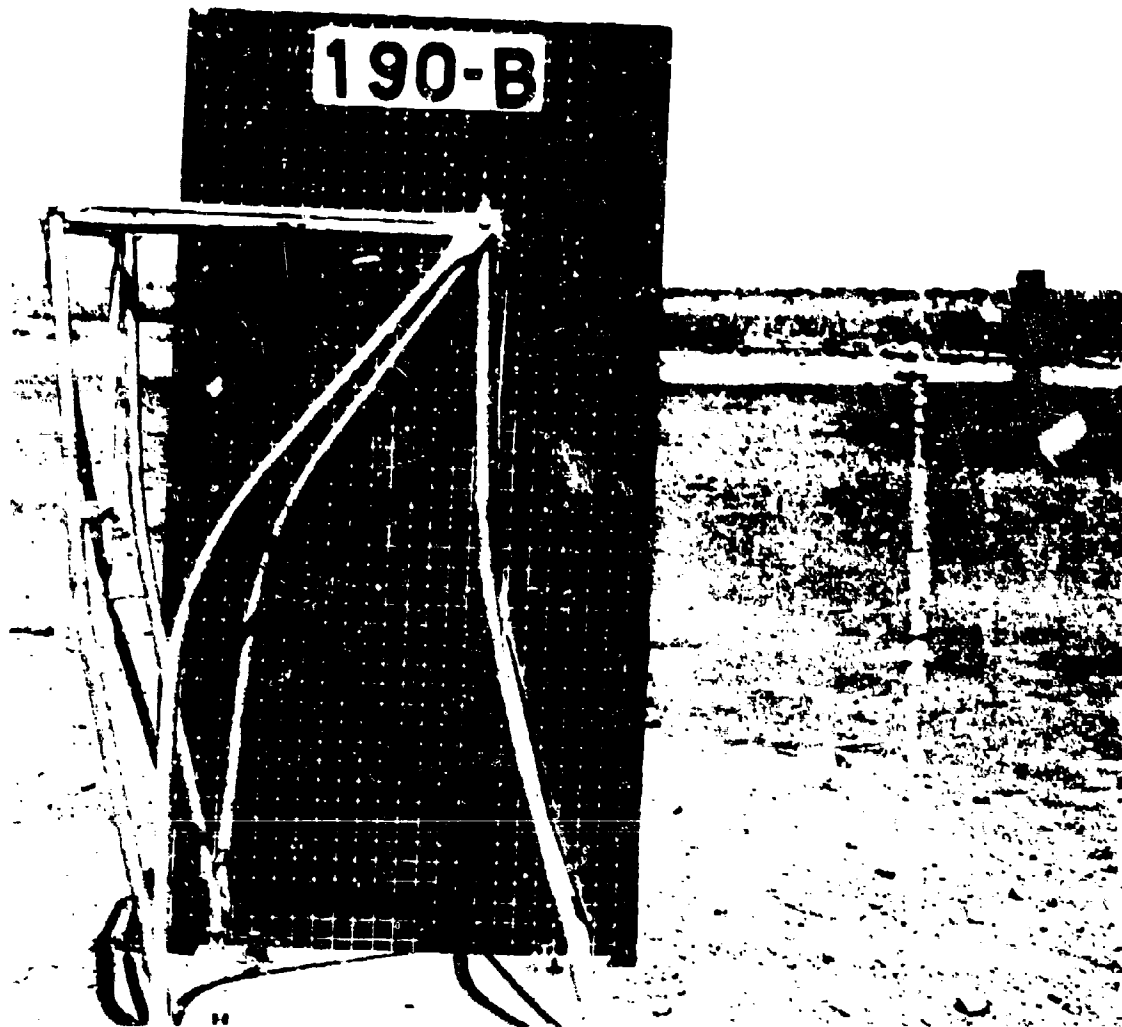
Fig. D-2.   Posttest Photo, U.S. Army Corps of Engineers Structure

TEST NO	DESCRIPTION TEST CONDITIONS	YIELD (%)	IGNITION TIME	DATA BANK	PRED. METHOD	REMARKS
001C	NWC 18-1b CAL.	--	--	--	--	Data presented in Section 4
002C	NWC 18-1b CAL.	--	--	--	--	Data presented in Section 4
001	NWC N_2O_4/50-50 Flat Wall	13	--	Yes	Yes	--
002	NWC N_2O_4/50-50 Shallow Wall	53	--	Yes	Yes	--
003C	NWC 18-1b CAL.	--	--	--	--	Data presented in Section 4
003	NWC N_2O_4/50-50 Deep Hole	29.5	--	Yes	Yes	--
004	NWC N_2O_4/50-50 Parallel Wall	40	--	Yes	Yes	--
005	N_2O_4/50-50 30-1b Spherical Shaped Charge Donor	--	--	--	--	Data presented in Section 4
006	NWC 18-1b CAL.	--	--	--	--	Data presented in Section 4
007	RWC N_2O_4/50-50 Flat Wall	5	--	Yes	Yes	--
008	NWC N_2O_4/50-50 Deep Hole	38	--	Yes	Yes	--
009	NWC N_2O_4/50-50 Deep Hole	56	--	Yes	Yes	--
010	NWC N_2O_4/50-50 Parallel Wall	26	--	Yes	Yes	--
011	NWC 18-1b CAL.	--	--	No	No	Data presented in Section 4
012	NWC 1000-1b N_2O_4/50-50 Flat Wall	15	--	Yes	Yes	--
013	NWC 1000-1b N_2O_4/50-50 Deep Hole	28	--	Yes	Yes	--
014	NWC 216-1b CAL.	--	--	No	No	Data presented in Section 4
015	NWC 216-1b CAL.	--	--	No	No	Data presented in Section 4
016	1R-1b CAL.	--	--	No	No	Data presented in Appendix A
017	N_2O_4/50-50 Test Article Filled With Water Using 30-1b Spherical Charge Donor	--	--	No	No	Data presented in Section 4
018	18-1b CAL.	--	--	No	No	Data presented in Appendix A
019	N_2O_4/50-50 30-1b Spherical Shaped Charge Donor	3.4	--	Yes	No	--
020	18-1b CAL.	--	--	No	No	Data presented in Appendix A
021	18-1b CAL.	--	--	No	No	Data presented in Appendix A
022	N_2O_4/50-50 Test Article Filled With Water Using 30-1b Spherical Charge Donor	--	--	No	No	Data presented in Section 4

TEST NO	DESCRIPTION TEST CONDITIONS	YIELD (%)	IGNITION TIME	DATA BANK	PRED. METHOD	REMARKS
023	18-lb CAL.	--	--	No	No	Data presented in Appendix A
024	18-lb CAL.	--	--	No	No	Data presented in Appendix A
025	N_2O_4/50-50 Linear Charge Donor	0.35	--	Yes	Yes	--
026	18-lb CAL.	--	--	No	No	Data presented in Appendix A
027	18-lb CAL.	--	--	No	No	Data presented in Appendix A
028	N_2O_4/50-50 Conical Charge Donor	1.2	--	Yes	Yes	--
029	N_2O_4/50-50 Conical Charge Donor	0.8	--	Yes	Yes	--
030	N_2O_4/50-50 30-lb Spherical Charge Donor	4	--	Yes	Yes	--
031	N_2O_4/50-50 In-Tank Failure	0.20	--	Yes	Yes	--
032	N_2O_4/50-50 In-Tank Failure	0.08	--	Yes	Yes	--
033	Frozen N_2O_4/50-50	8.8	--	Yes	Yes	--
034	Frozen N_2O_4/50-50	--	--	No	No	Failure of propellant transfer to test tank
035	N_2O_4/50-50 In-Tank Failure	0.15	--	Yes	Yes	--
036	N_2O_4/50-50 Linear Charge Donor	0.30	--	Yes	Yes	--
037	Frozen N_2O_4/50-50	13.7	--	Yes	Yes	--
038	N_2O_4/50-50 In-Tank Failure	--	--	No	No	No data test article failure
039	N_2O_4/50-50 30-lb Spherical Charge Donor	--	--	No	No	--
040	LO_2/RP-1 Time vs Pressure	43	--	No	No	No pressure on LO_2 tank before test. Cap ignition at 100 psi tank pressure
041	LO_2/LH_2 Time vs Pressure	--	--	No	No	(10)
042	LO_2/RP-1 CBM	48	290	Yes	Yes	Tank rupture ignition
043	LO_2/LH_2 CBM	--	--	No	No	Negligible explosion. Suspect no hydrogen
044	LO_2/RP-1 CBM	18	120	Yes	Yes	Tank rupture ignition
045	LO_2/RP-1 CBM	5.6	123	No	No	Suspect diaphragm breaker, cap ignition
046	LO_2/RP-1 CBM	17	143	Yes	Yes	Squib ignition
047	LO_2/RP-1 CBM	10	120	Yes	Yes	Cap ignition
048	LO_2/RP-1 CBM	0.8	310	No	No	Suspect diaphragm breaker, cap ignition

TEST NO	DESCRIPTION TEST CONDITIONS	YIELD (%)	IGNITION TIME	"A BANK	PRED. METHOD	REMARKS
049	LO_2/RP-1 CBM	12	316	Yes	Yes	Squib ignition
050	LO_2/RP-1 CBM	86	180	Yes	--	Tank rupture ignition 2 - LO_2/LH_2
051	LO_2/LH_2 CBM	22	80	Yes	--	Cap ignition at tank rupture
052	LO_2/LH_2 CBM	7	83	Yes	Yes	Squib ignition
053	LO_2/LH_2 CBM	4	1	Yes	Yes	Diaphragm rupture ignition
054	LO_2/LH_2 CBM	6	17	Yes	Yes	Diaphragm rupture ignition
055	LO_2/LH_2 CBM	1	1	Yes	Yes	Diaphragm rupture ignition
056	LO_2/LH_2 CBM	70	144	No	No	Breaker charge caused fire on top of tank.
057	LO_2/LH_2 CBM	1.3	12	Yes	Yes	Diaphragm rupture ignition
058	LO_2/RP-1 CBM	26	201	Yes	--	Squib ignition
059	18-1b CAL.	--	--	No	No	Data presented in Appendix A
060	18-1b CAL.	--	--	No	No	Data presented in Appendix A
061	105-1b CAL.	--	--	No	No	Data presented in Appendix A
062	SATURN S-IV LO_2/LH_2	6	183	No	No	Data presented in Section 5
063	1000-1b TNT CAL.	--	--	No	No	Data presented in Appendix A
064	1000-1b TNT CAL.	--	--	No	No	Data presented in Appendix A
065	NWC 18-1b CAL.	--	--	No	No	Data presented in Section 4
066	NWC CTF/Solid Deep Hole	0.6	--	No	No	Impact Velocity 590 ft/sec
067	NWC 18-1b CAL	--	--	No	No	Data presented in Section 4
068	NWC N_2O_4/50-50 Flat Wall	15	--	Yes	Yes	Impact Velocity 565 ft/sec
069	NWC N_2O_4/50-50 Deep Hole	37	--	Yes	Yes	Impact Velocity 555 ft/sec
070	NWC 18-1b CAL.	--	--	No	No	Data presented in Section 4
071	NWC 103-1b CAL.	--	--	No	No	Data presented in Section 4
072	NWC 1000-1b N_2O_4/50-50 Flat Wall	23	--	Yes	Yes	Impact velocity 585 ft/sec
073	NWC 1000-1b N_2O_4/50-50 Flat Wall	21	--	Yes	Yes	Impact Velocity 410 ft/sec
074	NWC 1000-1b N_2O_4/50-50 Deep Hole	34	--	Yes	Yes	Impact Velocity 557 ft/sec
075	NWC 1000-1b LO_2/RP-1 Flat Wall	21	--	Yes	Yes	Impact Velocity 526 ft/sec
076	NWC 1000-1b LO_2/RP-1 Deep Hole	57	--	Yes	Yes	Impact Velocity 523 ft/sec

TEST NO	DESCRIPTION TEST CONDITIONS	YIELD (%)	IGNITION TIME	DATA BANK	PRED. METHOD	REMARKS
077	NWC 1000-lb LO_2/RP-1 Flat Wall	20	--	Yes	Yes	Impact Velocity 523 ft/sec
078	NWC 1000-lb LO_2/RP-1 Deep Hole	77	--	Yes	Yes	Impact Velocity 518 ft/sec
079	NWC 1000-lb LO_2/LH_2 Flat Wall	121	--	Yes	Yes	Impact Velocity 597 ft/sec
080	NWC 1000-lb LO_2/LH_2 Deep Hole	163	--	Yes	Yes	Impact Velocity 519 ft/sec
081	NWC 216-lb CAL.	--	--	No	No	Data presented in Section 4
082	18-lb High Explosive Cal.	--	--	No	No	Data presented in Appendix A
083	18-lb High Explosive Cal.	--	--	No	No	Data presented in Appendix A
084	LO_2/RP-1 CBM	10	312	No	No	Test tank leaked, Cap Ignition
085	LO_2/RP-1 CBM	12	380	Yes	Yes	Cap Ignition, 108 psi internal pressure
086	LO_2/RP-1 CBM	14	100	Yes	Yes	Cap Ignition
087	LO_2/RP-1 CBM	--	--	No	No	No Ignition (3)
087A	LO_2/RP-1 CBM	16	70	Yes	Yes	Cap Ignition
088	LO_2/RP-1 CBM	8	60	Yes	Yes	Cap Ignition
089	18-lb High Explosive Cal.	--	--	No	No	Data presented in Appendix A
090	LO_2/LH_2 CBM	29	35 sec	Yes	Yes	Cap Ignition at 100 psi internal pressure
091	LO_2/LH_2 CBM	13	--	Yes	No	Diaphragm rupture ignition
092	LO_2/LH_2 CBM	28	3 min	Yes	Yes	Cap Ignition at 100 psi internal pressure
093	LO_2/LH_2 CBM	34	147	Yes	--	Cap Ignition
094	LO_2/LH_2 CBM	25	329	Yes	Yes	Ignition at 100 psi internal pressure
095	LO_2/RP-1 CBM	--	--	No	No	No Ignition (4)
095A	LO_2/RP-1 CBM	17	120	Yes	Yes	Cap Ignition
096	LO_2/RP-1 V - LV	14	50	Yes	--	Cap Ignition
097	LO_2/RP-1 V - LV (RPO)	32	240	Yes	--	Cap Ignition
098	LO_2/RP-1 V - LV	14	300	Yes	--	Cap Ignition
099	LO_2/RP-1 V - LV (RPO)	23	140	Yes	--	Fire on pad before ignition
100	LO_2/RP-1 CBM	23	220	Yes	Yes	Cap Ignition
101	LO_2/RP-1 CBM	35	245	Yes	Yes	Cap Ignition
102	18-lb High Explosive Cal.	--	--	No	Yes	Data presented in Appendix A
103	LO_2/LH_2 V - LV (RPO)	--	--	No	No	No ignition, ordnance wires reversed

TEST NO	DESCRIPTION TEST CONDITIONS	YIELD (%)	IGNITION TIME	DATA BANK	PRED. METHOD	REMARKS
103A	LO_2/LH_2 V - LV (RPO)	39	208	Yes	--	Cap Ignition
104	LO_2/LH_2 V - LV	6	258	Yes	--	Squib Ignition
105	LO_2/LH_2 V - LV	7	--	Yes	--	Cap Ignition
106	LO_2/LH_2 V - LV (RPO)	--	--	No	No	No ignition, tank dropped late, propellant spilled on pad
106A	LO_2/LH_2 V - LV (RPO)	22	325	No	No	Tank hit breaker
107	$LO_2/RP-1$ V - HV (RPO)	29	42	Yes	--	Cap Ignition
108	$LO_2/RP-1$ V - HV (RPO)	31	60	Yes	--	Cap Ignition
109	$LO_2/RP-1$ V - HV	10	40	Yes	--	Cap Ignition
110	$LO_2/RP-1$ V - HV	26	35	Yes	Yes	Cap Ignition
111	18-1b CAL.	--	--	No	No	Data presented in Appendix A
112	18-1b CAL.	--	--	No	No	Data presented in Appendix A
113	LO_2/LH_2 V - HV (RPO)	52	77	Yes	--	Cap Ignition
114	LO_2/LH_2 V - HV	54	74	Yes	Yes	Cap Ignition
115	LO_2/LH_2 V - HV (RPO)	15	93	Yes	--	Cap Ignition
116	LO_2/LH_2 V - HV	10	18	Yes	--	Ignition on impact with breaker
117	LO_2/LH_2 CBM	--	--	No	No	Breaker charge caused fire and early ignition
118	LO_2/LH_2 CBM	20	82	Yes	Yes	Cap Ignition at 100 psi
119	LO_2/LH_2 CBM	--	--	No	No	Test aborted (2)
119A	LO_2/LH_2 CBM	--	--	No	No	Test aborted, no data recorded
119B	$LO_2/RP-1$ H LV	--	--	No	No	Tanks dropped in reverse order, bad calibrations Cap Ignition. Data not usable.
120	$LO_2/RP-1$ H LV	30	238	No	No	No propellant out of bottom tank until impact of top tank
121	$LO_2/RP-1$ H LV	30	184	Yes	Yes	RP-1 dumped before start of film, cap ignition
122	$LO_2/RP-1$ H LV	28	338/139	Yes	Yes	Cap Ignition
123	$LO_2/RP-1$ H LV	25	362/53	Yes	Yes	Cap Ignition
124	$LO_2/RP-1$ H HV	5	238/0	Yes	--	Ignition at impact of top tank
125	$LO_2/RP-1$ H HV	52	142/76	Yes	Yes	Cap Ignition
126	$LO_2/RP-1$ H HV	--	--	No	No	Ignition at impact of top tank

TEST NO	DESCRIPTION TEST CONDITIONS	YIELD (%)	IGNITION TIME	DATA BANK	PRED. METHOD	REMARKS
127	LO_2/RP-1 H HV	42	510/55	Yes	Yes	Fluid at 7-8' at ignition, tank breakup ignition
128	18-lb CAL.	--	--	No	No	Data presented in Appendix A
129	18-lb CAL.	--	--	No	No	Data presented in Appendix A
130	LO_2/LH_2 CEM	--	--	No	No	Test aborted when tank pressure dropped
130A	$LO_2$$LH_2$ H - LV	--	--	No	No	Top tank did not drop, no data
130B	LO_2/LH_2 H - LV	--	--	No	No	Top tank caught on tower, no data
130C	LO_2/LH_2 H - LV	--	--	No	No	Self-ignition, LH_2 trench destroyed
131	LO_2/LH_2 H - LV	6	441/125	Yes	Yes	Cap Ignition
132	LO_2/LH_2 H - LV	5	--	Yes	Yes	Bottom tank did not release fluid until after impact of top tank, cap ignition
133	LO_2/LH_2 H - LV	--	--	No	No	Top tank did not drop
133A	LO_2/LH_2 H - LV	6	284/286	Yes	Yes	Cap Ignition
134	LO_2/LH_2 H HV	8	--	No	No	Cap Ignition, all propellant not on ground at ignition
135	LO_2/LH_2 H EV	5.5	--	No	No	Ignition at impact of top tank
136	LO_2/LH_2 H HV	--	--	No	No	Ignition at impact of top tank
137	LO_2/LH_2 H HV	6.4	--	No	No	Ignition at impact of top tank
138	LO_2/LH_2 CEM	17	100	Yes	Yes	Cap Ignition
139	LO_2/RP-1 H HV	4.2	--	No	No	Ignition at impact of top tank
140	LO_2/RP-1 H HV	12	420/10	Yes	Yes	Cap Ignition
141	LO_2/RP-1 V HV	5	--	Yes	--	Probable diaphragm rupture ignition (8)
142	LO_2/RP-1 V HV	14	33	Yes	--	Cap Ignition
143	LO_2/RP-1 V LV	34	210	No	No	Top and bottom tanks impacted together
144	LO_2/RP-1 V LV	24	190	Yes	Yes	Cap Ignition
145	18-lb CAL.	--	--	No	No	Data presented in Appendix A
146	16-lb Functional	--	--	No	No	Instrumentation checkout only, data not reduced
147	16-lb Functional	--	--	No	No	Instrumentation checkout only, data not reduced
148	Hypergolic V HV	--	--	No	No	Caught fire on top of tower, no data
149	18-lb CAL.	--	--	No	No	Data presented in Appendix A
150	LO_2/LH_2 V HV	35	40	Yes	Yes	Cap Ignition

TEST NO	DESCRIPTION TEST CONDITIONS	YIELD (%)	IGNITION TIME	DATA BANK	PRED. METHOD	REMARKS
151	LO_2/LH_2 V HV	46	167	Yes	--	Cap ignition, tank fell through stopper
152	LO_2/LH_2 V LV	14	480	Yes	Yes	Cap Ignition
153	LO_2/LH_2 V LV	14	121	Yes	Yes	Cap Ignition, bad timing
154	$LO_2/RP-1$ V LV	18	470	Yes	--	Cap Ignition
155	$LO_2/RP-1$ H LV (RPO)	55	314/202	Yes	Yes	Cap Ignition
156	$LO_2/RP-1$ H LV (RPO)	63	182/230	Yes	Yes	Cap Ignition
157	Hypergolic V HV	0.29	99	Yes	Yes	--
158	Hypergolic V HV	0.2	--	Yes	--	--
159	Hypergolic V HV	0.3	--	Yes	Yes	--
160	LO_2/LH_2 V HV	32	67	Yes	--	Cap Ignition
161	LO_2/LH_2 V HV	5	--	Yes	--	Cap Ignition
162	$LO_2/RP-1$ H HV	24	--	No	No	Bottom tank did not drop (6)
163	$LO_2/RP-1$ V HV	--	--	No	No	Two explosions, one early, one correct time
164	LO_2/LH_2 V LV	4	125	Yes	No	Tank leaked, self ignition
165	LO_2/LH_2 V LV	8	325	Yes	No	Cap ignites after propellant on pad, fire goes out, detonation at time given
166	LO_2/LH_2 CBM	--	--	--	--	0.7% open, cold flow test (10)
167	LO_2/LH_2 CBM	24	8.74 sec	Yes	--	Partial full cold flow, ignition caused by poor venting (10)
168	LO_2/LH_2 CBM	--	--	No	No	Cold flow test (10)
169	LO_2/LH_2 CBM	15	318	Yes	Yes	Cap Ignition
170	LO_2/LH_2 CBM	--	--	No	No	Cold flow test (10)
171	LO_2/LH_2 CBM	--	--	No	No	Cold flow test (10)
172	LO_2/LH_2 CBM	32	730	Yes	--	Fire on tank before ignition
173	LO_2/LH_2 CBM	15	56	Yes	Yes	Fire on tank before ignition
174	$LO_2/RP-1$ CBM	51	136	Yes	--	Tank ruptured before ignition
175	$LO_2/RP-1$ CBM	--	--	No	No	Tank came apart, deflagration at much later time. No data.
176	$LO_2/RP-1$ H LV	65	468/374	Yes	Yes	Cap Ignition
177	$LO_2/RP-1$ H LV	30	111/203	Yes	Yes	Cap Ignition
178	$LO_2/RP-1$ H HV	3.2	--	No	No	Bottom tank did not drop (6)

TEST NO	DESCRIPTION TEST CONDITIONS	YIELD (%)	IGNITION TIME	DATA BANK	PRED. METHOD	REMARKS
179	LO_2/RP-1 H HV	12	787/23	Yes	Yes	Probable impact ignition
180	LO_2/RP-1 H HV (RPO)	--	--	No	No	LO_2 outran RP-1, no ignition
181	LO_2/RP-1 H HV (RPO)	--	--	No	No	No tape recorder
182	LO_2/LH_2 H HV	2.7	--	No	No	Ignition at impact of top tank
183	LO_2/LH_2 H HV	15	448/0	Yes	--	Probable impact ignition
184	LO_2/LH_2 V LV	17	810	Yes	Yes	Cap Ignition
185	LO_2/LH_2 H LV	8	469/0	Yes	--	Probable impact ignition
186	LO_2/LH_2 H LV	9	597/61	Yes	No	Ignition source unknown
187	18-1b CAL.	--	--	No	No	Data presented in Appendix A
188	18-1b CAL.	--	--	No	No	Data presented in Appendix A
189	Hypergolic 1000-1b	0.35	--	Yes	Yes	--
190	LO_2/RP-1 V - HV 1000-1b	96	570	Yes	Yes	Cap fired early, propellant found other ignition source
191	LO_2/RP-1 V MV 1000-1b	13	0	No	No	Tank broke stopper and hit ground
192	LO_2/RP-1 CBM 1000-1b	14	216	Yes	Yes	Probable Cap Ignition
193	LO_2/RP-1 CBM 1000-1b	20	222	Yes	Yes	Probable Cap Ignition
194	LO_2/RP-1 CBM 1000-1b	5.5	5 sec	No	No	Tank separated at diaphragm (5)
195	LO_2/LH_2 V - HV	104	292	Yes	Yes	Cap Ignition
196	LO_2/LH_2 V HV	17	639/77	Yes	Yes	Cap Ignition
197	LO_2/LH_2 V MV	19	500	Yes	Yes	Cap Ignition
198	LO_2/LH_2 H LV	17	507/121	No	No	Top tank pushed bottom tank to ground
199	LO_2/LH_2 CBM	8	816	Yes	Yes	Cap Ignition
200	LO_2/LH_2 CBM	17	100	Yes	Yes	Cap Ignition
201	LO_2/LH_2 V LV	26	1524	Yes	Yes	Cap Ignition
202	LO_2/RP-1 V LV	42	870	Yes	Yes	Cap Ignition
203	LO_2/LH_2 V MV	31	800	Yes	Yes	Cap Ignition
204	LO_2/LH_2 V MV	42	317	Yes	Yes	Cap Ignition
205	LO_2/RP-1 V HV	41	40	Yes	Yes	Tank on fire on the way down
206	LO_2/RP-1 V HV	85	350	Yes	Yes	Cap Ignition
207	LO_2/RP-1 V HV	38	28	Yes	Yes	No obvious ignition source

TEST NO	DESCRIPTION TEST CONDITIONS	YIELD (%)	IGNITION TIME	DATA BANK	PRED. METHOD	REMARKS
208	LO₂/RP-1 V MV	39	460	Yes	Yes	Cap Ignition
209	LO₂/RP-1 CBM 1000-1b	10	121	Yes	Yes	Cap Ignition
210	LO₂/LH₂ CBM 1000-1b	7	20	Yes	Yes	Either tank rupture or diaphragm rupture ignition
211	LO₂/LH₂ V MV 1000-1b	12	0	Yes	No	Ignition at impact
212	LO₂/LH₂ CBM 1000-1b	27	1366	Yes	Yes	Cap Ignition
213	LO₂/LH₂ CBM 1000-1b	35	708	Yes	Yes	Cap Ignition
214	LO₂/LH₂ V HV 1000-1b	NG	--	No	No	No data, tank caught fire 50' up tower
215	LO₂/LH₂ V HV 1000-1b	20	23	Yes	No	Tank broke apart at impact
216	LO₂/LH₂ V HV 1000-1b	9	0	Yes	No	Ignition at impact
217	LO₂/LH₂ V MV 1000-1b	33	1490	Yes	Yes	Cap Ignition
218	LO₂/RP-1 V MV 1000-1b	4.5	--	Yes	No	Ignition at impact
219	LO₂/RP-1 V MV 1000-1b	14	1835	Yes	--	Cap Ignition
220	LO₂/RP-1 V MV 1000-1b	96	525	Yes	Yes	Cap Ignition
221	18-1b CAL.	--	--	No	No	Data presented in Appendix A
222	18-1b CAL.	--	--	No	No	Data Presented in Appendix A
223	LO₂/LH₂ H LV	18	708/157	Yes	Yes	Cap Ignition
224	LO₂/LH₂ H LV	16	899/621	Yes	Yes	Cap Ignition
225	LO₂/LH₂ V LV	34	933	Yes	Yes	Cap Ignition
226	LO₂/LH₂ V HV	51	283	Yes	Yes	Fire on pad before ignition
227	LO₂/LH₂ H HV	--	--	No	No	Tank on fire at impact
228	LO₂/LH₂ H HV	34	560/42	Yes	Yes	Unknown ignition source
229	LO₂/LH₂ V MV	52	1374	Yes	Yes	Cap Ignition
230	LO₂/LH₂ V MV	21	24	Yes	--	Fire visible at top of tank 10-15 msec before ignition
231	LO₂/LH₂ V MV	24	525	Yes	Yes	Cap Ignition
232	LO₂/RP-1 V MV	30	1220	Yes	Yes	Cap Ignition
233	LO₂/LH₂ H LV Pool	109	2182	Yes	Yes	Cap ignition, maximum yield trial
234	18-1b High Explosive Cal.	--	--	No	No	Data presented in Appendix A
235	18-1b High Explosive Cal.	--	--	No	No	Data presented in Appendix A
236	LO₂/RP-1 V HV	74	720	Yes	Yes	Cap Ignition

TEST NO.	DESCRIPTION TEST CONDITIONS	YIELD (%)	IGNITION TIME	DATA BANK	PRED. METHOD	REMARKS
237	LO₂/RP-1 CBM	33	127	Yes	Yes	Tank Rupture
238	LO₂/RP-1 CBM	19	85	Yes	Yes	Repeat of 87. Cap Ignition
239	LO₂/RP-1 CBM	33	156	Yes	Yes	Tank rupture ignition probable, could be cap
240	LO₂/RP-1 CBM	60*	156	Yes	Yes	Tank only 2/3 full, yield based on full tank, Cap Ignition
241	30-lb Comp B - Water	--	--	No	No	High explosive charge standard
242	LO₂/LH₂ H LV Pool	107	800	Yes	Yes	Maximum yield trial, Cap Ignition
243	Hybrid	--	--	No	No	**
244	Hybrid	--	--	No	No	**
245	LO₂/LH₂ H LV	--	--	No	No	Tape malfunction, no data
246	18-lb High Explosive Cal.	--	--	No	No	Data presented in Appendix A
247	18-lb High Explosive Cal.	--	--	No	No	--
248	LO₂/RP-1 V LV	25	210	Yes	Yes	Cap Ignition
249	LO₂/RP-1 V LV	50	710	Yes	Yes	Cap Ignition
250	LO₂/RP-1 V MV	52	200	Yes	Yes	Cap Ignition
251	LO₂/LH₂ V MV	64	775	Yes	Yes	Cap Ignition
252	LO₂/LH₂ V MV	38	325	Yes	Yes	Cap Ignition
253	LO₂/LH₂ H MV	57	561/108	Yes	Yes	Cap Ignition
254	LO₂/LH₂ V MV 200-lb	33	533	Yes	Yes	Cap Ignition
255	18-lb High Explosive Cal.	--	--	No	No	Data presented in Appendix A
256	18-lb High Explosive Cal.	--	--	No	No	--
257	N₂O₄/50-50 V MV 1000-lb	.3	--	Yes	Yes	--
258	N₂O₄/50-50 V MV 1000-lb	.25	--	Yes	Yes	--
259	Hybrid 30-lb Donor	--	--	No	No	**
260	Hybrid drop	--	--	No	No	No data
261	Hybrid drop	--	--	No	No	No data
262	LO₂/LH₂ V MV 1000-lb	42	900	Yes	Yes	Cap Ignition
263	LO₂/LH₂ V MV 1000-lb	--	--	No	No	Ignition before impact
264	LO₂/LH₂ V MV 1000-lb	21.5	20	Yes	No	Self ignition, suspect diaphragm break

* Pressure yields from AFRPL

** Data reported in Investigation of the Explosive Potential of the Hybrid Propellant Combinations N₂O₄/PBAN and CTF/PBAN, TDR No. AFRPL-TR-67-124, URS 652-26, March 1967

TEST NO	DESCRIPTION TEST CONDITIONS	YIELD (%)	IGNITION TIME	DATA BANK	PRED. METHOD	REMARKS
265	LO$_2$/LH$_2$ CBM 1000-lb	10	750	Yes	Yes	Cap Ignition
266	LO$_2$/LH$_2$ V MV 1000-lb	14	--	Yes	No	Fire at top of tank
267	LO$_2$/RP-1 V MV 1000-lb	64	1770	Yes	Yes	Cap Ignition
268	LO$_2$/RP-1 V MV 1000-lb	70	340	Yes	Yes	Cap Ignition
269	LO$_2$/RP-1 V HV 1000-lb	--	--	No	No	Test aborted
269A	LO$_2$/RP-1 V HV 1000-lb	44	77	Yes	Yes	Midsection of tank fails at impact
270	LO$_2$/RP-1 CBM 1000-lb	--	--	No	No	Test aborted, no data
270A	LO$_2$/RP-1 CBM 1000-lb	13	225	Yes	Yes	Cap Ignition
271	105-lb CAL.	--	--	No	No	Data presented in Appendix A
272	105-lb CAL.	--	--	No	No	--
273	100-lb Functional			No	No	A, B, C tests as well
274	500-lb CAL.	--	--	No	No	--
275	LO$_2$/RP-1 CBM 25,000-lb	4	515	Yes	Yes	Suspect only small hole in diaphragm (7)
276	500-lb CAL.	--	--	No	No	--
277	LO$_2$/LH$_2$ CBM 25,000-lb	0.2	31	Yes	No	Diaphragm rupture ignition
278	LO$_2$/RP-1 CBM 25,000-lb	13	530	Yes	Yes	Tank rupture ignition
279	LO$_2$/LH$_2$ CBM 25,000-lb	0.2	33	Yes	No	Diaphragm rupture ignition
280	500-lb CAL.	--	--	No	No	--
281	LO$_2$/LH$_2$ CBM 25,000-lb	0.1	0	Yes	No	Diaphragm rupture ignition
282	LO$_2$/RP-1 CBM 25,000-lb	13	540	Yes	Yes	Tank rupture before ignition
283	LO$_2$/RP-1 V MV 25,000-lo	--	--	No	No	Tank dropped early, no data
284	LO$_2$/RP-1 V MV 25,000-lb	2	89	Yes	No	Diaphragm rupture ignition, ignition before fluid hits ground
285	LO$_2$/LH$_2$ CBM 25,000-lb	37	465	Yes	No	Ignition source unknown
286	500-lb CAL.	--	--	No	No	--
287	500-lb CAL.	--	--	No	No	--
288C	LO$_2$/LH$_2$ V MV 25,000-lb	13	365	Yes	No	288A and B were aborted. Ignition source unknown
289	LO$_2$/LH$_2$ V MV 25,000-lb	4	166	Yes	No	Ignition source unknown
290	LO$_2$/LH$_2$ V MV 25,000-lb	4	105	Yes	No	Fire at top of tank after diaphragm rupture, ignition at bottom of tank

TEST NO	DESCRIPTION TEST CONDITIONS	YIELD (%)	IGNITION TIME	DATA BANK	PRED. METHOD	REMARKS
291	LO_2/LH_2 V MV 1000-lb	1.2*	--	No	No	No data reduced at URS, ignition at impact
292	LO_2/LH_2 V MV 1000-lb	3.6*	--	No	No	No data reduced at URS, ignition at impact
293	LO_2/LH_2 V MV 1000-lb	3.9*	--	No	No	No data reduced at URS, ignition at impact
294	LO_2/LH_2-LO_2/RP-1 V MV 1200-lb	5.6*	0	No	No	No data reduced at URS, fire on tank caused premature ignition
295	LO_2/LH_2-LO_2/RP-1 V MV 1200-lb	70	544	Yes	No	Cap ignition
296	LO_2/RP-1 V MV 1000-lb	22	740	No	No	Tank dropped to ground, slowing propellant release
297	LO_2/LH_2 V MV 200-lb	18*	2 sec	No	No	--
298	500-lb Pentolite CAL.	--	--	No	No	Data presented in Appendix A
299	LO_2/RP-1 CBM 200-lb	17	73 sec	No	No	AFRPL figures, data not reduced at URS
300	Titan LO_2/RP-1	--	--	No	No	Premature ignition, no data
301	Titan LO_2/RP-1	3.7	840	No	No	Source of ignition unknown
302	LO_2/LH_2 CBM 25,300-lb	--	--	No	No	No data reduced at URS
303	1000-lb Pentolite CAL.	--	--	No	No	--

* Pressure yields from AFRPL

E-14

Appendix F

PEAK OVERPRESSURE versus DISTANCE
AND POSITIVE-PHASE IMPULSE versus
DISTANCE REFERENCE CURVES
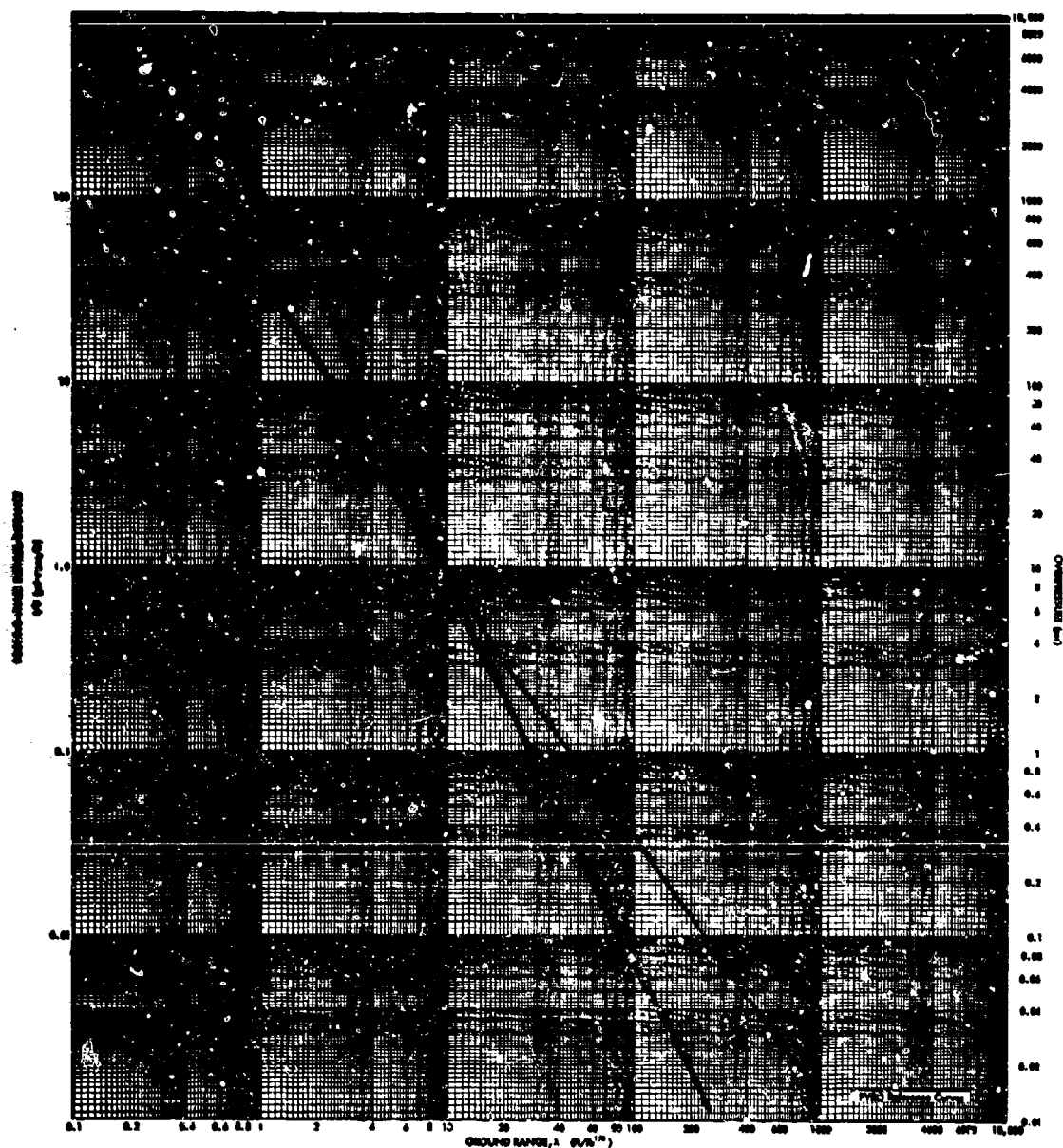
PEAK OVERPRESSURE and POSITIVE-PHASE IMPULSE vs SCALED DISTANCE for TNT SURFACE BURST

DOCUMENT CONTROL DATA - R & D

(Security classification of title, body of abstract and indexing annotation must be entered when the overall report is classified)

1. ORIGINATING ACTIVITY (Corporate author)	2a. REPORT SECURITY CLASSIFICATION
URS Research Company	Unclassified
	2b. GROUP

3. REPORT TITLE

Liquid Propellant Explosive Hazards

4. DESCRIPTIVE NOTES (Type of report and inclusive dates)

Final report

5. AUTHOR(S) (First name, middle initial, last name)

A.B. Willoughby, C. Wilton, and J. Mansfield

6. REPORT DATE	7a. TOTAL NO. OF PAGES	7b. NO. OF REFS
December 1968	637	53

8a. CONTRACT OR GRANT NO.	9a. ORIGINATOR'S REPORT NUMBER(S)
AF 04(611)10739	
b. PROJECT NO.	URS 652-35
c.	9b. OTHER REPORT NO(S) (Any other numbers that may be assigned this report)
d.	AFRPL TR 68-92

10. DISTRIBUTION STATEMENT

Distribution of this document is unlimited.

11. SUPPLEMENTARY NOTES	12. SPONSORING MILITARY ACTIVITY
Report is in three volumes	U.S. Air Force Rocket Propulsion Lab

13. ABSTRACT Project PYRO consisted of a comprehensive program to determine the blast and thermal characteristics of the three liquid propellant combinations in most common use in military missiles and space vehicles; liquid oxygen-RP-1 (LO$_2$/RP-1), liquid oxygen – liquid hydrogen (LO$_2$/LH$_2$), and nitrogen tetroxide/50% unsymmetrical dimethylhydrazine – 50% hydrazine (N$_2$O$_4$/50% UDMH – 50% N$_2$H$_4$). During the course of the program some 270 tests were conducted with these propellant combinations on weight scales ranging from 200 lb to 100,000 lb. This basic explosive test program was supplemented by analytical and statistical studies, laboratory-scale experimental studies, simulation tests with inert propellant combinations and a series of high-explosive tests for calibration and evaluation purposes.

The basic test program was designed to investigate the explosive characteristics of the three propellant combinations for the most credible ways that the propellants might accidentally come into contact with each other and result in a significant explosion.

The results of the basic test program in conjunction with the analytical studies and prior information regarding liquid propellant explosive behavior were used as the basis for developing methods for predicting the blast and thermal environment that would be expected for any given missile or space vehicle system and any specified failure mode. ( )

In the prediction method the thermal environment is given only as a function of propellant type, while the blast environment is given as a function of a number of controlling parameters. A failure mode analysis is required to select the appropriate values of the parameters needed to predict the blast environment for a specific system.

This report is presented in three volumes: Volume 1, Technical Documentary Report; Volume 2, Test Data; Volume 3, Prediction Methods.

14. KEY WORDS	LINK A		LINK B		LINK C	
	ROLE	WT	ROLE	WT	ROLE	WT
Liquid propellants						
Thermal measurements						
Propellant hazards						
Hazard analysis						
Propellant blast environment						